

NATIONAL AND KAPODISTRIAN UNIVERSITY OF ATHENS



SCHOOL OF SCIENCE

FACULTY OF GEOLOGY & GEOENVIRONMENT

**MINERALOGY AND GEOCHEMISTRY OF BAUXITES
FROM PARNASSOS-GHIONA MINES
AND THE IMPACT ON THE ORIGIN OF THE DEPOSITS**

PhD Thesis

PLATON N. GAMALETOS

Supervisor: Assistant Professor Dr. Athanasios Godelitsas

Athens, Greece

September, 2014

To my Beloved Parents,

Nikolaos Gamaletsos & Argyroula Paparizou

*And my Lovely Brother & Sister **George & Maria***

*To my Beloved **Georgia***

*To my Best Friends **George & Markellos***

*And finally... to my Lovely Godson **Lukas***

This PhD Thesis is also respectfully dedicated to my colleague **György Bárdossy**, who unexpectedly died on April 15, 2013, at the age of 88. Academician György Bárdossy was Hungarian geologist-geochemist whose pioneer work contributed to the geochemical investigation mainly of karst-type bauxites, laterite formation and occurrence worldwide. In 1991, he became member of the Croatian Academy of Sciences, while in 1993 he was elected to the Hungarian Academy of Sciences (HAS) correspondent, as well as in 1998 as full member (HAS). In 2009, he became member of the International Association of Mathematical Geology, and also an honorary citizen of HAS. In 2012, he received the Academic Gold Medal of HAS. I would like to express my respectful gratitude for György's precious guidance throughout my PhD Thesis. I have also been much honored for that György shared with me one of his last publications concerning bauxites (Nucl. Instrum. Meth. B. 269 (2011) 3067-3073 / DOI: 10.1016/j.nimb.2011.04.061).



In the memory of

Professor Dr. Vassilios J. Papazoglou

(1954 – 2014)

... I will always hold him in the highest regard and honor his memory ...



Professor **Vassilios J. Papazoglou** obtained his Diploma from the School of Naval Architecture and Marine Engineering, National Technical University of Athens, in 1975. He had two Masters in Science in the fields of (a) Naval Architecture and Marine Engineering (1978) and (b) Mechanical Engineering (1978) and a PhD in Ocean Engineering (1981), all from M.I.T. (Massachusetts Institute of Technology). He has been Research and Teaching Assistant (1975-1981), Postdoctoral Research Fellow (1981-1982) and Research Engineer (1982-1983) in the Department of Ocean Engineering, Massachusetts Institute of Technology. He has worked as Technical Consultant in various companies and government agencies of U.S.A. (1978-1983) and also in various companies and government agencies of Greece (from 1985). He was elected Assistant Professor (1985-1989), Associate Professor (1989-1994) and Professor (1994-2014), in the School of Naval Architecture and Marine Engineering of the National Technical University of Athens. He has been also appointed Director of the Laboratory of the Shipbuilding Technology (1989-2006). He has participated in over 60 sponsored research projects that resulted in the publication of over 90 articles in scientific journals and refereed international conferences and of more than 170 technical reports. He has served as reviewer and editor in several scientific journals, international conferences and research funding agencies. He was an internationally recognized scientist.

ACKNOWLEDGEMENTS

First and foremost, I am more than grateful to my precious supervisor Dr. Athanasios Godelitsas (Assistant Professor of Mineralogy-Mineral Chemistry at School of Science, Faculty of Geology & Geoenvironment, University of Athens, Greece; Visiting Professor of Environmental Mineralogy & Geochemistry at Complutense University of Madrid, Spain; Vice President of the International Natural Zeolite Association / INZA) for his crucial guidance during my PhD Thesis long journey. My scientific sufficiency has been validated under Athanasios' great expertise. I would also like to express my gratitude to my former supervisor, retired Associate Professor Dr. Magda Laskou who initially suggested the subject of this dissertation and inspired me to get interested in the science of bauxites.

"Aluminium S.A.", "S&B Industrial Minerals S.A." and "ELMIN S.A." are gratefully acknowledged for the provision of bauxite samples from active mines of Parnassos-Ghiona area and their collaboration during my PhD Thesis. Additionally, I would like to acknowledge "Aluminium S.A." for the supply of bauxite refining solid wastes (red mud) samples from its alumina plant at Antikyra (Gulf of Corinth, central Greece). Moreover, I do thank Mr. G. Georgalas, Mr. D. Kosmetatos, and Mr. S. Delipaltas ("Aluminium S.A." Management Directors) for authorizing the presentation and the publication of data that are included in this dissertation. Moreover, I thank Dr. V. Vassiliadou (Laboratory & Quality Manager of "Aluminium S.A."), and Mr. G. Delimichalis for offering me their authorization to visit the Pera Lakkos underground active mine of Parnassos-Ghiona area providing me with bauxite samples directly from its mining front.

Part of this dissertation has been benefited by the Institute for Photon Science and Synchrotron Radiation (IPS) and the ANKA Synchrotron Radiation Facility (KIT Campus South, Karlsruhe, Germany) in the frame of the provision of "Grant of Fellowship" allowing me to work as assistant beamline scientist at the SUL-X beamline of the Synchrotron Laboratory for Environmental Studies (Synchrotron Umwelt-Labor SUL) at the ANKA Synchrotron Radiation Facility. Thus, I would also like to acknowledge the administration of IPS & ANKA for their crucial financial support. Further, I am grateful to the ANKA for the provision of beamtime at the SUL-X beamline, several times during my dissertation. I do thank SUL-X beamline scientists Dr. Ralph Steininger, and Dr. Jörg Göttlicher for their help during XAFS

measurements. Especially, I would like to thank my precious colleague and friend Dr. Jörg Göttlicher for his fruitful discussion on XAFS study during my PhD Thesis.

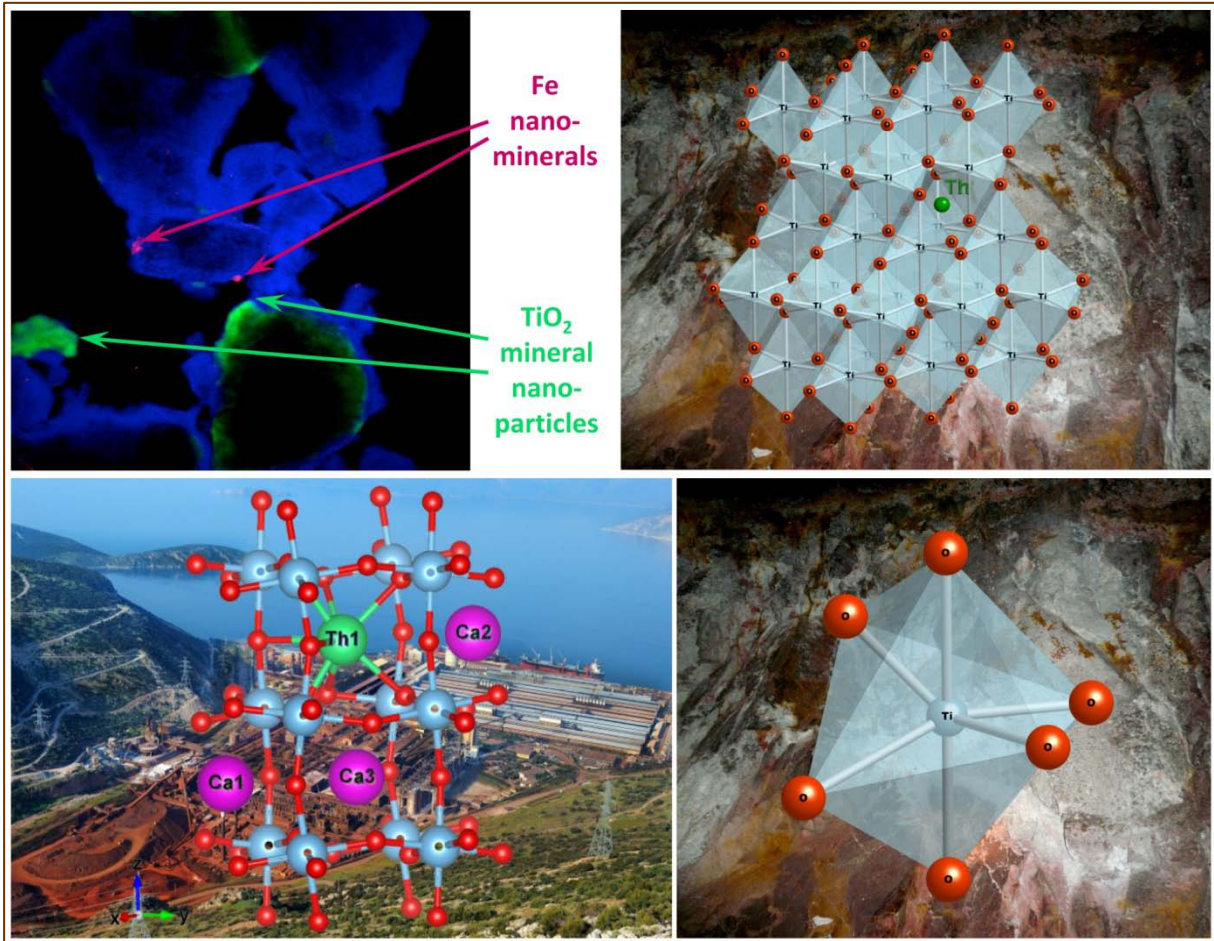
I am grateful to Professor Giovanni Mongelli (Professor at Università degli Studi della Basilicata, Italy) for the provision of geochemical data from his recent published paper (“Geochemistry of the Apulian karst bauxites (southern Italy): Chemical fractionation and parental affinities”) and for his kind permission, to use them. I am also grateful to my memorable colleague György Bárdossy† for his comments during my dissertation, and for the provision of Balkan and Hungarian industrial bauxite samples supplied by the Ajkai Timföldgyár alumina plant (MAL Magyar Alumínium Zrt).

Furthermore, Professor Dr. Maria Economou-Eliopoulos (School of Science, Faculty of Geology & Geoenvironment, University of Athens, Greece), Professor Dr. Anestis Filippidis (Faculty of Sciences, School of Geology, Department of Mineralogy-Petrology-Economic Geology, Aristotle University of Thessaloniki, Greece), and Vice Rector at University of Patras Professor Dr. George Angelopoulos (Department of Chemical Engineering, Laboratory of Metallurgy, University of Patras, Greece) are thankfully acknowledged for their long term collaboration during my PhD Thesis. Also, Professor Dr. Ioannis Paspaliaris (Dean of School of Mining and Metallurgical Engineering, National Technical University of Athens) is thankfully acknowledged for his cooperation in the examination Committee of the dissertation. This dissertation has been benefited from many stimulating discussions with our friends and colleagues. Dr. Theodore J. Mertzimekis (Assistant Professor at School of Science, Department of Physics, University of Athens), Dr. Alexios P. Douvalis (Assistant Professor at Department of Physics of University of Ioannina, Greece), and Dr. Stelios Xanthos (Department of Electrical and Computer Engineering, Aristotle University of Thessaloniki and Department of Automation Engineering, Alexander Technological Educational Institute of Thessaloniki, Greece) are grateful acknowledged for their critical discussion and comments concerning XAFS, Mössbauer, and Gamma-ray spectroscopy; also Professors Dr. K.M. Paraskevopoulos and Dr. K. Chrysafis (Faculty of Sciences, School of Physics, Department of Solid State Physics, Aristotle University of Thessaloniki, Greece) for their assistance in the FTIR and TG/DTG/DSC measurements and constructive comments. I would also wish to

thank Mr. Nikos Passalis for his guidance in contribution and editing of some of these images.

Finally, I would like to kindly thank Prof. Thomas J. Walsh, MD (Professor of Medicine in Microbiology and Immunology, Weill Cornell Medical College, USA) as mentor and friend for his precious encouragement! He was reminding me several times during this PhD Journey: *“The Journey in writing a dissertation is long and arduous. Knowing that others are there helping you and encouraging you on that journey makes an enormous difference”*.

Graphical Abstract



Fe-nanominerals and TiO₂ mineral nanoparticles (upper-left) into the studied Parnassos-Ghiona bauxite and possible extraframework position of Th⁴⁺ into anatase structure (upper-right); titanium octahedral sites (^[6]Ti⁴⁺ sites) occurring in Th-hosting nano-perovskite into the Bayer process solid residues -red mud- (lower-left) in contrast to anatase ^[6]Ti⁴⁺ sites existing in the parent bauxite material.

SUMMARY

Karst-type bauxite deposits have been exploited in central Greece, in the area of legendary Parnassos Mountain near the Oracle of Delphi, since 20's. The existence of bauxite in Parnassos-Ghiona was announced around 1922, giving possibilities of developing an aluminium industry in Greece. The Al-ores are hosted within Mesozoic carbonate formations of the Parnassos-Ghiona geotectonic zone, which is characterized by nearly continuous sedimentation of epicontinental reef-like carbonates from the Upper Triassic to the Upper Cretaceous. The exploitation is currently performed by three Greek mining companies ("Aluminium S.A.", "S&B Industrial Minerals S.A." and "ELMIN Hellenic Mining Enterprises S.A."), whereas there is also an Al industrial plant installed at the coastal zone of the Corinth gulf, which is the largest vertically integrated Al producer in the E.U.. Numerous geological studies have been published about the deposits, whereas their main mineralogical and geochemical characteristics have been described by several authors using various conventional microscopic and analytical methods, such as optical microscopy, SEM-EPMA, XRD, XRF, Fire-Assay/AAS/ICP and TGA/DTA.

The main purpose of the present dissertation was to combine -for first time in the literature with regard to karst-type bauxites of Greece and the globe- diffraction (PXRD), analytical in bulk and microscale (ICP-MS/OES, LA-ICP-MS), thermal (TGA/DTG, DSC), spectroscopic in bulk and microscale (FTIR, ⁵⁷Fe Mössbauer, high-resolution gamma-ray, Laser μ -Raman, SR μ -XRF, (μ)-XANES/(μ)-EXAFS), microscopic (optical, SEM-EDS/WDS), and nanoscopic (FEG TEM-EDS & EELS) techniques, together with magnetic susceptibility measurements, for the detailed mineralogical and geochemical characterization and the study of mineral nanoparticles and nanominerals in typical Fe-rich (low grade, red-brown) and Fe-depleted (high grade, white-grey, Al-rich: Al₂O₃ ca. 80 wt.%) from active mines of the Parnassos-Ghiona area. Nanoscopy, related to nanogeoscience, is expected to play a crucial role in the exploration and exploitation of basic, noble and strategic metal resources. The above novel mineralogical and geochemical data were used to illustrate new insights into the origin of the deposits. Moreover, STEM-HAADF and SF-ICP-MS techniques were additionally applied for characterization and leaching experiments with respect to bauxite metallurgical residues (so-called "red mud"), in order to provide with additional data which

are interesting not only to the mining but also to the metallurgical industry and environmental technology. In addition, stable isotope measurements ($\delta^{18}\text{O}$ and $\delta^{13}\text{C}$) were used in the case of hanging wall and footwall limestones of Pera Lakkos mine, to conclude about the mineralogy and geochemistry of the intercalated bauxites.

Bauxite samples were collected in collaboration with “Aluminium S.A.”, “S&B Industrial Minerals S.A.” and “ELMIN Hellenic Mining Enterprises S.A.” from currently active mines in the Parnassos-Ghiona area. The final composite samples concerned the Fe-rich and the Fe-depleted bauxites. The PXRD investigation confirmed the presence of AlOOH polymorphs (diaspore and/or boehmite), TiO_2 polymorphs (anatase and rutile), and Fe-oxides/oxyhydroxides, as the major mineral components. The laser μ -Raman results showed that the different bauxite types (diasporic or boehmitic) can easily be identified regardless of sample type by recording spectra in the low-wavenumber region ($250\text{ cm}^{-1} - 600\text{ cm}^{-1}$) where distinct bands of the natural AlOOH polymorphs are easily discernible (448 cm^{-1} for diaspore and 362 cm^{-1} for boehmite). The thermal analyses and FTIR measurements, also contributed to the elucidation of the volatile constituents (predominantly hydroxyls). The bulk geochemical analyses revealed that, except for major elements (mainly Al and Fe), the studied industrial bauxites contain an exceptional variety of trace elements, with remarkable positive geochemical anomalies with respect to High-Field Strength Elements (HFSE), Rare Earth Elements (REE), actinide elements (Th, U), as well as in most of compatible elements. Especial emphasis was given to Pera Lakkos mine where a case geochemical study was performed, including the surrounding coal and limestones. Among all trace elements studied, Th is stated to be important, related to mining, metallurgical and environmental issues. According to XRF and ICP-MS analyses Th, is relatively increased in Fe-depleted samples containing up to 62.75 ppm Th corresponding to 220 Bq/kg due to ^{228}Ac (^{232}Th -series), whereas Fe-rich samples are less Th-radioactive (up to 58.25 ppm Th, 180 Bq/kg due to ^{228}Ac). SEM-EDS indicated the presence of Ti-Fe-containing phases (e.g., ilmenite: FeTiO_3), chromites and besides LREE-minerals (mostly bastnäsite/parisite-group) and zircon (ZrSiO_4) hosting a part of the bulk Th. The presence of Th in diaspore and in Ti-containing phases (not detected by SEM-EDS as in the case of REE-minerals and zircon) was investigated, into distinct pisoliths of Fe-depleted bauxite, using μ -XRF and μ -XAFS. XAFS spectra of Th salts and Th-containing reference materials were obtained as well. Accordingly, it was revealed,

for the first time in the literature, that Ti-phases, and particularly anatase, host significant amounts of Th. This novel conclusion was complementary supported by LA-ICP-MS analyses indicating an average of 73 ppm Th in anatase grains together with abundant Nb (3356 ppm), Ta (247 ppm) and U (33 ppm). The Th L_{III} -edge XAFS spectra as compared to reference materials, gave also evidence that Th^{4+} may not replace Ti^{4+} in distorted $[\text{TiO}_6]$ fundamental octahedral units of anatase and ilmenite lattice (CN=6). The occupation of either extraframework sites of higher coordination (CN=6.9 or even CN=7.4), according to EXAFS signals evaluation, or of defected/vacant (\square) sites is more probable. This is likely explained by the difficulty of Th^{4+} to replace directly Ti^{4+} in [6]-coordinated (octahedral) sites due to the large difference in the relevant ionic radii (0.940 Å and 0.605 Å, respectively).

The discovery of Th-hosting anatase in microscale into karst-type bauxite, allowed further investigation concerning the study of *mineral nanoparticles* and *nanominerals* in Fe-depleted (high grade) samples, by means of a combined utilization of diffraction, spectroscopic, microscopic, and nanoscopic techniques. Initial characterization using SEM-EDS/WDS proved the presence of Fe-Cr-Ti-containing diasporite, anatase and minor rutile, together with traces of zircon, chrome-spinel and REE fluorocarbonates. The subsequent study by means of ^{57}Fe Mössbauer, in correlation with magnetic susceptibility vs temperature measurements, and complementary Synchrotron-based spectroscopic techniques in microscale (μ -XRF and μ -XANES/-EXAFS), indicated that Fe^{3+} , in contrast to $^{63}\text{Cr}^{3+}$, is not exclusively a component of the structure of α - AlOOH (diasporite). According to the Cr K -edge EXAFS spectral results, the interatomic distance between the central atom of Cr and the first neighbor of O of the first shell is calculated at 1.965 Å. The nanoscopic study, using FEG TEM-EDS & EELS, revealed TiO_2 polymorph *mineral nanoparticles*, particularly rounded anatase nanocrystals dispersed into the diasporite matrix (in areas appearing phase-homogeneous in microscale), as well as individual needle-shaped rutile. Additionally, it was proved that, except Fe^{3+} substituting Al^{3+} in the structure of diasporite, a percentage of the metal exists also in the form of peculiar Fe^{3+} *nanominerals* (probably maghemite-type phases or most likely semi-amorphous/disordered or even completely amorphous Fe phases in nanoscale) that are between 25 and 45 nm in size. Thus, diasporite in the studied karst-type bauxite concerns in fact a Fe-Cr- AlOOH low-T (sedimentary) phase, which was demonstrated for first time in the literature. On the other hand, the occluded Ti *mineral nanoparticles* and Fe *nanominerals*, revealed by HRTEM, were

hitherto unknown not only for the allochthonous karst-type bauxite deposits of central Greece, but also for the overall bauxite deposit groups worldwide. Thus, the present dissertation gives strong evidence for the importance of nano-mineralogy and -geochemistry in the characterization of Al-ores, and in general of metal oxide/hydroxide ore deposits, as has also been proved in the case of metals in sulfide ores. *Mineral nanoparticles* and *nanominerals*, related to nanogeoscience issues, seem to be the final frontier of ore mineralogy and geochemistry being playing a vital role in the exploration and exploitation of basic, noble and strategic metal resources.

The findings about the mineralogy and geochemistry of the studied bauxites gave robust proof for the origin of the Parnassos-Ghiona karst-type bauxites. The vital contribution of the pre-Cretaceous (Middle-Upper Jurassic) ophiolites of the Hellenides is more than obvious, due to the presence of detrital chromite grains, of possible zircon crystals from the basic members (gabbros) and the plagiogranites, and also of positive geochemical anomalies for relevant compatible elements (Ti, Cr, V, Ni, Sc). This is in accordance to all previous observations. It is evident that the enrichment in other trace elements, namely some HFSE (Zr, Ce) and actinides (U, Th), can hardly be attributed to contribution of ophiolites and must be derived from pre-existing acidic geological formations. Specific information were obtained using discrimination geochemical diagrams based on ratios of “contrasting elements” (occurring either in acidic or mafic rocks), such as Th/Sc vs Zr/Sc, as well as on REE anomalies, i.e. Eu/Eu* and Ce/Ce*. Thus, it was stated evident that acidic igneous rocks, predominantly volcanic, also contributed, besides ophiolites, to the formation of Parnassos-Ghiona bauxite deposits. It is proposed that Triassic volcanic rocks showing a variable composition, from sub-alkaline basalts to rhyolite, volcano-sedimentary complexes formed during the rifting stage of Permo-Triassic age, and perhaps also Paleozoic igneous rocks (~300 Ma) occurring in the pre-Alpine basement of areas, such as the central Evia Island, have contributed to formation of later (Jurassic-Cretaceous) bauxites of Parnassos-Ghiona.

Finally, bauxite refining solid wastes (red mud) from Greece were characterized using a combination of diffraction, microscopic, analytical, and spectroscopic techniques (XRD, SEM-EDS, STEM-EDS/EELS, XRF, ICP-OES/MS, HR γ -ray Spectrometry, and XANES/EXAFS). The bulk XRD-detected crystalline phases concern hematite (α -Fe₂O₃), calcite (CaCO₃), gibbsite &

diaspore (AlOOH-polymorphs), Na-Ca-Al-silicate-carbonate & Ca-Al-hydroxysilicate phases (cancrinite- & “hydrogarnet”-type phases), quartz (SiO₂), anatase (TiO₂) and phyllosilicates/clays while the microscale study by SEM-EDS indicated a dominant “Al-Fe-Ca-Ti-Si-Na-Cr matrix”. Bulk Fe *K*-edge XANES proved the abundance of Fe³⁺ and also revealed the existence of minor Fe²⁺. Bulk analyses showed that except major Fe, Al, Ca, Si, Ti, Na and C (86.5 wt.%) and significant volatiles (LOI: 13.6 wt.%), the material contains Cr (2403 ppm), V (1081 ppm), Ni (902 ppm), As (164 ppm), Pb (120 ppm), as well as remarkable Th (111 ppm). The latter, and also minor U (15 ppm), are responsible for radioactivity (352 and 134 Bq Kg⁻¹ for ²³²Th and ²³⁸U respectively) with total dose rate 285 nGy h⁻¹. The radioactivity of parent material (typical Greek bauxites) was also measured for comparison. Leaching experiments, in conjunction with SF-ICP-MS, using Mediterranean seawater from Greece, indicated significant release of V, depending on solid/liquid ratio, and negligible release of Th, and therefore of radioactivity, at least after 12 months leaching tests. However, almost all trace elements, including REE, are relatively mobile in concentrated acetic acid solution implying potential recovery technologies. Similar seawater- and acid-leaching were also applied in industrial bauxite samples. Subsequent STEM-EDS/EELS study of leached red mud revealed that the significant immobility of Th⁴⁺ is due to its incorporation into an insoluble nano-perovskite phase with a major composition Ca_{0.8}Na_{0.2}TiO₃. Various elemental impurities, such as Ce, Nb, Zr, are detectable into the low-T & low-P nano-perovskite. Additionally, nanoscale -Th-free- insoluble Fe-oxides (nano-hematite/Ti-hematite, and nano-magnetite/Ti-magnetite), as well as nano-anatase, and nano-diaspore, were also found as constituents of the “Al-Fe-Ca-Ti-Si-Na-Cr matrix”. Th *L*_{III}-edge EXAFS spectra showed, for first time in the literature, that Th⁴⁺, hosted in this novel Ca-Na-(Ce-Nb-Zr-Cr)-nano-perovskite of red mud, occupies Ca²⁺ sites rather than Ti⁴⁺ sites. It is therefore, herein, stated that the above nanophase is the reason of low Th release in acid medium, and subsequently of the Th immobility into Greek red mud exposed in Mediterranean seawater.

TABLE OF CONTENTS

<i>Acknowledgements</i>	<i>i</i>
<i>Graphical Abstract</i>	<i>v</i>
<i>Summary</i>	<i>vii</i>
<i>Table of Contents</i>	<i>xiii</i>
<i>Abbreviations</i>	<i>xvi</i>
1. INTRODUCTION	1
1.1. Aluminium and bauxites	1
1.2. Bauxite formation	13
1.3 Karst bauxites and formation of Parnassos-Ghiona deposits	27
1.4 Parnassos-Ghiona bauxite mining and aluminium industry	43
1.5 Scale effect in ores and the role of mineral nanoparticles and nanominerals	49
1.6 Overview of previous work and scope of the present dissertation concerning Parnassos-Ghiona bauxite deposits and their metallurgical residues (red mud)	55
2. MATERIALS AND METHODS	59
2.1 Bauxite samples and preparation	59
2.2. Mineralogical and geochemical characterization of bauxite in macroscale (bulk)	63
2.2.1. Powder X-Ray diffraction (PXRD)	63
2.2.2. X-Ray Fluorescence Spectrometry (XRF)	63
2.2.3. Inductively Coupled Plasma Mass Spectrometry (ICP-MS) and ICP-Atomic Emission Spectrometry (ICP-OES)	65
2.2.4. Fourier Transform Infrared Spectrometry (FTIR)	67
2.2.5. Thermo-Gravimetric Analysis (TGA) and Differential Scanning Calorimetry (DSC)	67
2.2.6. Iron-57 Mössbauer Spectroscopy	67
2.2.7. Magnetic Susceptibility	69
2.2.8. Gamma-Ray Spectrometry (HPGe)	69
2.2.9. Synchrotron Radiation (SR) measurements in bulk (XAFS: XANES / EXAFS)	69
2.2.10. Stable isotope ratio analyses ($\delta^{18}\text{O}$ and $\delta^{13}\text{C}$)	73

2.3. Mineralogical and geochemical characterization of bauxite in microscale	75
2.3.1. Optical Microscopy	75
2.3.2. Laser micro-Raman	75
2.3.3. Scanning Electron Microscopy-Energy Dispersive Spectrometry/Wavelength Dispersive Spectrometry (SEM-EDS/WDS)	75
2.3.4. Laser-Ablation Inductively Coupled Plasma Mass Spectrometry (LA-ICP-MS)	76
2.3.5. Synchrotron Radiation (SR) measurements in microscale (μ -XRF, μ -XAFS: μ -XANES / μ -EXAFS)	77
2.4. Mineralogical and geochemical characterization of bauxite in nanoscale by High- Resolution Transmission Electron Microscopy (HRTEM) and Electron Energy Loss Spectroscopy (EELS)	82
2.5. Red mud samples and characterization	82
2.6. Leaching experiments for red mud and bauxites using Sector field Inductively Coupled Plasma Mass Spectrometry (SF-ICP-MS)	83
3. RESULTS AND DISCUSSION	87
3.1. Bulk mineralogy and geochemistry of bauxite	87
3.1.1. PXRD investigation	87
3.1.2. Bulk geochemistry	93
3.1.3. The case study of B3 horizon in Pera Lakkos underground mine	135
3.1.4. Hydrous components and thermal behavior (FTIR and TG-DTG/DSC)	157
3.1.5. Bulk Fe solid-state speciation (Mössbauer and Fe K-edge XANES) and magnetic susceptibility	163
3.1.6. Bulk radionuclide content (γ -ray spectrometry)	191
3.2. Mineralogy and geochemistry of bauxite in microscale	197
3.2.1. Optical microscopy investigation	197
3.2.2. AlOOH polymorph identification (Laser μ -Raman)	199
3.2.3. Chemical composition and element distribution and speciation in microscale (SEM- EDS/WDS, LA-ICP-MS, SR μ -XRF, μ -XAFS)	203
3.3. Mineralogy and geochemistry (phase identification, element distribution and solid- state speciation) of bauxite in nanoscale (FEG TEM-EDS & EELS)	239

3.4. Impact of mineralogy and geochemistry to the origin of the deposits	247
3.5. Comparison of bauxite with red mud	269
3.5.1. Red mud characterization in bulk, microscale and nanoscale	269
3.5.2. Leaching experiments for red mud and bauxites	293
4. BIBLIOGRAPHY	309
5. <i>Platon N. Gamaletsos Curriculum Vitae</i>	357
6. <i>Platon N. Gamaletsos Publications</i>	359

ABBREVIATIONS***Techniques***

XRD: X-Ray diffraction

PXRD: Powder XRD

XRF: X-Ray Fluorescence Spectrometry

ICP-MS: Inductively Coupled Plasma Mass Spectrometry

ICP-OES: ICP Optical Emission Spectrometry

FTIR: Fourier Transform Infrared Spectrometry

Far-IR: Far-infrared FTIR

Mid-IR: Mid-infrared FTIR

TGA: Thermo-Gravimetric Analysis

DTG: Differential Thermo-Gravimetric Analysis

TG-DSC: Thermo-Gravimetric – Differential Scanning Calorimetry

HPGe: High-purity Germanium Detector

SEM: Scanning Electron Microscopy

SEM-EDS: Scanning Electron Microscopy – Energy Dispersive Spectrometry

SEM-WDS: Scanning Electron Microscopy – Wavelength Dispersive Spectrometry

LA-ICP-MS: Laser-Ablation ICP-MS

SR: Synchrotron Radiation

XAS: X-Ray Absorption Spectroscopy

XAFS: X-Ray Absorption Fine Structure Spectroscopy

XANES: X-Ray Absorption Near-Edge Structure Spectroscopy

EXAFS: Extended X-Ray Absorption Fine Structure Spectroscopy

μ -XANES: micro-XANES

μ -XAFS: micro-XAFS

μ -EXAFS: micro-EXAFS

SR μ -XRF: SR micro-XRF

SR μ -XRD: SR micro-XRD

RDF: Radial Distribution Function

LCF: Linear Combination Fitting procedure

FT: Fourier transform

SUL-X beamline: X-ray beamline of the Synchrotron Laboratory for Environmental Studies (Synchrotron Umwelt-Labor SUL) of ANKA Synchrotron Light Source

FEG: Field Emission Gun

TEM: Transmission Electron Microscopy

HRTEM: High-Resolution TEM

FEG-TEM: Field Emission Gun TEM

STEM: Scanning TEM

STEM-EDX: Scanning TEM mapping by Energy Dispersive X-ray spectroscopy

HR-STEM: High-Resolution STEM

HAADF: High-Angle Annular Dark-Field imaging

EELS: Electron Energy Loss Spectroscopy

BF image: Bright Field image

SAED pattern: Selected Area Electron Diffraction pattern

SF-ICP-MS: Sector field ICP-MS

Mineralogy & Geochemistry

Avg.: Average

Ant: Anatase

Chr: Chromite

Dsp: Diaspore

Hem: Hematite

Mgt: Magnetite

Zrn: Zircon

REE: Rare Earth Elements

LREE: Light REE

HREE: Heavy REE

Σ REE: Total REE

Σ LREE: Total LREE

Σ HREE: Total HREE

HFSE: High-Field Strength Elements

LILE: Large Ion Lithophilic Elements

UCC: Upper Continental Crust

NASC: North America Shale Composite

PAAS: Post-Archaean average Australian Sedimentary rock

ES: European Shale

OC: Ordinary Chondrites

CI: Carbonaceous Chondrites

“Masuda-Coryell” diagram: REE normalized diagram

Ce^A: Ce anomaly

Eu^A: Eu anomaly

1. INTRODUCTION

1.1. Aluminium and bauxites

Aluminum is the sixth most abundant element in the Earth. It is a highly refractory lithophile element. The radioactive isotope ^{26}Al quickly decayed into ^{26}Mg in the first millions of years of the Solar System's evolution. It provided substantial heating to the early planetary bodies, and the isotopic composition of Mg is one of the most widely used extinct radioactivity chronometers. Thus, aluminium is an abundant element in Solar System (**Figure 1.1.1**), showing the possibility to form various phases in the Solar Gas (**Figure 1.1.2**).

Figure 1.1.1: Abundances of the element in the Solar System (modified after [Lodders, 2010](#)).

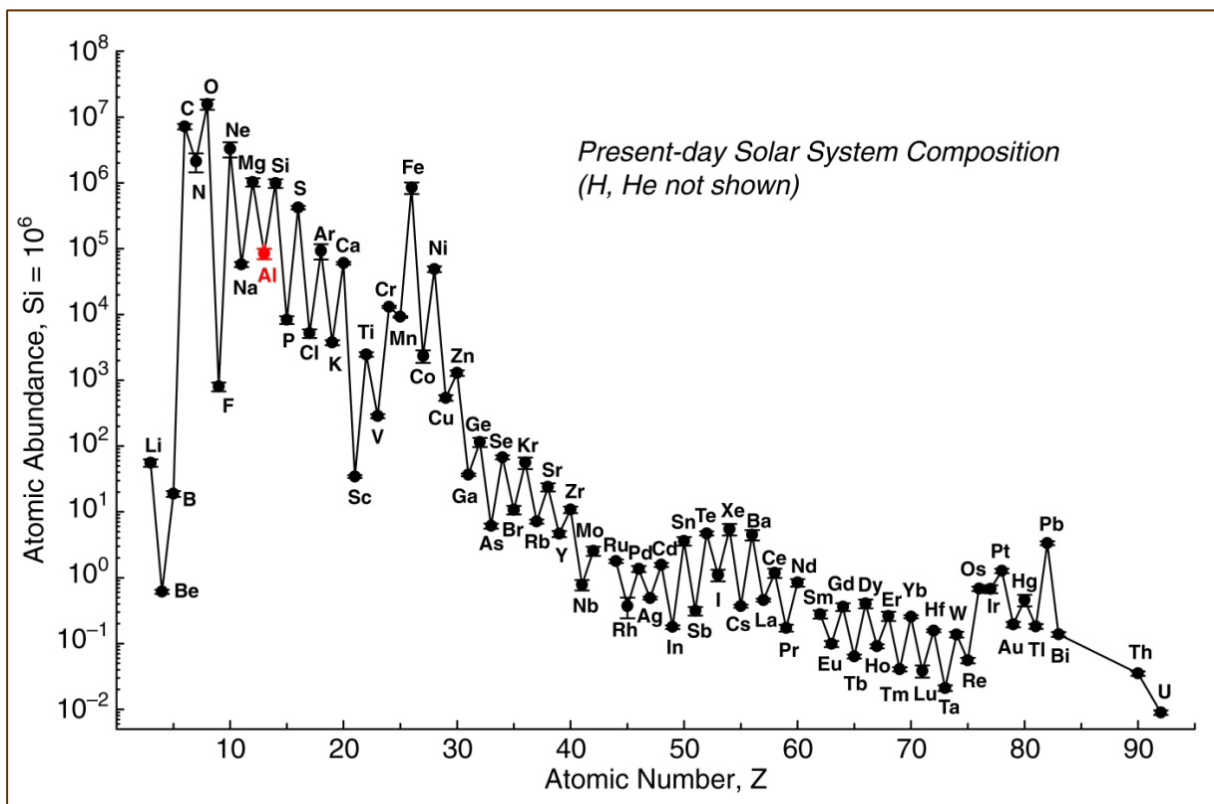
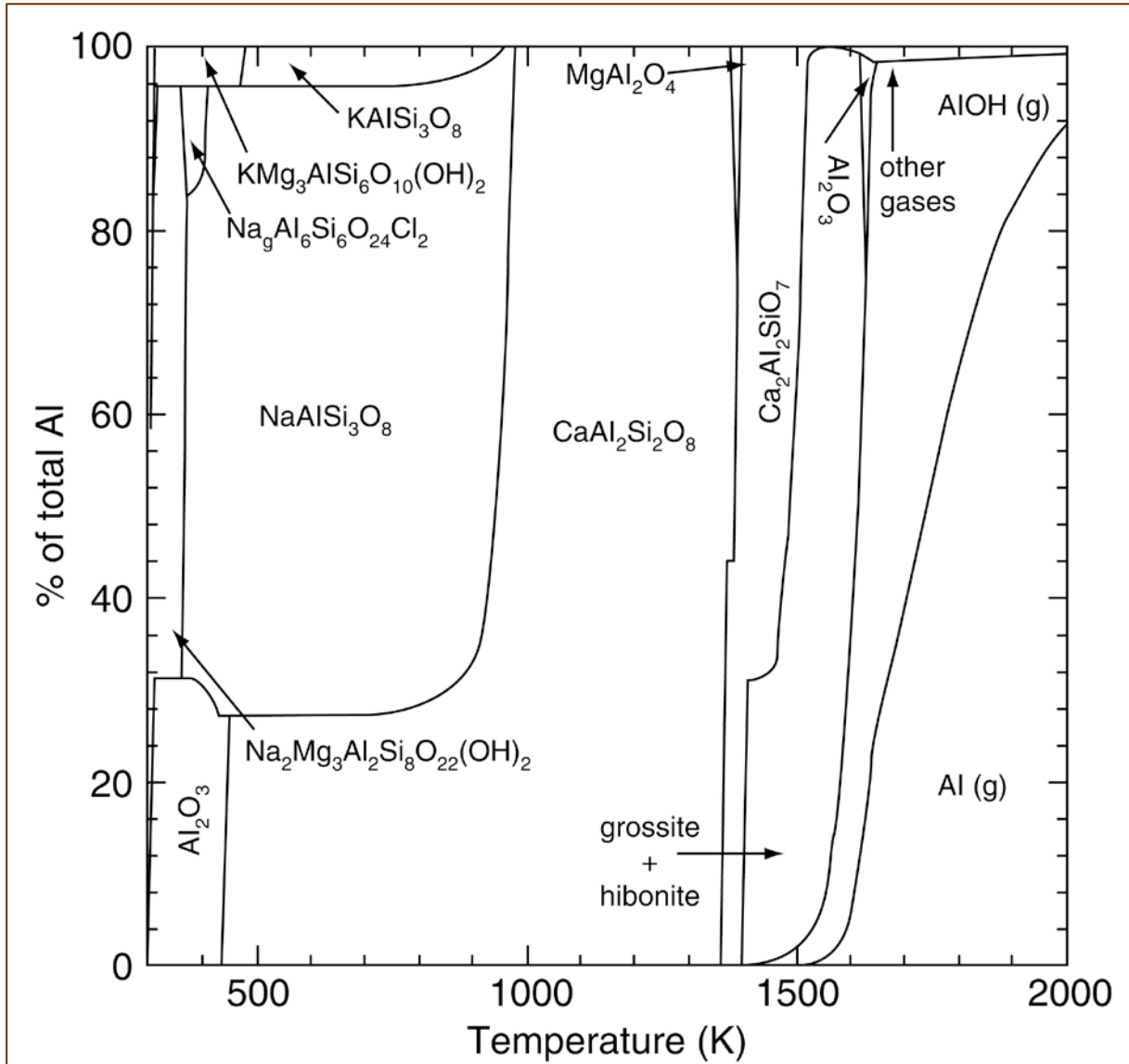
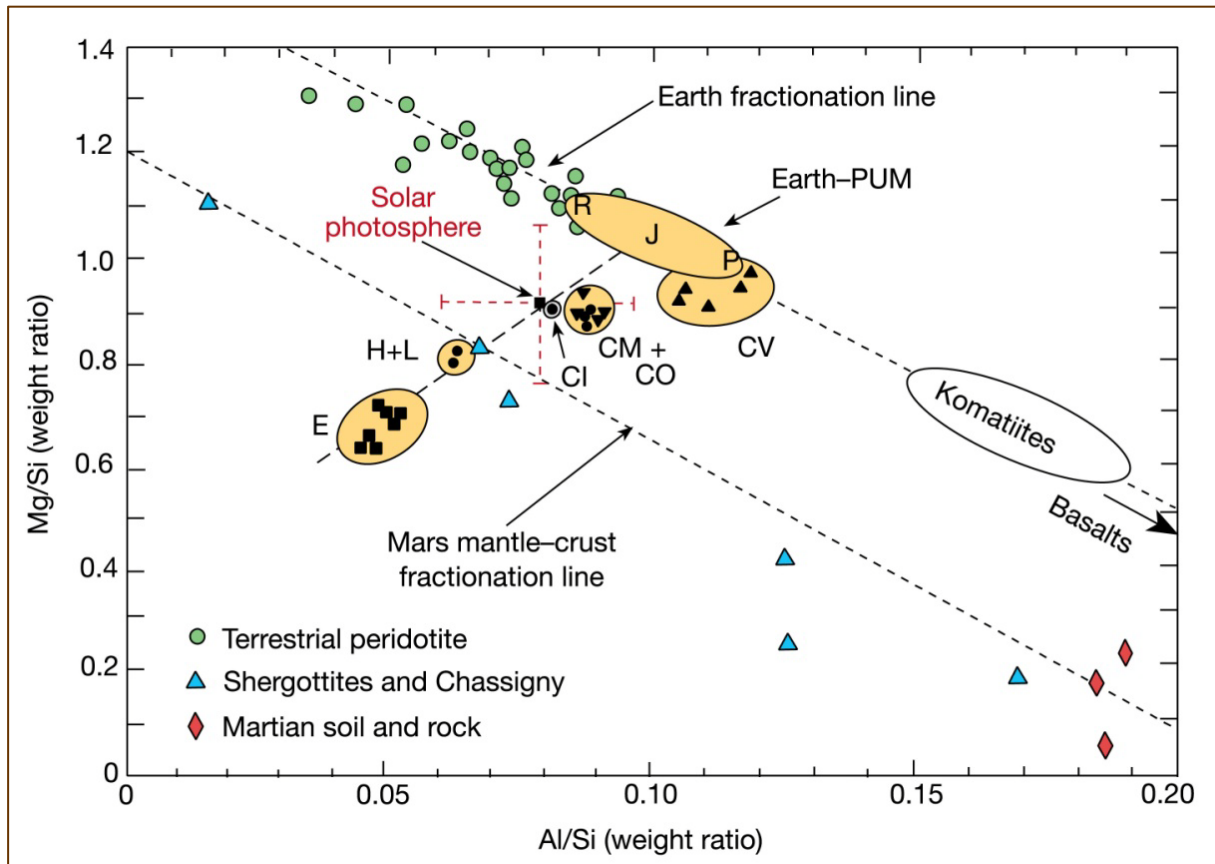


Figure 1.1.2: Percentage distribution of aluminum between different phases in a solar composition gas. Species are indicated with (g) correspond to gaseous, whereas other are condensed matters (Fegley & Schaefer, 2010).



Aluminium micro- and nanomineral phases identified from interstellar grains in chondritic meteorites concern corundum (Al_2O_3), spinel (MgAl_2O_4) and hibonite ($\text{CaAl}_{12}\text{O}_{19}$), while primary Al mineral phases in chondrules of type 3.0 chondrites concern augite, spinels and feldspars (Hazen et al., 2008). Moreover, it is known that the matrices of many primitive CI chondrites are dominated (>50 to 60%) by clay minerals, including saponite $[(\text{Ca},\text{Na})_{0.3}(\text{Mg},\text{Fe}^{2+})_3(\text{Si},\text{Al})_4\text{O}_{10}(\text{OH})\cdot 4\text{H}_2\text{O}]$ (Hazen et al., 2013).

Figure 1.1.3: The major-element composition of primitive material in the inner Solar System (Drake & Righter, 2002).



Although it is unlikely for Al to enter in large proportions in the core, however, it is a major constituent of many major minerals at any depth in the Mantle and in the Crust. In the mantle, it enters plagioclase up to pressures of about 1 GPa, spinel to 2 GPa, and garnet beyond. At these high pressures, Al also enters clinopyroxene (Al-pyroxene) in large proportions: garnet and clinopyroxene dissolve into each other to form majorite, an essential mineral phase of the mantle above the 660 km discontinuity. At higher depth, Al is hosted in a perovskite structure and also occurs as δ -AlOOH (e.g., Mierdel et al., 2007; Nishi et al., 2014; see Figure 1.1.4). In general, it should be mentioned that Mantle contains much less aluminium, and in general in the interior of the Earth, aluminium exists in high-pressure (HP) minerals and ultra high-pressure (UHP) minerals.

Figure 1.1.4: Distribution of aluminium and aluminium minerals in the Earth (upper image: data from McDonough & Sun, 1995; Rudnick & Gao, 2003; middle image: Ballaran et al., 2004; lower image: Nishi et al., 2014).

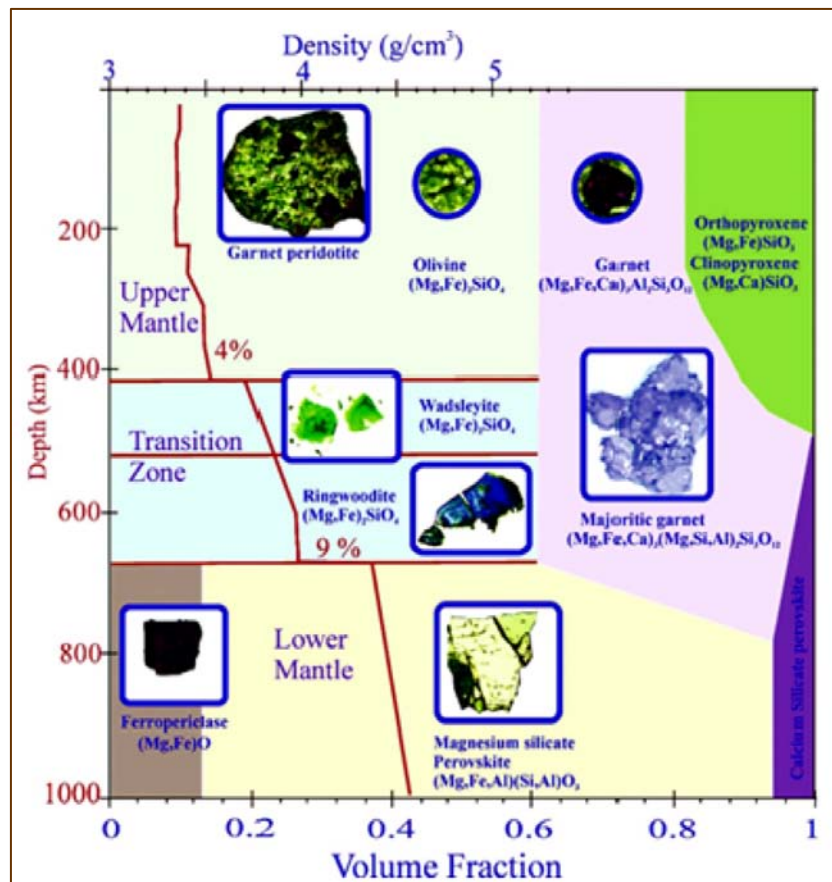
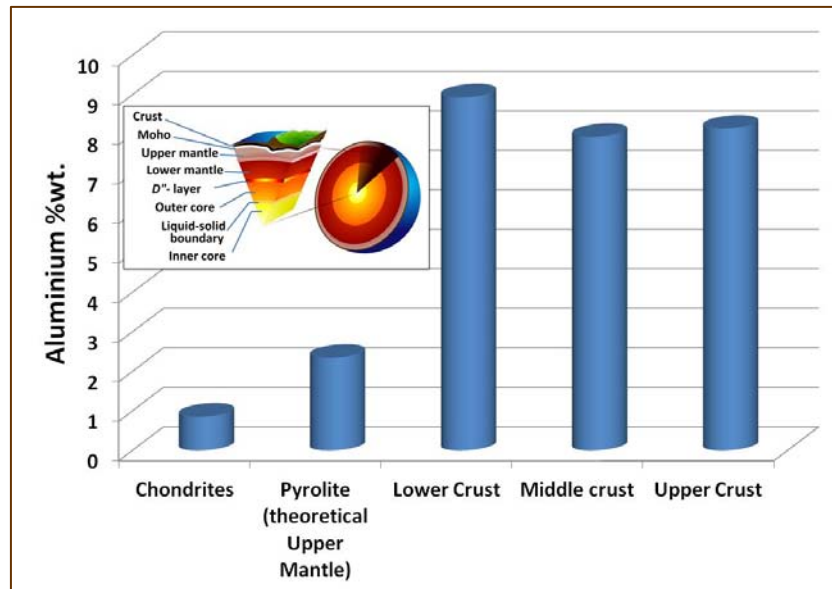
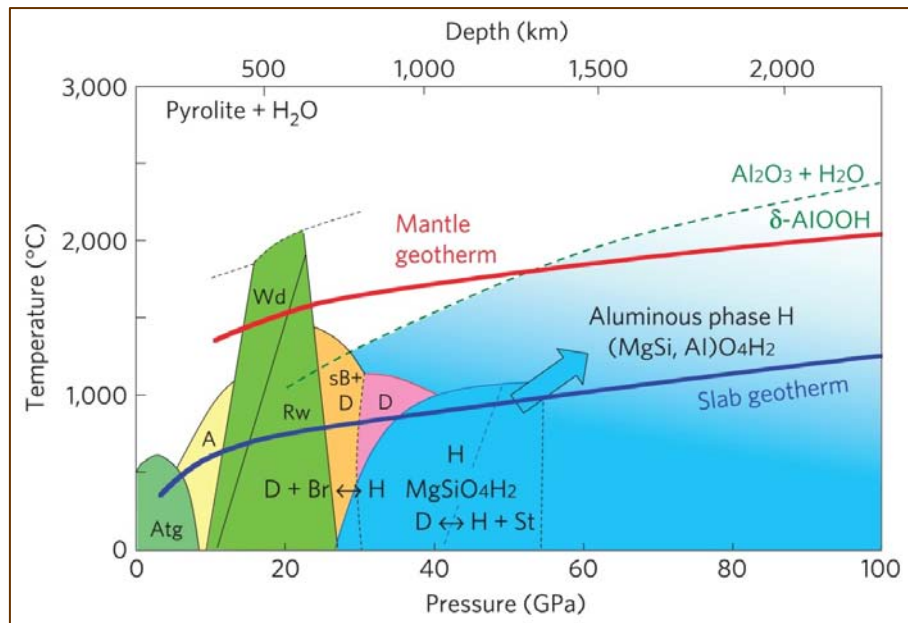


Figure 1.1.4: Continued.


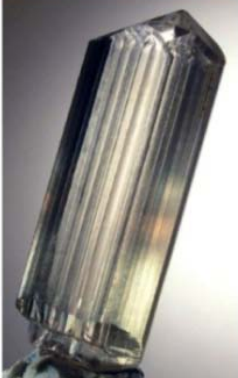



The major mineral that hosts Al in igneous rocks is feldspar: only plagioclase occurs in basalts, while plagioclase and alkali feldspar may occur together in felsic rocks. Biotite mica may occur in both types of rocks but normally accounts for only a small part of the Al inventory. In sedimentary rocks, Al is hosted in clay minerals, such as kaolinite and illite and, occasionally, in detrital feldspars. In metamorphic gneisses and schists, Al largely resides in feldspars and micas. Aluminum can be tetrahedrally coordinated and in this coordination it replaces Si in the center of oxygen tetrahedra. It can also be octahedrally coordinated and form solid solutions with elements, such as Ca, Mg, and Fe. During melting, the Al-rich minerals (feldspar, spinel, garnet) quickly dissolve into the melt and Al therefore behaves as a moderately incompatible element. During low-pressure fractionation of basalts, Al is removed by plagioclase precipitation. At higher pressure, plagioclase solubility in silicate melts increases, and this mineral does not precipitate until a late stage in the magmatic differentiation. Aluminum is therefore useful in assessing the depth of differentiation of basaltic series. In mid-ocean ridge and continental flood basalts, Al concentrations do not vary much with fractionation because they are buffered by plagioclase removal: these lavas are differentiated at low pressure in the plagioclase stability field. In contrast, Al concentrations increase steadily with fractionation of Hawaiian basalts: these rocks evolve at

higher pressure in the absence of plagioclase. Typical concentrations of Al_2O_3 in basaltic and granitic melts average 15 wt.%.

Thus, aluminium on the Earth occurs in a variety of minerals, including common rock-forming minerals (**Figure 1.1.5**), and rocks, but the only reliable resource, worldwide, still remains bauxite. It is notable that Al minerals are not specially included in minerals produced by biological mineralization processes, and thus Al biominerals are not common (Hazen et al., 2008).

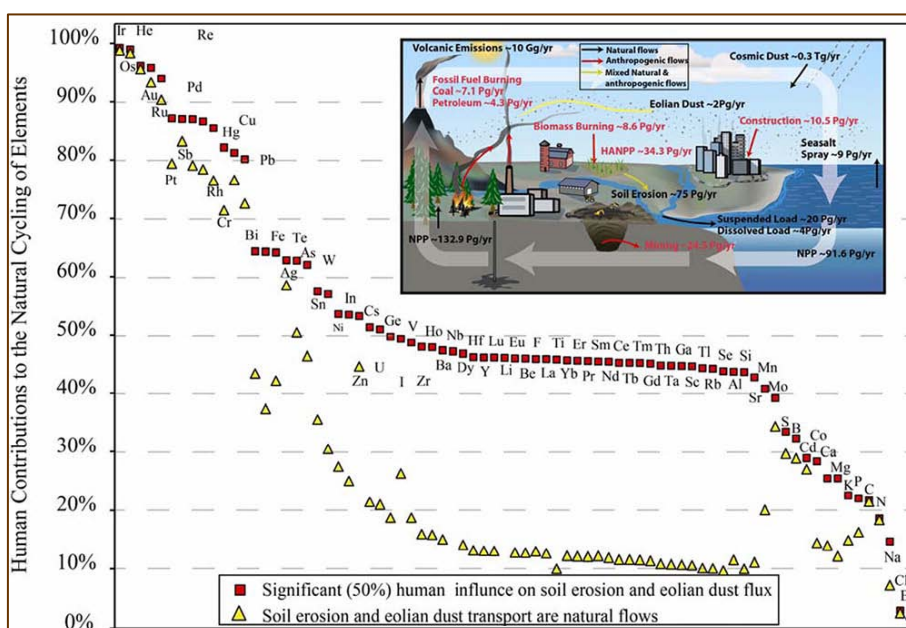
Figure 1.1.5: Earth minerals (corundum: <http://www.mindat.org/XHK-AND>; diaspore: <http://www.mindat.org/2TM-TR6>; kyanite: <http://www.mindat.org/HQ6-FHN>) containing the highest amount of aluminium.

Al (wt.%)	Mineral	Formula	MW
52.93	Corundum 	Al_2O_3	101.96
44.98	Diaspore 	$\alpha\text{-AlOOH}$	59.99
33.3	Kyanite 	Al_2SiO_5	162.05

Bauxite is a supergene aluminium ore, formed under surficial processes (Robb, 2005), consisting predominantly of AlOOH polymorphs (α -AlOOH: diaspore, β -AlOOH: boehmite, γ -AlOOH: gibbsite), Fe-oxides (mainly α -Fe₂O₃: hematite) and TiO₂ polymorphs (mainly anatase). The Upper Crust, where bauxites occur, contains 8.15 wt.% Al (McDonough & Sun, 1995; Rudnick & Gao, 2003), whereas higher concentration has been reported for the Lower Crust (Figure 1.1.4).

Aluminium (Al) is basic non-ferrous metal widely used in myriads of applications by humankind in modern society. The metal was first produced in 1825 in an impure form by Danish scientist Hans Christian Ørsted. Friedrich Wöhler, a German chemist, is considered to have isolated Al in pure form. The recent global production is more than 40 million tonnes, and has exceeded any other metal except Fe. According to recent studies (Sen & Peucker-Ehrenbrink, 2012; Liu & Müller, 2013a; Liu & Müller, 2013b; see Figures 1.1.6 – 1.1.10), the human contribution to Al natural cycling is significant, whereas the per-capita use of Al varies significantly across countries, with a global average of 7.2 kg in 2008. Average industrialized countries used about 10–60 kg of aluminum per-capita.

Figure 1.1.6: Anthropogenic disturbance of element cycles at the Earth's surface (Sen & Peucker-Ehrenbrink, 2012).



Between different countries, there are differences regarding with the reservation of Al stocks in form of ore (bauxite) and the possession of Al stocks in use. It is evident that Greece reserves considerable amounts of bauxite while the use of the metal is not always rational. It is notable that Western Europe (mainly Germany), North America (mainly USA) and, of course, China and Japan, are the major consumers of Al. The global aluminum demand is anticipated to triple at least by 2050 (Liu et al., 2011 and references therein), indicating the necessity for more bauxite exploration and exploitation worldwide.

Figure 1.1.7: Density-equalizing maps of the aluminum stocks in 2010 in bauxite reserves (top) and in use (bottom). Country sizes are distorted in proportion to their absolute aluminum stocks. Color scale indicates per-capita aluminum stocks (Liu & Müller, 2013a).

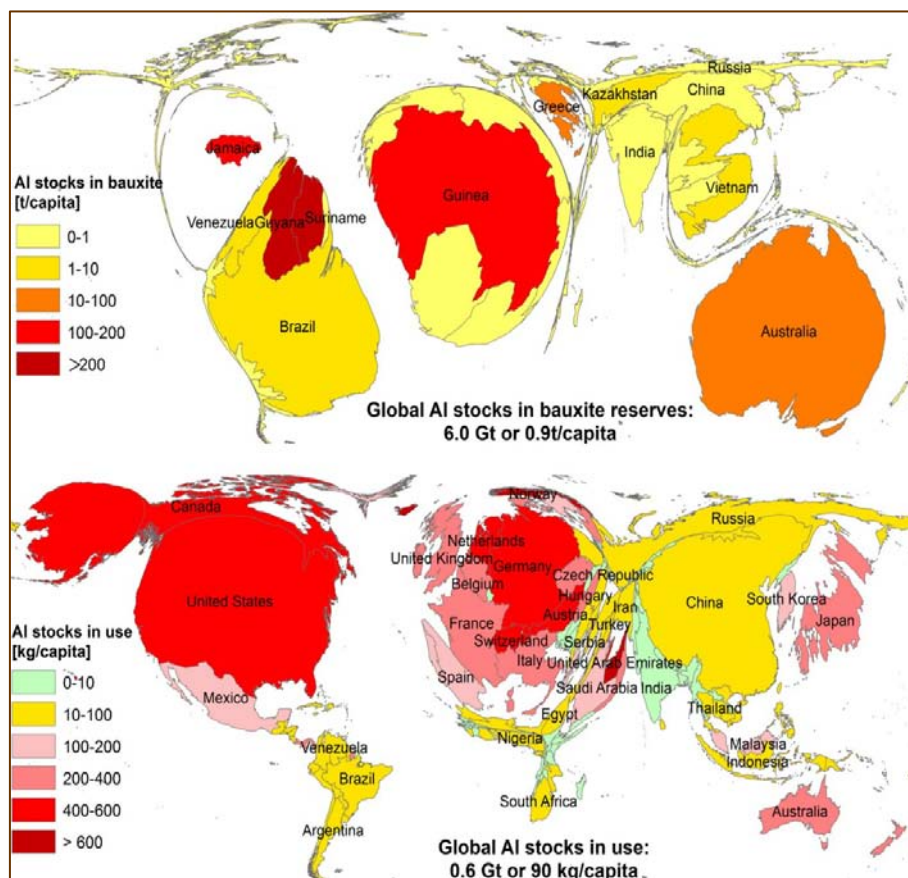


Figure 1.1.8: Historical global aluminum stocks in principal repositories, 1900-2100 (Liu & Müller, 2013a).

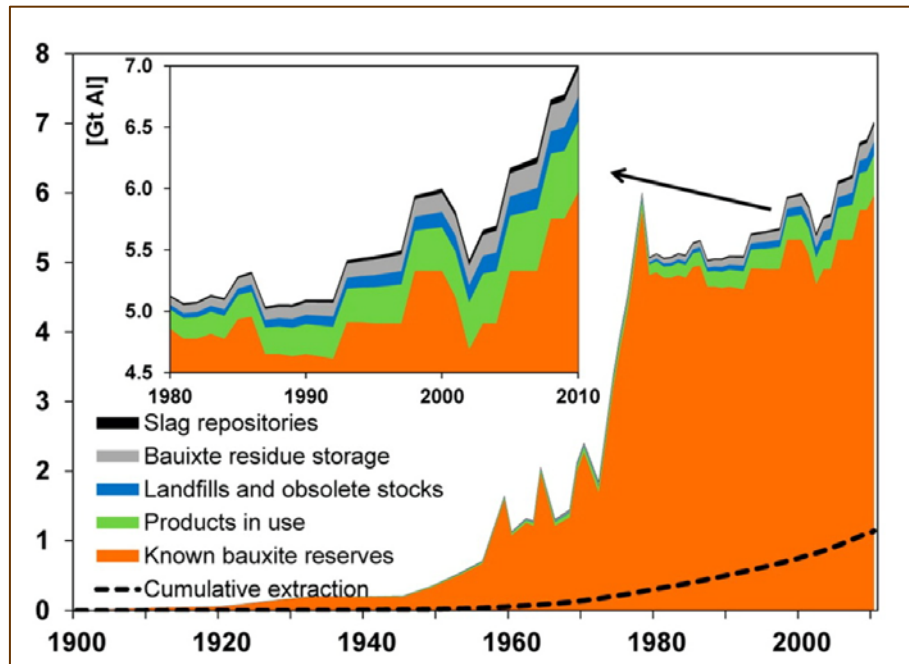


Figure 1.1.9: The global aggregated trade flows of aluminum in bauxite, alumina, unwrought aluminum, semis, finished products, and scrap for the year 2008 (Liu & Müller, 2013b).

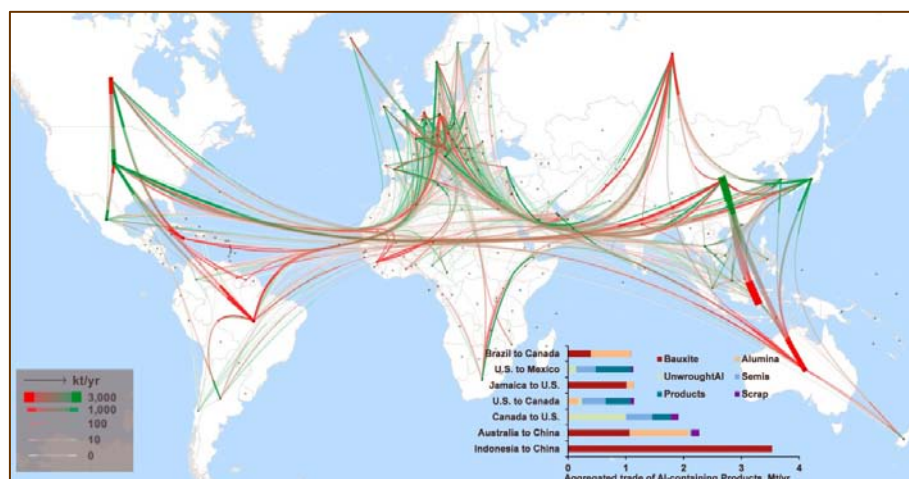
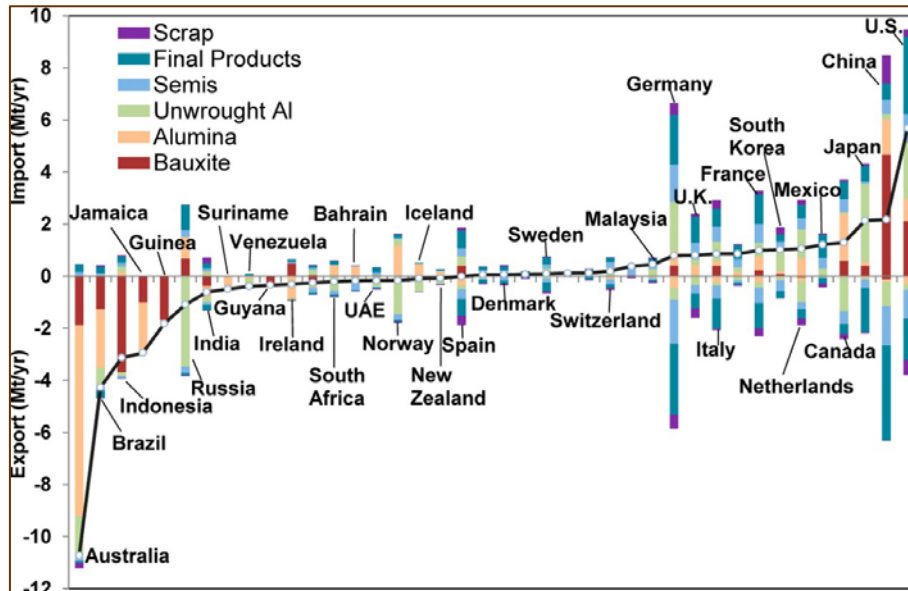
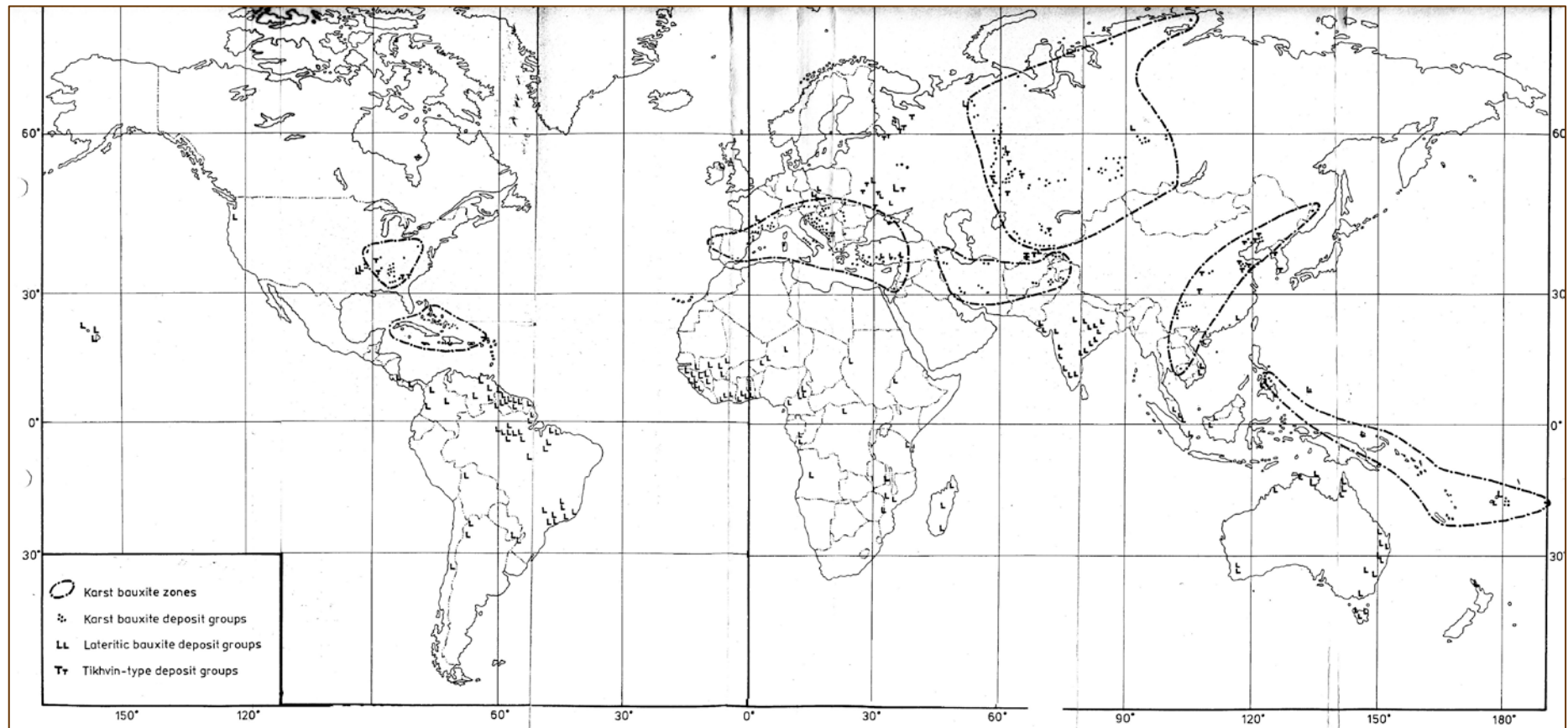


Figure 1.1.10: International trade of aluminum in bauxite, alumina, unwrought aluminum, semis, final products, and scrap in 2008 (Liu & Müller, 2013b).



Bauxite was firstly recognized as aluminium (Al) ore in the Les Baux village (Southern France) by the French geologist P. Berthier in 1821. This geological material was formed under hot and humid climate in upper Mesozoic Era, more than 100 million years ago, due to intense weathering of various rock types of the ancient continent. After prolonged dissolution of the rocks and subsequent complex geochemical reactions, the insoluble chemical compounds (mostly $AlOOH$ polymorphs) and residual minerals were deposited into cavities of older limestones (karstic surfaces). Further geological processes contributed to the final formation of the so-called “karst-type” (Valeton, 1972; Bárdossy, 1982; see **Figure 1.1.11**) allochthonous bauxite (ca. 15% of the world deposits), which is predominant in the Mediterranean belt, in contrast to lateritic autochthonous bauxite occurring in Australia, Brazil, India, etc (ca. 85%).

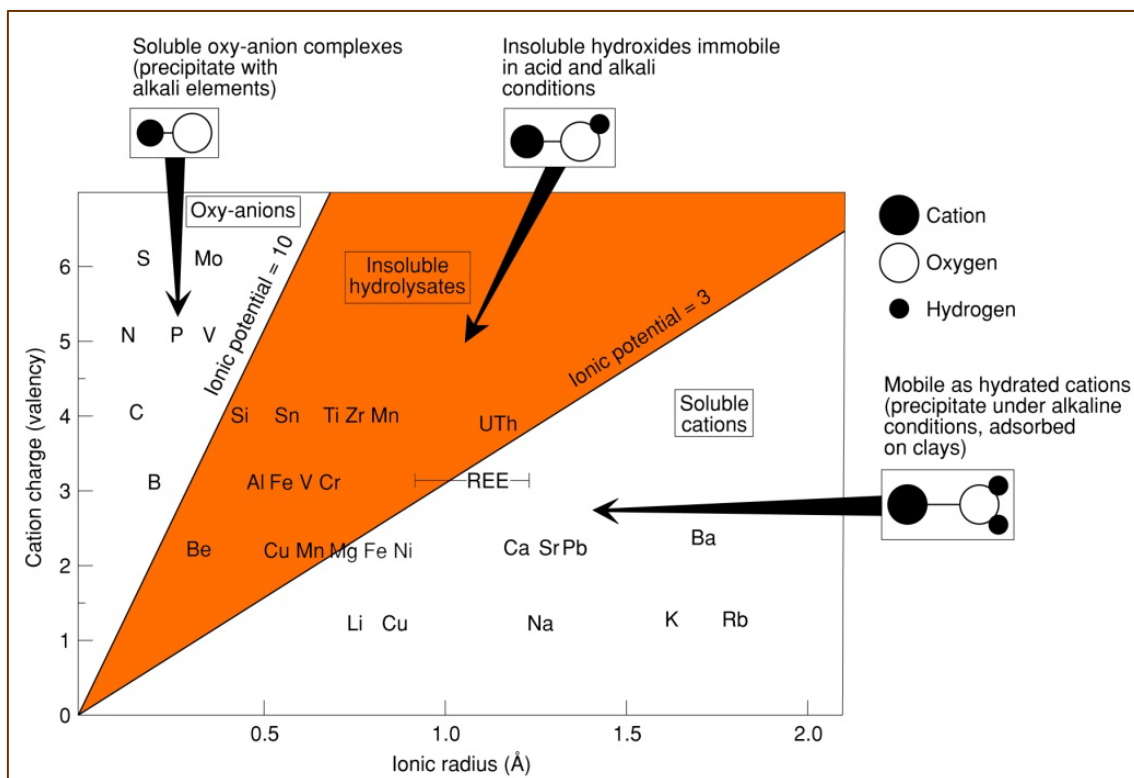
Figure 1.1.11: Bauxites, lateritic and karst, in the globe (Bárdossy, 1982).



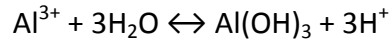
1.2. Bauxite formation

There are several deposit types where the final enrichment stage is related to surficial weathering processes. Some of these deposit types are economically very important and contain ores, such as bauxites, which do not occur in any other form (Robb, 2005). The main chemical processes that contribute to weathering include dissolution, oxidation, hydrolysis, and acid hydrolysis. The relative solubilities of different elements in surface waters depend on a variety of factors, but can be qualitatively predicted (Figure 1.2.1) in terms of their ionic potential (or the ratio of ionic charge to ionic radius).

Figure 1.2.1: Relative mobility of selected ions in aqueous solutions in the surficial environment (Robb, 2005).

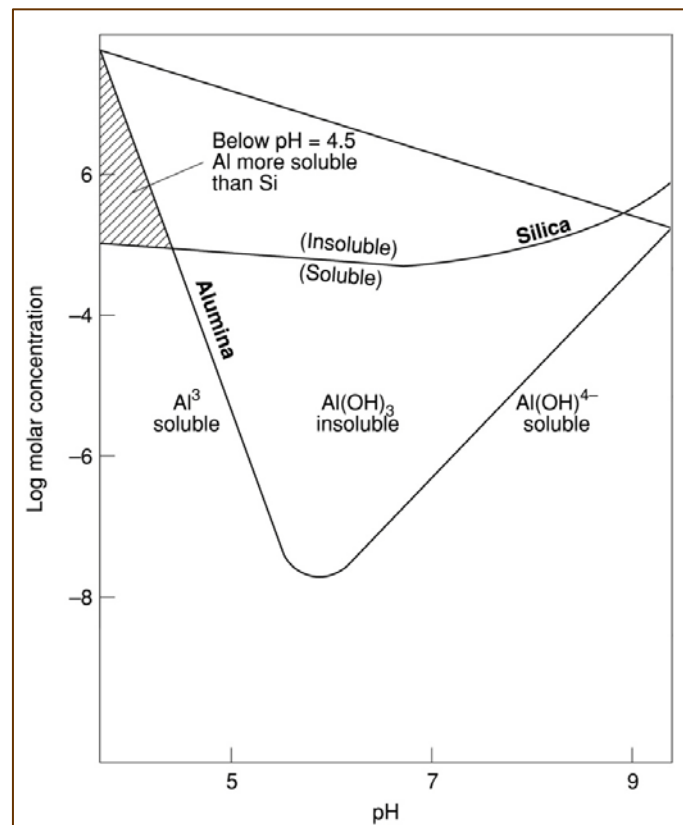


Hydrolysis is defined as a chemical reaction in which one or both of the O–H bonds in the water molecule are broken. The hydrolysis of aluminum, yielding an aluminum hydroxide precipitate, is illustrated by reaction:

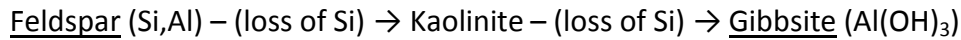


It is this type of process that results, for example, in the concentration of aluminum (as gibbsite $\text{Al}(\text{OH})_3$) and ferric iron (as goethite FeOOH) in lateritic soils. The accumulation of an alumina rich residuum, as opposed to one enriched in iron, is a function of higher rainfall, and also of lower average temperatures (around 22 °C rather than 28 °C for ferricretes) and of higher humidity. Actual alumina enrichment is due, at least in part, to relatively high Si mobility compared to Al, and probably reflects near neutral pH conditions (between 4.5 and 9; see **Figure 1.2.2**).

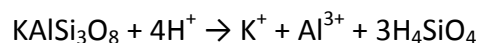
Fig. 1.2.2: The solubility of Si and Al as a function of pH (Robb, 2005).



This results in incongruent dissolution of minerals such as feldspar and kaolinite, where Si is leached in preference to Al, yielding a gibbsite-like residue. This process is shown schematically as:



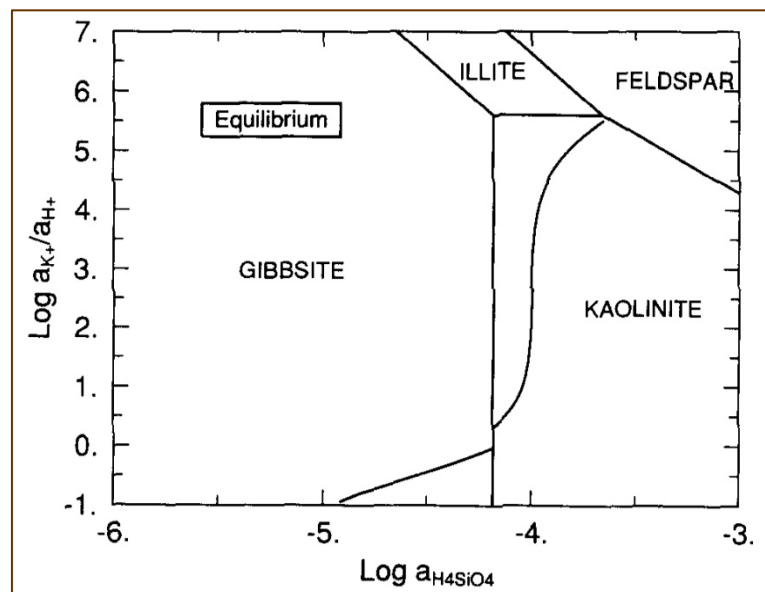
In the case of K-feldspar the dissolution is slow and irreversible. The dissolution rate of K-feldspar is lower compared to plagioclases and has been estimated 12.5 mol/m²/s (Lasaga et al., 1994).



However, upon saturation of the aqueous medium with any of the erosion/weathering products, equilibrium between the fluid and the solid phase is achieved. As shown in **Figure 1.2.3**:

Figure 1.2.3: Activity-activity diagram showing the chemical composition path of a solution in equilibrium with dissolving feldspar (Lasaga et al., 1994).

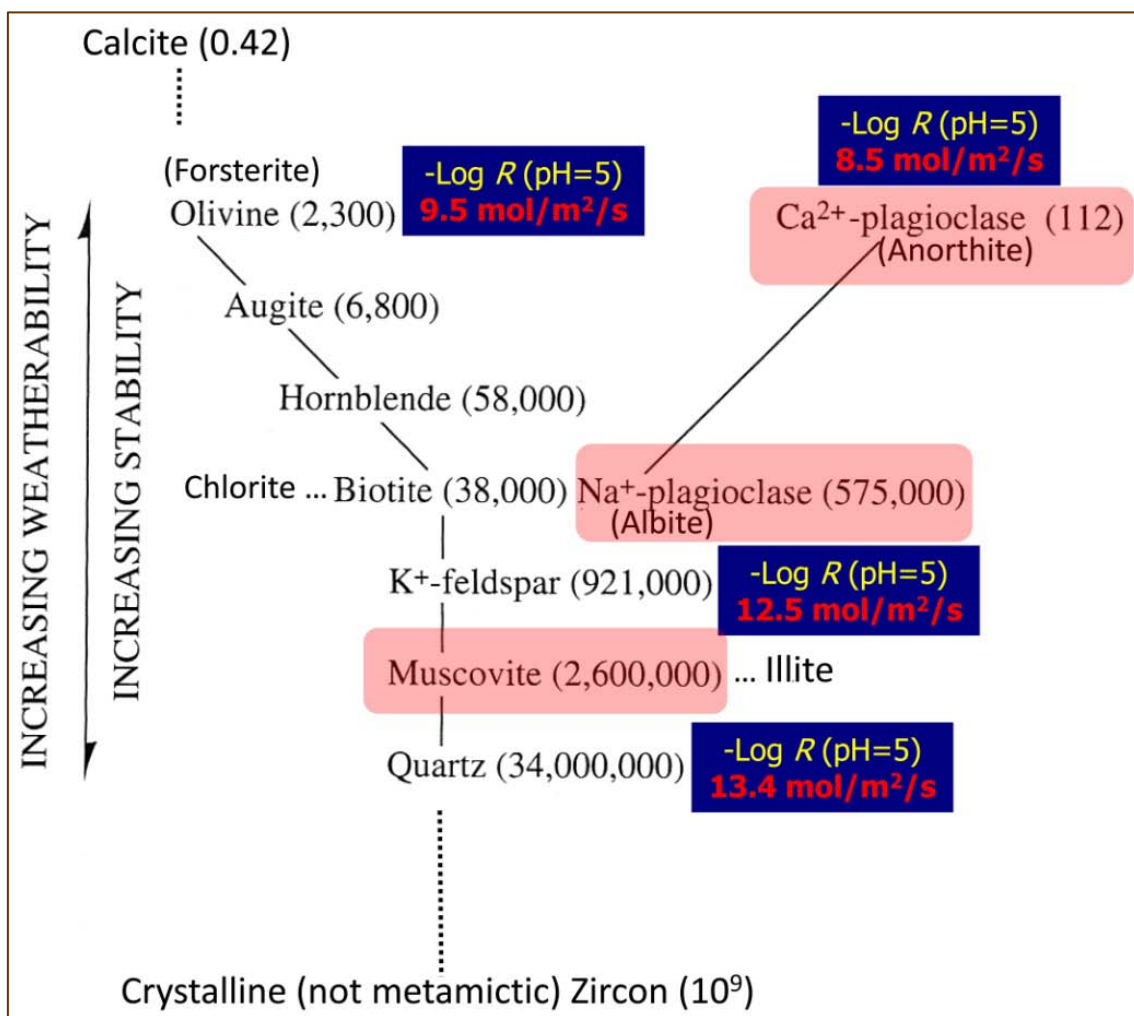
1.2.3 (Lasaga et al., 1994) in the beginning, gibbsite precipitates and later on supersaturation with regard to kaolinite, causes the precipitation of kaolinite and the subsequent dissolution of gibbsite. At the end, gibbsite dissolves, and the fluid composition goes into kaolinite stability field. In due course, the system reaches equilibrium with feldspar (**Figure 1.2.3**).



Feldspars are rather soluble, among various rock-forming minerals, with relatively high dissolution rates (**Figure 1.2.4**). However, it should be mentioned that among feldspars, plagioclases, and particularly anorthite (CaAl₂Si₂O₈, Al = 18.97 wt.%), are the most soluble

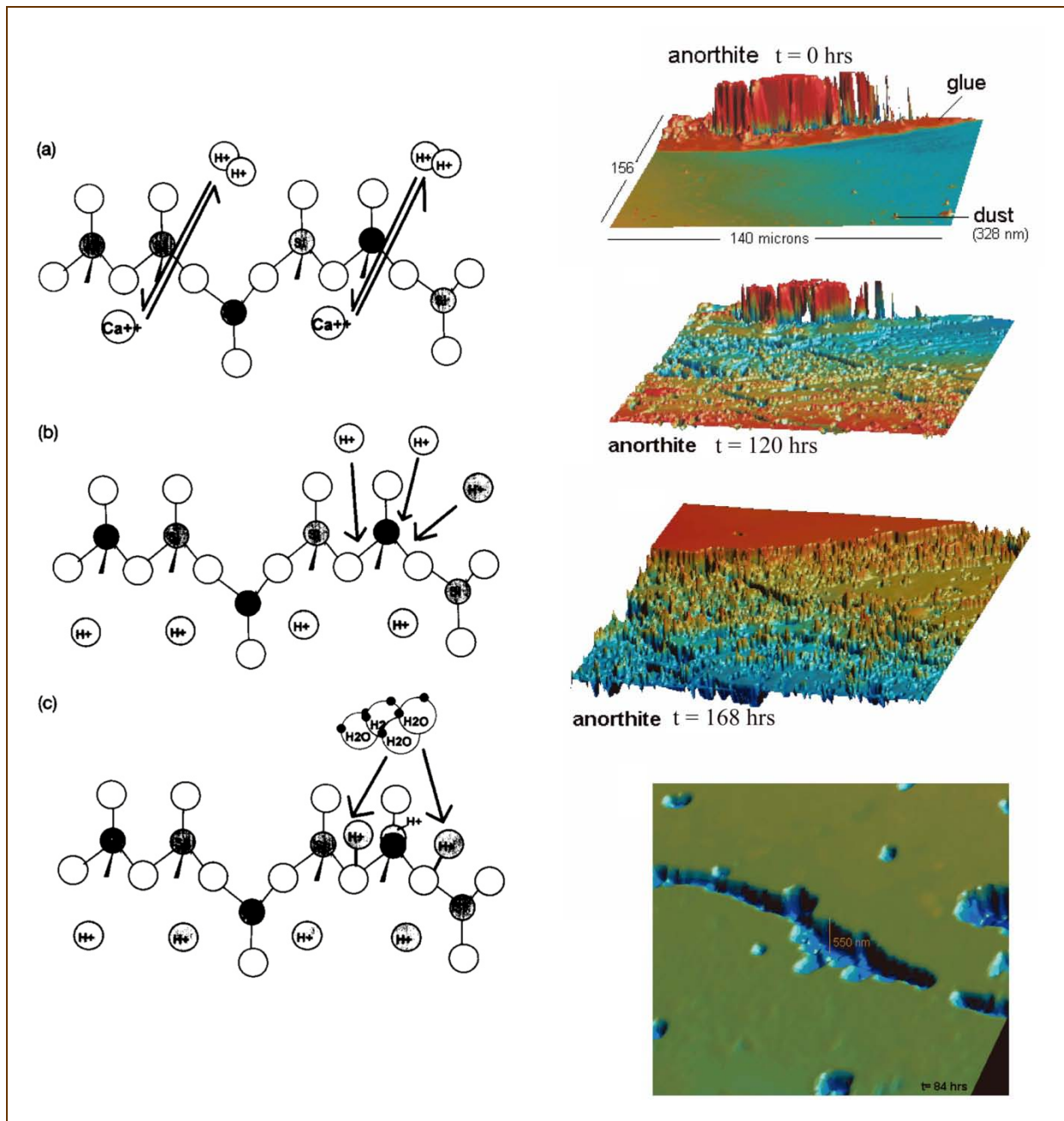
and Al-bearing minerals and hence the most favorable source of Al in erosion/weathering followed by laterization and bauxitization processes (Bowen, 1922; Lasaga et al., 1994).

Figure 1.2.4: Dissolution rates (1 mm crystal, pH = 5, 25 °C) and lifetime (yrs) of rock-forming minerals of igneous rocks as related to Bowen Reaction Series (modified after Bowen, 1922 and Lasaga et al., 1994). The minerals with higher Al content are marked with red-shaded rounded rectangles.

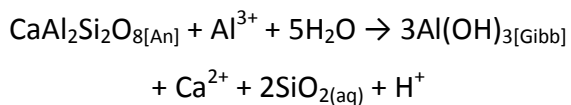


The dissolution of plagioclase, and particularly of anorthite, starting from the surface of the mineral, includes three major steps and leads to characteristic etch-pits (Oelkers & Schott, 1995; Lüttge et al., 1999; see Figure 1.2.5).

Figure 1.2.5: Dissolution of anorthite (after Oelkers & Schott, 1995; Lüttge et al., 1999).

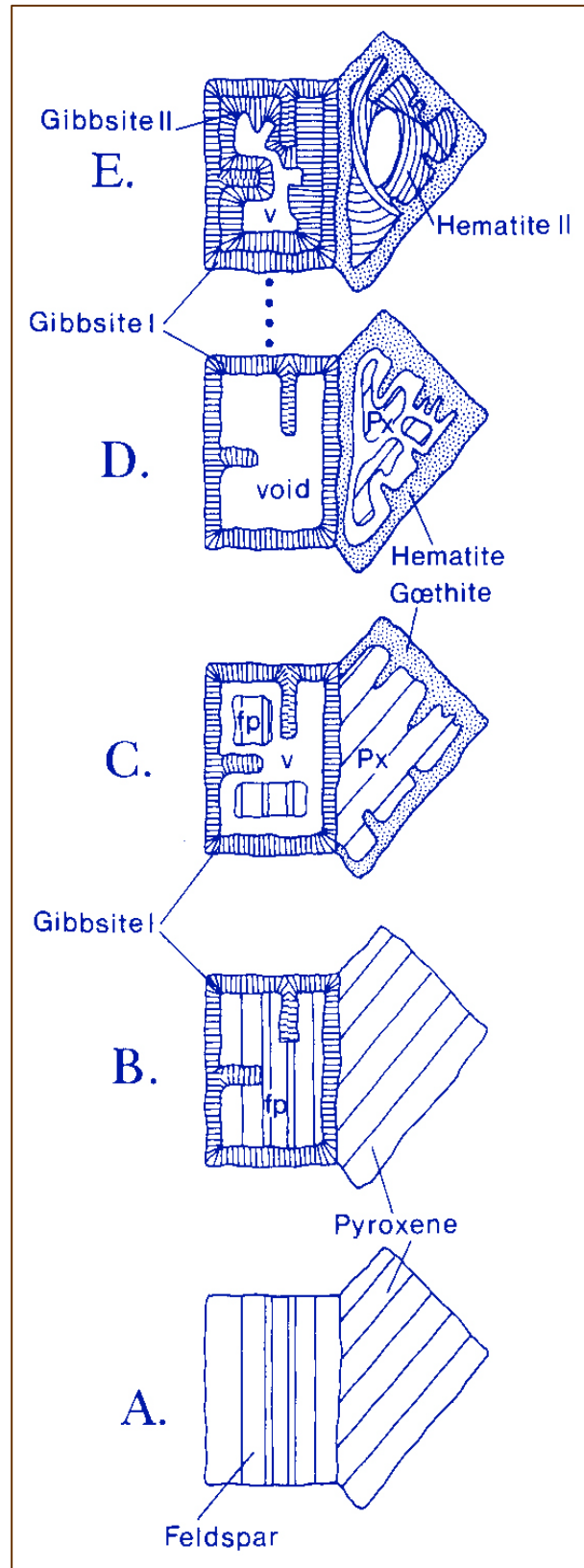


In relatively higher temperature (210 °C) secondary Al oxyhydroxides -including boehmite- can be precipitated, in microscale, on the dissolved surface of anorthite (Murakami et al., 1998). Moreover, when anorthite occurs together with pyroxene, i.e., in the case of gabbroic rocks, a pseudomorphic replacement of the feldspar by gibbsite, after surface dissolution, takes place (Merino et al., 1993; see Figure 1.2.6) through the following reaction:



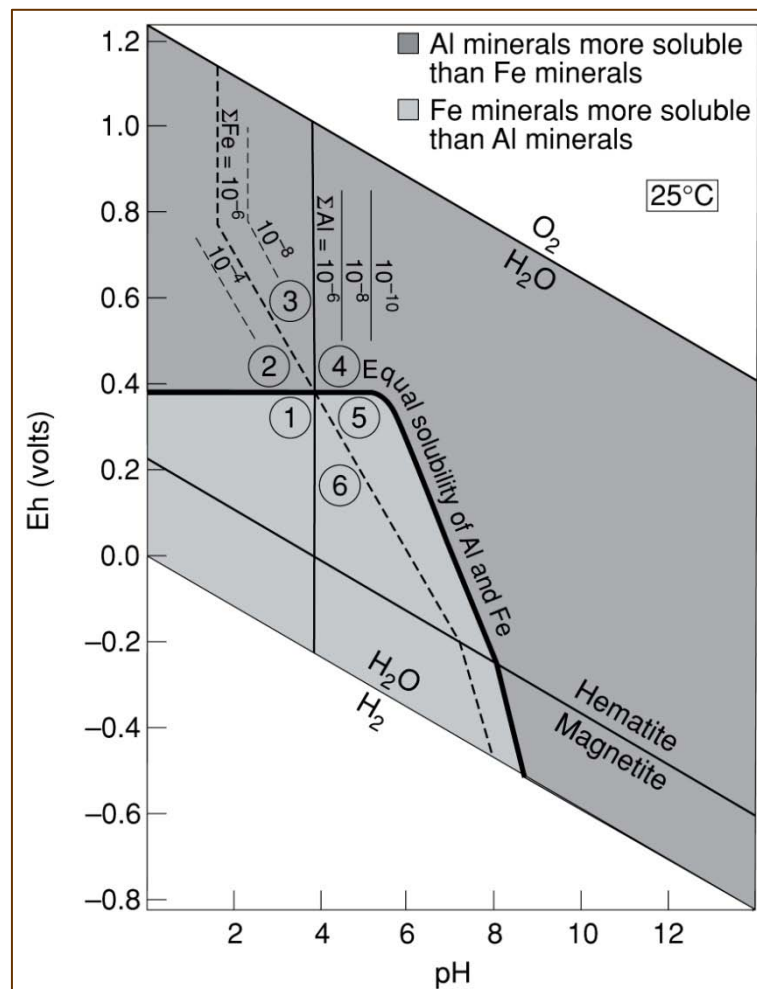
In the case of bauxitization, the redistribution of Fe, and the segregation of Al and Fe, is a necessary process in bauxite formation because ferruginous minerals tend to contaminate the ore. High quality bauxitic ores require that both Fe and Si be removed, but not alumina, whereas ferricretes and conventional laterites are characterized by different combinations of element leaching. The interplay of Eh and pH is critical to the formation of high quality bauxitic ores (Figure 1.2.7). The optimum conditions for bauxite formation

Figure 1.2.6: Pseudomorphic replacement of anorthite by gibbsite and pyroxene by hematite (Merino et al., 1993).



are provided in field 6 where groundwater solutions will preferentially remove Fe. In this field Al hydrolysates are stable, especially at pH between 5 and 7, and gibbsite will accumulate (Norton, 1973; Robb, 2005).

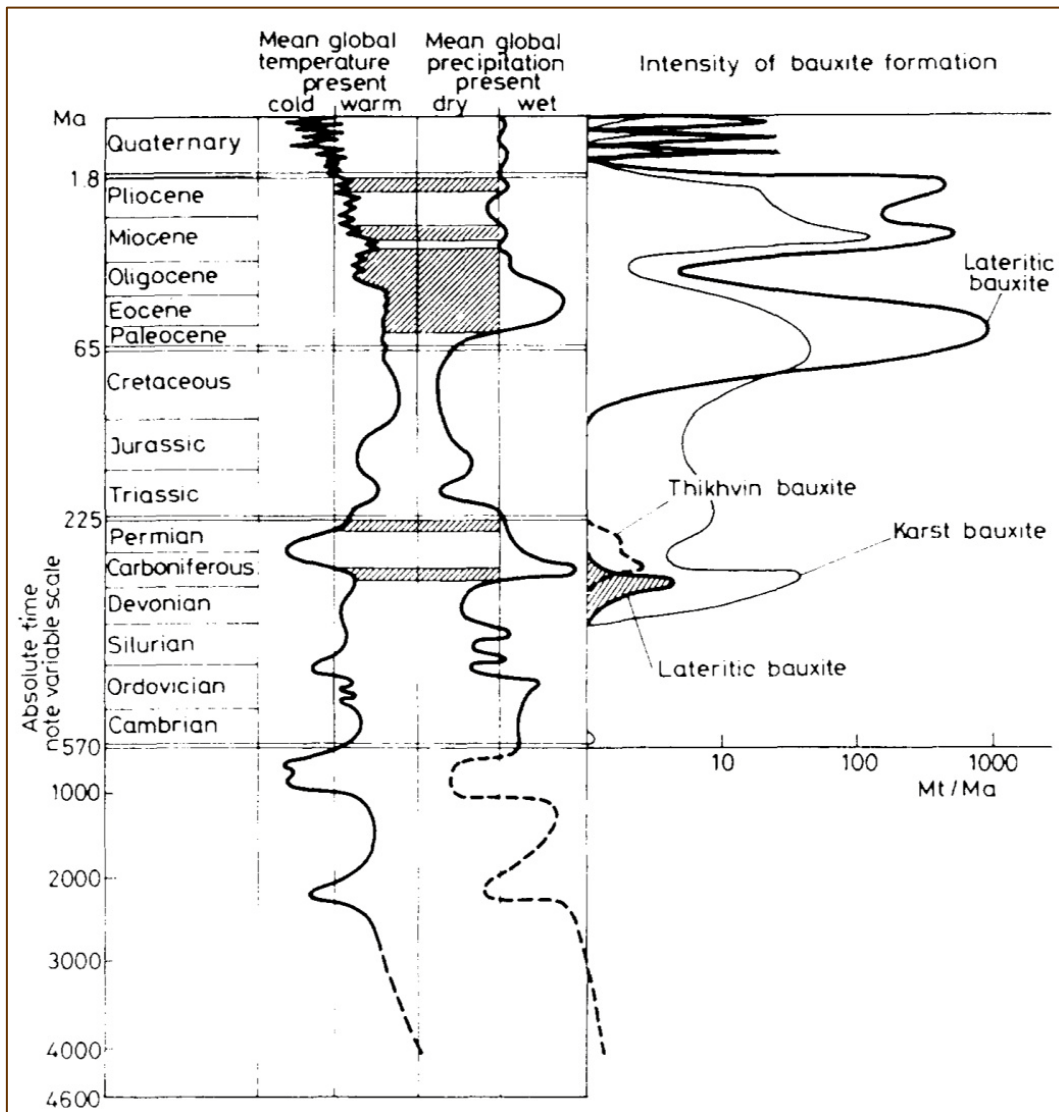
Figure 1.2.7: Eh–pH diagram showing conditions relevant to the formation of laterites and bauxite ore (Robb, 2005).



Seasonal climatic variations are also considered important to the formation of bauxitic ores as the alternation of wet and dry spells promotes fluctuations in groundwater levels and, hence, dissolution and mass transfer. Thus, most of the bauxites are ordered after their age, according to alignments indicating the existence of palaeoclimatic belts of humid

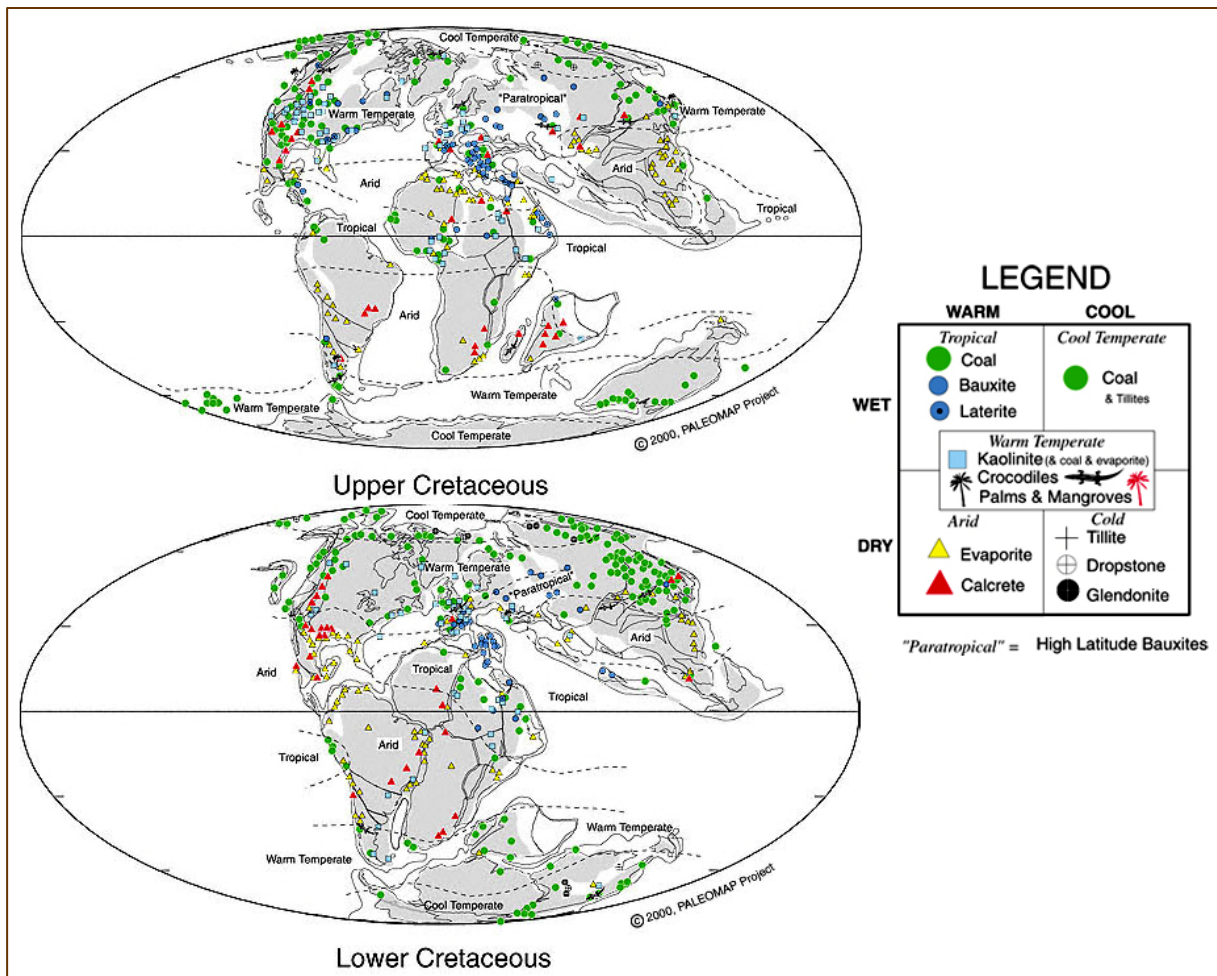
intertropical type that were susceptible of having generated a laterizing pedogenesis, during geological time when these bauxites and laterites were formed (Nicolas & Bildgen, 1979; Robb, 2005). Subsequently, special climatic periods during Earth history with a greenhouse effect, allowed intense lateritic weathering during limited time intervals and therefore, formation of bauxite deposits (Bardossy & Aleva, 1990; Valeton, 1994; see Figure 1.2.8).

Figure 1.2.8: Generalized temperature and precipitation curves of the Phanerozoic and the distribution of bauxite in time (Bardossy & Aleva, 1990; Valeton, 1994).



Among various weathering periods that have been recorded in the European continent during Late Mesozoic and Tertiary, the Upper Jurassic to Eocene, and particular the Cretaceous interval, is considered the most important for bauxitization processes (Bárdossy, 1982). The Cretaceous period is generally considered to have been a time of typical warm climate (Figure 1.2.9).

Figure 1.2.9: Cretaceous climate and supergene ore deposits, i.e., bauxites and laterites, (Scotese, 2001).



Moreover, [Steuber et al. \(2005\)](#) studied rudist bivalves (*Hippuritoidea*) to record intra-shell variations in $\delta^{18}\text{O}$ values and hence the evolution of the seasonality of Cretaceous sea surface temperatures. The study indicated high maximum temperatures (~ 35 to 37°C) and relatively low seasonal variability ($<12^\circ\text{C}$) between 20° and 30°N during the warmer episodes (**Figure 1.2.10**).

It is evident that Cretaceous seas of the Tethys paleo-Ocean were exceptionally warm (between 6 and 14°C warmer than today) and the growth of rudists, as major reef-building organisms, was favored in carbonate platforms ([Skelton et al., 2006](#); see **Figure 1.2.11**). During this geological period, rudist reefs were so dominant that they pushed scleractinian corals out of many tropical environments, including shelves that they occur now in Caribbean and the Mediterranean.

Figure 1.2.10: Palaeo-positions (palaeolatitudes between 8° and 31°N) of early Aptian / 119Myr ago and Maastrichtian / 67Myr ago rudist bivalves (*Hippuritoidea*) used to record intra-shell variations in $\delta^{18}\text{O}$ values and hence the evolution of the seasonality of Cretaceous sea surface temperatures; green: central Greece ([Steuber et al., 2005](#)).

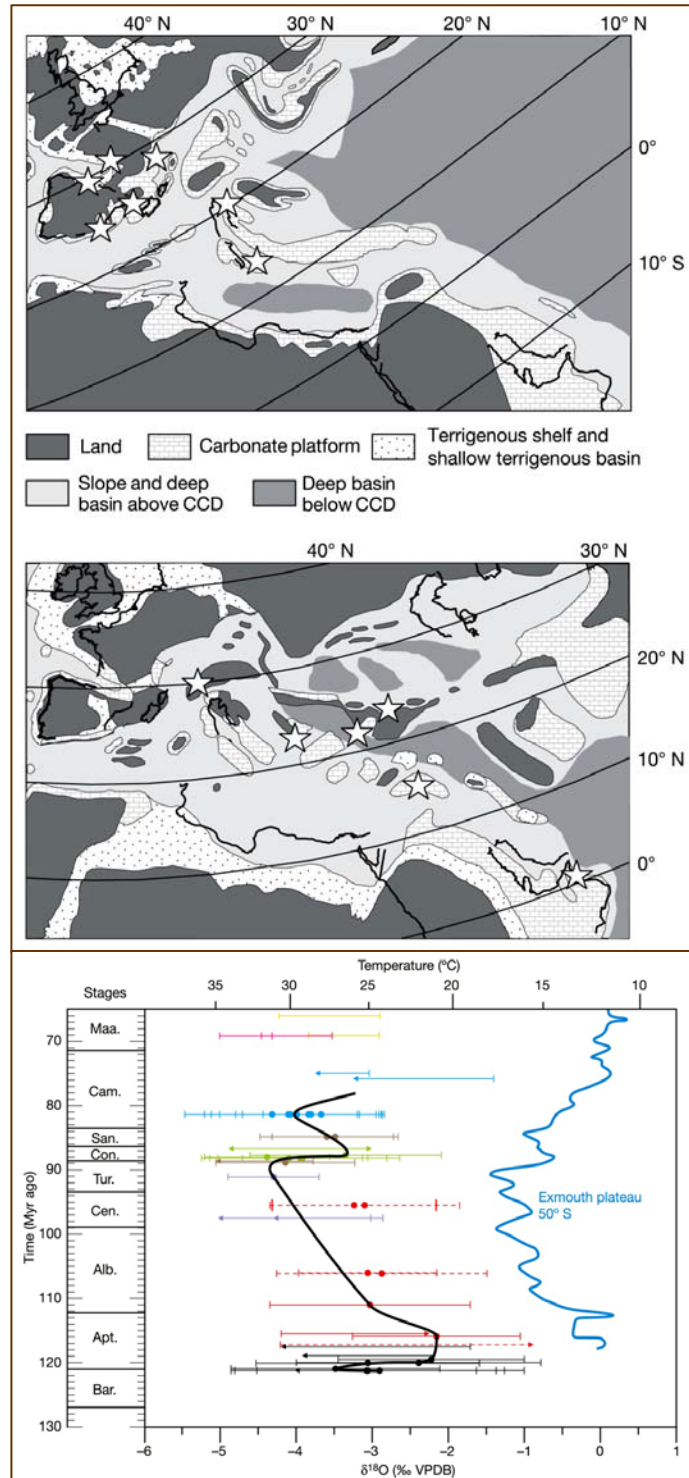
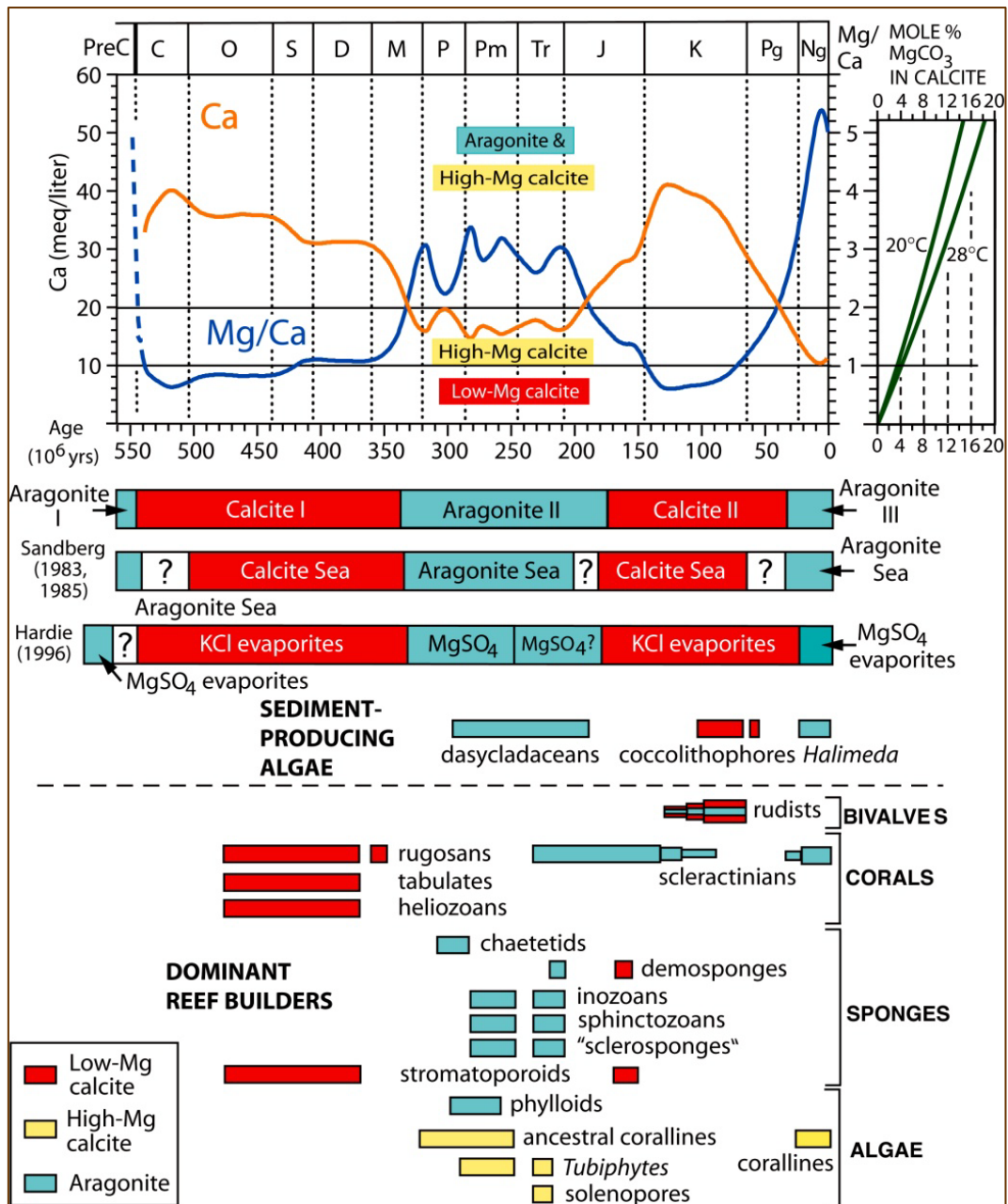


Figure 1.2.11: Reconstruction of a representative carbonate platform emphasizing the dominance of rudists ([Skelton et al., 2006](#)).



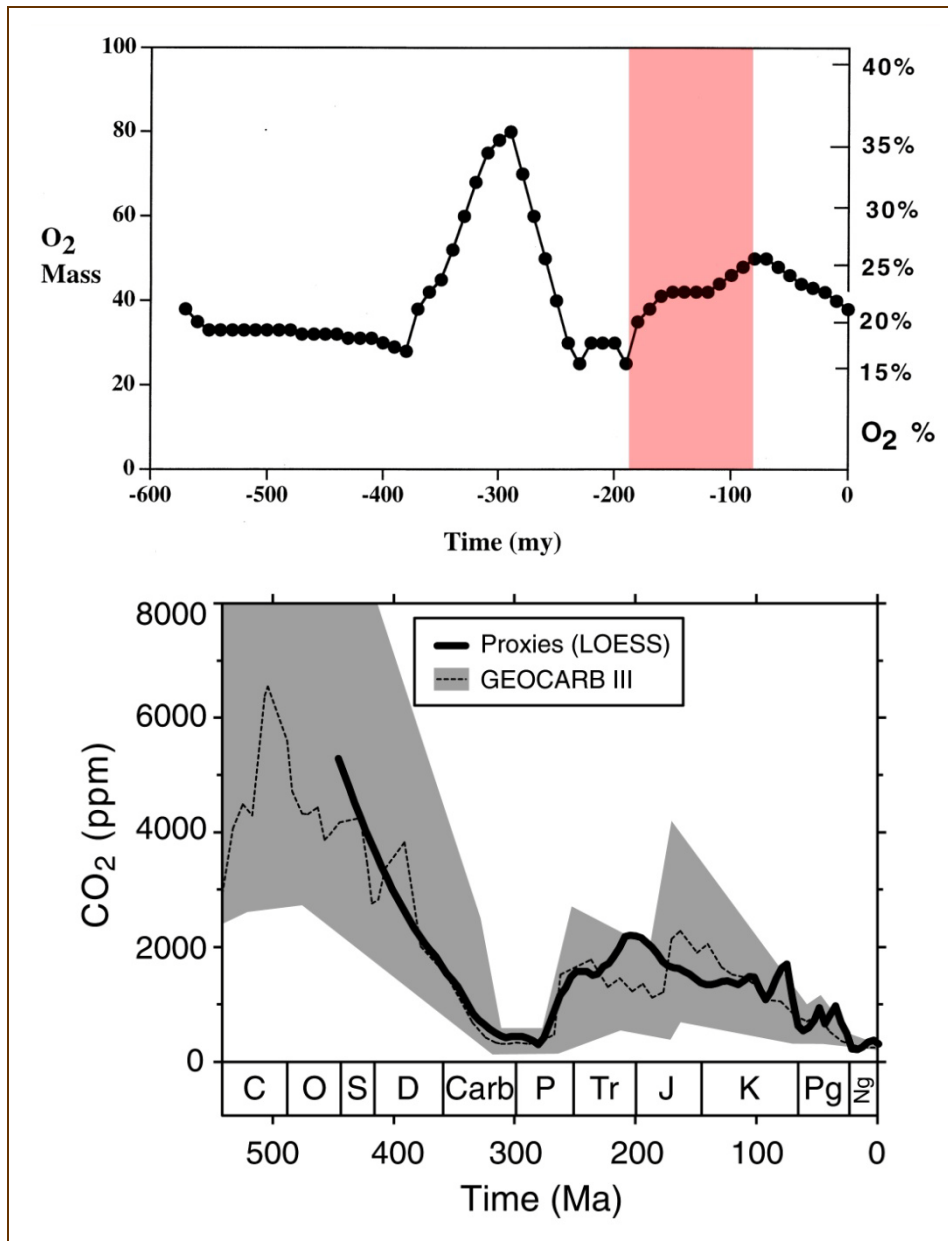
During Cretaceous seawater was also more saline, and therefore it was an appropriate environment for rudists and not so convenient for coral growth. On the other hand, it should be emphasized that Cretaceous seas were characterized by low Mg/Ca ratio related to typical “calcite sea” ([Stanley, 2008](#); see **Figure 1.2.12**).

Figure 1.2.12: “Calcite” and “aragonite seas” (Stanley, 2008).



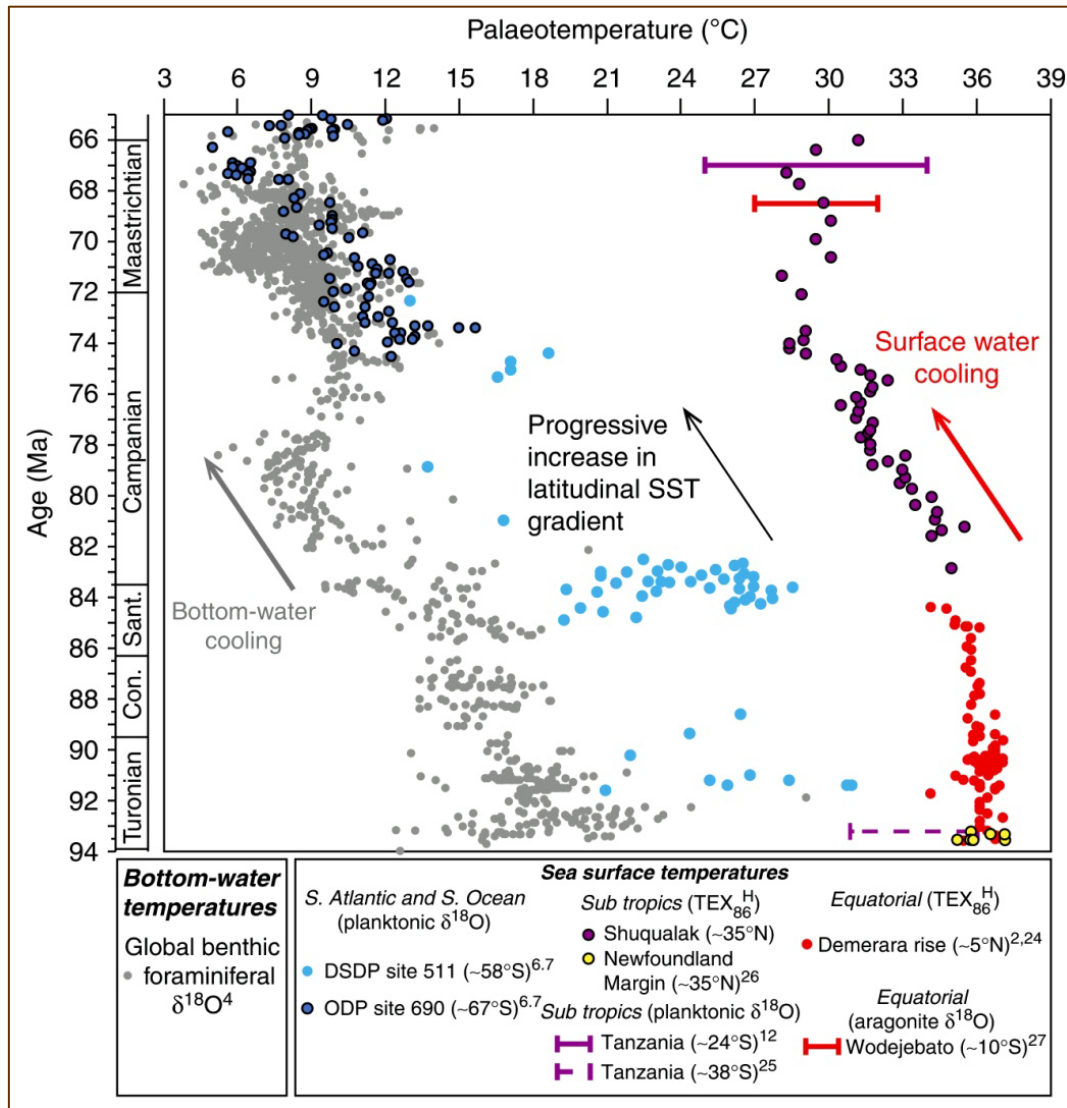
In general, Cretaceous, except for the characteristic warm climate, is characterized by low atmospheric O₂, and in parallel by high CO₂, related to severe greenhouse effect (Berner, 1999; Royer, 2006; see Figure 1.2.13). This also stands for Upper Jurassic, implying that atmospheric and climate conditions in the entire period of Upper Jurassic – Upper Cretaceous promoted the intense lateritic weathering and bauxitization processes.

Figure 1.2.13: Atmospheric O₂ and CO₂ level vs. time for the Phanerozoic (Berner, 1999; Royer, 2006).



However, in recent study, on the basis of organic geochemical palaeothermometer (TEX₈₆), it has been suggested that the high sea surface temperature (SST) in north Atlantic during earliest Campanian (~35 °C) was followed by significant cooling (~9) after this to <~28 °C during the Maastrichtian (Linnert et al., 2014; see Figure 1.2.14). That means, lateritic weathering and bauxitization processes may be slowed down in Late Cretaceous, worldwide.

Figure 1.2.14: Benthic and planktonic foraminiferal estimates of temperature in Late Cretaceous (Linnert et al., 2014).



1.3. Karst bauxites and formation of Parnassos-Ghiona deposits

This type of bauxite is wide-spread in the Mediterranean and in the West-Indian part of the world (**Figure 1.3.1**). The bauxites are connected with platform evolution in the orogen mountain chains and in other tectonic mobile shelf areas. They occur as intercalations in carbonate sediments and on top of clastic sediments during the Mesozoic-Early Cenozoic time in the Mediterranean and during the Miocene-Pliocene in the Caribbean ([Valeton, 1972](#); [Bárdossy, 1982](#); [Valeton, 1994](#); [Robb, 2005](#)).

Karst bauxites in the so-called Mediterranean belt ([Valeton, 1972](#); [Bárdossy, 1982](#); [Özlü, 1983](#)), including parts of central Europe, Balkans and Middle East / western Asia, are fundamentally hosted in Mesozoic marine sedimentary carbonate rocks, limestones, derived from the Tethys paleo-Ocean (**Figure 1.3.2**).

Thus, as already mentioned, karst bauxites are hosted into pre-existing irregular karst cavities (**Figures 1.3.3 & 1.3.4**) and/or as rather regular beds into limestone layers of different geological age.

The huge bauxite deposits of Jamaica represent a good example of the controls involved in the formation of aluminum ores. Thick deposits of bentonitic volcanic ash were laid down on limestone bedrock and the former are considered to be the ultimate source of residual alumina in the bauxite deposits. Desilication of volcanic glass and other silicate minerals by rapid and efficient drainage through the underlying karst limestone is considered to have been responsible for the gibbsite-dominated ores (**Figure 1.3.5**).

Figure 1.3.1: Karst bauxites in the Mediterranean belt (Bárdossy, 1982).

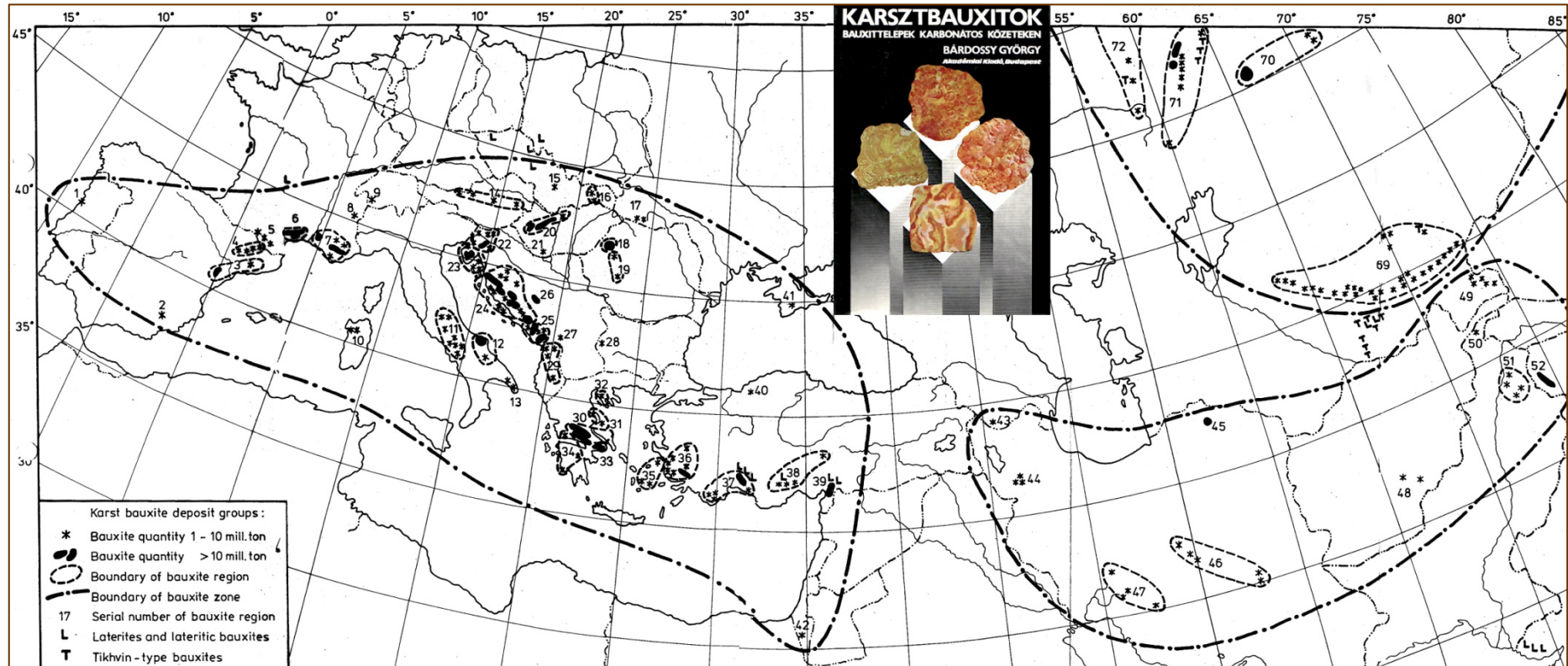


Figure 1.3.2: Distribution and stratigraphic order of bauxites in southern Europe (modified after [Valeton, 1972](#)).

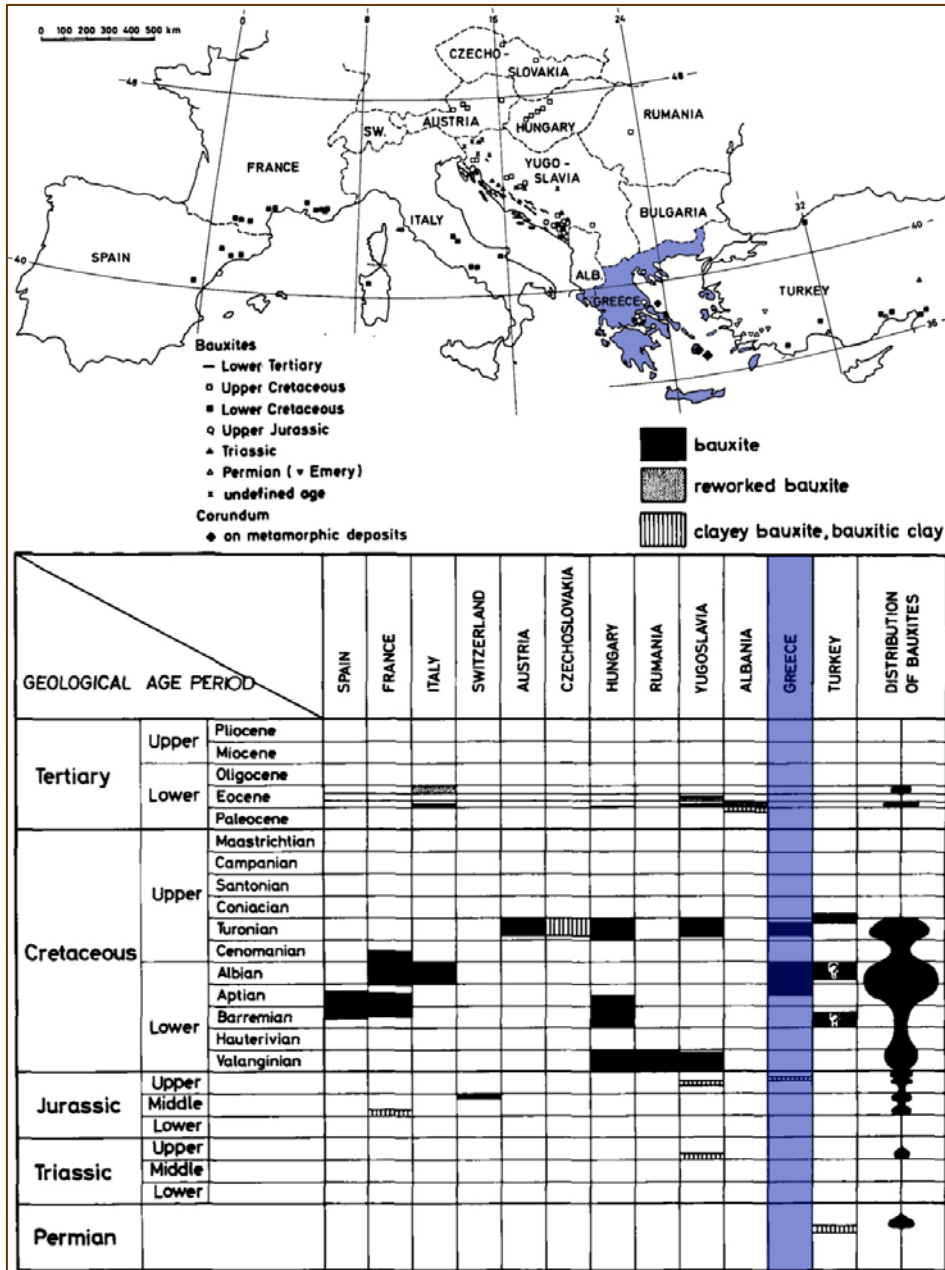


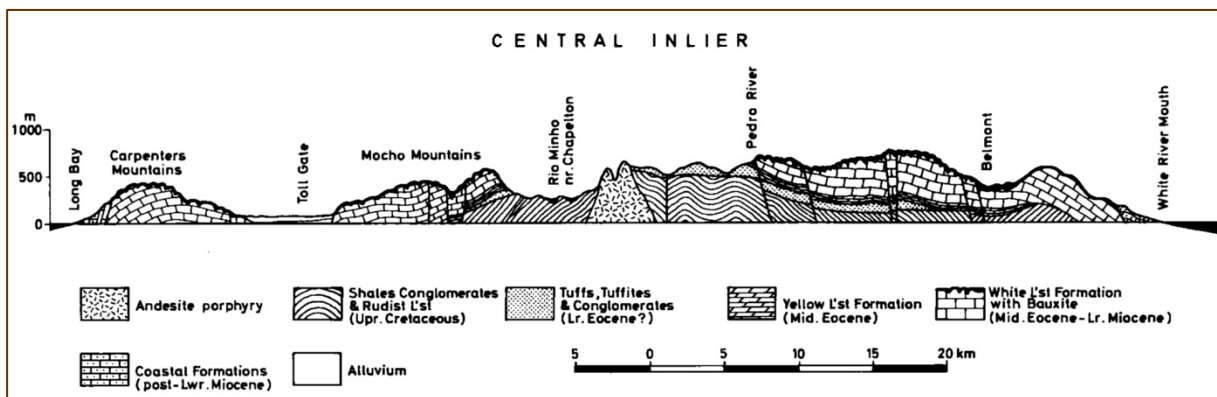


Figure 1.3.3: Karst cavity in Mesozoic limestone which was filled with bauxitic material before exploitation in an abandoned bauxite mine of Parnassos-Ghiona area.

Figure 1.3.4: Mesozoic carbonate formations at Parnassos-Ghiona area (left image) and entrance of an active bauxite mine / Pera Lakkos mine (right image).



Figure 1.3.5: Section across the central part of Jamaica (Valeton, 1972).



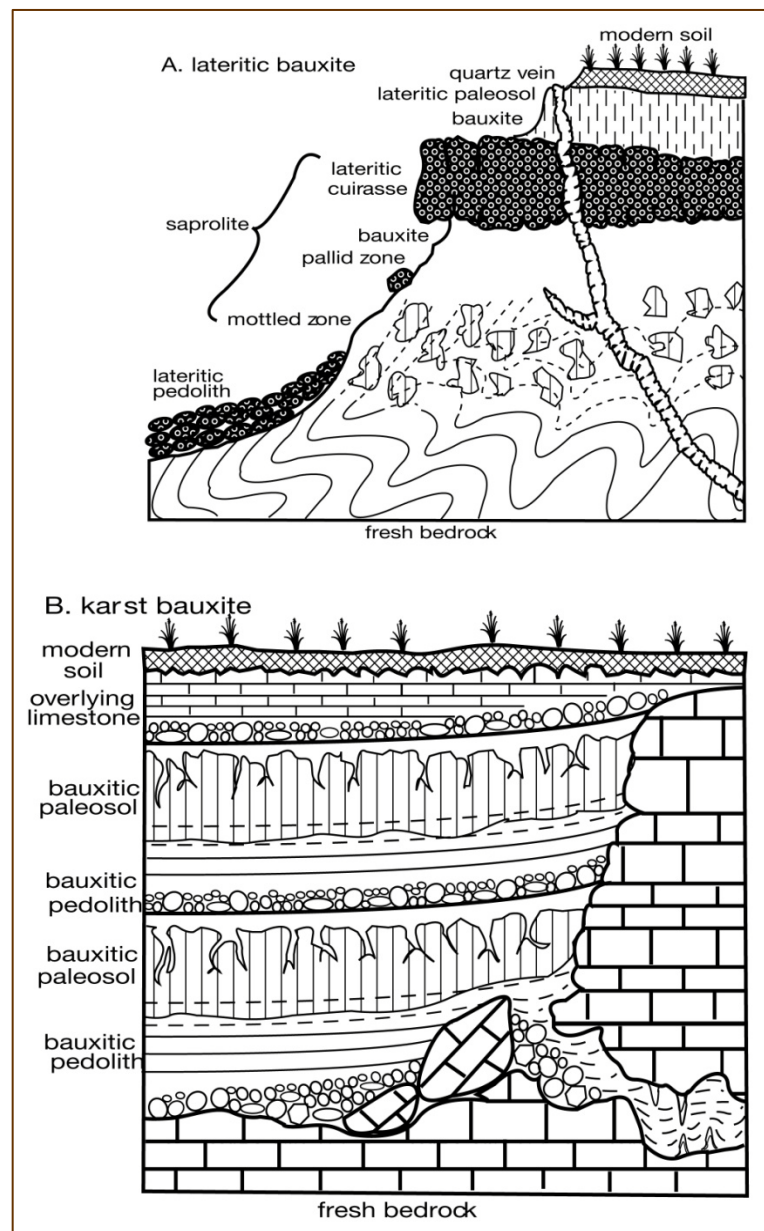
In Venezuela, by contrast, lateritic bauxites (**Figure 1.3.6**) are derived by deep weathering of granitic bedrock during prolonged uplift and erosion of the Guyana Shield (Soler & Lasaga, 1996; Robb, 2005). Taking into account all the above, it is evident that feldspars and volcanic glass may be critical sources of aluminium in bauxite and karst bauxite formation.

Almost one century after the **Figure 1.3.6: Section of lateritic and karst bauxite** discovery of bauxite, karst-type (Retallack, 2010).

bauxite deposits, similar to French ones, were exploited in central Greece, in the area of legendary Parnassos Mountain near the Oracle of Delphi. As mentioned by Georgalas (1946), the existence of karst-type bauxite in Parnassos-Ghiona was announced around 1922, giving possibilities of developing an aluminium industry in Greece.

Numerous geological studies have been published about the Parnassos-Ghiona allochthonous karst bauxite deposits (Aronis, 1955; Papastamatiou, 1960; Papastamatiou, 1964; Bárdossy & Mack, 1967; Nia, 1971; Valeton, 1972; Maksimović & Papastamatiou, 1973;

Papastavrou, 1974; Mack & Petrascheck, 1978; Nicolas & Bildgen, 1979; Combes et al., 1981; Bárdossy, 1982; Biermann, 1983; Combes & Andreou, 1983; Arp, 1985; Papastavrou, 1986;



Valeton et al., 1987; Petrascheck, 1989; Valeton, 1991; Vgenopoulos & Daskalakis, 1991; Economopoulos & Vgenopoulos, 1998). These ores are hosted within Mesozoic carbonate formations (**Figure 1.3.7**). The Parnassos-Ghiona geotectonic zone is characterised by nearly continuous sedimentation of epicontinental reef-like carbonates from the Upper Triassic to the Upper Cretaceous (Valeton et al., 1987).

Figure 1.3.7: Simplified geological map (upper image; Mettos et al., 2009) and stratigraphy (lower image; lithostratigraphic column has been modified after Valeton et al., 1987 and Kalaitzidis et al., 2010 and references therein) of Parnassos-Ghiona Mesozoic geotectonic zone hosting the bauxite deposits.

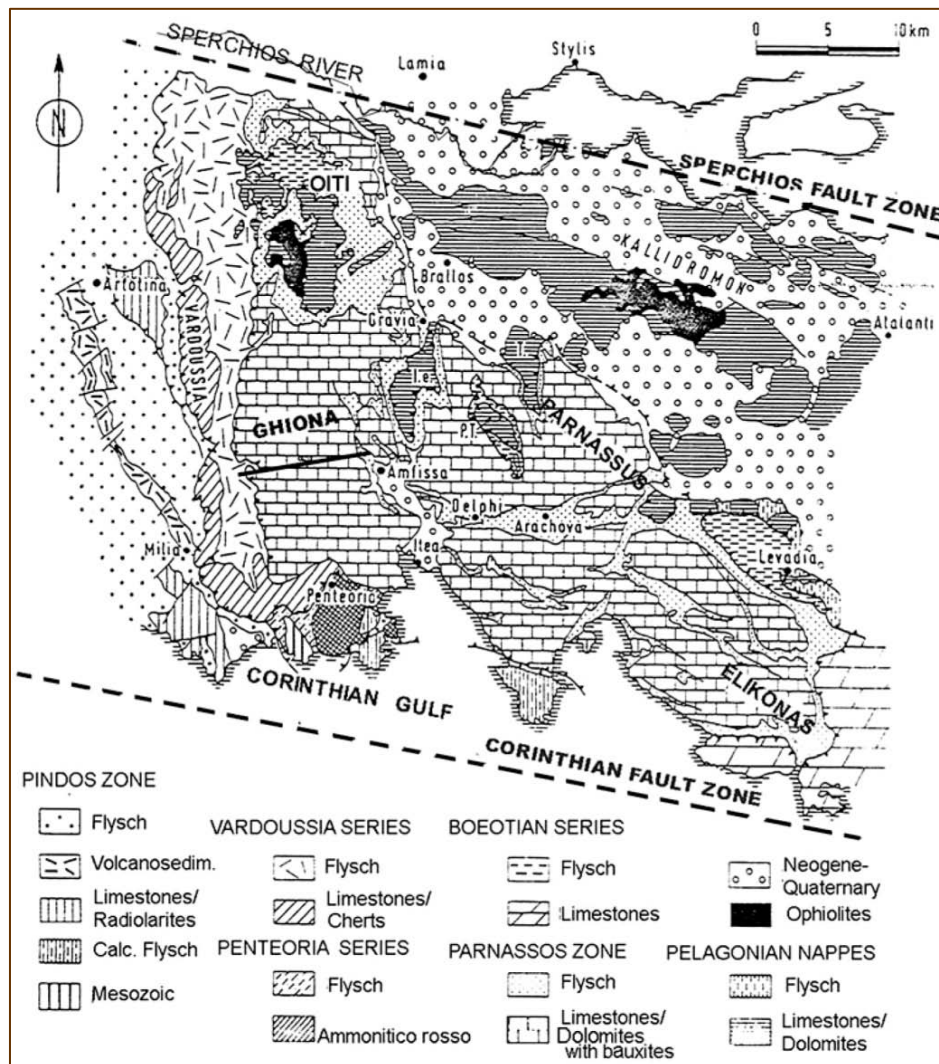
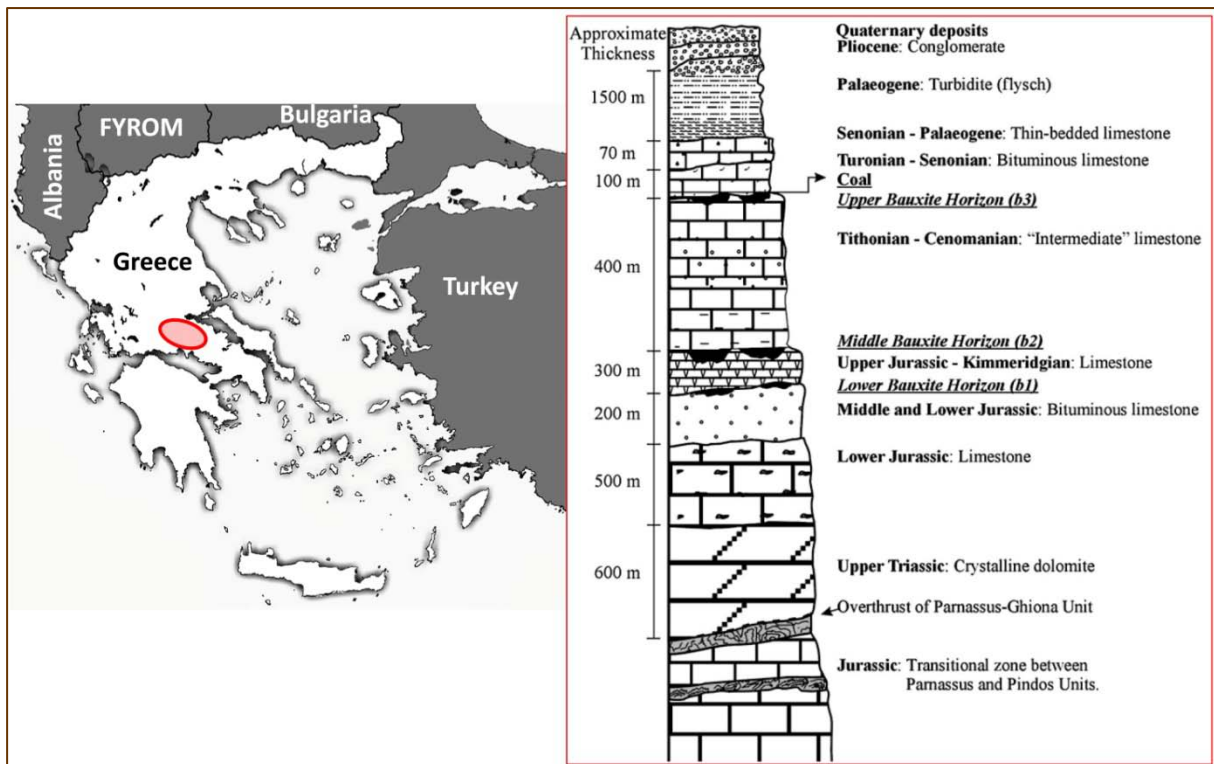


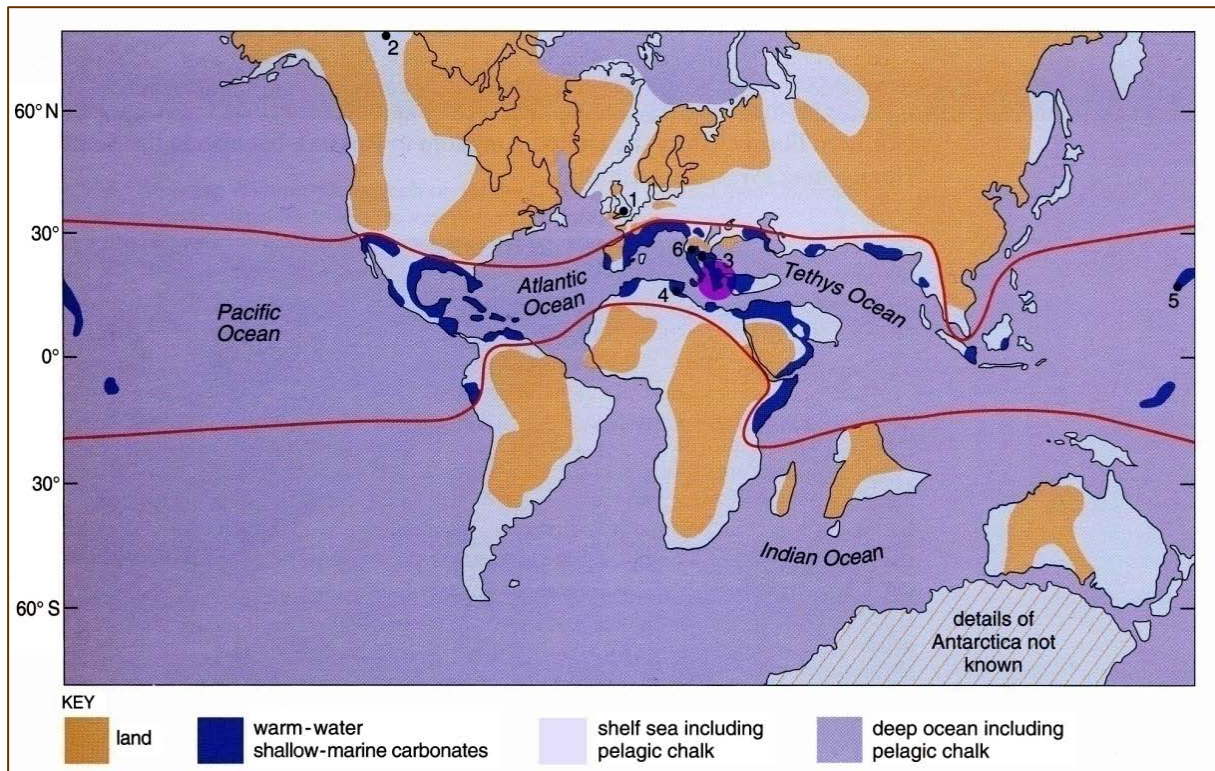
Figure 1.3.7: continued.



In this carbonate sequence, three bauxite horizons (from bottom to top: B1, B2 and B3) can be distinguished and they were caused by epirogenic emersion phases and formation of coastal karst reliefs (Valeton et al., 1987; Petrascheck, 1989). Horizon B1 is hosted in the carbonate Middle-Upper Jurassic units, horizon B2 in the carbonate Upper/Jurassic – Lower Cretaceous units (Tithonian and Neokomian respectively), whereas horizon B3 is hosted in carbonate Upper Cretaceous units (Cenomanian – Turonian). Thus, the most important geological period for for bauxitization, and formation of deposits in the Parnassos-Ghiona area, can be considered the period between Middle-Upper Jurassic and Upper Cretaceous, and particularly the whole Cretaceous. In the frame of the present dissertation, representative composite samples from active mines of the B2 and B3 horizons were studied. In the case of the B2 horizon typical Fe-rich bauxite deposits occur, while in B3 horizon, both Fe-rich and Fe-depleted (high alumina/quality) bauxite deposits are exploited. It should be noted that there are no active mines or any other current exploitation in the B1 horizon of the Parnassos-Ghiona area.

The Cretaceous period (**Figure 1.3.8**) in southern Europe is related to the partial closure of the Tethys paleo-Ocean accompanied by collision, exhumation of ophiolites, and the uplift of carbonate platforms.

Figure 1.3.8: Paleo-map of Late (Upper) Cretaceous (Skelton et al., 2006).



Concerning the Hellenides, within the Tethyan system in the Eastern Mediterranean, the paleogeodynamic and paleogeographic evolution included continental drifting and contemporaneous oceanic opening of Tethyan basins in between the continental terranes during Triassic–Paleogene with shallow-water carbonate platforms on the continental terranes and ophiolite suites interlayered with pelagic sediments within the Tethyan basins (Papanikolaou, 2009 and Papanikolaou, 2013; see **Figure 1.3.9**).

Figure 1.3.9: The geodynamic evolution of the terranes within the Tethyan segment of the Hellenides (from Early Triassic to Present) and the tectonic emplacement of the internal ophiolite belt (Papanikolaou, 2009; Papanikolaou, 2013).

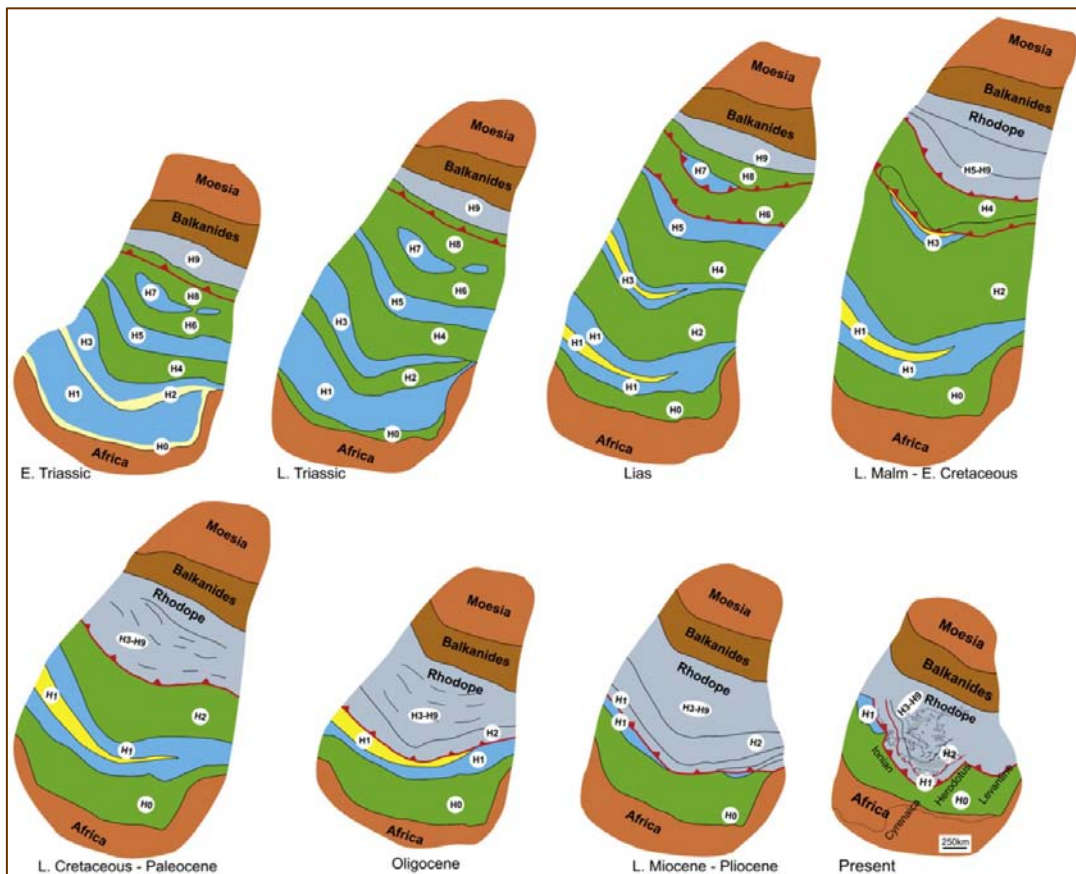
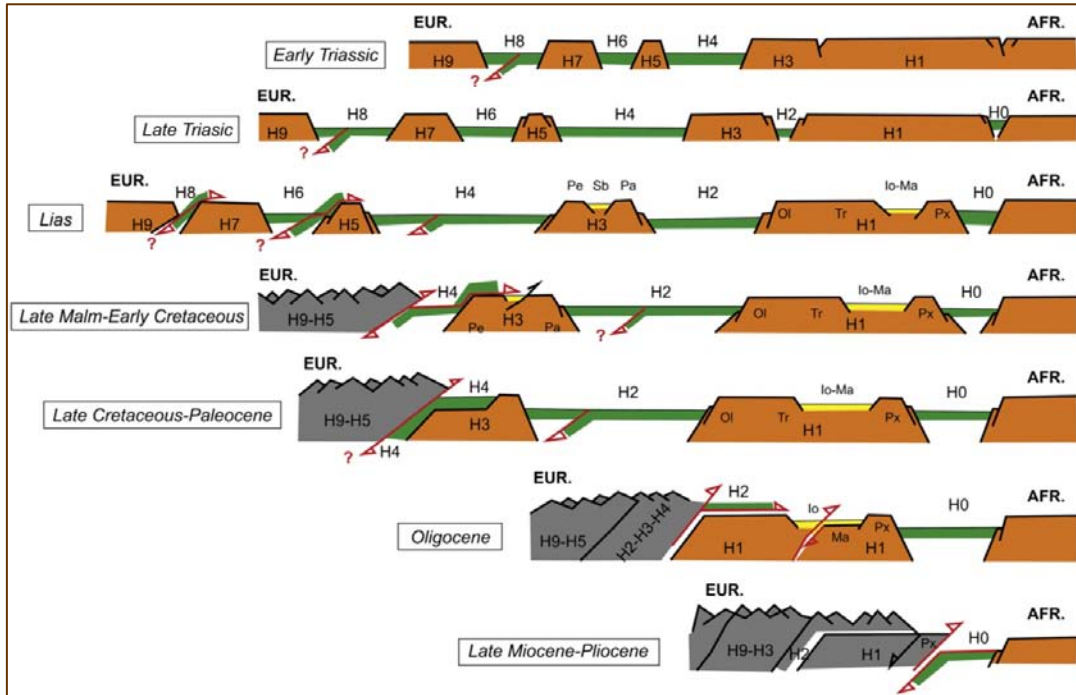
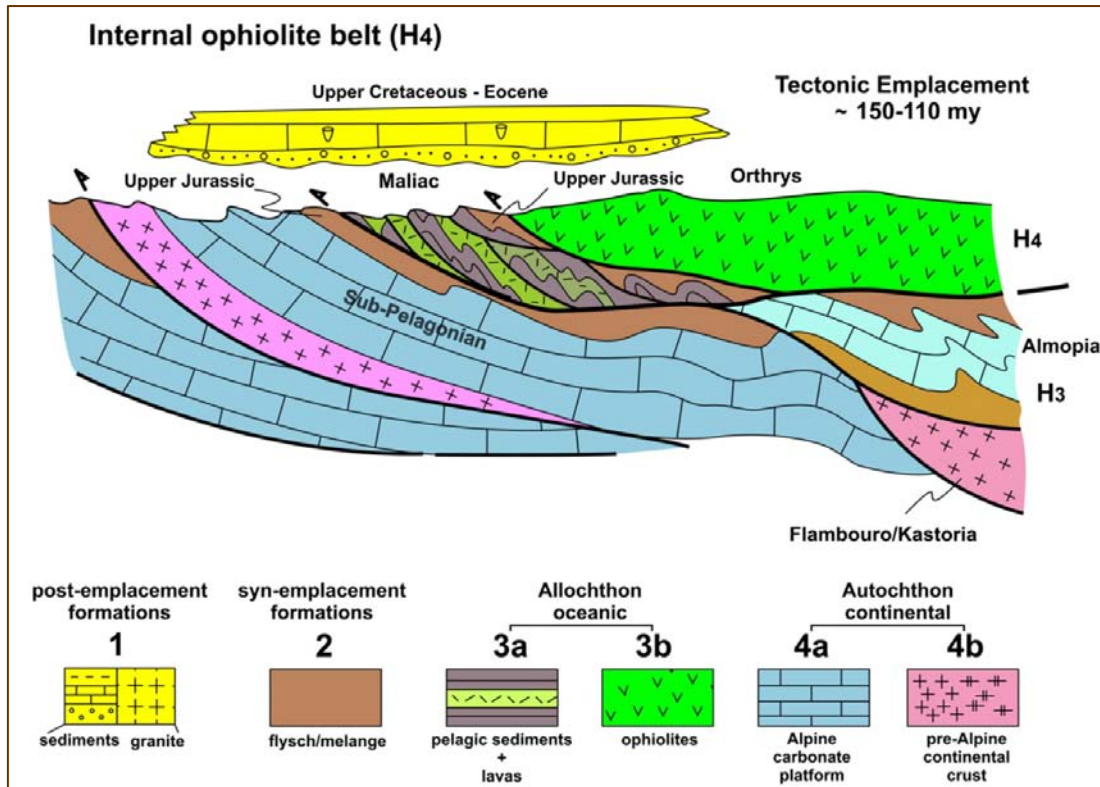


Figure 1.3.9: continued.



It is evident that the paleogeography is important for the formation of karst bauxites. A model for the paleogeographic situation in central Greece during nickel-laterite evolution on ophiolites and bauxite formation on laterite-derived facies covering the carbonate platform of the foreland has been reported by [Valeton \(1994\)](#). In the Mesozoic coastal area from the land to the seaward side in several sequences bauxite events occur, which are each related to a transgressive phase (**Figures 1.3.10 & 1.3.11**).

Figure 1.3.10: Paleogeography of Parnassos-Ghiona area in early Cretaceous (upper image; Combes et al., 1981) and of 2nd (B2) and 3rd (B3) horizons paleo-karst before bauxitization (middle & lower images; Combes, 1984).

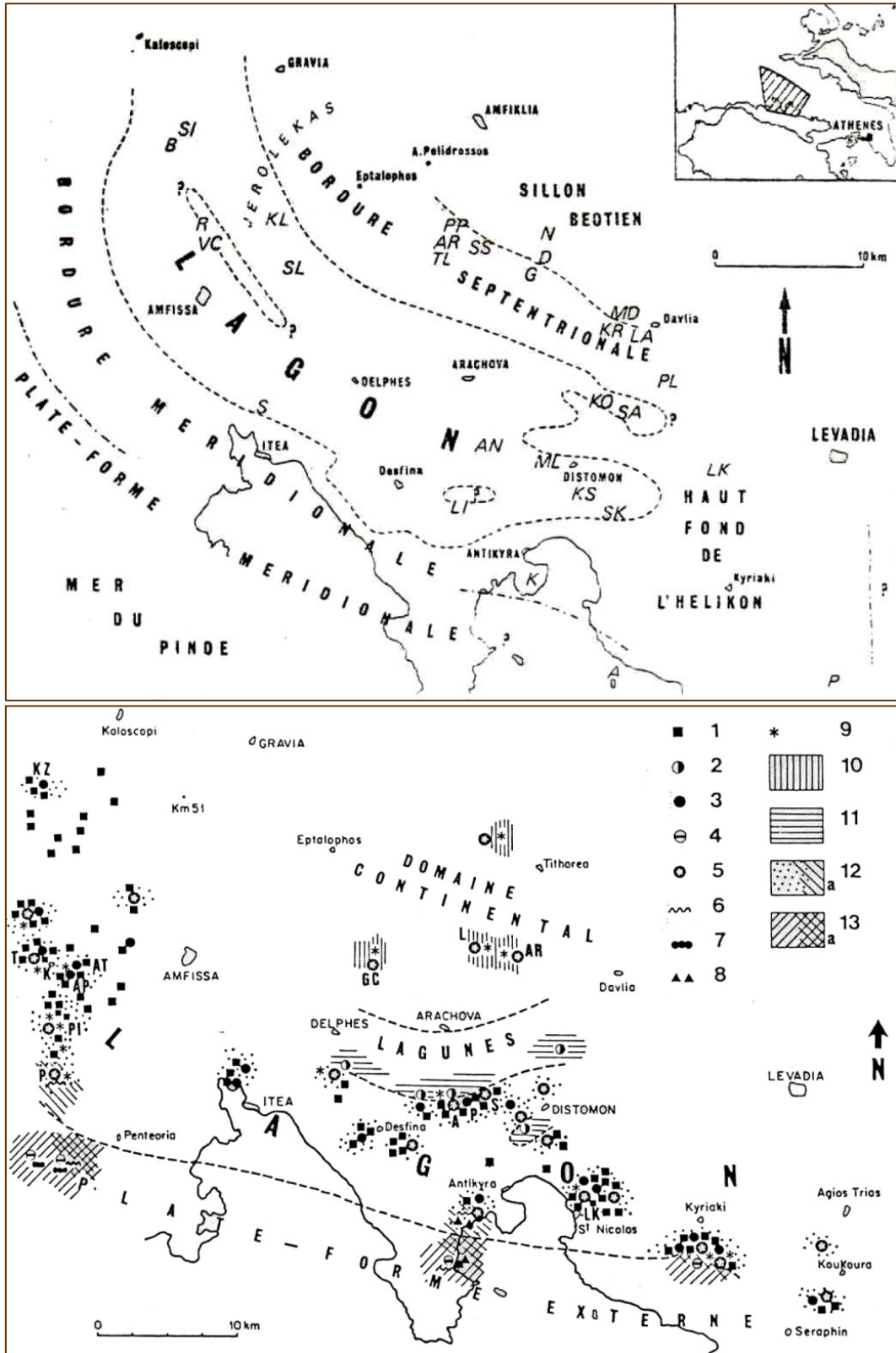


Figure 1.3.10: continued.

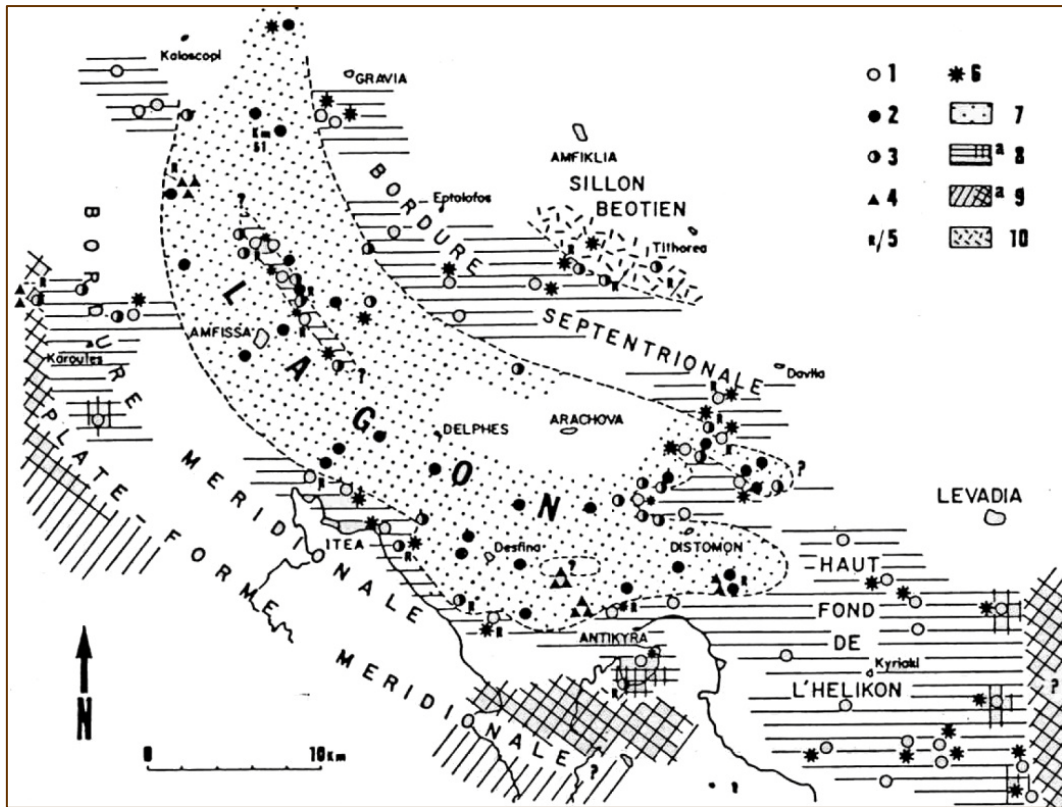
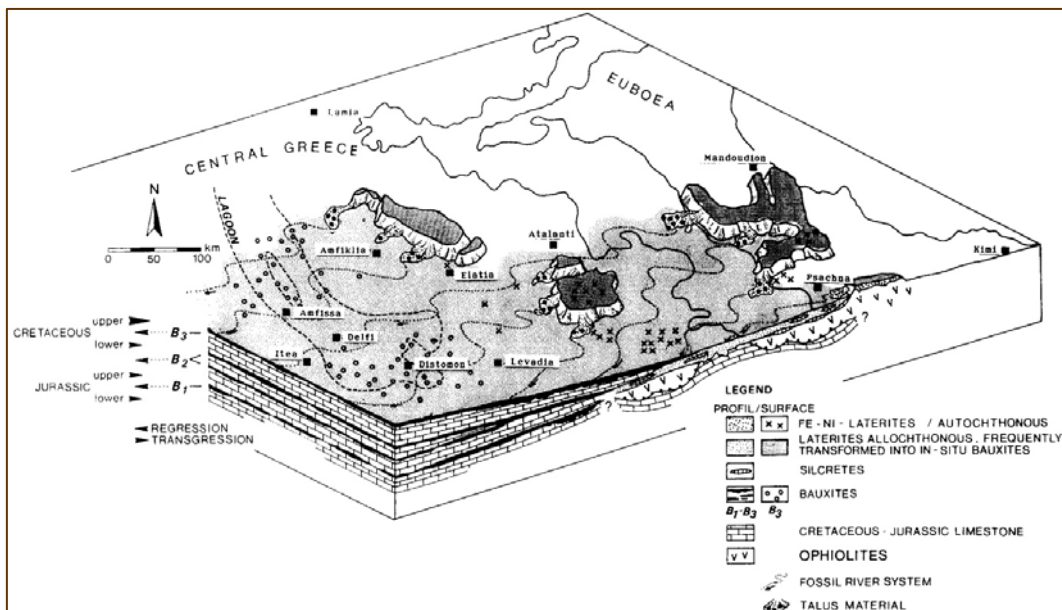


Figure 1.3.11: Model of sequences of marine re- and transgressions during Jurassic and Cretaceous times on a carbonate platform of the Alpine Orogen in central Greece and Euboea (Valeton, 1994).



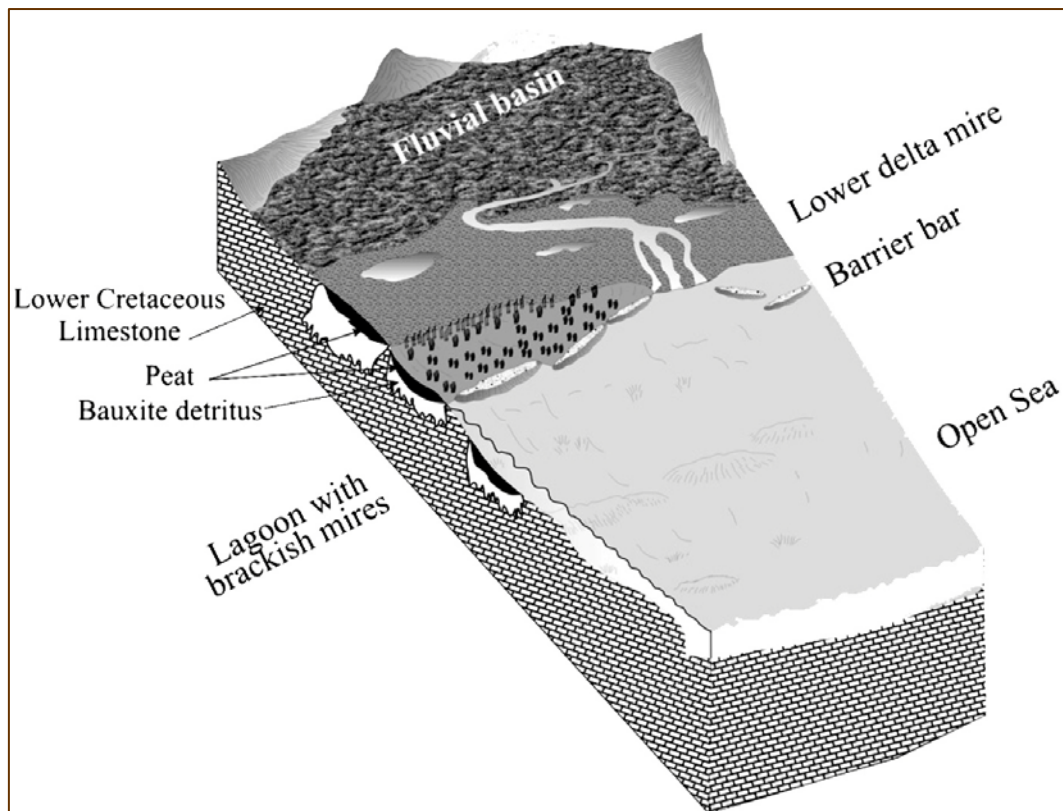
In particular, short-lived emergence episodes due to regression of the sea interrupted the marine sedimentation, resulting in exposure of the carbonate platform to freshwater alteration and development of karst. Bauxitic material, derived from erosion of lateritic bauxites exposed in the adjacent Pelagonian geotectonic Zone, was transported and deposited into the karst. The bauxite formation (bauxitization) is related to the coastal areas and to the times of beginning transgression. During three times of regression and uplift of the terrestrial hinterland, the laterites on ophiolites and surrounding rocks were reworked in the northeast and deposited as "laterite-derived facies" (LDF) in the southwest. Due to the rise of the ground-water level during the subsequent transgression, the LDF was transformed into bauxite. It is also believed that degradation of lateritic weathering crusts resulted in deposition of bauxitic material as talus and colluvium on the slopes, followed by reworking and transport by river systems.

Further diagenesis resulted in (i) leaching of silica and Fe under partly reducing conditions, and (ii) re-crystallization of Fe minerals and crystal growth of AlOOH (diaspore and/or boehmite) and TiO_2 (anatase) polymorphs. Additionally, intense supergene/epigenetic processes caused re-distribution of more mobile elements like Fe, Mn, Ba and Zn, which were precipitated, commonly as black crusts, in traps near the limestone footwall. The Fe minerals species and their location indicate several phases of Fe mobilization, (i) the first Fe mobilization and re-precipitation as hematite is contemporaneous with the crystallization of diaspore, (ii) a subsequent second mobilization of Fe under reducing and stagnating groundwater conditions resulted in the growth of Fe-sulfides (pyrite), which is followed by (iii) a final epigenetic Fe migration/epigenetic Fe bleaching related, most likely, to formation of Fe-depleted bauxite in the topmost part of the B3 horizon (Valeton, 1987; Valeton, 1994).

Moreover, it has been reported that the deposition of a coal layer lying unconformably over the B3 bauxite horizon, and covered by the Turonian–Senonian bituminous limestone, took place in a paralic sedimentary environment characterized by reotrophic, high groundwater-table (lacustrine) conditions for the peat forming stage except the uppermost part, which was affected by oxidizing conditions. The karst cavities of the footwall limestone, filled with bauxite during a period of sea regression, were suitable sites for the formation of

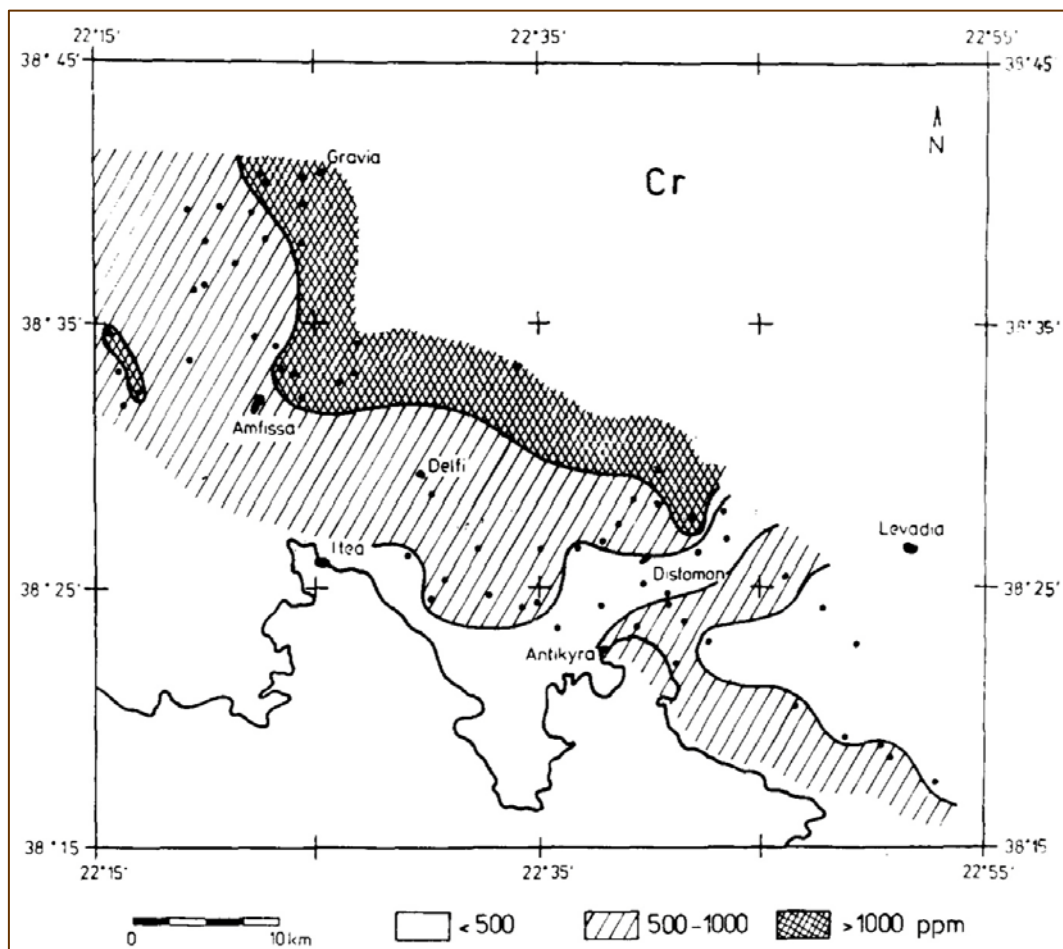
lagoons, possibly behind barrier bars formed on the shallow carbonate platform. Oxidation of the upper part of the pyrite-rich coal might result in bleaching of the bauxite by downwards penetrating acidic ($\text{SO}_4^{=}$ -containing) solutions. The oxidation was probably caused syngenetically at the palaeomire surface by the wave action of the transgressing sea or epigenetically in the coal layer by drainage waters. Either or both of the above mentioned effects may explain the contribution of coal to the formation of Fe-depleted bauxite (Kalaitzidis et al., 2010; see **Figure 1.3.12**). According to other authors, the driving force, for formation of Fe-depleted (grey-white, high-grade) bauxites, could be micro-organisms involved in biomineralization processes (Laskou & Economou-Eliopoulos 2007; Laskou et al., 2010; Laskou & Economou-Eliopoulos, 2013).

Figure 1.3.12: The depositional setting of the B3 bauxite horizon coal in the Parnassos-Ghiona area (Kalaitzidis et al., 2010).



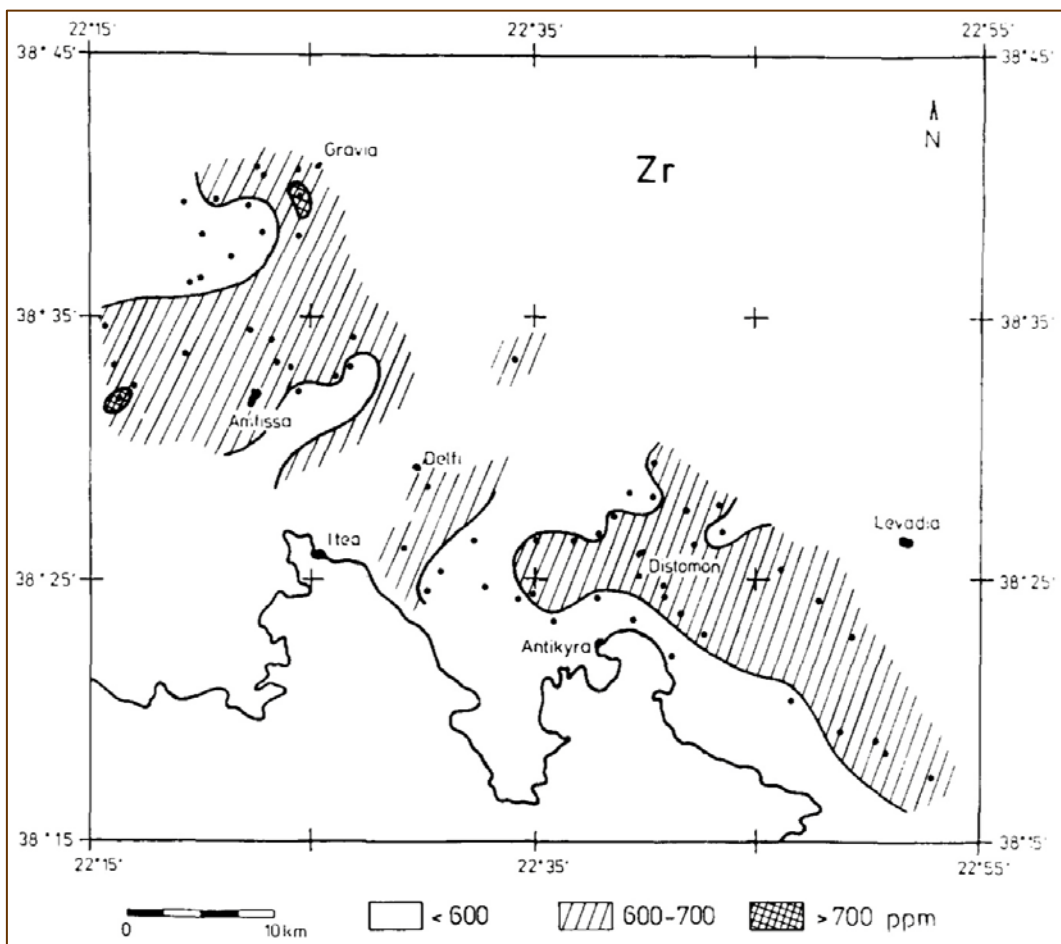
On the basis of the above, almost all investigators have concluded that Parnassos-Ghiona bauxite deposits are allochthonous. The bauxites of B2 and B3 horizons have a high content of several hundred to 2,400 ppm Cr, and also Ni, indicating the provenance to be the Jurassic serpentinites in the northeast, which are covered by Ni-laterite ores (Petrascheck, 1989). In this setting, the regional distribution of Cr, mainly related to detrital chromites (Cr-spinels), increases from southwest to northeast (Valeton, 1987; see **Figure 1.3.13**).

Figure 1.3.13: Cr distribution in the Parnassos-Ghiona karst bauxite deposits (Valeton, 1987).



However, [Valeton \(1985\)](#) and [Valeton \(1987\)](#), considering high contents of Th and REE as well as characteristic detrital minerals such as zircon (**Figure 1.3.14**), came to the conclusion that not only the ophiolites, but also Al-bearing felsic volcanic rocks were the source of the karst bauxites. In accordance, [Papastavrou & Perdikatsis \(1987\)](#), considering actinide and lanthanide analyses, agreed that both ophiolitic and acid volcanic rocks (most likely tuffs) of the Pelagonian Zone contributed to the formation of the Parnassos-Ghiona bauxites.

Figure 1.3.14: Zr distribution in the Parnassos-Ghiona karst bauxite deposits ([Valeton, 1987](#)).

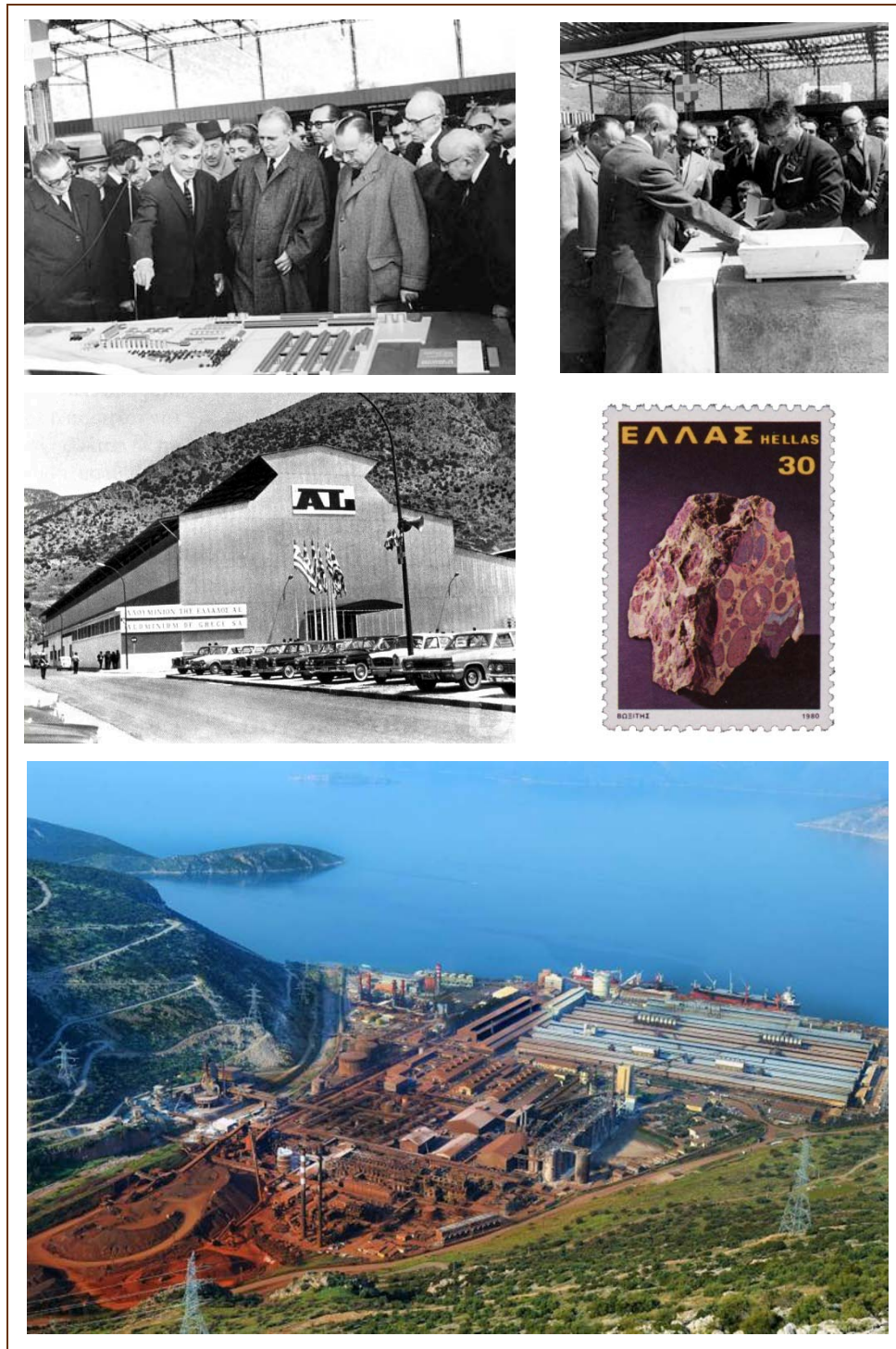


1.4. Parnassos-Ghiona bauxite mining and aluminium industry

Parnassos-Ghiona bauxite mining and aluminium industry of Greece is under private sector's exploration and exploitation. The exploitation of karst-type deposits in Parnassos-Ghiona area (central Greece) is currently performed by three Greek mining companies ("Aluminium S.A.", "S&B Industrial Minerals S.A." and "ELMIN Hellenic Mining Enterprises S.A."), whereas there is also an Al industrial plant installed at the coastal zone of the Corinth gulf. Of special interest is the fully modernized and highly automated industrial complex of "Aluminium S.A." (<http://www.alhellas.com>) at Antikyra area (Corinth Gulf), which is the largest vertically integrated Al producer in the E.U., covering an area of 1 Km² (**Figure 1.4.1**). The fully vertical production facility consists mainly of:

- (1) The area used for delivery of the raw material (bauxite).
- (2) The alumina refinery plant, which is among the largest metallurgical Al producers globally.
- (3) Other aluminium production plant facilities (e.g., electrolysis lines, production of electrodes, and smelter).
- (4) The on-site port facilities for large tonnage ships.
- (5) The on-site co-generation high-efficiency plant using natural gas. Of great environmental concern is the isolated area inside the industrial plant (**Figure 1.4.1**) complex for the disposal of the bauxite metallurgical residue after the Bayer process (http://www.umobit.com/Interactive_document/mytilineos/eN/Sustainability_Report_2010/index.html).

Figure 1.4.1: History of Greek aluminium industrial plant of Aluminium S.A. (former Aluminium of Greece) at the coast of Gulf of Corinth, based on exploitation of Parnassos-Ghiona deposits (<http://www.alhellas.com/>).



Nowadays, according to USGS, Greece is now considered to be the 16th alumina (Al_2O_3) producer in the world and the 4th among the European Union member-states, related to the exploitation of Al-ore (bauxite) deposits by Greek mining companies. Thus, Greece is the 12th bauxite producer worldwide, but also the largest in E.U. zone with an annual production of 2.1×10^6 metric dry tons in 2011. At the present time, the part of the Greek bauxite reserves, which could be economically produced, is estimated to be approx. 600×10^6 metric dry tons (Lee Bray, 2012). Most of the raw material is processed by Aluminium S.A. at its industrial complex at Antikyra (Gulf of Corinth) for the production of alumina (800×10^3 metric dry tons) and metallic Al (165×10^3 metric dry tons) to be used in industry and constructions (Tsirambides & Filippidis, 2012a; Tsirambides & Filippidis, 2012b). There are also ports where bauxite ore is concentrated and exported to both the Greek and global market (Figure 1.4.2).

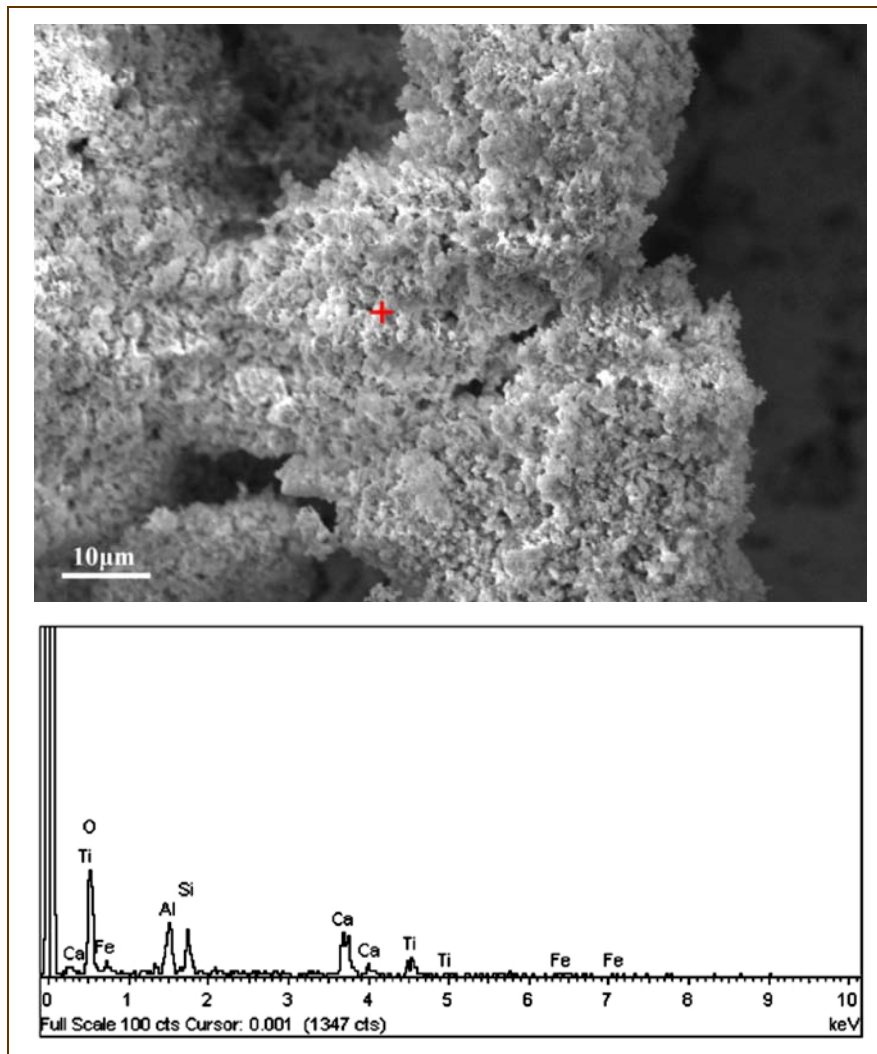
Figure 1.4.2: Port facilities of ELMIN S.A. in Ag. Marina at Maliakos gulf (upper image) and S&B S.A. at Corinth gulf (lower image).



Figure 1.4.2: continued.

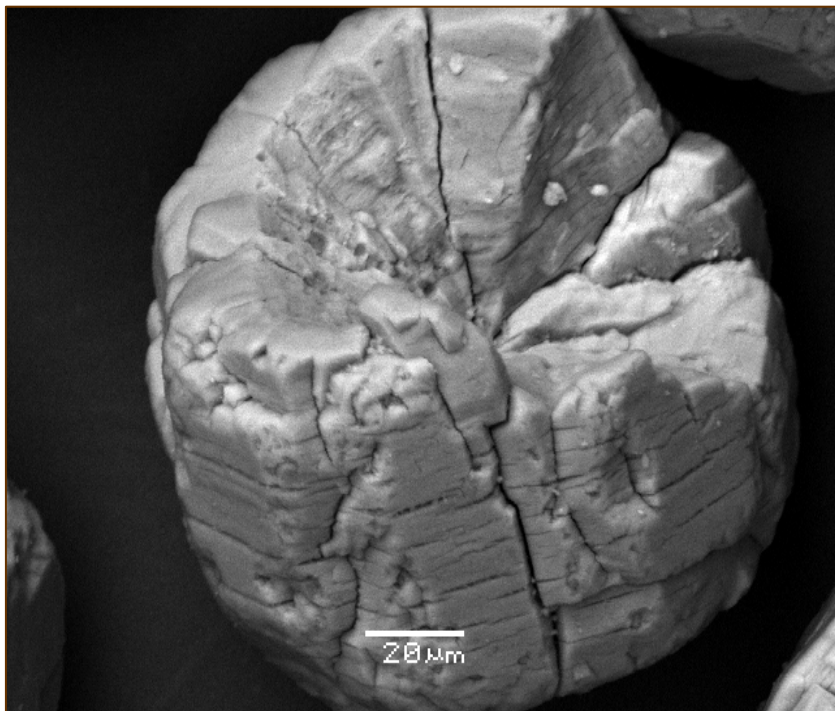
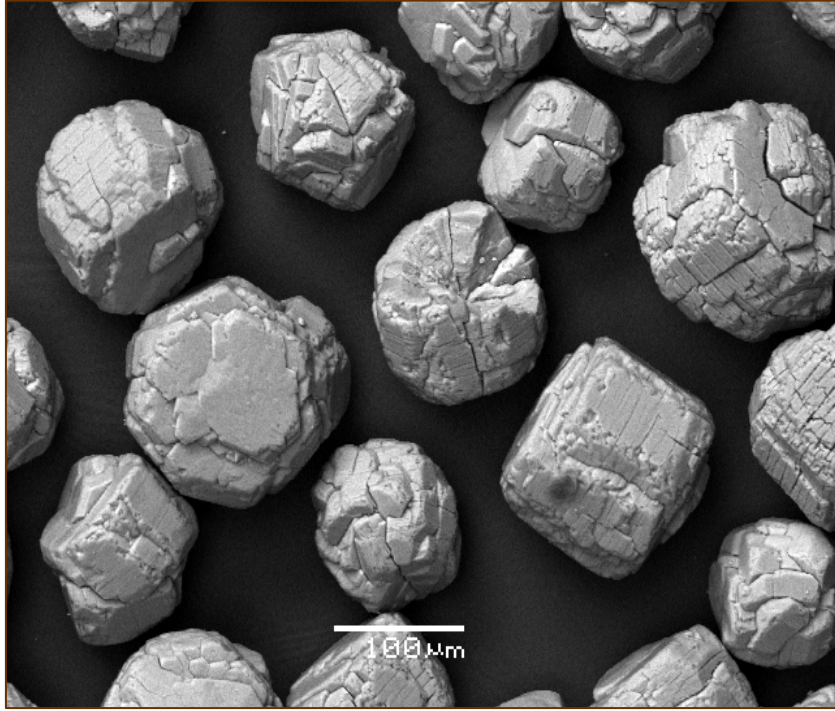
Worldwide, the refining of bauxite to alumina through the Bayer process results in production of huge quantities of a solid waste, the so-called “red mud”. It is estimated that 2 tons of red mud is produced per ton of alumina and that $60 - 120 \times 10^6$ tons of this residue are deposited every year by the global Al industry (e.g., [Burke et al., 2013](#); [Liang et al., 2014](#)). The handling of such quantities may occasionally cause severe environmental problems, such as the historical deadly accident occurred at the Ajkai Timföldgyár alumina plant (MAL Magyar Alumínium Zrt) near Ajka city, Veszprém County, Hungary, on Oct. 4th 2010 (e.g., [Schiermeier & Balling, 2010](#); [Enserink, 2010](#)). In that accident, it was proved that red mud acted as a source of V, and As in the environment ([Mayes et al., 2011](#); [Burke et al., 2012](#); [Burke et al., 2013](#)), whereas radioactivity issues, due to ^{232}Th , ^{238}U and ^{40}K , were also concerned ([Ruyters et al., 2011](#)). That also fosters debates on potential health effects due to respirable fugitive dust ([Gelencsér et al., 2011](#)). In Greece, the production of red mud (**Figures 1.4.3 & 1.4.4**) from the Aluminium S.A. processing plant is approx. $500 - 680 \times 10^3$ tons year⁻¹ ([Vavadakis et al., 2006](#); [Agatzini-Leonardou et al., 2008](#)).

Figure 1.4.3: SEM-EDS data for red mud (Agatzini-Leonardou et al., 2008).



During last decades, red mud was pumped through pipes from the Antikyra refinery to the sea bed of the Antikyra bay, Gulf of Corinth, Mediterranean Sea. However, Aluminium S.A. has recently carried out major investments for the installation of four filter presses, and exploration of the potential for the utilization of red mud in the production of other industrial materials, such as cements and ceramics (Tsakiridis et al., 2004; Pontikes et al., 2006; Pontikes, 2007; Vangelatos et al., 2009). Thus, after 2011, the company's goal to dispose all bauxite residues on land was achieved. However, millions of tons of Greek red mud still remain in the bottom of the sea in the Gulf of Corinth.

Figure 1.4.4: SEM image of alumina (crystalline Al_2O_3) produced in Greece (present dissertation).



1.5. Scale effect in ores and the role of mineral nanoparticles and nanominerals

In the last two decades, technological developments have revitalized a field in mineralogy emphasizing on the structure and reactivity of mineral surfaces (e.g., [Vaughan & Patrick, 1995](#); [Brady, 1996](#); [Godelitsas & Astilleros, 2010](#)). The combined use of advanced microscopic and spectroscopic techniques has enabled the study of physicochemical processes occurring in-situ and ex-situ at mineral interfaces on a molecular scale (nanoscale). Mineral surface science is closely associated to the fields of molecular geochemistry and biogeochemistry in that it investigates geochemical processes at the molecular level. Mineral surface science and molecular geochemistry contributed to the founding of nanogeoscience dealing with the study of nanoparticles in nature and the probe of geological processes in nanoscale (1 nm – 100 nm, see [Figures 1.5.1 & 1.5.2](#)). Moreover, accelerator-/Synchrotron-based techniques, including PIXE, NRA, RBS, SR-micro-XRF, SR-micro-XRD and micro-XANES/-EXAFS, provide with new opportunities to nanogeoscience being itself a revolution in Earth & Environmental Sciences by bringing together the macro-/micro- & nano-Worlds ([Hochella, 2002a](#); [Hochella, 2002b](#); [Hochella, 2006](#); [Miranda & Matsuoka, 2008](#); [Hochella, 2008](#); [Brenker & Jordan, 2010](#)).

Figure 1.5.1: Scaling of Earth's system; from gigascale system to nanoscale system ([Velde & Meunier, 2008](#)).

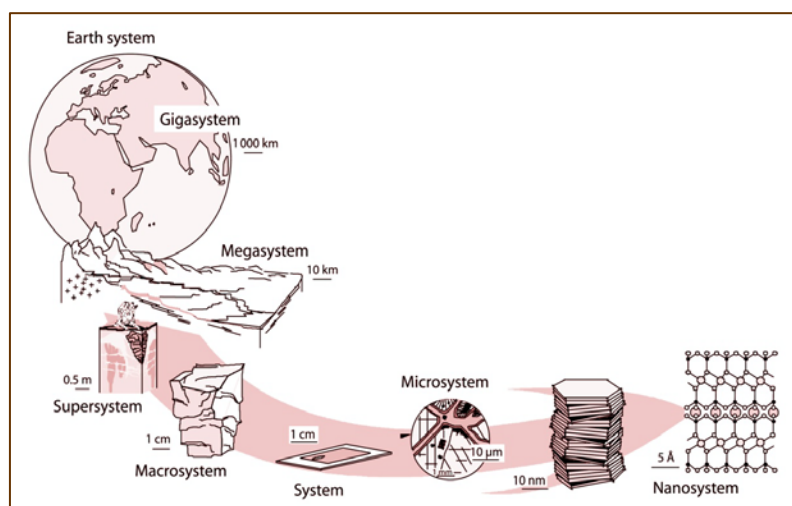
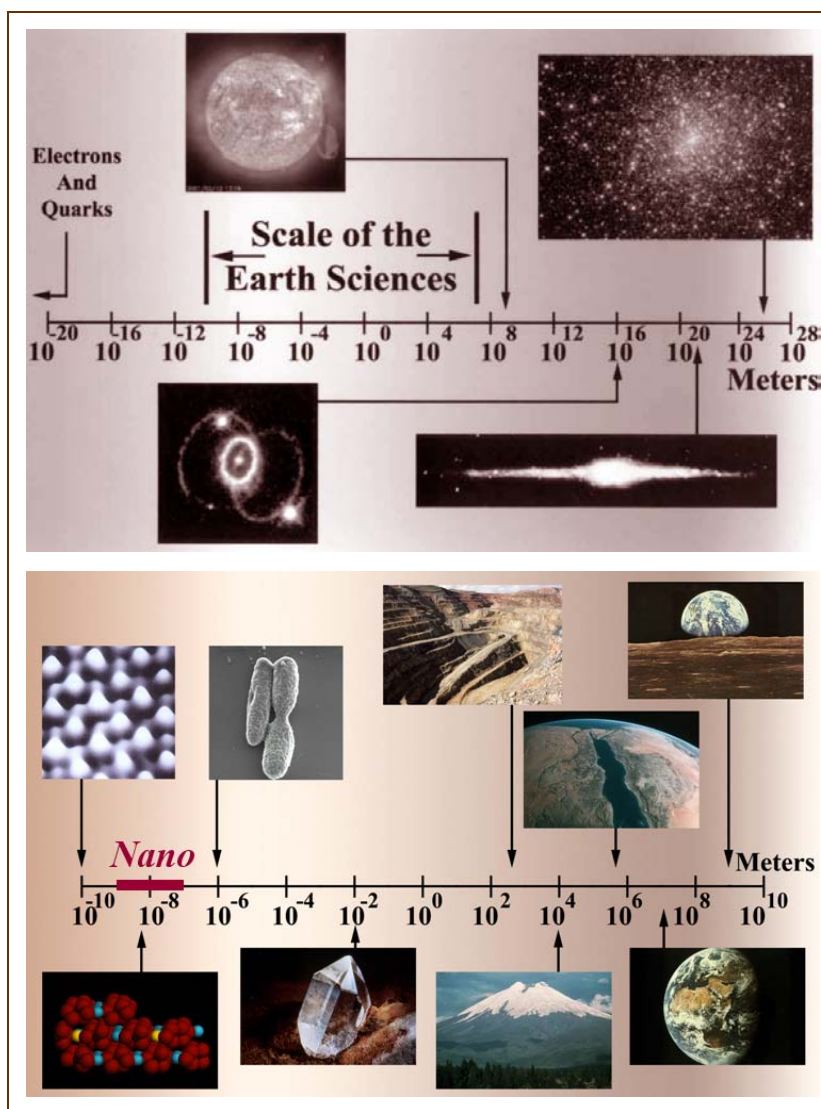
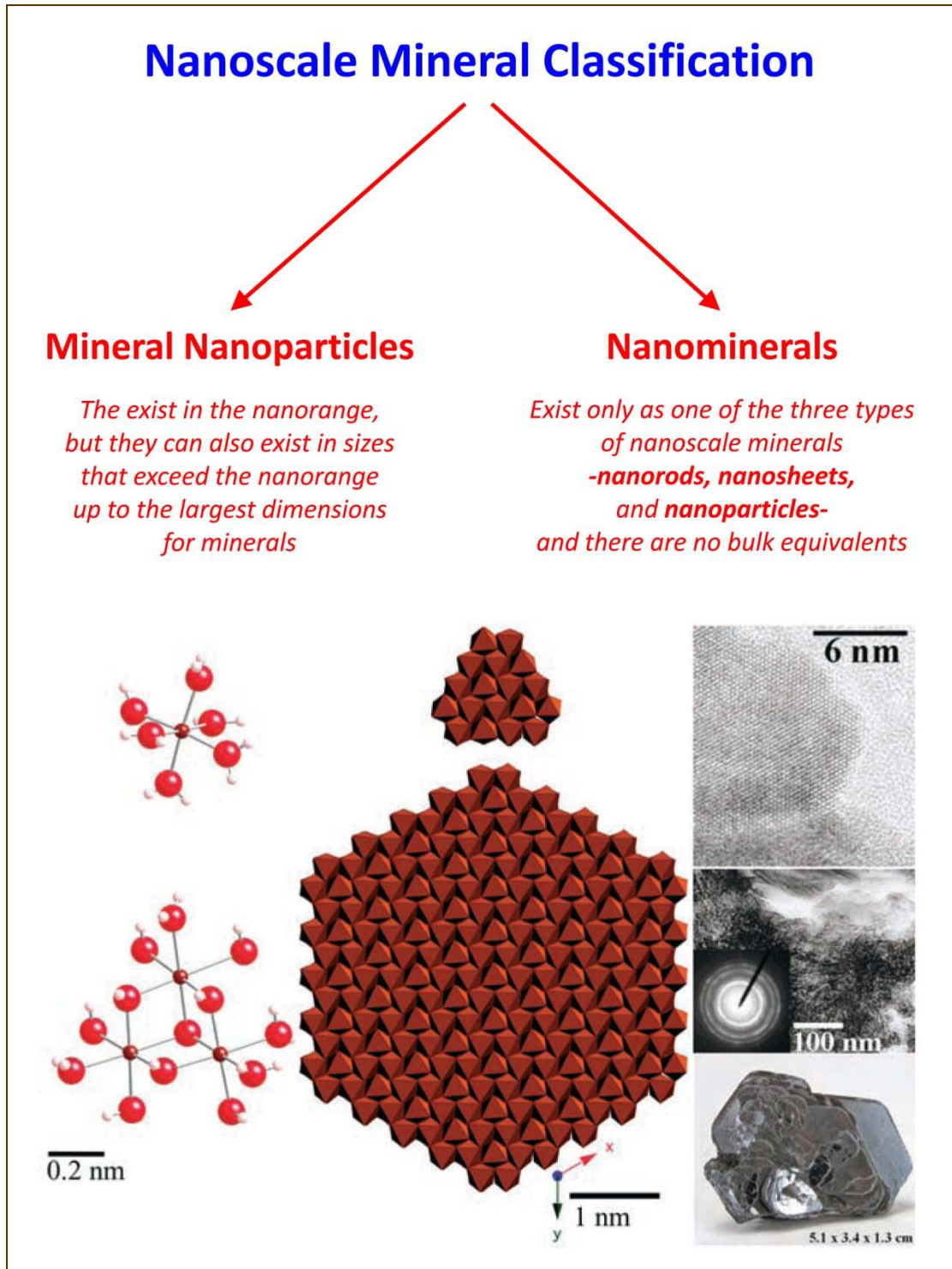


Figure 1.5.2: Scales in Science and Earth Sciences (Hochella, 2002a).



The role of nanogeoscience in solid-Earth science, and moreover in raw material resources, is greatly enhanced by the abundant presence of nanometer-sized crystalline minerals or even poorly-, non-crystalline minerals, such as mineral nanoparticles, and nanominerals in the geosphere (Hochella, 2008; Hochella et al., 2008a; Hochella et al., 2008b; see Figure 1.5.3). Mineral nanoparticles constitute the nanoscale-version of common minerals (exhibiting although different physicochemical properties compared to the micro- and macro-scale analogues), whereas nanominerals are distinct phases existing only in nanoscale without equivalents at larger scales (i.e., Waychunas, 2001; Udubasa et al., 2007;

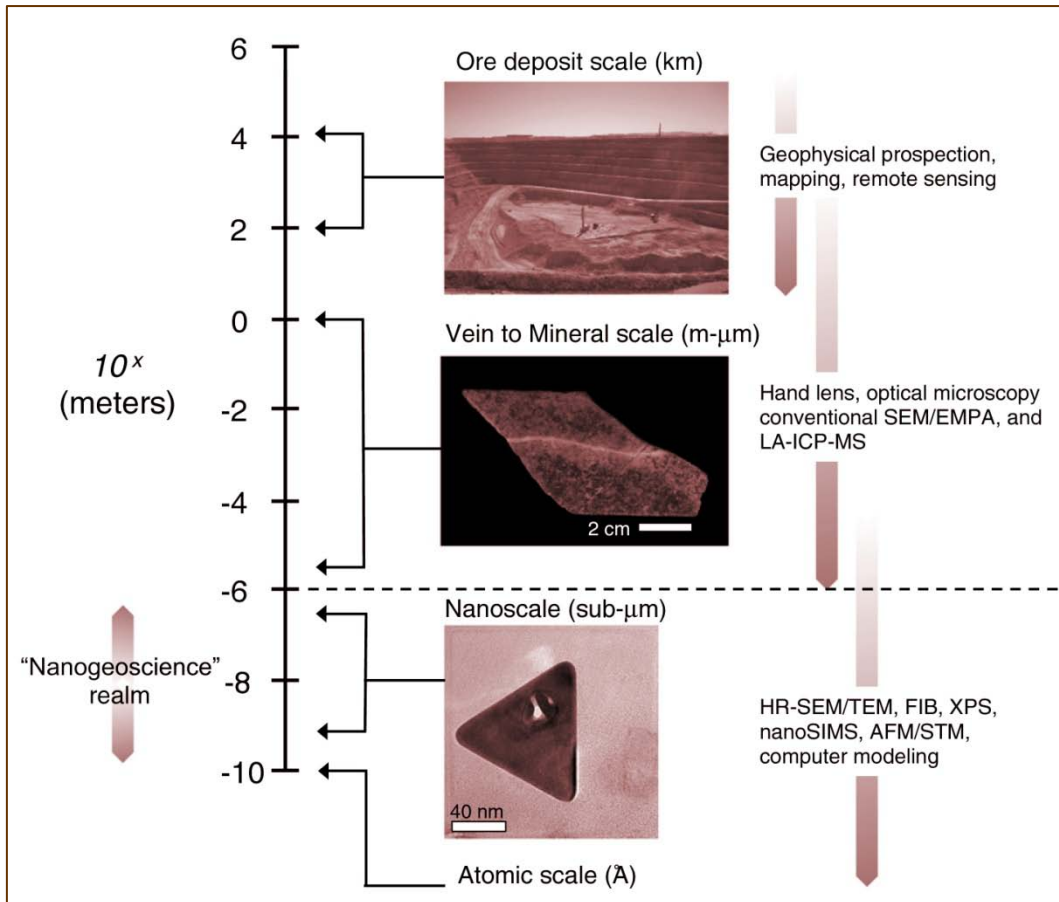
Figure 1.5.3: Mineral nanoparticles and nanominerals and the example of Fe^{3+} (Hochella, 2008; Hochella et al., 2008a; Hochella et al., 2008b).



Hochella et al., 2008a; Hochella et al., 2008b; Wauchunas & Zhang, 2008; Plathe et al., 2010). Moreover, Hochella et al. (2013) suggested that the classic definition of the term “mineral” has unquestionably to be redefined, upon to the deep knowledge of atomic structure. This is generated by the necessity of incorporation within that term of the entire understudied and unnoticed natural non-crystalline (amorphous) and poorly crystalline materials, which are also in abundance in the Earth’s regimes playing a crucial role in the understanding of the environmental mineralogy, nano-mineralogy and -geochemistry. Even well-known gemstones have to be re-considered, due to nanominerals giving their precious identity (Ma & Rossman, 2013). The study of well-, poorly-, and non-crystalline mineral nanoparticles and nanominerals, “the Earth’s last unexplored major geochemical components”, giving proof to nano-mineralogy and -geochemistry, will contribute to the future of Sustaining Earth, including the various types of ores providing metals to the modern industry, technology and humanity (Hochella, 2002c; Wang et al., 2003; Casey et al., 2005; Nadin, 2007; Xu & Barnad, 2008; Hochella et al., 2011; Hochella, 2012; Hochella et al., 2012). The environmental significance of mineral nanoparticles and nanominerals is now critically arising, due to their severe role to the dictation of toxic elements’ transformation in nature (e.g., Plathe et al., 2013).

The nanogeoscience, and particularly nano-mineralogy and nano-geochemistry, issues, have been apprehensively started to infiltrate into the economic geology field, revealing that large-scale ore systems may be controlled significantly by unknown parameters occurring in the nano-scale ore-processes (e.g., Reich et al., 2011, see **Figure 1.5.4**).

Figure 1.5.4: The dimensional scale of ore deposits research (Reich et al., 2011).



The necessity for considering different scales in the study of ore deposits has been recently approved by articles with regard to sulfides. For instance, it has been demonstrated that the old-standing problem of “invisible Au” in pyrite, arsenian pyrite and arsenopyrite, and of other elements (e.g., Ag, Pb and Te), as well as of “colloidal Au”, could finally be resolved by applying micro- and nano-mineralogy and -geochemistry methodologies (Palenik et al., 2004; Reich et al., 2006; Hough et al., 2008; Barker et al., 2009; Deditius et al., 2010; Hough & Noble, 2010; Koneev et al., 2010; Mayanovic et al., 2010; Weldt et al., 2010; Ciobanu et al., 2011; Deditius et al., 2011; Hough et al., 2011; Ciobanu et al., 2012; Hough et al., 2012; Pačevski et al., 2012). There are also scarce studies about nanoparticles of Zn-phases from disseminated mineralization of metasomatic rocks in the Dukat ore field in Russia (Filimonova & Trubkin, 2008), as well as about magnetite nanoparticles in the mineralized zones of the Pena Colorado Fe-ore deposit in Mexico (Rivas-Sánchez et al.,

2009), both indicating that the mineral macro- and nano-size dependence reflects to the formation stages of ore-forming systems. Besides, latest data yielded by Reich et al. (2013) thoroughly revealed the distribution of precious metals, metalloids and heavy metals in nano-scale of pyrite crystals from the Dexing porphyry Cu deposit (China). Furthermore, confirmatory evidences for the existence of PGE-bearing arsenide and sulfide nanocrystals of the Merensky Reef PGE ore deposit of the Bushveld complex in South Africa have been provided recently (Wirth et al., 2013). Additionally, a recent study (Helmy et al., 2013), provided convincing evidence that the preexisting noble metal nanophases, nanoclusters, and nanoparticles preceding the formation of stable phases in natural complex systems are the building blocks of them. Finally, the importance of nano-mineralogy and -geochemistry has been mentioned for phosphate ore deposits (Cosmidis et al., 2013).

The nano-mineralogical and -geochemical investigation of karst-type bauxite ore deposits has not been adequately demonstrated in the literature. Since the pioneering work by Bárdossy (i.e., Bárdossy & Mack, 1967; Bárdossy & White, 1979) who presented for first time TEM images of bauxite minerals from karst-type bauxites, only recently Gan et al. (2013) presented TEM images of *mineral nanoparticles* from karst-type bauxites of northern Europe and Jamaica. Bárdossy (1982) also presumed that colloid geochemistry (colloidal systems, i.e. nanoparticles) also rules the Al-ore (bauxite) deposits, which are in fact natural low-T inorganic nanomaterials consisting of dispersed-phase particles. Microscale investigation of Greek karst-type bauxite using LA-ICP-MS and Synchrotron-based techniques (μ -XRF and μ -XANES/-EXAFS) has been recently carried out, for first time in the literature, in the frame of the present dissertation. A relevant Zr *K*-edge XAFS investigation has been performed for non-karst type bauxite (lateritic) from Brazil, only (Douvallet et al., 1999).

1.6. Overview of previous work and scope of the present dissertation concerning Parnassos-Ghiona bauxite deposits and their metallurgical residues (red mud)

The main mineralogical and geochemical characteristics of the Parnassos-Ghiona bauxite deposits, together with the neighboring Marmara (Attica) bauxite deposits belonging to the same bauxite region of central Greece, have been described by several authors using various conventional microscopic and analytical methods, such as optical microscopy, SEM-EPMA, XRD, XRF, Fire-Assay/AAS/ICP and TGA/DTA (Kiskyras, 1960; Nia, 1968a; Nia, 1968b; Bárdossy & Pantó, 1971; Ochsenkühn & Parissakis, 1977; Augustithis et al., 1978; Bárdossy & Brindley, 1978; Bárdossy et al., 1978; Maksimović & Bish, 1978; Combes, 1979; Augustithis et al., 1980; Laskou, 1981; Ochsenkühn & Ochsenkühn-Petropoulou, 1982; Biermann, 1983; Arp, 1985; Paspaliaris, 1985; Kritsotakis et al., 1986; Papastavrou & Perdikatsis, 1987; Economopoulou-Kyriakopoulou, 1991; Laskou, 1991; Laskou & Economou, 1991; Perdikatsis, 1992; Ochsenkühn-Petropulu et al., 1994; Ochsenkühn-Petropoulou & Ochsenkühn, 1995; Laskou, 2001; Laskou & Andreou, 2003; Laskou, 2005; Laskou & Economou-Eliopoulos, 2005; Laskou & Economou-Eliopoulos, 2007; Solymár et al., 2005; Kalaitzidis et al., 2010; Papassiopi et al., 2010; Laskou et al., 2010; Laskou et al., 2011). More detailed characterization techniques, such as instrumental neutron activation analysis – INAA, carbon, sulfur and oxygen isotopic analysis have also been used (Laskou and Economou, 1991; Maksimović & Pantó, 1991; Ochsenkühn-Petropoulou et al., 1991; Ochsenkühn et al., 1995; Lympelopoulou, 1996; Ochsenkühn et al., 2002; Eliopoulos & Economou-Eliopoulos, 2010; Laskou & Economou-Eliopoulos, 2013). The presence of detrital zircons as well as chlorite group minerals and various REE mineral phases in the Parnassos-Ghiona bauxite samples has already been reported (Kritsotakis et al., 1986; Maksimović & Pantó, 1996; Ochsenkühn-Petropoulou & Ochsenkühn, 1995; Laskou, 2001; Laskou & Andreou, 2003; Laskou et al., 2011). In general, previous works on karst-type bauxites from the Mediterranean bauxite belt gave emphasis to trace element distribution of selective samples (Özlü, 1983) and to the conditions related to the genesis of the deposits (Valeton et al., 1987; Öztürk et al., 2002; Kalaitzidis et al., 2010).

Concerning Parnassos-Ghiona bauxites, except for the general geology, it is evident that only the basic (in macro- and micro-scale) mineralogy and geochemistry have been investigated. Thus, the main purpose of the present dissertation was to combine, for first time in the literature for karst-type bauxites of Greece and the globe, diffraction (PXRD), analytical in bulk and microscale (ICP-MS/OES, LA-ICP-MS), thermal (TGA/DTG, DSC), spectroscopic in bulk and microscale (FTIR, ⁵⁷Fe Mössbauer, high-resolution gamma-ray, Laser μ -Raman, SR μ -XRF, (μ)-XANES/(μ)-EXAFS), microscopic (optical, SEM-EDS/WDS), and nanoscopic (FEG TEM-EDS & EELS) techniques, together with magnetic susceptibility measurements, for the detailed mineralogical and geochemical characterization and the study of *mineral nanoparticles* and *nanominerals* in typical Fe-rich (low grade, red-brown) and Fe-depleted (high grade, white-grey, Al-rich: Al₂O₃ ca. 80 wt.%) from active mines of the Parnassos-Ghiona area, central Greece. Nanoscopy (e.g., [Brenker & Jordan, 2010](#)), related to nanogeoscience, is expected to play a crucial role in the exploration and exploitation of basic, noble and strategic metal resources. The above novel mineralogical and geochemical data were used to illustrate new insights into the origin of the deposits.

Furthermore, since the presence of actinide elements are of great concern in the metallurgical industry, the existence of Th in bauxite, and, especially, in the Greek karst-type bauxite, is already known from few previous studies containing, however, only bulk analytical data ([Adams & Richardson, 1960](#); [Papastavrou & Perdikatsis, 1987](#); [Ochsenkühn et al., 1995](#); [Ochsenkühn et al., 2002](#); [Laskou & Economou-Eliopoulos, 2007](#)). Despite the fact that Th could be penalty element in the metallurgy and radiotoxic for the environment, relevant papers regarding Th partitioning (element distribution among the mineral phases) in bauxite from Greece or any other place of the world are still absent. Consequently, another critical goal of the present dissertation was to give new insights, for the first time in the literature, into the partitioning of Th in Greek industrial bauxite by combining diffraction (XRD), bulk analytical (XRF, ICP-MS, X-ray spectroscopy), microscopic (SEM-EDS), and microscale-sensitive advanced spectroscopic techniques (Synchrotron μ -XRF and -XAFS as well as Laser-Ablation-ICP-MS). It should be emphasized that Synchrotron and laser-based techniques have never been applied for the study of Greek bauxites whereas, as far as we know, there is only one previous work with XAFS spectra with regard to Zr in non-karst type bauxite ([Duvallet et al., 1999](#)).

Finally, a relevant research was carried out, for comparison reasons, with regard to bauxite residues (red mud), in order to provide additional data which are of interest not only to the mining but also to the metallurgical industry and environmental technology. Previous works concerned the distribution of the discharged material onto the sea bed of the Antikyra Bay and the basic chemical composition (Varnavas et al., 1986; Varnavas & Achilleopoulos, 1995; Iatrou et al., 2010). Moreover, severe questions arise for the nature of actinides in the material due to previous papers indicating elevated radioactivity and potential release of radionuclides in the environment of the Antikyra Bay (Papatheodorou et al., 2005; Pontikes et al., 2006; Pontikes, 2007; Karagiannidi et al., 2009; Samouhos et al., 2013). With regard to the leachability of the material, the recovery of Ti, and Fe was attempted in previous works (Agatzini-Leonardou et al., 2008; Samouhos et al., 2013). The determination of REEs (lanthanides+Y+Sc) in Greek red mud, and the subsequent recovery of lanthanides, and Y in short time (24 h), using various acids (HNO₃, HCl, H₂SO₄) under moderate conditions of heating and pressure, have been reported (Ochsenkühn-Petropulu et al., 1994; Lympelopoulou, 1996; Ochsenkühn-Petropulu et al., 1996; Ochsenkühn-Petropoulou et al., 2002). The extraction using di(2-ethylhexyl)phosphoric acid in hexane resulted in the selective separation of Sc (Ochsenkühn-Petropulu et al., 1995). Additionally, the usage of chromatographic methods, using α -hydroxyisobutyric acid, gave evidence for separation of all REEs (Tsakanika et al., 2004). Similar experiments with sulfuric acid have been recently performed for red mud from India (Abhilash et al., 2014), whereas Liang et al. (2014) mentioned the importance of red mud acid-leaching towards fluoride adsorption. In the frame of present dissertation, emphasis was given to the mobility of metals and metalloids, including Th related to radioactivity, into Mediterranean seawater from Greece. Leaching tests with acetic acid, instead of typical TCLP, as recently proposed for red mud in case potentially hazardous elements (Rubinos & Barral, 2013), was applied for Th, REE, and selected HFSE (Nb, Ta), in long time intervals (2 weeks to 1 year). Similar leaching experiments were additionally performed -also for first time in the literature- using typical Greek bauxites, for comparison reasons. It should be mentioned that investigation of actinides, and namely of Th, aiming at the chemical behavior of the contaminant in the environment, has never been carried out with regard to red mud from Greece, despite previous reports indicating the problem in Japan (Sato et al., 1986) and, recently, in China (Gu & Wang, 2013; Qu & Lian, 2013). It is notable that, although Gu & Wang (2013) have

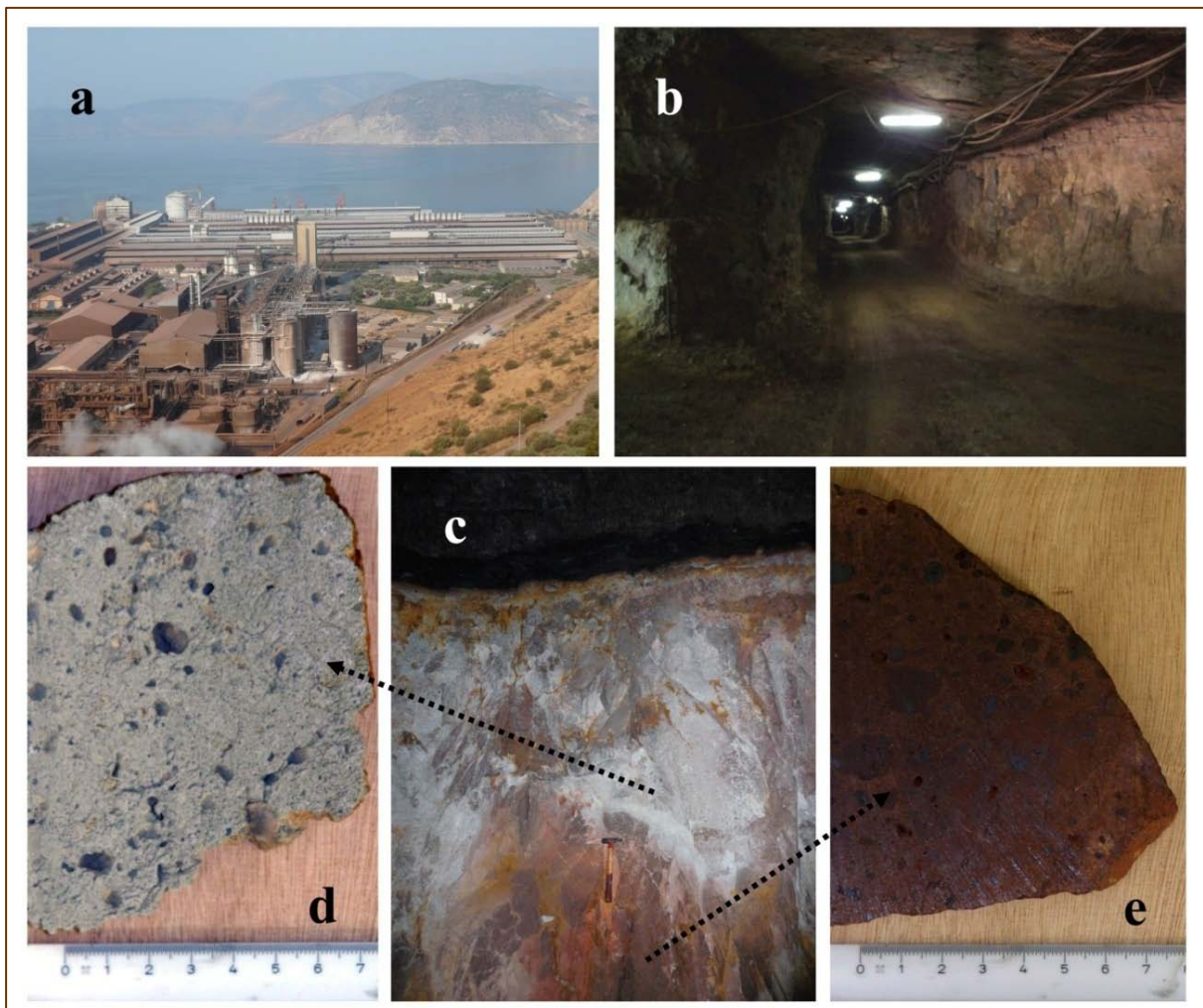
studied high-Th (88 – 257 ppm) red mud by TEM, they have not determined the “accessory” and/or “neo-formational minerals” hosting the actinide element. In addition, there was not any attempt in the literature to determine the structural environment of Th, particularly by XAFS, as it was performed by other authors in the case of other metals sorbed by Australian red mud (Collins et al., 2014). The final perspective of the present dissertation, additional to the study of bauxites, is to prospectively contribute to solutions of one of the world’s largest chronic problems, concerning the reuse of mining and mineral-processing wastes impacting the future of sustainable development (e.g., Bian et al., 2012). The criticality of global aluminum demand (Liu et al., 2011; Liu & Müller, 2013a; Liu & Müller, 2013b), resulting in expansion of aluminum industry and relevant solid wastes, enhances the necessity for detailed studies on the chemical, structural and environmental characteristics of red mud.

2. MATERIALS AND METHODS

2.1. Bauxite samples and preparation

The bauxite samples, used in the present study, are composite mining materials which were created by taking the appropriate number of specimens vertically at mining fronts along the underground mining sites and using standard mixing procedures and sample

Figure 2.1.1: The Aluminium S.A. plant (a); general view of the underground works leading to the mining front (b); underground mining front at Pera-Lakkos mine where the Fe-rich and Fe-depleted karst-type bauxite (together with footwall & hanging wall limestone and coal) was sampled (c); representative Fe-depleted (high-grade) white-grey bauxite (d) and Fe-rich (low-grade) red-brown bauxite (e) used in the present dissertation.



splitters. The investigated industrial bauxite samples were collected from underground mining sites (**Figure 2.1.1**) of the three Greek mining companies (“Aluminium S.A.,” “ELMIN Hellenic Mining Enterprises S.A.” and “S&B Industrial Minerals S.A.”) exploiting bauxite from the 2nd (intermediate: B2) and the 3rd (upper: B3) bauxitic horizon in the Parnassos-Ghiona area (central Greece).

All bauxite ore samples were crushed to appropriate size (**Figure 2.1.2**) and a further portion was sliced by diamond wheel for preparation of polished and thin-polished sections, and pulverized in WC mortar, for mineralogical and geochemical characterization.

Figure 2.1.2: Bauxite (and limestone) samples in the laboratory before mineralogical and geochemical characterization.



Additionally, representative bauxite samples from active mines of Balkan countries (i.e., Bosnia, and Montenegro) and Hungary, supplied by the Ajkai Timföldgyár alumina plant (MAL Magyar Alumínium Zrt) and provided by György Bárdossy† ([Bárdossy, 2011 – personal communication](#)) were investigated (**Figure 2.1.3**). In particular, bauxite samples from Bosnian mines (Jajce deposit), Montenegrin (Niksic deposit), and Hungarian (Halimba deposit) mining areas were simultaneously studied for comparison reasons.

Figure 2.1.3: Karst-bauxite samples from Balkan countries and Hungary used for comparison reasons in the present dissertation ([Bárdossy, 2011 – personal communication](#)).



2.2. Mineralogical and geochemical characterization of bauxite in macroscale (bulk)

2.2.1. Powder X-Ray diffraction (PXRD)

Bulk mineralogical composition was determined by means of powder X-ray diffraction (PXRD) using a Bruker AXS D8 ADVANCE Diffractometer. Powder XRD patterns were overnightly recorded ($\text{CuK}\alpha$ radiation, dwell time of 8 s per 2θ step with a step of 0.02°). The identification of mineral phases was initially obtained using the database from ICDD (International Centre for Diffraction Data) and the EVA software (BRUKER AXS). The semi-quantitative phase analysis was based on the “Reference Intensity Ratio” method (RIR-method) (De Wolff & Visser, 1964) and performed using the MATCH! version 1.9a software for phase identification from powder diffraction data. Furthermore, Rietveld method has attempted to define the lattice constants of the sample using the GSAS (Larson & Von Dreele, 2004) as well as the FullProf (Rodríguez-Carvajal, 1993) refinement software packages. Both the necessary good preparation of the bauxitic sample (i.e., appropriate grain size, homogeneous powder material on the XRD holder), and the fully rotation during the XRD measurement have been followed according to the literature (e.g., Perdikatsis, 1992).

2.2.2. X-Ray Fluorescence Spectrometry (XRF)

The bulk XRF analyses were performed using a Philips (now: PANalytical B.V.) MagiX PRO equipment, with Rh Anode at 3.6 kW, in University of Mainz (Germany) and under experimental conditions presented in **Table 2.2.2.1**. Additional XRF analyses, concerning specific lanthanides and actinides were also performed in PANalytical laboratories (Almelo, Netherlands) using an in-house X-ray Fluorescence/XRF equipment.

Table 2.2.2.1: Experimental conditions of bulk XRF analyses.

Nachweisgrenzen und Fehlerbetrachtung der Spurenelementeichung (Routineprogramm)

für das RFA-Spektrometer MagiXPRO, Fa. Philips, Bj 2002

Anode Rh, Anregungsleistung 3,6 kW

Präparation: unverdünnte Pulverpresslinge

Element	mittl. Konz. (ppm)	RMS (ppm)	LLD (ppm)	Messzeit Peak (sec)	max.Konz. der Eichung (ppm)	RMSrel (%)
Sc	32	1.6	2.7	40	60	5.0
V	317	8.1	6.1	40	600	2.6
Cr	289	6.8	5.3	30	400	2.4
Co	45	2.1	2.2	20	70	4.7
Ni	121	3.5	3.7	18	300	2.9
Cu	100	2.9	1.6	10	400	2.9
Zn	224	3.6	1.1	6	500	1.6
Ga	39	1	1	6	70	2.6
Rb	152	3.7	1.2	12	600	2.4
Sr	403	5.4	1.5	12	1500	1.3
Y	184	1.6	1.3	8	200	0.9
Zr	780	11	0.9	8	1200	1.4
Nb	110	1.3	1.1	10	300	1.2
Ba	800	22	10.5	40	2500	2.8
Pb	39	2.2	2.7	20	5000	5.6
Th	18.5	1.6	1.7	40	400	8.6
U	4.6	1.1	1.1	40	150	23.9

$$\text{RMS} = \frac{1}{n-1} \times \sqrt{\sum_{i=1}^N (X_i - \bar{X})^2} \quad (\text{root mean square})$$

$$\text{LLD} = \frac{n\sqrt{2}}{s} \times \sqrt{\frac{r_b}{t_b}} \quad (\text{lower limit of detection})$$

Verwendete Standards:

BIR-1	W-2	RGM-1	MAG-1	STM-1	SCO-1	DNC-1
SY-2	QLO-1	SGR-1	G-2	W-1	BCR-1	GSN
GSS-3	SO-4	AGV-1	BR	GSP-1	DR-N	BE-N
BHVO-1	NIM-G	NIM-S	SDC-1	JG-2	JB-2	AN-G
GSS-2	GSS-4	GSR-1	GSR-6	GSD-02	GSD-08	GSD-09
GSD-12	GSS-5	GSS-6	GSS-1	GSR-4	BCR-32	NBS278
NBS688	BX-N	AC-E	BM	NIST2710	SGD-1a	SG-1a
LKSD-4	JR-2	GXR-6	JR-1	JB-3		

Konzentrationen aus: K.Govindaraju, Special Issue of Geostandards Newsletters, July 1989

2.2.3. Inductively Coupled Plasma Mass Spectrometry (ICP-MS) and ICP-Atomic Emission Spectrometry (ICP-OES)

Bulk analyses for major and trace elements were performed using a Perkin Elmer ICP-OES and a Perkin Elmer Sciex Elan 9000 ICP-MS following a $\text{LiBO}_2/\text{LiB}_4\text{O}_7$ fusion and HNO_3 digestion of a 0.2 g sample. The chemical composition of investigated bauxite composited samples, was achieved using strict QA/QC procedures including, of course, three analytical replicates. Blanks (analytical and method), duplicates and standard geological and synthetic reference materials provided a measure of background noise, accuracy and precision. QA/QC protocol incorporates a granite or quartz sample-prep blank(s) carried through all stages of preparation and analysis as the first sample(s) in the job, a pulp replicate (REP) to monitor analytical precision, a -10 mesh reject duplicate (DUP) to monitor sub-sampling variation, a reagent blank (BLK) to measure background and an aliquot of In-house Reference Materials and Certified Reference Materials (CRM) to monitor accuracy. In-house Reference Materials were prepared and certified against internationally Certified Reference Materials (CRM), such as CANMET and USGS standards where possible, and they were externally verified at a minimum of three commercial laboratories. The QA/QC data, using four different Reference Materials (STD1, In-house Reference Material based on soil samples; STD2, In-house Reference Material, matrix of geological samples with additional elements spiked into the material; STD3, In-house Reference Material, based on geological samples; STD4, CRM from Ore Research & Exploration PTY Ltd. Australia for carbon and sulphur analyses), and appropriate blanks (BLK), are summarized in **Table 2.2.3.1**. Concentrations exceeding 5 % of the lowest sample concentration or 5 times the detection limit for that element, (whichever is higher) the blank reporting > DL were confirmed by re-analysis of the same solution. Elements whose concentration exceeded 5 times the detection limit and did not repeat values within 10 % were flagged and investigated. In that case, solutions were rerun and, if confirmed, the pulp material was retrieved from the sample to inspect the material for homogeneity and fineness. The process for evaluating reject reruns is the same as for pulp reruns except 30 % is the acceptable tolerance. If reported concentrations are higher than expected values, contamination may have occurred. Preparation blanks were used to monitor contamination only. Concentration of preparation blanks greater than 50 times the sample concentration should be rechecked by

first re-analysis of a group of samples followed by re-weighing, if the contamination is confirmed.

Table 2.2.3.1: QA/QC data concerning bulk chemical analyses of composite bauxite samples by ICP-MS.

Analyte	SiO₂	Al₂O₃	Fe₂O₃	MgO	CaO	Na₂O	K₂O	TiO₂	P₂O₅	MnO	Cr₂O₃	Sc	Ba	Co
Unit	%	%	%	%	%	%	%	%	%	%	%	ppm	ppm	ppm
MDL	0.01	0.01	0.04	0.01	0.01	0.01	0.01	0.01	0.01	0.01	0.002	1	1	0.2
STD1	58.25	14.08	7.58	3.33	6.34	3.68	2.13	0.69	0.82	0.39	0.545	25	499	26.2
STD1	58.12	14.09	7.62	3.34	6.36	3.68	2.15	0.69	0.83	0.39	0.546	25	497	26.7
STD1 Expected	58.47	14.23	7.67	3.35	6.42	3.71	2.17	0.69	0.83	0.39	0.55	25	514	26.2
BLK (Blank)	<0.01	<0.01	<0.04	<0.01	<0.01	<0.01	<0.01	<0.01	<0.01	<0.01	<0.002	<1	<1	<0.2
Analyte	Cs	Ga	Hf	Nb	Rb	Sn	Sr	Ta	Th	U	V	W	Zr	Y
Unit	ppm	ppm	ppm	ppm	ppm	ppm	ppm	ppm	ppm	ppm	ppm	ppm	ppm	ppm
MDL	0.1	0.5	0.1	0.1	0.1	1	0.5	0.1	0.2	0.1	8	0.5	0.1	0.1
STD1	6.7	17.1	9.3	20.5	27.8	15	398.4	6.8	9.9	16	200	14.5	278.3	30.5
STD1	6.5	17	9.5	20.4	27.5	14	398.7	6.8	9.7	16	200	14.6	278.1	30.5
STD1 Expected	7.1	17.6	9.8	21.3	28.7	15	407.4	7.4	9.9	16.4	200	14.8	280	31
BLK (Blank)	<0.1	<0.5	<0.1	<0.1	<0.1	<1	<0.5	<0.1	<0.2	<0.1	<8	<0.5	<0.1	<0.1
Analyte	La	Ce	Pr	Nd	Sm	Eu	Gd	Tb	Dy	Ho	Er	Tm	Yb	Lu
Unit	ppm	ppm	ppm	ppm	ppm	ppm	ppm	ppm	ppm	ppm	ppm	ppm	ppm	ppm
MDL	0.1	0.1	0.02	0.3	0.05	0.02	0.05	0.01	0.05	0.02	0.03	0.01	0.05	0.01
STD1	11.7	27.1	3.3	13.5	2.89	0.85	2.82	0.5	2.86	0.59	1.72	0.27	1.72	0.27
STD1	12	27.4	3.3	13.5	2.82	0.85	2.82	0.49	2.83	0.6	1.71	0.24	1.68	0.26
STD1 Expected	12.3	27.1	3.45	14	3	0.89	2.93	0.53	3	0.62	1.84	0.27	1.79	0.27
BLK (Blank)	<0.1	<0.1	<0.02	<0.3	<0.05	<0.02	<0.05	<0.01	<0.05	<0.02	<0.03	<0.01	<0.05	<0.01
Analyte	Mo	Cu	Pb	Zn	Ni	As	Cd	Sb	Bi	Ag	Au	Hg	Tl	Se
Unit	ppm	ppm	ppm	ppm	ppm	ppm	ppm	ppm	ppm	ppm	ppb	ppm	ppm	ppm
MDL	0.1	0.1	0.1	1	0.1	0.5	0.1	0.1	0.1	0.1	0.5	0.01	0.1	0.5
STD2	20.8	105.5	72.6	407	58.5	54.2	6.4	5	5	0.9	63.4	0.18	4.3	4
STD2 Expected	20.5	109	70.6	411	56	48.2	6.4	4.6	4.5	0.9	70	0.2	4.2	3.5
STD3	1.1	607.1	18.9	123	295.1	3.6	0.1	0.2	0.2	0.3	41.2	0.02	<0.1	0.6
STD3 Expected	0.9	600	19	119	281	4.2	0.09	0.13	0.18	0.3	43	0.03	0.07	0.54
BLK (Blank)	<0.1	<0.1	<0.1	<1	<0.1	<0.5	<0.1	<0.1	<0.1	<0.1	<0.5	<0.01	<0.1	<0.5
Analyte	C	S												
Unit	%	%												
MDL	0.02	0.02												
STD4	0.17	18.85												
STD4 Expected	0.16	18												
BLK (Blank)	<0.02	<0.02												

2.2.4. Fourier Transform Infrared Spectrometry (FTIR)

Fourier-transformed infrared spectroscopy (FTIR) was used to characterize the investigated samples. FTIR measurements were carried out with a Bruker IFS 113v Fourier transform spectrometer. Samples were powdered using an agate mortar, in order to reach a mean grain size of 20 μm . The IR spectra were being collected in the transmittance mode and were obtained in the mid-infrared FTIR (Mid-IR) region (4000-400 cm^{-1}) and in the far-infrared (Far-IR) region (400-200 cm^{-1}), respectively. For the Mid-IR region a specific amount (0.8 mg) of each powdered sample was mixed with KBr powder (250 mg) and pressed into pellets in a vacuum press under 7 kbar pressure for accurate time of 60 s and a spectrum of a freshly KBr pellet was used as background whereas, for the Far-IR region, an amount (1.5 mg) of each powdered sample was mixed with CsJ powder (300 mg) and pressed into pellets in a vacuum press under 7.5 kbar pressure for 60 s and a spectrum of the CsJ pellet was used as background, as well. For each spectrum, 32 scans were recorded with a resolution of 2 cm^{-1} , in room temperature conditions.

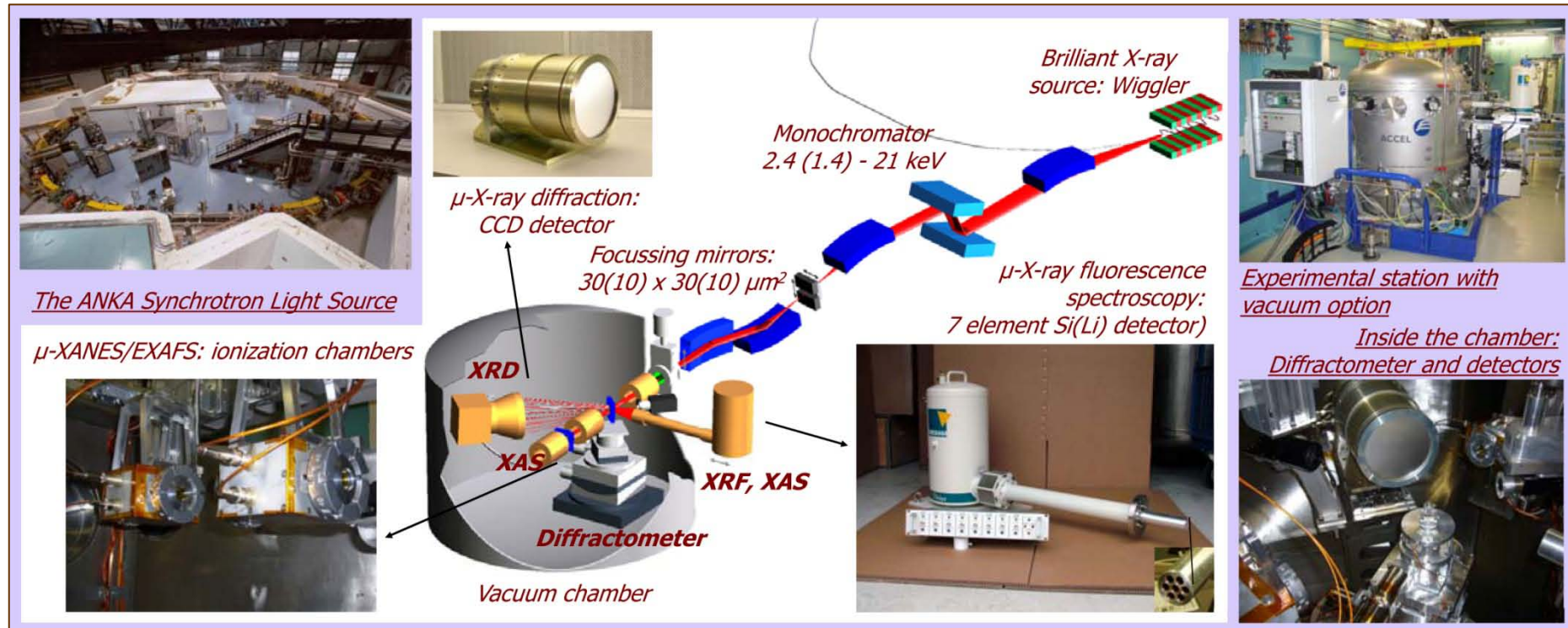
2.2.5. Thermo-Gravimetric Analysis (TGA) and Differential Scanning Calorimetry (DSC)

Thermal characterization of bauxite samples was evaluated with Thermo-Gravimetric – Differential Scanning Calorimetry (TG-DSC) simultaneous analyses, performed with a Setaram thermogravimetric-differential thermal analyzer SETSYS 16/18-TG-DSC (1750 $^{\circ}\text{C}$ rod). After powdering in agate mortar in order to reach a mean grain size of 20 μm , samples (80 mg) were placed in alumina crucibles, while an empty alumina crucible was used as reference. Samples were heated from ambient temperature up to 1000 $^{\circ}\text{C}$, with a heating rate 10 $^{\circ}\text{C min}^{-1}$, in argon atmosphere.

2.2.6. Iron-57 Mössbauer Spectroscopy

^{57}Fe Mössbauer spectra of the samples were recorded in transmission geometry at 300 K, 200 K, 180 K, 77 K and at 10 K, using a constant-acceleration Mössbauer spectrometer equipped with a ^{57}Co (Rh) source kept at room temperature (RT).

Figure 2.2.9.1: The SUL-X beamline, for combined μ -XRF, μ -XAFS and μ -XRD investigation, at the ANKA Synchrotron facility (KIT, Germany).



2.2.7. Magnetic Susceptibility

The susceptibility measurements were conducted on an AGICO MFK1 kappabridge with cryostat and furnace attachments, allowing acquisition over a temperature range from approximately -200 deg C to 700 deg C in an AC field of 200 A/m and a frequency of 976 Hz. Multiple specimens of powdered bauxite were analyzed, some in heating runs that spanned the full temperature range, and others in more complex sequences which iteratively heated the same sample to initially moderate and then progressively higher temperatures, cooling between each run. Heating runs were conducted in air to minimize the formation of reduction products (notably magnetite) that may be produced from natural samples in 'inert' argon atmospheres.

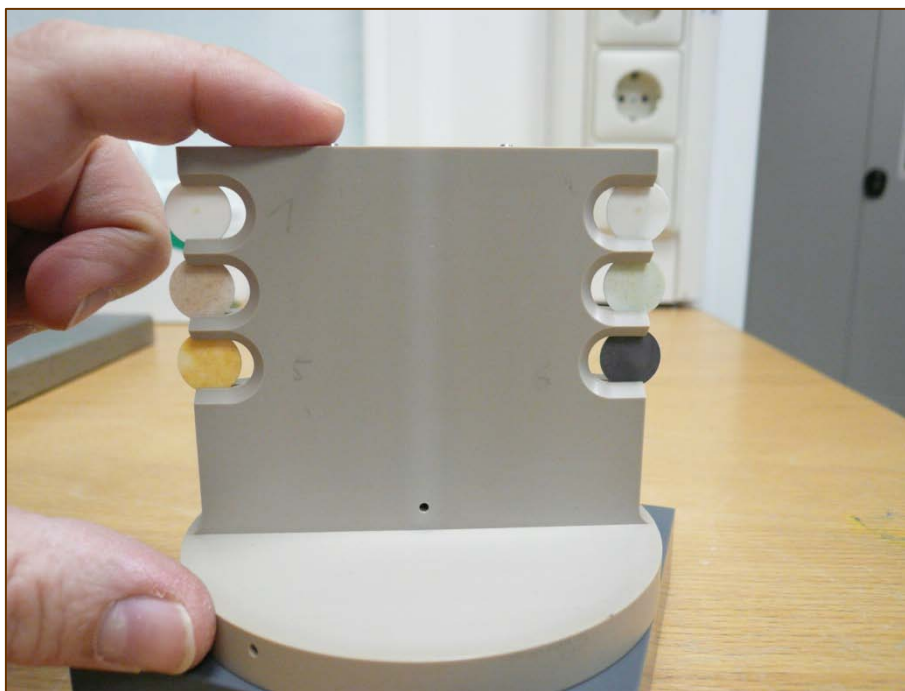
2.2.8. Gamma-Ray Spectrometry (HPGe)

HP γ -ray spectra, of red mud and bauxite samples towards the determination of natural radionuclides and radioactivity (total dose rate) were performed using a Canberra system with High-purity Germanium (HPGe) Detector.

2.2.9. Synchrotron Radiation (SR) measurements in bulk (XAFS: XANES / EXAFS)

Bulk XAFS spectroscopic study of bauxite and red mud samples was performed at the SUL-X beamline of ANKA Synchrotron Radiation Facility (e.g., [Göttlicher et al., 2006](#); [ANKA Instrumentation Book, 2012](#); KIT, Germany; [Figure 2.2.9.1](#)) using powder of the material into pressed with cellulose to pellets ([Figure 2.2.9.2](#)). Bulk XAFS data were obtained for Th in Fe-depleted bauxite (for comparison to μ -XAFS spectra; see text below), as well as for Fe in representative Fe-rich and Fe-depleted samples. Concerning Th, data were obtained at the Th L_{III} -edge (16,300 eV) and at the Fe K -edge (7,112 eV), respectively. For the Th L_{III} -edge XAFS spectra thorium compounds ($\text{Th}(\text{NO}_3)_4 \cdot 4\text{H}_2\text{O}$ and ThO_2) and minerals containing Th impurities, such as zircon (ZrSiO_4), were used as reference materials.

Figure 2.2.9.2: Bulk XAFS spectroscopic study of bauxite and red mud samples using powder of the material into pressed with cellulose to pellets at the SUL-X beamline of the ANKA Synchrotron facility (KIT, Germany).



Spectra were measured at the Th L_{III} -edge (16,300 eV; energy was calibrated using Y metal foil) and processing was performed using initially the ATHENA (Ravel & Newville, 2005) and, furthermore, the EDA (Kuzmin, 1995) software packages for the XANES and EXAFS processing and evaluation. The EXAFS signal corresponding to the first main peak in Fourier transforms (FTs) was isolated using the Fourier filtering procedure. The range of the back-FT was 1 – 3 Å for $\text{Th}(\text{NO}_3)_4 \cdot 4\text{H}_2\text{O}$ and 0.8 – 2.5 Å for other samples. Thus, obtained EXAFS signals were best fitted using two different approaches, namely, the conventional Gaussian model and the regularization method (Kuzmin & Purans, 2000). The theoretical backscattering amplitude and phase shift functions for Th-O were used in the simulations. They were calculated by the *ab initio* FEFF8 code (Ankudinov et al., 1998) using a complex Hedin-Lundqvist exchange-correlation potential accounting for inelastic effects. Additionally, data were obtained at the Fe K -edge (7,112 eV), and at the Th L_{III} -edge (16,300 eV), respectively.

In the case of Fe, XAFS spectra of the studied samples were measured at the Fe *K*-edge (7,112 eV). Taking into account the importance (Manceau & Gates, 1997) of the usage of references and compounds with quite similar electronic properties and expected analogous crystalline structure as the investigated bauxite selected crystalline references and standards with known iron oxidation state (e.g., Waychunas et al., 1983; Bajt et al., 1994; Manceau & Gates, 1997; Dyar et al., 1998; England et al., 1999; Wilke et al., 2001; Quartieri et al., 2002; Berry et al., 2003; Sánchez del Río et al., 2005; Arčon et al., 2007; Hurai et al., 2008; Sigrist et al., 2011; Oakes et al., 2012; Regelink et al., 2014), such as natural Fe³⁺-oxide (pure-grey hematite: α -Fe₂O₃), synthetic Fe³⁺-oxyhydroxide (goethite: α -FeOOH), and natural mixed-valence (Fe³⁺/ Σ Fe \neq 1) iron oxide (magnetite: Fe²⁺Fe³⁺₂O₄) as well as synthetic Fe²⁺-standards by Merck Inc. (Fe(II)-chloride: Fe²⁺Cl₂•4H₂O; Fe(II)-sulfate: Fe²⁺SO₄•7H₂O), were used for Fe *K*-edge XANES spectra analysis. Energy was calibrated to 7,112 eV (1st derivative of the Fe *K*-edge, Fe metal foil). XAFS data for the references and the studied bauxite sample were measured at both transmission and fluorescence mode. XAFS processing and evaluation was performed using the Athena (Ravel & Newville, 2005) software package.

Herein, it should be mentioned that the qualitative results with regard to the Fe oxidation state of the studied bauxite were not approached by the peak fitting procedure (e.g., Calas & Petiau, 1983; Westre et al., 1997; Galois et al., 2001; Wilke et al., 2001; Quartieri et al., 2002; Berry et al., 2003; Hurai et al., 2008) of the characteristic pre-edge features of the experimental Fe *K*-edge XANES spectra, inasmuch the precise evaluation of bonding environment and local distortion around Fe is still too difficult for this kind of condensed glassy-like material, and beyond the scope of the paper. Objectively, relevant difficulties can be assigned either to several differences in site symmetries between references and studied sample or to uncertainties related to “accuracy & reproducibility” factors associated with the monochromator’ motors and, in general, this is a complicated approach that requires ab initio Full-Multiple-Scattering simulations. As the feasibility and reliability of the determination of Fe oxidation state using the Fe *K*-edge XANES analysis – alternatively without any peak fitting procedure- has been successfully investigated (Arčon et al., 2007), mentioning that the proper usage of references with similar structure, and same type of neighboring atoms around the Fe absorbing atom arranging in similar local symmetry plays a crucial role for that, of particular interest was to examine the shifting of the energy position

of pre-edge features -between the Fermi energy and the threshold- of the bauxite together with the proper Fe-references and, subsequently to reliably determine its Fe valence.

Thus, the determination of the valence state of iron in the bauxite was approached by the relationship between published XANES data of mixed-valence magnetites ([Bajt et al., 1994](#); [Berry et al., 2003](#)) and the relative energy shift of pre-edge features, and not the edge shift, as it is disturbed by EXAFS oscillations. The energy of pre-edge features, which is due to the $1s \rightarrow 3d$ transition, is more or less related to the bottom of the conduction band (e.g., 1st hole, relaxation effects etc.), which is sensitive to the effective charge (valence) of iron. Besides, it is powerful precise tool for the determination of the Fe oxidation state as $3d$ crystal field levels are more tightly bound and, thus, less sensitive to effects that can cause changes in the local environment (e.g., [Waychunas et al., 1983](#); [Manceau et al., 1992](#); [Bajt et al., 1994](#); [Westre et al., 1997](#); [Wilke et al., 2001](#); [Berry et al., 2003](#); [Henderson et al., 2014](#)).

2.2.10. Stable isotope ratio analyses ($\delta^{18}\text{O}$ and $\delta^{13}\text{C}$)

The oxygen and carbon stable isotope ratios were measured, in footwall (ALM0306_PL1_WLS) and hanging wall (ALM0306_PL1_DLS1 & DLS2) limestones of the Pera Lakkos underground mine, using a VG Micromass 903 Ratio Mass Spectrometer (analyzer vacuum $<1 \times 10^{-6}$ Torr). Carbonate-bearing rocks (i.e. limestones) were converted to CO_2 by reaction with 100% H_3PO_4 at 50 °C. $\delta^{18}\text{O}$ and $\delta^{13}\text{C}$ of the CO_2 were determined by SIRA with a suitable correction applied to the oxygen ratio to adjust the oxygen isotopic fractionation.

The $\delta^{13}\text{C}_{\text{PDB}}$ value of the CO_2 is calculated as follows:

$$\delta^{13}\text{C}_{\text{PDB}} = [1.0673 * (\delta^{13}\text{C-ZE}^{13}\text{C}) - 0.0336 * (\delta^{18}\text{O-ZE}^{18}\text{O})] + [\delta^{13}\text{C}_{\text{PDBstd}}] + [1.0673 * (\delta^{13}\text{C-ZE}^{13}\text{C}) - 0.0336 * (\delta^{18}\text{O-ZE}^{18}\text{O})] * [\delta^{13}\text{C}_{\text{PDBstd}}] / 1000$$

The $\delta^{18}\text{O}_{\text{SMOW}}$ value of the CO_2 is calculated as follows:

$$\delta^{18}\text{O}_{\text{SMOW}} = 1.03086 * \delta^{18}\text{O}_{\text{PDB}} + 30.86$$

and,

$$\delta^{18}\text{O}_{\text{PDB}} = [1.0010 * (\delta^{18}\text{O-ZE}^{18}\text{O}) - 0.0021 * (\delta^{13}\text{C-ZE}^{13}\text{C})] + [\delta^{18}\text{O}_{\text{PDBstd}}] + [1.0010 * (\delta^{18}\text{O-ZE}^{18}\text{O}) - 0.0021 * (\delta^{13}\text{C-ZE}^{13}\text{C})] * [\delta^{18}\text{O}_{\text{PDBstd}}] / 1000$$

where $\delta^{13}\text{C}$ and $\delta^{18}\text{O}$ are the delta values of the sample relative to the COR-0101 working reference gas, ZE^{13}C and ZE^{18}O are zero enrichment corrections (which are usually zero) and $\delta^{13}\text{C}_{\text{PDBstd}}$ (0.05 ‰ PDB) and $\delta^{18}\text{O}_{\text{PDBstd}}$ (1.8‰ PDB) are the values relative to PDB of the COR-0101 working reference gas. The internal standard deviations of the results should be less than +/- 0.2 ‰. If the standard deviations are unusually high, or if any non-random signals are observed in the analysis trace, repeat the analysis of the gas.

2.3. Mineralogical and geochemical characterization of bauxite in microscale

2.3.1. Optical Microscopy

Both typical Fe-rich and Fe-depleted bauxite samples were investigated in polished and polished-thin sections. All bauxite samples were investigated in polished sections using a Zeiss Axio Imager.Z1m (with AXIOVISION 4.7 software) motorized optical microscope in transmitted and reflected light.

2.3.2. Laser micro-Raman (Laser μ -Raman)

The Laser μ -Raman spectra were obtained on the polished-thin sections using Renishaw Ramascope RM 1000 equipment with a HeNe laser at 633 nm, a spectrometer with a grating of 1800 lines/mm, and a CCD Peltier-cooled detector. The laser beam diameter was adjusted depending on resolution requirements. In any case, its maximum energy did not exceed 4mW. Moreover, Laser micro-Raman spectra were additionally obtained, prior to Synchrotron study (see text below) on polished sections using a Kaiser RXN1 Analyzer portable Laser micro-Raman spectrometer equipped with two-wavelength excitation lasers (at 532 nm and 785 nm).

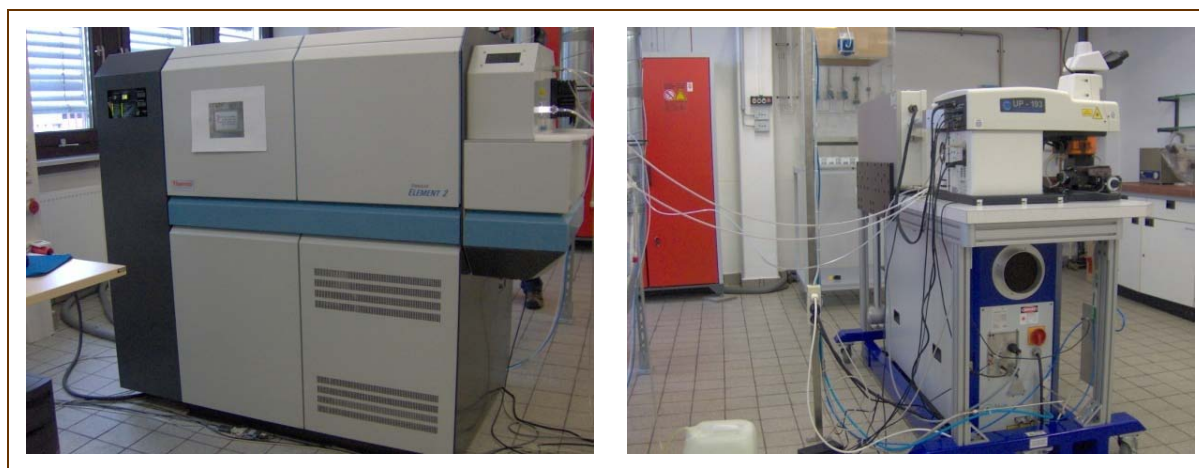
2.3.3. Scanning Electron Microscopy-Energy Dispersive Spectrometry/Wavelength Dispersive Spectrometry (SEM-EDS/WDS)

Details of mineralogical and chemical composition in microscale were obtained using a Jeol JSM-5600 scanning electron microscope (SEM) equipped with an Oxford Instruments INCA EDS and also a 20 kV FEI Quanta 200 FEG SEM equipped with both EDS and WDS. The acquisition of EDS and WDS spectra and their analyses were performed with INCA software. Variations of Al, Fe, Ti and Cr contents were performed with linescan analysis and quantified using a database of measurements given by the manufacture (i.e., standardless analysis).

2.3.4. Laser-Ablation Inductively Coupled Plasma Mass Spectrometry (LA-ICP-MS)

According to SR μ -XRF (see text below), distinct mineral phases hosting Th, were point-analyzed for trace element distribution by means of Laser Ablation Inductively Coupled Plasma Mass Spectrometry / LA-ICP-MS at WWU Münster, Germany (Engvik et al., 2009; **Figure 2.3.4.1**).

Figure 2.3.4.1: The LA-ICP-MS facility at WWU Münster (Germany).



Sample ablation for trace elements analysis has been done with a 193 nm ArF excimer laser (UP193HE, New Wave Research). The energy density was $\sim 9 \text{ J/cm}^2$ and the laser repetition rate was set to 5 Hz. Depending on the size of the distinct mineral phases the beam spot diameter was varied from 12 to 25 μm . Elemental analysis has been carried out with an Element 2 mass spectrometer (ThermoFisher). Gas-flow rates were 0.73 l/min for the He carrier gas, 0.99 l/min and 1 l/min for the Ar-auxiliary and sample gas, respectively. Cooling gas flow rate was set to 16 l/min. Before starting measurements, the system was tuned on the SRM 612 standard glass from NIST to ensure high sensitivity and stability of the signal. A total of five (5) elements were analyzed using the NIST 612 glass as an external standard, and ^{49}Ti as internal standard. Groups of five (5) spots on a given sample were bracketed with 2 calibration standards on both sides, to follow instrumental drift. The overall measuring time for a single spot analysis was 60 s (20 s for background and 40 s for

the peak signal). Concentrations of measured elements were calculated using the Glitter software (Jackson, 2001).

2.3.5. Synchrotron Radiation (SR) measurements in microscale (μ -XRF, μ -XAFS: μ -XANES / μ -EXAFS)

Synchrotron radiation (SR) micro-X-ray Fluorescence (μ -XRF) and micro X-ray Absorption Fine Structure (μ -XAFS) spectra were obtained using powders (for reference materials) and polished sections of the bauxite samples (**Figure 2.3.5.1**) in the X-ray beamline of the Laboratory for Environmental Studies (SUL-X) of ANKA Synchrotron Radiation Facility, KIT, Germany (e.g., Göttlicher et al., 2006; ANKA Instrumentation Book, 2012). The μ -XAFS spectra in the case of polished sections were obtained in micro-areas previously selected on the basis of optical microscopy, Laser μ -Raman and elemental maps from SR μ -XRF.

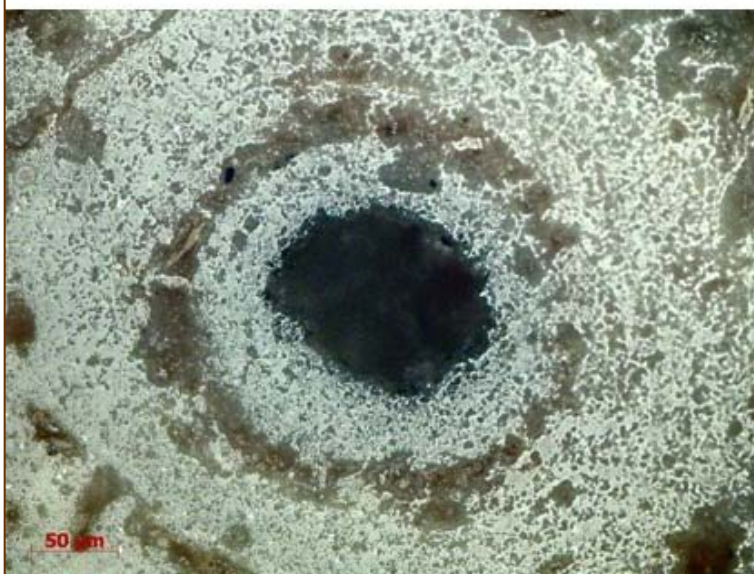


Figure 2.3.5.1: Polished-section of Fe-depleted diasporic Greek industrial bauxite sample (upper) and detail of pisoliths in the optical microscope (lower) prior the μ -XRF and μ -XAFS measurements in the SUL-X beamline of ANKA.

The μ -XAFS spectra were recorded in order to investigate the distribution and solid-state speciation of Cr, Th, As, V and Ga in the studied Parnassos-Ghiona bauxites. Micro-XAFS investigation, for Fe-depleted bauxite, was performed for Cr in the diaspore matrix. Chromium 3+ and 6+ compounds, such as chromium nitrate ($\text{Cr}(\text{NO}_3)_3$), potassium dichromate ($\text{K}_2\text{Cr}_2\text{O}_7$), and FeCr_2O_4 (chromite), as well as Cr-oxyhydroxide (grimaldiite-type) were used as reference materials. XAFS measurements were carried out at room temperature in both fluorescence and transmission mode at the Cr *K*-edge (5,989 eV). Energy was calibrated for the Cr *K*-edge XAFS measurements to 5,989 eV (1st derivative of the Cr *K*-edge, Cr metal foil between the ionization chambers 2 and 3). The spectra were processed using the ATHENA and the ARTEMIS software packages (Ravel & Newville, 2005). For the overall EXAFS fitting procedure, structural data from a grimaldiite (α -CrOOH) reference from the literature (Christensen et al., 1977) were imported from its atoms.inp file for the FEFF calculation. This reference was used as a “Cr-analogue” of diaspore (α -AlOOH) and particularly for EXAFS fitting of first shell parameters depicting the Cr-O bonds into the diaspore of the studied bauxite. The crystal-chemistry investigation of Th was also performed in the diaspore matrix of the Fe-depleted bauxite. Thorium compounds ($\text{Th}(\text{NO}_3)_4 \cdot 4\text{H}_2\text{O}$ and ThO_2) and minerals containing Th impurities, such as zircon (ZrSiO_4), were used as reference materials. Spectra were measured at the Th *L*_{III}-edge (16,300 eV) and processing was performed using initially the ATHENA (Ravel & Newville, 2005) and, furthermore, the EDA (Kuzmin, 1995) software packages. The EXAFS signal corresponding to the first main peak in Fourier transforms (FTs) was isolated using the Fourier filtering procedure. The range of the back-FT was 1-3 Å for $\text{Th}(\text{NO}_3)_4 \cdot 4\text{H}_2\text{O}$ and 0.8-2.5 Å for other samples. Thus, obtained EXAFS signals were best-fitted using two different approaches and namely the conventional Gaussian model and the regularization method (Kuzmin & Purans, 2000). The theoretical backscattering amplitude and phase shift functions for Th-O were used in the simulations. They were calculated by the *ab initio* FEFF8 code (Ankudinov et al., 1998) using a complex Hedin-Lundqvist exchange-correlation potential accounting for inelastic effects. In the case of As and V, the Synchrotron study aimed in element distribution and speciation (As^{3+} , As^{5+} and V^{3+} , V^{4+} , V^{5+}) in areas of the Fe-rich bauxite samples previously mapped by SR μ -XRF. Spectra were measured at the As *K*-edge (11,867 eV) and the V *K*-edge

Figure 2.3.5.2: Measurements in the SUL-X beamline of ANKA Synchrotron facility in sealed vacuum chamber.

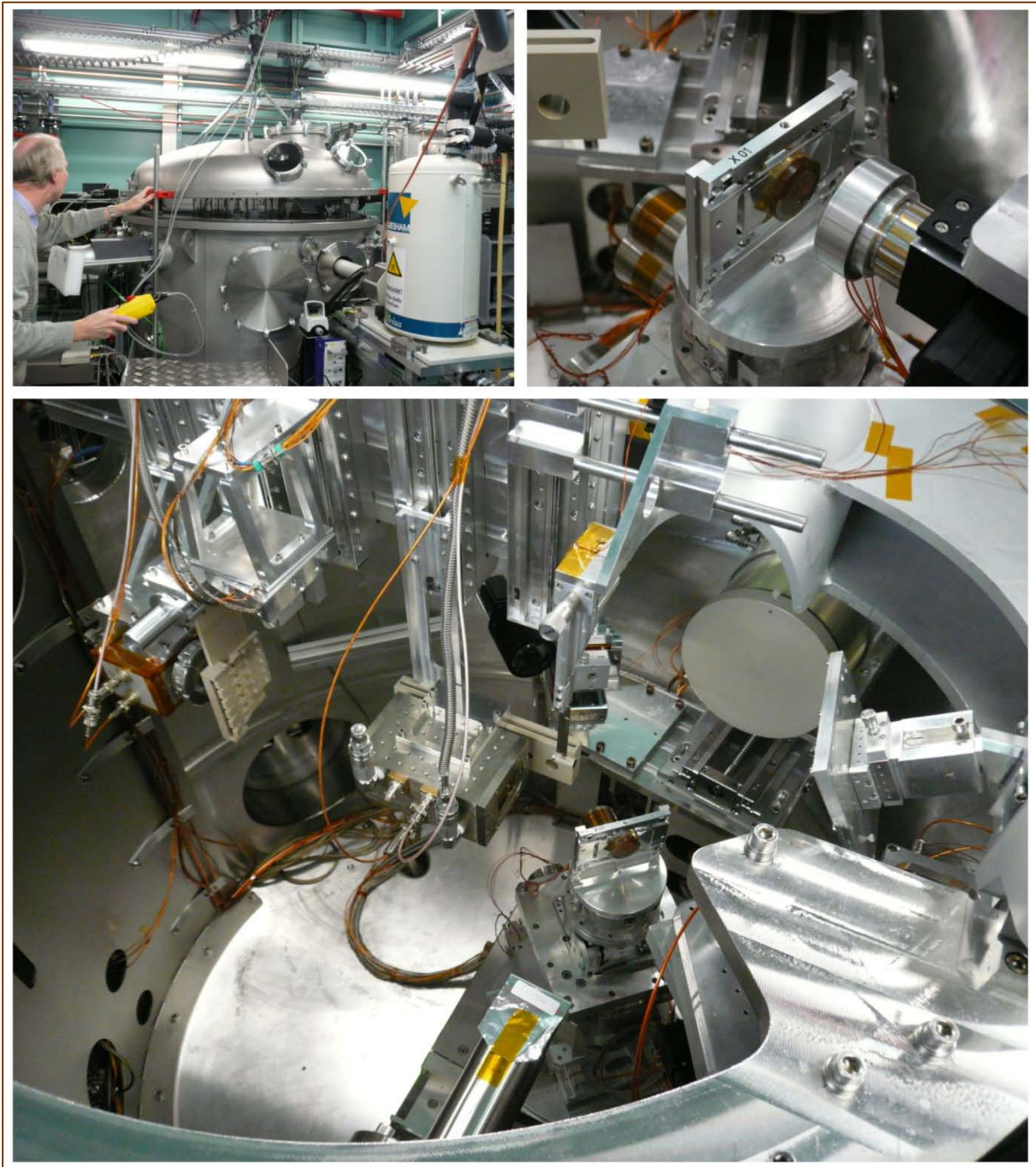


Figure 2.3.5.2: Continued.

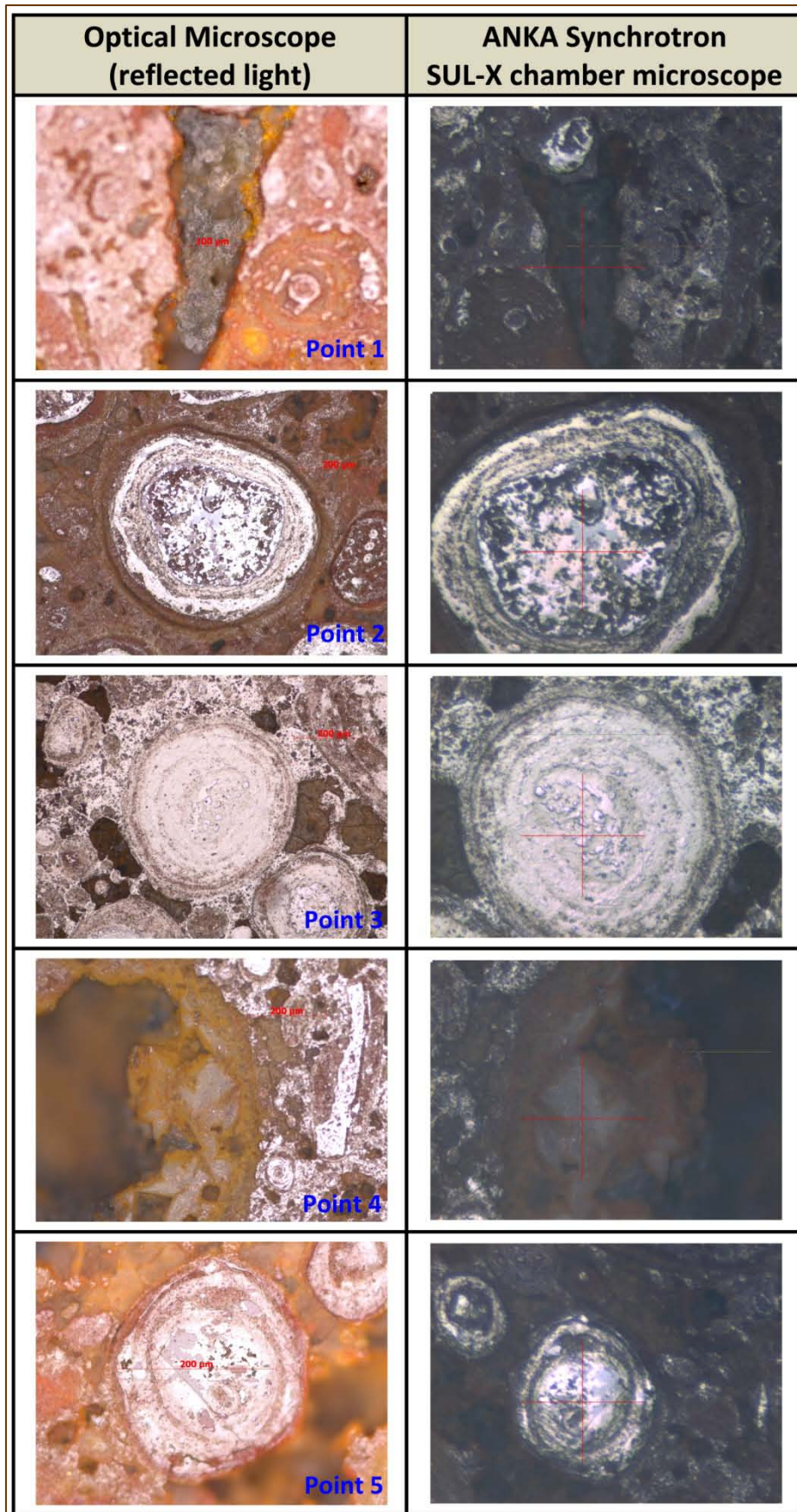
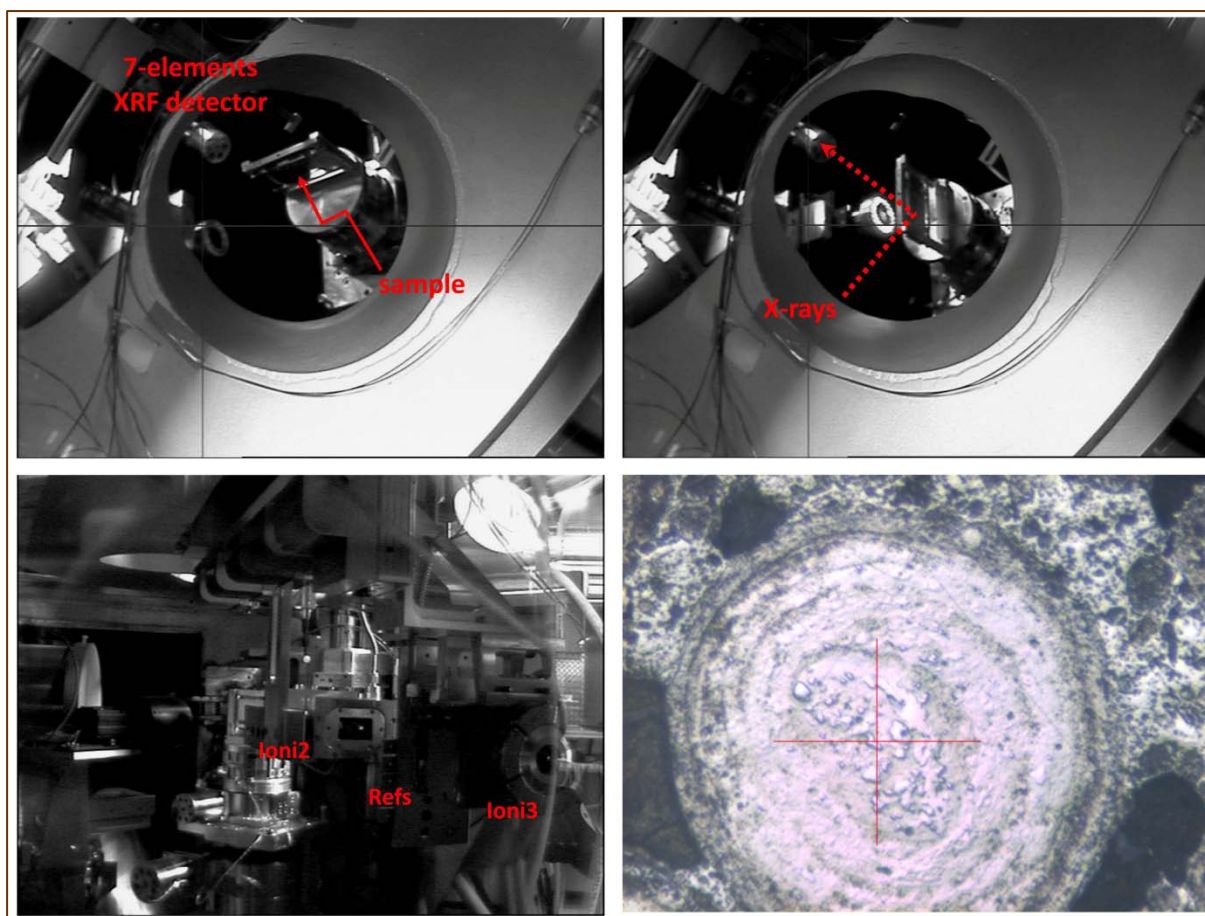


Figure 2.3.5.2: Continued.



($K\alpha$ at 5,465 eV). Natural minerals of known As oxidation state, such as arsenopyrite (FeAsS), orpiment (As_2S_3), and arsenates (i.e., annabergite: $\text{Ni}_3(\text{AsO}_4)_2 \cdot 8\text{H}_2\text{O}$ and scorodite: $\text{FeAsO}_4 \cdot 2\text{H}_2\text{O}$), as well as synthetic As^{3+} compounds, such as As_2O_3 (arsenolite) and NaAsO_2 (sodium meta-arsenite) were used as reference materials. In the case of V, numerous V minerals (e.g., cavansite containing V^{4+} and vanadinite containing V^{5+}) and compounds were used as reference materials. At the same time, a variety of other elements were mapped in microscale, using a sealed vacuum chamber (Figure 2.3.5.2), whereas Ga K -edge μ -XANES spectra at 10,367 eV were successively obtained.

2.4. Mineralogical and geochemical characterization of bauxite in nanoscale by High-Resolution Transmission Electron Microscopy (HRTEM) and Electron Energy Loss Spectroscopy (EELS)

TEM-EDS & EELS measurements were carried out using an FEI Tecnai F20 field-emission-gun transmission electron microscope (FEG-TEM) operated at 200 kV and an FEI Titan 80-300ST FEG TEM operated at 300 kV. Elemental mapping by energy-filtered TEM and electron energy-loss spectroscopy were obtained using a Gatan imaging filter equipped to the Titan TEM. Three-window elemental maps were yielded using O (centered at 542 eV), Ti (centered at 468 eV), and Fe (centered at 718 eV) core-loss edges with a 20 eV energy window. For comparison reasons, the elemental maps were colored for better visualization. EELS were acquired with an energy dispersion of 0.2 eV/pixel and an energy resolution of 0.8 eV, which could give a practical resolution of better than 1 eV. Qualitative TEM-EDS measurements were carried out using an electron beam with <10 nm in size. The bauxite samples were polished down to approximately 30 nm, thinned to electron transparency using Ar ion milling and coated lightly with carbon.

2.5. Red mud samples and characterization

Bauxite refining solid wastes (red mud) samples were supplied by Aluminium S.A. alumina plant at Antikyra, Gulf of Corinth, central Greece. The company manages the red mud through the installation of four filter presses, disposing the final dehydrated metallurgical residue onto a special configured area inside its plant. The final red mud sample, used in the study, concerned composite sample which was created by taking the appropriate number of specimens ($n=10$), using standard mixing procedures and sample splitters. The bulk characterization was performed using a combination of microscopic, analytical, and spectroscopic techniques (PXRD, SEM-EDS, STEM-EDS/EELS, XRF, ICP-OES/MS, HR γ -ray Spectrometry, and XANES/EXAFS; for descriptions of the techniques see sections above). Furthermore, simultaneously to bulk mineralogical composition of the raw material, additional PXRD studies were performed on the acetic acid-leached red mud using a

SIEMENS D5005 (currently BRUKER AXS) diffractometer with CuK_α radiation ($\lambda = 1.54 \text{ \AA}$) at an accelerating voltage of 40 kV. For this reason, the identification of mineral phases was complementary recorded for the coarse ($>2\mu\text{m}$) and fine fraction ($<2\mu\text{m}$) of the acetic acid-leached red mud separated using standard wet-chemical and centrifugation procedures (Moore & Reynolds, 1997).

2.6. Leaching experiments for red mud and bauxites using Sector field Inductively Coupled Plasma Mass Spectrometry (SF-ICP-MS)

Leaching experiments on the investigated Greek red mud and typical bauxites were carried out using (a) Mediterranean seawater from the Gulf of Corinth (Greece), and (b) concentrated acetic acid (Merck), over a period ranged from 2 weeks to 1 year. Acetic acid was used, instead of typical TCLP, according to recent relevant work for red mud (Rubinos & Barral, 2013). The analyses of leachates, for potentially hazardous metals and metalloids (Cr, V, Ni, As, Pb), Th, Ta, Nb, and REE, were performed using a SF-ICP-MS (Thermo Scientific Element 2/XR) at KIT-INE (Figure 2.6.1). The red mud sample, used in the leaching experiments, was composite sample which was created by taking the appropriate number of specimens ($n=10$), using standard mixing procedures and sample splitters. Simultaneously, similar leaching tests on Greek typical bauxites were also carried out for comparison reasons. For this purpose the bauxite samples subjected to leaching tests, constituted composite sample, which was created by taking the appropriate number of specimens, using standard mixing procedures and sample splitters. Such composited samples are typically obtained from bauxite mines of "Aluminium S.A." for the material's characterization either going to be proceeded through Bayer process for the alumina production or to be used as direct commercial products at the aluminium industry, worldwide. Thus, the final composited leached bauxite samples represent both the typical types of karst-type of Greek bauxites (i.e., Fe-depleted (white-grey in color) diasporic type; Fe-rich (red-brown in color) diasporic and/or boehmitic type) from the Parnassos-Ghiona active mining area.

Figure 2.6.1: The SF-ICP-MS of KIT-INE.



On a first step, powder from the red mud, as well as from both the typical bauxite types (typically between ~ 10 and 100 mg; details are given in **Table 2.6.1**) were weighted in zinser vials, which were then filled with 20 mL of the leaching solution (i.e., seawater or concentrated acetic acid).

In addition, 2 experimental blank experiments (only seawater and concentrated acetic acid) were also prepared in the same way using zinser vials filled with 20 mL of the particular solution. Sampling of the experimental, as well as the blank solutions was performed at certain periods of time after the start of the leaching procedure (after 2 weeks, 1 month, 2 months, 3 months, 5 months, 7 months, 10 months, 12 months). Typically, 1 mL was taken from each vial and filtered with a syringe filter to remove particles. 500 μL of the filtered leachate was then further diluted using 2 vol% HNO_3 (prepared from concentrated Merck

ultrapure HNO₃ and deionized water with a resistance of 18 mΩ) to a total of 5 mL. The concentrations of trace elements, including actinides, HFSE and REE, in the leachates were determined using a SF-ICP-MS (Thermo Scientific Element 2/XR) at KIT-INE. Lanthanides and As were measured in high resolution mode ($m/\Delta m = 10.000$), whereas other elements, such as Cr, and V were measured in medium resolution ($m/\Delta m = 4.000$) or in case of Ta, Y, Th, and

Table 2.6.1: Details of leaching experiments with regard to the studied red mud and Greek typical high grade (i.e., Fe-depleted; diasporic; white-grey in color) and low grade (i.e., Fe-rich; diasporic & boehmitic; red-brown in color) bauxite samples.

Starting Date	Treatment Solution	Sample Type		Sample Code	Sample Weight (mg)	Amount of Solution (mL)	
6.11.2012	Concentrated Acetic Acid (Merck)	Red Mud		RM-AC-1	102.4	20	
6.11.2012				RM-AC-2	12.5	20	
6.11.2012		Greek Industrial Bauxite	High Grade		HGB-AC-1	99.1	20
6.11.2012					HGB-AC-2	11.8	20
6.11.2012			Low Grade		LGB-AC-1	104.2	20
6.11.2012					LGB-AC-2	9.2	20
6.11.2012	Mediterranean seawater (Gulf of Corinth – Greece)	Red Mud		RM-SW-1	98.9	20	
6.11.2012				RM-SW-2	18.7	20	
6.11.2012				RM-SW-3	9.1	20	
6.11.2012		Greek Industrial Bauxite	High Grade		HGB-SW-1	102.7	20
6.11.2012					HGB-SW-2	20.9	20
6.11.2012					HGB-SW-3	10.8	20
6.11.2012			Low Grade		LGB-SW-1	99.2	20
6.11.2012					LGB-SW-2	19.9	20
6.11.2012					LGB-SW-3	9.9	20

Pb in low resolution mode ($m/\Delta m = 300$). Rhodium was added to the solutions and used as an internal standard (final Rh concentration was 1 ng/g). Plasma parameters and sample uptake conditions were optimized at the beginning of each instrumental session to achieve optimal signal stability and maximum sensitivity at low oxide ratios. Typical instrumental parameters and measured isotopes are listed in **Table 2.6.2**.

Table 2.6.2: Instrumental parameters for SF-ICP-MS measurements.

<i>Instrumental settings</i>	
Forward Power (W)	1250
Cooling gas flow rate (L min ⁻¹)	16
Auxiliary gas flow rate (L min ⁻¹)	0.9
Sample gas flow rate (L min ⁻¹)	1.195
Cones	Nickel
<i>Sample introduction</i>	
Nebulizer	PFA micro-concentric
Spray chamber	PC ³ -System
<i>Data acquisition</i>	
Monitored masses	²³² Th, ²⁰⁷ Pb, ²⁰⁸ Pb, ⁸⁹ Y, ¹⁸¹ Ta (low resolution mode) ⁵³ Cr, ⁵¹ V, ¹¹³ Cd (medium resolution mode) ¹³⁹ La, ¹⁴⁰ Ce, ¹⁴¹ Pr, ¹⁴⁶ Nd, ¹⁴⁹ Sm, ¹⁵³ Eu, ¹⁵⁸ Gd, Dy, ¹⁵⁹ Tb, ¹⁶⁵ Ho, ¹⁶⁷ Er, ¹⁶⁹ Tm, ¹⁷³ Yb, ¹⁷⁵ Lu, ⁷⁵ As (high resolution mode)

Calibrations were generally performed with adjusted solutions using acetic acid and Mediterranean seawater for matrix matching. The accuracy of the measurements was verified with various water reference materials (TM26.3 and SPS-SW1) which were also adjusted with Mediterranean seawater and acetic acid for matrix matching. Since the river water reference materials are not certified for Ta a diluted matrix matched reference solution of BHVO-1 (rock reference standard material) was used. All certified values could be reproduced throughout the measurements except for Dy, which is therefore not listed in **Table 2.6.2**. The analyzed reference solutions yielded consistently higher Dy concentrations probably caused by Carbon based interferences such as ¹³⁴Ba, ¹⁶O, ¹²C⁺ and ¹³⁵Ba, ¹⁶O, ¹²C⁺, which were not completely resolved from the analyte peaks of ¹⁶²Dy⁺ and ¹⁶³Dy⁺ respectively.

3. RESULTS AND DISCUSSION

3.1. Bulk mineralogy and geochemistry of bauxite

3.1.1. PXRD investigation

The bulk mineralogical composition of the studied bauxite samples were initially investigated by means of conventional powder XRD (PXRD). The PXRD patterns of representative Fe-rich diasporic and Fe-rich boehmitic bauxite samples together with Fe-depleted diasporic sample, which unexpectedly contains minor hematite, are illustrated in **Figure 3.1.1.1**. PXRD data, including the semi-quantitative crystalline phase analyses using both the EVA and the MATCH! version 1.9a software packages, are shown in **Table 3.1.1.1**. In general, the studied Fe-depleted bauxites appear as porous white-grey (high grade) and they concern only diasporic type, while the Fe-rich are massive, red-brown (low grade) and both are present as diasporic and/or boehmitic type. Except the above cases, Fe-depleted bauxite samples usually contain diasporic, and TiO₂ polymorphs, i.e., abundant anatase and minor rutile (possibly detrital) in macroscale, see **Figure 3.1.1.2**. Nevertheless, in the case of the Fe-rich samples, except major solid crystalline phases (AlOOH polymorphs, anatase and hematite), rutile (possibly detrital), clays (kaolin-group), goethite (FeOOH), and magnetite (Fe₃O₄) are occasionally present (**Figure 3.1.1.3** and **Table 3.1.1.1**). Accessory crystalline phases (i.e., detrital zircons, and chromites as well as REE fluorocarbonates) detected by SEM-EDS/WDS (see text below), and occurring as rare irregular microcrystals and aggregates into the diasporic matrix, were not detected by XRD. Rietveld refinement of the XRD patterns were applied, using both GSAS ([Larson & Von Dreele, 2004](#)) and FullProf ([Rodríguez-Carvajal, 1993](#)) refinement software packages, to Fe-depleted (high grade) bauxite samples, while previous work referred to typical Fe-rich (low grade) bauxite ([Perdikatsis, 1992](#)). The R values (R_w and R_p) yielded by the GSAS are lower than those of the FullProf software. According to the GSAS, the unit cell parameters of the AlOOH and TiO₂ phases calculated by the refinement (**Table 3.1.1.2**) are in good agreement with the values reported in the

literature for the aforementioned minerals (Cromer & Herrington, 1955; Klug & Farkas, 1981; Hazemann et al., 1991; Howard et al., 1991; Hummer et al., 2007). Thus, it can be argued that there is no practical distortion of the diaspore unit cell, despite the presence of metal, namely Fe and Cr, impurities revealed by electron and Synchrotron-based microanalyses (see text below). Moreover, the unit cell of anatase also remains undistorted, regardless of incorporation of HFSE, such as Th, U, Nb, and Ta detected by LA-ICP-MS investigation (see text below).

Figure 3.1.1.1: PXRD patterns of representative Fe-depleted diasporic (black lower pattern: ① ALM0306_BIW), Fe-rich diasporic (red middle pattern: ② ELM0206_DV_B1) and Fe-rich boehmitic (red upper pattern: ③ ALM0306_PL1_B2) bauxite samples from Parnassos-Ghiona active mining area; kaolinite, boehmite, goethite, diaspore, anatase, rutile, hematite, and magnetite strongest reflections at 12.37 (7.15), 14.48 (6.11), 21.37 (4.16), 22.26 (3.99), 25.35 (3.51), 27.50 (3.24), 33.27 (2.69), and 35.46 (2.53) 2θ (d in Å).

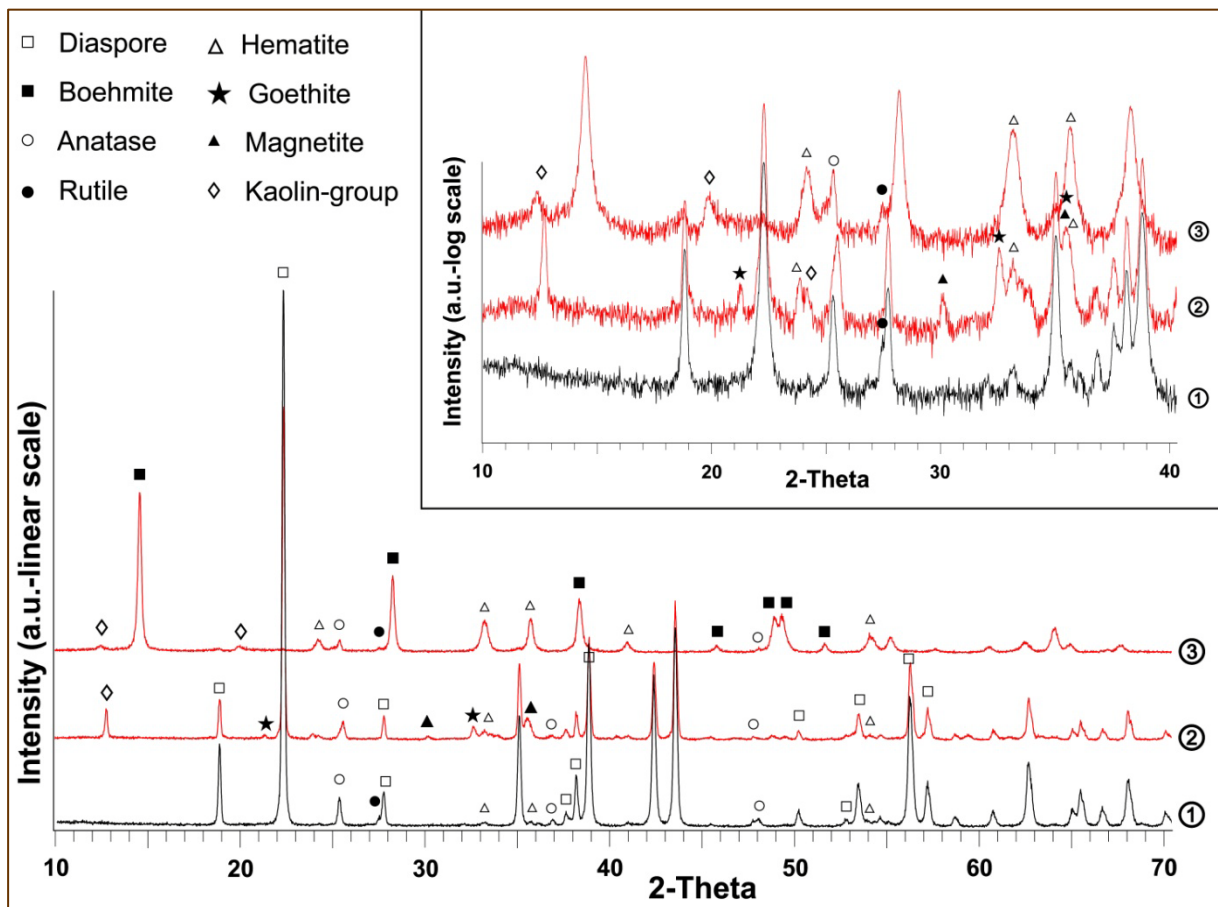


Table 3.1.1.1: Powder XRD results for the studied Parnassos-Ghiona bauxites using both EVA and MATCH! version 1.9a software packages for phase identification.

PARNASSOS-GHIONA BAUXITES			Crystalline Phases								
			<i>Semi-Quantitative Phase Analysis based on Powder X-ray diffraction patterns (wt.%)</i>								
Type	Code	Description	Diaspore	Boehmite	Anatase	Rutile	Goethite	Hematite	Magnetite	Kaolinite	
DIASPORIC	Fe-depleted (high-grade) High Al ₂ O ₃ component between ~ 79 and ~ 80 wt.% Low Fe ₂ O ₃ component between ~ 1 and ~ 3 wt.% White-grey	ALM0306_PL1_BIW	3rd bauxitic horizon (B3), white-grey, porous	97.9		1.6	0.5				
		ALM0306_BIW	3rd bauxitic horizon (B3), white-grey to pale-brown, highly porous	98.4		1.1	0.2		0.3		
		ALM0306_PL1_WB	3rd bauxitic horizon (B3), white-grey to pale-pink, highly porous	98.2		1.3	0.5				
		ALM0306_PL1_BS2	3rd bauxitic horizon (B3), white-grey-yellow, highly porous	98.2		1.4	0.4				
		ELM0206_SK_B1a	3rd bauxitic horizon (B3), white-grey, highly porous	98.0		1.5	0.5				
		ELM0206_SK_B1b	3rd bauxitic horizon (B3), white-grey-yellow, highly porous	98.4		1.3	0.3				
	Typical Fe-rich (low-grade) Low Al ₂ O ₃ component between ~ 44 and ~ 68 wt.% High Fe ₂ O ₃ component between ~ 14 and ~ 28 wt.% Red-brown	ELM0206_SK_B2	3rd bauxitic horizon (B3), yellow-red-brown, highly porous	92.2		1.7	0.4	5.7			
		ALM0306_PL1_B1	3rd bauxitic horizon (B3), red-brown to pale-brown, massive	83.9		1.9	0.6		10.9	0.5	2.2
		ALM0306_PL1_B3	3rd bauxitic horizon (B3), red-brown, massive	84.8		1.1	0.7		13.3		
		ALM0306_PL1_B4	3rd bauxitic horizon (B3), red-brown, slightly porous	93.7		1.2	0.4	4.7			
		ELM0206_DV_B1	2nd bauxitic horizon (B2), red-brown, massive	89.6		0.5		1.2	1.0	1.4	6.3
		SAB0306_ASV	3rd bauxitic horizon (B3), red-brown, massive	84.0		1.6	0.4		13.9		
		ALM0306_PL1_B2	3rd bauxitic horizon (B3), red-brown, massive		74.2	1.9	1.4		13.7		8.9
		ELM0206_KV_B1	2nd bauxitic horizon (B2), red-brown, massive		64.9	2.0	1.8		21.8		9.5
BOEHMITIC	ELM0206_2H1	2nd bauxitic horizon (B2), red-brown-orange, massive	6.3	63.5	4.2	1.4	8.1		0.4	16.1	
	SAB0306_SKR	2nd bauxitic horizon (B2), red-brown, massive		70.0	1.7	1.2		19.8		7.2	

Figure 3.1.1.2: PXRD pattern of representative Fe-depleted bauxite containing only diaspore, anatase and rutile (possibly detrital).

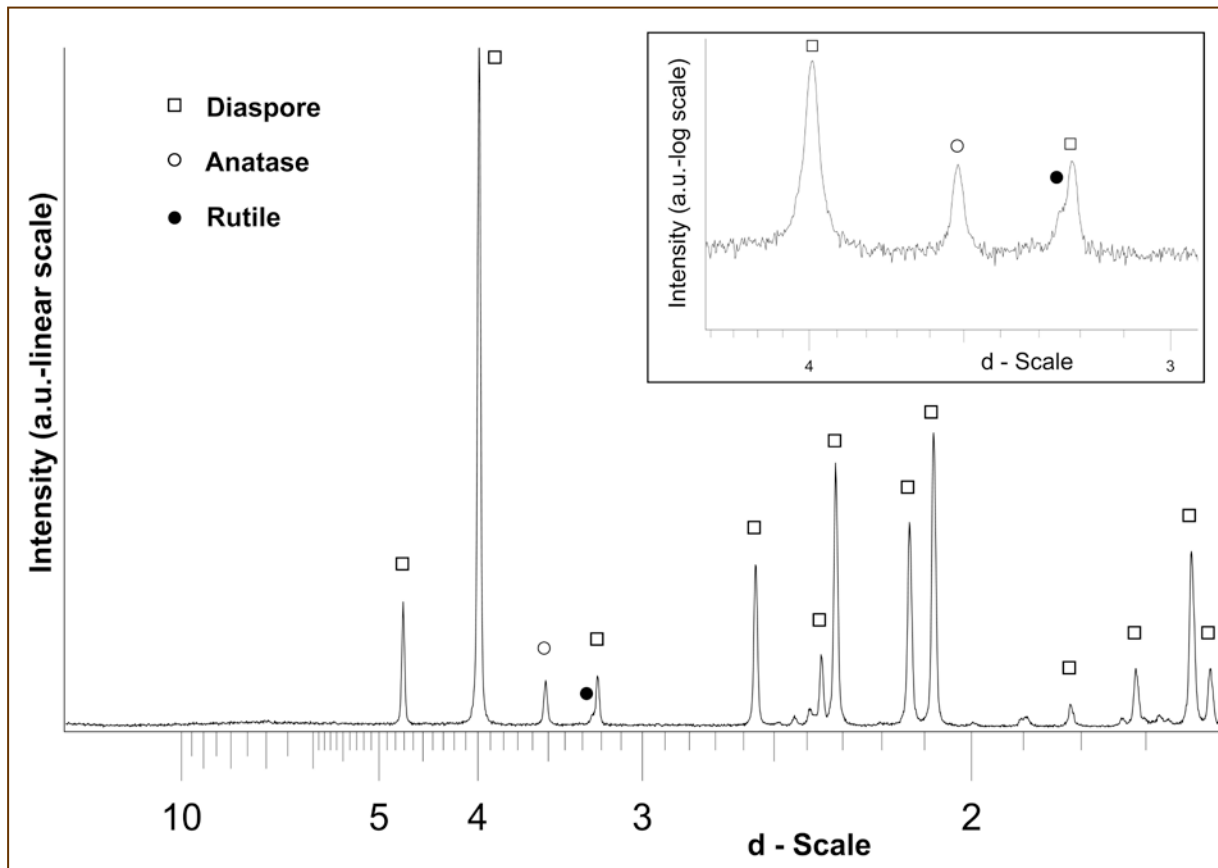


Figure 3.1.1.3: Processed, using MATCH! software, PXRD pattern of representative Fe-rich bauxite containing all crystalline phases observed in Parnassos-Ghiona bauxites.

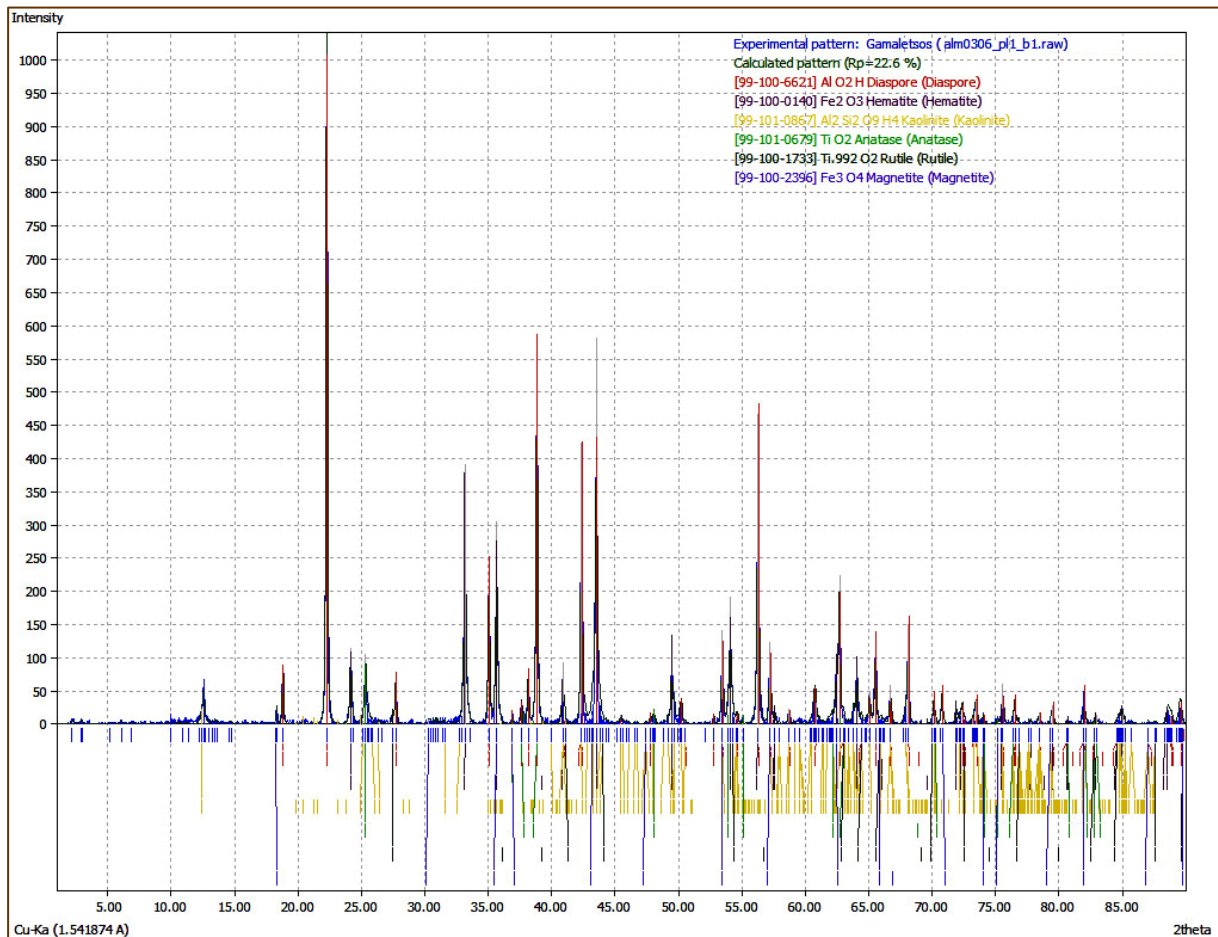


Table 3.1.1.2: Unit cell parameters of diaspore, anatase, and rutile in Fe-depleted (high grade) bauxite yielded by Rietveld method, using the GSAS (Larson & Von Dreele, 2004), and the FullProf (Rodríguez-Carvajal, 1993) refinement software packages.

Refinement Software	Mineral	Space Group	a (Å)	b (Å)	c (Å)	Weight (%)	Cell Volume (Å ³)	R values	
								Rwp	Rp
GSAS	diaspore	P b n m	4.402554 (0.000078)	9.424099 (0.000144)	2.845213 (0.000056)	96.603 (4.71544)	118.048		
	anatase	I 41/a m d	3.783301 (0.000368)	3.783301 (0.000368)	9.502564 (0.002090)	3.1342 (4.3628)	71.902		
	rutile	P 42/m n m	4.590689 (0.001167)	4.590689 (0.001167)	2.958973 (0.002198)	0.26286 (0.37694)	27.167		
								0.088	0.0678
FullProf	diaspore	P b n m	4.40511 (0.00004)	9.43015 (0.00008)	2.84717 (0.00003)	98.95 (0.75)	118.274		
	anatase	I 41/a m d	3.78660 (0.00016)	3.78660 (0.00016)	9.50218 (0.00080)	0.39 (0.01)	71.962		
	rutile	P 42/m n m	4.59424 (0.00059)	4.59424 (0.00059)	2.95845 (0.00074)	0.66 (0.05)	27.184		
								0.128	0.0966

3.1.2. Bulk geochemistry

The bulk chemical composition of the studied Fe-rich and Fe-depleted bauxites from Parnassos-Ghiona mines has been yielded by means of XRF and ICP-OES/MS measurements. Analytical findings provide convincing evidence that all the illustrated elements, herein, can be accurately measured by both these analytical techniques. Representative correlations of XRF and ICP-OES/MS analyses are given in **Figure 3.1.2.1**. The bulk chemical composition of all the studied Fe-rich and Fe-depleted bauxites is presented in **Table 3.1.2.1**.

Figure 3.1.2.1: Correlations of XRF and ICP-OES/MS analyses for lithophile (upper image), chalcophile (middle image) and siderophile (lower image) elements.

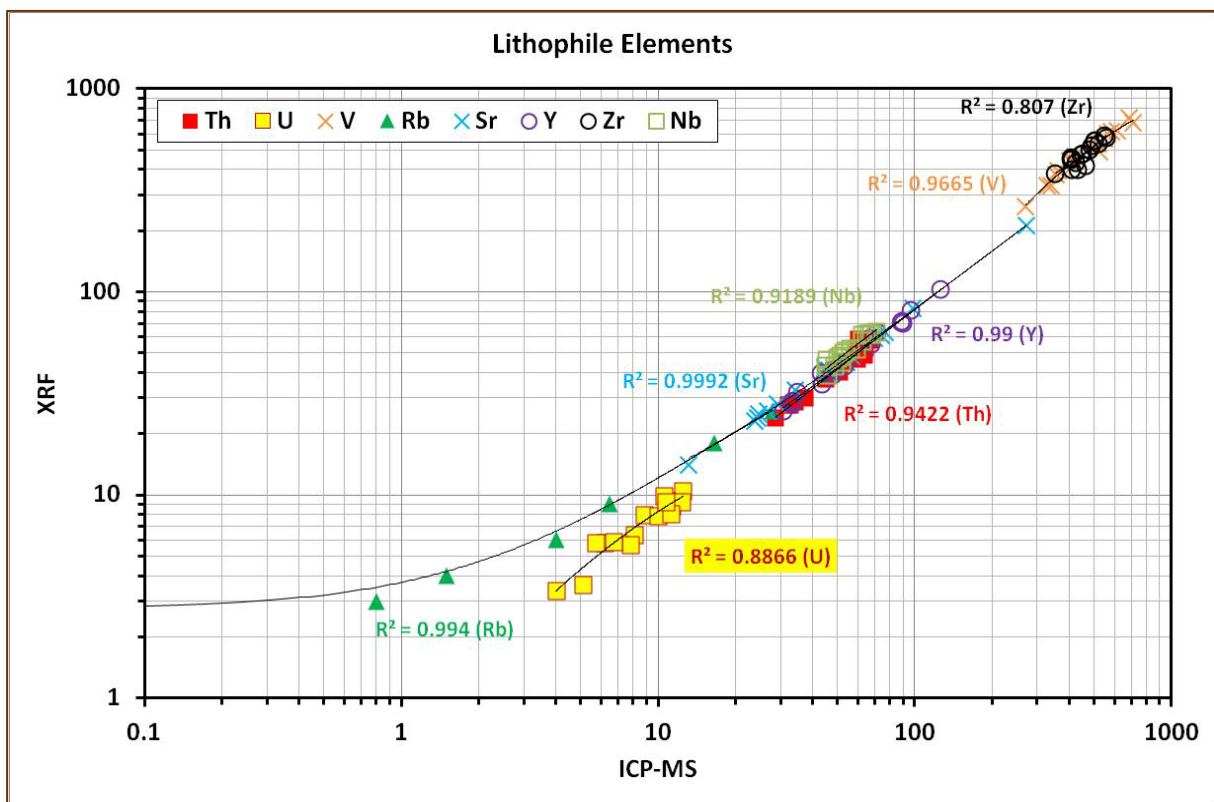


Figure 3.1.2.1: continued.

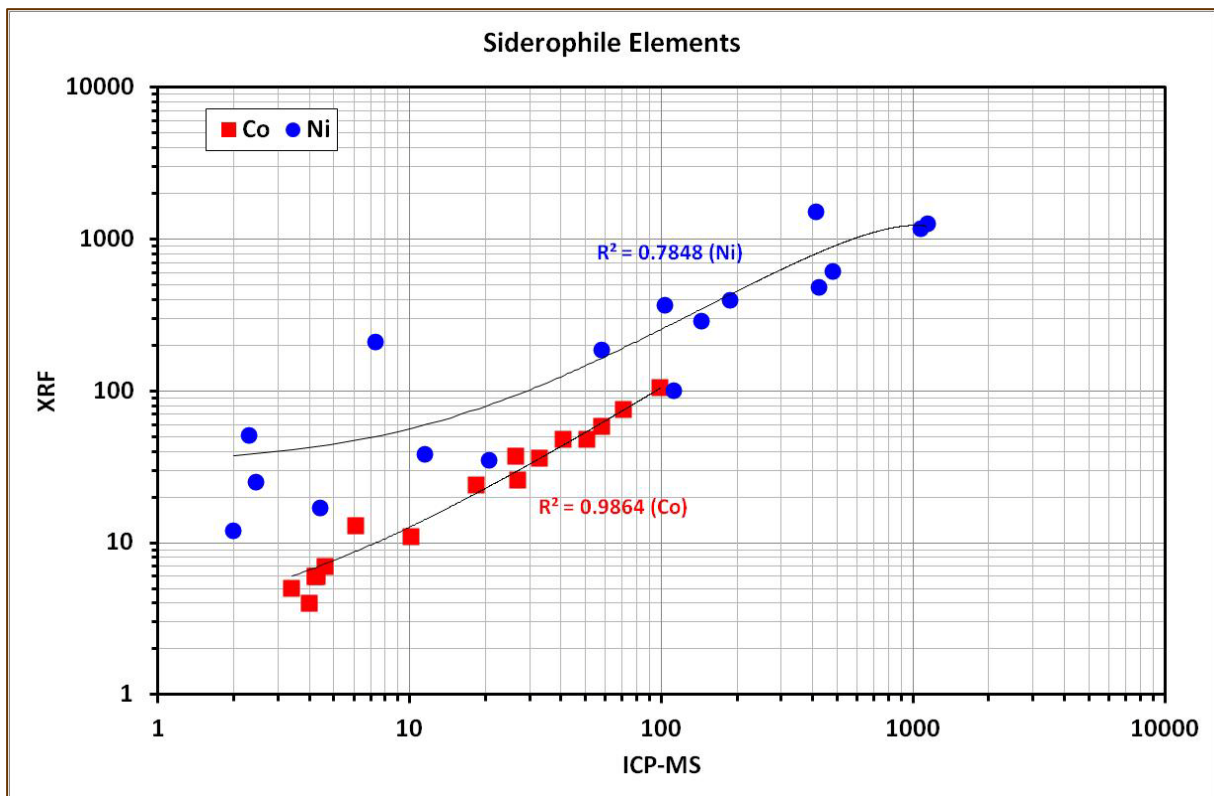
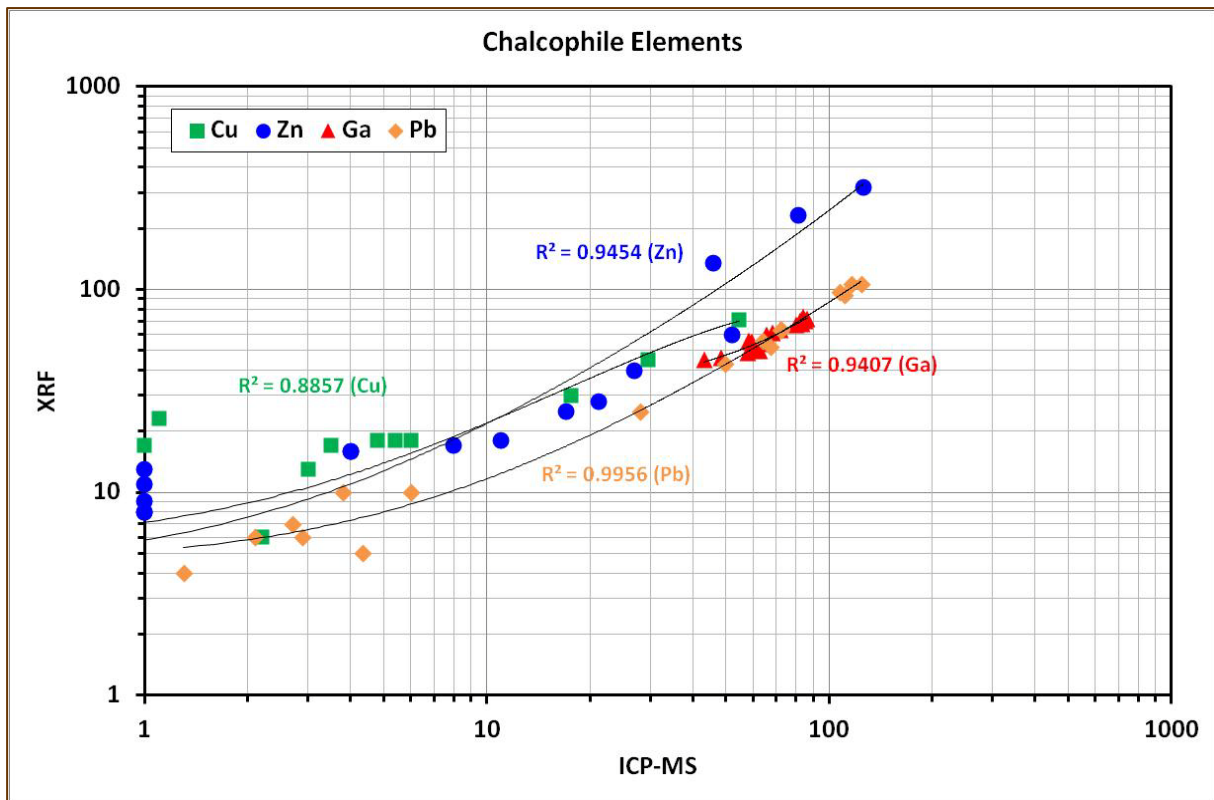


Table 3.1.2.1: Major and trace element concentrations in the studied bauxites from Parnassos-Ghiona active mining area. Commonly, the elements comprise the LREE and HREE groups are arbitrary defined (Mariano & Mariano, 2012; Gambogi, 2013; Zepf, 2013).

Sample Code	ALM0306_PL1_BIW <i>Fe-depleted</i>	ALM0306_BIW	ALM0306_PL1_WB	ALM0306_PL1_BS2	ELM0206_SK_B1a	ELM0206_SK_B1b	ELM0206_SK_B2 <i>Fe-rich</i>	ALM0306_PL1_B1
Description	<i>High-grade Diasporic White-grey</i>						<i>Low-grade</i>	
							<i>Red-brown</i>	
<i>wt.%</i>								
SiO ₂	0.08	0.17	0.2	0.14	0.32	0.28	0.34	1.95
Al ₂ O ₃	79.24	78.79	79.22	79.31	79.62	80.22	67.64	61.53
Fe ₂ O ₃ (T)	1.71	2.81	1.98	1.95	0.95	1.08	14.12	20.58
MnO	0	0	0	0	0	0	0	0.01
MgO	0.11	0.12	0.12	0.12	0.13	0.13	0.13	0.16
CaO	0	0.01	0.02	0.02	0.04	0.03	0.04	0.02
Na ₂ O	bdl	bdl	bdl	bdl	bdl	bdl	bdl	bdl
K ₂ O	0	0	0	0	0	0	0	0
TiO ₂	3.35	2.92	3.42	3.09	3.26	2.67	2.78	2.69
P ₂ O ₅	0.01	0.02	0.02	0.02	0.03	0.02	0.05	0.01
Cr ₂ O ₃	0.14	0.12	0.10	0.15	0.14	0.12	0.14	0.12
LOI	14.91	14.84	14.70	14.91	15.06	15.15	14.59	12.39
Total	99.55	99.80	99.78	99.71	99.55	99.70	99.83	99.46
<i>ppm</i>								
Be	4.5	6	9	4	6	9	5	8
Sc	29.1	31	38	29	39	32	38	57
V	521	362	414	561	402	354	415	548
Cu	0.05	0.1	0.6	0.2	0.3	0.5	2.2	5.4
Co	4.1	4	4.3	4.6	4.2	3.4	10.1	40.7
Ni	37	7.3	2.3	11.5	4.4	2.0	20.7	1076
Zn	24.6	7	6	4.5	5	3	4.5	52
Ga	84.2	80.1	83.5	86.3	82.2	84.9	72.1	68.3
As	0.5	0.49	0.45	0.5	0.44	0.39	30.2	0.7
Se	0	0.5	0.5	0.5	0.5	0.5	0.5	0.5
Rb	0.25	0.5	0.5	0.5	0.5	0.5	0.5	0.5
Sr	31.8	54.3	46.2	45.8	98.1	74	56.9	24.5
Y	31.2	47.8	88.4	30.7	49.2	43.4	33.4	67.2
Zr	568.1	478.2	550.6	488.4	502.8	443.4	451.1	404.8
Nb	62.3	59.5	68	62.3	62.5	54	56.2	53
Mo	0.6	0.5	2.4	2.7	0.8	0.3	6.7	3
Ag	bdl	bdl	bdl	bdl	bdl	bdl	bdl	bdl
Cd	0.1	0.1	0.1	0.1	0.1	0.1	0.1	0.1
Sn	11.9	13	15	11	10	11	11	12
Sb	4.9	3.1	2.8	4.1	1.6	0.7	2	7.6
Cs	1	0.1	0.1	0.1	0.1	0.1	0.1	0.1
Ba	4.7	8.3	5.9	5.1	4.4	5.1	5.7	24.5
Hf	14.35	13.9	15.9	13.9	14.8	13.5	13.4	12.3
Ta	2.88	2.9	3.1	3	3	2.7	3.3	3.2
W	51.3	33.4	47.3	48.6	37.8	37.1	88.9	94.5
Hg	0.04	0.02	0.02	0.05	0.01	0.01	0.02	0.02
Tl	0	0.07	0.08	0.07	0.1	0.06	0.09	0.1
Pb	4.35	3.8	2.1	1.3	2.7	2.9	6	64.1
Bi	0.53	1.4	1.7	1	2.8	0.8	2.6	2.4
La	6.1	36.1	46.9	7.9	38.8	25	12.3	32
Ce	106.1	153.5	118.5	124.6	101.8	66.9	80.9	216.1
Pr	1.75	5.92	7.63	2.14	6.07	3.68	2.09	6.41
Nd	6.3	16.8	20	7.7	17.5	11.4	6.4	21.7
Sm	2.32	2.84	3.84	1.65	2.86	2.22	1.4	6.33
Eu	0.41	0.58	0.97	0.38	0.71	0.53	0.37	1.65
Gd	2.03	2.44	4.95	1.65	3.24	2.76	2.05	7.36
Tb	0.68	0.83	1.96	0.58	1.04	0.81	0.69	2.44
Dy	4.73	6.31	15.6	4.34	7.4	5.47	4.74	16.59
Ho	1.05	1.5	3.63	0.92	1.59	1.19	1.04	3.7
Er	3.49	5.22	12.29	3.07	5.17	3.95	3.26	11.33
Tm	0.59	0.99	2.21	0.58	0.91	0.69	0.56	1.68
Yb	3.05	7.12	15.59	3.85	6.33	4.57	4.01	10.33
Lu	0.68	1.13	2.49	0.62	1.01	0.77	0.63	1.65
Th	60.5	28.6	34.4	59.6	32.2	37.5	32.9	48.3
U	9.33	8.1	11.1	10.8	6.2	4	5.1	10.5
<i>ppb</i>								
Au	2.6	2.4	2	0.5	1.2	0.8	0	1.6
<i>ppm</i>								
Σ LREE ⁽¹⁾	125	218	203	146	171	112	106	292
Σ HREE ⁽¹⁾	45	71	142	45	73	61	48	115
Σ REE ⁽¹⁾	199	320	383	220	283	205	192	463
[Eu/Eu*] _{ch}	0.56	0.66	0.69	0.70	0.72	0.66	0.67	0.74
[Ce/Ce*] _{ch}	7.87	2.17	1.30	7.20	1.34	1.37	3.31	3.28
[Eu/Eu*] _{ch} ⁽²⁾	0.57	0.68	0.69	0.71	0.72	0.66	0.67	0.74
[Eu/Eu*] _{NASC} ⁽²⁾	0.58	0.68	0.69	0.71	0.72	0.66	0.67	0.75
[Eu/Eu*] _{NASC}	0.54	0.64	0.59	0.65	0.64	0.57	0.56	0.66
[Ce/Ce*] _{NASC}	7.94	2.39	1.44	7.32	1.48	1.51	3.62	3.49
[La/Sm] _{ch}	1.55	7.55	7.25	2.84	8.06	6.69	5.22	3.00
[La/Sm] _{NASC}	0.50	2.44	2.35	0.92	2.61	2.17	1.69	0.97
[La/Yb] _{ch}	1.31	3.33	1.98	1.35	4.03	3.60	2.02	2.04
[La/Yb] _{NASC}	0.20	0.51	0.30	0.21	0.61	0.55	0.31	0.31
[Gd/Yb] _{ch}	0.55	0.28	0.26	0.35	0.42	0.50	0.42	0.59
[Gd/Yb] _{NASC}	0.83	0.43	0.40	0.53	0.64	0.75	0.64	0.89

Table 3.1.2.1: continued.

Sample Code	ALM0306_PL1_B3	ALM0306_PL1_B4	ELM0206_DV_B1	SAB0306_ASV	ALM0306_PL1_B2	ELM0206_KV_B1	ELM0206_ZH1	SAB0306_SKR	ALM0306_PL1_B51
Description	Fe-rich								Sulfur-bearing
	Low-grade								
	Diasporic								
	Boehmitic								
	Red-brown								Red-grey
<i>wt.%</i>									
SiO ₂	0.75	0.4	1.96	0.50	6.1	13.9	8.57	8.94	1.63
Al ₂ O ₃	61.70	56.84	62.49	63.36	55.25	49.70	44.25	52.83	55.28
Fe ₂ O ₃ (T)	21.95	24.57	19.30	20.29	22.52	20.28	27.66	22.45	27.66
MnO	0.01	0	0.01	0.01	0.02	0.08	0	0.42	0.02
MgO	0.11	0.1	0.2	0.1	0.3	0.4	0.2	0.39	0.08
CaO	0.08	0.10	0.02	0.05	0.09	0.13	0.21	0.11	0.02
Na ₂ O	bdl	bdl	bdl	bdl	bdl	bdl	bdl	bdl	bdl
K ₂ O	0	0.01	0	0	0.16	0.35	0.2	0.21	0.07
TiO ₂	2.63	2.29	3.44	3.36	2.49	2.23	2.58	2.41	2.57
P ₂ O ₅	0.02	0.03	0.01	0.01	0.01	0.04	0.06	0.04	0.01
Cr ₂ O ₃	0.13	0.10	0.14	0.16	0.11	0.03	0.17	0.05	0.13
LOI	12.18	15.07	11.96	12.19	12.16	11.93	15.61	11.96	10.18
Total	99.56	99.51	99.53	100.03	99.21	99.07	99.51	99.81	97.64
<i>ppm</i>									
Be	9	6	5	5	10	4	5	7	5
V	51	45	73	71	57	54	46	56	48
Cu	617	683	271	420	711	340	518	329	523
Co	6	1	4.8	3	29.6	17.6	3.5	54.6	1.1
Ni	18.4	6.1	57.7	26.3	70.8	27	32.9	98.9	50.7
Zn	479	112	1142	188	412	58	144	103	423
Ga	27	17	11	4	46	81	8	126	4
As	65.5	48.4	59.5	60.1	58.4	62.5	58	63	43.1
Se	1.2	43.5	0	0.5	5	11.5	176.7	9.6	162.3
Rb	0.5	0.5	0.5	0.5	0.5	0.5	3.5	0.5	3.6
Sr	44.6	29.2	13.2	23.9	34.2	76.4	271.7	69.4	24.7
Y	71.2	35	89.2	68	96.2	89.8	53.4	126.5	43
Zr	410.8	353.3	520.4	556.4	407.3	408.7	433.4	425.1	465.2
Nb	51.6	44.9	71.1	66.3	50.2	46	51.9	48.7	45.3
Mo	3.6	64.8	0.9	0.7	2.6	1.1	2.7	1.4	17.8
Ag	bdl	bdl	bdl	bdl	bdl	bdl	bdl	bdl	bdl
Cd	0.2	0.3	0.1	0.1	0.1	0.3	0.3	0.9	0.1
Sn	12	8	17	15	11	11	8	11	11
Sb	8.9	22.5	0.6	4.8	12.5	1.9	2.8	2.4	15.9
Cs	0.1	0.1	0.1	0.1	2.8	9.4	0.6	6.4	0.2
Ba	18.6	19.8	9.1	16.7	44.5	74.2	7.8	62.3	15.5
Hf	12.3	10.6	14.7	16.1	11.4	11.7	12.8	12.4	10.8
Ta	3.1	2.7	3.7	3.6	3.1	2.8	3.2	2.9	2.8
W	50.5	57.4	66.5	133.8	19	13	62.2	28.9	28.8
Hg	0.01	0.77	0.01	0.01	0.01	0.02	0.16	0.02	0.15
Tl	0.1	0.2	0.08	0.1	0.1	0.1	0.07	0.1	0.1
Pb	72.6	28	49.6	72.2	107.2	111	123.9	116.1	67.6
Bi	2.2	1.4	1.8	2.7	2.3	1.8	2.6	2.1	2.4
La	82.7	23.7	106	52.2	140.1	167.1	45.9	140.5	22.7
Ce	99.1	99.9	655	350.5	251.4	286.4	203.4	291.6	83.5
Pr	12.1	7.45	25.13	9.83	36.8	23.27	12.97	28.89	6.07
Nd	35.2	29.3	90.8	33.3	136.1	79.2	49.1	109.8	22.5
Sm	7.82	6.77	19.29	7.57	29.94	14.64	9.69	23.37	4.96
Eu	1.9	1.35	3.75	1.63	5.82	2.7	1.61	4.57	1.1
Gd	9.14	5.39	12.74	6.72	20.42	9.94	5.49	18.44	4.77
Tb	2.76	1.19	2.39	1.85	4.37	2.19	1.36	3.66	1.22
Dy	18.33	6.4	12.08	10.85	22.88	12.32	8.7	19.22	7.37
Ho	3.87	1.2	2.26	4.16	2.23	2.5	1.68	3.69	1.44
Er	12.52	3.6	6.84	6.85	12.24	7.78	5.53	10.98	4.36
Tm	2.03	0.6	1.14	2.06	1.31	1.31	0.98	1.75	0.76
Yb	13.02	4.04	7.84	7.92	13.25	9	7.08	11.71	4.91
Lu	2.12	0.64	1.22	1.23	2.05	1.4	1.11	1.82	0.78
Th	58.8	44.9	50.7	64	48.4	51	63.7	53	60.4
U	11.3	12.4	8.8	7.8	10	5.7	11.2	6.7	10.7
<i>ppb</i>									
Au	0.5	3.5	0	1.3	6.8	0	0.7	1.3	0.9
<i>ppm</i>									
Σ LREE ⁽¹⁾	248	174	913	462	621	583	328	617	146
Σ HREE ⁽¹⁾	126	53	123	100	157	126	80	179	64
Σ REE ⁽¹⁾	425	272	1109	633	835	764	454	853	257
[Eu/Eu*] _{ch}	0.69	0.67	0.69	0.69	0.69	0.65	0.62	0.65	0.69
[Ce/Ce*] _{ch}	0.62	1.82	2.89	3.29	0.82	0.87	1.98	0.99	1.67
[Eu/Eu*] _{ch} ⁽²⁾	0.69	0.69	0.74	0.70	0.73	0.69	0.68	0.68	0.68
[Eu/Eu*] _{NASC} ⁽²⁾	0.69	0.69	0.74	0.71	0.73	0.69	0.68	0.68	0.68
[Eu/Eu*] _{NASC}	0.61	0.66	0.72	0.66	0.71	0.67	0.67	0.65	0.64
[Ce/Ce*] _{NASC}	0.68	1.80	2.99	3.52	0.83	0.96	1.99	1.03	1.70
[La/Sm] _{ch}	6.28	2.08	3.26	4.10	2.78	6.78	2.81	3.57	
[La/Sm] _{NASC}	2.03	0.67	1.06	1.33	0.90	2.19	0.91	1.16	
[La/Yb] _{ch}	4.18	3.86	8.89	4.33	6.95	12.21	4.26	7.89	3.04
[La/Yb] _{NASC}	0.64	0.59	1.35	0.66	1.06	1.86	0.65	1.20	0.46
[Gd/Yb] _{ch}	0.58	1.10	1.34	0.70	1.27	0.91	0.64	1.30	0.80
[Gd/Yb] _{NASC}	0.87	1.66	2.02	1.06	1.92	1.38	0.97	1.96	1.21

Note:

Eu/Eu* = [2* (Eu_{measured} / Eu_{ch}) / ((Sm_{measured} / Sm_{ch}) + (Gd_{measured} / Gd_{ch})); after: Liu et al. (2013).Ce/Ce* = [3* (Ce_{measured} / Ce_{ch}) / 2* ((La_{measured} / La_{ch}) + (Nd_{measured} / Nd_{ch})); after: German & Elderfield (1990).⁽¹⁾ The Σ LREE group includes the lanthanide elements from La through Gd (Gambogi, 2013; Zepf, 2013); The Σ HREE group includes the lanthanide elements from Tb through Lu, including Y (Gambogi, 2013; Zepf, 2013); The Σ REE group comprises of the 15 lanthanide elements including Sc, and Y (Gambogi, 2013; Zepf, 2013).⁽²⁾ In this case, Eu anomaly has been quantified using the equation: Eu/Eu* = [Eun / (Smn * Gdn)] (Mongelli et al., 2014); Chondrite values are depicted using the average chondrite values (see text below).

* NASC values are from Gromet et al. (1984).

** Chondrite values are the average of selected average values of ordinary chondrites / OC (Haskin et al., 1968a; Haskin et al., 1968b; Haskin et al., 1971; Wakita et al., 1971), and carbonaceous chondrites / CI (Boynton, 1985; Taylor & McLennan, 1985) as well as of values reported by Korotev (1996a & 1996b) - who utilized the CI values from Anders & Grevesse (1989) multiplied by 1.3596. This approach is based on comments by Rollinson (1993) and suggestions by Korotev (2010). Values from CI chondrites have been selectively chosen in order to be consistent with the average values of OC chondrites by Haskin et al. (1968a), Haskin et al. (1968b), Haskin et al. (1971), and Wakita et al. (1971).

The UCC-normalized spider diagrams (Rudnick & Gao, 2003) have indicated a clear enrichment in High-Field Strength Elements (HFSE), Rare Earth Elements (REE), actinide elements (Th, U), and in most of compatible elements, while there is a depletion in Large Ion Lithophilic Elements (LILE), P, Sr, and certain compatible elements such as Zn, Cu, and As (Figure 3.1.2.2). Except the values presented in the above table (Table 3.1.2.1), individual analyses were performed with regard to Ge, Te and Br in a representative composite sample (2.45 ppm, 8 ppm and 3 ppm, respectively). The general enrichment of Parnassos-Ghiona bauxite in certain HFSE and actinides (Nb, Ta, Th, U) is due to Ti-oxides, namely anatase, as it

Figure 3.1.2.2: UCC-normalized (Rudnick & Gao, 2003) spider diagrams for the studied Fe-rich (upper image) and Fe-depleted bauxites (middle image). The average for all chemical elements occurring in Parnassos-Ghiona bauxites is also presented (lower image).

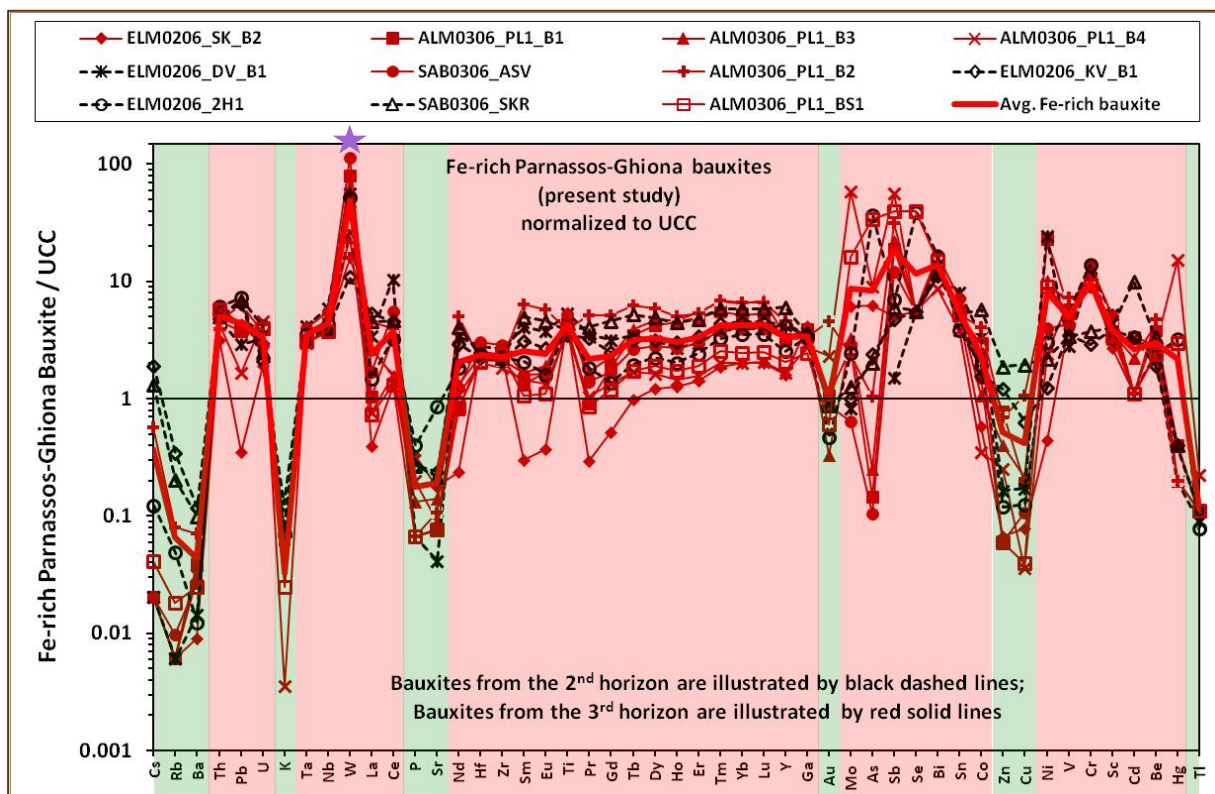
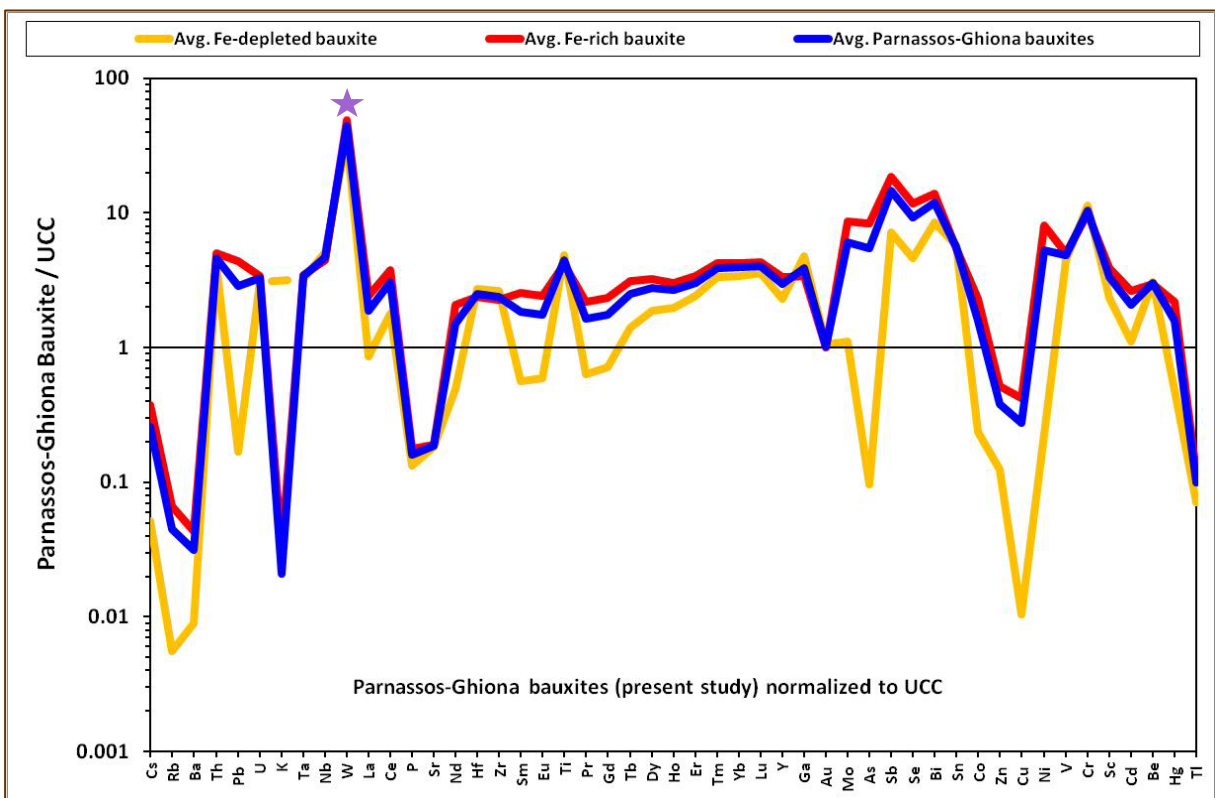
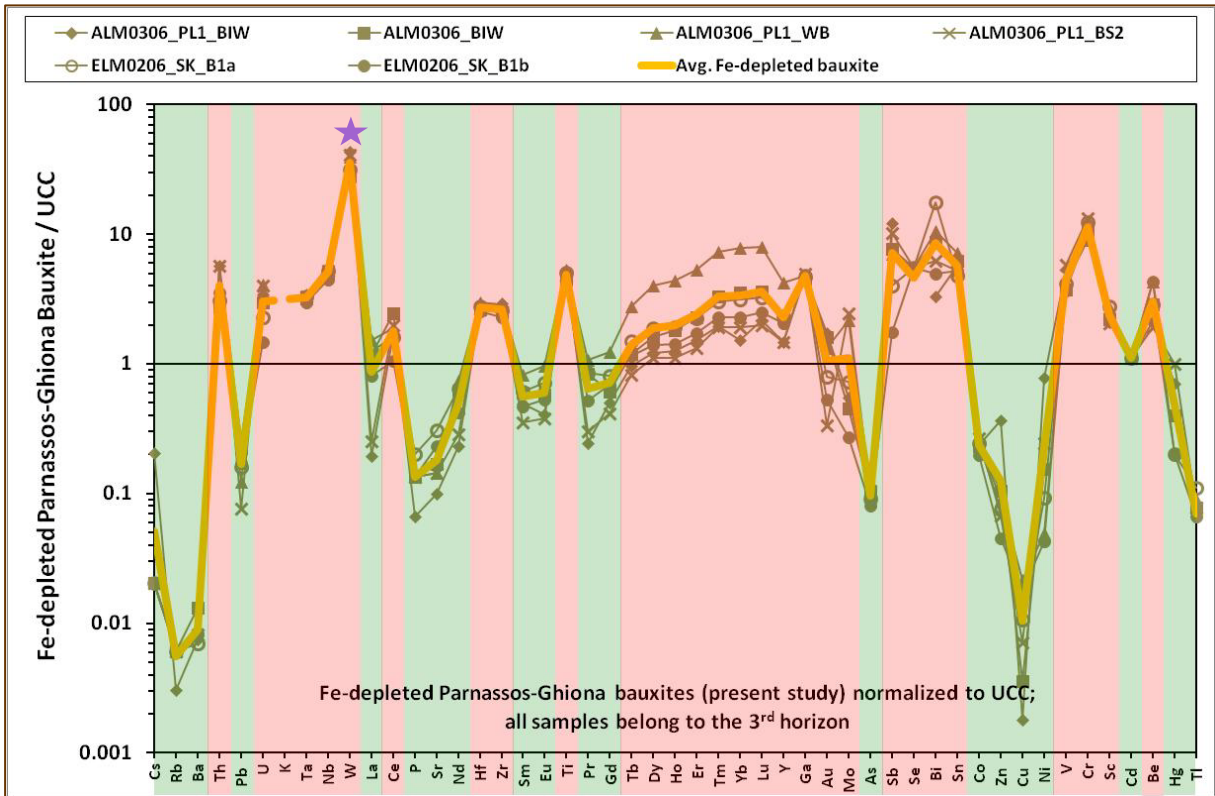


Figure 3.1.2.2: continued.

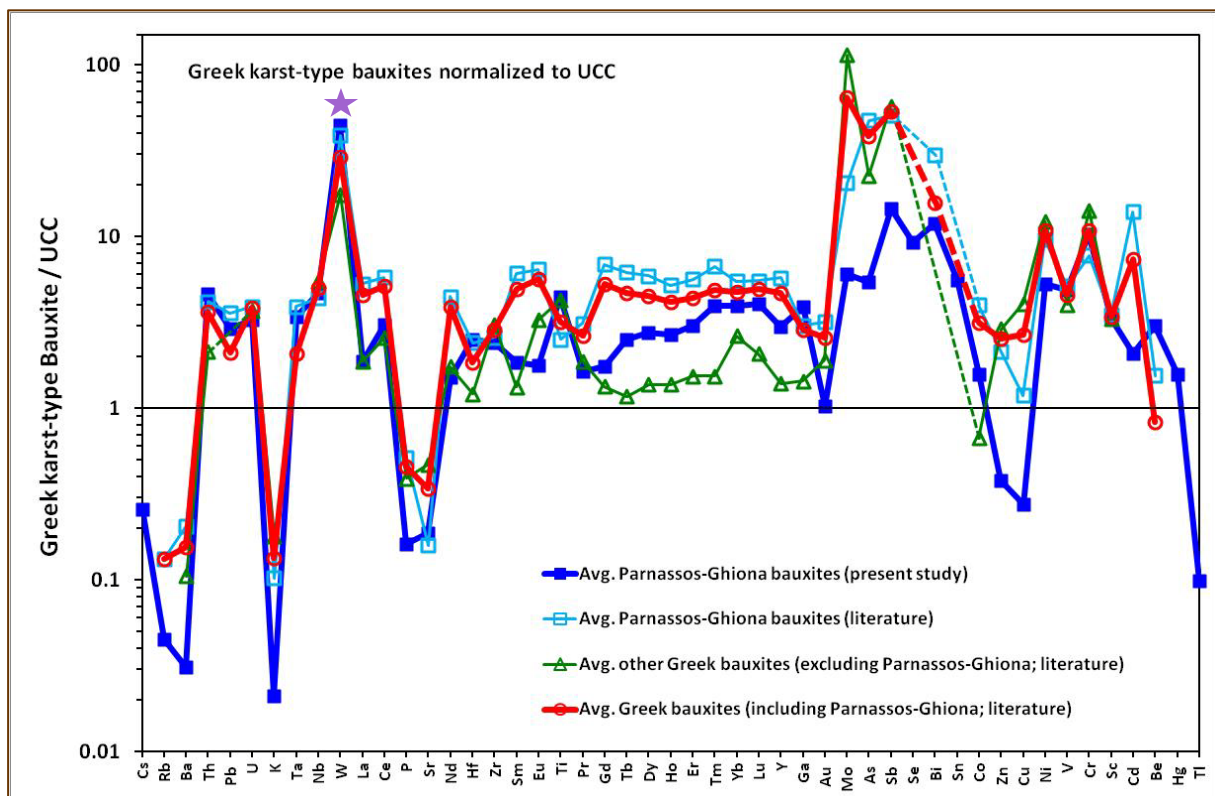


it was revealed by a combined Laser- and Synchrotron-based analytical investigation in microscale (see text below). Taking into account the literature for all Greek bauxites (i.e., Kiskyras, 1960; Papastamatiou & Maksimovic, 1970; Maksimović & Papastamatiou, 1973; Ochsenkühn & Parissakis, 1977; Biermann, 1983; Arp, 1985; Retzmann, 1986; Papastavrou & Perdikatsis, 1987; Laskou, 1991; Ochsenkühn-Petropoulou et al., 1991; Ochsenkühn-Petropoulou et al., 1994; Ochsenkühn et al., 1995; Papastavrou & Perdikatsis, 1987; Laskou & Economou, 1991; Laskou, 2001; Laskou & Andreou, 2003; Laskou & Economou-Eliopoulos, 2007; Eliopoulos & Economou-Eliopoulos, 2010; Papassiopi et al., 2010; Laskou et al., 2011; Laskou & Economou-Eliopoulos, 2013) it is agreed that there are similar enrichment/depletion trends, though in some cases there are favorable concentrations of As, Sb and REE (**Figure 3.1.2.3**).

It is evident that Fe-rich bauxites are preferentially enriched in Pb, REE and As, in comparison to Fe-depleted bauxites. In particular, the Fe-rich bauxites contain an average of 74.4 ppm Pb (avg. in Fe-depleted: 2.9 ppm), 40.1 ppm As (avg. in Fe-depleted: 0.5 ppm) and 568.7 ppm Σ REE (avg. in Fe-depleted: 268.4 ppm). The elevated Pb concentrations in Fe-rich samples are rather reasonable; in fact, a positive correlation of Fe with Pb has been found (see text below), and thus Pb must be contained in Fe-oxides and/or oxyhydroxides.

In a similar way, As is also related to Fe, and particularly to Fe-Cr-Ti in pisoliths, as revealed by Synchrotron Radiation (SR) μ -XRF (see text below). The REE content in Fe-rich bauxites is higher, simply due to higher content of REE minerals (of diagenetic and/or epigenetic origin), mostly REE fluorocarbonates, as indicated by SEM-EDS investigation (see text below).

Figure 3.1.2.3: UCC-normalized (Rudnick & Gao, 2003) spider diagrams for all Greek karst bauxites (Kiskyras, 1960; Papastamatiou & Maksimovic, 1970; Maksimović & Papastamatiou, 1973; Ochsenkühn & Parissakis, 1977; Biermann, 1983; Arp, 1985; Retzmann, 1986; Papastavrou & Perdikatsis, 1987; Laskou, 1991; Ochsenkühn-Petropoulou et al., 1991; Ochsenkühn-Petropoulou et al., 1994; Ochsenkühn et al., 1995; Papastavrou & Perdikatsis, 1987; Laskou & Economou, 1991; Laskou, 2001; Laskou & Andreou, 2003; Laskou & Economou-Eliopoulos, 2007; Eliopoulos & Economou-Eliopoulos, 2010; Papassiopi et al., 2010; Laskou et al., 2011; Laskou & Economou-Eliopoulos, 2013).



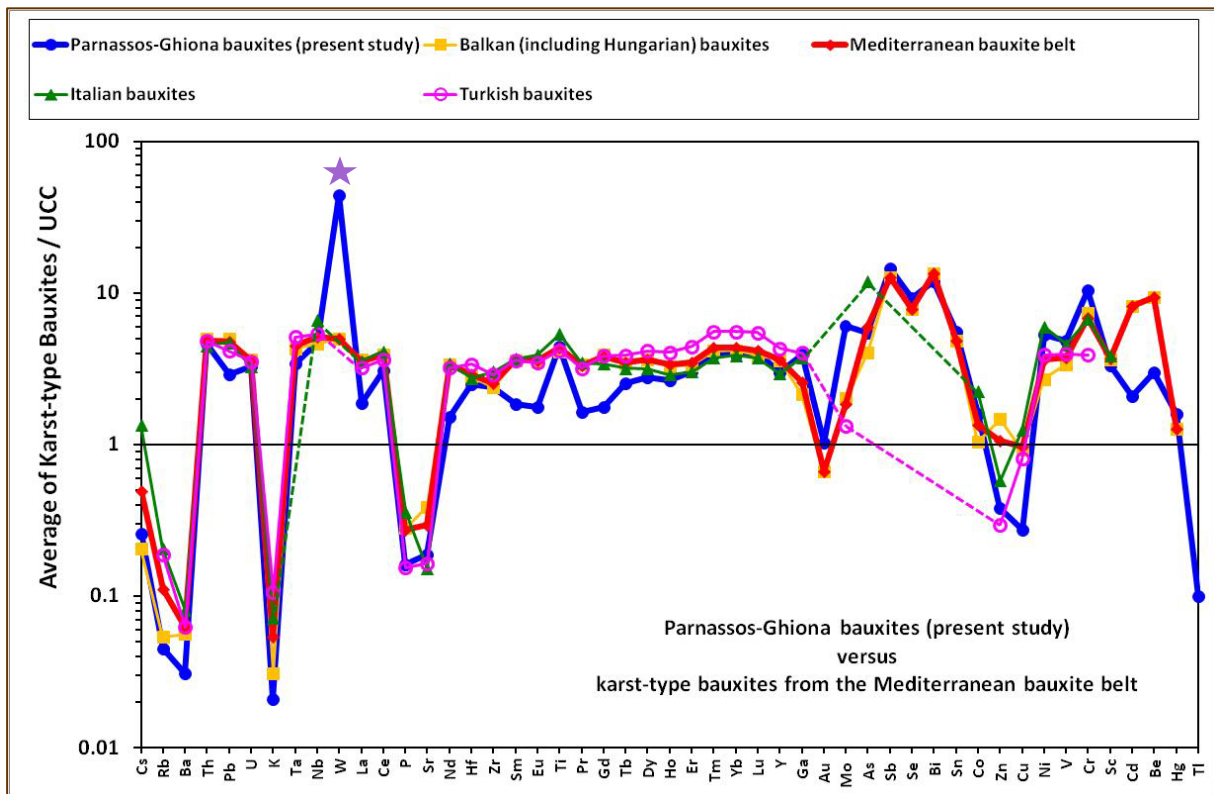
Regarding HFSE, the Parnassos-Ghiona bauxites, analyzed in the frame of the present dissertation, seem to be enriched in W (if it is not contamination from sample preparation – powdering- in WC apparatus; mentioned by purple solid star) when compared to the average of bauxites from the Mediterranean belt and particularly bauxites from Italy (Mongelli, 1997; MacLean et al., 1997; Mameli et al., 2007; Mondillo et al., 2011; Boni et al., 2013; Mongelli et al., 2014), and Turkey (Özlu, 1983; Öztürk et al., 2002; Karadağ et al., 2009; Haniçli et al., 2013), as well as from Balkan countries (i.e., Bosnia, and Montenegro) and

Hungary (Bárdossy, 2011 – personal communication: new data in the frame of the present dissertation; Tables 3.1.2.1 & 3.1.2.2 and Figure 3.1.2.4). In general, the bulk geochemical trends of the Greek bauxites are similar to karst-type bauxites of neighboring countries.

Table 3.1.2.2: New analytical data concerning representative bauxite samples from active mines of Balkan countries (i.e., Bosnia, and Montenegro) and Hungary, supplied by the Ajkai Timföldgyár alumina plant (MAL Magyar Alumínium Zrt) and provided by György Bárdossy† (Bárdossy, 2011 – personal communication: new data in the frame of the present dissertation: see experimental section).

Sample code	MAL-Jajce	MAL-Halimba	MAL-Niksic	Sample code	MAL-Jajce	MAL-Halimba	MAL-Niksic
Country	Bosnia	Hungary	Montenegro	Country	Bosnia	Hungary	Montenegro
<i>Unit</i>	<i>data</i>	<i>data</i>	<i>data</i>	<i>Unit</i>	<i>data</i>	<i>data</i>	<i>data</i>
<i>wt. %</i>				<i>ppm</i>			
SiO ₂	0.92	5.83	6.42	Ag	0	1.7	0
Al ₂ O ₃	58.57	52.77	57.14	Cd	0.2	0.2	1.8
Fe ₂ O ₃ (T)	25.12	21.8	19.84	Sn	12	12	11
MnO	0.02	0.13	0.12	Sb	3.9	9.5	1.8
MgO	0.05	0.17	0.23	Cs	0.3	0.2	2.5
CaO	0.35	2.05	0.21	Ba	10	18	42
Na ₂ O	0.01	0.07	0.02	Hf	15.7	15.2	13.8
K ₂ O	0	0.06	0.2	Ta	3.9	3.3	4.4
TiO ₂	2.67	2.59	2.75	W	5.5	5.8	6.6
P ₂ O ₅	0	0.12	0.05	Hg	0.04	0.06	0.09
Cr ₂ O ₃	0.083	0.055	0.063	Tl	0	0	0
LOI	11.9	14	12.6	Pb	70.8	65.8	94.9
Total	99.69	99.65	99.64	Bi	2.8	1	2.7
<i>ppm</i>				La	112.1	77.8	153.1
Be	7	3	5	Ce	287.2	126.2	330.8
Sc	63	44	64	Pr	27.3	13.7	30.3
V	324	805	284	Nd	107.7	49	117.1
Cu	4	8.2	38.7	Sm	20.04	7.75	22.83
Co	16.2	24.1	20	Eu	4.26	1.72	4.62
Ni	128	70	115	Gd	19.32	7.78	19.97
Zn	7	10	98	Tb	2.84	1.34	2.99
Ga	45.1	52	47.7	Dy	15.47	9.16	17.9
As	37.5	16.5	4.3	Ho	2.82	1.91	3.47
Se	0.8	0.6	0.7	Er	7.5	5.8	9.67
Rb	0.2	1.3	11.7	Tm	1.15	0.91	1.68
Sr	43.9	120	83.4	Yb	7.86	5.75	11.37
Y	52.9	54.6	100.2	Lu	1.13	0.91	1.55
Zr	519.5	580.5	543.1	Th	61.3	46.6	48.3
Nb	48.3	51.4	56.7	U	6.7	15.4	7.5
Mo	0.9	5.4	0.5	<i>ppb</i>			
				Au	0	1.1	1.9

Figure 3.1.2.4: UCC-normalized (Rudnick & Gao, 2003) spider diagrams for the average of the Parnassos-Ghiona bauxites in comparison with the average of karst bauxites from Italy (Mongelli, 1997; MacLean et al., 1997; Mameli et al., 2007; Mondillo et al., 2011; Boni et al., 2013; Mongelli et al., 2014), Turkey (Özlü, 1983; Öztürk et al., 2002; Karadağ et al., 2009; Haniçi et al., 2013), and Balkan countries (i.e., Bosnia, and Montenegro) and Hungary (Bárdossy, 2011 – personal communication: new data in the frame of the present dissertation), as well as with the average of the karst bauxites from the Mediterranean bauxite belt (excluding Greek bauxites).



On the other hand, when Parnassos-Ghiona bauxite is normalized to the average of karst bauxites from the Mediterranean belt ,excluding Greek bauxites, i.e., using data from the Bosnian, Montenegrin, and Hungarian bauxites (Bárdossy, 2011 – personal communication: new data in the frame of the present dissertation), data from the Bulgarian, Croatian, and Romanian bauxites (Özlü, 1983 and references therein) data from Italian bauxites (Mongelli, 1997; MacLean et al., 1997; Mameli et al., 2007; Mondillo et al., 2011; Boni et al., 2013; Mongelli et al., 2014) and data from Turkish karst bauxites: Özlü, 1983;

Öztürk et al., 2002; Karadağ et al., 2009; Hanilçi et al., 2013), significantly enriched in W (if it is not contamination from sample preparation –powdering- in WC apparatus; mentioned by purple solid star), Mo, Co, Ni, Sb and Hg was revealed (Figure 3.1.2.5). The same geochemical trends also stand for all Greek bauxites (Figure 3.1.2.6). According to SEM-EDS investigation (see text below), Co and Ni are present, at least, in distinct Ni-Co-sulfides corresponding to detrital pentlandite-type phases. The distribution, partitioning, and solid-state speciation of Mo, Sb and Hg have not been concluded yet, despite detailed study of the samples using a combination of microscopic and spectroscopic techniques in various scales.

Figure 3.1.2.5: Mediterranean bauxite belt-normalized (Özlü, 1983 and references therein; Mongelli, 1997; MacLean et al., 1997; Öztürk et al., 2002; Mameli et al., 2007; Karadağ et al., 2009; Mondillo et al., 2011; Boni et al., 2013; Hanilçi et al., 2013; Mongelli et al., 2014 and new data of the present dissertation: Bárdossy, 2011 – personal communication) spider diagrams for the studied Fe-rich (upper image) and Fe-depleted bauxite (middle image). The average for all chemical elements occurring in Parnassos-Ghiona bauxite is presented (lower image).

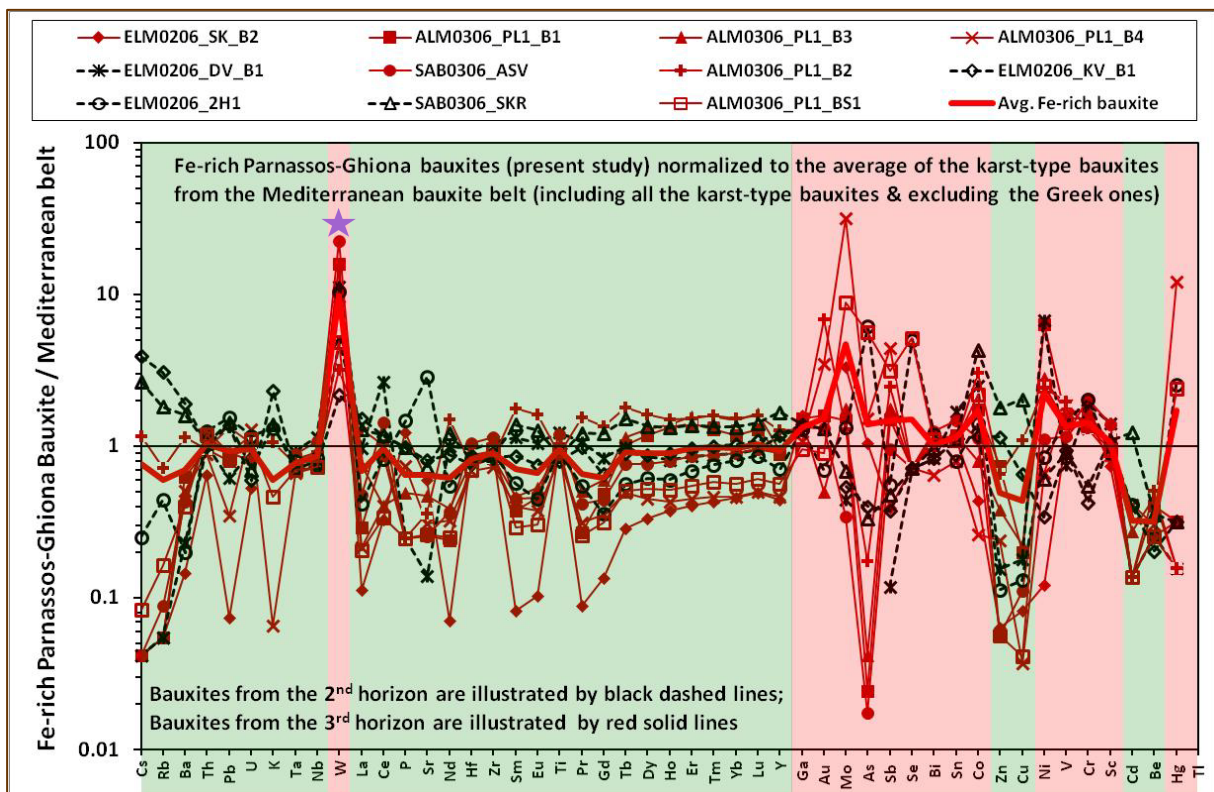


Figure 3.1.2.5: continued.

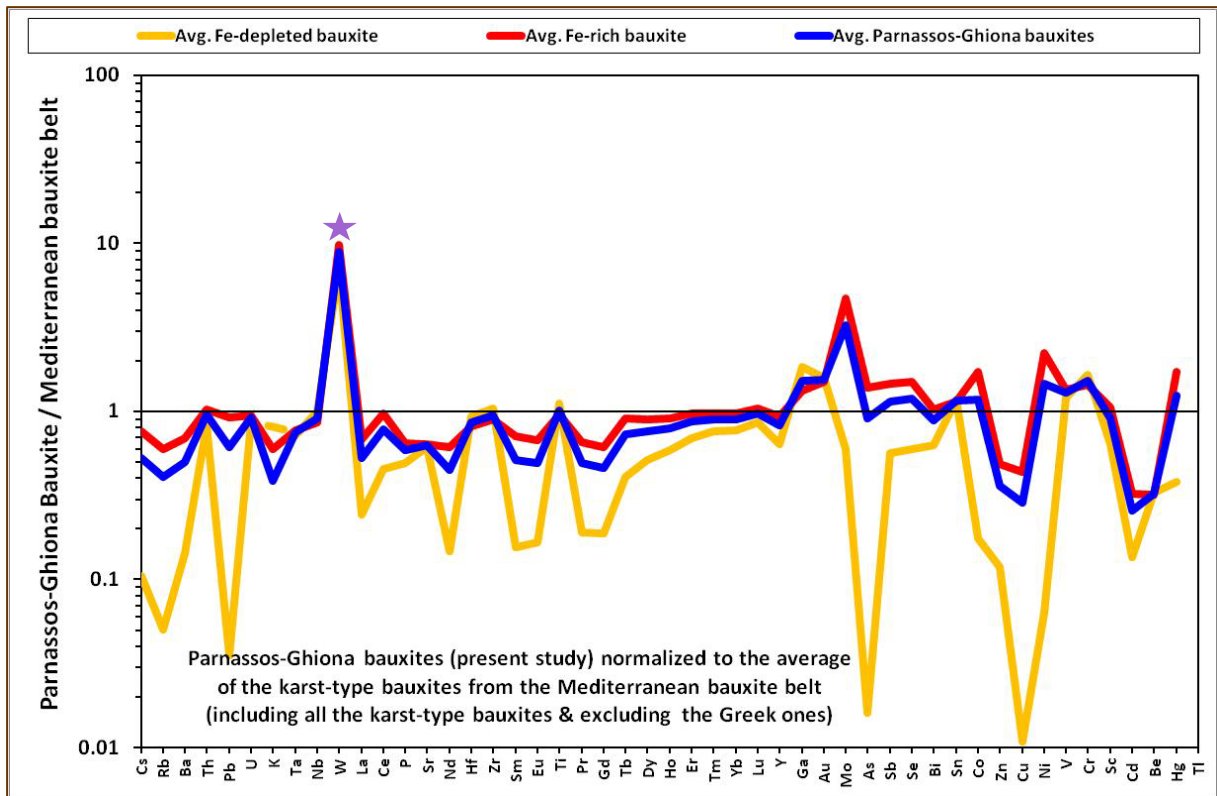
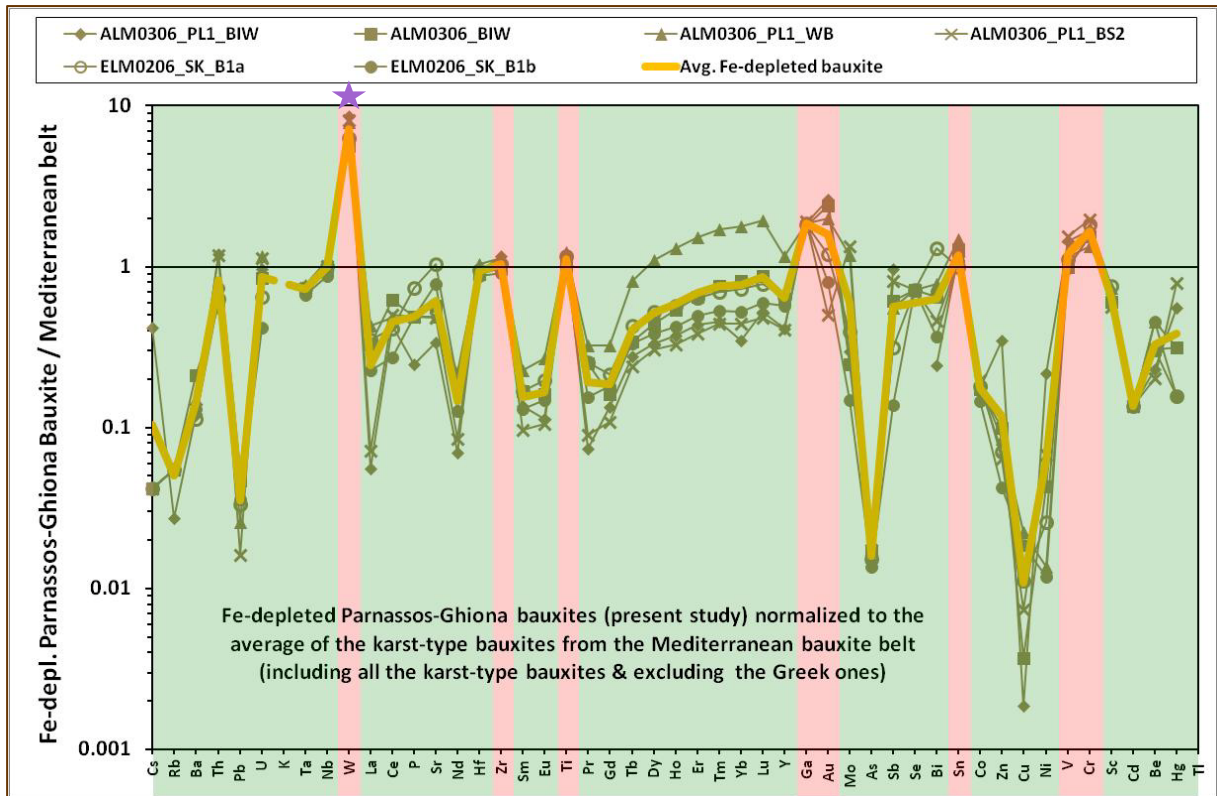
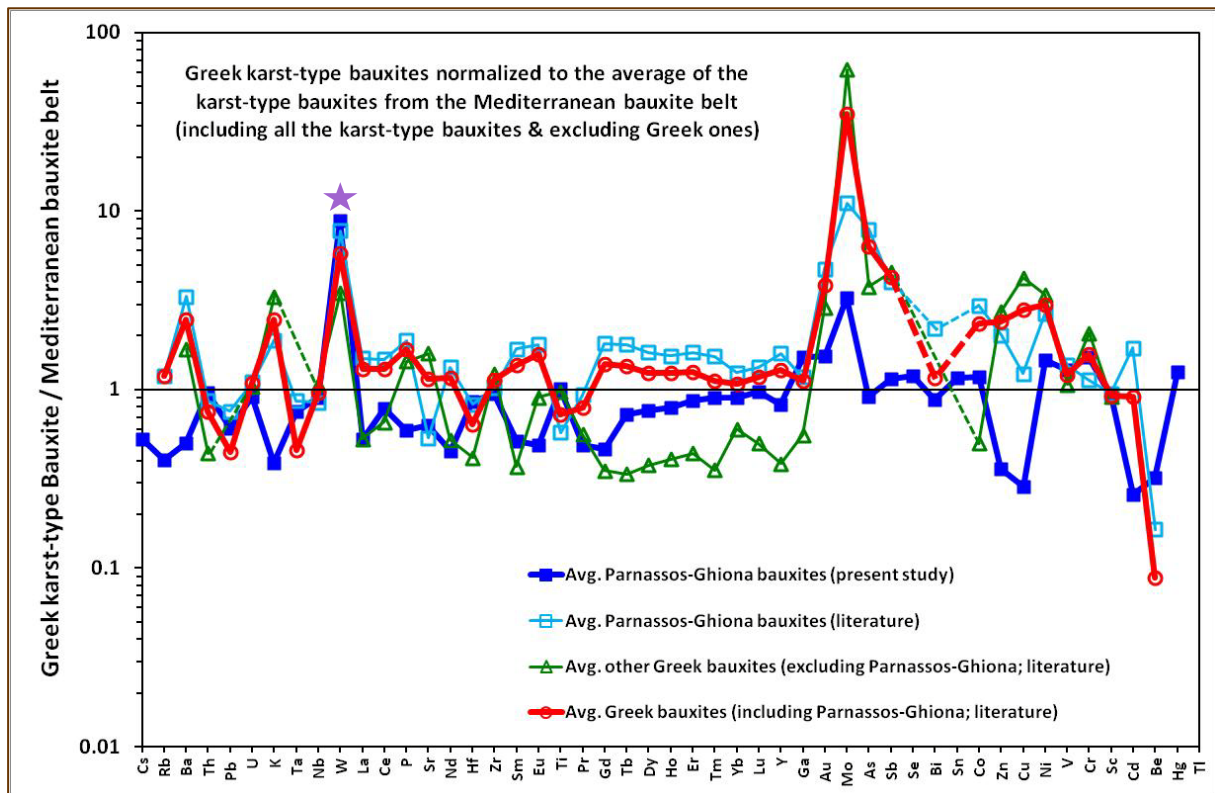


Figure 3.1.2.6: Mediterranean bauxite belt-normalized (for relevant literature: see caption of previous **Figure 3.1.2.5**) spider diagrams for all Greek bauxites (Kiskyras, 1960; Papastamatiou & Maksimovic, 1970; Maksimović & Papastamatiou, 1973; Ochsenkühn & Parissakis, 1977; Biermann, 1983; Arp, 1985; Retzmann, 1986; Papastavrou & Perdikatsis, 1987; Laskou, 1991; Ochsenkühn-Petropoulou et al., 1991; Ochsenkühn-Petropoulou et al., 1994; Ochsenkühn et al., 1995; Papastavrou & Perdikatsis, 1987; Laskou & Economou, 1991; Laskou, 2001; Laskou & Andreou, 2003; Laskou & Economou-Eliopoulos, 2007; Eliopoulos & Economou-Eliopoulos, 2010; Papassiopi et al., 2010; Laskou et al., 2011; Laskou & Economou-Eliopoulos, 2013).



On the basis of bulk chemical analyses, it can be argued that there is a correlation between certain chemical elements (**Figures 3.1.2.7 – 3.1.2.14**). First of all, there is a negative correlation between SiO_2 and Al_2O_3 , meaning that Si-containing minerals (i.e., kaolinite) are more abundant in Fe-rich (low grade) bauxites, as has been also revealed by powder XRD. Also, there is a strong correlation of SiO_2 with distinct LILE such as K, Rb, Cs and

Ba. Potassium is most likely related to unidentified minor micro-/nano-sized silicate minerals (clays), which could also be true for Rb and Cs, as well as for Ca. The strong correlation between Al and Fe, especially in the case of Fe-depleted bauxites, is mainly due to the presence of Fe into diaspore which concerns in fact a low-T natural Fe-Cr-AlOOH phase, described for first time in literature (see text below). The correlation of Al and Cr is not obvious in bulk geochemistry, and it is only revealed in microscale and nanoscale studies. A strong correlation is observed between Zr and Ti, Zr and Nb, and especially Zr-Hf implying the presence of Hf into detrital zircon crystals. Al and Ga are reasonably correlated due to similarities in ionic radii and valence, but it can be concluded that Ga (avg. for all bauxites: 68.2 ppm) is obviously not absolutely contained in AlOOH polymorphs (diaspore and boehmite). Lead is not correlated to any other metal except Fe, implying that Pb must be contained in Fe-oxides and/or -oxyhydroxides. It is known that Pb shows a strong affinity for hematite and moreover, for goethite, during metal uptake (sorption) geochemical processes in aqueous environments (e.g. [O'Reilly & Hochella, 2003](#); [Ostergren et al., 1999](#)). On the other hand, V, which is an element of increased importance in bauxite industry due to its involvement in red mud ([Burke et al., 2013](#); [present dissertation](#)), is not correlated to Fe or any other metal in bulk. According to SR μ -XRF and μ -XAFS investigation (see text below), high-valence V is related to Ca and K (and also possibly Sc), in micro-areas between Fe-Cr-Ti and Al-(Ga) pisoliths. Titanium, except Zr, is also correlated to Nb, Hf and Ta. However, the relevance of Ti with Ta stands for Fe-rich samples, whereas the relevance with Nb is valid for all types of bauxites. In fact, the correlation of Ti and Nb (and Nb to Ta) is the most remarkable in bulk geochemistry and shows that Nb is most probably hosted in anatase (as also proved by LA-ICP-MS analyses; see text below). Another significant element is Th, related to the observed radioactivity in Parnassos-Ghiona bauxites and the red mud ([Papatheodorou et al., 2005](#); [Pontikes et al., 2006](#); [Pontikes, 2007](#); [Karagiannidi et al., 2009](#); [Samouhos et al. 2013](#); [present dissertation](#)). The evaluation of the bulk geochemical data gave no evidence of any correlation with other metals. However, the detailed microscopic, analytical, and spectroscopic investigation in microscale revealed the occurrence of Th in anatase particles (see text below). The LREE and HREE are well-correlated to Y, which is geochemically reasonable, as well as Gd and Eu themselves.

Figure 3.1.2.7: Binary diagram of Al_2O_3 and SiO_2 (upper image) showing the dominance of AIOOH polymorphs and the almost absence of kaolinite-group minerals, as well as plot of Si, K, Cs, Rb, and Ba (lower image) illustrating the correlation between the more mobile Large Ion Lithophile Elements (LILE) for the studied Parnassos-Ghiona bauxites.

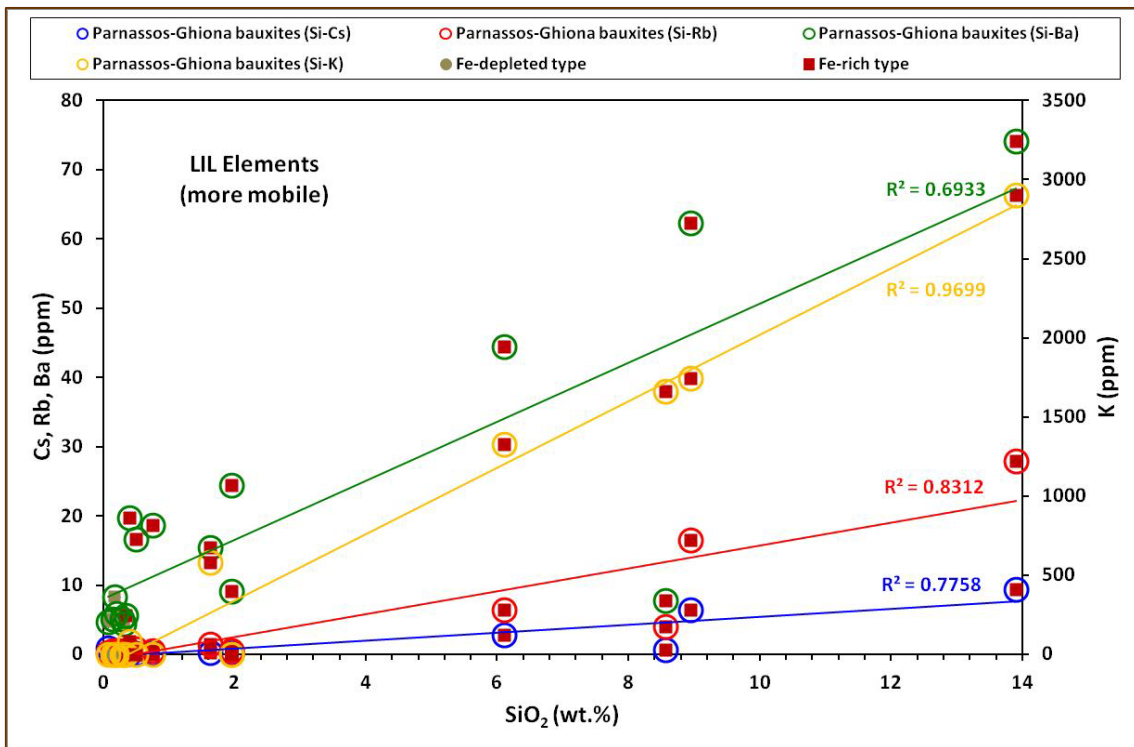
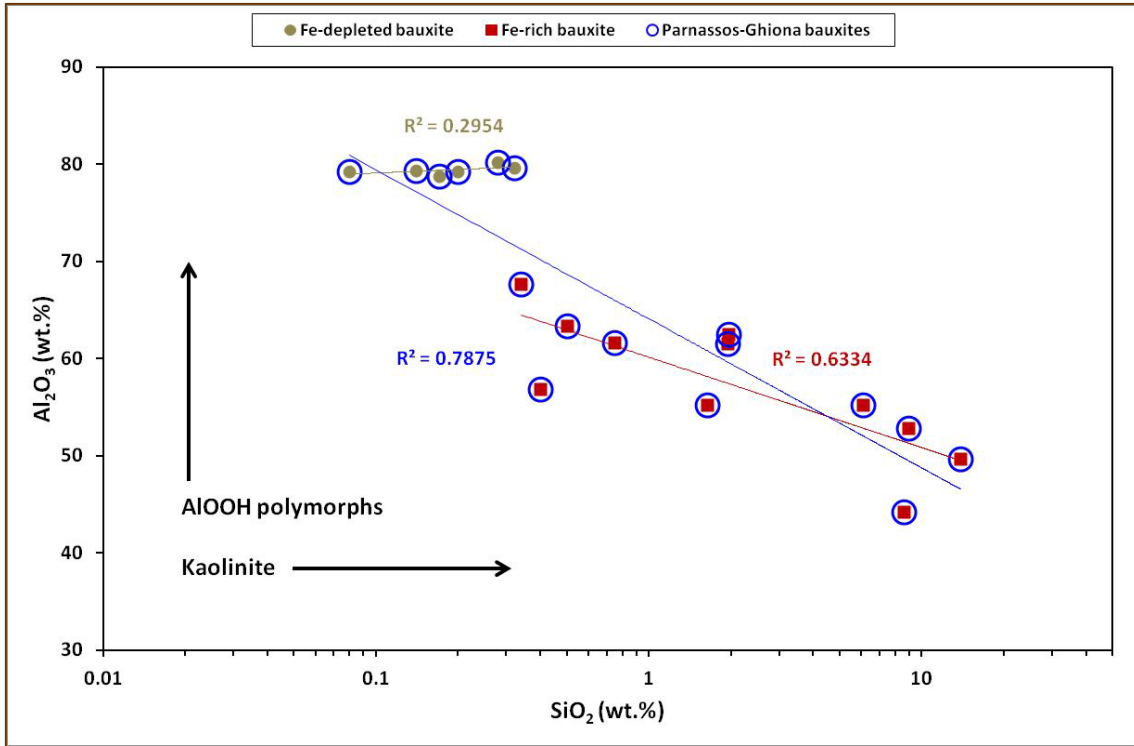


Figure 3.1.2.8: Binary diagrams of some major elements (such as Fe_2O_3 vs Al_2O_3 and Cr_2O_3 vs Al_2O_3 ; in wt.%) showing the correlation between them for the studied Parnassos-Ghiona industrial bauxites.

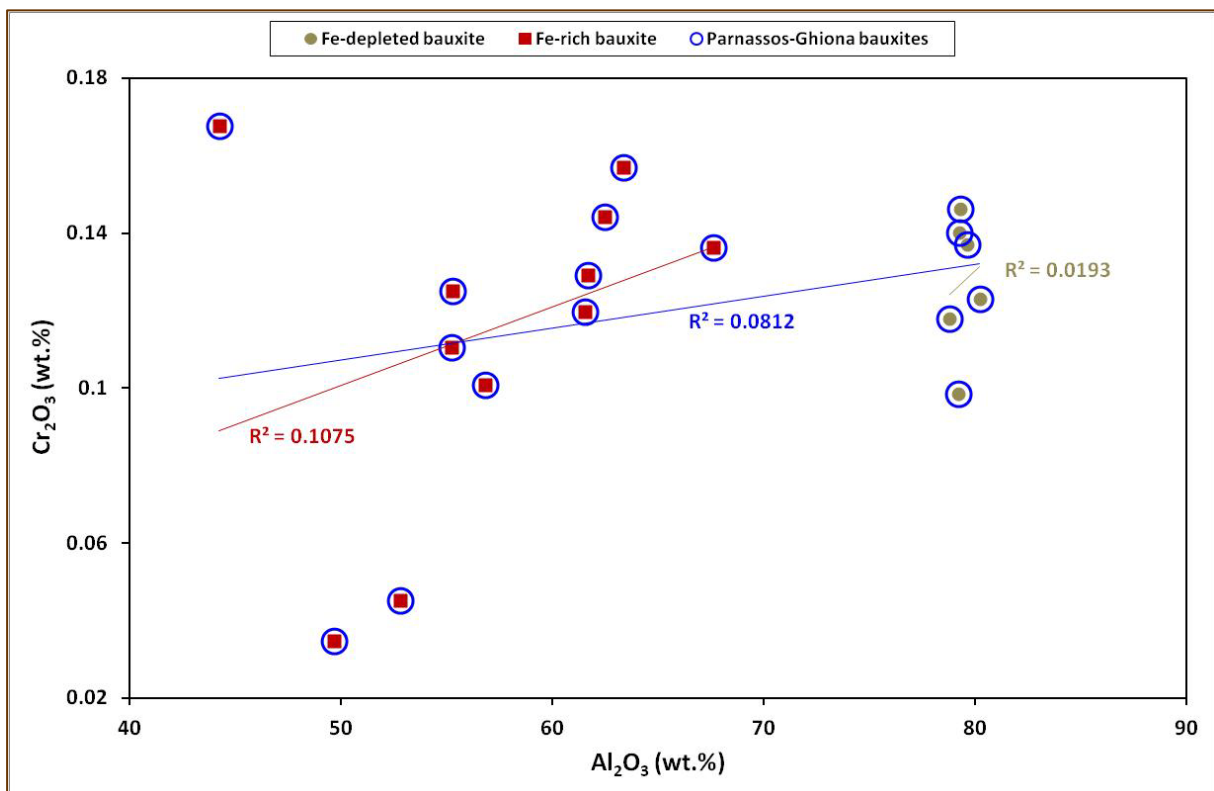
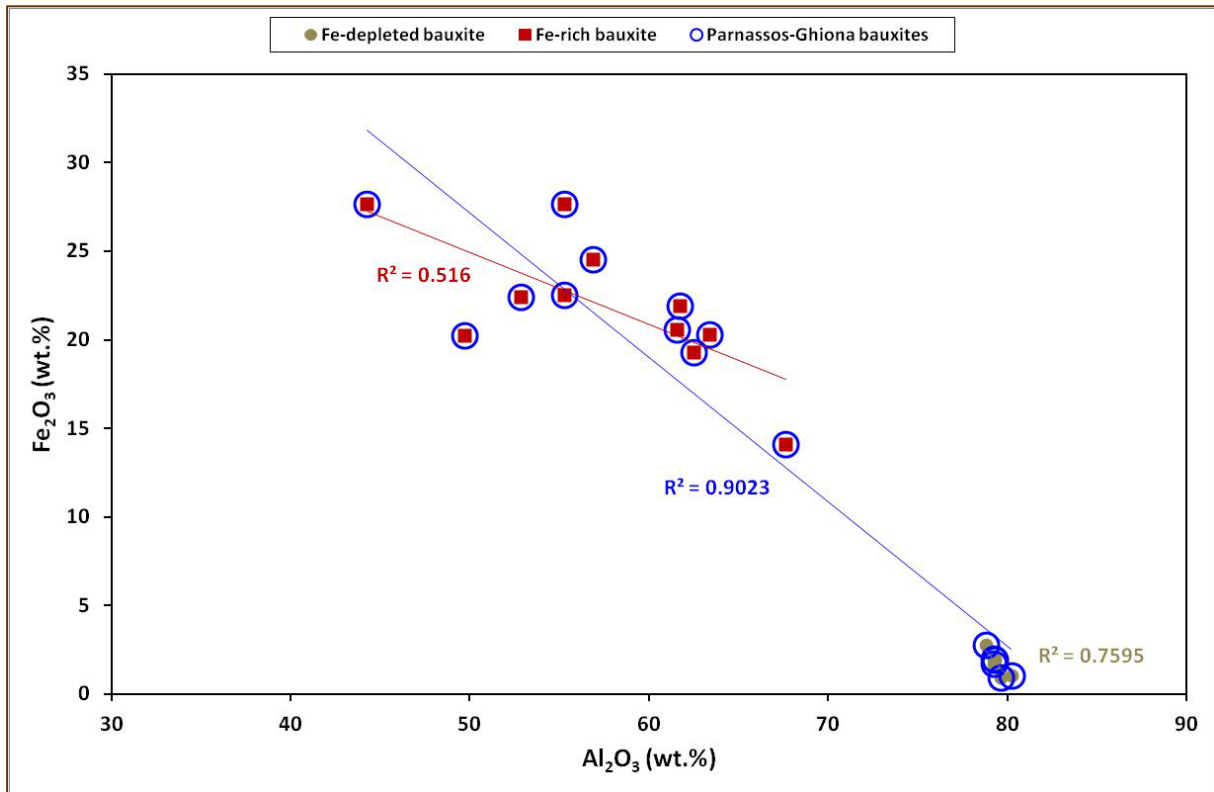


Figure 3.1.2.9: Plot of Zr, Ti, Nb, and Hf (upper image) illustrating the correlation between the less mobile lithophile High Field Strength Elements (HFSE), as well as binary diagram of Ga (ppm) and Al₂O₃ (wt.%) illustrating their correlation for the studied Parnassos-Ghiona industrial bauxites.

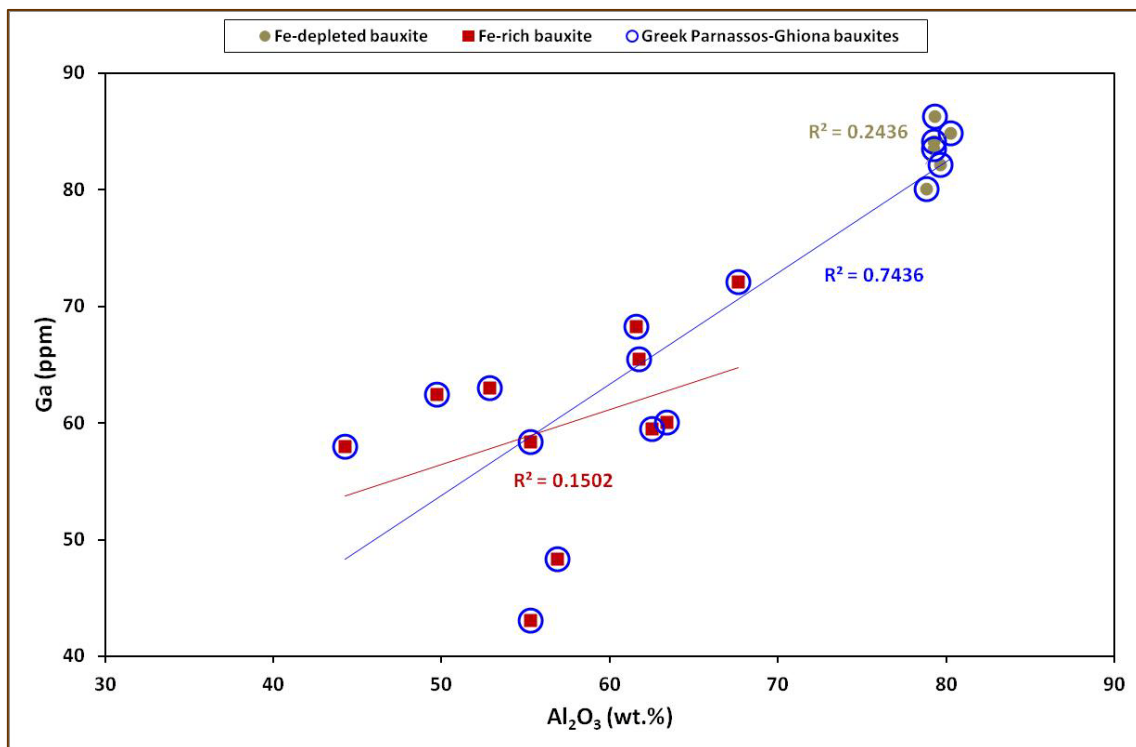
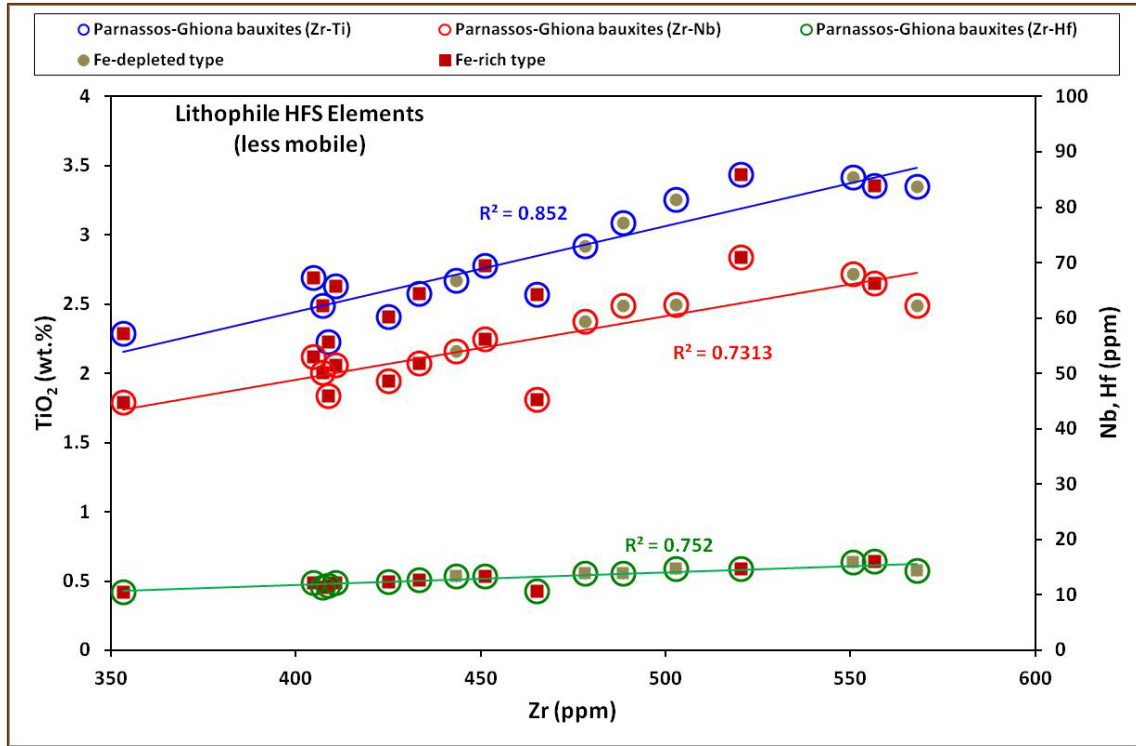


Figure 3.1.2.10: Binary diagrams illustrating the correlation between Fe₂O₃ (wt.%) the Pb, and the V (ppm) for the studied Parnassos-Ghiona industrial bauxites.

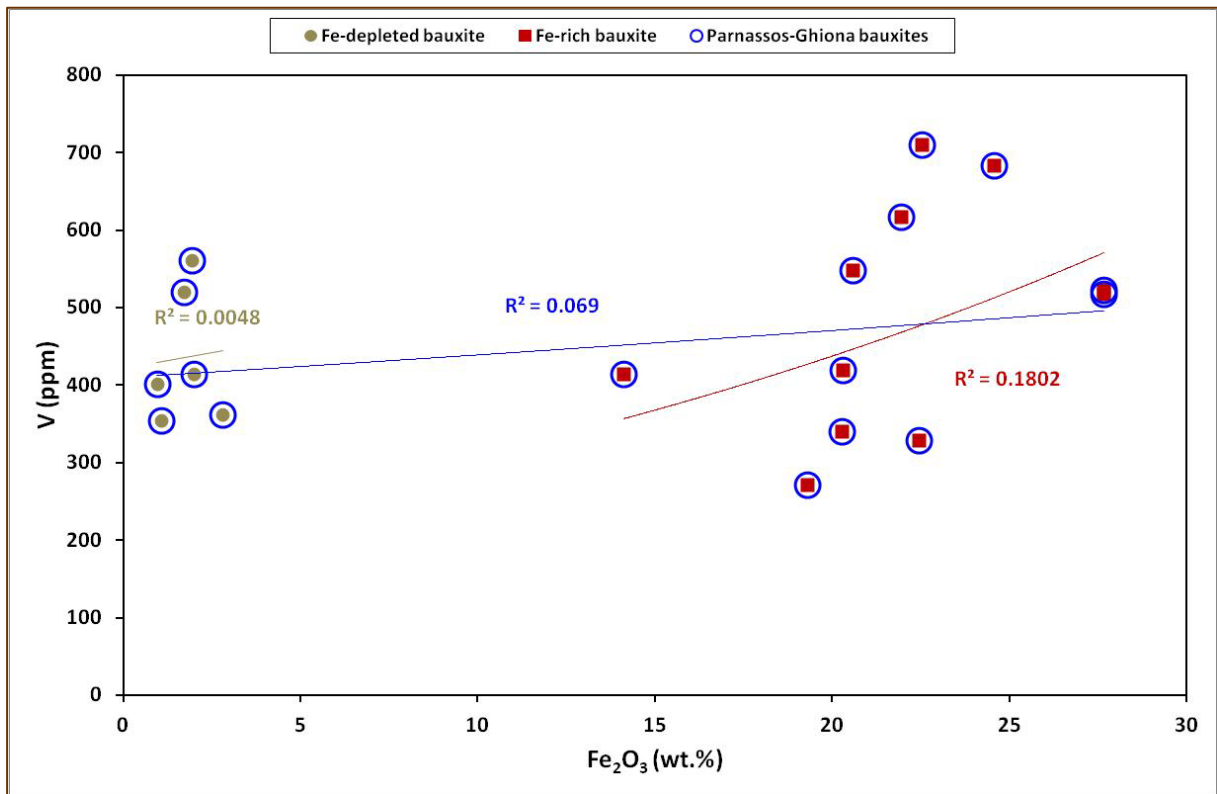
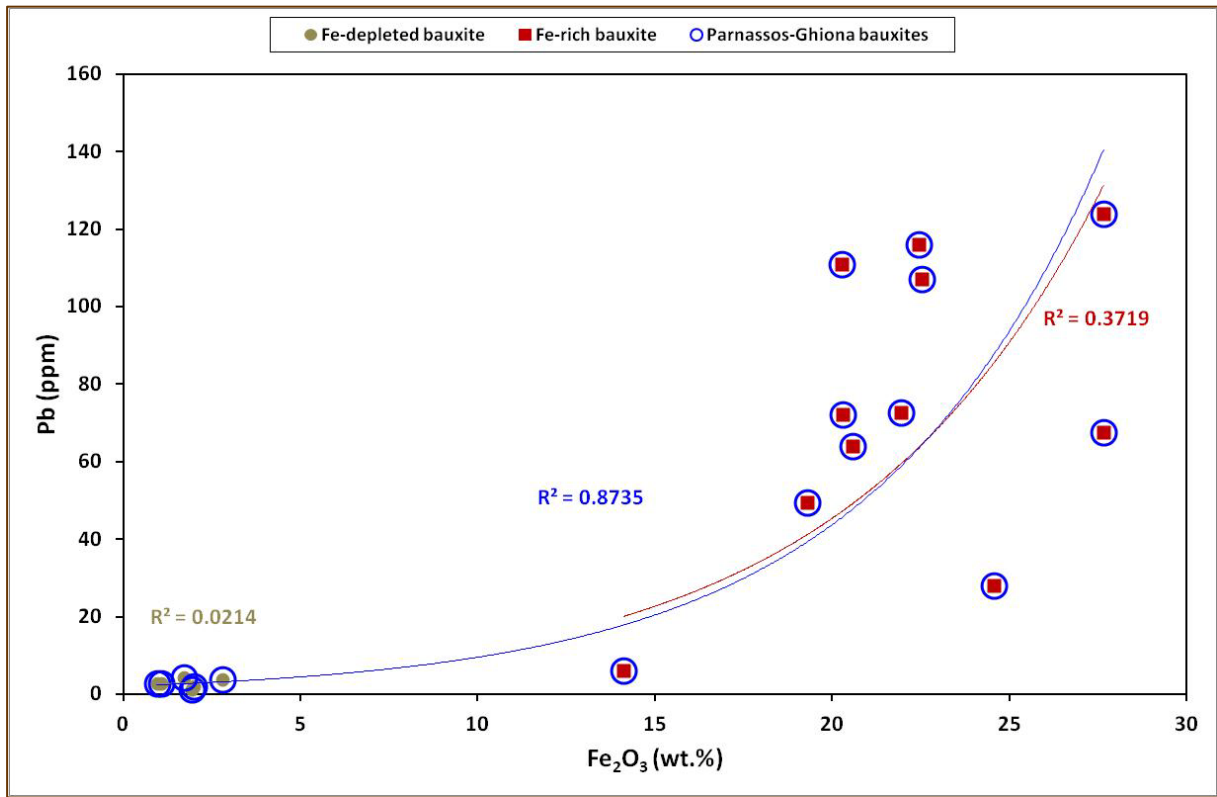


Figure 3.1.2.11: Binary diagrams illustrating the correlation between TiO_2 (wt.%), and Ta, Nb, Hf (ppm) as well as correlation between Nb (ppm), and Ta (ppm) for the studied Parnassos-Ghiona industrial bauxites.

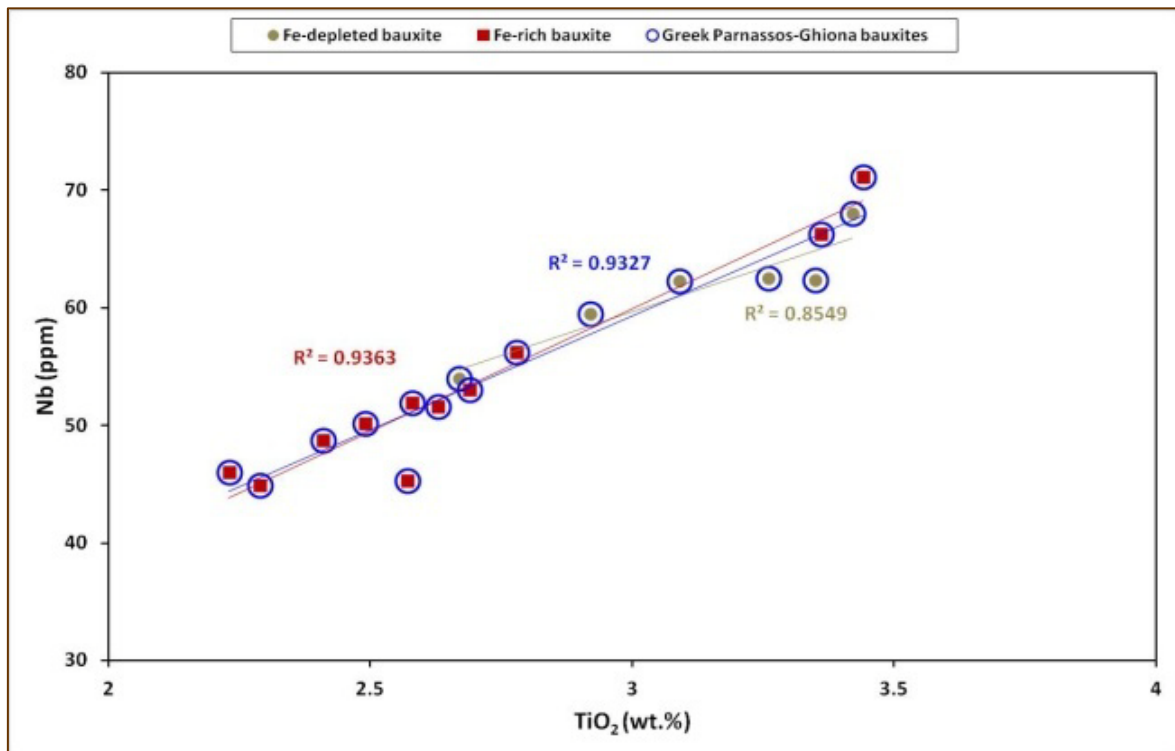
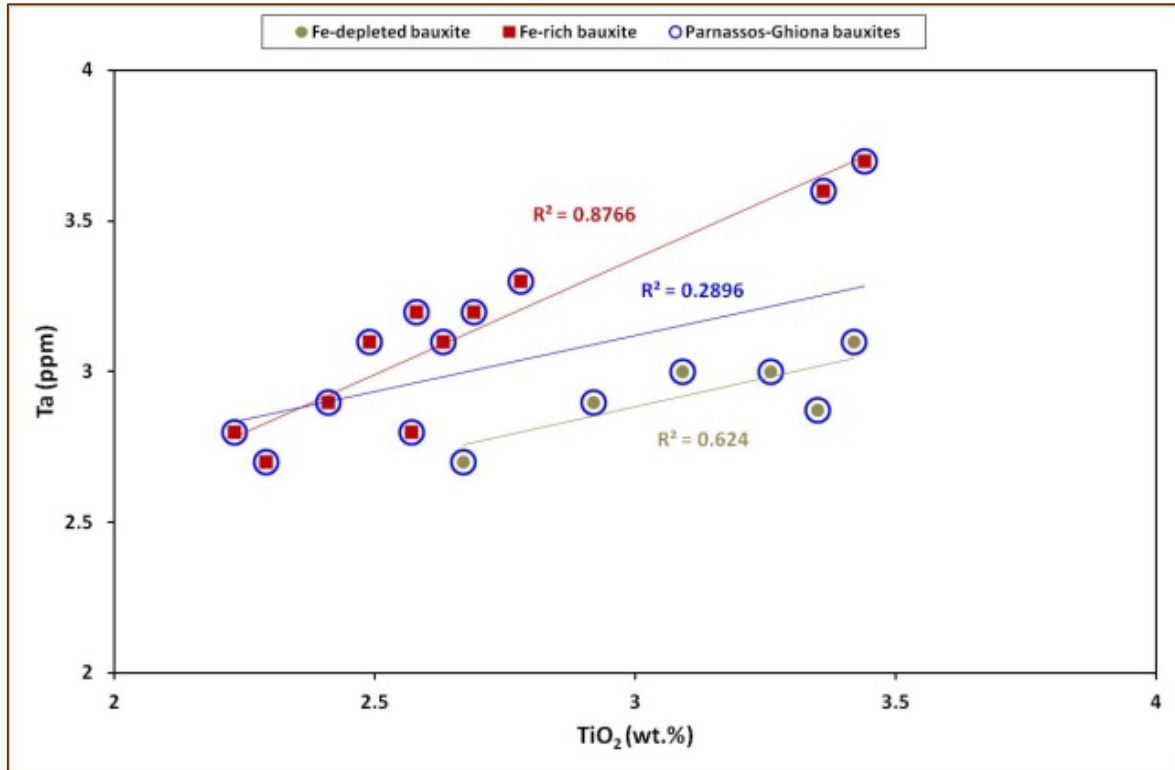


Figure 3.1.2.11: continued.

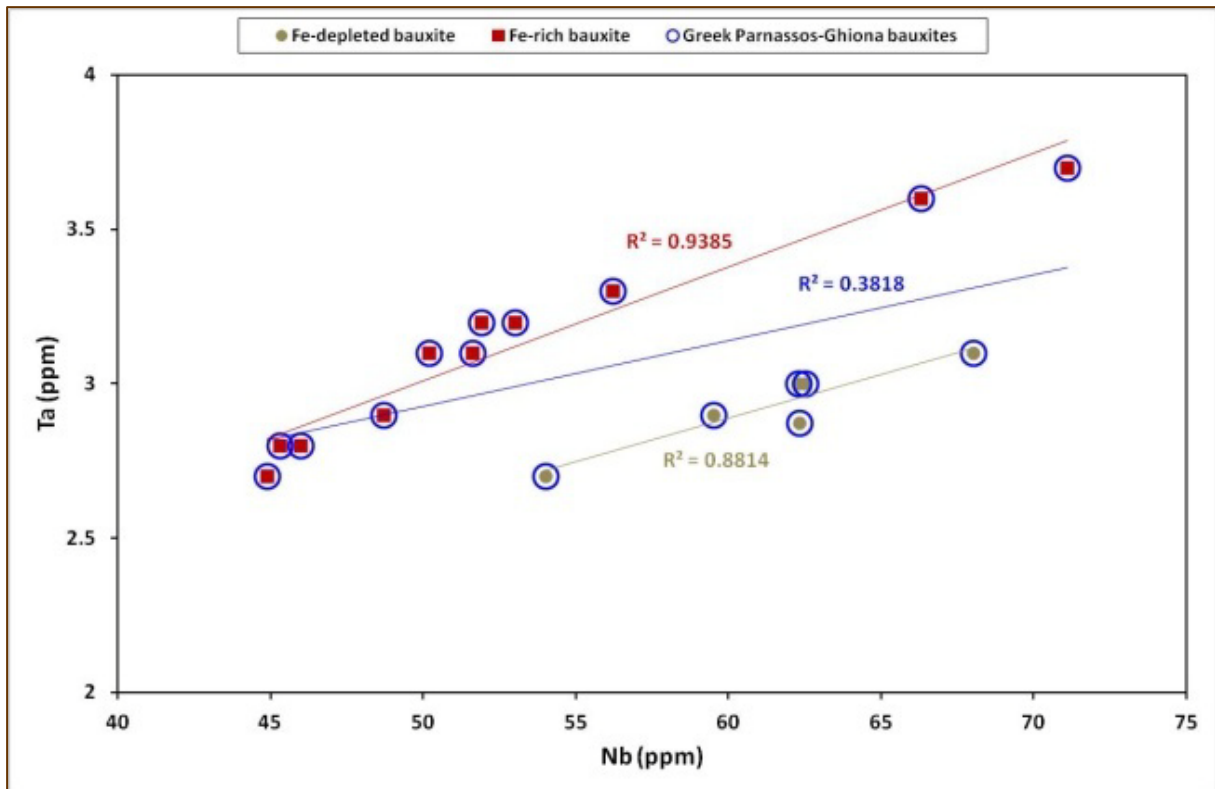
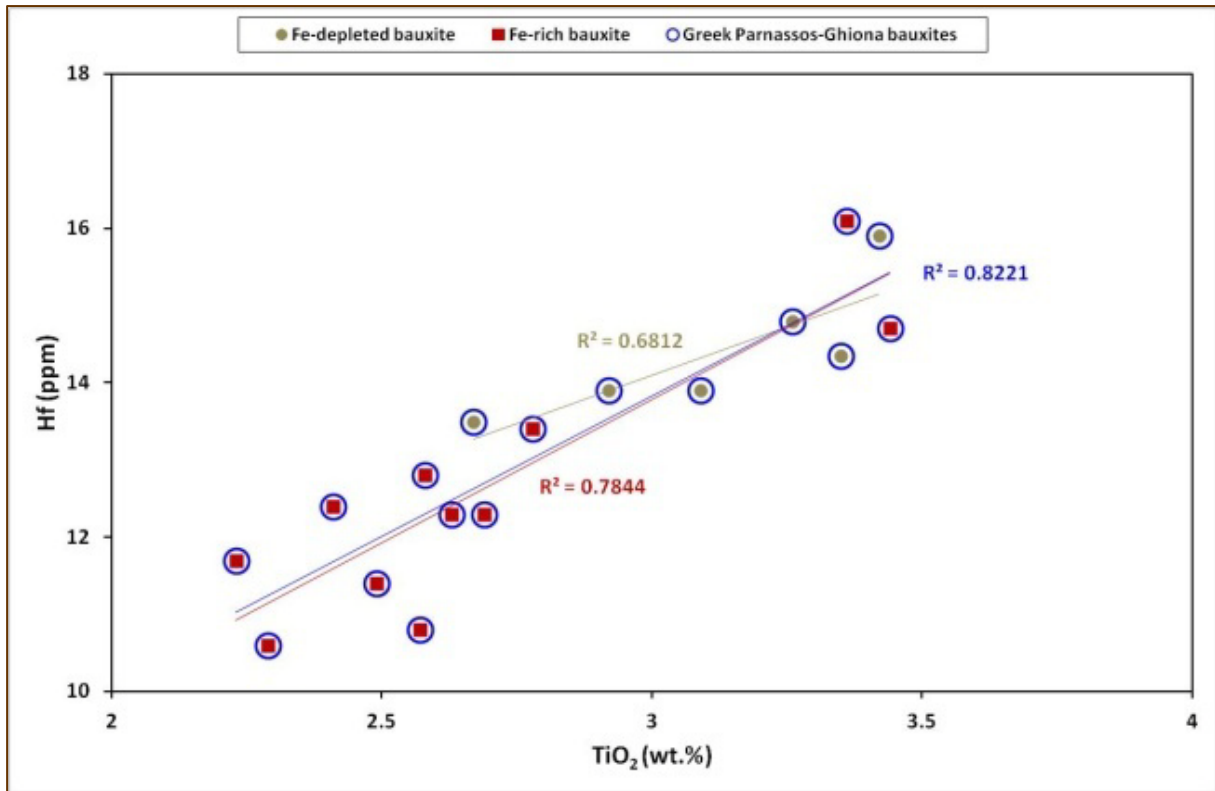


Figure 3.1.2.12: Binary plots of Al₂O₃, Fe₂O₃, TiO₂, and SiO₂ (in wt.%) and Th (in ppm).

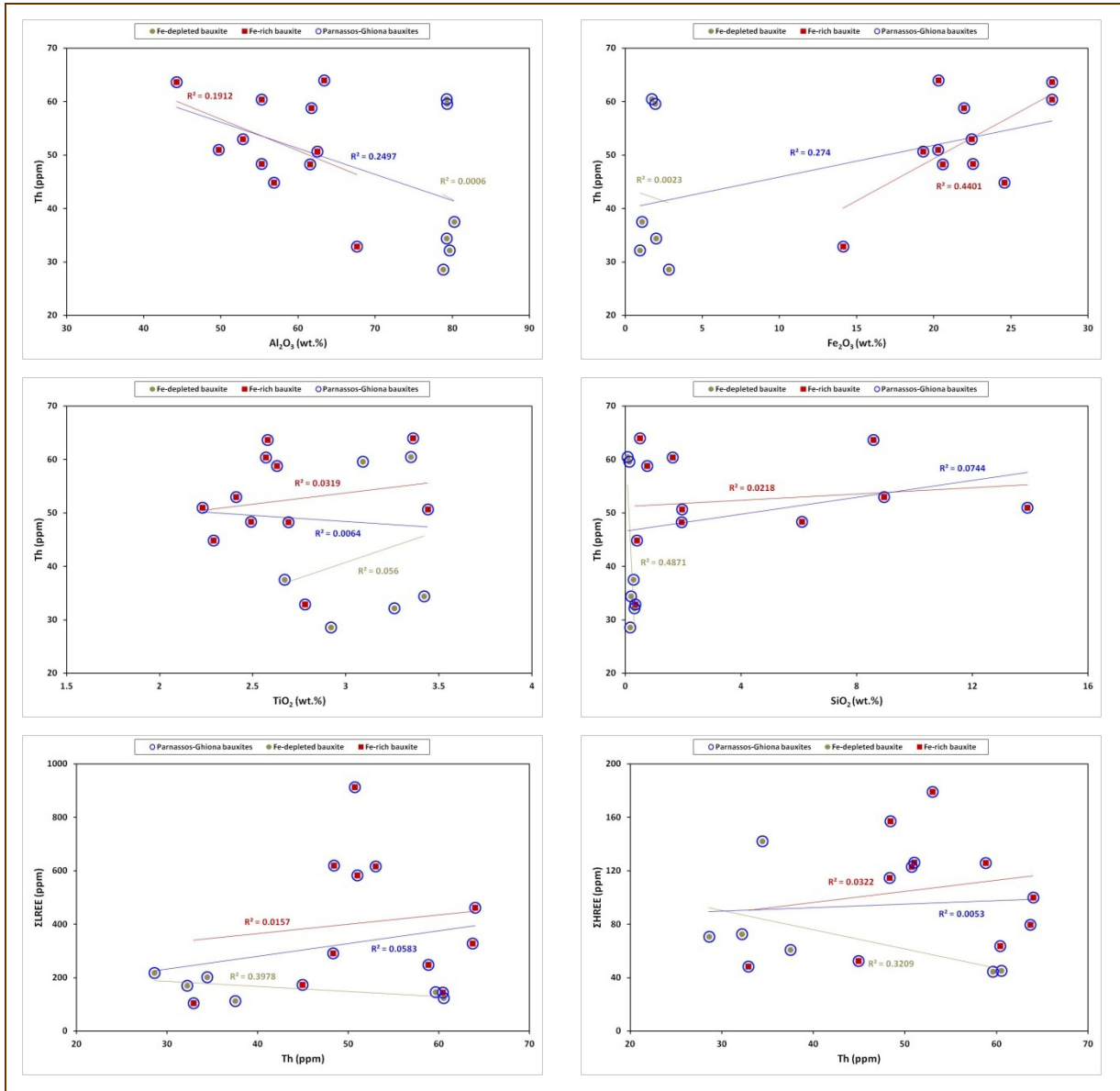


Figure 3.1.2.13: Binary diagrams illustrating the correlation between Y (ppm), the Σ LREE, and the Σ HREE content (ppm) for the studied Parnassos-Ghiona industrial bauxites.

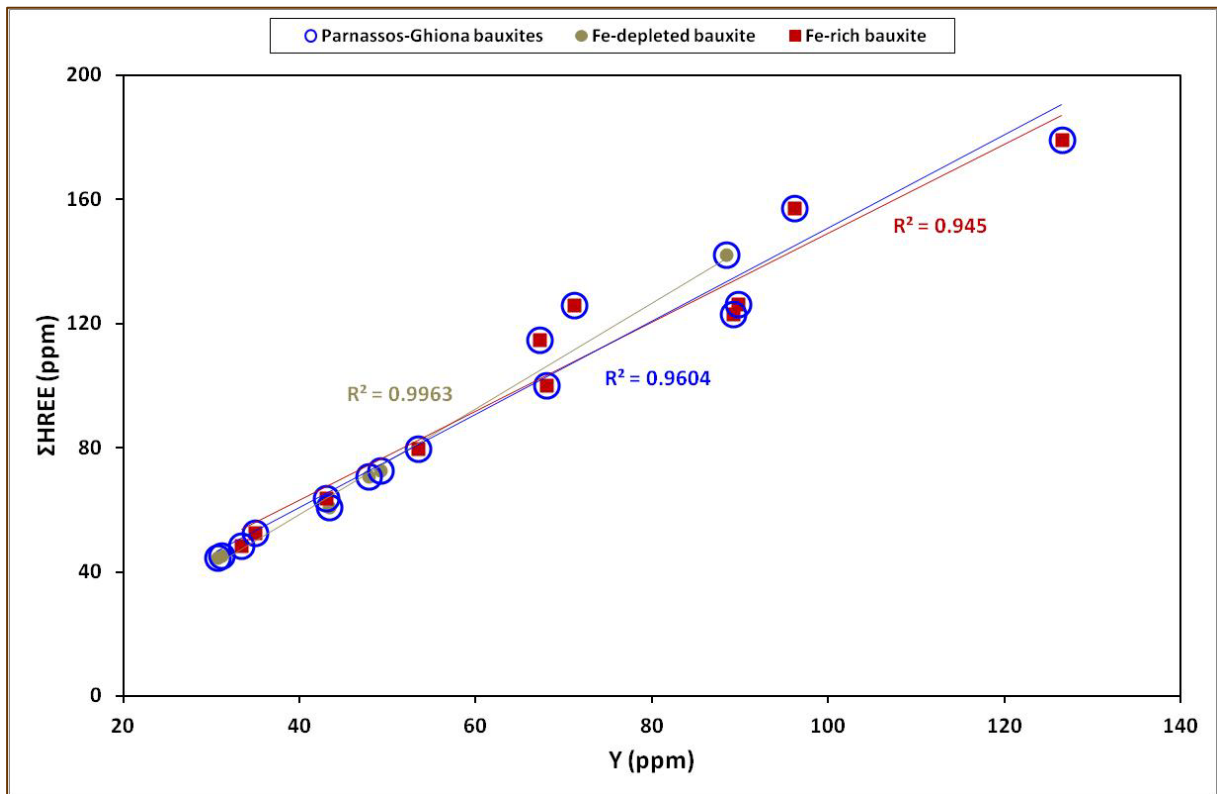
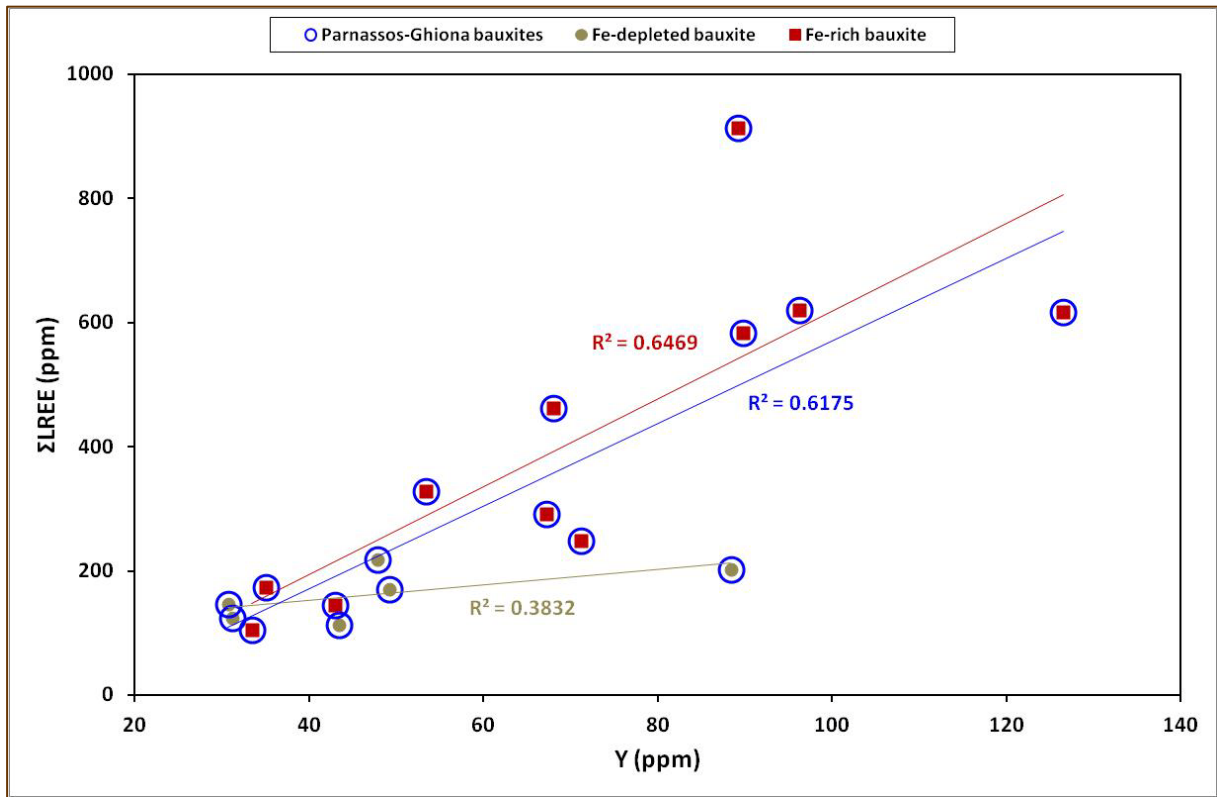
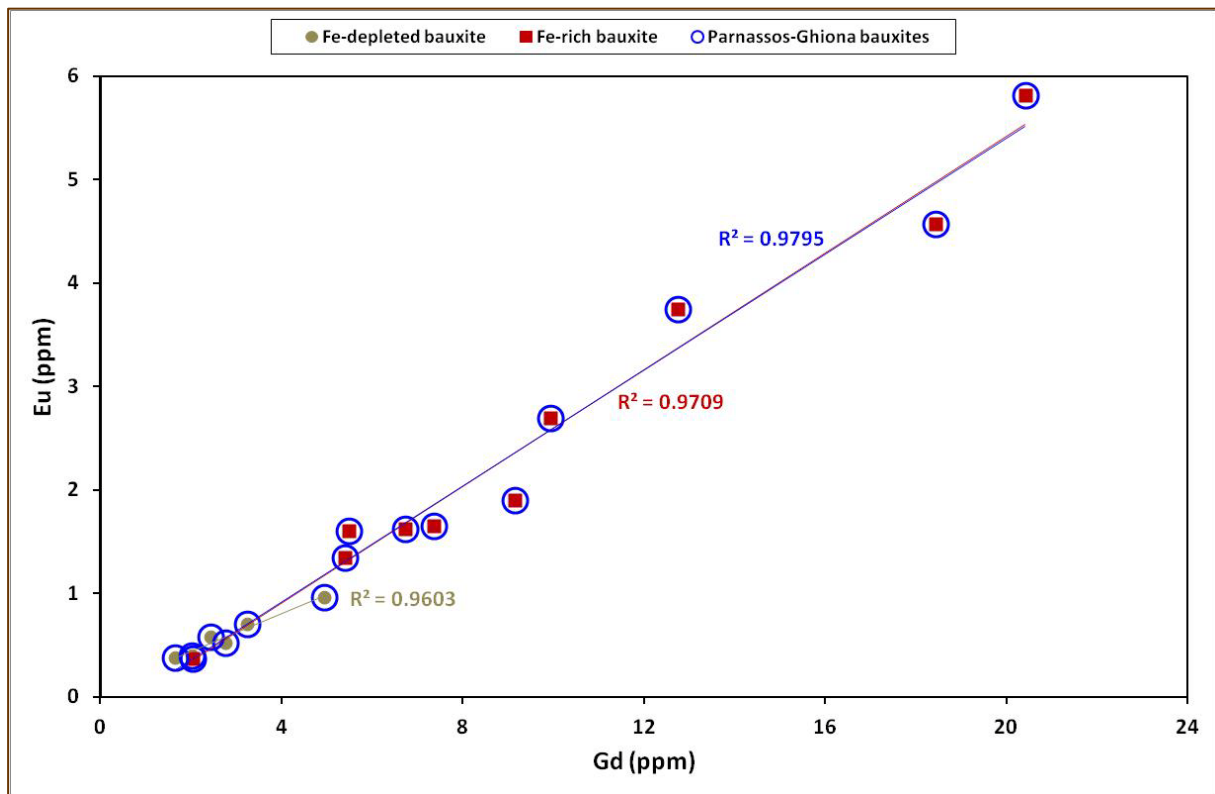
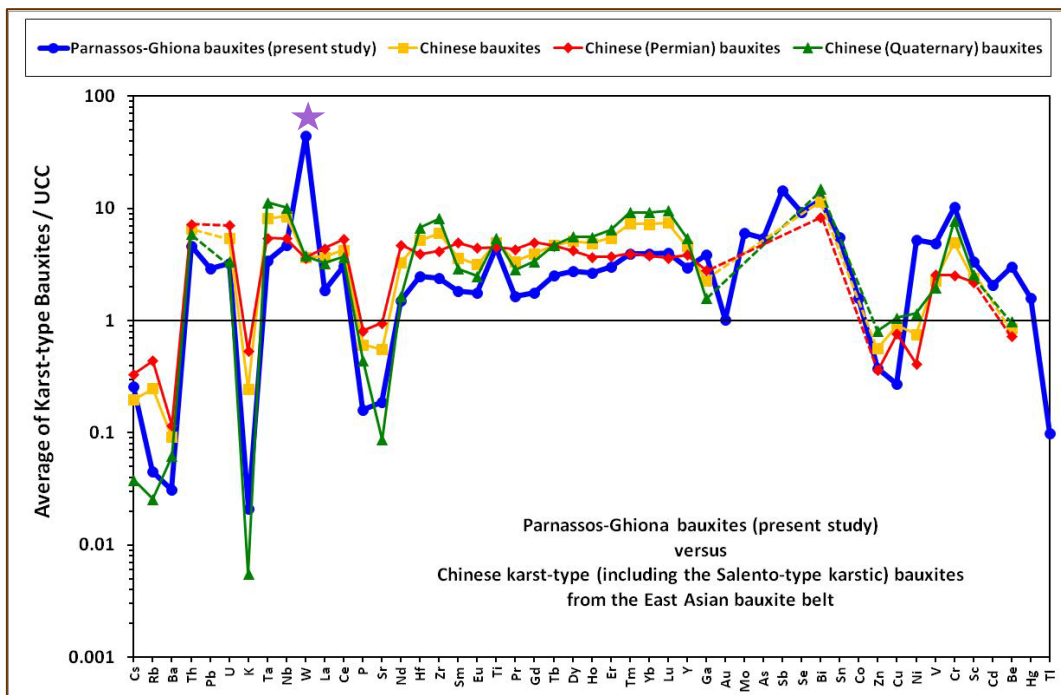
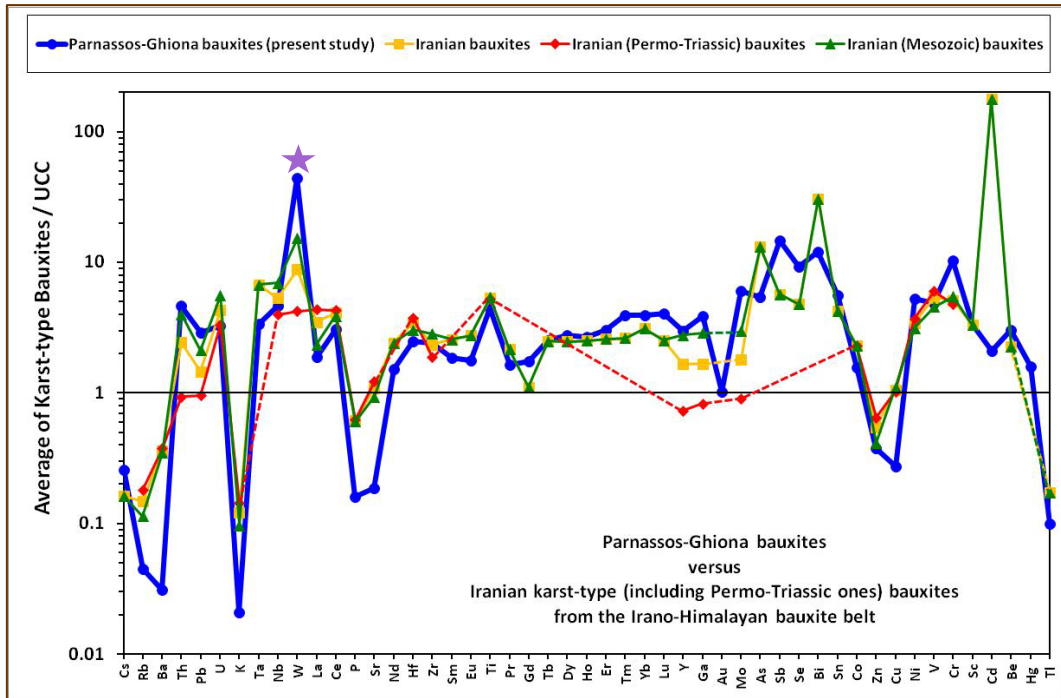


Figure 3.1.2.14: Binary diagram showing the correlation between Eu and Gd contents (ppm) for the studied Parnassos-Ghiona industrial bauxites.



Since Greek bauxite deposits have never been compared to that of Irano-Himalayan, as well as of East-Asian bauxite belt in the literature, yet, it is quite interesting to compare the studied Parnassos-Ghiona industrial bauxites with bauxites from Iran (**Figure 3.1.2.15**: upper image) and China (**Figure 3.1.2.15**: lower image). The Iranian bauxites (Calagari & Abenini, 2007; Rafiei et al., 2008; Zarasvandi et al., 2008; Esmaily et al., 2010; Zarasvandi et al., 2012) are more enriched in Rb, K and Cd, whereas the Chinese ones (Liu et al., 2010; Wang et al., 2010; Wang et al., 2012; Li et al., 2013; Liu et al., 2013) are enriched in K, REE, Ni and V. It should be noted that the relative depletion in K observed in Salento-type (i.e., Quaternary bauxites: Liu et al., 2010; Wang et al., 2010) bauxites from China is due to post-weathering surface processes.

Figure 3.1.2.15: UCC-normalized (Rudnick & Gao, 2003) spider diagrams for the avg of Parnassos-Ghiona bauxites compared to the avg. of karst bauxites from Iran (upper image: Permo-Triassic bauxites: Calagari & Abenini, 2007 and Mesozoic bauxites: Rafiei et al., 2008; Zarasvandi et al., 2008; Esmaeily et al., 2010; Zarasvandi et al., 2012), and to the avg. of karst bauxites from China (lower image: Quaternary bauxites: Liu et al., 2010; Wang et al., 2010 and Permian bauxites: Wang et al., 2010; Wang et al., 2012; Li et al., 2013; Liu et al., 2013).



The studied Parnassos-Ghiona bauxites contain rather significant amounts of REE. In Fe-rich bauxites Σ LREE, Σ HREE and Σ REE reach the values of 912.7 ppm, 179.3 ppm and 1108.7 ppm respectively. In the case of Fe-depleted samples Σ LREE, Σ HREE and Σ REE reach the values of 218.2 ppm, 142.2 ppm and 383 ppm respectively. The average of Σ REE in Fe-rich is 568.7 ppm and in Fe-depleted is 268.4 ppm, clearly indicating that typical Fe-rich (red in color) Greek industrial bauxites contain the highest amount of REE, as also mentioned above. The Fe-depleted bauxites contain LREE³⁺-minerals, mostly bastnäsite/parisite-group (Grice et al., 2007 and Maksimović & Pantó, 1996) with up to 2.5 wt.% ThO₂, as well as zircon (ZrSiO₄) detrital crystals (see text below concerning microscale measurements). When both Fe-rich and Fe-depleted Greek bauxites are normalized to North America Shale Composite (NASC; Gromet et al., 1984) there is an evident positive Ce geochemical anomaly, i.e., positive Ce^A (Figure 3.1.2.16). In case of NASC-normalization, there is also a Gd positive anomaly (not evident in chondrite-normalization; see text below) and also a relative enrichment in HREE, especially in the case of Fe-depleted samples.

Figure 3.1.2.16: REE NASC-normalized (Gromet et al., 1984) diagrams for the studied Fe-rich (upper image) and Fe-depleted bauxites (middle image). The averages for all chemical elements occurring in Parnassos-Ghiona bauxites are also presented (lower image).

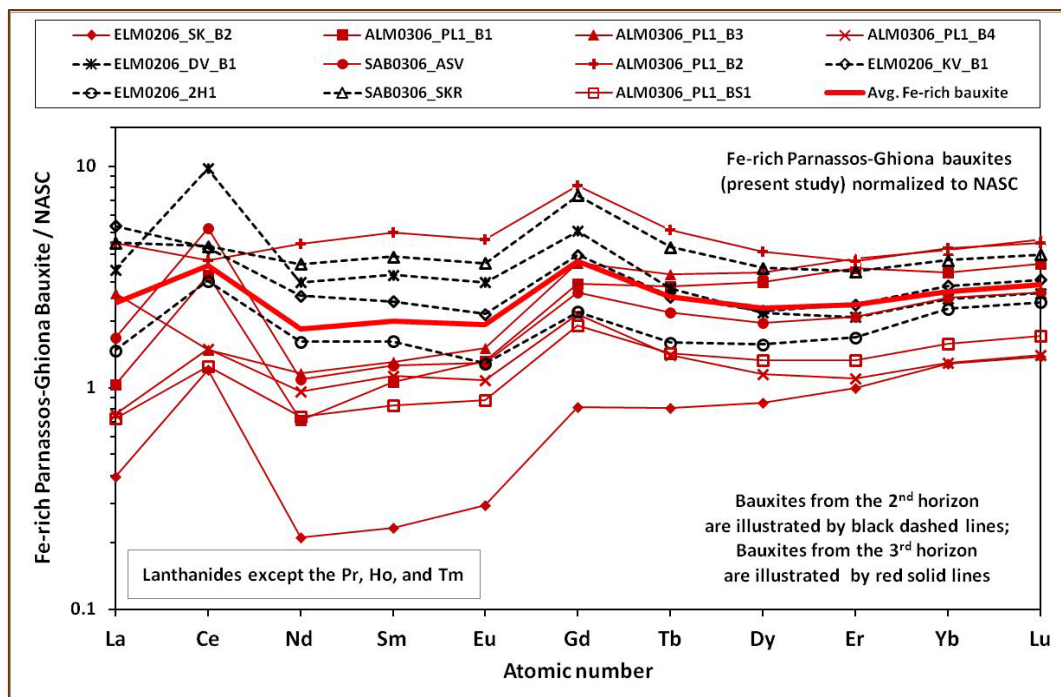
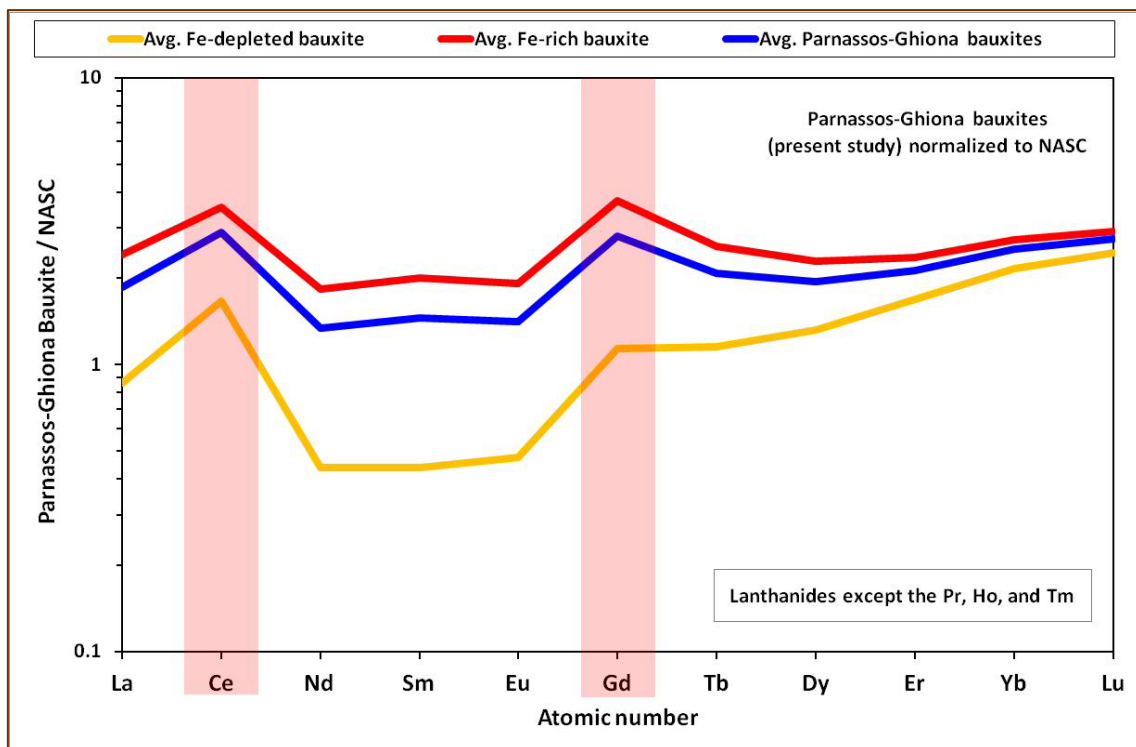
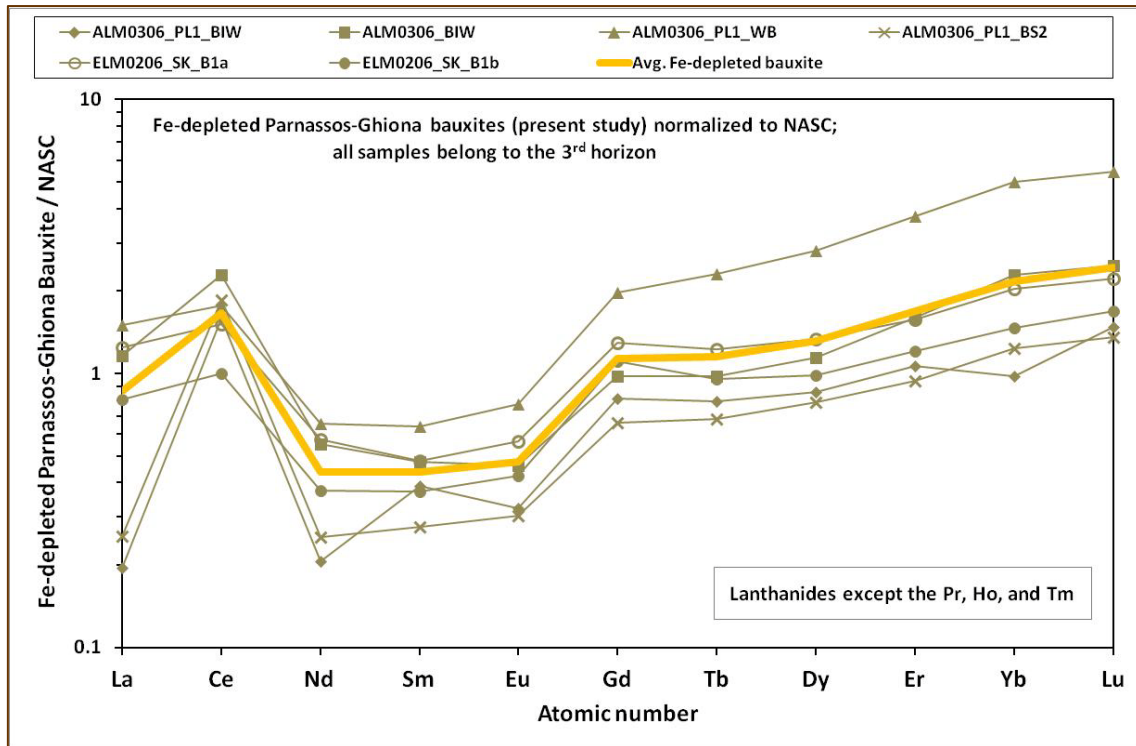


Figure 3.1.2.16: continued.



The chondrite-normalized diagrams (Haskin et al., 1968a; Haskin et al., 1968b; Haskin et al., 1971; Wakita et al., 1971; Boynton, 1985; Taylor & McClennan, 1985; Korotev, 1996a; Korotev, 1996b), concerning REE in average, of the Fe-rich and the Fe-depleted bauxites are presented in **Figure 3.1.2.17** and **Figure 3.1.2.18**. These diagrams are also referred as Masuda-Coryell diagrams (e.g., Rollinson, 1993).

In particular, for choosing the most proper set of chondrite-normalization values, selected average values of ordinary chondrites / OC (Haskin et al., 1968a; Haskin et al., 1968b; Haskin et al., 1971; Wakita et al., 1971), and carbonaceous chondrites / CI (Boynton, 1985; Taylor & McClennan, 1985), as well as values reported by Korotev (1996a & 1996b) -who utilized the CI values from Anders & Grevesse (1989) multiplied by 1.3596- were carefully used from an overall set of available published data (i.e., Haskin et al., 1968a; Haskin et al., 1968b; Haskin et al., 1971; Wakita et al., 1971; Masuda et al., 1973; Nakamura, 1974; Evensen et al., 1978; Laul et al., 1979; Anders & Ebihara, 1982; Boynton, 1985; Taylor & McClennan, 1985; Palme, 1988; Anders & Grevesse, 1989; McDonough & Sun, 1995; Korotev, 1996a; Korotev, 1996b). This approach is based on comments by Rollinson (1993) and suggestions by Korotev (2010). Furthermore, values from CI chondrites have been selectively chosen in order to be consistent with the average values of OC chondrites reported by Haskin et al. (1968a), Haskin et al. (1968b), Haskin et al. (1971), and Wakita et al. (1971).

Similar to the case of NASC-normalization (**Figure 3.1.2.16**), there is an evident positive Ce^A ; besides there is also a negative Eu^A . In both cases, the REE-normalized curves show similar geochemical trends.

As it has been observed in the literature, analogous to the above approach, the “Masuda-Coryell” diagrams were yielded using different average REE values for normalization than that of the average abundance of REE in chondrites (**Figure 3.1.2.17** and **Figure 3.1.2.18**), such as the average abundance of REE in the European Shale / ES (Haskin & Haskin, 1996; see **Figure 3.1.2.19**), the Upper Continental Crust / UCC (Rudnick & Gao, 2003; see **Figure 3.1.2.20**), the Post-Archaean average Australian Sedimentary rock / PAAS (Taylor & McClennan, 1985; McClennan, 1989; see **Figure 3.1.2.21**) and, for the first time in the literature, the average abundance of REE in the Mediterranean bauxite belt excluding the Greek ones (for literature: see caption of previous **Figure 3.1.2.5**; see **Figure 3.1.2.22**).

Figure 3.1.2.17: Comparative REE chondrite-normalized diagrams initially using all the chondrite values from literature (upper image) and finally utilizing the selected ones (lower image), according to suggestions provided by Rollinson (1993) and Korotev (2010).

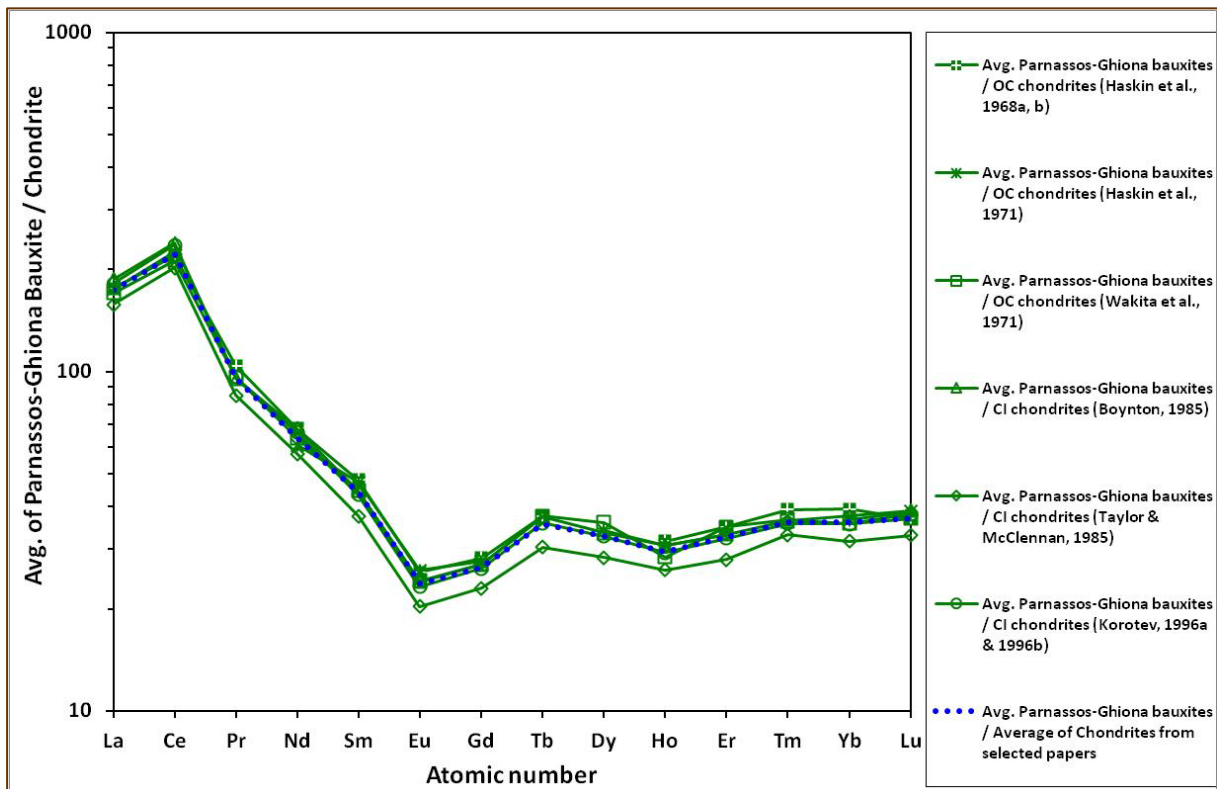
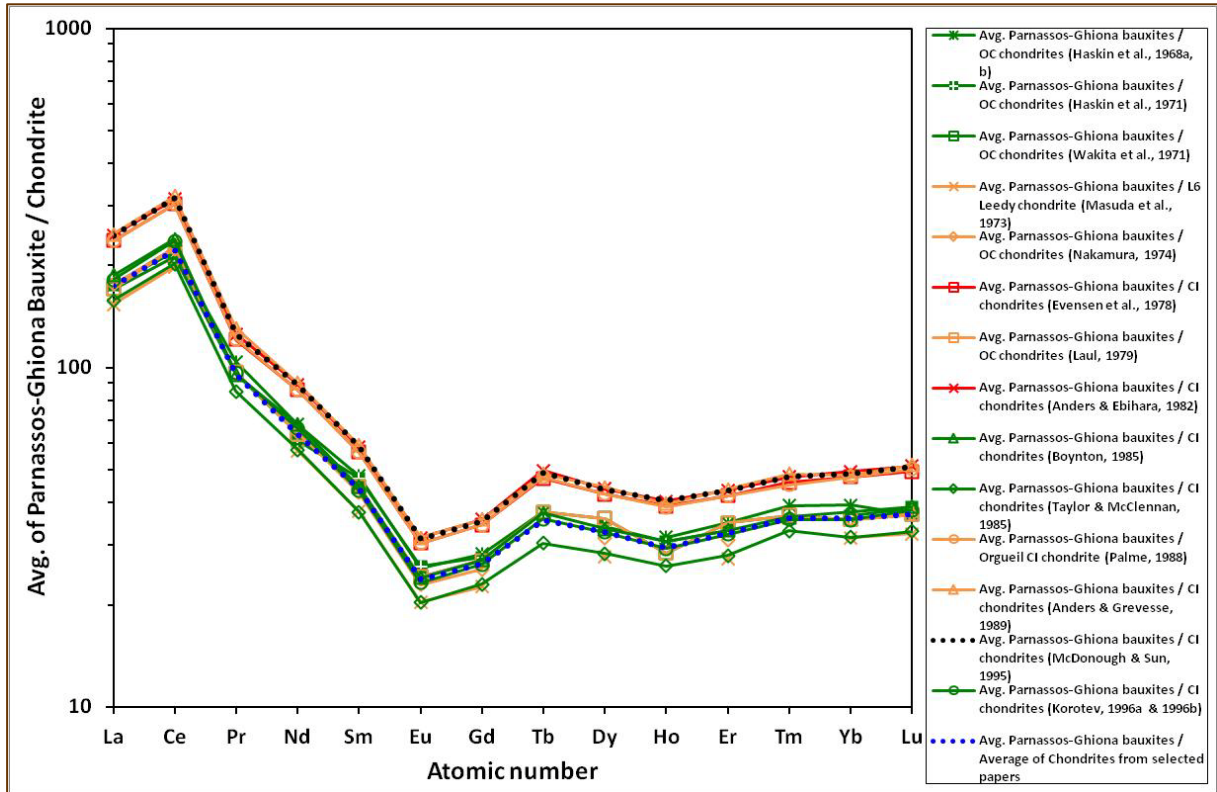


Figure 3.1.2.18: REE chondrite-normalized (Haskin et al., 1968a; Haskin et al., 1968b; Haskin et al., 1971; Wakita et al., 1971; Boynton, 1985; Taylor & McClennan, 1985; Korotev, 1996a; Korotev, 1996b) diagrams for the studied Fe-rich (upper image) and Fe-depleted bauxites (middle image). The average for all chemical elements occurring in Parnassos-Ghiona bauxites is also presented (lower image).

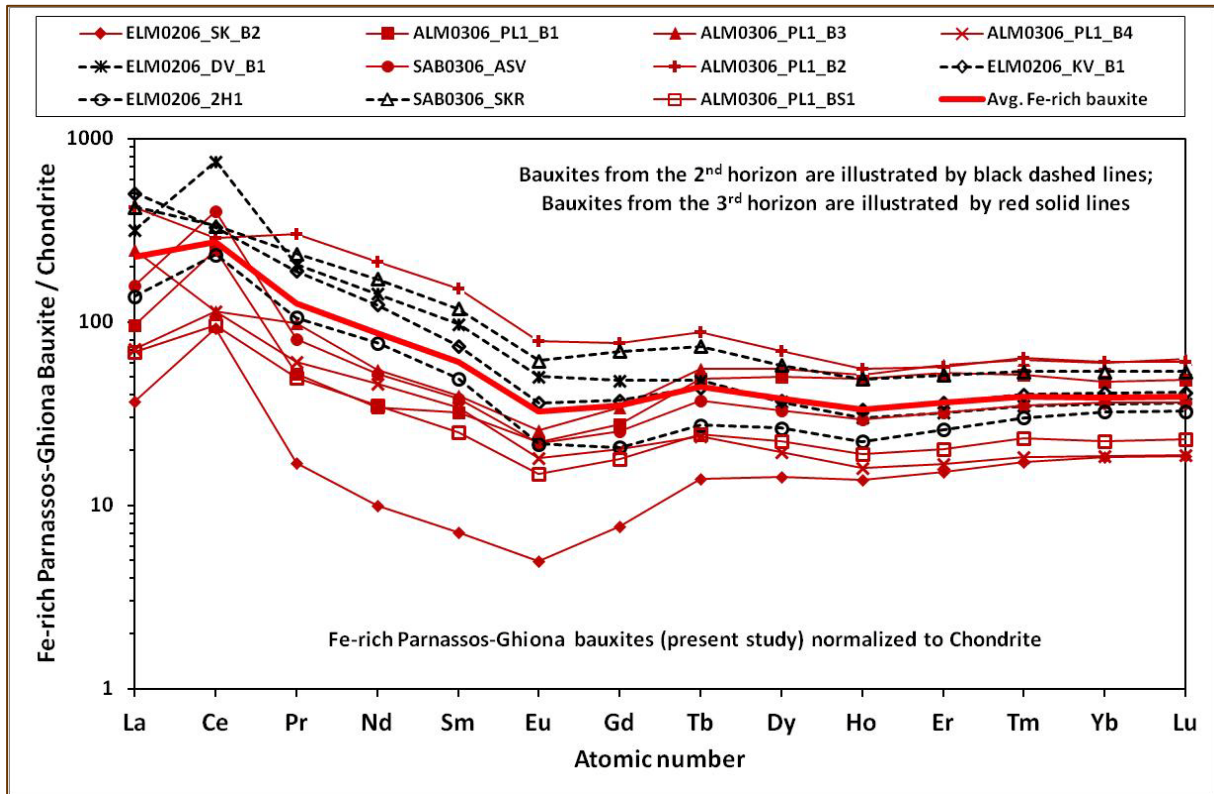


Figure 3.1.2.18: continued.

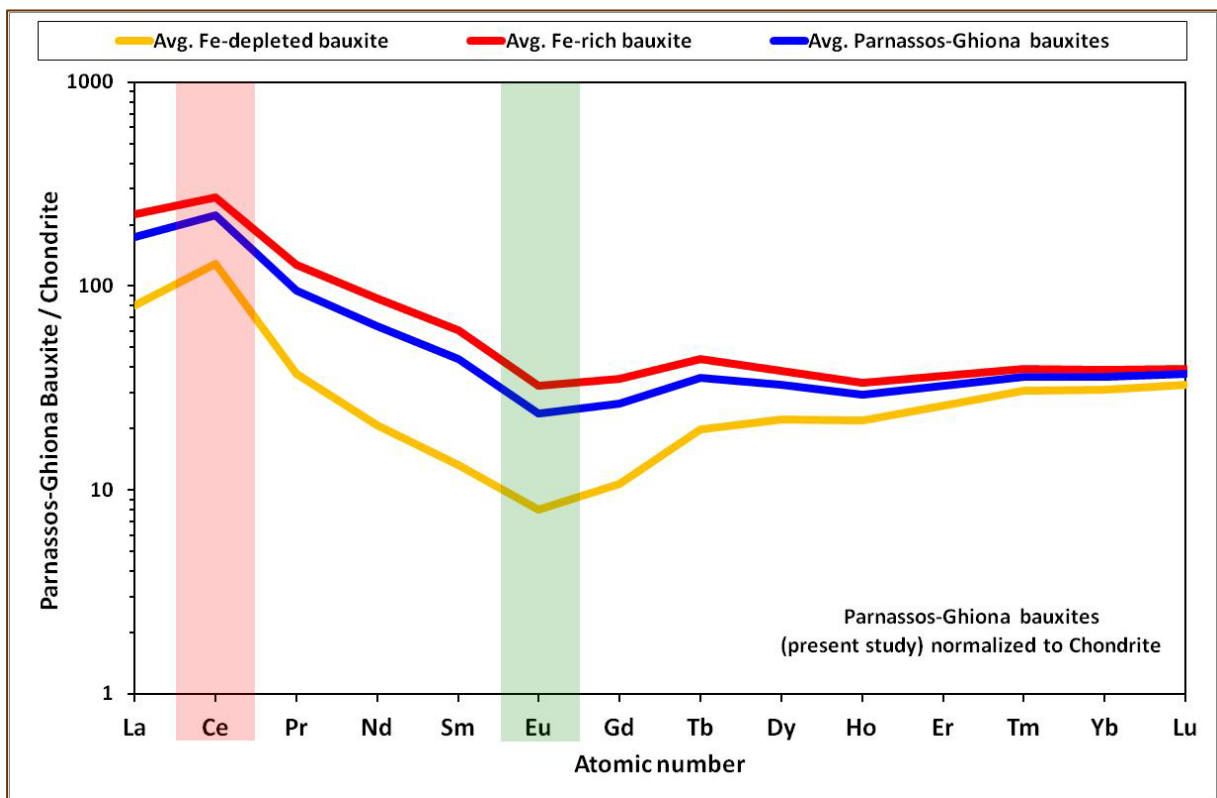
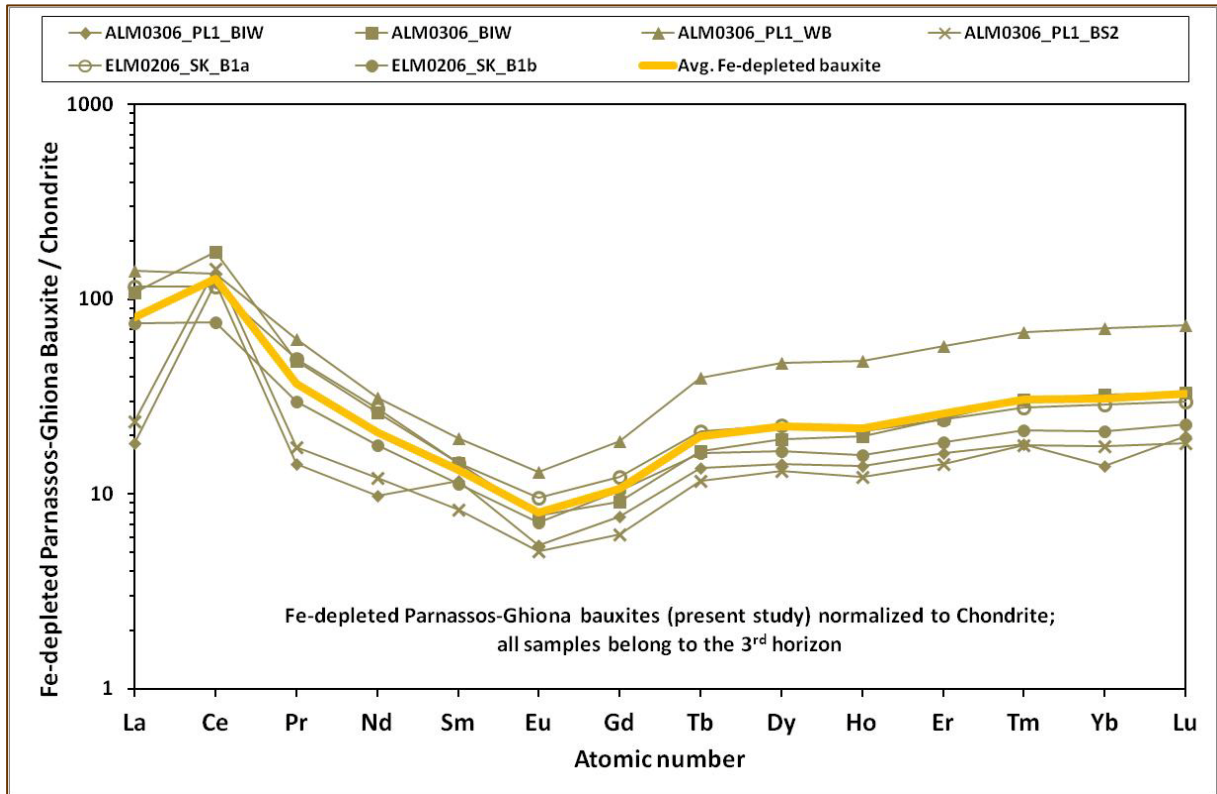


Figure 3.1.2.19: REE ES-normalized (Haskin & Haskin, 1996) diagrams for the studied Fe-rich (upper image) and Fe-depleted bauxites (middle image). The average for all chemical elements occurring in Parnassos-Ghiona bauxites is also presented (lower image).

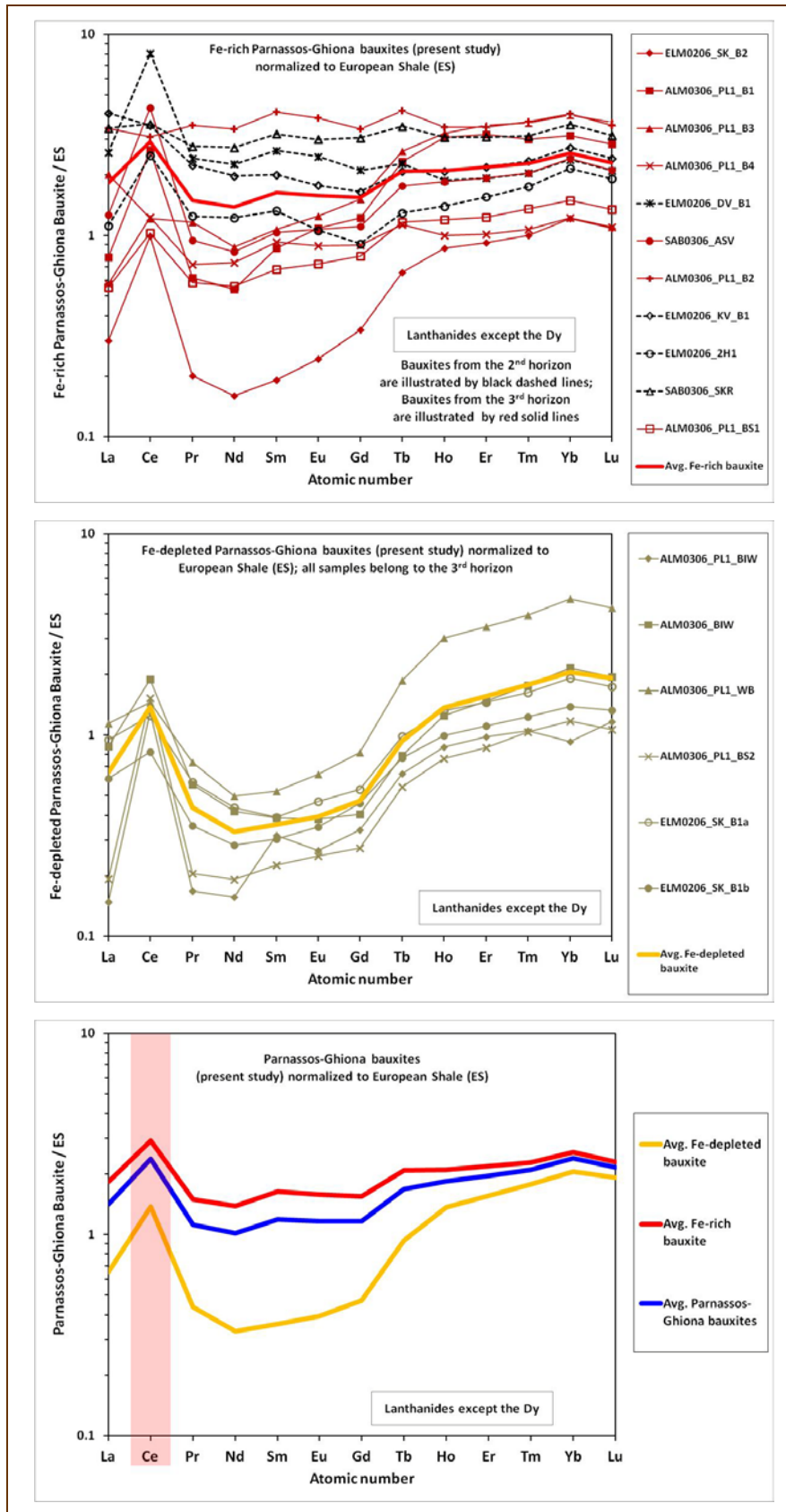


Figure 3.1.2.20: REE UCC-normalized (Rudnick & Gao, 2003) diagrams for the studied Fe-rich (upper image) and Fe-depleted bauxites (middle image). The average for all chemical elements occurring in Parnassos-Ghiona bauxites is also presented (lower image).

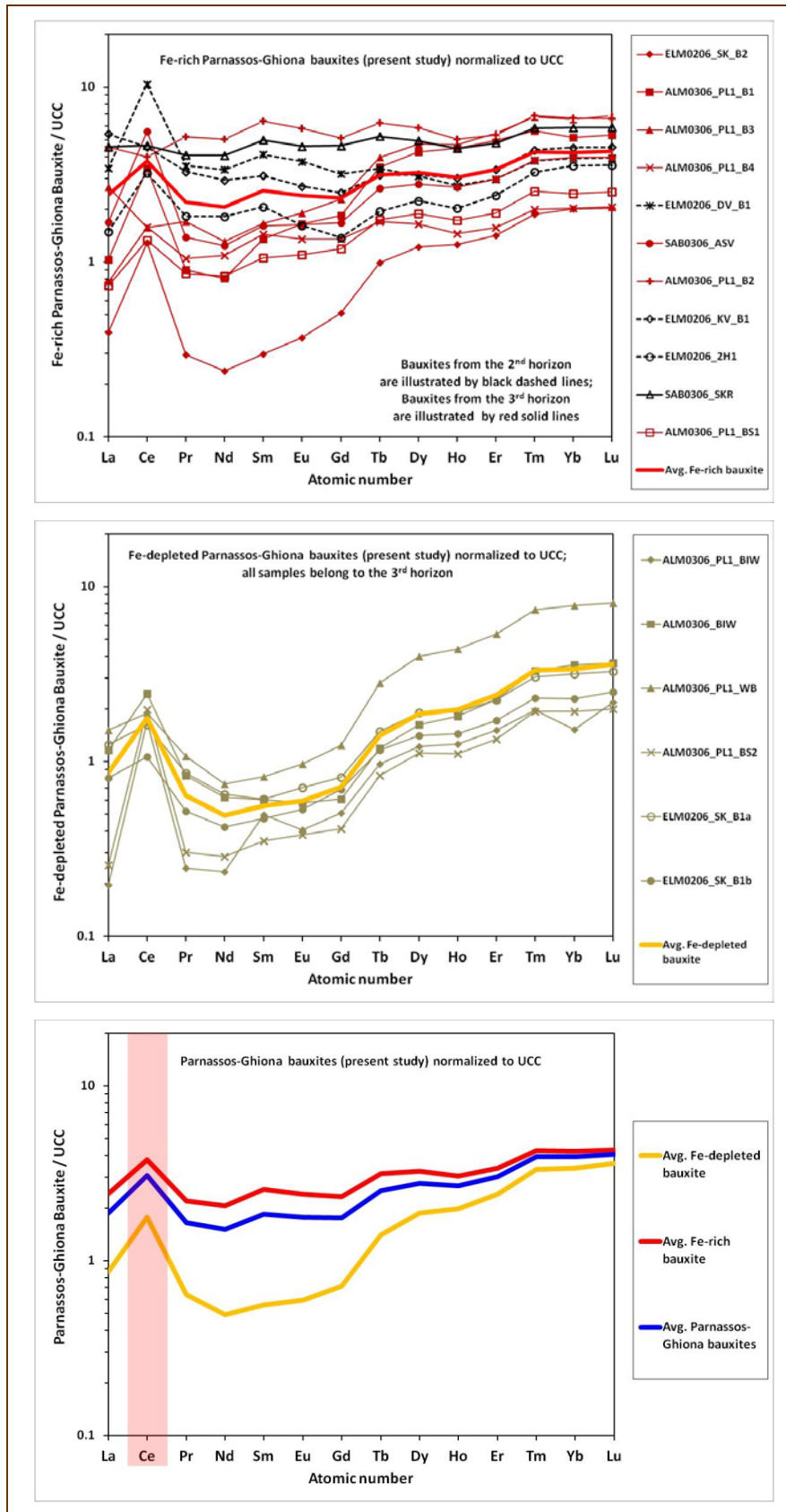


Figure 3.1.2.21: REE PAAS-normalized (Taylor & McClennan, 1985; McClennan, 1989) diagrams for the studied Fe-rich (upper image) and Fe-depleted bauxites (middle image). The average for the REEs occurring in the studied bauxites is also presented (lower image).

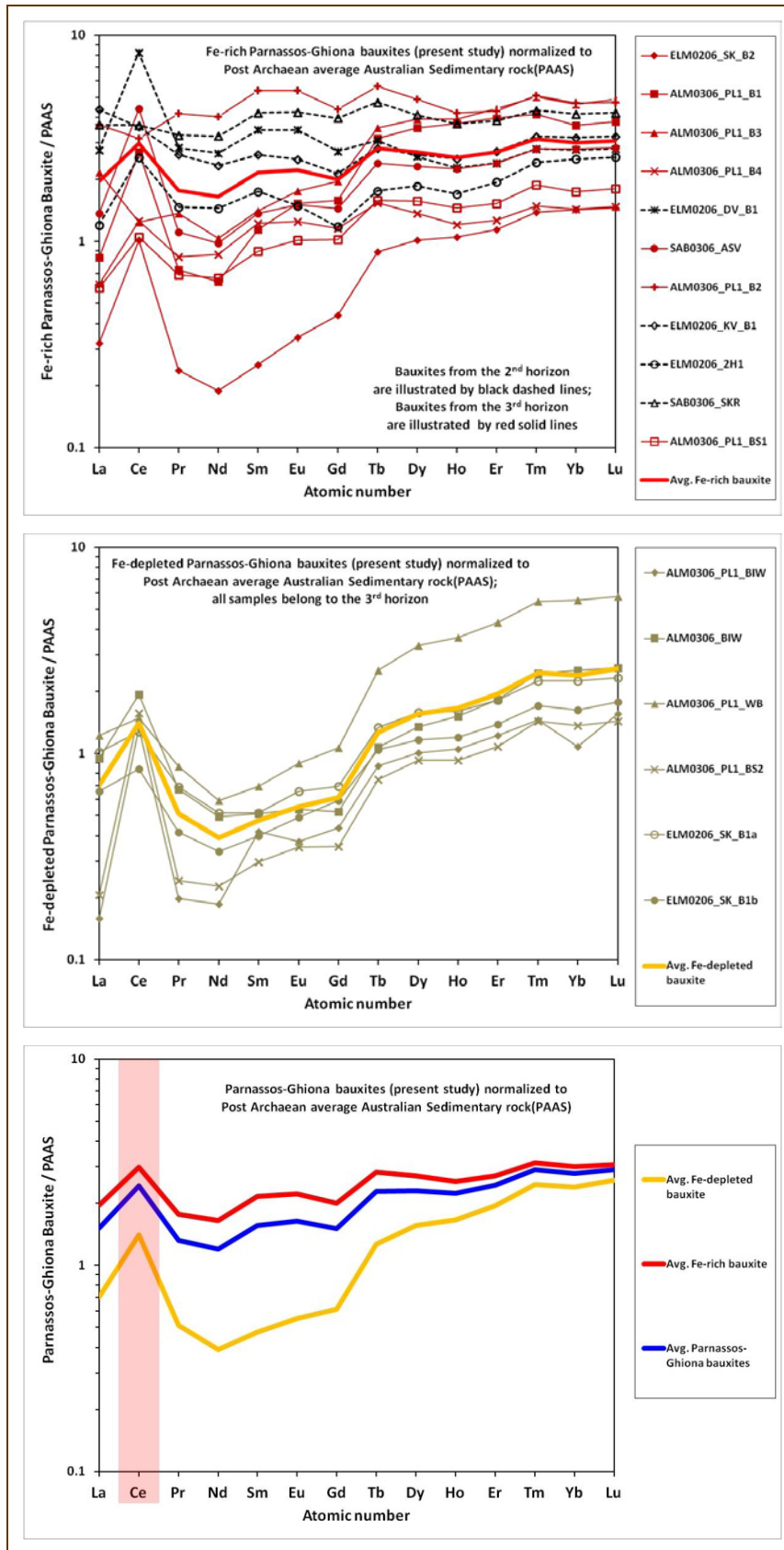


Figure 3.1.2.22: Rare earth element abundances normalized to the average of the karst-type bauxites from the Mediterranean belt (Özlü, 1983 and references therein; Mongelli, 1997; MacLean et al., 1997; Öztürk et al., 2002; Mameli et al., 2007; Karadağ et al., 2009; Mondillo et al., 2011; Boni et al., 2013; Haniçi et al., 2013; Mongelli et al., 2014 and new data of the present dissertation: Bárdossy, 2011 – personal communication) for the studied Fe-rich (upper image) and Fe-depleted bauxite (middle image). The average for all chemical elements occurring in Parnassos-Ghiona bauxites is also presented (lower image).

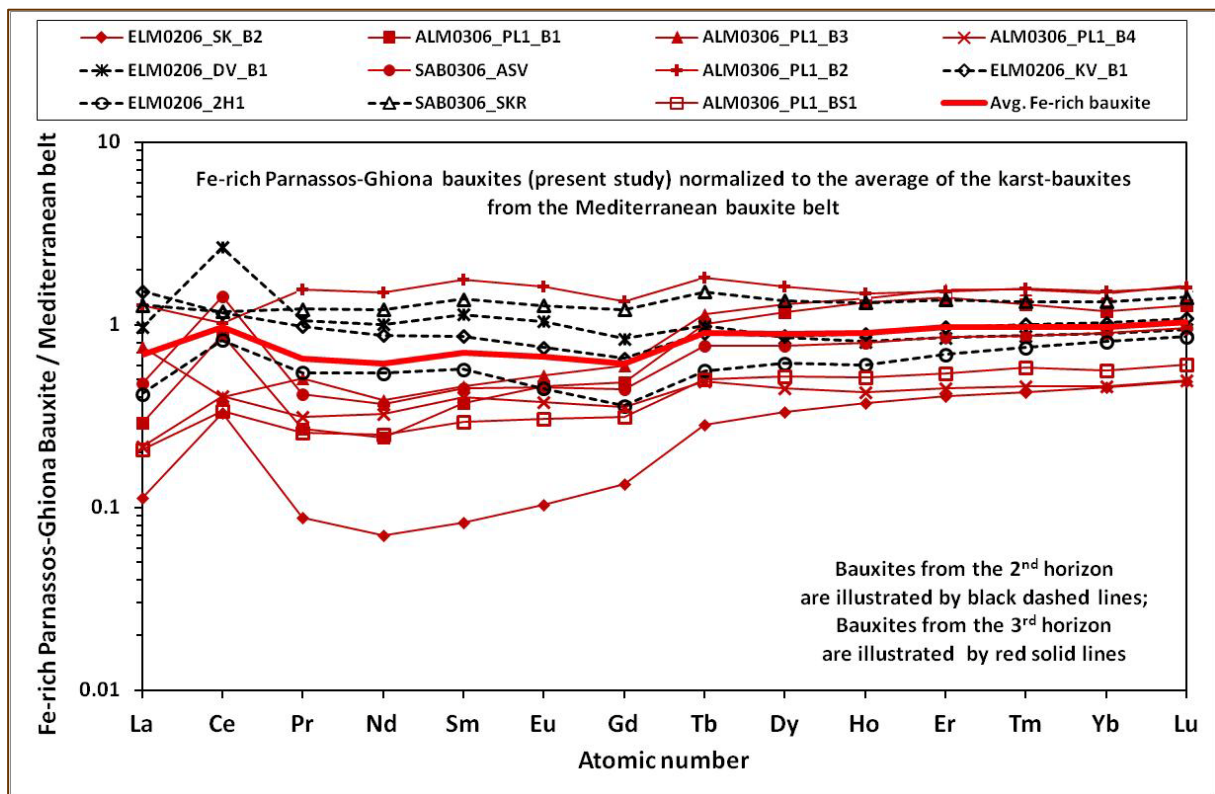
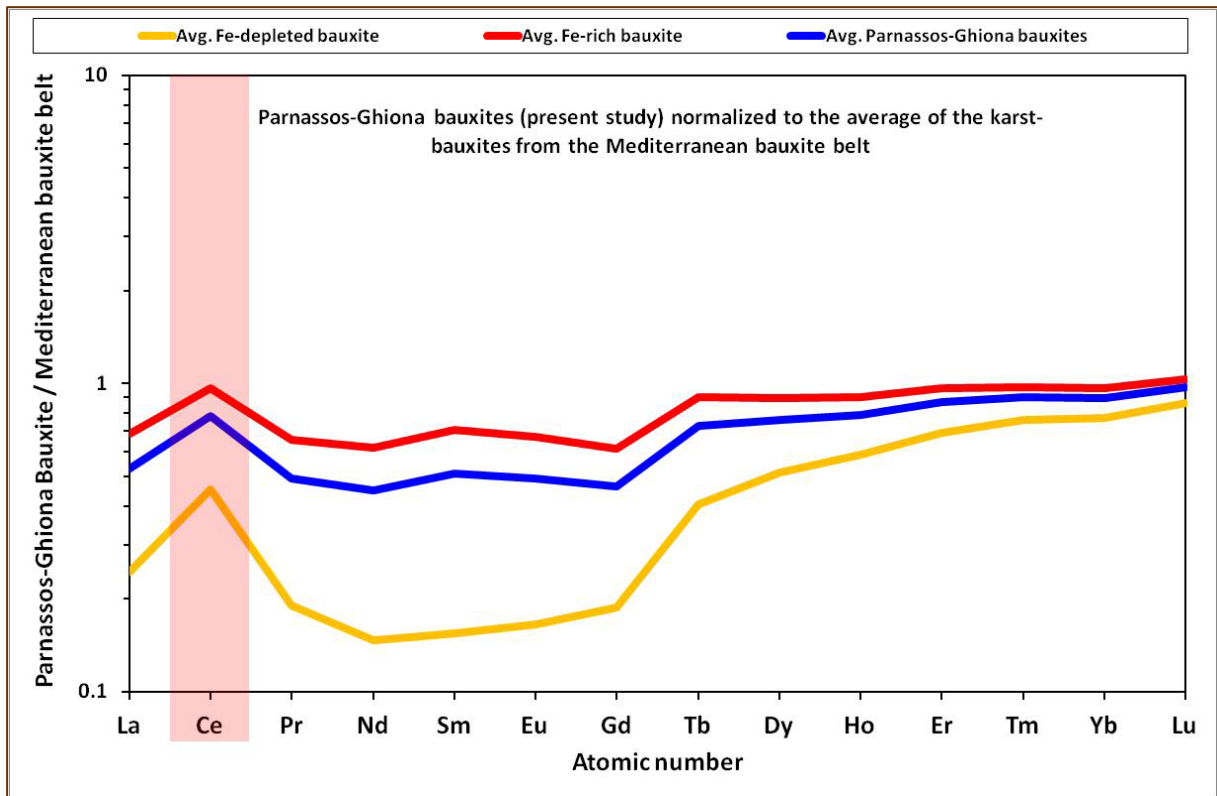
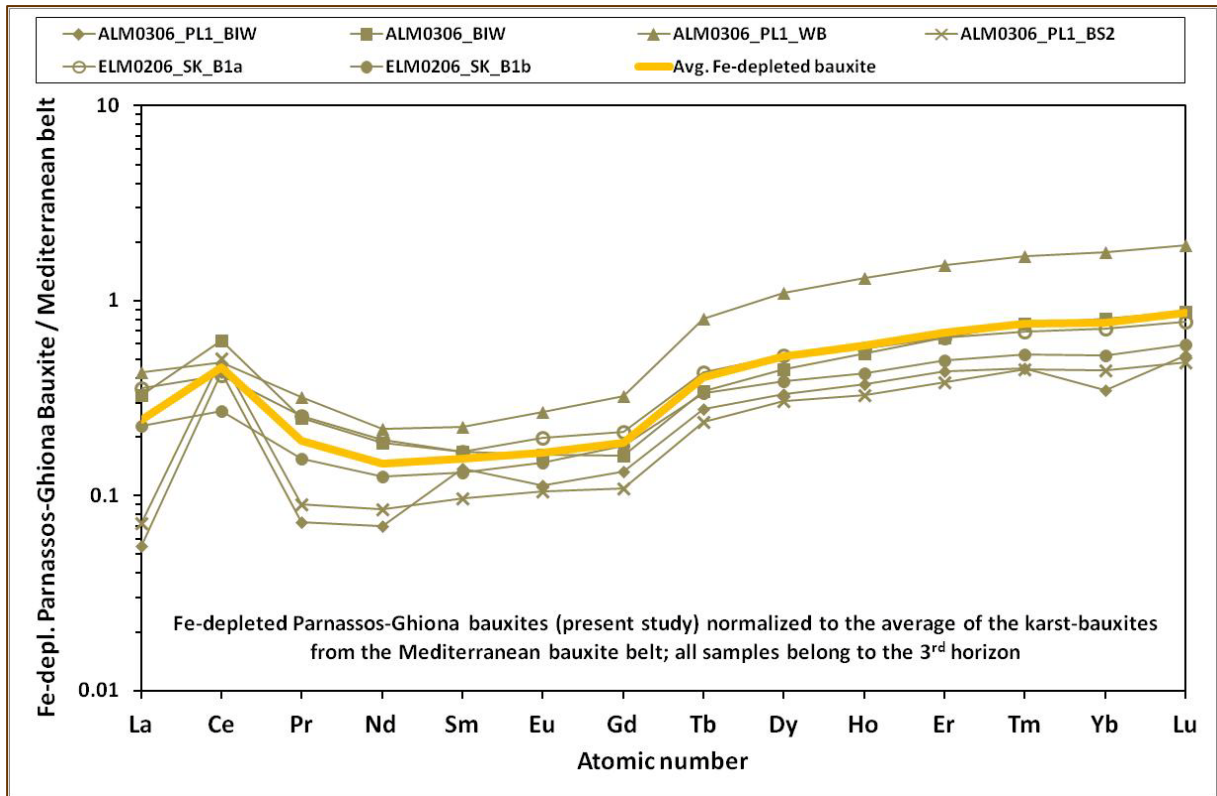
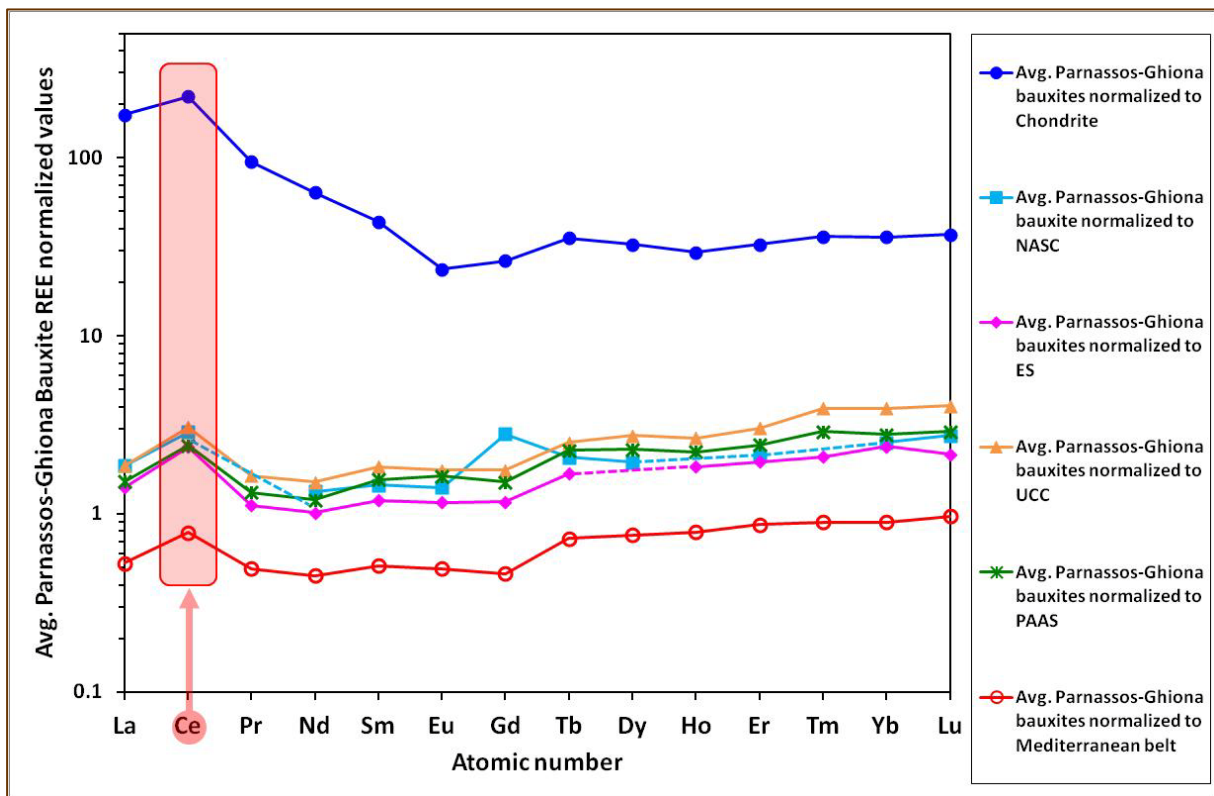


Figure 3.1.2.22: continued.



Conclusively, similar to the case of NASC-normalization (Figure 3.1.2.16) and chondrite-normalization (Figure 3.1.2.17 and Figure 3.1.2.18), an evident positive Ce^A can be observed in the “Masuda-Coryell” diagrams for the studied Parnassos-Ghiona bauxite when are normalized to ES (Figure 3.1.2.19), to UCC (Figure 3.1.2.20), to PAAS (Figure 3.1.2.21) or even to Mediterranean bauxite belt (Figure 3.1.2.22). On the other hand, contrary to the similar negative Eu^A for the first two cases, in all the other cases there is no considerable Eu anomaly. Finally, one can say that the REE-normalized curves show similar geochemical trends. The strong similarities of all the above “Masuda-Coryell” diagrams are illustrated in Figure 3.1.2.23.

Figure 3.1.2.23: Comparison of all the “Masuda-Coryell” diagrams for the studied Parnassos-Ghiona bauxite showing the strong similarities between them.



The same geochemical trends also stand for the studied Parnassos-Ghiona bauxites and, also for all Greek bauxites (for relevant literature: see caption below) when their REE values are normalized to the average abundance of REE in the chondrite (for relevant literature: see text above), PAAS (for relevant literature: see text above), and Mediterranean bauxite belt (for relevant literature: see text above) excluding Greek ones (**Figure 3.1.2.24**).

Figure 3.1.2.24: REE abundances normalized to chondrite (upper image), to PAAS (middle image), and to Mediterranean bauxite belt excluding Greek ones (lower image) for the studied Parnassos-Ghiona bauxites (present dissertation), as well as for all Greek bauxites (Kiskyras, 1960; Papastamatiou & Maksimovic, 1970; Maksimović & Papastamatiou, 1973; Ochsenkühn & Parissakis, 1977; Biermann, 1983; Arp, 1985; Retzmann, 1986; Papastavrou & Perdikatsis, 1987; Laskou, 1991; Ochsenkühn-Petropoulou et al., 1991; Ochsenkühn-Petropoulou et al., 1994; Ochsenkühn et al., 1995; Papastavrou & Perdikatsis, 1987; Laskou & Economou, 1991; Laskou, 2001; Laskou & Andreou, 2003; Laskou & Economou-Eliopoulos, 2007; Eliopoulos & Economou-Eliopoulos, 2010; Papassiopi et al., 2010; Laskou et al., 2011; Laskou & Economou-Eliopoulos, 2013).

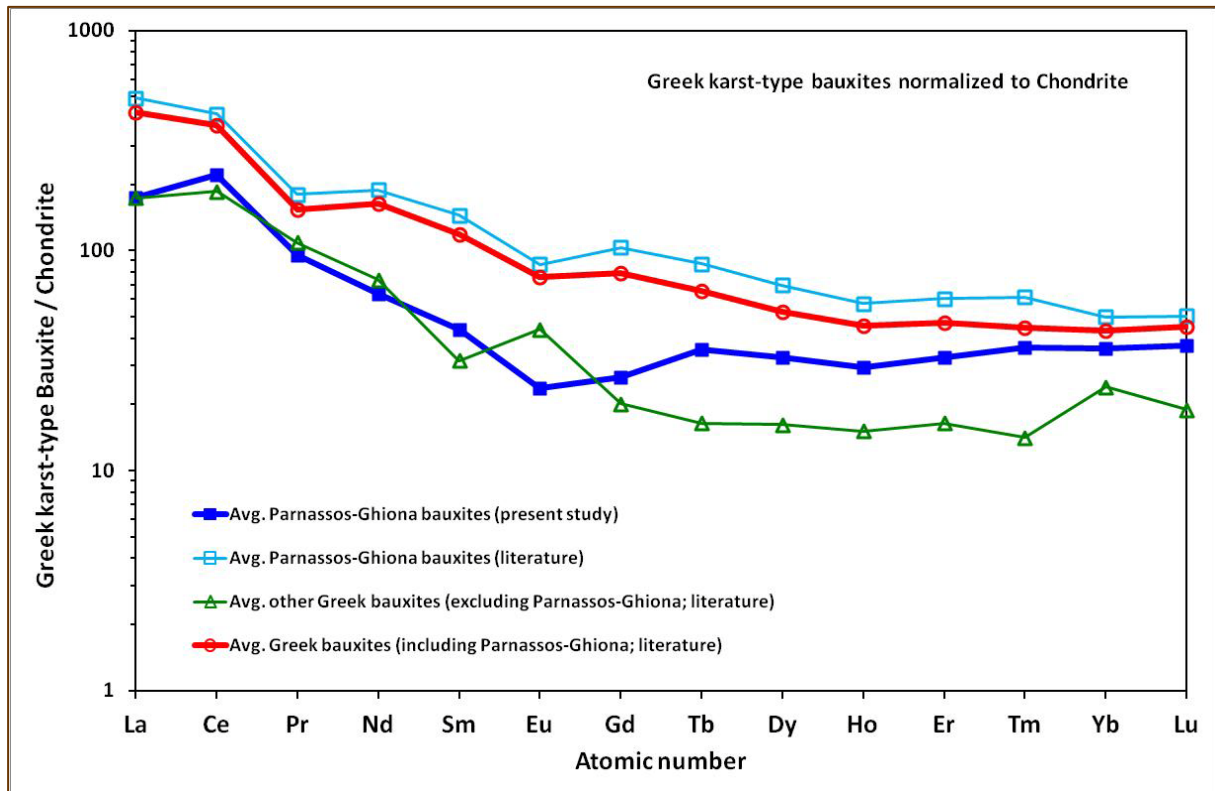
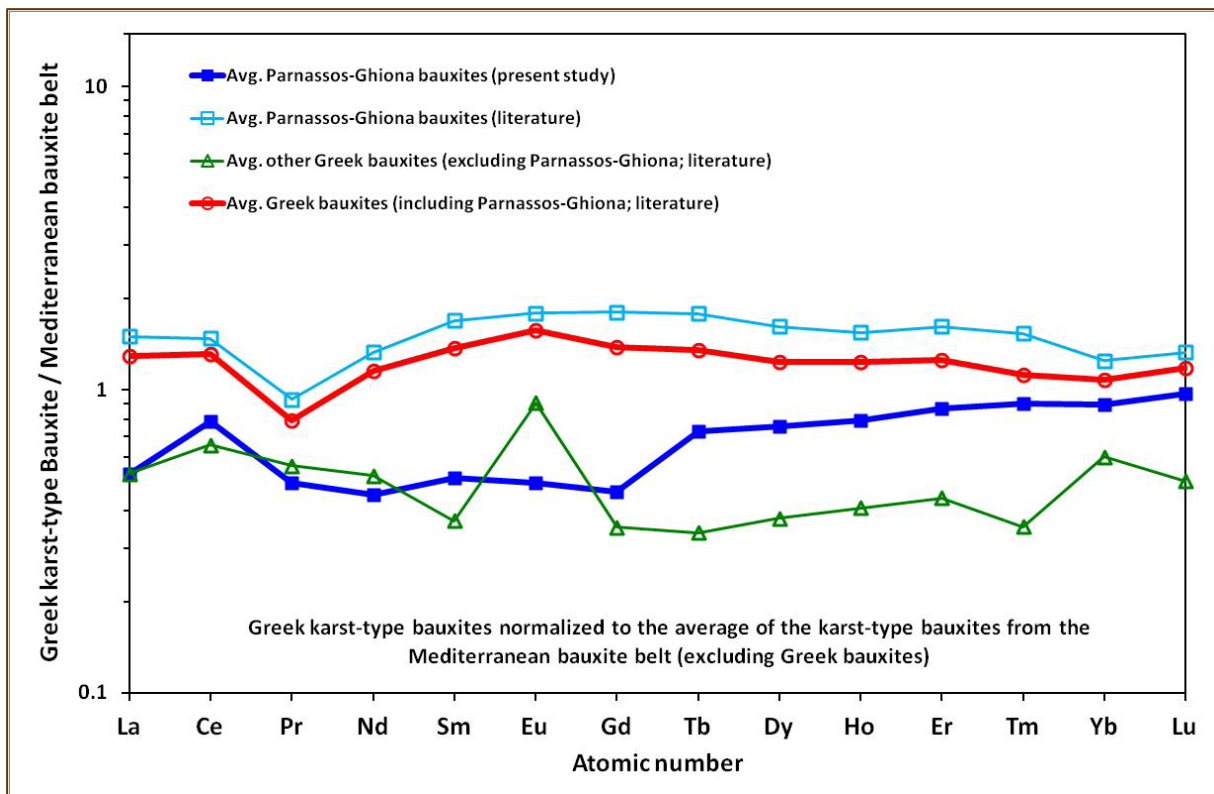
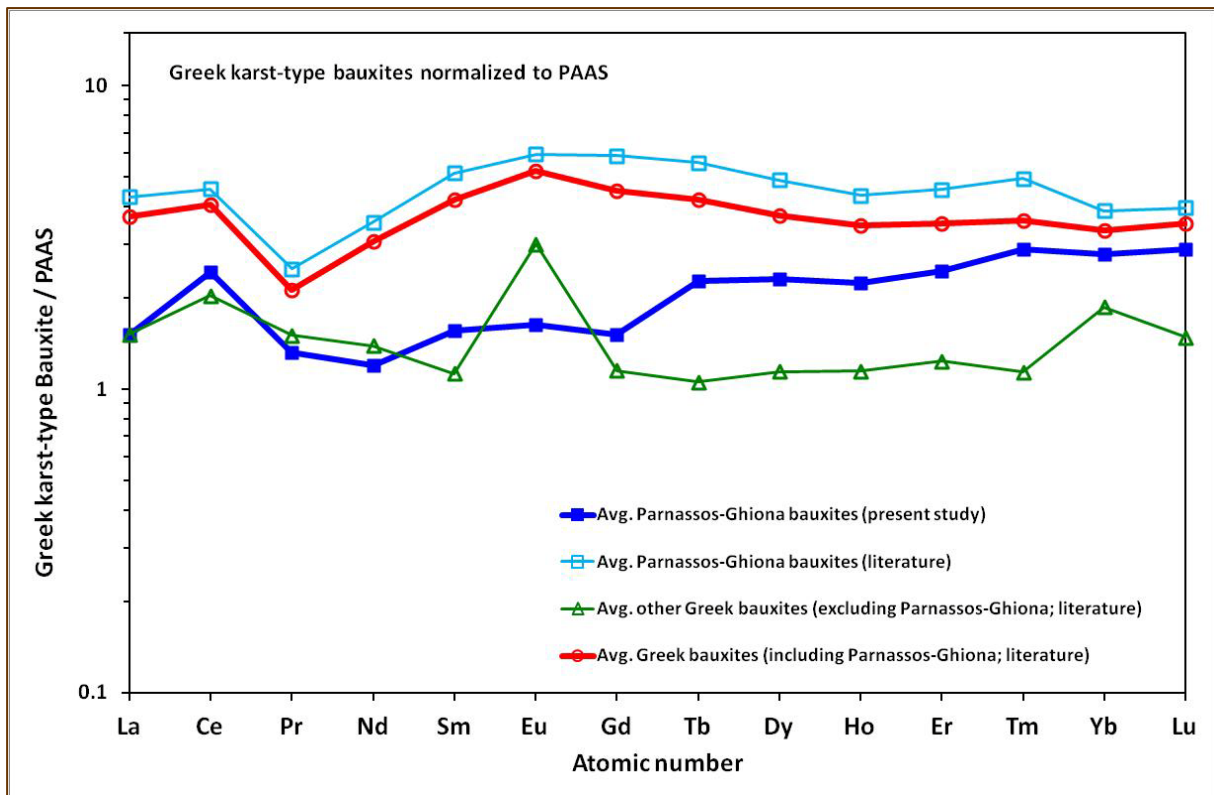


Figure 3.1.2.24: continued.



In contrast to the majority of igneous REE deposits, such as carbonatites etc., which do not significantly show evidence of neither positive nor negative Ce^A when normalized to primitive mantle (Chakhmouradian et al., 2012 and references therein), the studied Parnassos-Ghiona bauxites exhibit significant Ce^A , which calculated using the equation suggested by German & Elderfield (1990); see **Figure 3.1.2.1**, when normalized to any reference material (chondrite, NASC, PAAS, ES, UCC and the average of Mediterranean belt karst-type bauxites; see **Figures 3.1.2.16 – 3.1.2.24**). However, it is worthy to note that karst-type bauxites from other areas of Greece do not exhibit similar positive Ce^A and also relative enrichment in HREE (**Figure 3.1.2.24**). Most of the characteristically REE-enriched geological materials exhibit negative Ce^A , as well as the seawater (Li, 1991) when they are normalized to NASC (**Figures 3.1.2.25**) and/or to chondrite (**Figure 3.1.2.26**). It has long been suggested that the negative Ce^A in seawater reflects the oxidation of soluble Ce^{3+} to insoluble Ce^{4+} , which can be then removed as $Ce(OH)_4$ (e.g., Liu et al., 1988; Piepgras & Jacobsen, 1992 and references therein). Besides, Ce^{4+} can be incorporated into deep-sea sediments, and preferentially into Fe-Mn-nodules and Fe-Mn-crusts, exhibiting a characteristic positive Ce^A (Piper, 1974; Elderfield & Greaves, 1981; Murphy & Dymond, 1984; Aplin, 1984; De Carlo et al., 1992; Wen et al., 1997; Ohta et al., 1999; Hein et al., 2000; Rajani et al., 2005; see **Figures 3.1.2.25** and **3.1.2.26**). Another geological material showing positive Ce^A is the desert varnish consisting of Fe-Mn-oxyhydroxides (Thiagarajan & Aeolus Lee, 2004). Nevertheless, except, bauxites, positive Ce^A show specific types of laterites and xenoliths derived from laterites (Boulangé & Colin, 1994; Zou et al., 2004). On the other hand, in the case of Middle Proterozoic Fe-REE-Nb deposit of Bayan Obo, which is the world's largest REE resource, though there is a typically enormous enrichment in LREEs relative to HREEs (occurring as REE fluorocarbonate minerals and monazite into dolomite marbles), there is no apparent positive nor negative Ce^A (**Figures 3.1.2.25** and **3.1.2.26**, Ling et al., 2013). This strong HREEs enrichment may be attributed to a very low degree (<1%) of partial melting of parental magmas derived from a source, enriched in incompatible elements (including REE), from subcontinental upper mantle (Chakhmouradian et al., 2012 and references therein). A strong positive Ce^A is also observed, in zircon crystals (**Figures 3.1.2.26**), where Ce^{3+} substitutes in Zr^{4+} sites resulting in a charge deficiency (Grimes et al., 2007). In order to ensure that zircon maintains charge neutrality, incorporation of trivalent REE is thought to involve the so-called “xenotime” substitution ($Zr^{4+} + Si^{4+} \rightarrow REE^{3+} + P^{5+}$), requiring a

pentavalent element like P^{5+} substituting for Si^{4+} (Hanchar & Wenstrenen, 2007 and references therein).

Figure 3.1.2.25: Ce positive anomaly of Parnassos-Ghiona bauxites (present dissertation) compared with the Ce positive anomaly of various geological materials, such as granite (Mason & Moore, 1982; Krauskopf & Bird, 1994), Fe-Mn-nodules (Piper, 1974; Elderfield & Greaves, 1981; Ohta et al., 1999), Fe-Mn-crust (Elderfield & Greaves, 1981; Aplin, 1984; De Carlo et al., 1992; Wen et al., 1997; Hein et al., 2000; Rajani et al., 2005), Brazilian lateritic bauxite (Boulangé & Colin, 1994), desert varnish (Thiagarajan & Aeolus Lee, 2004), Bayan Obo REE deposit (Ling et al., 2013), and xenoliths (Zou et al., 2004), including seawater (inset image; Li, 1991), normalized to NASC (except Pr, Ho, and Tm; Gromet et al., 1984). Ce negative anomaly of seawater is also depicted for comparison reason (inset; Li, 1991).

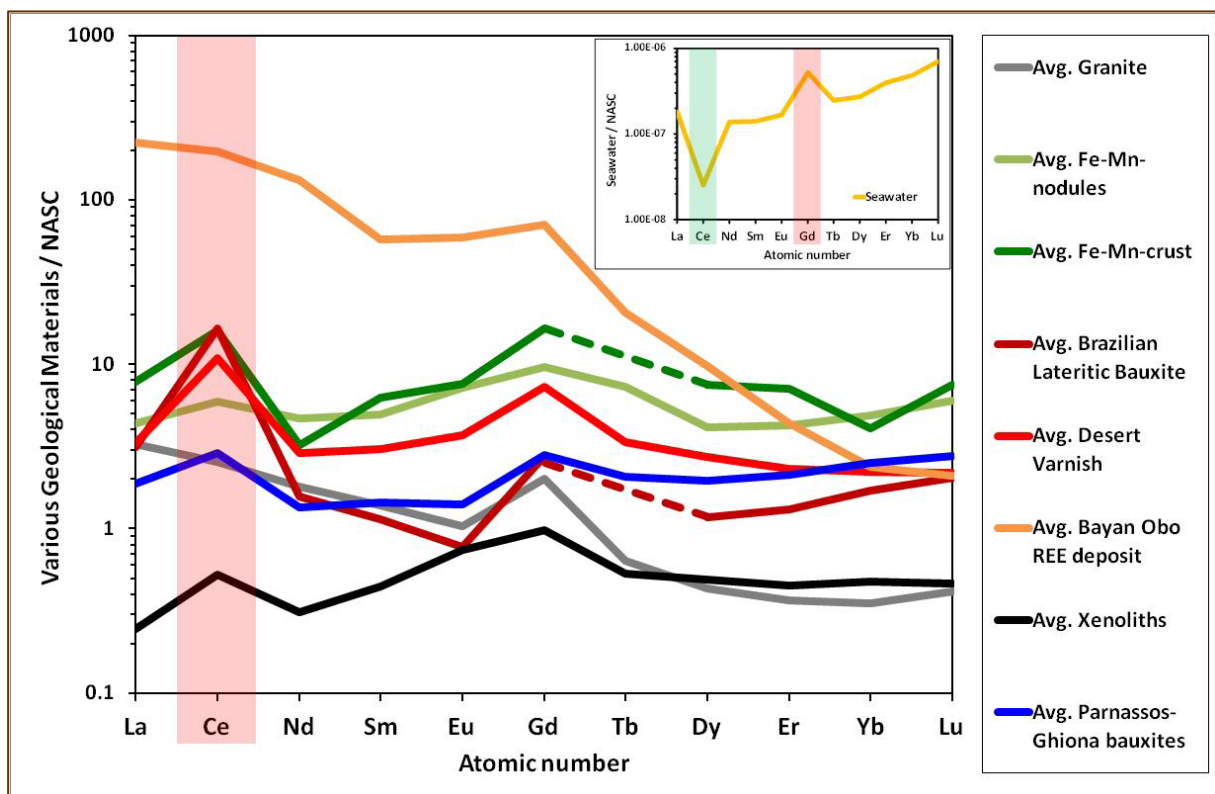
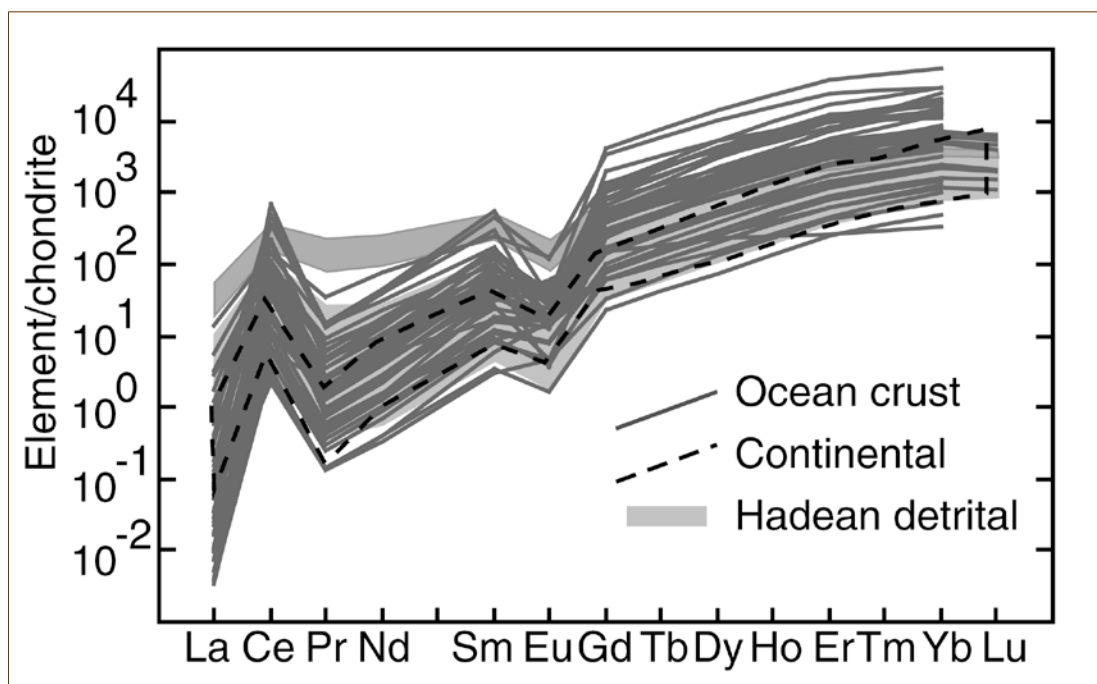
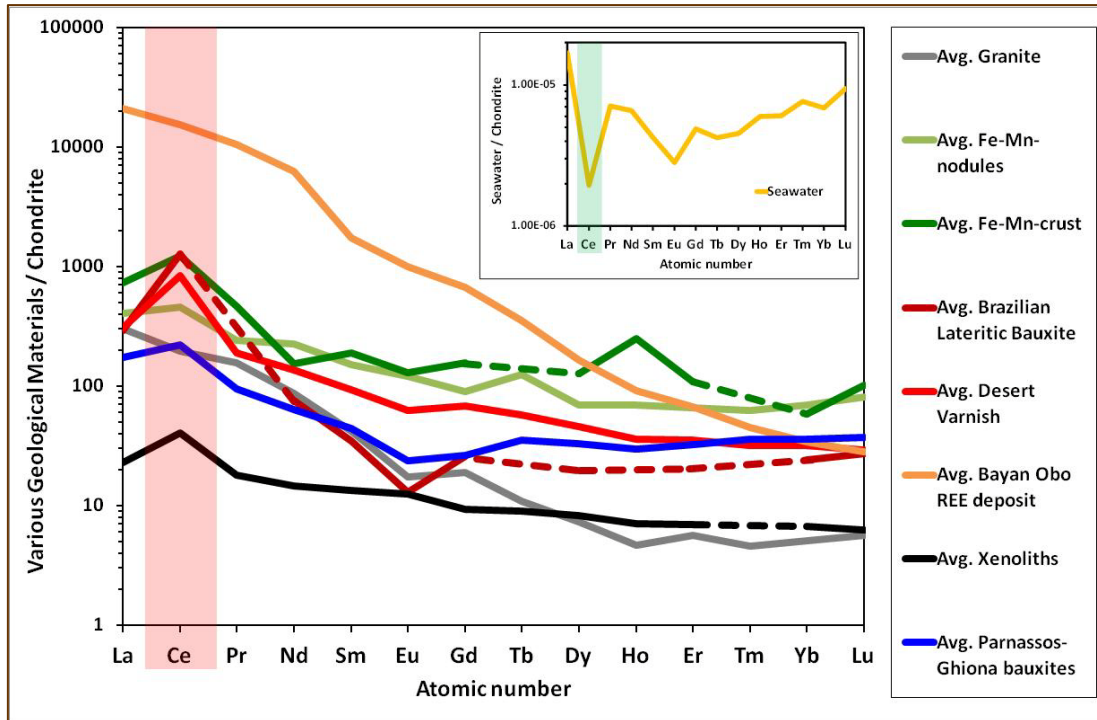


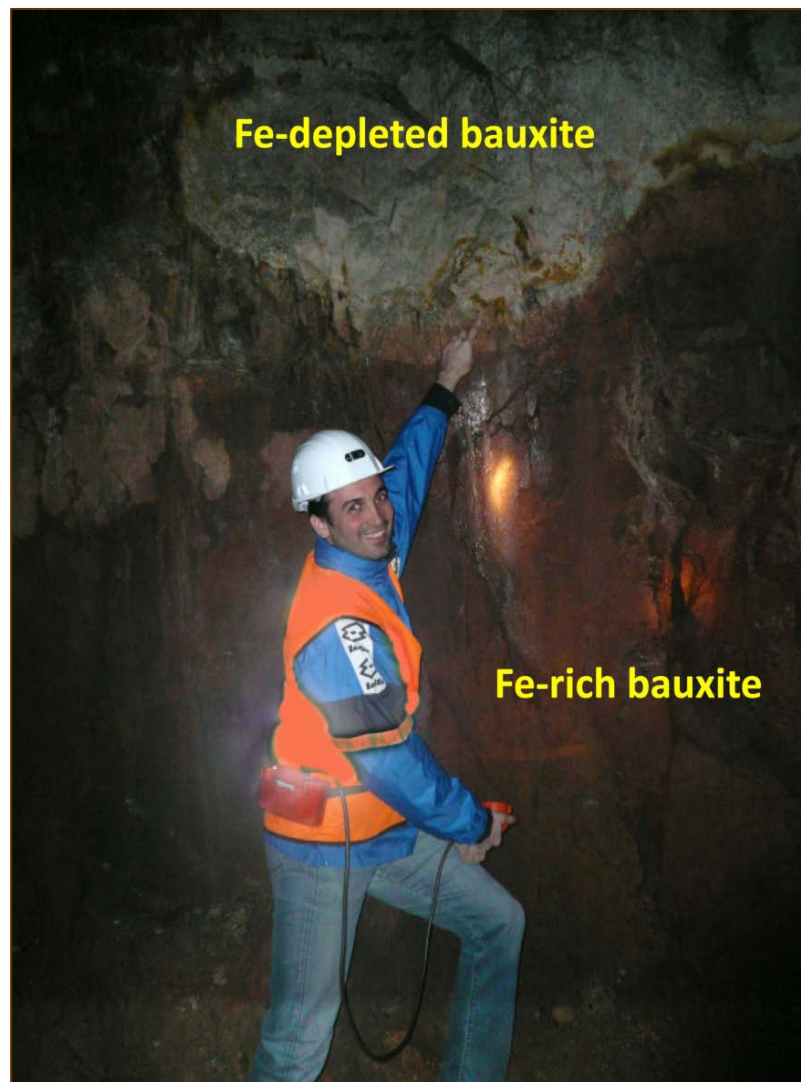
Figure 3.1.2.26: Ce anomaly of Parnassos-Ghiona bauxites (present dissertation) compared with the Ce anomaly of various geological materials (for literature: see previous caption of **Figure 3.1.2.25**) normalized to chondrite (upper image; for literature: [Haskin et al., 1968a](#); [Haskin et al., 1968b](#); [Haskin et al., 1971](#); [Wakita et al., 1971](#); [Boynton, 1985](#); [Taylor & McClennan, 1985](#); [Korotev, 1996a](#); [Korotev, 1996b](#)). Ce positive anomaly of ocean crust zircon is also depicted (lower image; [Grimes et al., 2007](#) and references therein).



3.1.3. The case study of B3 horizon in Pera Lakkos underground mine

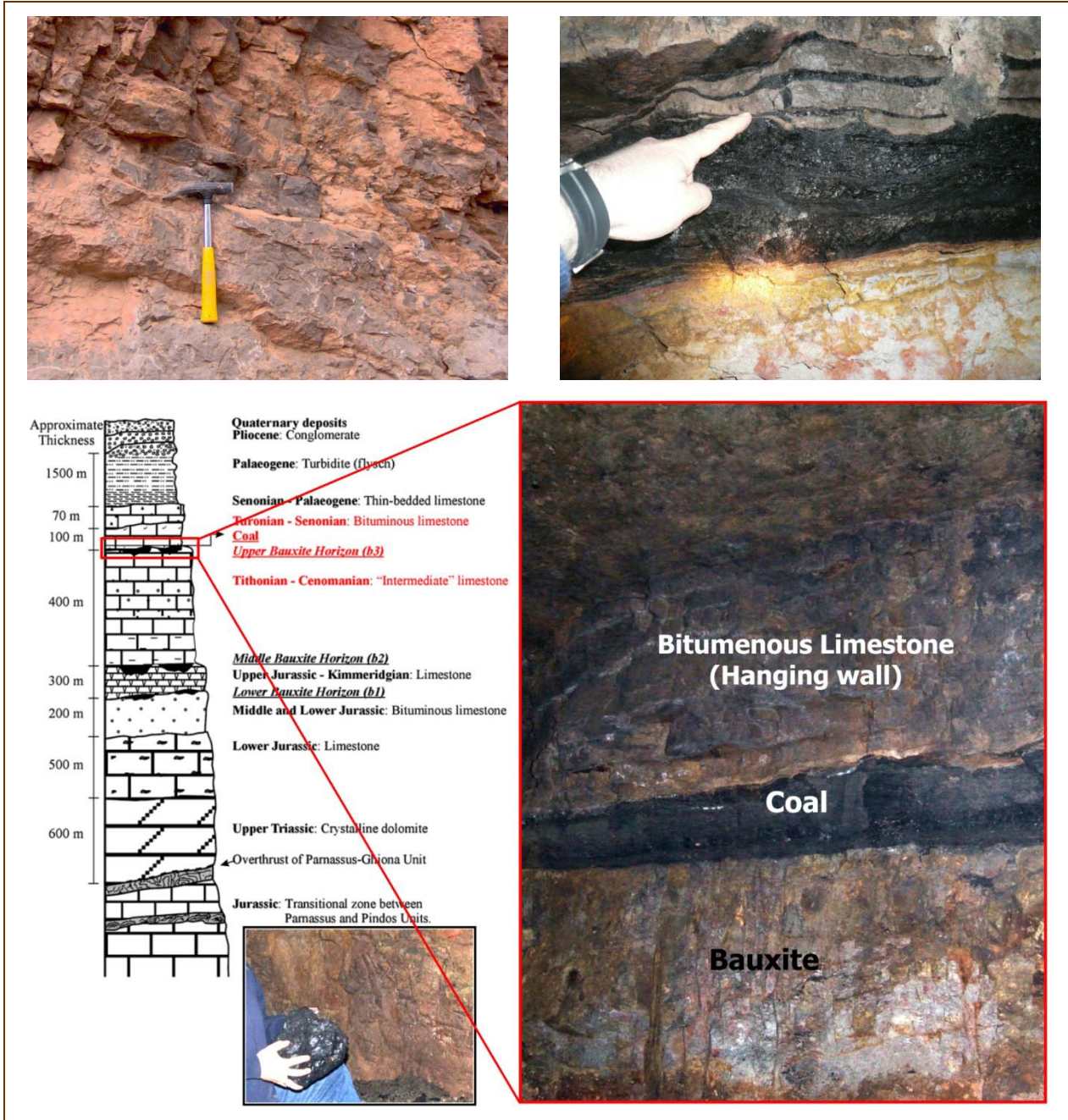
In the frame of the present dissertation, a specific mining site situated into the Cretaceous B3 horizon, and particularly the mining front of the Pera Lakkos active underground mine was geochemically investigated, in details. In this case, both typical Fe-rich and Fe-depleted bauxite, embedded between ordinary white footwall limestone and black to dark bituminous hanging wall limestone, occur (**Figure 3.1.3.1** and **Figure 3.1.3.2**).

Figure 3.1.3.1: The typical Fe-rich and Fe-depleted bauxite layers embedded between the black to dark bituminous hanging wall limestone and the ordinary white footwall limestone at the investigated mining front of the in Pera Lakkos underground mine (Parnassos-Ghiona mining area).



Additionally, there are also local intercalations of sulfide-bearing bauxite (see also [Laskou & Economou-Eliopoulos, 2007](#)), into the Fe-depleted bauxite, overlaid by a rare Cretaceous coal layer with thickness 35-40 cm (**Figure 3.1.3.2**; [Aluminium S.A. – personal communication](#); [Kalaitzidis et al., 2010](#)).

Figure 3.1.3.2: The coal interstratified between the bauxite ore and the black to dark bituminous hanging wall limestone, at the mining front of Pera Lakkos underground mine. Lithostratigraphic column has been modified after [Valeton et al., 1987](#) and [Kalaitzidis et al., 2010](#) and references therein.



The bulk chemical compositions of black (ALM0306_PL1_DLS1) to dark (ALM0306_PL1_DLS2) bituminous hanging wall limestone and the ordinary white footwall limestone (ALM0306_PL1_WLS), as well as the composition of the coal (ALM0807_PL1_COAL; including its relevant flying ash / ALM0807_PL1_ASH) interstratified between the bauxite ore and the hanging wall limestone at Pera Lakkos underground mine are presented in **Tables 3.1.3.1** and **3.1.3.2**, respectively. For comparison reasons, the chemical composition of the flying ash of coal is also illustrated.

Table 3.1.3.1: Major and trace element concentrations of the black (ALM0306_PL1_DLS1) to dark (ALM0306_PL1_DLS2) bituminous hanging wall limestone and the ordinary white footwall limestone (ALM0306_PL1_WLS).

Sample code	ALM0306_PL1_WLS	ALM0306_PL1_DLS1	ALM0306_PL1_DLS2	Sample code	ALM0306_PL1_WLS	ALM0306_PL1_DLS1	ALM0306_PL1_DLS2
Description	Footwall	Hanging wall	Hanging wall	Description	Footwall	Hanging wall	Hanging wall
	Limestone	Limestone	Limestone		Limestone	Limestone	Limestone
	White	Black	Dark		White	Black	Dark
Mine Locality	Pera Lakkos	Pera Lakkos	Pera Lakkos	Mine Locality	Pera Lakkos	Pera Lakkos	Pera Lakkos
Unit	<i>data</i>			Unit	<i>data</i>		
wt. %				ppm			
SiO ₂	0.11	0.04	0.08	Ag	bdl	bdl	bdl
Al ₂ O ₃	0.53	0.11	0.08	Cd	0.3	0.1	0.1
Fe ₂ O ₃ (T)	0.07	0.39	0.08	Sn	1	1	1
MnO	0.01	0.01	0.01	Sb	0.1	0.2	0.1
MgO	0.11	1.06	1.47	Cs	0.1	0.1	0.1
CaO	55.69	54.06	53.52	Ba	1.6	5.4	2
Na ₂ O	0.02	0.02	0.02	Hf	0.5	0.5	0.5
K ₂ O	bdl	bdl	bdl	Ta	0.1	0.1	0.1
TiO ₂	0.06	0.04	0.04	W	11.2	16.6	6
P ₂ O ₅	-	-	-	Hg	0.01	0.02	0.01
Cr ₂ O ₃	-	-	-	Tl	0.09	0.1	0.1
LOI	43.17	44.09	44.18	Pb	0.6	0.4	0.1
Total	99.77	99.82	99.48	Bi	0.1	0.1	0.1
ppm				La	1.8	1.3	0.9
Be	1	1	1	Ce	2.2	1.2	0.7
Sc	-	-	-	Pr	0.27	0.19	0.08
V	6	23	5	Nd	0.9	0.8	0.4
Cu	0.1	0.2	0.1	Sm	0.19	0.11	0.06
Co	3.5	2.7	1.4	Eu	0.05	0.02	0.02
Ni	1.3	30.8	11.2	Gd	0.22	0.15	0.12
Zn	3	1	1	Tb	0.03	0.02	0.01
Ga	0.5	0.5	0.5	Dy	0.19	0.1	0.05
As	0.8	7.5	1.5	Ho	0.04	0.02	0.02
Se	0.5	0.7	0.6	Er	0.07	0.05	0.03
Rb	0.6	0.7	0.5	Tm	0.02	0.01	0.02
Sr	48.3	517	617.8	Yb	0.09	0.05	0.05
Y	1.6	0.8	0.5	Lu	0.02	0.01	0.01
Zr	4.6	0.9	0.7	Th	0.2	0.1	0.1
Nb	0.6	0.5	0.5	U	0.4	2	1.1
Mo	0.1	2.6	0.3	ppb			
				Au	0.6	0.5	0.5

Table 3.1.3.2: Major and trace element concentrations of the coal (ALM0807_PL1_COAL) interstratified between the bauxite ore and the hanging wall limestone at Pera Lakkos underground mine. The bulk chemical composition of the flying ash (ALM0807_PL1_ASH) of coal is also depicted for comparison reasons.

Sample code	ALM0807_PL1_COAL	ALM0807_PL1_ASH	Sample code	ALM0807_PL1_COAL	ALM0807_PL1_ASH
Mine Locality	Pera Lakkos	Pera Lakkos	Mine Locality	Pera Lakkos	Pera Lakkos
<i>Unit</i>	<i>data</i>	<i>data</i>	<i>Unit</i>	<i>data</i>	<i>data</i>
<i>wt.%</i>			<i>ppm</i>		
SiO ₂	0.22	30.85	Mo	9.5	62.7
Al ₂ O ₃	0.67	33.93	Ag	bdl	0.9
Fe ₂ O ₃ (T)	1.45	22.01	Cd	bdl	bdl
MnO	bdl	0.01	Sn	bdl	5
MgO	0.09	1.02	Sb	3	1.7
CaO	0.27	2.92	Cs	0.2	21.5
Na ₂ O	0.02	1.88	Ba	2	175
K ₂ O	0.01	1.49	Hf	0.3	8.5
TiO ₂	0.01	1.45	Ta	0	2.3
P ₂ O ₅	0.01	0.08	W	bdl	4.1
Cr ₂ O ₃	bdl	0.07	Hg	0.31	0.01
LOI	96.6	3.4	Tl	bdl	0.7
Total	99.35	99.114	Pb	0.9	9.6
TOT/C	78.37	0.1	Bi	bdl	0.3
TOT/S	5.62	0.48	La	23.4	293.5
<i>ppm</i>			Ce	289.9	1531
Be	2	13	Pr	11.63	73.63
Sc	16	38	Nd	48.7	282
V	36	338	Sm	12.56	44.89
Cu	1.5	13.3	Eu	3.17	8.96
Co	2.7	35	Gd	12.39	40.21
Ni	257.1	488.3	Tb	1.99	4.71
Zn	7	3	Dy	10.82	23.92
Ga	8.6	74.8	Ho	2.18	4.5
As	41.5	36.4	Er	5.83	11.22
Se	3	bdl	Tm	0.8	1.45
Rb	1.1	80.5	Yb	4.73	8.64
Sr	166.9	799.7	Lu	0.62	1.12
Y	57.3	226.7	Th	0.6	28.1
Zr	8.7	285.6	U	30.4	135.1
Nb	0.3	31.3	<i>ppb</i>		
			Au	bdl	10

The bulk chemical compositions (with regard to the trace elements) of the geological materials composing the Pera Lakkos, normalized to UCC (Rudnick & Gao, 2003), are presented in **Figure 3.1.3.3**. It is obvious that both hanging wall and footwall limestones contain relatively low concentrations of trace elements. On the other hand, hanging wall limestone is slightly enriched in Sr, Mo, Se, Cd, whereas footwall limestone differs from the latter as is relative depleted in Sr, and Mo comparing to UCC (Rudnick & Gao, 2003). Similar

observation was reported by [Spathi \(1972\)](#) who analyzed footwall limestones for Pb, Cr, Cu, Co and Sr. It is noteworthy to mention that sulfur-bearing Fe-rich bauxite is highly enriched in As, and Sb, less enriched in metals (such as Ni, V, Cr, Pb, Co, Sn, and Hg) and, also, in actinides (Th, and U). Moreover, these sulfur bauxitic fragments are relative enriched in Sc, Zr, Ti, Ta, Nb, and REE. Furthermore, comparing the UCC-normalized spider diagram ([Rudnick](#)

Figure 3.1.3.3: The UCC-normalized ([Rudnick & Gao, 2003](#)) spider diagrams for the studied dark (ALM0306_PL1_DLS2) and black (ALM0306_PL1_DLS1) hanging wall limestone, the coal layer (ALM0807_PL1_COAL) including the relevant flying ash (ALM0807_PL1_ASH), the Fe-rich/sulfide-bearing bauxite (Fe-rich/S-bearing bauxite), the average of Fe-depleted bauxite (n=3), the average of Fe-rich bauxite (n=4), and the footwall limestone (ALM0306_PL1_WLS) in the Pera Lakkos mine.

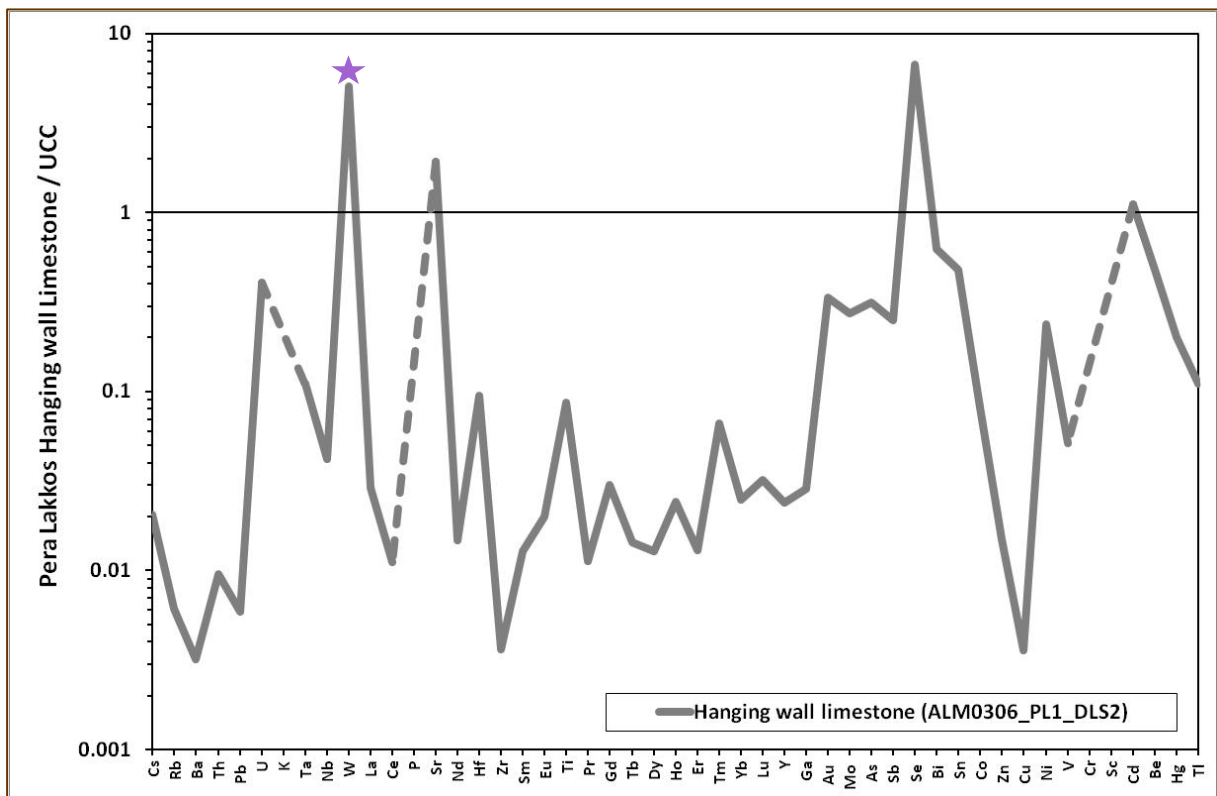


Figure 3.1.3.3: continued.

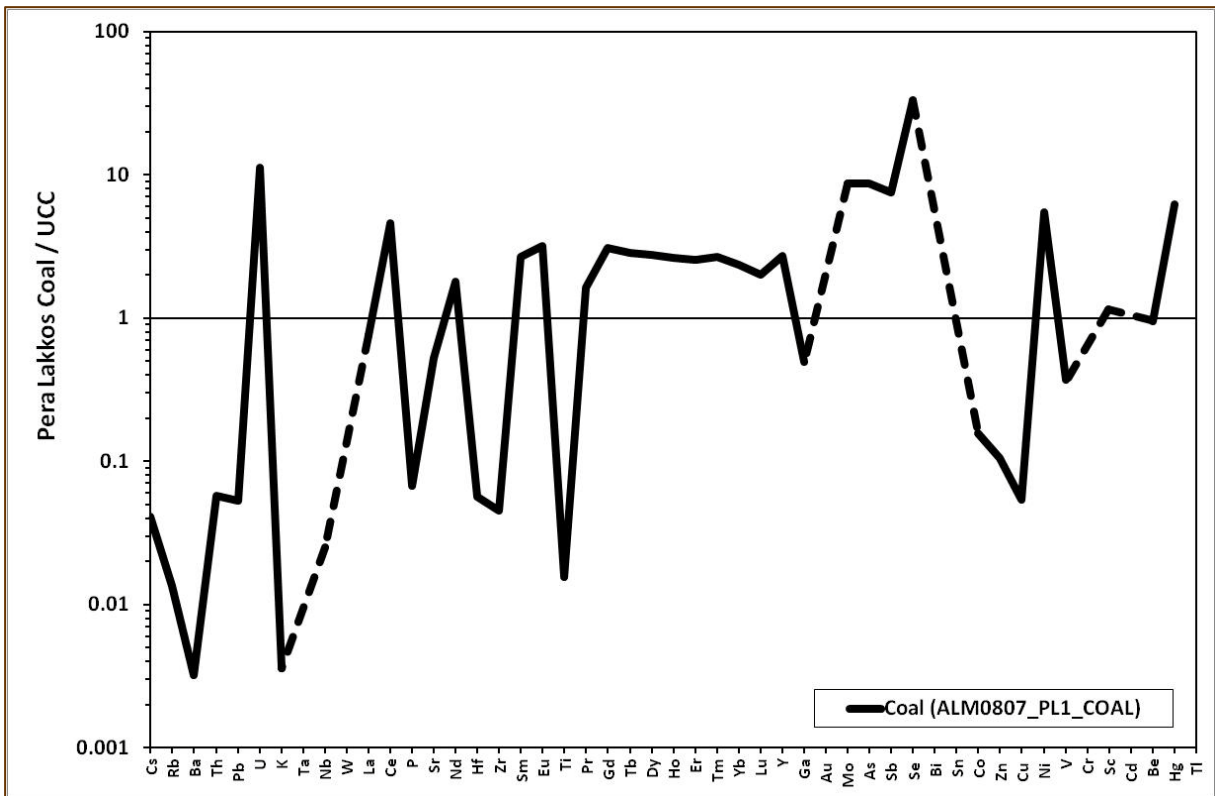
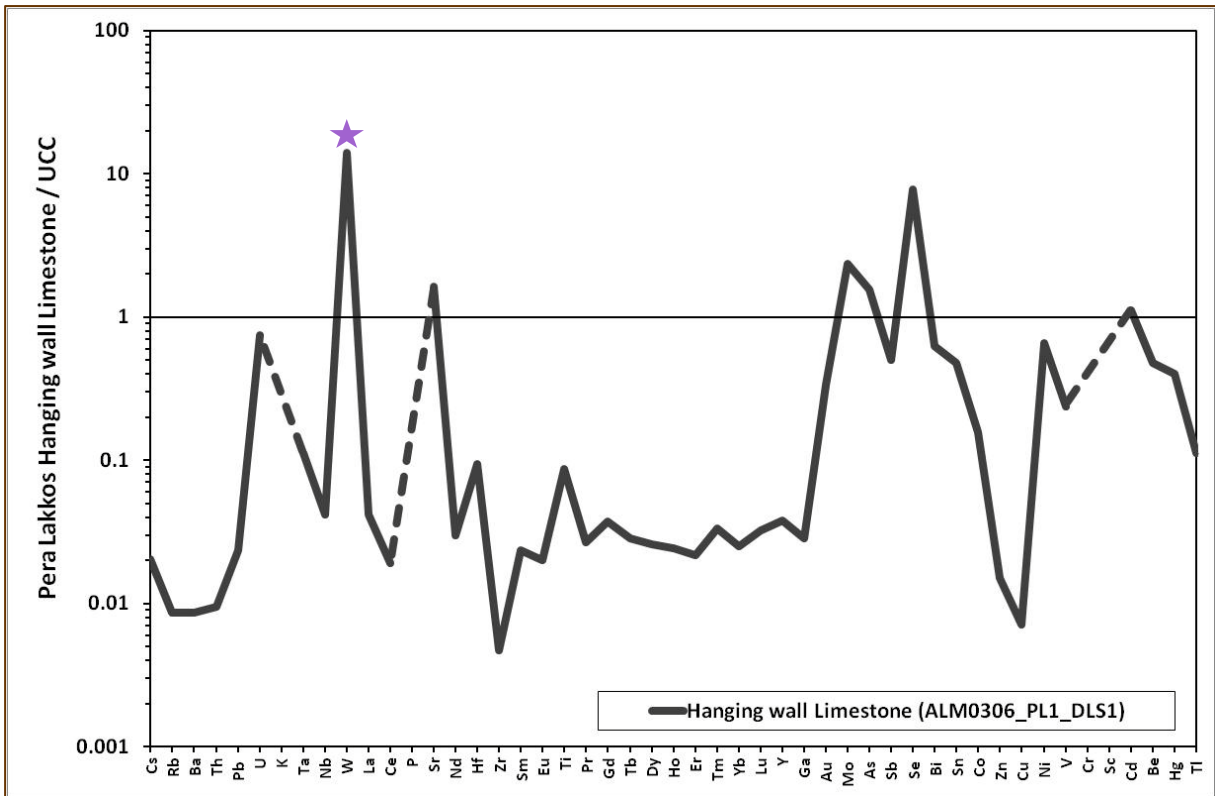


Figure 3.1.3.3: continued.

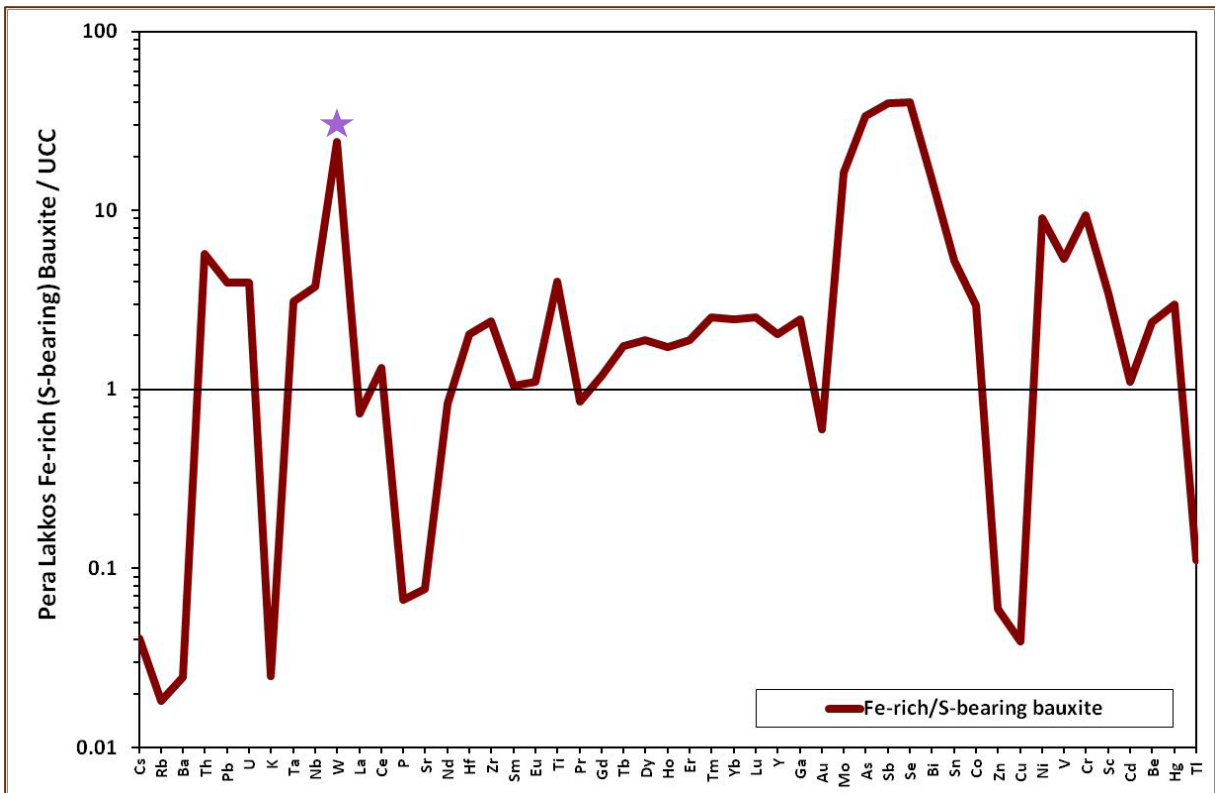
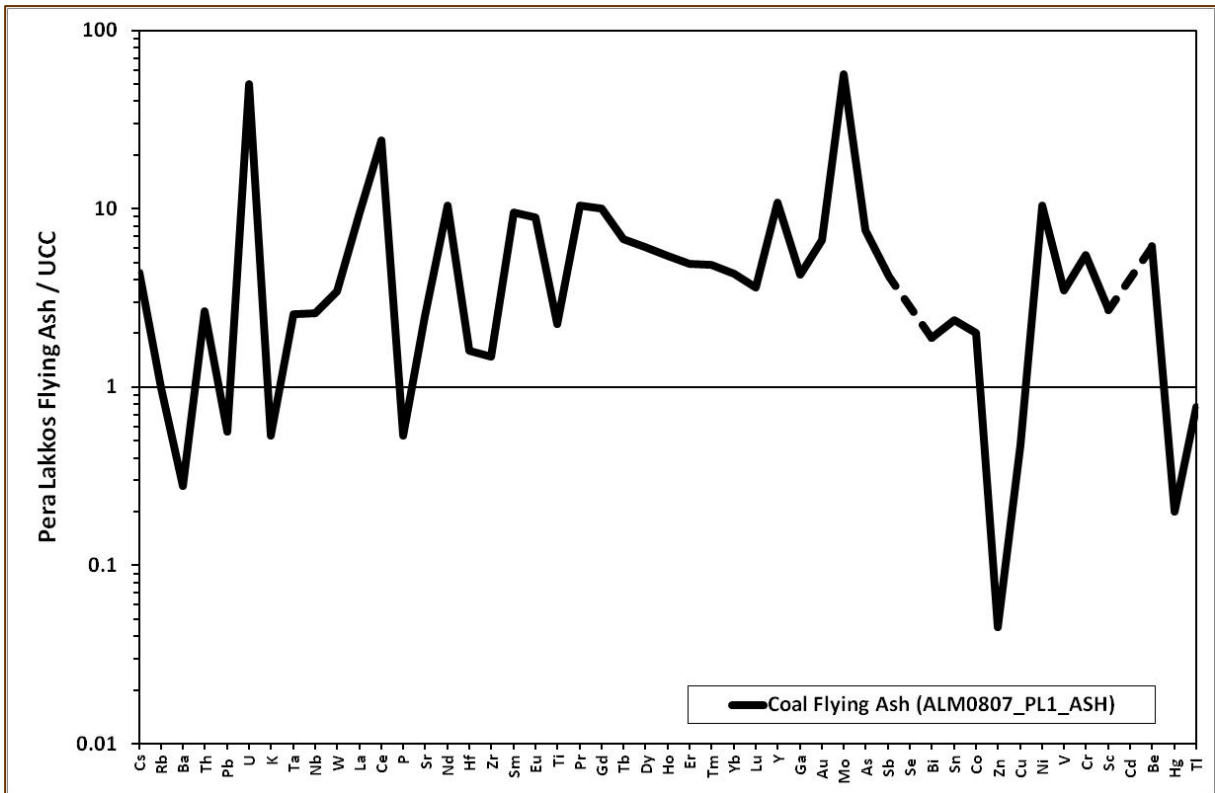


Figure 3.1.3.3: continued.

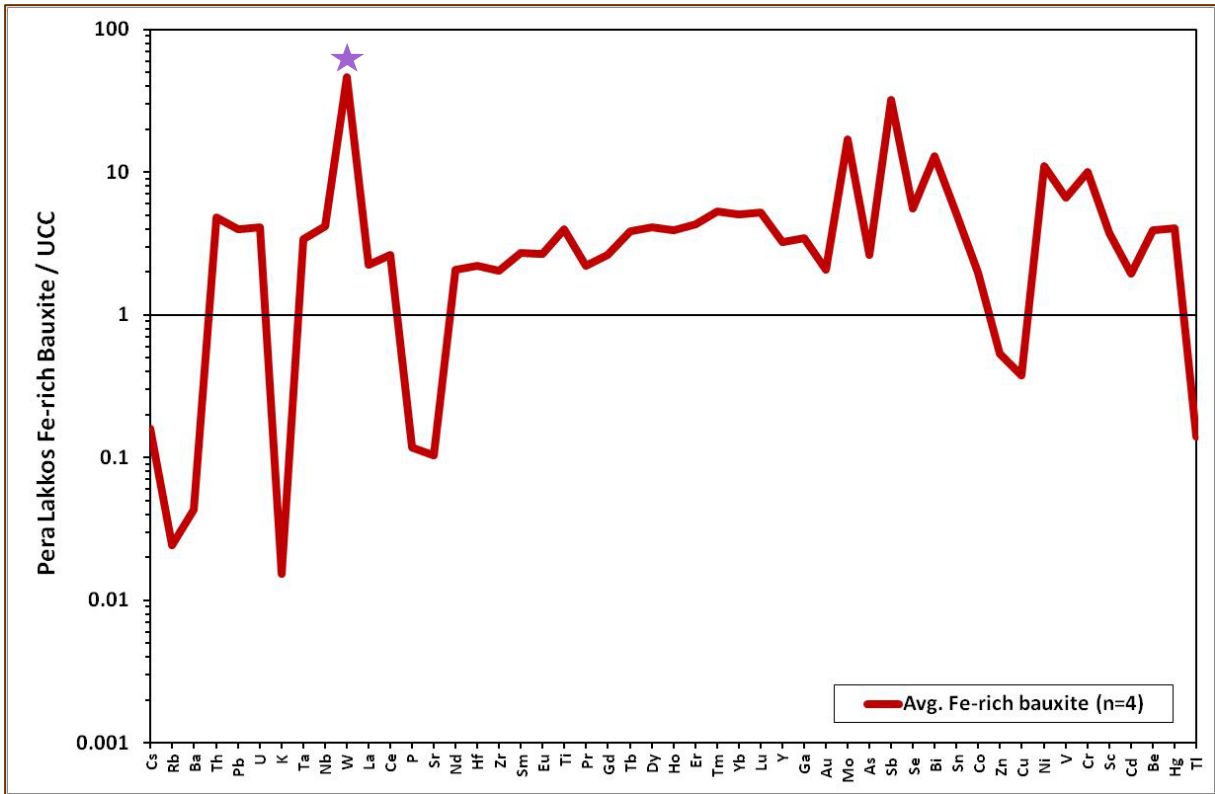
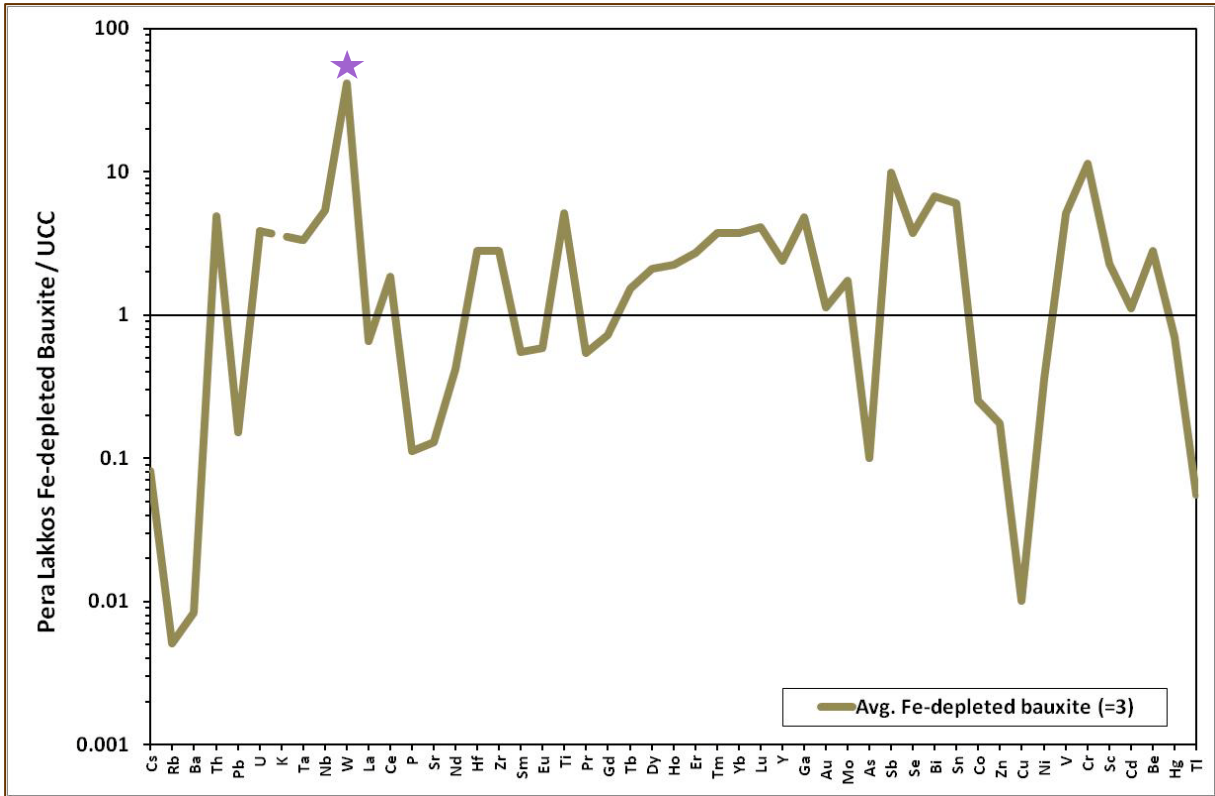
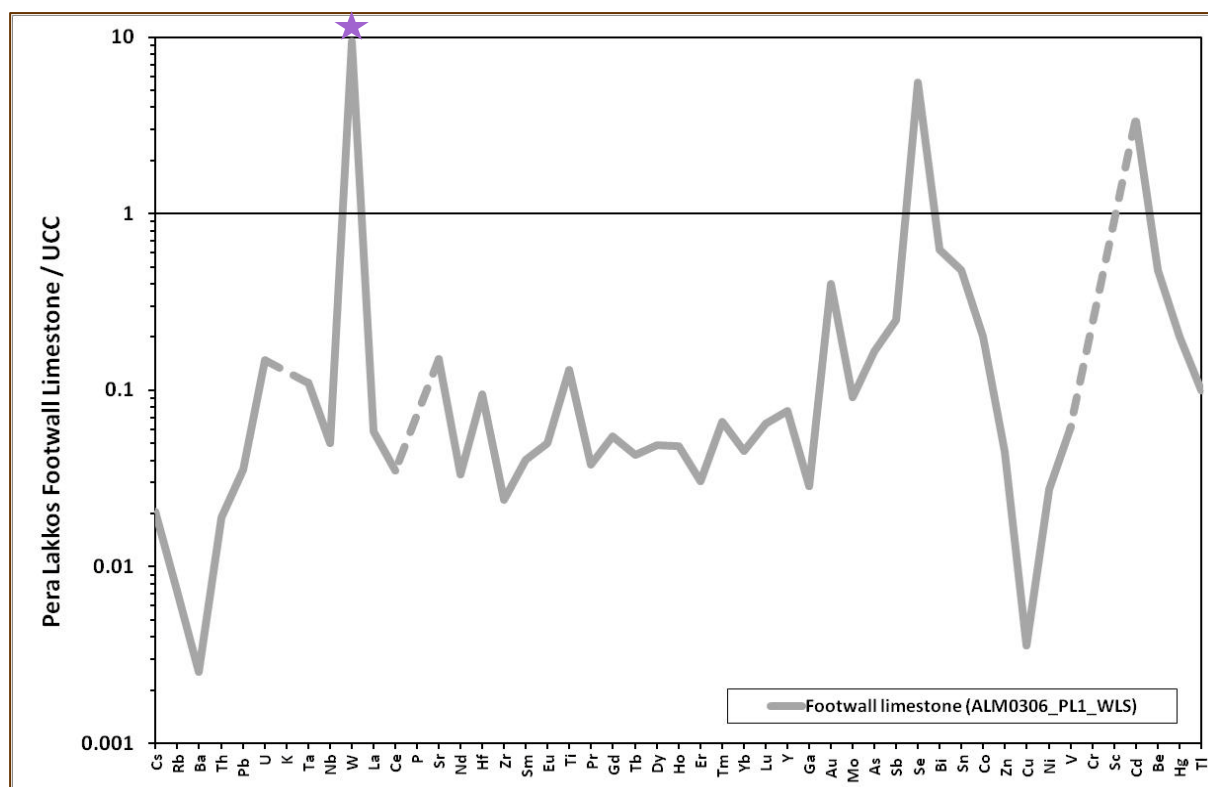


Figure 3.1.3.3: continued.



& Gao, 2003) of Fe-depleted and Fe-rich bauxite, significant enrichment and depletion differences in selected elements -among the two bauxitic types- can be confirmed. Hence, Fe-depleted bauxite is depleted in As, Sm, and Eu. Additionally, both bauxitic types are enriched in Th, U, REE, and Ti, whereas are depleted in Pb. The coal is highly enriched in Se, U, Mo, As, Sb, Ni, REE and Hg. Similar observations have been reported by Kalaitzidis et al. (2010) for most of elements, though there is no mention for elevated content of Cu, Se, REE and Hg. Moreover, the relevant flying ash, representing the “inorganic” part of the material, is exceptionally enriched in U, Mo, REE, Ni and Cr. That means U, Mo, Ni and REE are in either case concentrated in the above geological material.

According to PXRD diagrams the studied footwall and hanging wall limestones contain only calcite as major crystalline phase, whereas most of the trace elements must be associated to detrital and authigenic crystalline phases such as chromites, magnetites, zircons, rutiles, clays, goethite, and pyrite (Figure 3.1.3.4 and Figure 3.1.3.5). The presence

of characteristic framboids and/or relevant pseudomorphs into the dark and black hanging wall limestone indicates potential anoxic palaeo-environment.

Figure 3.1.3.4: Detrital and authigenic crystalline phases separated, by CH_3COOH dissolution, from the white footwall limestones (ALM0306_PL1_WLS): chromite (left images); zircon (upper right); rutile (middle right); chromite with zircon and rutile crystal (lower right).

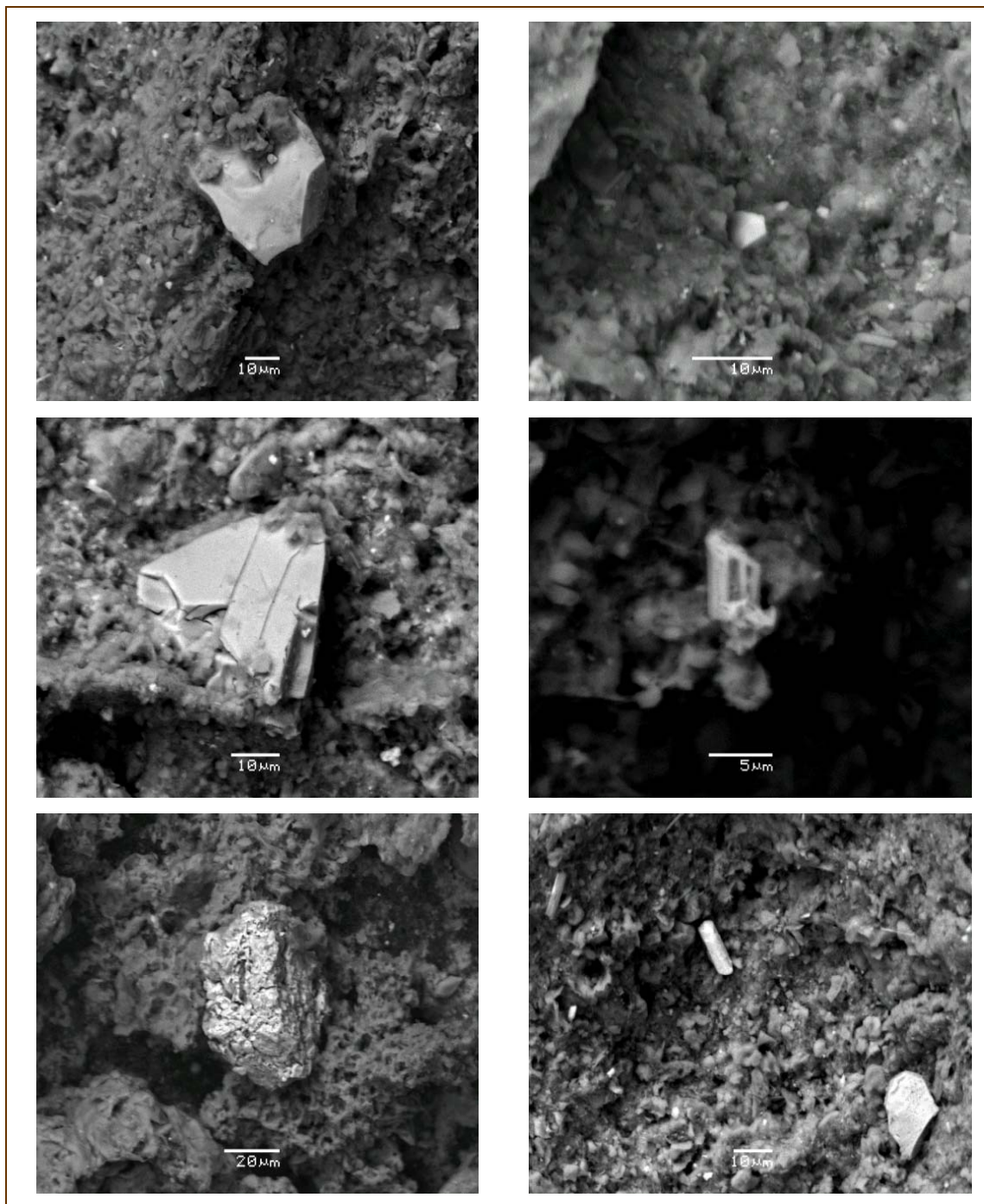
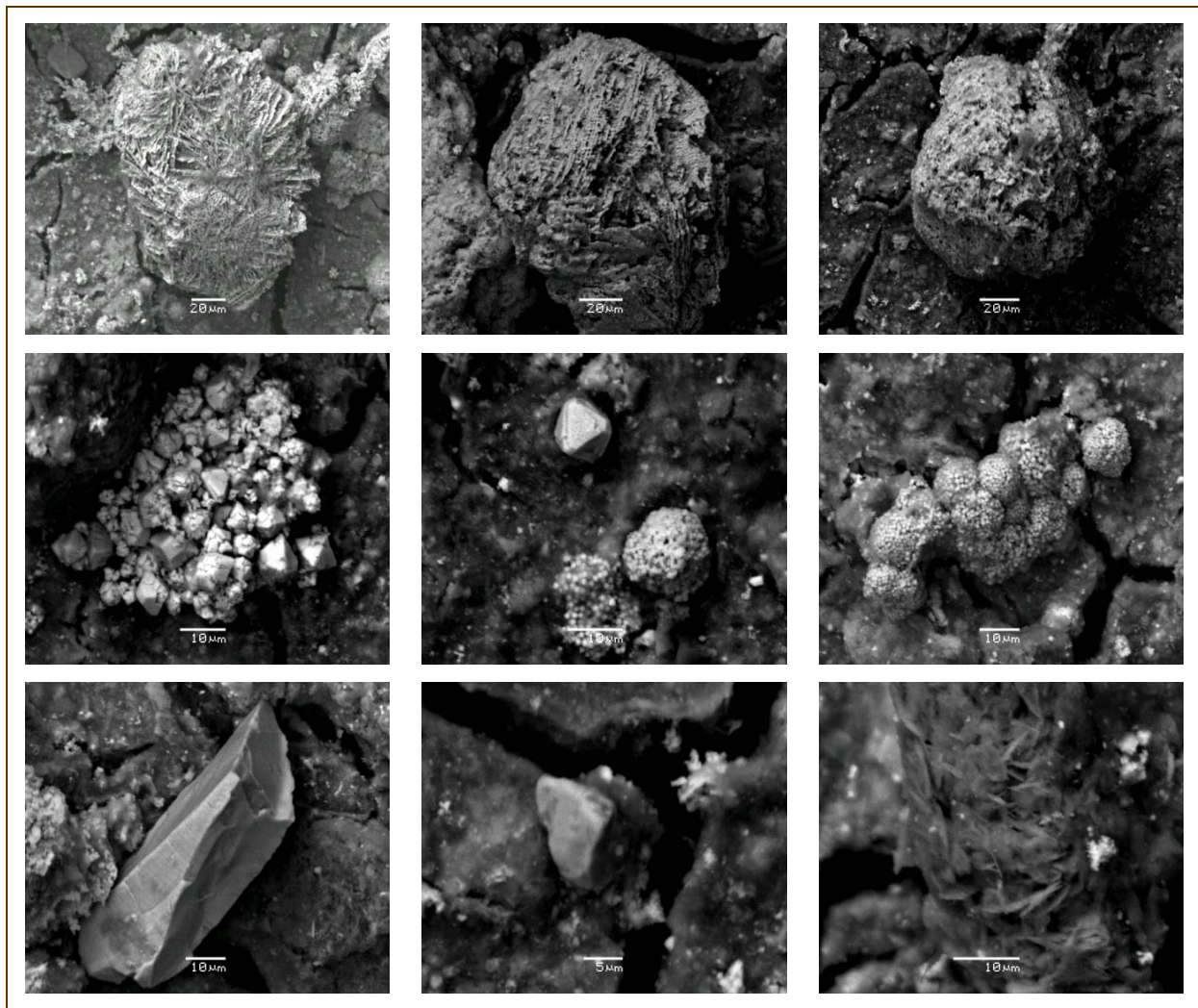


Figure 3.1.3.5: Detrital and authigenic crystalline phases separated, by CH_3COOH dissolution, from the dark hanging wall (ALM0306_PL1_DLS2): goethite (upper left), its pseudomorph after pyrite (upper middle), and pyrite (upper right); magnetite crystals (middle left), magnetite with framboids (middle), and framboids (middle right); chromite (lower left); rutile (lower middle); clays with REE (lower left).



The REE chondrite-normalized (Haskin et al., 1968a; Haskin et al., 1968b; Haskin et al., 1971; Wakita et al., 1971; Boynton, 1985; Taylor & McClennan, 1985; Korotev (1996a & 1996b; see text above) diagrams for all geological materials for the Pera Lakkos profile are presented in **Figure 3.1.3.6**. It is more than evident that there is a remarkable variation in the Ce/Ce* (Ce anomaly / Ce^A) from negative to positive values and back, downward from hanging wall limestones to coal and bauxite, towards the footwall limestone (Ce^A: 0.44 -> 0.49 -> 4.18 -> 1.70 -> 3.10 -> 1.18 -> 0.68). The Ce anomalies in marine limestones could indicate paleo-redox conditions in paleo-oceans, and particularly in Tethys (e.g., Liu et al., 1988). According to the above authors, Tethyan middle-Triassic limestone in China yielded a Ce^A of 0.53 when U/Th was found to be 2.6. In the case of Parnassos-Ghiona B3 horizon Tethyan Cretaceous limestones, the hanging wall samples show Ce^A close to Chinese Triassic, but much higher U/Th ratios, in the range 11 to 20, and therefore Ce^A values should be carefully considered (Liu et al., 1988). It is also notable that other factors, including $\delta^{18}\text{O}$ and $\delta^{13}\text{C}$ values (see text below), might indicate that the hanging wall limestones have been subjected to significant alteration, due to epigenetic processes, and subsequently their composition does not reflect the primary Cretaceous Tethys seawater. On the other hand, the footwall limestones exhibits Ce^A = 0.68 and low U/Th = 2. However, also in this case the stable isotope measurements (see text below) indicated that the carbonate rock undergone through lithification related to diagenetic processes. Regarding Fe-depleted and Fe-rich bauxite occurring in Pera Lakkos underground mine, it is also rather hard to conclude on the paleo-redox conditions by using various redox-sensitive elements such as U, As, Mo and V, and geochemical parameters such as Ce/Ce*, U/Th and V/V+Ni (e.g. Hatch et al., 1992; Jones et al., 1994; Liu et al., 1988, see **Figure 3.1.3.7**). According to Mazumdar et al. (1999) positive Ce^A in early Cambrian chert-phosphorite assemblages indicate anoxic palaeo-conditions. If this is true for Cretaceous bauxites, Ce must exist in reduced state (Ce³⁺); in fact, this growing claim is strongly supported by the study of bauxites in microscale showed Ce³⁺ fluorocarbonate minerals (see text below). The precipitation of such phases in the karts-type

Figure 3.1.3.6: The REE chondrite-normalized (Haskin et al., 1968a; Haskin et al., 1968b; Haskin et al., 1971; Wakita et al., 1971; Boynton, 1985; Taylor & McClennan, 1985; Korotev (1996a & 1996b) diagrams for the studied dark (ALM0306_PL1_DLS2) and black (ALM0306_PL1_DLS1) hanging wall limestone, the coal layer (ALM0807_PL1_COAL) including the relevant flying ash (ALM0807_PL1_ASH), the Fe-rich/sulfide-bearing bauxite (Fe-rich/S-bearing bauxite), the average of Fe-depleted bauxite (n=3), the average of Fe-rich bauxite (n=4), and the footwall limestone (ALM0306_PL1_WLS) in the Pera Lakkos mine.

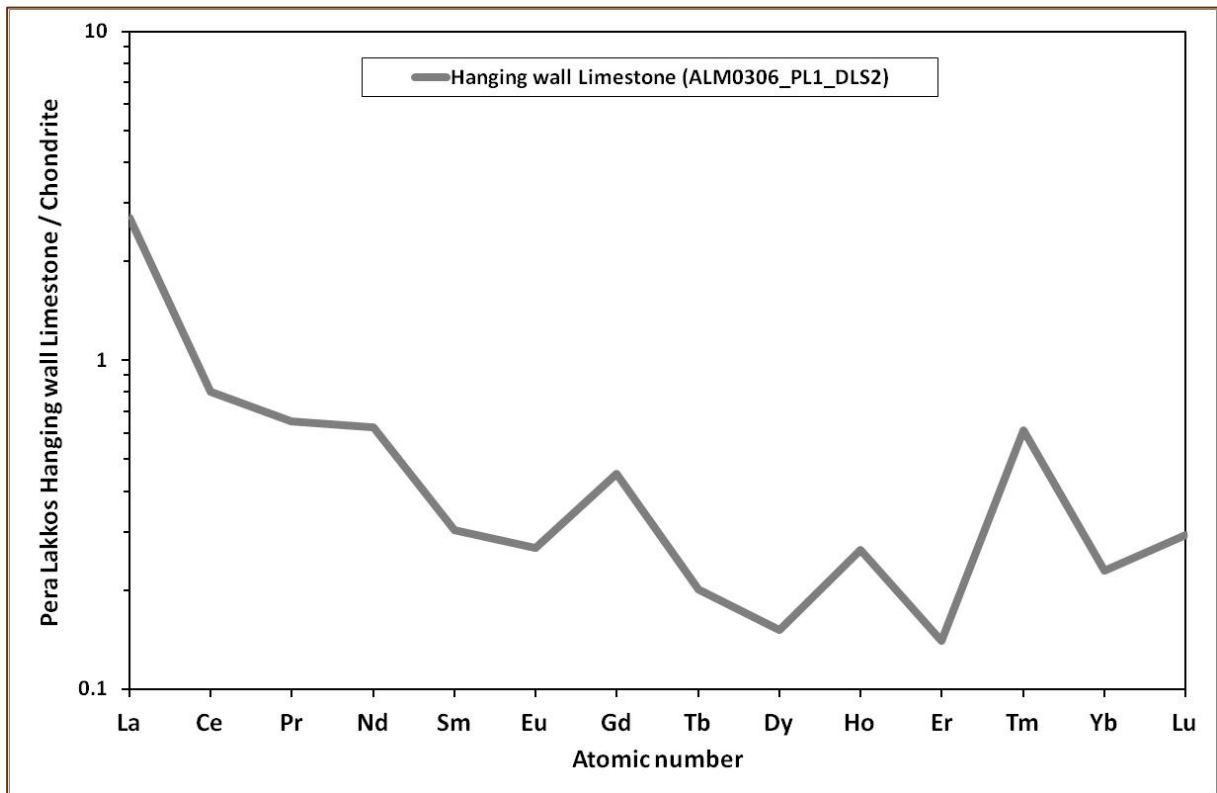


Figure 3.1.3.6: continued.

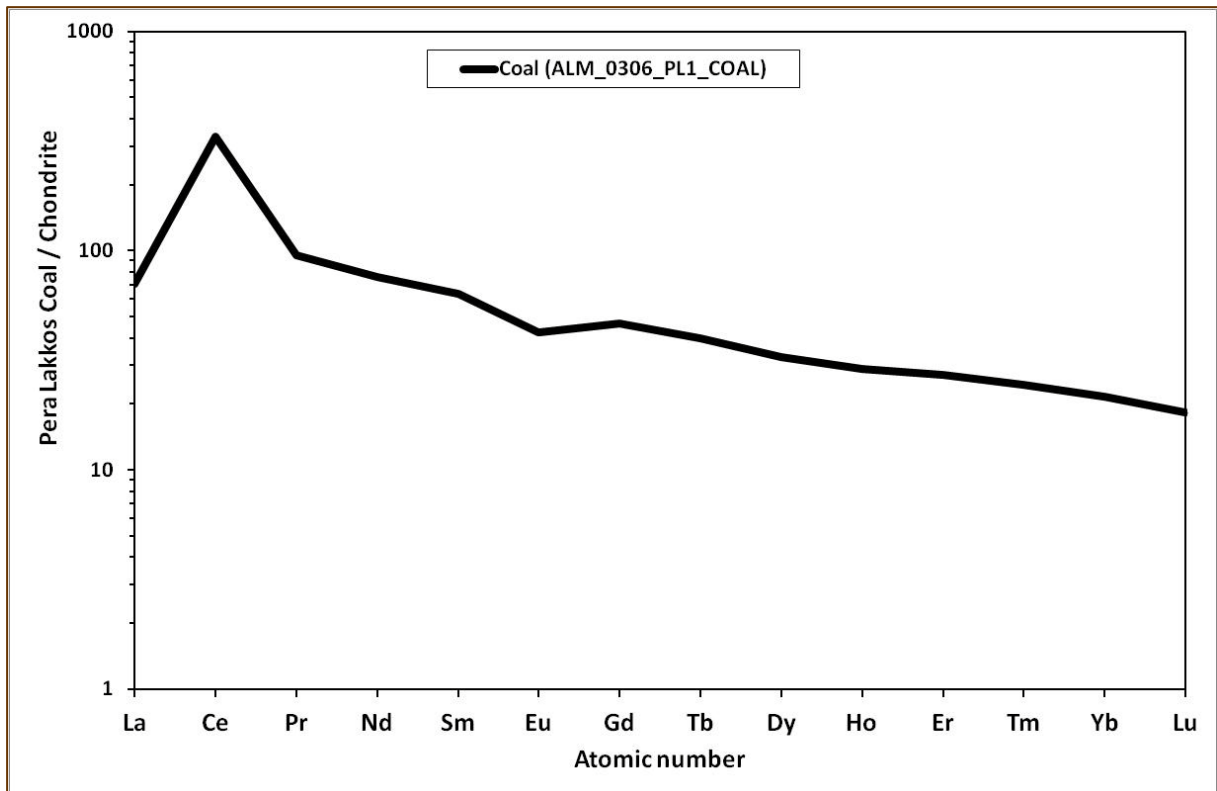
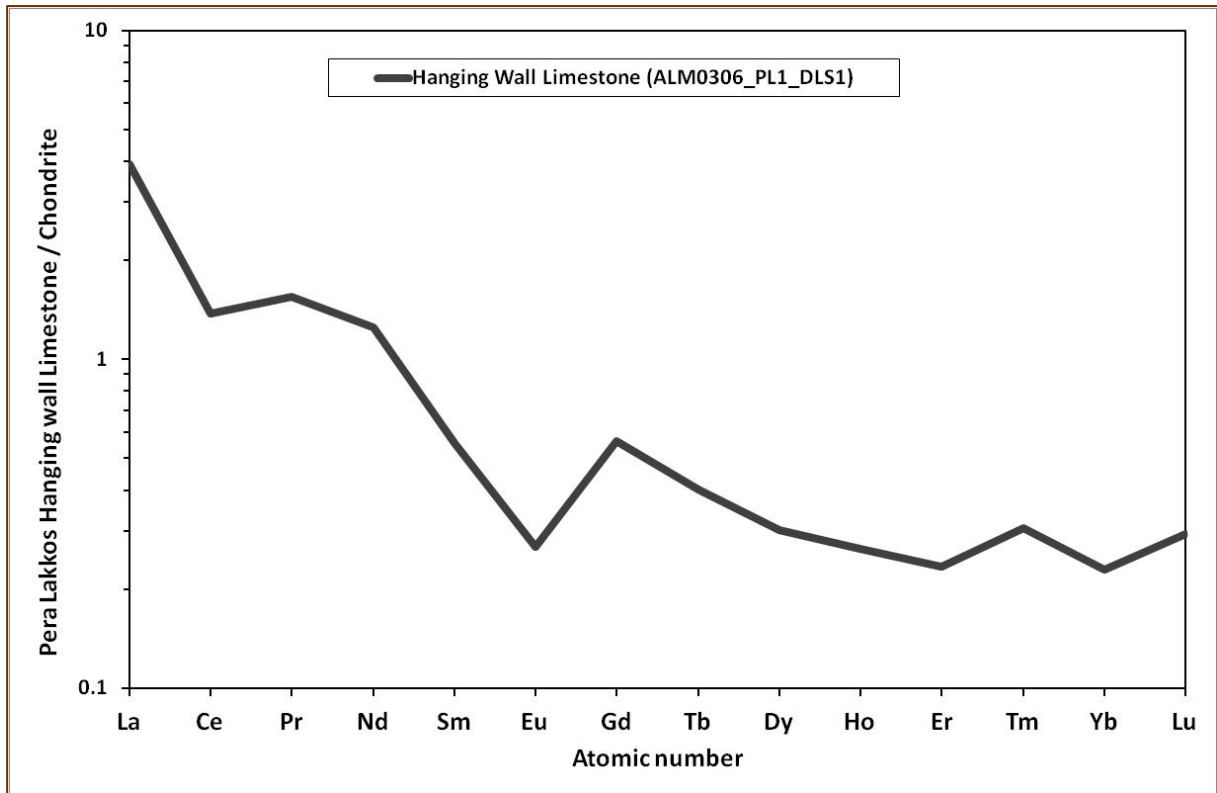


Figure 3.1.3.6: continued.

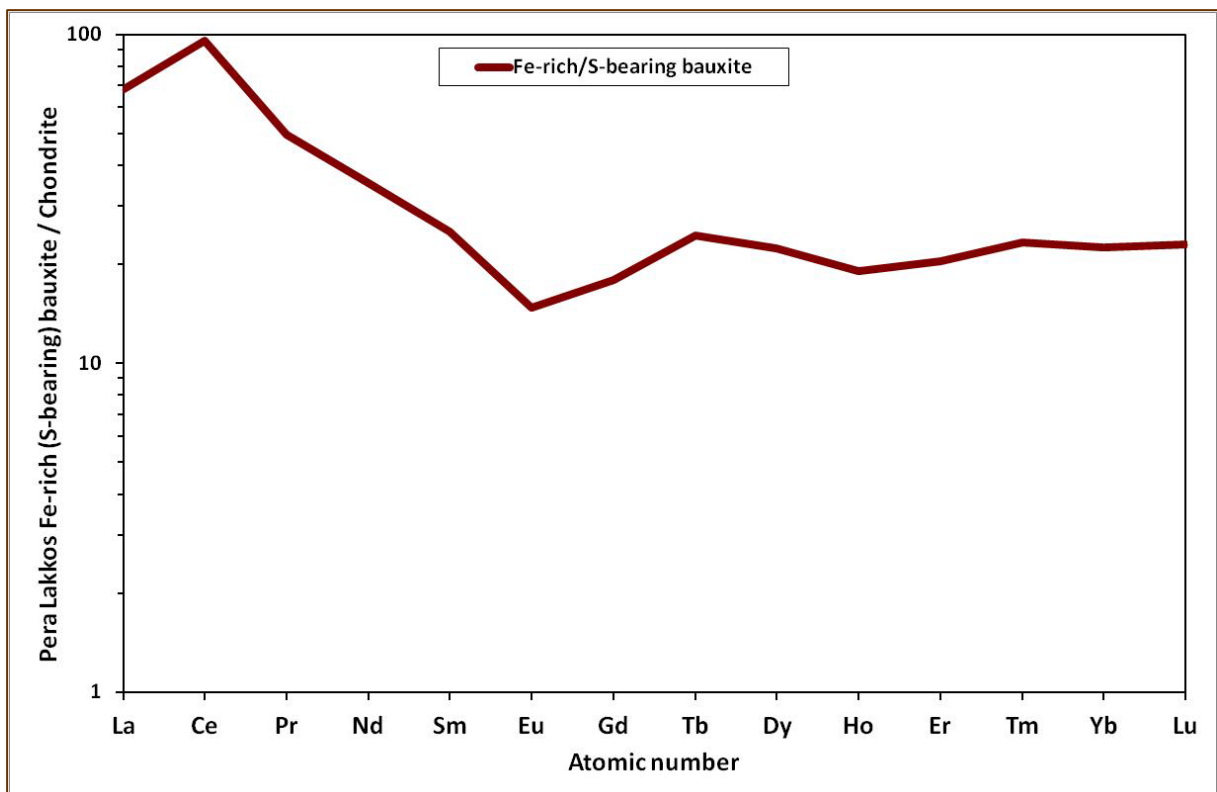
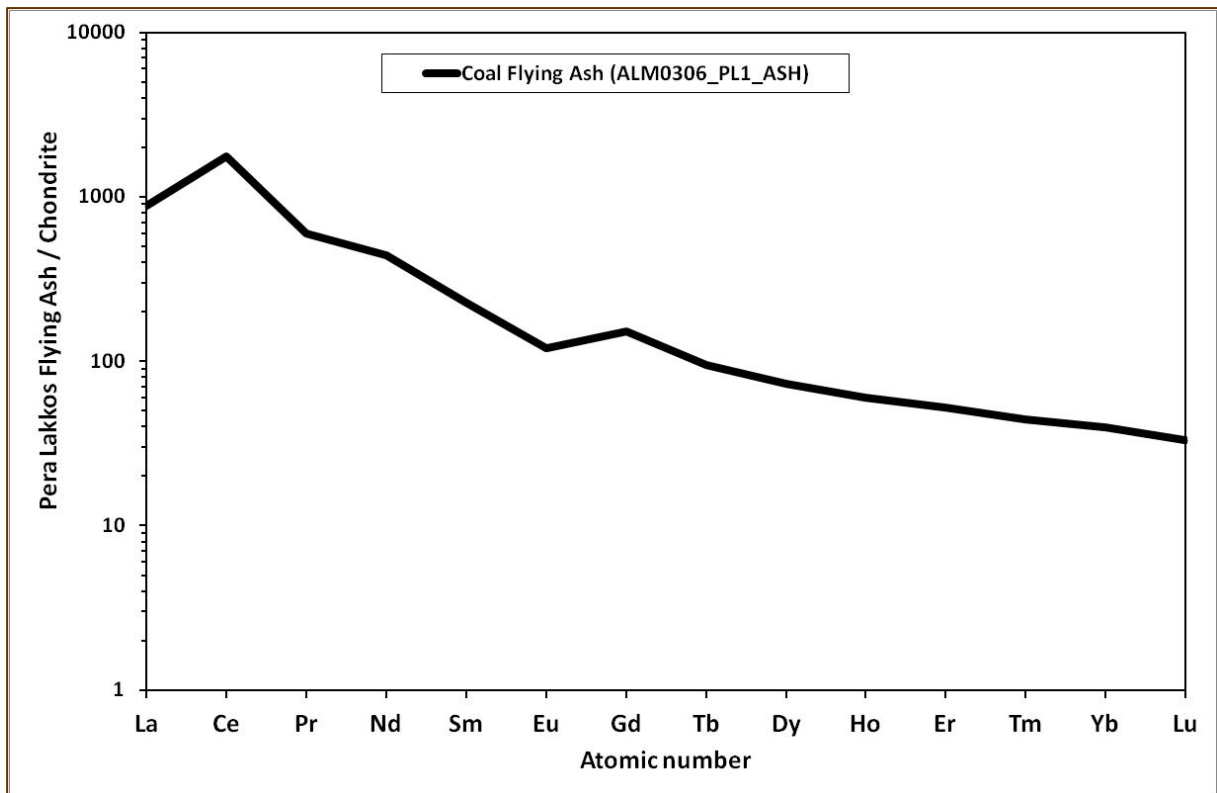


Figure 3.1.3.6: continued.

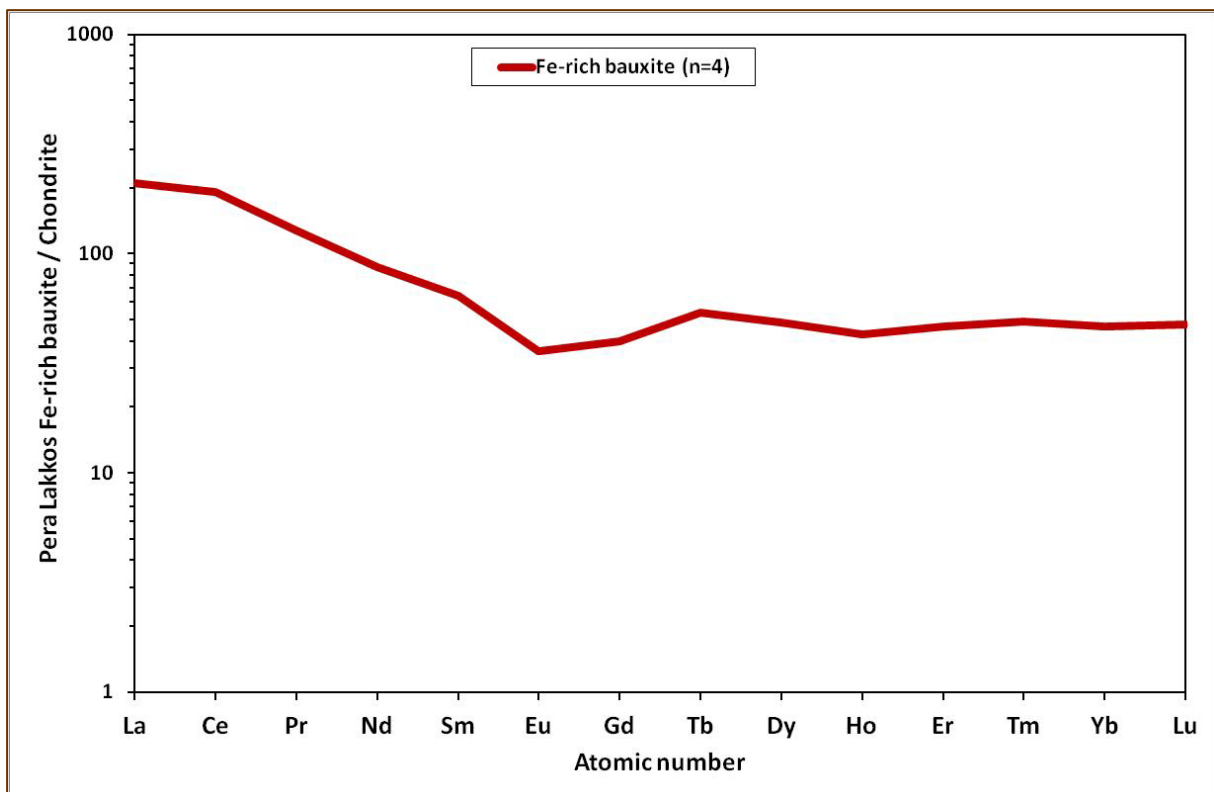
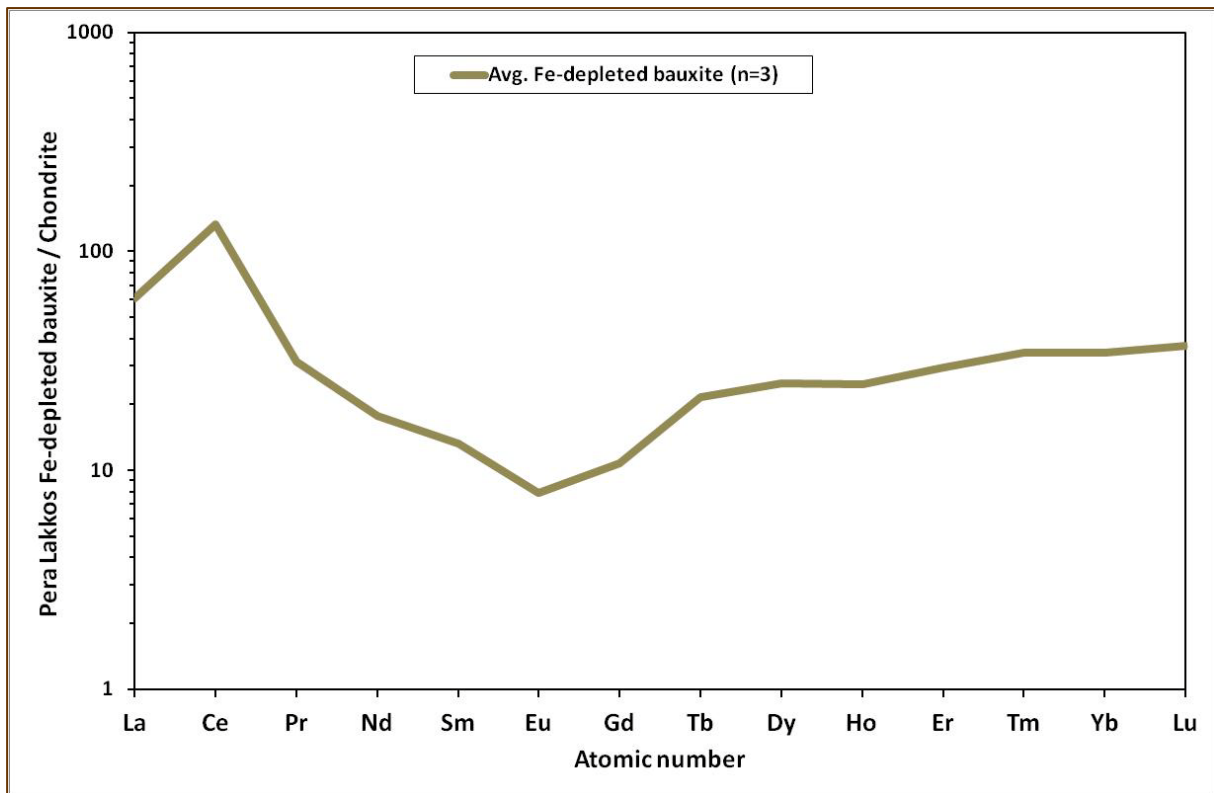
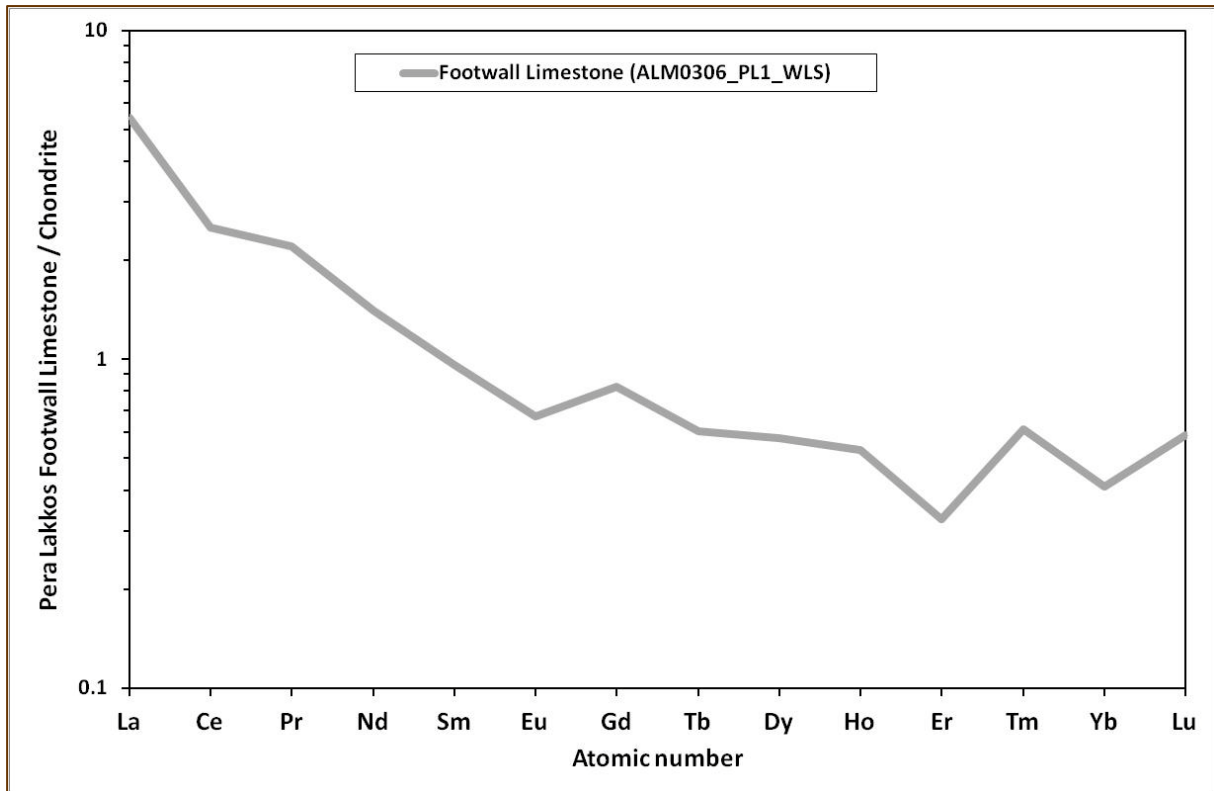


Figure 3.1.3.6: continued.



bauxites also requires alkaline conditions (Wang et al., 2010). In a more recent paper, Mongelli et al. (2014) have also discussed about oxic-anoxic conditions in bauxites on the basis of Ce^A, but for an open pit with periodic fluctuation of the groundwater table in an overall rising trend. Concerning the Pera Lakkos bauxite ore deposit, it is rather tricky to conclude whether precipitation of REE fluorocarbonates took place during diagenesis (when crystals of diasporite and/or boehmite together with primary Fe- & Ti-oxides were grown) or in the frame of further supergene/epigenetic processes. Nevertheless, it should be noted that the enrichment of the studied bauxites in rare earth elements has been recorded in all mass of the ore; thus, it is not necessarily related to the neighborhood of footwall limestone, where potential alkaline conditions (the so called “alkaline barrier”, Valetton et al., 1987; Skarpelis et al., 1989) might had occur during that enrichment.

Figure 3.1.3.7: Elemental and geochemical parameters in geological materials (from top to bottom: black hanging wall limestone; dark hanging wall limestone; coal; Fe-rich/sulfide-bearing bauxite; Fe-depleted bauxite; Fe-rich bauxite; white footwall limestone) from Pera Lakkos mine.

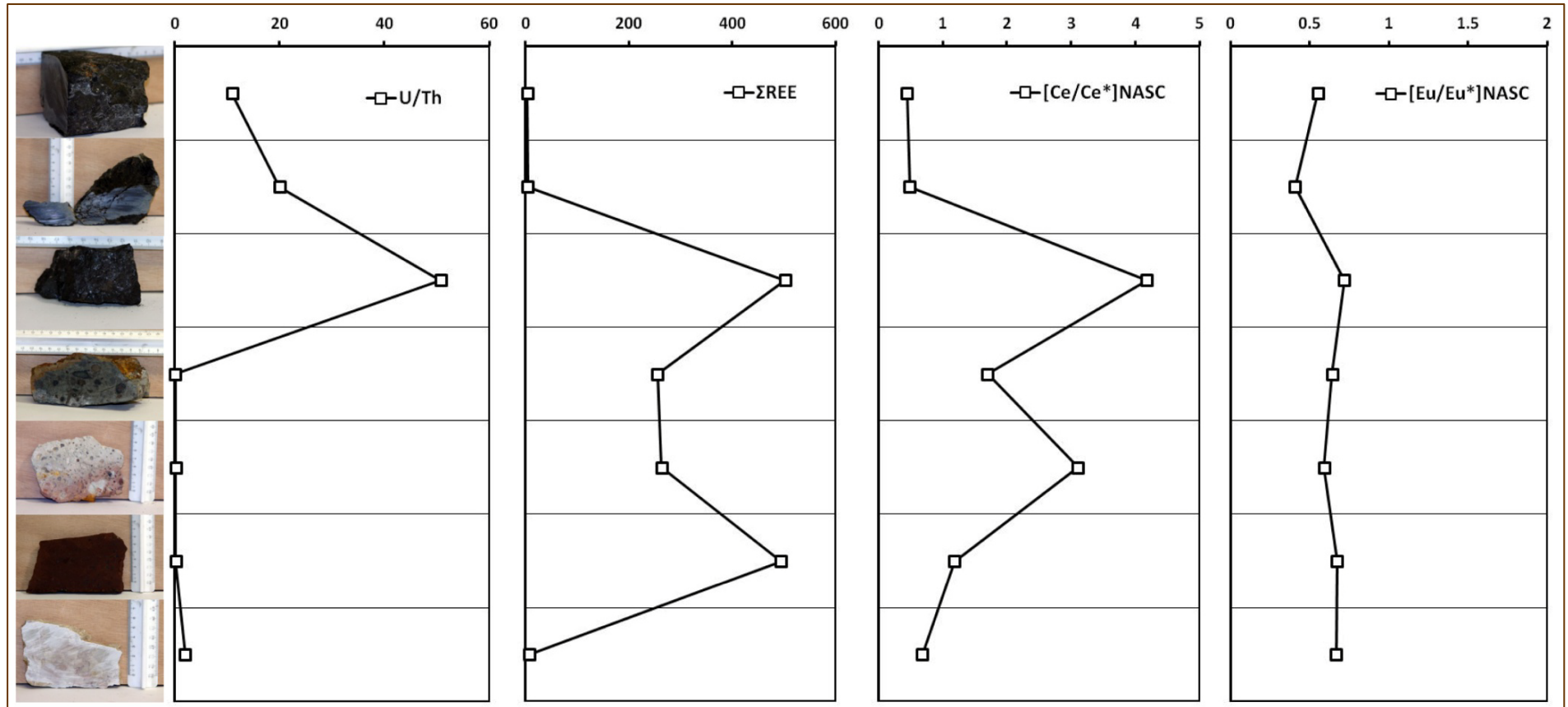
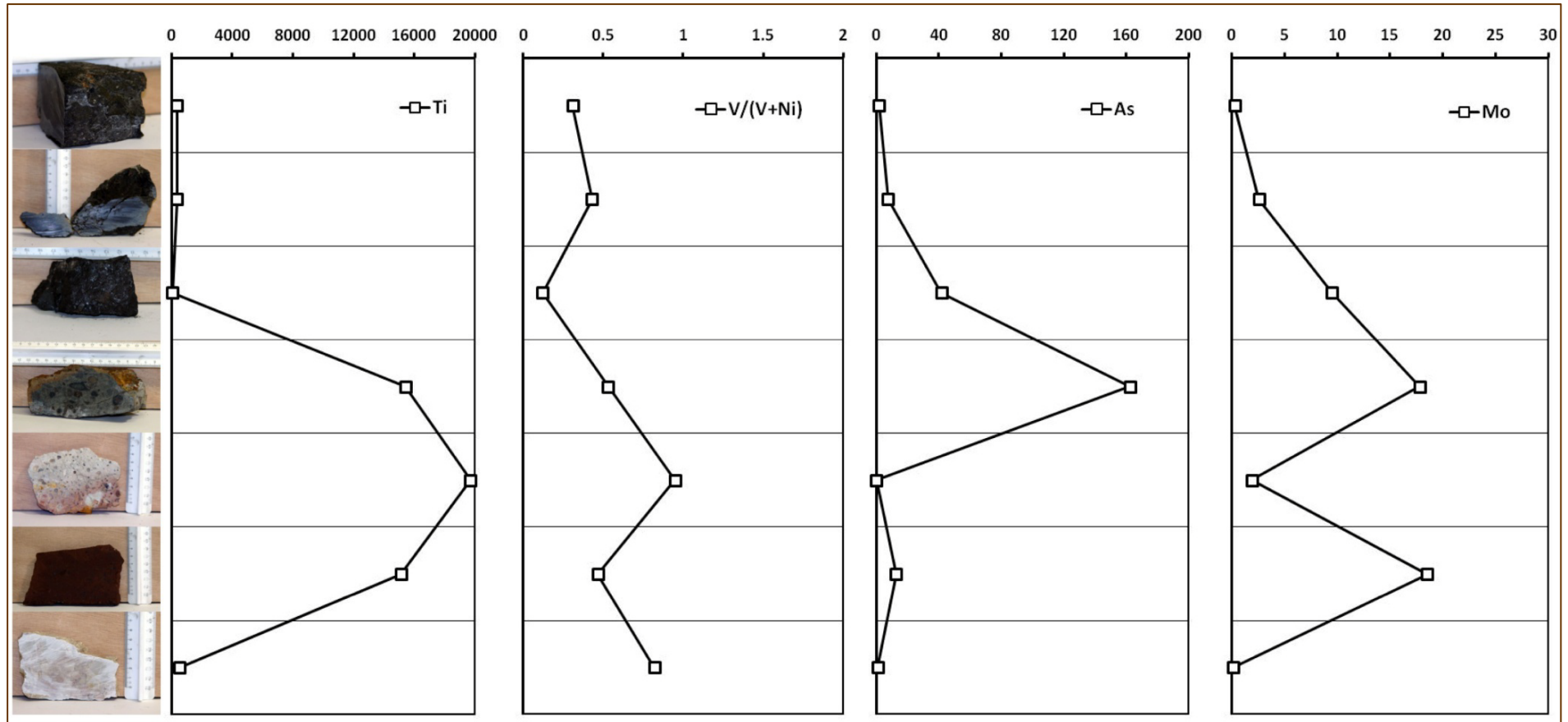


Figure 3.1.3.7: continued.

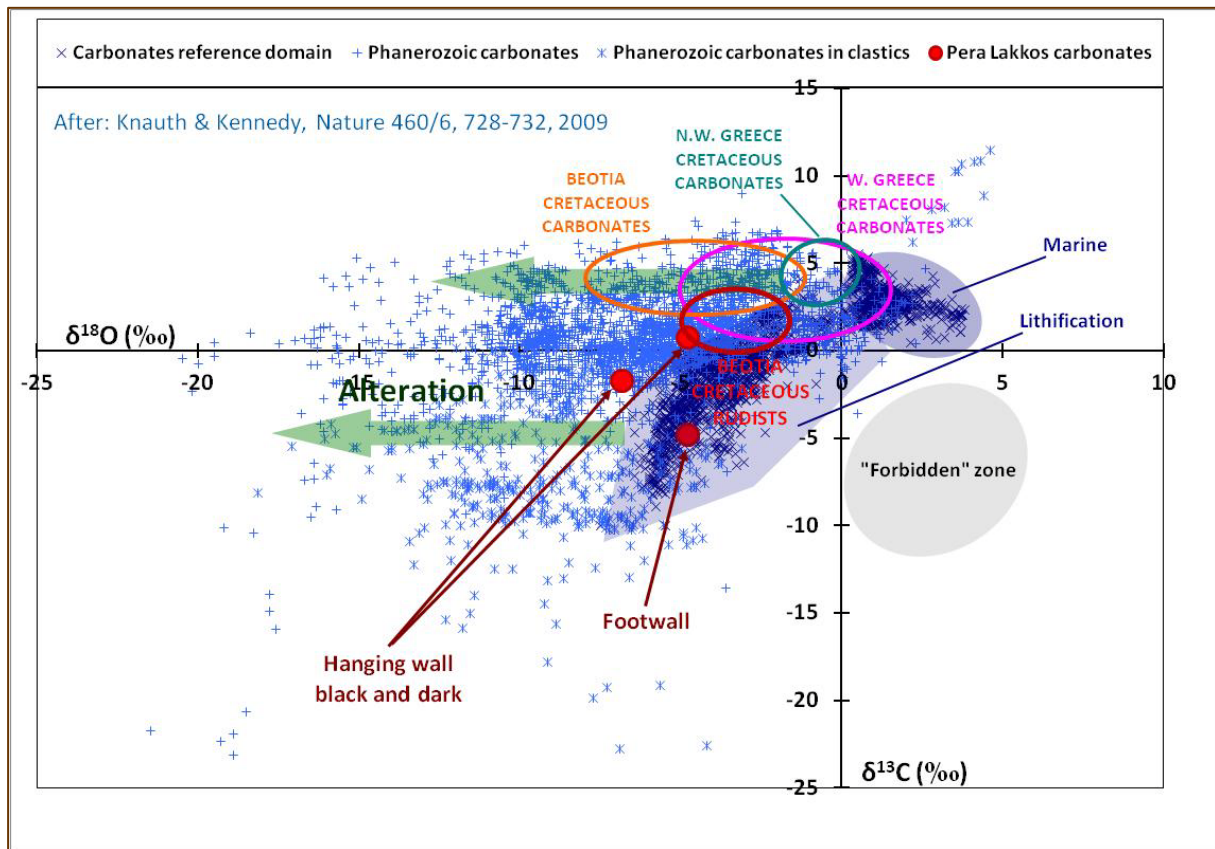


The whole rock oxygen and carbon stable isotopic compositions (**Table 3.1.3.3**) are rather typical for common limestones (after Hudson, 1977). However, taking into account the data for all Phanerozoic carbonates (including carbonates in clastics) and the carbonates reference domain (Knauth & Kennedy, 2009), it can be supported that the hanging wall limestones (dark: ALM0306_PL1_DLS2; black: ALM0306_PL1_DLS1), and particularly the black sample (ALM0306_PL1_DLS1) overlying the coal, are out of the marine and lithification fields related to marine deposition and diagenesis (**Figure 3.1.3.8**). These rocks have been subjected to intense alteration, due to epigenetic processes, in contrast to the footwall limestone (ALM0306_PL1_WLS) that seems to be, as mentioned above, an ordinary carbonate sedimentary rock subjected to diagenetic processes.

Table 3.1.3.3: Whole rock oxygen and carbon stable isotopic compositions for the studied black (ALM0306_PL1_DLS1) to dark (ALM0306_PL1_DLS2) bituminous hanging wall limestones and ordinary white footwall limestone (ALM0306_PL1_WLS), from the Pera Lakkos underground mine.

Sample Code	Description	$\delta^{18}\text{O}$ (PDB)	$\delta^{13}\text{C}$ (PDB)
ALM0306_PL1_DLS2	Hanging wall (dark) limestone	-4.81	0.8
ALM0306_PL1_DLS1	Hanging wall (black) limestone overlying coal layer	-6.85	-1.7
ALM0306_PL1_WLS	Footwall (white) limestone	-4.81	-4.8

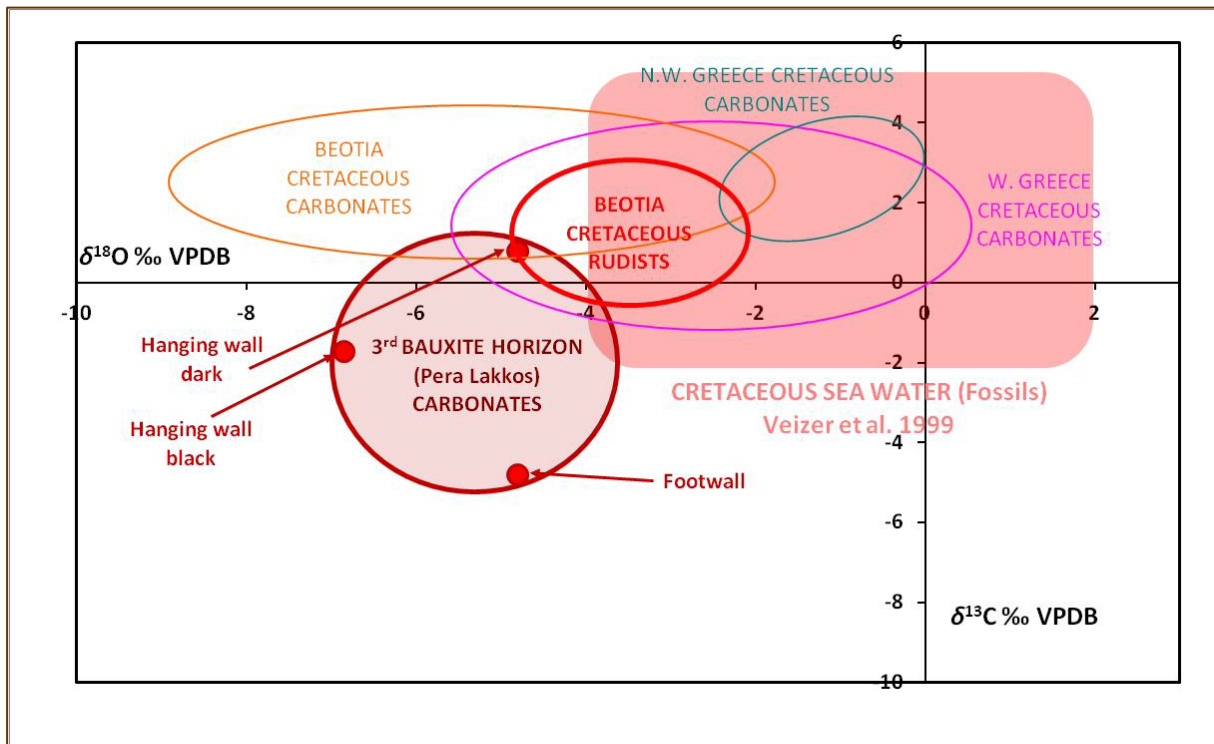
Figure 3.1.3.8: $\delta^{18}\text{O}$ and $\delta^{13}\text{C}$ of black (ALM0306_PL1_DLS1) to dark (ALM0306_PL1_DLS2) bituminous hanging wall limestones and ordinary white footwall limestone (ALM0306_PL1_WLS), from the Pera Lakkos underground mine, plotted in the diagram of Knauth & Kennedy (2009) and compared to Cretaceous carbonates from Greece (Steuber et al., 1994; Karakitsios et al., 2004; Tsikos et al., 2004; Steuber et al., 2005).



It is evident someone can hardly find primary marine (Cretaceous) signatures in these carbonate rocks. In fact, the investigated Parnassos-Ghiona carbonate rocks are different to Cretaceous carbonates from western and north-western Greece derived from Pindos palaeo-ocean and also to Cretaceous carbonates from Beotia area (Steuber et al., 1994; Karakitsios et al., 2004; Tsikos et al., 2004). Moreover, the B3 horizon carbonates from Pera Lakkos mine, in contrast to other Cretaceous carbonates from External Hellenides, seem not to deserve any isotopic signature from the Cretaceous seawater (Veizer et al., 1999). Thus, more work is needed towards determination of stable isotope ratios in fossil shells from the

bauxite-hosting carbonates, as presented by [Veizer et al. \(1999\)](#) for the globe and by [Steuber et al. \(2005\)](#) for Cretaceous of Greece (**Figure 3.1.3.9**).

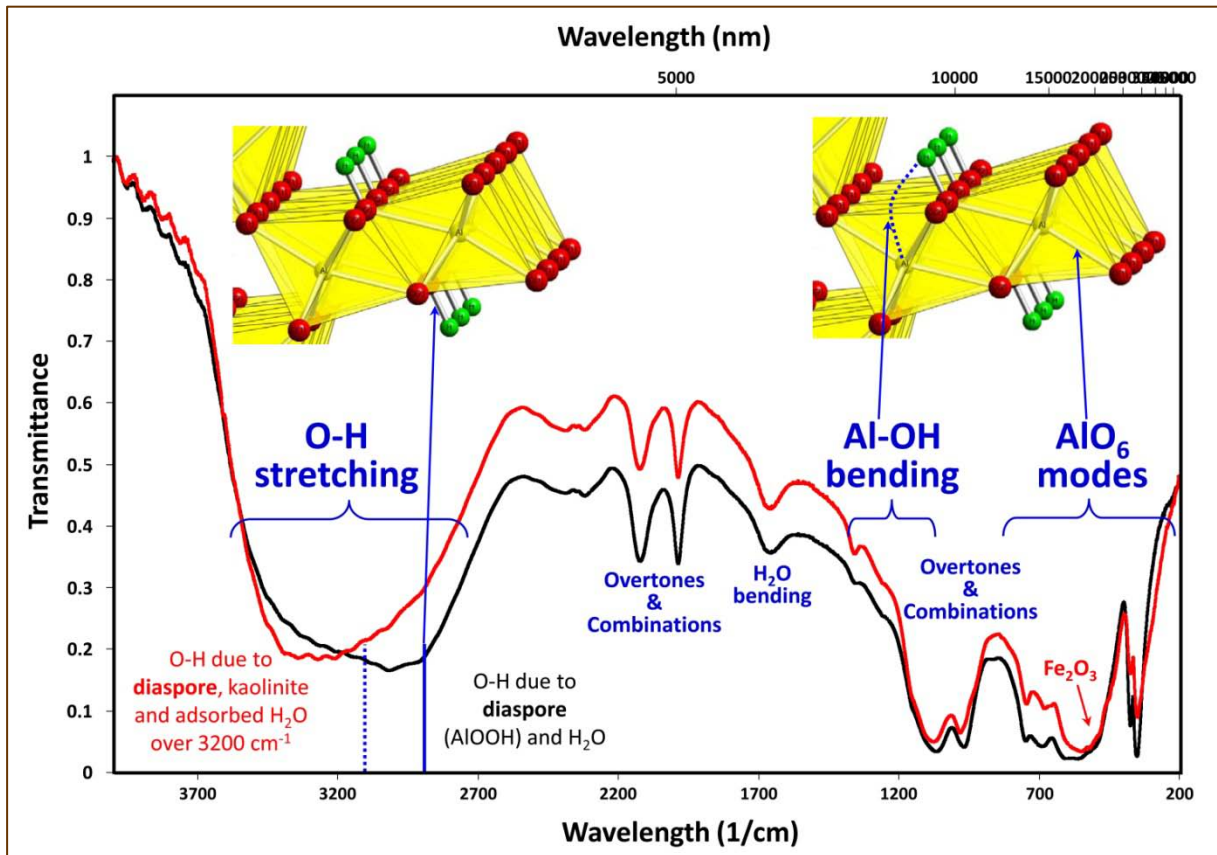
Figure 3.1.3.9: $\delta^{18}\text{O}$ and $\delta^{13}\text{C}$ of black (ALM0306_PL1_DLS1) to dark (ALM0306_PL1_DLS2) bituminous hanging wall limestones and ordinary white footwall limestone (ALM0306_PL1_WLS), from Pera Lakkos underground mine, compared to Cretaceous carbonates from Greece ([Steuber et al., 1994](#); [Karakitsios et al., 2004](#); [Tsikos et al., 2004](#)), Cretaceous seawater ([Veizer et al., 1999](#)) and Cretaceous fossil shells (rudist bivalves) from Greece ([Steuber et al., 2005](#)).



3.1.4. Hydrous components and thermal behavior (FTIR and TG-DTG/DSC)

The hydrous components (fundamentally OH^- and H_2O) of the Parnassos-Ghiona bauxites, related to weight loss upon heating, were investigated by FTIR spectroscopy and thermal analytical techniques (TGA/DSC). This is important not only for the mineralogy and geochemistry point of view, but also for metallurgical and technological aspects. According to powder XRD and SEM-EDS study (see text above) the hydrous minerals correspond only to hydroxylated minerals, namely diaspore and boehmite (AlOOH polymorphs), goethite (FeOOH) and kaolinite ($\text{Al}_2\text{Si}_2\text{O}_5(\text{OH})_4$). The FTIR spectra of representative diasporic Fe-rich and Fe-depleted bauxites are shown in **Figure 3.1.4.1** and confirm the abundance of hydrous components represented mainly by OH^- in Al- and/or Fe-hydroxylated mineral phases (AlOOH and FeOOH). The contribution of Fe-oxides (hematite), in the case of Fe-rich bauxite, is rather evident in low wavenumbers, while the slight shift of the Fe-rich spectrum to higher wavenumbers in the O-H stretching vibrations region can be attributed to the presence of kaolin-group minerals. Differences between theoretical vibrational spectra of AlOOH polymorphs (Kolesova & Ryskin, 1962; Wickersheim & Korpi, 1965; Bárdossy et al., 1977; Kloprogge et al., 2002; Demichelis et al., 2007) and the observed ones, can be attributed to metal ion impurities (Fe^{3+} and Cr^{3+} according to Mössbauer and XANES spectra; see text below) modifying the AlO_6 octahedra of the structure. Thus, the bauxitic diaspore and boehmite show different spectra because they are, in fact, Fe-Cr-containing AlOOH compounds and not pure AlOOH . A small contribution of H_2O molecules, most likely due to adsorbed (physisorbed) water, is related to H_2O (H-O-H) bending vibrations and to broadening of O-H stretching vibrations. Thus, a small weight loss at low temperature should be expected in the corresponding TG-DSC curves (see text below). It should be noted that there are no peaks due to other volatile components, such as sulfates and carbonates, which could interfere in the thermal behavior the materials.

Figure 3.1.4.1: FTIR spectra of representative Fe-rich (ELM0206_DV_B1; red line) and Fe-depleted (ALM0306_PL1_BS2; black line) bauxites.



The TG-DTG curves together with the heat flow curves of the studied Fe-rich and Fe-depleted bauxites are presented in **Figure 3.1.4.2** and **Figure 3.1.4.3**. The weight loss recorded for all studied Parnassos-Ghiona bauxites has been recorded in the range 12 - 15 %, while the corresponding dehydroxylation peak has been recorded in the range 512 – 550 °C (Smykatz-Kloss et al., 2003). The higher temperature in the case of Fe-rich samples may be attributed to the kaolinite component (Paulik & Paulik, 1978; Smykatz-Kloss et al., 2003), not measured by PXRD in Fe-depleted, whereas the slightly higher temperature for certain Fe-rich samples is attributed to the presence of boehmite (Laskou et al., 2006). Herein, it should

Figure 3.1.4.2: Simultaneous TG-DTG (left images) and the heat flow (right images) curves of the studied Fe-rich bauxites.

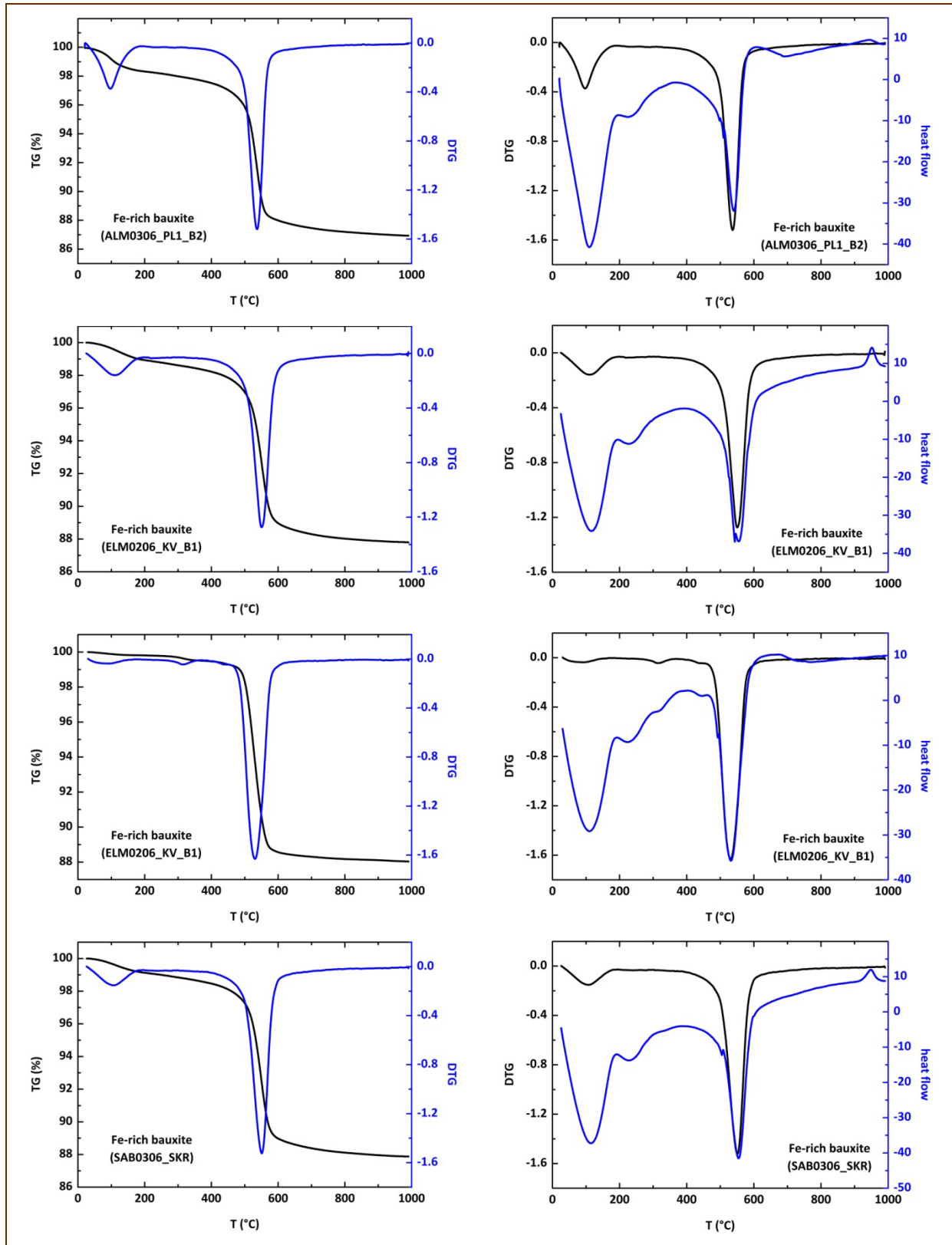
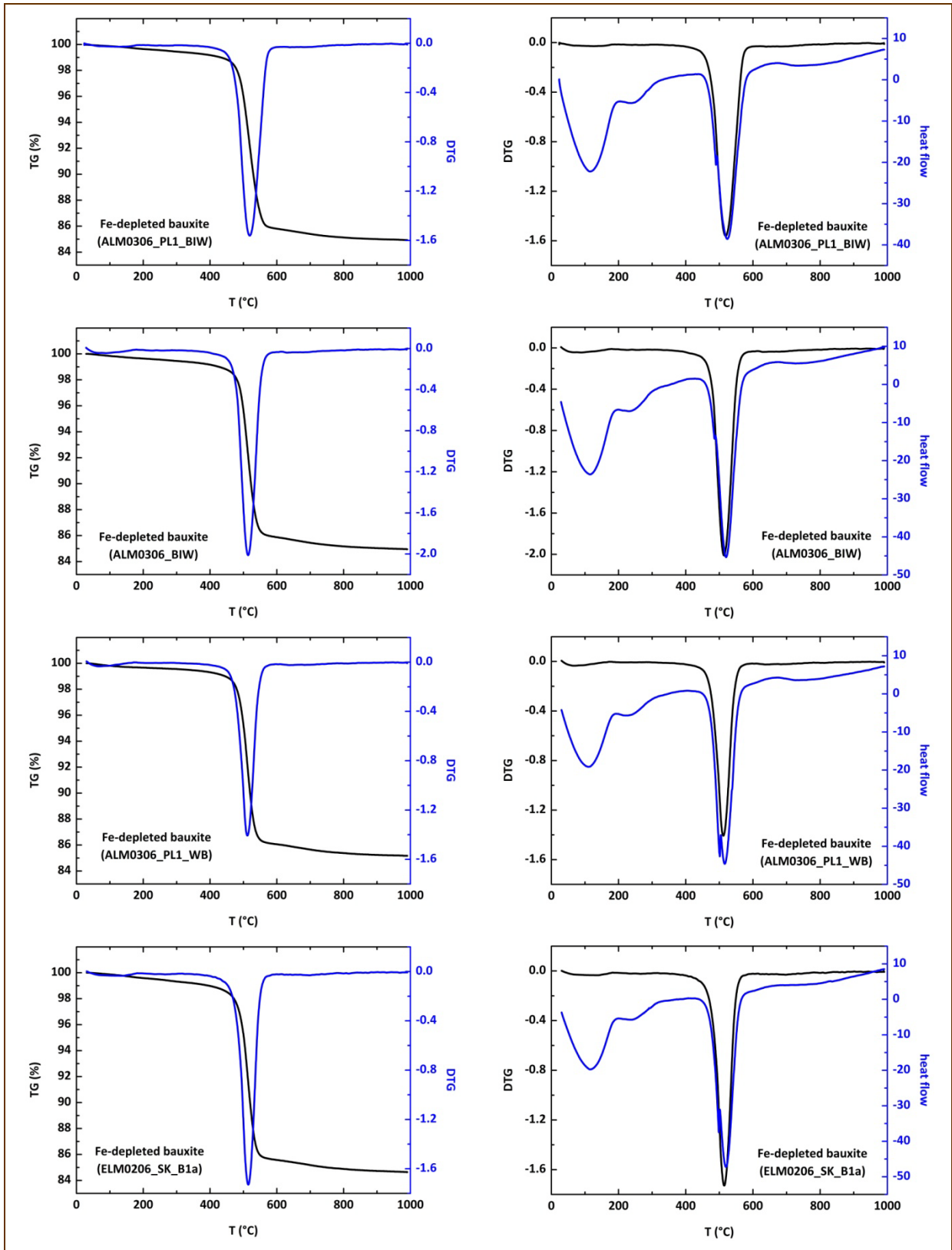
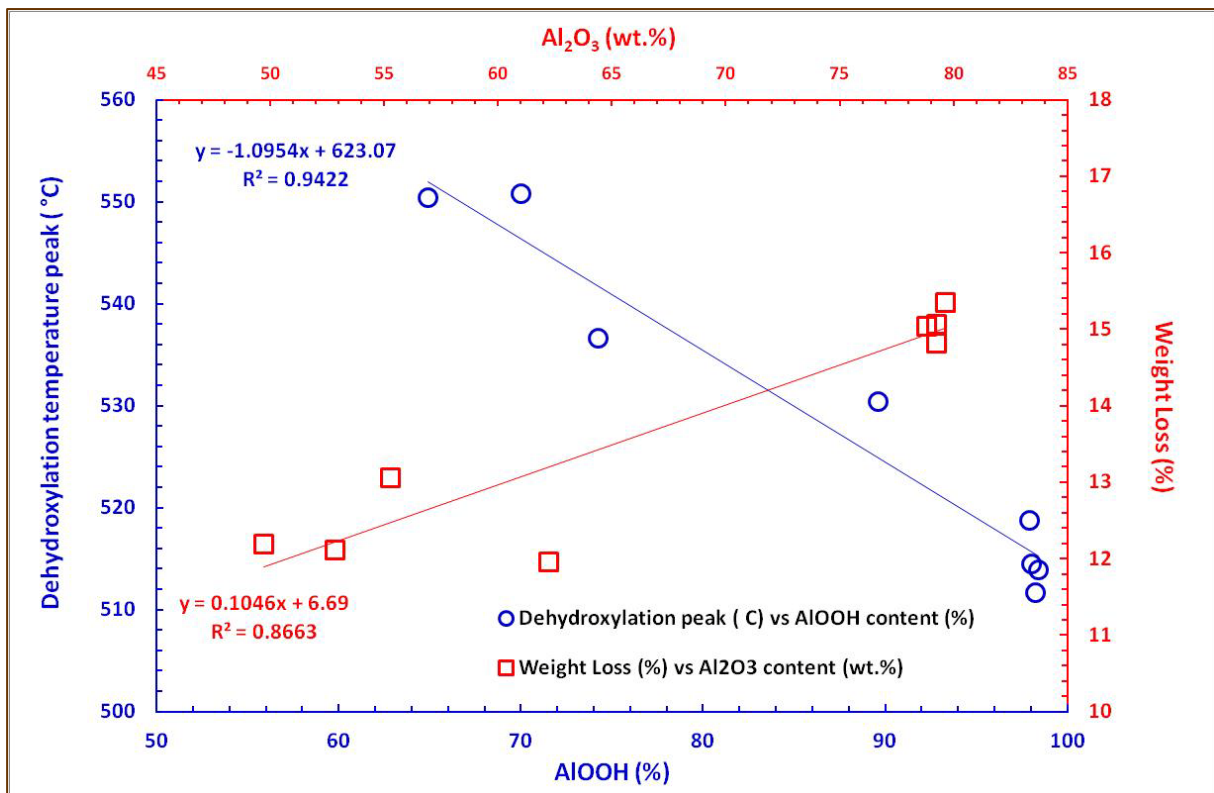


Figure 3.1.4.3: Simultaneous TG-DTG (left images) and the heat flow (right images) curves of the studied Fe-depleted bauxites.



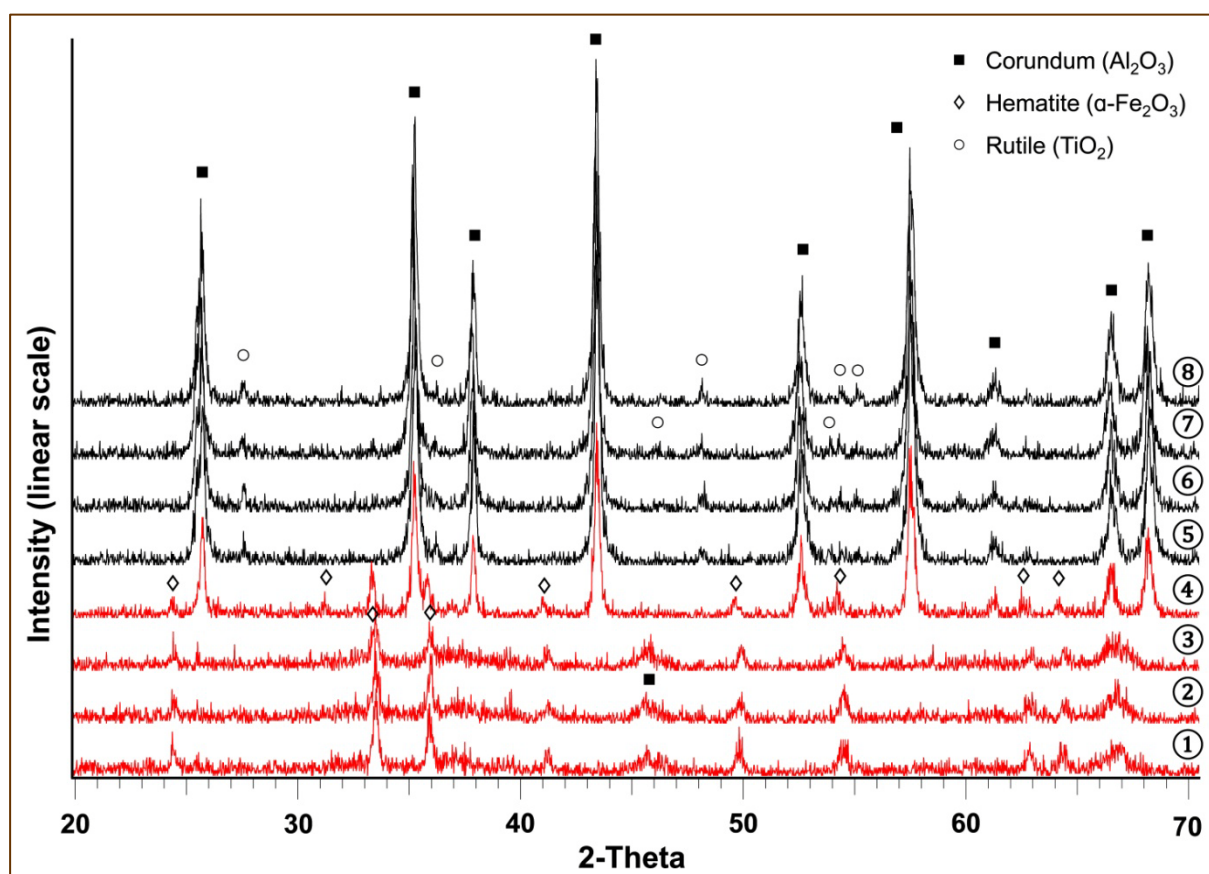
be mentioned that the dehydroxylation temperature is disproportionally correlated to the AlOOH content, as shown in **Figure 3.1.4.4**. In contrast to the latter, it is also remarkable the fact that the weight loss is proportionally related with the Al₂O₃ content. The thermal behavior of the studied Fe-rich bauxites is rational to that reported for Balkan bauxites and Greek bauxites other than those of Parnassos-Ghiona (Zivkovic & Blecic, 1988; Zivkovic et al., 1994; Laskou et al., 2006). However, the relatively low dehydroxylation temperature in the highly diasporic (ca. 98 %, see PXRD results in **Table 3.1.1.1**) Fe-depleted bauxites, might be attributed to metal ion impurities (Fe³⁺ and Cr³⁺ according to Mössbauer and XANES spectra; see text below).

Figure 3.1.4.4: Decrement of dehydroxylation temperature disproportional to AlOOH content increment (blue colored plot) and increment of weight loss proportional to Al₂O₃ content (red colored plot) for the studied Parnassos-Ghiona industrial bauxite samples.



Finally, PXRD patterns obtained in the materials derived from TG/DSC measurements, indicated that in 1000 °C the major bauxite components are transformed to anhydrous Al and Fe oxides, namely to corundum (Al_2O_3), hematite ($\alpha\text{-Fe}_2\text{O}_3$), whereas anatase is transformed to rutile (**Figure 3.1.4.5**).

Figure 3.1.4.5: PXRD patterns of the Fe-rich (red patterns: ① ELM0206_KV_B1; ② SAB0306_SKR; ③ ALM0306_PL1_B2; ④ ELM0206_DV_B1) and Fe-depleted (black patterns: ⑤ ELM0206_SK_B1a; ⑥ ALM0306_PL1_WB; ⑦ ALM0306_BIW; ⑧ ALM0306_PL1_BIW) bauxite samples after thermal analysis (TG-DSC) at 1000 °C.

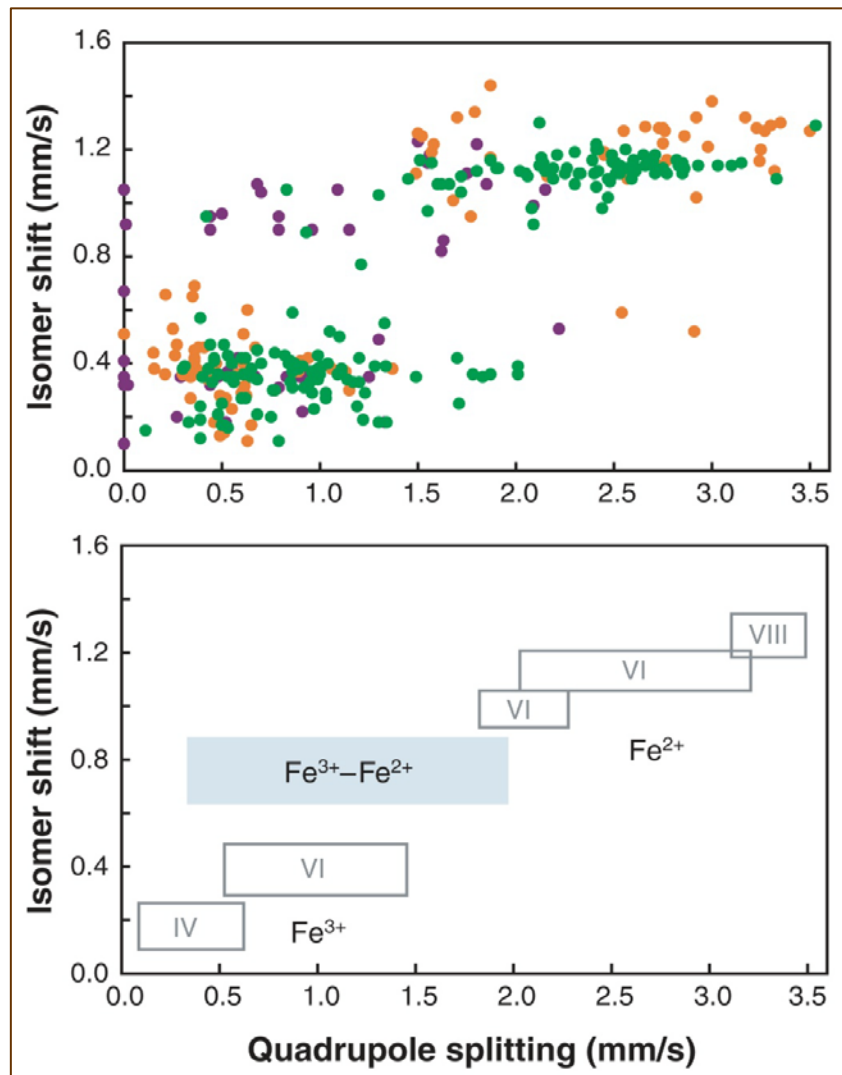


3.1.5. Bulk Fe solid-state speciation (Mössbauer and Fe K-edge XANES) and magnetic susceptibility

Though Greek bauxite is a quite important industrial material, the number of publications dealing with the characterization by ^{57}Fe Mössbauer spectroscopy is almost absent in the literature (Hill et al., 1978; Musić et al., 1980; Fysh & Clark, 1983; Cashion et al., 1986; Raj et al., 1993; Raj, et al., 2004; Murad, 2005; Kirwan et al., 2009). Therefore, the Mössbauer data presented herein absolutely concern the very first study that attempts to address Mössbauer investigation of Parnassos-Ghiona industrial bauxites. Mössbauer spectroscopy is ideal for the determination of the Fe solid-state speciation and specifically for the identification of Fe^{2+} and Fe^{3+} mineral phases (Figure 3.1.5.1; Dyar et al., 2006).

The investigation of Fe-rich (high grade) bauxite samples using ^{57}Fe Mössbauer spectroscopy (Figures 3.1.5.2-3.1.5.5 and Table 3.1.5.1) revealed that Fe occurs predominantly as Fe^{3+} ($\text{Fe}^{3+}/\Sigma\text{Fe}$ in the range 92 – 100 %) due to hematite and goethite. On the other hand the presence of Fe^{2+} could be associated with detrital micron-sized chromites (Cr-spinel

Figure 3.1.5.1: Room temperature isomer shift versus quadrupole splitting data for common rock-forming minerals (Dyar et al., 2006).



grains: FeCr_2O_4) as well as with minor Fe-containing aluminosilicate and silicate phases. Even kaolinite may contain Fe^{2+} and provide with relevant Mössbauer effect (e.g., Fysh et al., 1983). The presence of mixed valence Fe-oxides, i.e. magnetite detected by powder XRD, is not clear may be due to overlapping with the rest Fe phases.

Figure 3.1.5.2: Characteristic ^{57}Fe Mössbauer spectra measured at room temperature (300 K) of Fe-rich bauxite samples (i.e., ALM0306_PL1_B1; ALM0306_PL1_B2; ALM0306_PL1_B3; ALM0306_PL1_B4) from Parnassos-Ghiona mining area.

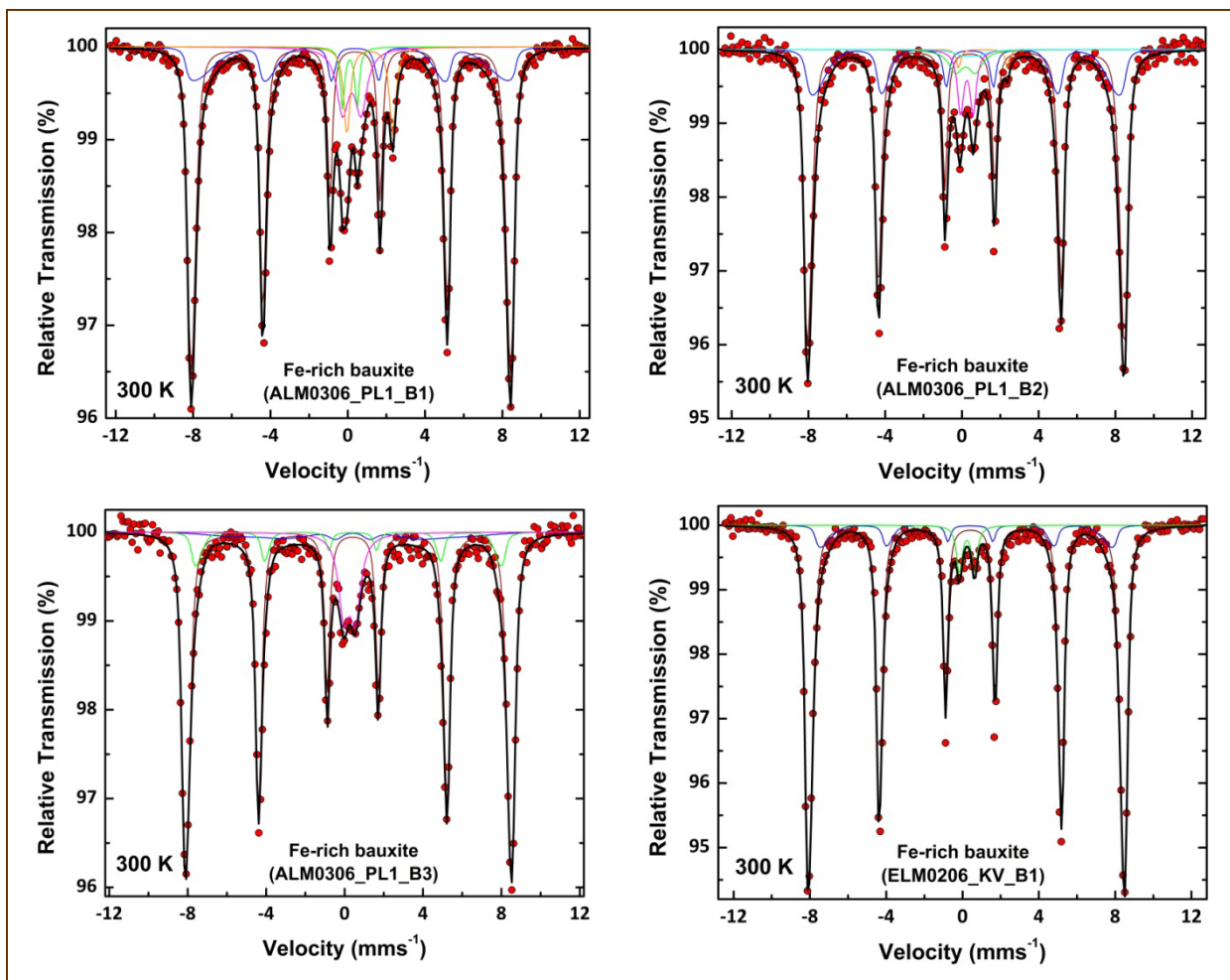


Figure 3.1.5.3: Characteristic ^{57}Fe Mössbauer spectra measured at room temperature (300 K; left-column) and at 77 K (right-column) of Fe-rich bauxite samples (SAB0306_SKR: upper series; SAB0306_ASV: lower series) from Parnassos-Ghiona mining area.

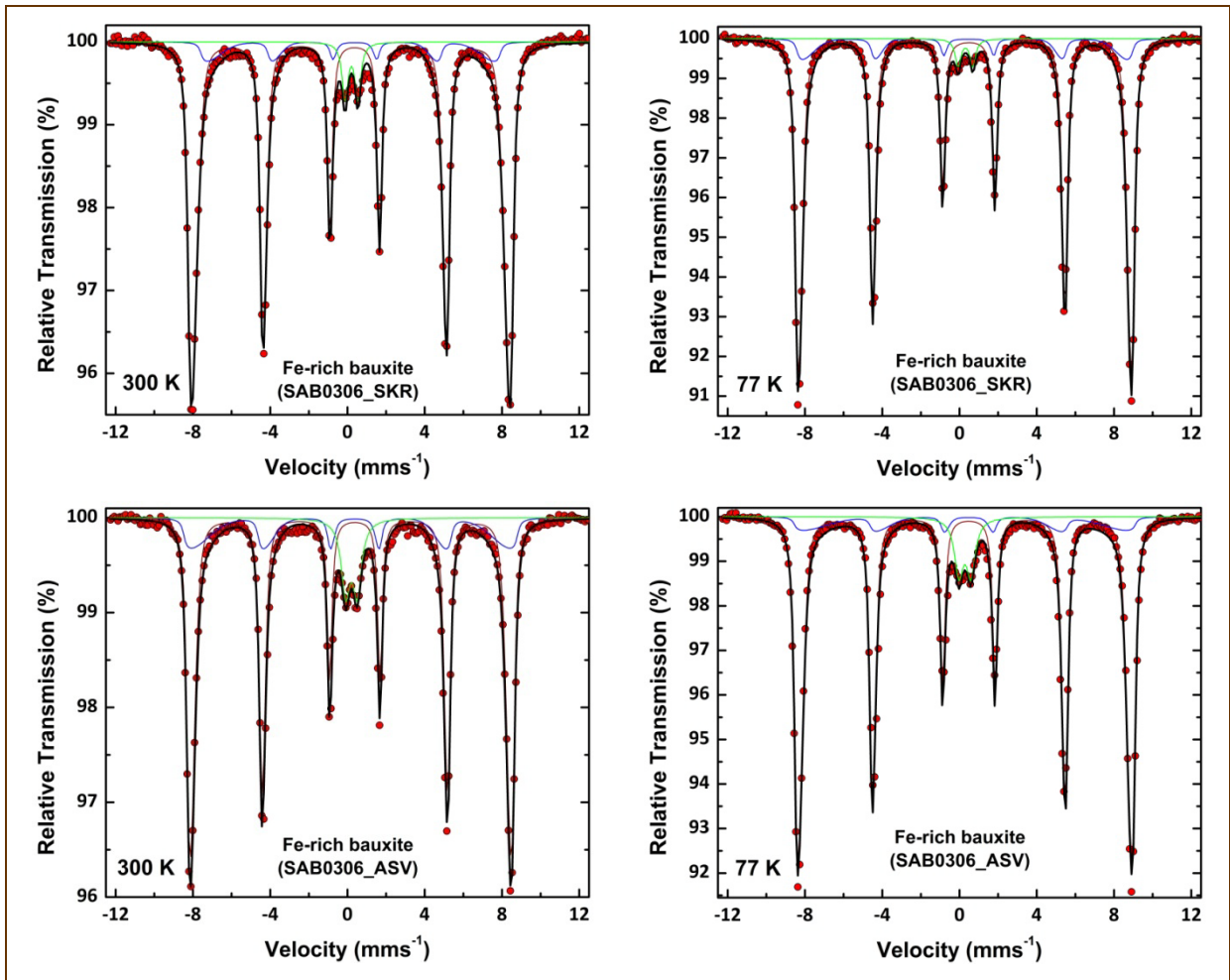


Figure 3.1.5.4: Characteristic ^{57}Fe Mössbauer spectra measured at room temperature (300 K; upper image), at 200 K (middle image), and at 77 K (lower image) of a Fe-rich bauxite sample (ELM0206_2H1) from Parnassos-Ghiona mining area.

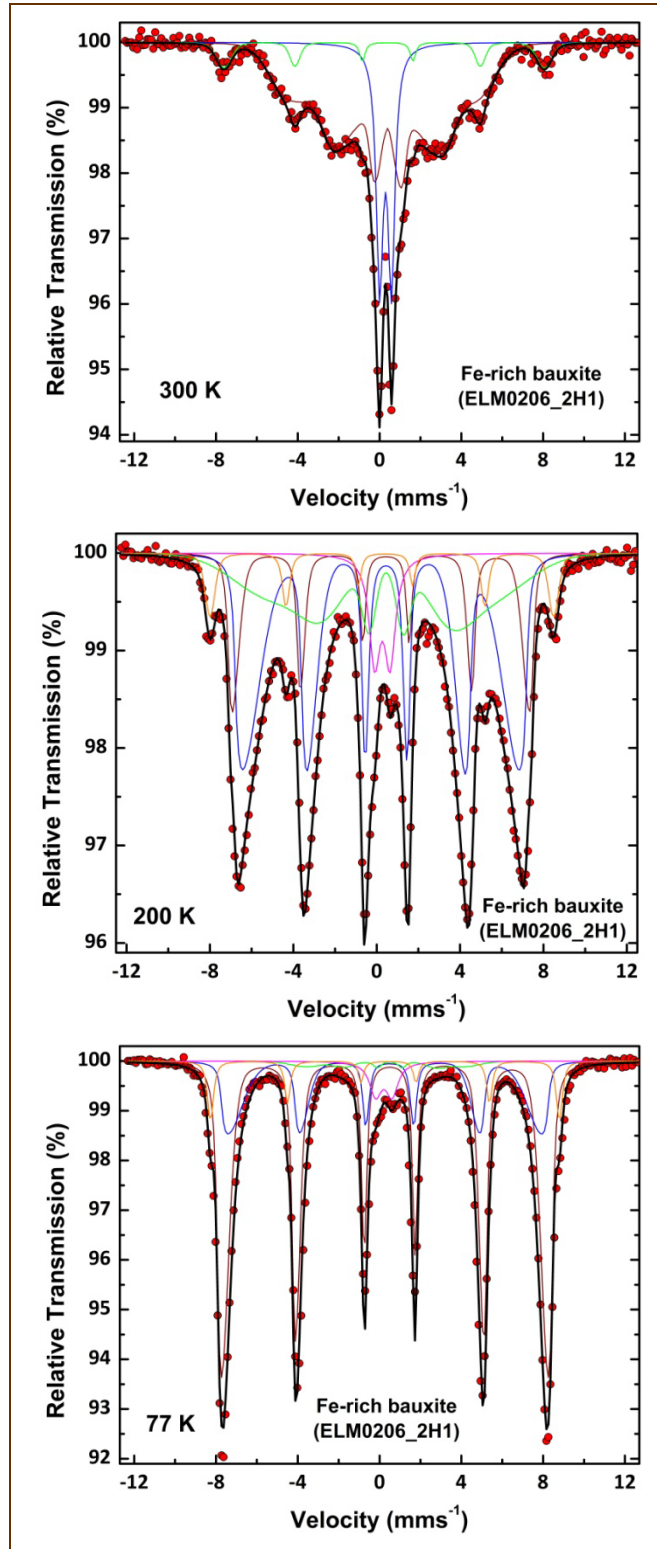


Figure 3.1.5.5: Characteristic ^{57}Fe Mössbauer spectra measured at room temperature (300 K; upper series), at 180 K (middle series), and at 77 K (lower series) of Fe-rich bauxite samples (ALM0306_PL1_B4: left-column images; ELM0206_SK_B2: right-column images) from Parnassos-Ghiona mining area.

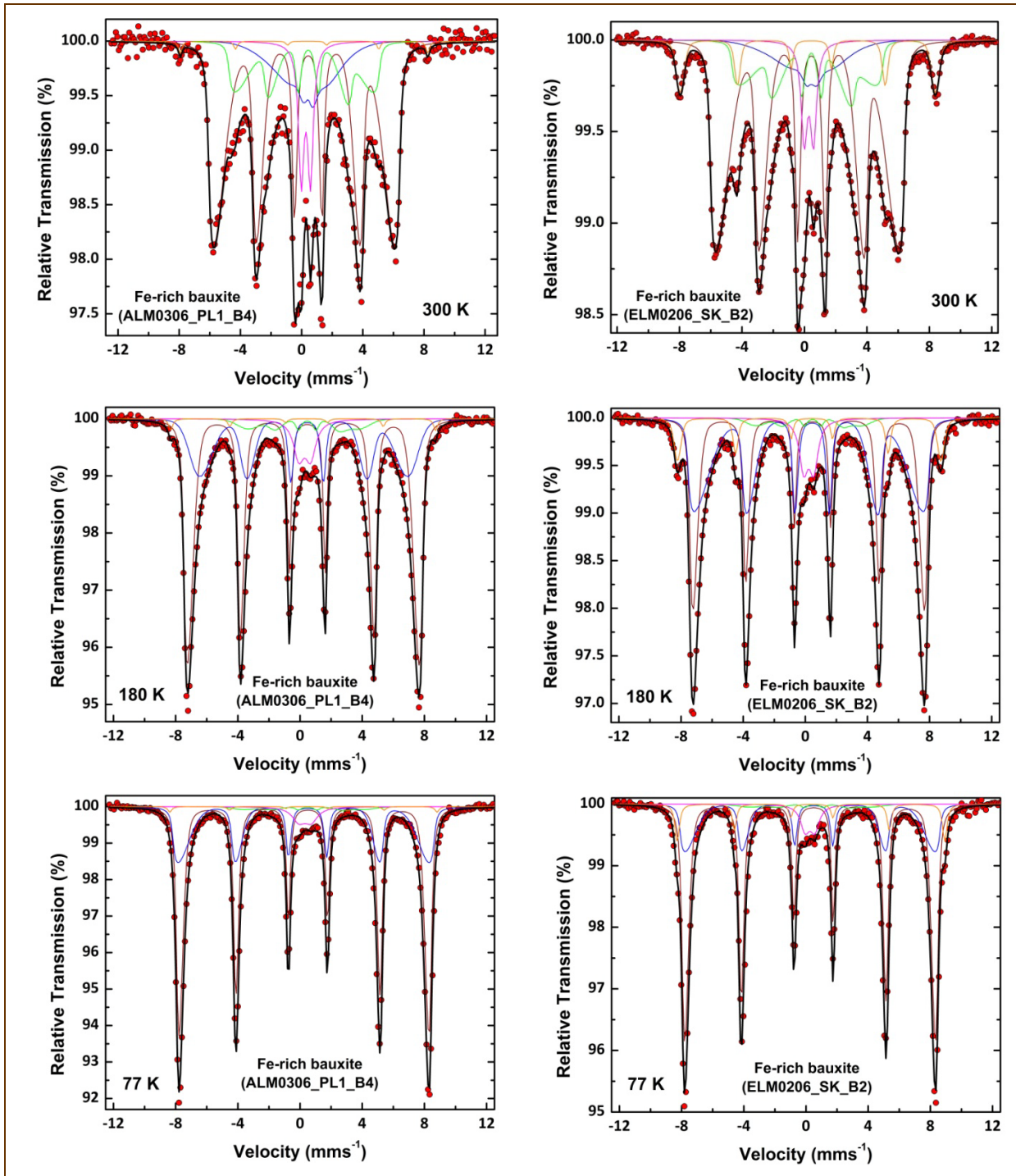


Table 3.1.5.1: ^{57}Fe Mössbauer fitted parameters for all the Fe-rich (low grade) bauxite samples from Parnassos-Ghiona mining area.

Mössbauer Fitted Parameters											
Sample	T	δ ($\alpha\text{-Fe}$)	$\Gamma/2$	2ϵ or QS	B_{hf}	$\Delta B_{\text{hf}}(<B_{\text{hf}})$	$\Delta B_{\text{hf}}(>B_{\text{hf}})$	Area	Component	Fe valence	$\text{Fe}^{3+}/\Sigma\text{Fe}$
						kOe	kOe				
		K	mms^{-1}	mms^{-1}	mms^{-1}	kOe	ΔB_{hf} (kOe)	%			
ALM0306_PL1_B1	300	0.38	0.15	-0.22	519	7	1	61	$\alpha\text{-Fe}_2\text{O}_3$	3+	92
		0.38	0.15	-0.22	527	35	0	17	$\alpha\text{-Fe}_2\text{O}_3$	3+	
		0.22	0.13	0.76	0	0	0	4	$\alpha\text{-Fe}_2\text{O}_3 / \alpha\text{-FeOOH}$	3+	
		0.32	0.37	0.96	0	0	0	10	$\alpha\text{-Fe}_2\text{O}_3 / \alpha\text{-FeOOH}$	3+	
		1.25	0.20	2.36	0	0	0	8	Fe-silicate / FeCr_2O_4	2+	
ALM0306_PL1_B2	300	0.42	0.15	-0.20	520	7	1	67	$\alpha\text{-Fe}_2\text{O}_3$	3+	99
		0.42	0.15	-0.20	510	22	3	20	$\alpha\text{-Fe}_2\text{O}_3$	3+	
		0.30	0.44	1.03	0	0	0	5	$\alpha\text{-Fe}_2\text{O}_3 / \alpha\text{-FeOOH}$	3+	
		0.37	0.19	0.66	0	0	0	6	$\alpha\text{-Fe}_2\text{O}_3 / \alpha\text{-FeOOH}$	3+	
		1.21	0.12	2.54	0	0	0	1	Fe-silicate / FeCr_2O_4	2+	
		0.56	0.54	0.78	0	0	0	1	?	3+	
ALM0306_PL1_B3	300	0.42	0.15	-0.22	520	6	2	73	$\alpha\text{-Fe}_2\text{O}_3$	3+	100
		0.42	0.15	-0.22	494	11	0	9	$\alpha\text{-Fe}_2\text{O}_3$	3+	
		0.42	0.15	-0.22	290	117	0	6	$\alpha\text{-Fe}_2\text{O}_3$	3+	
		0.37	0.31	0.58	0	0	0	12	$\alpha\text{-Fe}_2\text{O}_3 / \alpha\text{-FeOOH}$	3+	
ALM0306_PL1_B4	300	0.41	0.15	-0.26	385	25	0	58	$\alpha\text{-FeOOH}$	3+	100
		0.41	0.15	-0.26	302	34	0	18	$\alpha\text{-FeOOH}$	3+	
		0.41	0.15	-0.26	102	84	0	14	$\alpha\text{-FeOOH}$	3+	
		0.38	0.21	0.60	0	0	0	9	$\alpha\text{-FeOOH}$	3+	
		0.37	0.14	-0.20	502	0	0	1	$\alpha\text{-Fe}_2\text{O}_3$ (?)	3+	
	180	0.44	0.14	-0.25	473	12	0	58	$\alpha\text{-FeOOH}$	3+	
		0.45	0.14	-0.22	418	24	17	30	$\alpha\text{-FeOOH}$	3+	
		0.45	0.14	-0.26	220	40	0	5	$\alpha\text{-FeOOH}$	3+	
		0.41	0.41	0.76	0	0	0	6	$\alpha\text{-FeOOH}$	3+	
		0.42	0.15	-0.22	529	0	0	1	$\alpha\text{-Fe}_2\text{O}_3$ (?)	3+	
	77	0.49	0.14	-0.26	507	8	0	61	$\alpha\text{-FeOOH}$	3+	
		0.47	0.14	-0.26	519	25	0	31	$\alpha\text{-FeOOH}$	3+	
		0.47	0.14	-0.26	236	45	0	3	$\alpha\text{-FeOOH}$	3+	
		0.43	0.50	0.79	0	0	0	4	$\alpha\text{-FeOOH}$	3+	
		0.44	0.15	-0.22	534	0	0	1	$\alpha\text{-Fe}_2\text{O}_3$ (?)	3+	
ELM0206_SK_B2	300	0.42	0.14	-0.26	383	29	0	59	$\alpha\text{-FeOOH}$	3+	100
		0.42	0.14	-0.26	105	49	0	9	$\alpha\text{-FeOOH}$	3+	
		0.42	0.14	-0.26	296	88	0	18	$\alpha\text{-FeOOH}$	3+	
		0.39	0.24	0.59	0	0	0	7	$\alpha\text{-FeOOH}$	3+	
		0.43	0.14	-0.23	508	12	0	7	$\alpha\text{-Fe}_2\text{O}_3$ (?)	3+	
	180	0.44	0.14	-0.25	472	10	0	39	$\alpha\text{-FeOOH}$	3+	
		0.44	0.14	-0.23	478	33	0	43	$\alpha\text{-FeOOH}$	3+	
		0.45	0.14	-0.26	210	36	0	3	$\alpha\text{-FeOOH}$	3+	
		0.33	0.34	0.64	0	0	0	7	$\alpha\text{-FeOOH}$	3+	
		0.44	0.15	-0.17	527	9	0	8	$\alpha\text{-Fe}_2\text{O}_3$ (?)	3+	
	77	0.48	0.14	-0.23	508	8	0	61	$\alpha\text{-FeOOH}$	3+	
		0.49	0.14	-0.24	516	24	0	25	$\alpha\text{-FeOOH}$	3+	
		0.49	0.14	-0.24	239	45	0	2	$\alpha\text{-FeOOH}$	3+	
		0.36	0.35	0.62	0	0	0	5	$\alpha\text{-FeOOH}$	3+	
		0.46	0.15	-0.05	535	3	0	7	$\alpha\text{-Fe}_2\text{O}_3$ (?)	3+	

Table 3.1.5.1: continued.

Mössbauer Fitted Parameters											
Sample	T	δ (α -Fe)	$\Gamma/2$	2ε or QS	B_{hf}	$\Delta B_{hf}(<B_{hf})$	$\Delta B_{hf>(>B_{hf})$	Area	Component	Fe valence	$Fe^{3+}/\Sigma Fe$
	K	mms^{-1}	mms^{-1}	mms^{-1}	kOe	kOe	kOe				
ELM0206_KV_B1	300	0.41	0.14	-0.21	522	7	0	86	α -Fe ₂ O ₃	3+	100
		0.41	0.14	-0.21	489	18	0	9	α -Fe ₂ O ₃	3+	
		0.34	0.17	0.79	0	0		5	α -Fe ₂ O ₃ (?)	3+	
ELM0206_2H1	300	0.39	0.14	-0.26	283	82	26	71	α -FeOOH	3+	100
		0.40	0.20	0.58	0	0		21	α -FeOOH	3+	
		0.42	0.14	-0.17	487	19		8	α -Fe ₂ O ₃ (?)	3+	
	200	0.43	0.14	-0.25	452	10	0	16	α -FeOOH	3+	
		0.43	0.14	-0.25	431	29	0	44	α -FeOOH	3+	
		0.44	0.14	-0.26	323	110		27	α -FeOOH	3+	
		0.38	0.32	0.74	0	0		7	α -FeOOH	3+	
		0.44	0.15	-0.17	512	10		6	α -Fe ₂ O ₃ (?)	3+	
	77	0.48	0.14	-0.23	506	12	0	62	α -FeOOH	3+	
		0.49	0.14	-0.24	493	25	0	24	α -FeOOH	3+	
		0.49	0.14	-0.24	239	45		3	α -FeOOH	3+	
		0.32	0.35	0.80	0	0		4	α -FeOOH	3+	
		0.46	0.15	-0.17	530	3		7	α -Fe ₂ O ₃ (?)	3+	
SAB0306_SKR	300	0.38	0.14	-0.21	520	9	0	86	α -Fe ₂ O ₃	3+	100
		0.38	0.14	-0.21	479	26	0	9	α -Fe ₂ O ₃	3+	
		0.32	0.17	0.67	0	0		5	α -Fe ₂ O ₃	3+	
	77	0.49	0.14	-0.20	542	6	0	86	α -Fe ₂ O ₃	3+	
		0.49	0.14	-0.20	538	22	0	11	α -Fe ₂ O ₃	3+	
		0.42	0.17	0.76	0	0		3	α -Fe ₂ O ₃	3+	
SAB0306_ASV	300	0.38	0.14	-0.21	523	7	0	72	α -Fe ₂ O ₃	3+	100
		0.38	0.14	-0.21	533	34	0	18	α -Fe ₂ O ₃	3+	
		0.31	0.27	0.60	0	0		10	α -Fe ₂ O ₃	3+	
	77	0.49	0.14	-0.20	544	8	0	81	α -Fe ₂ O ₃	3+	
		0.49	0.15	-0.20	544	44	0	11	α -Fe ₂ O ₃	3+	
		0.39	0.27	0.62	0	0		8	α -Fe ₂ O ₃	3+	

Uncertainties: δ , $\Gamma/2$, 2ε , QS, $\pm 0.02 mms^{-1}$, $B_{hf} \pm 5 kOe$, Area $\pm 3\%$

Mössbauer spectroscopy results for the Fe-depleted (high grade) diasporic karst-type bauxite sample are presented in **Figures 3.1.5.6 – 3.1.5.8** and **Table 3.1.5.2**. The spectra were analyzed using a combination of two quadrupole split doublets and two magnetically split components. The quadrupole doublets are well resolved, but the magnetic components possess large line broadening (we allowed a spreading of hyperfine magnetic fields ΔB_{hf} for each component to describe this broadening), indicating that they correspond to Fe containing phases with either reduced particle size and/or low crystallinity. That implies the presence of Fe *mineral nanoparticles* and/or Fe *nanominerals* as also supposed by electron microscopy in nanoscale (see text below). The isomer shift (IS-given relative to α -Fe at 300 K) values indicate that the main contribution originates from paramagnetic Fe^{3+} ions, while the second paramagnetic minor component is attributed to Fe^{2+} ions and that both magnetic components correspond to Fe^{3+} ions (e.g., Hill et al., 1978; Fysh and Clark, 1983; Raj et al., 1993; Cornell and Schwertmann, 2003; Kuzmann et al., 2003; Murad, 2005; Dyar et al., 2006). It is therefore argued that the recorded major Fe^{3+} (up to 65 %) components correspond to Fe-Cr-diaspore ($Fe-Cr-AlOOH$ where Fe^{3+} substitutes for Al^{3+} ions in octahedral sites, i.e. $[^6]Fe^{3+} \leftrightarrow [^6]Al^{3+}$) and to potential occluded Fe *mineral nanoparticles* and/or *nanominerals* (see text below). The latter might be responsible for the magnetic component with the high hyperfine field (B_{hf}), coming from contribution of a ferrimagnetic mineral with large Fe content, which is probably maghemite-type phase ($\gamma-Fe_2O_3$), and also for the collapsing magnetic component attributed to either not well crystallized nano-maghemite or Fe^{3+} dispersed in amorphous minor phases not detected by powder XRD. The possible influence by microcrystal fragments of trace chromite could be excluded, due to the rarity of the phase detectable only by careful SEM-EDS/WDS investigation (see text below), but it could also be used to explain the existence of Fe^{2+} (ca. 4 %).

Figure 3.1.5.6: ^{57}Fe Mössbauer spectra measured at room temperature (300 K; left image) and at 10 K (right image) of a representative Fe-depleted bauxite sample (ALM0306_PL1_BIW) from Parnassos-Ghiona mining area.

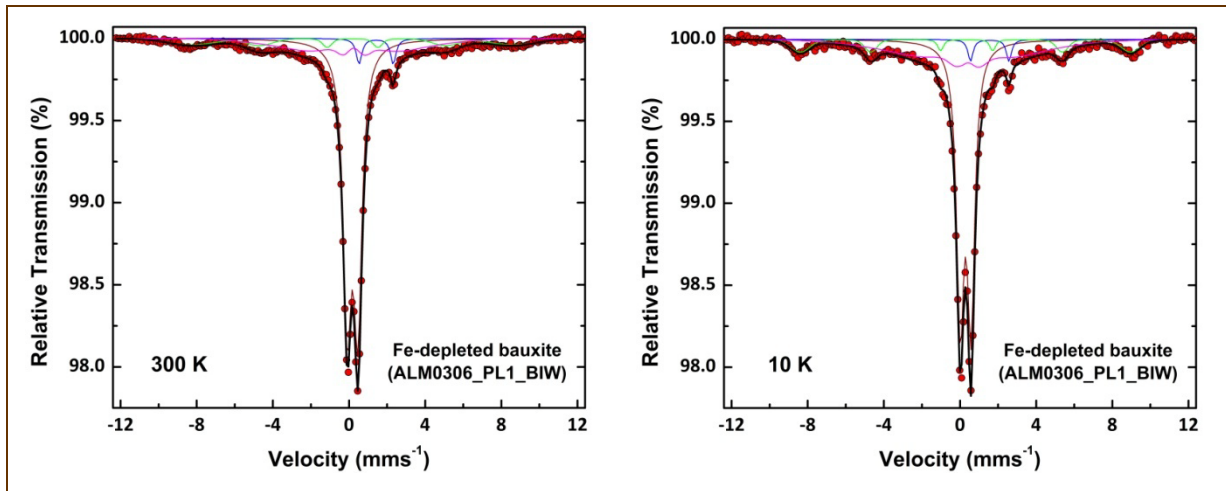


Figure 3.1.5.7: Characteristic ^{57}Fe Mössbauer spectra measured at room temperature (300 K) of other Fe-depleted bauxite samples (ELM0206_SK_B1a: left image; ELM0206_SK_B1b: right image) from Parnassos-Ghiona mining area.

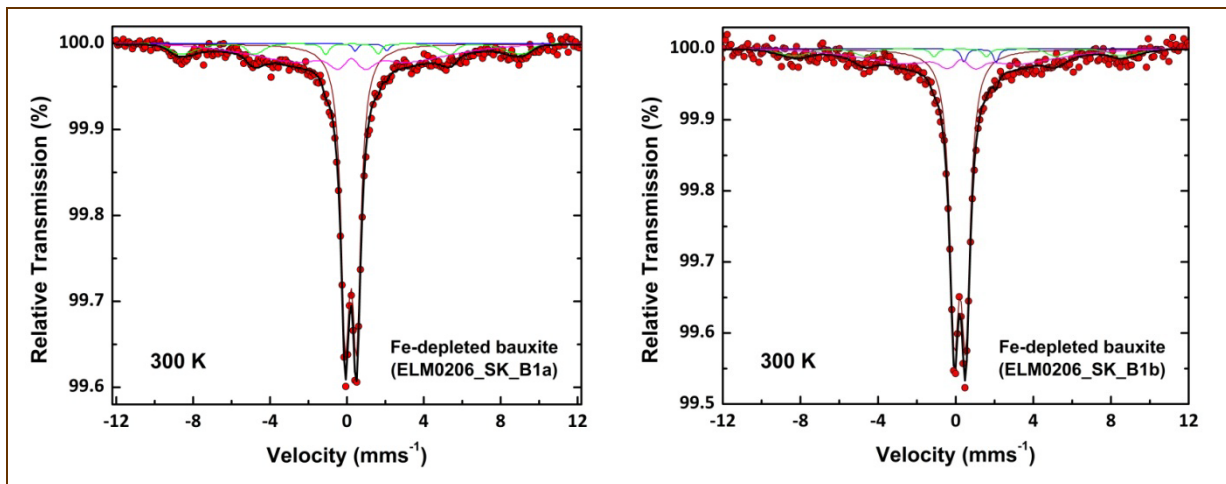


Figure 3.1.5.8: Characteristic ^{57}Fe Mössbauer spectra measured at room temperature (300 K) of other Fe-depleted bauxite samples (ALM0306_BIW: upper image; ALM0306_PL1_WB: middle image; ALM0306_PL1_BS2: lower image) from Parnassos-Ghiona mining area.

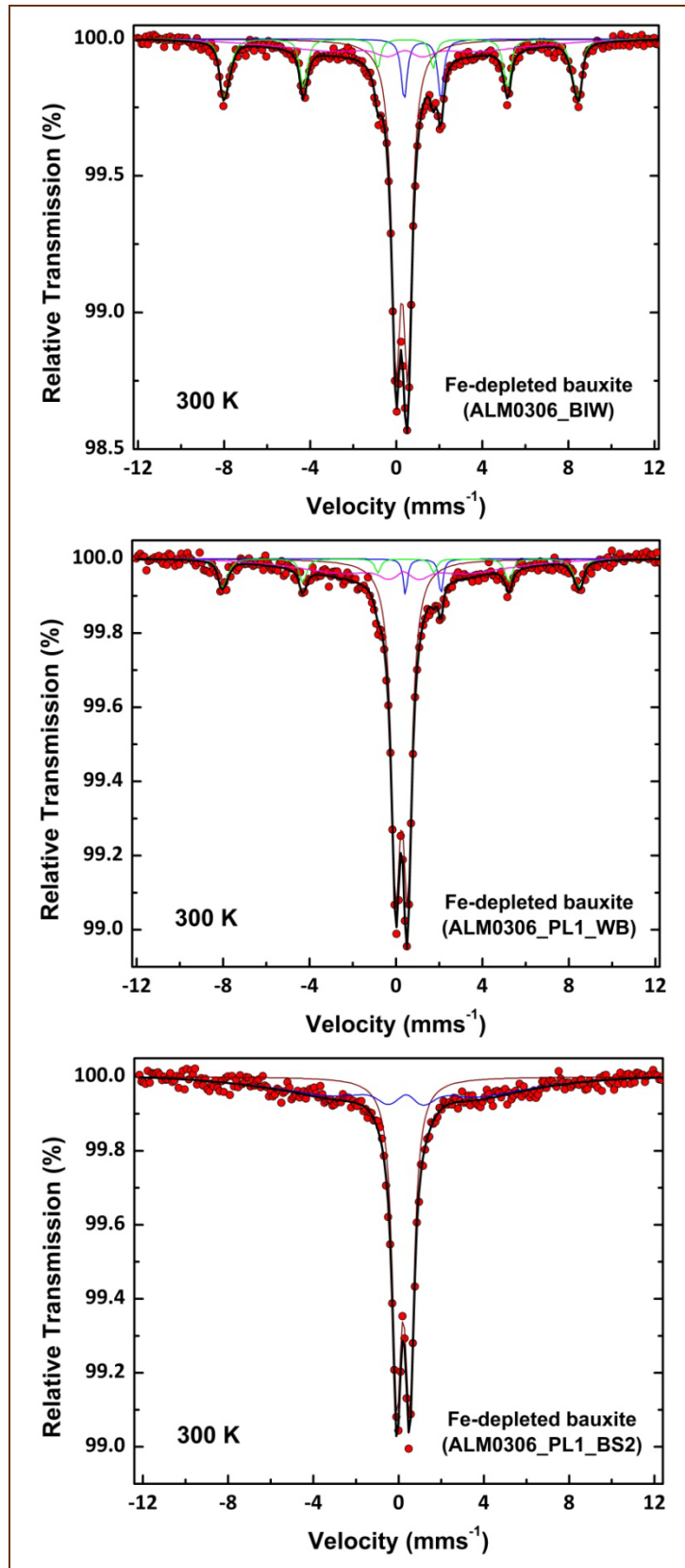


Table 3.1.5.2: ^{57}Fe Mössbauer fitted parameters for all the Fe-depleted (high grade) bauxite samples from Parnassos-Ghiona mining area.

Mössbauer Fitted Parameters											
Sample	T K	δ ($\alpha\text{-Fe}$) mms^{-1}	$\Gamma/2$ mms^{-1}	2ϵ or QS mms^{-1}	B_{hf} kOe	ΔB_{hf} (kOe)		Area %	Component	Fe valence	$\text{Fe}^{3+}/\Sigma\text{Fe}$ %
						$\Delta B_{\text{hf}}(<B_{\text{hf}})$ kOe	$\Delta B_{\text{hf}}(>B_{\text{hf}})$ kOe				
ALM0306_PL1_BIW	300	0.29	0.26	0.56	0	0		65	Fe ³⁺ substituting Al ³⁺ in diaspore	3+	96
		1.53	0.17	1.80	0	0		4	Fe ²⁺ in chromite	2+	
		0.30	0.14	0.00	525	69		12	Fe ³⁺ possibly in maghemite-type phase	3+	
		0.31	0.14	-0.12	214	115		19	Fe ³⁺ most likely in nano-maghemite and amorphous phases	3+	
	10	0.40	0.23	0.57	0	0		57	Fe ³⁺ substituting Al ³⁺ in diaspore	3+	
		1.67	0.16	2.02	0	0		3	Fe ²⁺ in chromite	2+	
		0.42	0.14	-0.06	540	27		10	Fe ³⁺ possibly in maghemite-type phase	3+	
		0.41	0.14	-0.21	202	160		30	Fe ³⁺ most likely in nano-maghemite and amorphous phases	3+	
ALM0306_BIW	300	0.37	0.24	0.55	0	0		52	Fe ³⁺ substituting Al ³⁺ in diaspore	3+	93
		1.32	0.16	1.70	0	0		7	Fe ²⁺ in chromite	2+	
		0.43	0.15	-0.21	520	9	0	20	Fe ³⁺ possibly in maghemite-type phase	3+	
		0.46	0.15	-0.09	295	176		21	Fe ³⁺ most likely in nano-maghemite and amorphous phases	3+	
ALM0306_PL1_WB	300	0.37	0.25	0.55	0	0		61	Fe ³⁺ substituting Al ³⁺ in diaspore	3+	96
		1.36	0.11	1.65	0	0		4	Fe ²⁺ in chromite	2+	
		0.45	0.15	-0.23	522	8	0	11	Fe ³⁺ possibly in maghemite-type phase	3+	
		0.45	0.15	-0.06	250	155		24	Fe ³⁺ most likely in nano-maghemite and amorphous phases	3+	
ALM0306_PL1_BS2	300	0.32	0.25	0.60	0	0		62	Fe ³⁺ substituting Al ³⁺ in diaspore	3+	100
		0.32	0.15	-0.27	302	181		38	Fe ³⁺ most likely in nano-maghemite and amorphous phases	3+	
ELM0206_SK_B1a	300	0.31	0.27	0.59	0	0		58	Fe ³⁺ substituting Al ³⁺ in diaspore	3+	99
		1.36	0.15	1.66	0	0		1	Fe ²⁺ in chromite	2+	
		0.33	0.15	-0.07	557	26	12	10	Fe ³⁺ possibly in maghemite-type phase	3+	
		0.33	0.15	-0.04	265	154		31	Fe ³⁺ most likely in nano-maghemite and amorphous phases	3+	
ELM0206_SK_B1b	300	0.32	0.28	0.59	0	0		64	Fe ³⁺ substituting Al ³⁺ in diaspore	3+	98
		1.36	0.15	1.66	0	0		2	Fe ²⁺ in chromite	2+	
		0.31	0.15	-0.05	518	16	26	8	Fe ³⁺ possibly in maghemite-type phase	3+	
		0.33	0.15	-0.17	265	142		26	Fe ³⁺ most likely in nano-maghemite and amorphous phases	3+	

Uncertainties: δ , $\Gamma/2$, 2ϵ , QS, $\pm 0.02 \text{ mms}^{-1}$, $B_{\text{hf}} \pm 5 \text{ kOe}$, Area $\pm 3\%$

The characterization of the Fe solid-state speciation by XAFS spectroscopy (Fe *K*-edge XANES) has been performed for representative Parnassos-Ghiona bauxite samples (i.e., Fe-depleted diasporic bauxite: ALM0306_PL1_BIW; Fe-rich diasporic: SAB0306_ASV; Fe-rich boehmitic: ELM0206_2H1; see **Figures 3.1.5.9 – 3.1.5.13**). A similar study has been applied for soils (Regelink et al., 2014), atmospheric particles (Oakes et al., 2012), historical iron inks (Proost et al., 2004; Arçon et al., 2007; Wilke et al., 2009), ancient Roman glasses (Quartieri et al., 2002), ancient “Maya blue” pigments (Sánchez del Río et al., 2005), geological samples, such as silicate melts and lavas (Hurai et al., 2008), and natural minerals (e.g.,

Waychunas et al., 1983; Bajt et al., 1994; Dyar et al., 1998; England et al., 1999; Galois et al., 2001; Wilke et al., 2001; Di Benedetto et al., 2010; Figueiredo et al., 2010), as well as for synthesized crystals, materials and silicate glasses (e.g., Calas & Petiau, 1983; Manceau & Gates, 1997; Kim et al., 1998; Galois et al., 2001; Berry et al., 2003; Heijboer et al., 2004; Berry et al., 2010; Sigrist et al., 2011), even for proteins (e.g., Shulman et al., 1976). Accordingly, the determination of Fe oxidation state of the studied bauxite has never been approached since the present dissertation.

Figure 3.1.5.9: Normalized Fe *K*-edge XANES spectra of representative Parnassos-Ghiona bauxites, together with the Fe³⁺ natural (hematite), and synthetic (goethite) measured references, comparing to the Fe²⁺ synthetic standards (Fe(II)-chloride, Fe(II)-sulfate). A normalized XANES spectrum of a natural mixed-valence iron oxide (magnetite: Fe²⁺Fe³⁺₂O₄), is also depicted. All spectra are offset for clarity (a); the energy shift at the main rising of the *K* absorption edge assigning to the 1*s*→4*s* transition of the normalized Fe *K*-edge XANES spectra of the references and the studied bauxites (b).

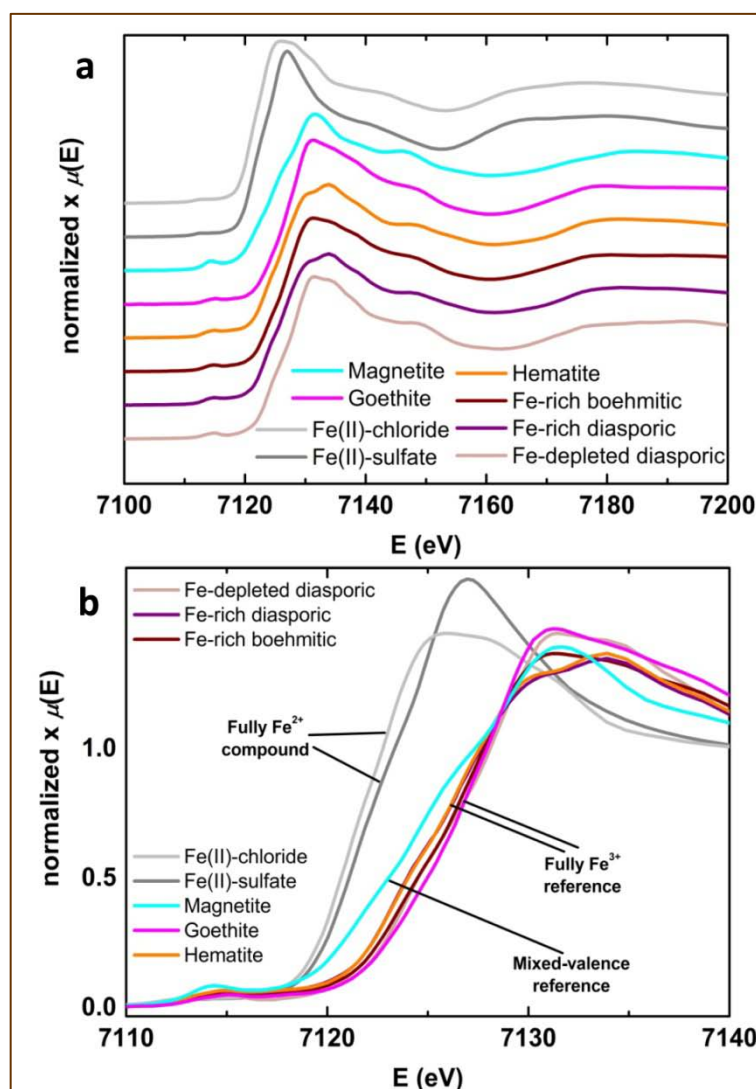
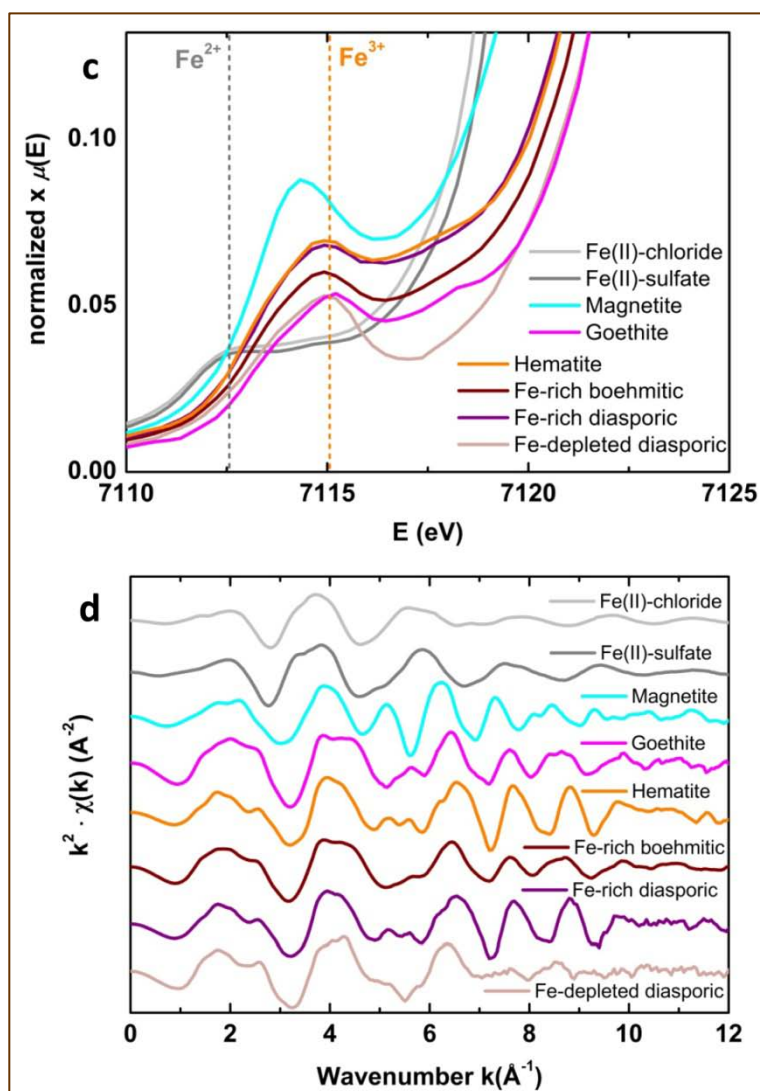


Figure 3.1.5.9: continued: The zoom at the pre-edge region illustrate the characteristic pre-edge features, and the characteristic energy separation between them related to the differences of their Fe oxidation state. The energy site of each of the Fe^{2+} and Fe^{3+} references is marked by a vertical grey and orange dashed line, respectively. These lines indicate the outer boundaries of the energy grid, within the Fe valence of the studied bauxites varies (c); the Fourier transform (FT) of $\chi(k)$ of the experimental Fe K-edge EXAFS signals of the references and the studied bauxites (d).

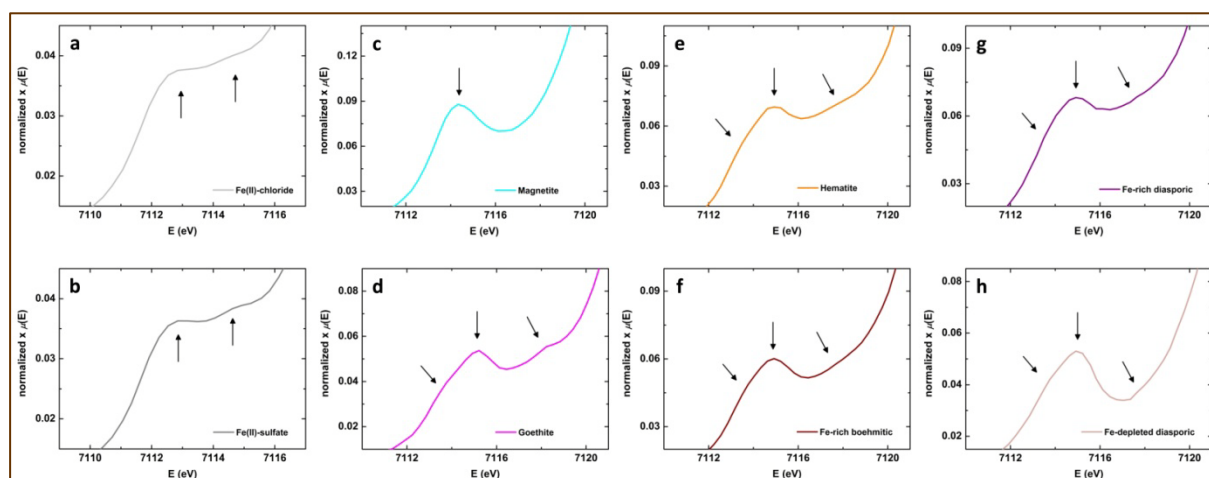


It is known that Fe K-edge XANES spectra exhibit significant differences in the energy position of characteristic features at the pre-edge region below the threshold, as the energy position sensitively shifts toward to higher values in proportion to the increment of Fe oxidation state (e.g., Shulman et al., 1976; Calas & Petiau, 1983; Bajt et al., 1994; Manceau & Gates, 1997; Westre et al., 1997; England et al., 1999; Galois et al., 2001; Wilke et al., 2001; Quartieri et al., 2002; Arčon et al., 2007; Hurai et al., 2008; Berry et al., 2010; Oakes et al., 2012; Henderson et al., 2014) with linear correlation among them (Bajt et al., 1994; Berry et al., 2003). The Fe K-edge XANES features are primarily ascribed to several transitions to bound states; especially the pre-edge features are due to transition from 1s core state to 3d

crystal field levels ($1s \rightarrow 3d$ transition) and, eventually, to final electron states (Shulman et al., 1976; Calas & Petiau, 1983; Waychunas et al., 1983; Bajt et al., 1994; Westre et al., 1997; Wilke et al., 2001; Berry et al., 2003). This electron transition, particularly in the case of Fe^{3+} and Fe^{2+} in sites with O_h symmetry, gains intensity through the allowed electric quadrupole transition giving rise to weak pre-edge features, in contrast to the more intense pre-edge features for Fe in tetrahedral environment (Westre et al., 1997; Wilke et al., 2001; Berry et al., 2003). Furthermore, the energy of the shoulder at the K absorption edge (i.e., the main rising part above the threshold, primarily due to the absorbing Fe atom) is ascribed to the $1s \rightarrow 4s$ transition (Shulman et al., 1976; Waychunas et al., 1983; Berry et al., 2003), while at higher energies the $1s \rightarrow 4p$ electronic transition contribute to the edge crest of the XANES spectrum (Shulman et al., 1976; Westre et al., 1997; Wilke et al., 2001; Berry et al., 2003). The latter is followed by the EXAFS region dominated by either SS and/or MS processes. In conclusion, the energy position of the pre-edge features, ascribed to the $1s \rightarrow 3d$ transition, was used for the qualitative determination of Fe oxidation state. On the other hand, spectral similarities of the oscillations of the studied sample, compared to those of known standards existing at higher energies above the threshold in the edge, the near-edge, and the post-edge region can only be useful for the determination of structural characteristics of the material. This comparison method is also known as “fingerprinting” (Henderson et al., 2014 and references therein). The usage of this powerful tool can be supported by the statement previously suggested (Waychunas et al., 1983) that the shape of the edge crest, its broadness, and its energy variation in the near-edge region are closely related to the first neighbor interatomic distances, to the Fe site symmetry, and the bond length, respectively. Based on these implications (Waychunas et al., 1983), observed differences and similarities between the edge crest of the measured reference materials (see images **a**, **b**, and **c** of **Figure 3.1.5.9**), and references from the literature (e.g., Waychunas et al., 1983; Bajt et al., Manceau & Gates, 1997; Dyar et al., 1998; England et al., 1999; Wilke et al., 2001; Quartieri et al., 2002; Sánchez del Río et al., 2005; Arčon et al., 2007; Hurai et al., 2008; Sigrist et al., 2011; Oakes et al., 2012; Regelin et al., 2014) can be logically attributed to analogous differences and similarities of the shape, broadness, and energy variation of edge crest, and the different experimental conditions.

The experimental spectra of the ferrous compounds (Fe(II)-chloride, and Fe(II)-sulfate; see images **a** and **b** of **Figure 3.1.5.10**, respectively) exhibit two very weak pre-edge features split by ~ 2 eV. A predicted third pre-edge feature is undistinguishable in the experimental spectra due to site distortion effect that impacts to this feature in the pre-edge region decreasing its intensity (e.g., [Wilke et al., 2001](#); [Henderson et al., 2014](#)). The observed two very weak features at the pre-edge region imply that Fe^{2+} atoms occupy centrosymmetric octahedral sites surrounded by 6 O_2 atoms ([Westre et al., 1997](#); [Arrio et al., 2000](#); [Wilke et al., 2001](#); [Henderson et al., 2014](#)). The lower energy pre-edge feature is more intense relative to the second feature that exists at higher energy positioned at almost the same energy grid of the trivalent references. It is noteworthy to mention that theoretical calculations based on the ligand field theory predict three pre-edge peaks ([Westre et al., 1997](#); [Arrio et al. 2000](#); [Galoisy et al., 2001](#); [Wilke et al., 2001](#); [Henderson et al., 2014](#)) contrary to the visible two very weak pre-edge features in the experimental pre-edge region.

Figure 3.1.5.10: Expanded views focusing in the $1s \rightarrow 3d$ pre-edge region of the experimental Fe *K*-edge XANES spectra of selected synthetic ferrous standards (**a**: Fe(II)-chloride; **b**: Fe(II)-sulfate), natural mixed-valence ($\text{Fe}^{3+}/\Sigma\text{Fe}\neq 1$) iron oxide (magnetite: **c**), synthetic and natural ferric crystalline references (goethite: **d**; hematite: **e**), and the representative bauxite sample (**f**: Fe-rich boehmitic; **g**: Fe-rich diasporic; **h**: Fe-depleted diasporic bauxite). All pre-edge features are indicated by arrows.



It is known that the lowest energy peak is ascribed to ${}^4T_{1g}$ electron state, whereas the ${}^4T_{2g}$ and ${}^4T_{1g}$ states, predicted by ligand field analysis, give rise to two peaks at higher energy values in the pre-edge region (Westre et al., 1997). Any transition to the ${}^4A_{2g}$ state is not expected (Galoisy et al., 2001).

Furthermore, it is well known (e.g., Manceau & Gates, 1997; Wilke et al., 2001) that magnetites consist of ${}^{[6]}Fe^{2+}$, ${}^{[4]}Fe^{3+}$ and ${}^{[6]}Fe^{3+}$ atoms. Theoretical calculations (Wilke et al., 2001) predict three pre-edge components that may contribute to the high intensity pre-edge feature at the pre-edge region of Fe *K*-edge XANES spectra of magnetites. The component that mainly affects the intensity of the pre-edge feature is ascribed to tetrahedrally coordinated atoms (${}^{[4]}Fe^{3+}$) confirming that its relative high intensity is sensitively influenced by tetrahedral symmetry site (e.g., Waychunas et al., 1983; Wilke et al., 2001). In addition, the lower and the higher components from the theory are due the impact of the presence of ${}^{[6]}Fe^{2+}$ and ${}^{[6]}Fe^{3+}$ atoms, respectively. Potential energy shift in the position of the pre-edge feature between different magnetites reported in other papers (e.g., Bajt et al., 1994; Manceau & Gates, 1997; Wilke et al., 2001; Quartieri et al., 2002) can also be attributed to the $Fe^{3+}/\Sigma Fe$ ratio. In the present dissertation, the magnetite used for interpretation of the Fe oxidation state (see image **c** of **Figure 3.1.5.10**) is consistent with previous papers mentioned herein.

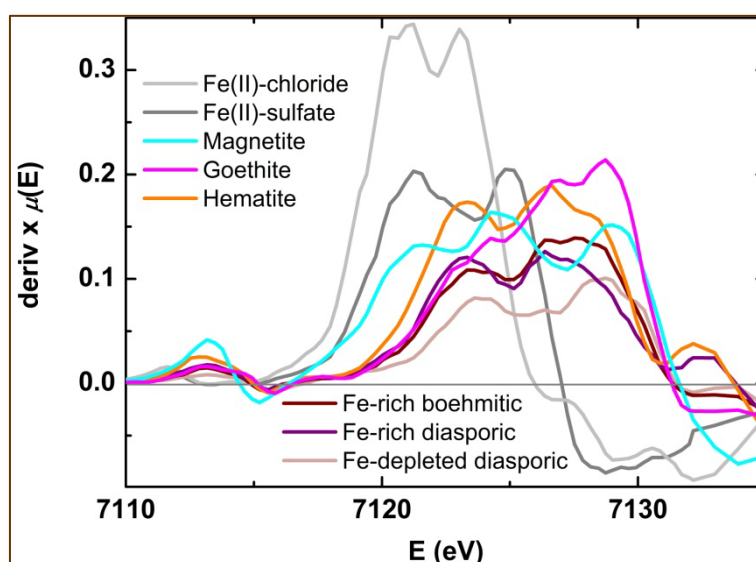
The $1s \rightarrow 3d$ pre-edge features of the bulk recorded normalized Fe *K*-edge XANES spectra of the bauxite samples (see images **f**, **g**, and **h** of **Figure 3.1.5.10**) were compared with the pre-edge features of the XANES spectra of the trivalent (goethite, hematite; see images **d**, and **e** of **Figure 3.1.5.9**), mixed-valence (magnetite; see image **c** of **Figure 3.1.5.10**) references, and the divalent compounds (Fe(II)-chloride, Fe(II)-sulfate; see images **a**, and **b** of **Figure 3.1.5.10**). The evaluation of the Fe oxidation state can be based on the potential energy shift of the pre-edge features of the studied bauxites compared with the energy values of the pre-edge features of the hematite, and the goethite putting them almost to the same energy grid, and residing them at significantly higher energy position than that of the mixed-valence reference (magnetite), but far away from that of the Fe^{2+} compounds (see image **c** of **Figure 3.1.5.9**). The potential energy shift could be attributed to different structural modulation (Di Benedetto et al., 2010) and can also be assigned to the possible

presence of fraction of Fe^{2+} content. In our case, the latter justification seems to be more reliable viewing the fact that, according to previously Mössbauer study, Fe depleted diasporic bauxite contains a small proportion of divalent iron. Besides, as magnetites and hematites can be precisely used as energy reference standards (Berry et al., 2003), a supplementary spectral comparison involving them and the studied bauxites was approached for further investigation of the valence of iron in the studied samples. For this reason, based on the published Fe *K*-edge XANES data (Bajt et al., 1994; Berry et al., 2003) that defined that $\text{Fe}^{3+}/\Sigma\text{Fe}$ ratio in magnetites varies from 0.72 to 0.94, the interpretation of them, judging against the energy site of the pre-edge peak of the studied bauxites (see image **b** of **Figure 3.1.5.9**), fosters the argument that iron in the studied bauxites is most probably a mixture of traces of divalent and abundances of trivalent components, with specific Fe^{3+} content to be quantified to an order of value above the upper limit of published magnetites (94 %). In conclusion, our Fe *K*-edge XANES evaluation revealed that the dominant component of iron in the investigated bauxite samples is the trivalent (see images **a**, **b**, and **c** of **Figure 3.1.5.9**). In particular, Fe^{3+} seems to be exclusively present in the Fe-rich diasporic and boehmitic samples. However, a very small contribution of Fe^{2+} atoms as minor component in the Fe-depleted diasporic investigated sample cannot be excluded reportedly by the Mössbauer study. Consequently, the Fe *K*-edge XANES study of the representative bauxite samples is in line with the Mössbauer results.

Complementary, it is known that the energy of the shoulder at the *K* absorption edge (i.e., the main rising part above the threshold; see image **b** of **Figure 3.1.5.9**), appearing as a tip of the peak of the first derivative (Manceau & Gates, 1997; Berry et al., 2003; Arçon et al., 2007; see **Figure 3.1.5.11**), is assigned to the known forbidden $1s \rightarrow 4s$ electron transition (Shulman et al., 1976; Berry et al., 2003). Besides, the examination of the Fe valence based on the energy position of the shoulder in the main rising part of the *K* absorption edge (see image **b** of **Figure 3.1.5.9**), excluding the usage of the pre-edge features, resulted in some differences compared with the study of the energy position of the $1s \rightarrow 3d$ pre-edge features characteristics (e.g., Quartieri et al., 2002; Berry et al., 2003; Oakes et al., 2012). These deviations are most probably due to some Fe coordination changes related with different kind of sample preparation (Berry et al., 2003). Nevertheless, resemblances of the spectral features (joining with additional resemblances of their shape, broadness, and energy

variation of the edge crests; Waychunas et al., 1983) between the investigated Fe-rich boehmitic and Fe-rich diasporic bauxites, the hematite, and the goethite at their main rising parts of the *K* absorption edge (see image **b** of **Figure 3.1.5.9**) provide evidence for further spectral similarities between them. These matches can be fortified by the spectral similarities between oscillations of the studied Fe-rich samples, the hematite, and the goethite existing at higher energies above the threshold, particularly, in the edge, the near-edge, and the post-edge region (see text below; image **d** of **Figure 3.1.5.9**).

Figure 3.1.5.11: The first derivative spectra of the Fe *K*-edge XANES of the measured studied bauxite samples and the reference standards.



Focusing in the pre-edge region, both the experimental Fe *K*-edge XANES spectra of the goethite and hematite (see images **d**, and **e** of **Figure 3.1.5.10**) exhibit one distinct low intensity pre-edge feature with a very weak shoulder at slightly lower energy, matching with the examined hematite and goethite from the literature (Manceau & Gates, 1997). Additionally, their spectral pre-edge features seem to be quite similar to those from the low-spin centrosymmetric octahedral ferric complexes (Westre et al., 1997). Accordingly, as the experimental low intensity pre-edge feature of the bauxites (see images **f**, **g**, and **h** of **Figure**

3.1.5.10) is similar to that of goethite (see image **d** of **Figure 3.1.5.10**) and hematite (see image **e** of **Figure 3.1.5.10**), containing a very weak shoulder difficult to split at slightly lower energy, it can be implied that Fe^{3+} atoms occupy octahedral centrosymmetric sites in the structure of the measured ferric references and, most probably, occupy similar octahedral sites in the structure of the studied bauxites. The comparison between the heights of the experimental pre-edge feature of the bauxites, and the octahedral ferric references, reveal local structural similarities of their centrosymmetric sites of the octahedral Fe^{3+} atoms, inasmuch as the height of the pre-edge feature of the Fe-rich boehmitic bauxite seems to be equal to that of goethite, and the pre-edge feature of the Fe-rich diasporic bauxite seems to be equal to that of hematite. These similarities indirectly indicate that Fe^{3+} atoms site symmetry in the studied Fe-rich boehmitic and diasporic bauxites resemble to that of goethite and of hematite, respectively. In contrast to the ferric references of the present dissertation, a distinguishable splitting of the pre-edge feature was appeared in the pre-edge region of hematite and goethite examined by [Wilke et al. \(2001\)](#) due to crystal-field splitting. Based on previously remarks ([Westre et al., 1997](#)), this wide splitting indicates that the published references ([Wilke et al., 2001](#)) could be ranked as “high-spin” in contradiction to the measured “low-spin” octahedral ferric compounds of the present dissertation. In either case, the totally undetectable two different well-splitting pre-edge features, as in the case of other octahedrally coordinated Fe^{3+} published references such as andradite ([Wilke et al., 2001](#)), presumptively signifies that the octahedral units of O_2 atoms surrounding Fe^{3+} atoms, in both the measured (present dissertation) and the previously examined ([Wilke et al., 2001](#)) hematite and goethite, may not be distorted, too. Since the pre-edge features of all the investigated bauxites (see images **f**, **g**, and **h** of **Figure 3.1.5.10**) are similar to those of the measured ferric references (see images **d**, and **e** of **Figure 3.1.5.10**), the latter assumption also stands for the studied bauxite samples.

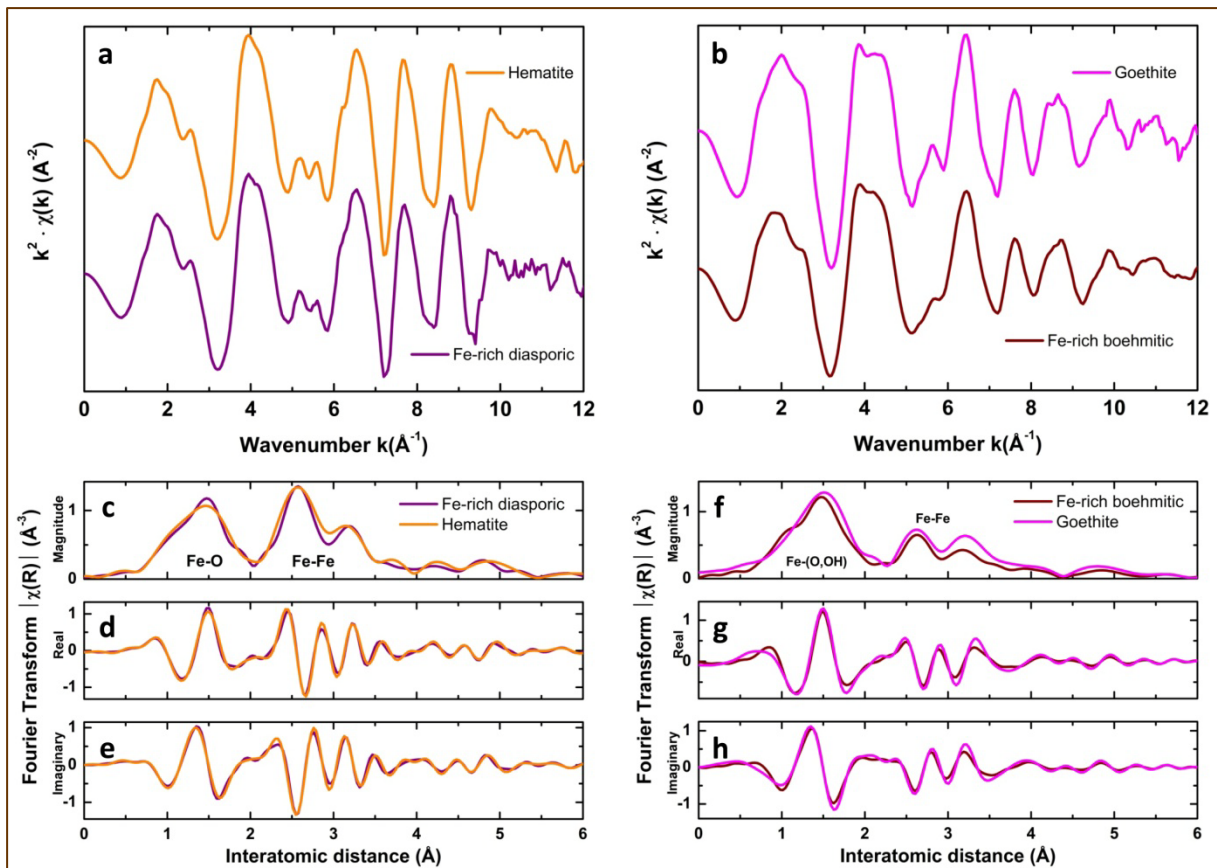
In the case of low-spin octahedral ferric complexes (such as the measured hematite, goethite, and the studied Fe-rich bauxites), it is known that the ligand field theory predicts three pre-edge peaks that mainly contribute to the pre-edge feature and, also, to the neighboring weak shoulders ([Westre et al., 1997](#)). The lowest energy pre-edge peak is ascribed to ${}^4\text{A}_{1g}$ state appearing as a very weak shoulder just below the centroid position of the pre-edge feature, while the ${}^1\text{T}_{2g}$ electron state appears as a very weak shoulder between

the centroid position of the pre-edge feature and the threshold, as can be more observed in the case for the measured goethite (see image **d** of **Figure 3.1.5.10**), but less in the case for the hematite (see image **d** of **Figure 3.1.5.10**) and all the studied bauxites (see images **f**, **g**, and **h** of **Figure 3.1.5.10**). Besides the $^3T_{1g}$, $^3T_{2g}$, and $^1T_{1g}$, electron states give rise to the main pre-edge feature (Westre et al., 1997). In contrast to our results, it can be supported that the visible distinguishable splitting of the pre-edge feature of the high-spin octahedral hematite and goethite from the literature (Wilke et al., 2001) attributed to the two pre-edge peaks yielded by the theoretical calculations (Westre et al., 1997). In this case, it is known (Westre et al., 2001) that ligand field theory predicts that these peaks are ascribed to the $^5T_{2g}$ and 5E_g states, respectively. The latter is also supported by other published work (Galoisy et al., 2001). On the other hand, one to three extra theoretical contributions at higher energies just above the centroid position, which are not predicted by theory, were previously noticed (Wilke et al., 2001). In line with published results (Wilke et al., 2001), these extra pre-edge theoretical peaks may give some contribution and, consequently, cause considerably enhancement of the intensity of the very weak shoulder just above the pre-edge feature making it somehow visible in the pre-edge characteristics of both the measured ferric references (see images **d**, and **e** of **Figure 3.1.5.10**), and the studied bauxites (see images **f**, **g**, and **h** of **Figure 3.1.5.10**). These extra contributions could be related to possible Fe clustering phenomenon (Wilke et al., 2001) directly attributed to Fe-Fe contribution (Heijboer et al., 2004) and, particularly, could be interpreted as Fe-O-Fe multiple scattering as previously suggested (Hurai et al., 2008). It is noteworthy to mention that exactly the same argument can indirectly be applied for the measured hematite and, especially, for the goethite and, consequently, the same also stands for the resembled bauxite samples.

To stress potential structural relationships between the studied bauxite samples and the measured hematite and goethite, a comparison method -known as “fingerprinting” (Henderson et al., 2014) mentioned above- has been successfully applied. In the beginning, the Fourier transform (FT) of $\chi(k)$ of the experimental Fe *K*-edge EXAFS signals of all the studied bauxite samples were compared with EXAFS signals of the hematite, the goethite, and the magnetite as well as with EXAFS signals of the divalent standards (see image **d** of **Figure 3.1.5.9**). Whereupon, further comparison between the FT of $\chi(k)$ of the Fe *K*-edge EXAFS signals of the “Fe-rich diasporic bauxite – hematite” pair (see image **a** of **Figure**

3.1.5.12) and the “Fe-rich boehmitic bauxite – goethite” pair (see image **b** of **Figure 3.1.5.12**), addressed significant spectral similarities between the Fe-rich diasporic sample and the hematite and, further, between the Fe-rich boehmitic sample and the goethite, respectively, as their FT $\chi(k)$ EXAFS signals match perfectly each other.

Figure 3.1.5.12: The Fourier transform (FT) of $\chi(k)$ of the experimental Fe *K*-edge EXAFS signal of the studied Fe-rich diasporic bauxite comparing with the EXAFS signal of the hematite (**a**), and experimental FT of $\chi(k)$ Fe *K*-edge EXAFS signal of the studied Fe-rich boehmitic bauxite comparing with the EXAFS signal of the goethite (**b**). The experimental FT of $\chi(R)$ Fe *K*-edge EXAFS plots in the magnitude (**c** and **f**), the real (**d** and **g**), and the imaginary part (**e** and **h**) stressing the observed spectral similarities, using the ATHENA software package (Ravel & Newville, 2005).



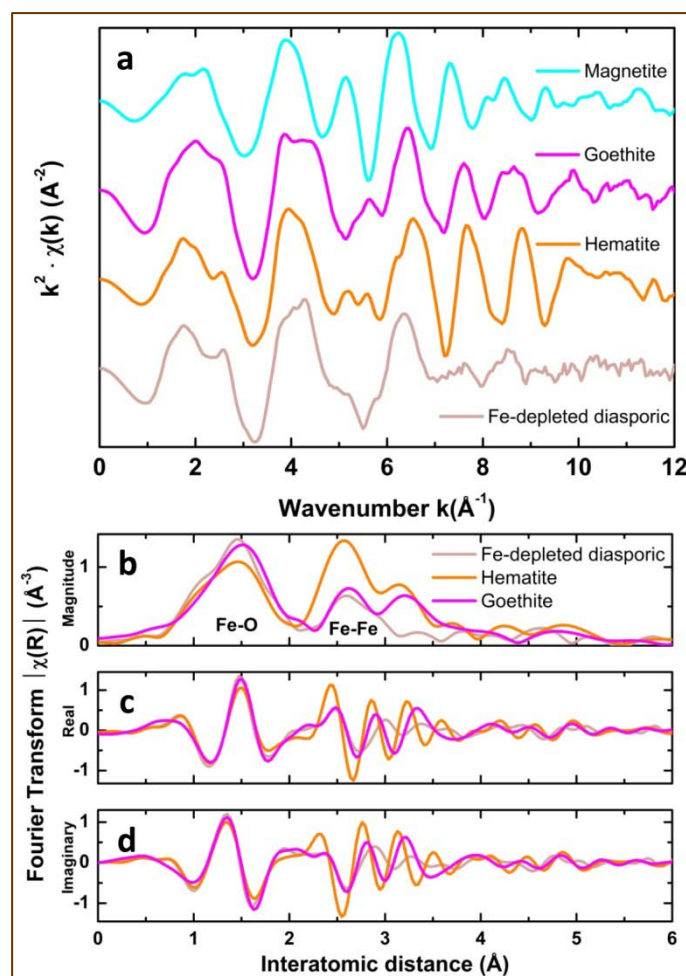
In general, a distinguishable well-formed first peak is appeared, while a splitting phenomenon at higher interatomic distance, dividing the next to the first neighbor Fe-Fe atomic shell into two sub-shells, is also observed creating the second and the third peak, respectively (see images **c**, and **f** of **Figure 3.1.5.12**). This split is common for Fe oxides and oxyhydroxides (e.g., Manceau & Combes, 1988; Manceau & Drits, 1993; Singh et al., 2000; Cornell & Schwertmann, 2003, and references therein). It is noteworthy to mention that the ratio of the second to third peak intensity varies depending on the studied material (Manceau & Combes, 1988), and its intensity is equally enhanced both in the Fe-rich diasporic bauxite and the hematite. In contrast, this ratio is proportionally lesser in the Fe-rich boehmitic bauxite and the goethite FT EXAFS signals. Since the experimental FT of $\chi(R)$ in the magnitude part of the Fe *K*-edge EXAFS signal of the Fe-rich diasporic bauxite strongly resemble with that of hematite (see image **c** of **Figure 3.1.5.12**), significant structural similarities between them can be extrapolated. This hypothesis can alternatively be supported by the similarities appearing at the experimental FT plot in the real (see image **d** of **Figure 3.1.5.12**) and the imaginary part (see image **e** of **Figure 3.1.5.12**) of $\chi(R)$ of their comparative Fe *K*-edge EXAFS signals. Proportionally, the latter assessment also stands for the “Fe-rich boehmitic bauxite – goethite” pair (see images **f**, **g**, and **h** of **Figure 3.1.5.12**) driving to the similar conclusion. Intensity and shape differences between the peaks of the measured hematite and those of literature (Manceau & Combes, 1988; Manceau & Drits, 1993; Singh et al., 2000) can be attributed to different type of hematite (i.e., present sample is a natural pure-grey hematite type contrary to the natural or synthetic red hematite type usually was used), to transition metals incorporation into hematite structure (Singh et al., 2000) and to different experimental conditions. The above peak-to-peak comparison of the FT of $\chi(R)$ of the EXAFS signals directly illustrates that the first peak of the Fe-rich diasporic bauxite matches with the first peak of hematite corresponding to an O₂ first neighbor (Fe-O shell) surrounding by Fe atoms, while the Fe-rich boehmitic bauxite matches with the first peak of goethite corresponding to an O₂ and/or OH⁻ first neighbors (Fe-O and/or Fe-OH shell) surrounding by Fe atoms, too (e.g., Manceau & Combes, 1988; Manceau & Drits, 1993; Singh et al., 2000; Cornell & Schwertmann, 2003). In both cases, the presence of second and third peaks establishes the existence of extended local environment around the Fe absorbing atom beyond its first coordination shell in the Fe-rich bauxites (either diasporic or boehmitic). The resemblances of the second strongest and third peaks between the FT of

$\chi(R)$ EXAFS signal of Fe-rich diasporic bauxite and hematite (see image **c** of **Figure 3.1.5.12**) can be attributed to the structural similarities between the Fe-Fe shells corresponding to the nearest and the next-to-nearest Fe neighboring atom, respectively (e.g., [Manceau & Combes, 1988](#); [Manceau & Drits, 1993](#); [Singh et al., 2000](#); [Cornell & Schwertmann, 2003](#)). Similar resemblances of the second and third peaks between the FT of $\chi(R)$ EXAFS signal of Fe-rich boehmitic bauxite and goethite (see image **f** of **Figure 3.1.5.12**) drive to the argument that the local environment around the absorbing Fe atoms of the Fe-rich boehmitic bauxite resembles to that of goethite. Hence, the latter comparative finding denotes that the first peak of the Fe-rich boehmitic bauxite can be related not only to the first O^{2-} neighbor anion (as in the previous case of hematite structure) but, also, to an OH^- neighbor anion (as in the case of goethite structure), while the presence of Fe-Fe configuration in the local structural environment around the absorbing atoms of the Fe-rich boehmitic bauxite is affirmed by the depiction of the second and third peaks corresponding to edge- and corner-sharing linkages (case of goethite structure; e.g., [Manceau & Combes, 1988](#); [Manceau & Drits, 1993](#); [Cornell & Schwertmann, 2003](#)). Conclusively, in both cases the spectral similarities of the experimental Fe *K*-edge EXAFS signals testify that the signal of the Fe-rich diasporic bauxite is strongly influenced by hematite component, while the Fe-rich boehmitic is strongly influenced by goethite component, too. Under this statement, this specifies that ferric octahedral basic structural units of the investigated Fe-rich diasporic bauxite correspond to the $Fe(O)_6$ octahedra of hematite, whereas in the case of the studied Fe-rich boehmitic bauxite the $^{6}Fe^{3+}$ structural units match to the $FeO_3(OH)_3$ octahedra of goethite. Besides, on the basis of local structural differences between well-crystalline hematite and goethite ([Manceau & Drits, 1993](#)) and the proved spectral similarities, the latter implication can, consequently, drive to the assumption that the $^{6}Fe^{3+}$ basic structural units of the Fe-rich diasporic bauxite are linked to each other by face-linkages (due to structural similarities of this bauxite sample with hematite; see images **a**, **c**, **d**, and **e** of **Figure 3.1.5.12**), whereas the other two type of linkages (corner- and edge-sharing) exist only in Fe-rich boehmitic bauxite local structure (due to structural similarities between this bauxite sample and the goethite; see images **b**, **f**, **g**, and **h** of **Figure 3.1.5.12**). Nevertheless, the differences in the intensity between the third peak of the Fe-rich boehmitic bauxite and the third peak of the goethite FT EXAFS signal (see image **f** of **Figure 3.1.5.12**) could be circuitously attributed to a possible less proportion of ferric octahedra linked by corner-

linkages. This assumption is based on the fact that the second and the third peaks at the FT plot of $\chi(R)$ of goethite correspond to different type of linkage of octahedra and, particularly, to edge- and to corner-sharing, respectively (Manceau & Drits, 1993); interatomic distances across edge- and face-sharing octahedra are too close to be separated by EXAFS (Manceau & Combes, 1988).

The comparison between the FT of $\chi(k)$ of the Fe *K*-edge EXAFS signals of the Fe-depleted diasporic bauxite, the hematite, the goethite, and the magnetite (see image **a** of **Figure 3.1.5.13**) revealed that significant spectral differences can be inferred between the investigated Fe-depleted diasporic bauxite sample and the measured references, and no spectral similarities can be observed as their FT $\chi(k)$ EXAFS signals cannot match each other.

Figure 3.1.5.13: The Fourier transform (FT) of $\chi(k)$ of the experimental Fe *K*-edge EXAFS signal of the studied Fe-depleted diasporic bauxite comparing with the EXAFS signal of the hematite, goethite, and magnetite (**a**), and experimental FT of $\chi(k)$ Fe *K*-edge EXAFS signal of the studied Fe-depleted diasporic bauxite comparing with the EXAFS signal of the hematite, and the goethite (**b**). The experimental FT of $\chi(R)$ Fe *K*-edge EXAFS plots in the magnitude (**c** and **f**), the real (**d** and **g**), and the imaginary part (**e** and **h**) using the ATHENA software package (Ravel & Newville, 2005).



This is enhanced by the demonstration of the experimental FT of $\chi(R)$ in the magnitude part of the Fe *K*-edge EXAFS signal of the Fe-depleted diasporic bauxite, which strongly differ to that of hematite, and goethite (see image **b** of **Figure 3.1.5.12**). Thus, significant structural differences between them can be confirmed. This statement can be supported by the spectral differences appearing at the experimental FT plot in the real (see image **c** of **Figure 3.1.5.13**) and the imaginary part (see image **d** of **Figure 3.1.5.13**) of $\chi(R)$ of their comparative Fe *K*-edge EXAFS signals.

In conclusion, the spectral similarities between the Fe-rich boehmitic bauxite (ELM0206_2H1) and the goethite as well as between the Fe-rich diasporic (SAB0306_ASV) and the hematite can be profoundly described in terms of the structural relationships between the studied bauxite samples, the goethite, and the hematite components. The consideration about the structural similarities between the Fe-rich bauxites (either boehmitic or diasporic) and the ferric reference standards is in accordance with the previously mentioned PXRD (see text above; **Table 3.1.1.1**) and Mössbauer results (see text above; **Table 3.1.5.1**). Fe-rich diasporic sample has been found to contain only hematite, whereas in the case of Fe-rich boehmitic bauxite the existence of goethite, the possible presence of maghemite traces, and the totally absence of hematite has been proved. On the other hand, based on the Mössbauer study, minor amounts of hematite cannot be excluded to be present in the latter bauxite sample. The demonstrated structural differences between the Fe-depleted diasporic bauxite and the measured magnetite, goethite, and hematite, are in line with the PXRD (see text above; **Table 3.1.1.1**) and Mössbauer data (see text above; **Table 3.1.5.2**) that proved the absence of Fe-oxides and -oxyhydroxides (see text above) in microscale, as Fe-depleted diasporic sample (ALM0306_PL1_BIW) has been found to contain Fe³⁺ atoms possibly substituting Al³⁺ in diasporic (according to FEG TEM-EDS with EELS observations; see text below), whereas minor quantities of Fe³⁺ most likely can be possibly occluded in maghemite-type phase, in nano-maghemite and/or in amorphous phases. In either case, the presence of Fe nanominerals in the Fe-depleted diasporic bauxite, detected by FEG TEM-EDS with EELS (see text below) and influenced both by Mössbauer and Fe *K*-edge XANES study, indicates that Fe³⁺ is not exclusively present in novel Fe-Cr-AlOOH (see text below), but also in novel Fe nanoparticles of unknown structure and crystallinity.

The examination of magnetic transitions during temperature cycling is a diagnostic method to observe even low concentration of magnetic minerals. These transitions manifest as abrupt increases or decreases in magnetization and/or magnetic susceptibility when the sample is heated or cooled through a critical temperature. The primary feature of the mass-normalized magnetic susceptibility measurement for Fe-depleted bauxite, presented in **Figure 3.1.5.14**, is the irreversibility of the susceptibility after heating the sample to approximately 700 °C. When heating above 500 °C, susceptibility begins to increase before dropping sharply just below 600 °C. During the cooling run, susceptibility increases as the sample is cooled through 600 °C and remains higher than its initial values. There is a similar but smaller and less abrupt increase as the sample cools through approximately 235 °C; a small deviation at a similar temperature can be observed in the heating run but magnitude has been greatly enhanced by the time at high temperature. The two abrupt changes in magnetic susceptibility described above indicate two magnetic phases, which either increase in quantity or undergo some magnetic enhancement as a function of heating. The lower temperature transition (~235 °C) is very close to the Curie temperature of Fe₂CrO₄ (Francombe, 1957), i.e. chromite which was observed directly with SEM-EDS/WDS analyses (see text below). The Curie temperature as calculated by point of maximum slope (Tauxe 1998) is slightly above 200 °C, that of pure Fe₂CrO₄, suggesting a slight deviation from endmember composition. The phase that shows a high-temperature transition is more uncertain. The Curie temperature of the phase produced during heating is indistinguishable from that of pure magnetite, and there are notably no further magnetic transitions above 600 °C that would indicate the presence of hematite or maghemite, which can be stable to high temperatures with the presence of Al. Neither the initial (unheated) low-temperature measurements nor those acquired after the high-temperature run show any magnetic transitions below room temperature that would indicate primary or secondary magnetite or end-member hematite. The Verwey transition at ~-150 °C (~120 - 125 K; Verwey, 1939) is diagnostic of magnetite, but is difficult to observe in susceptibility measurements of single-domain carriers (Muxworthy, 1999). It may also be suppressed by even small degrees of cation substitution (Kakol et al., 1992) or non-stoichiometry (Aragon et al., 1985) so the inability to identify any inflections in the susceptibility curve in this temperature range does not rule out magnetite as the phase created at high-temperature. The Morin transition of hematite, which occurs at approx. -10 °C (Morin, 1950) is likewise diagnostic of the presence

of that mineral; the lack of any magnetic transitions at this temperature or at the Neel temperature of 675 °C indicate that there is little hematite initially present or generated during the heating run. The lower image of **Figure 3.1.5.14** shows the repeat of the susceptibility measurements by cycling to increasing temperature in order to observe the point at which alteration in the sample becomes irreversible. The heating and cooling curves appear similar up to a maximum temperature of 510 °C, after which increasing amounts of ferromagnetic material is produced and the susceptibility curves become dissimilar. The onset of alteration occurs at a notably higher temperature than that of the dehydroxylation of potential Fe-oxyhydroxide precursors, such as lepidocrocite, ferrihydrite, and goethite, which has been observed at temperatures as low as 200 °C (e.g. [Gendler et al., 2005](#)). This higher temperature is similar to that of the inversion of maghemite and titanium-substituted maghemite; while a range of inversion temperatures have been reported, the onset above 510 °C corresponds precisely to the values reported in at least one study ([Özdemir & Banerjee, 1984](#)). The Curie temperature of the ferromagnetic phase generated at high temperatures is strongly suggestive of magnetite, but the precursors are less certain. The increase in susceptibility suggests either a compositional or crystallographic change, and the nature of that change would indicate the starting material. The susceptibility curves are qualitatively very similar to magnetization measurements acquired during the inversion of titanium-substituted maghemite ([Readman & O'Reilly, 1970](#); [Özdemir, 1987](#)), a process which produces pure magnetite and a weakly magnetic second phase. A second possibility for the development of magnetite is a minor crystallographic change from a non-magnetic magnetite precursor. This lack of magnetic signal could be caused by the phase being amorphous or with a sufficiently defect-rich lattice that magnetization is reduced and the particle exhibits superparamagnetic behavior. Upon heating, the development of crystalline ordering from a previously amorphous phase would create a new single-domain phase. Alternatively, enhancement of magnetization by the annealing of lattice defects would effectively increase the relaxation time of superparamagnetic particles so generating a single-domain magnetic phase can be observed laboratory timescales. This final possibility, while unproven is suggestive of the Fe nanominerals implied by the Mössbauer spectroscopy and directly observed by the study of Fe-depleted bauxite in nanoscale (FEG TEM-EDS & EELS; see text below).

Figure 3.1.5.14: Magnetic susceptibility versus temperature measurements. *Upper image:* Full temperature run, illustrating measurement protocol of heating run from -192 °C to 700 °C, followed by cooling to room temperature. Both magnetite and chromite (chrome-spinel) are present after heating to high-temperature, indicating a chemical or structural change from some Fe-containing precursor (most likely the Fe nanominerals; see text below). *Lower image:* Recursive heating of the same sample to progressively higher temperatures to establish critical temperature of magnetite development. Heating up to 510 °C produces little irreversible change, but the successive run to 560 °C (of which a total of 13 min between 510 - 560 °C) causes the formation of magnetite, a process which continues in further runs to yet higher temperatures.

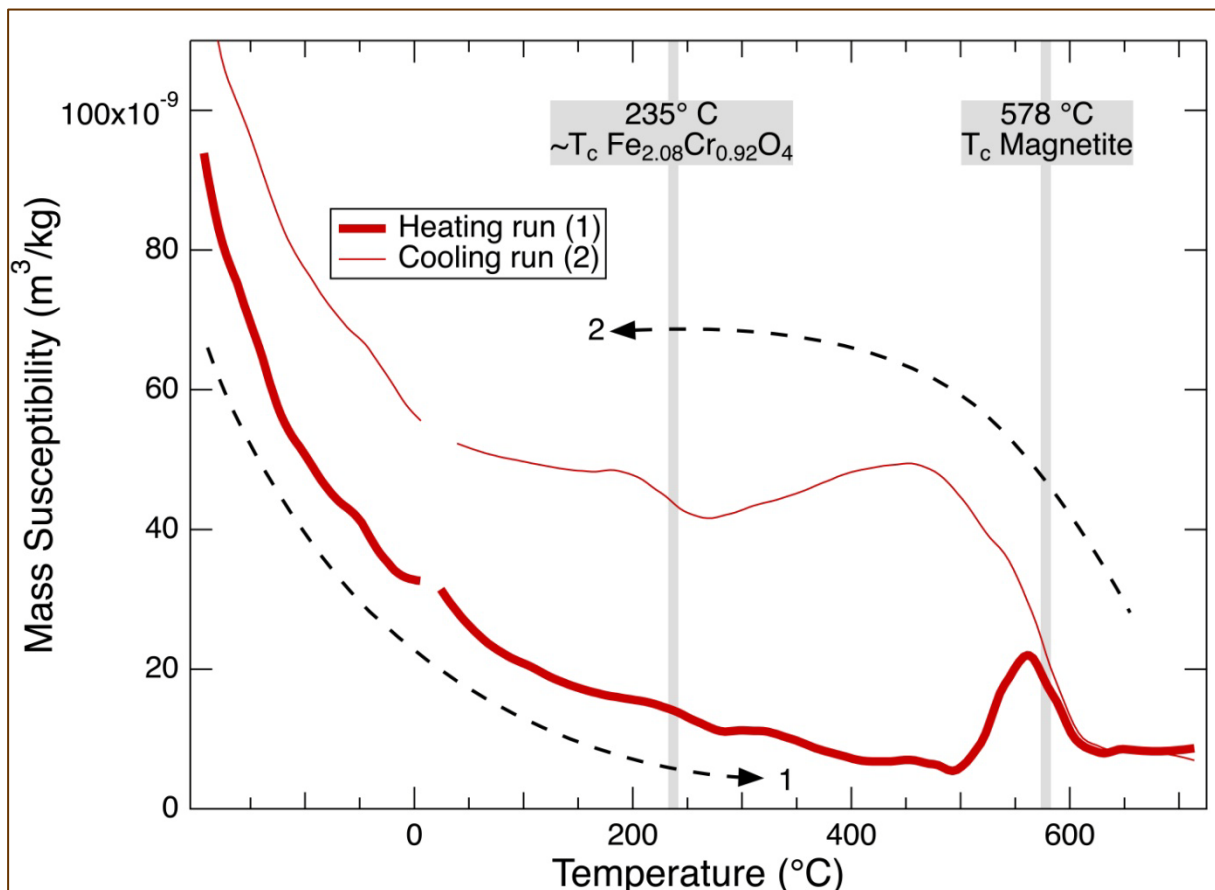
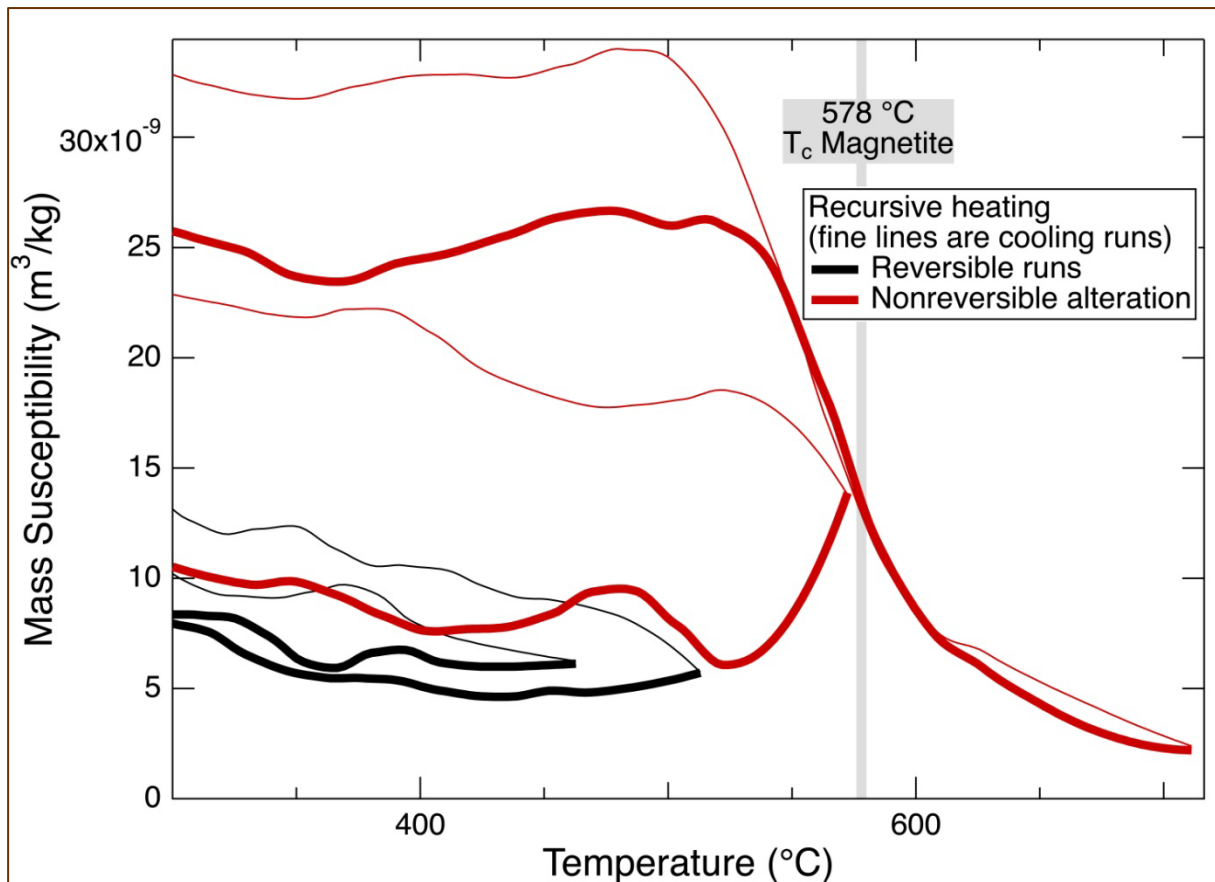


Figure 3.1.5.14: continued.



3.1.6. Bulk radionuclide content (γ -ray spectrometry)

The studied bauxites contain significant amounts of natural actinides (U, Th) as well as K. According to bulk geochemical data, the materials contain avg. 48.8 ppm Th and avg. 8.8 ppm U. Potassium is preferentially concentrated in Fe-rich bauxites (avg. 754.7 ppm), while the content of Fe-depleted is practically insignificant. It is obvious that the studied Greek bauxites from Parnassos-Ghiona active mining area exhibit high natural radionuclides concentration, mainly due to ^{232}Th (calculated by ^{228}Ac and ^{208}Tl), ^{238}U (calculated by ^{234}Th and ^{234}Pa), ^{226}Ra , and ^{40}K , related to considerable radioactivity. It is worthy to mention that both the radioactivity (due to ^{228}Ac ; Bq/Kg) and the Th concentration (in bulk; ppm) are significant higher in the metallurgical residue (red mud; see text below), and totally

inexistent (practically equal to zero) in the alumina product compared to those of the bauxite ore deposit (**Figure 3.1.5.14**). Results of the bulk radionuclide content for representative Fe-rich and Fe-depleted samples are presented in **Table 3.1.5.3**, compared to those of the alumina (Al_2O_3) industrial product derived from bauxite ore and, also, to that of the metallurgical residue (red mud; see text below) after the Bayer process at the Aluminium S.A. industrial plant at Antikyra bay (**Table 3.1.5.4**). The average activity corresponding to ^{232}Th -series for Fe-depleted bauxites was found to be 210 Bq/kg (max. 229 Bq/kg), as compared to an average of 175 Bq/kg for Fe-rich bauxite (max. 203 Bq/kg). The total average of ^{232}Th , for all types of Greek bauxite examined, is 182 Bq/kg ($n = 10$), in general agreement with data from a previous investigation (216 Bq/kg, $n = 2$; [Papatheodorou et al., 2005](#)). This value is lower than the average of Hungarian bauxite (256 Bq/kg, $n = 46$) and much lower than the international average (400 Bq/kg; [Somlai et al., 2008, and references therein](#)). The summary of γ -ray spectrometry measurements is presented in **Table 3.1.5.5**.

Figure 3.1.5.14: Binary plot of ^{228}Ac (Bq/Kg) versus Th (ppm) of the studied Parnassos-Ghiona bauxites relative to their metallurgical residues (red mud; see text below) and to alumina production after the Bayer process.

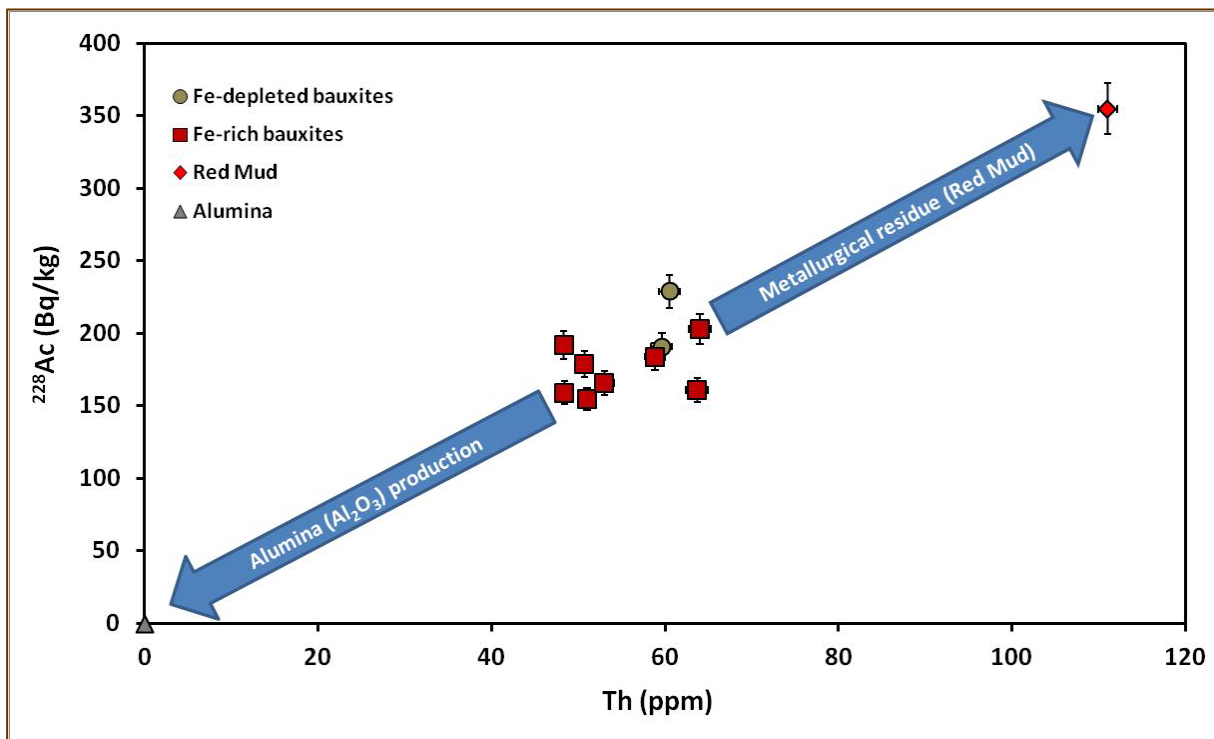


Table 3.1.5.3: Bulk radionuclide content for representative Fe-rich (ALM0306_PL1_B1; upper image) and Fe-depleted (ALM0306_PL1_BIW; lower image) bauxite samples from Parnassos-Ghiona active mining area.

NUCLIDE	ENERGY	AREA	±	c/s	±	BKG	±	BKG/s	±	NET c/s	± NET	Efficiency eeae	± Efficiency	FY	Corrections	Bq/kg	Total Dose Rate	± Bq/kg	nGy/h
²³⁴ Th	63	530	136	0.02315	0.00594	465.1	80	0.00465	0.00080	0.01850	0.00600	0.01335	0.00067	0.037		69		22.6875	32
²³⁵ U	143	370	146	0.01616	0.00638	172.7	51.81	0.00173	0.00052	0.01444	0.00640	0.02920	0.00146	0.109	0.72	6.03		3.7365	
²¹⁴ Pb	352	9956	131	0.43495	0.00572	1477	64	0.01477	0.00064	0.42018	0.00576	0.01868	0.00093	0.356		117		6.0503	54
²¹⁴ Bi	609	7624	107	0.33307	0.00467	1037	52.7	0.01037	0.00053	0.32270	0.00470	0.01280	0.00064	0.448		104		5.4117	48
²¹⁴ Bi	1764	1425	44	0.06225	0.00192	236	23.6	0.00236	0.00024	0.05989	0.00194	0.00615	0.00031	0.1531		117		6.9922	55
²²⁸ Ac	911	6774	85	0.29594	0.00371	411	39.3	0.00411	0.00039	0.29183	0.00373	0.00970	0.00048	0.29		192		9.8879	119
²⁰⁸ Tl	583	9385	116	0.41000	0.00507	564	39.7	0.00564	0.00040	0.40436	0.00508	0.01319	0.00066	0.307		184		9.5057	115
²³⁴ Pa	1001	80	33	0.00349	0.00144	87.9	14.943	0.00088	0.00015	0.00262	0.00145	0.00909	0.00045	0.01021		52		28.9565	24
⁴⁰ K	1461	435	34	0.01900	0.00149	1313	42	0.01313	0.00042	0.00587	0.00154	0.00701	0.00035	0.1067		15		3.8820	1
²²⁶ Ra + ²³⁵ U	186	2748	167	0.12005	0.00730	819	79.3	0.00819	0.00079	0.11186	0.00734	0.02899	0.00145	0.0355		201		16.5598	
²²⁶ Ra (after Gilmore correction)	186	2748	167	0.12005	0.00730	819	79.3	0.00819	0.00079	0.11186	0.00734	0.02899	0.00145	0.0355	0.571	114.63		16.5598	
²²⁶ Ra ONLY ²³⁵ U from ²³⁴ Th	186	2748	167	0.12005	0.00730	819	79.3	0.00819	0.00079	0.08281	0.00734	0.02899	0.00145	0.0355		149	Average ²²⁶ Ra	15.1225	69
²²⁶ Ra ONLY ²³⁵ U from ²³⁴ Pa	186	2748	167	0.12005	0.00730	819	79.3	0.00819	0.00079	0.09001	0.00734	0.02899	0.00145	0.0355		162	138	15.4502	75
²²⁶ Ra ONLY ²³⁵ U from 143 keV	186	2748	167	0.12005	0.00730	819	79.3	0.00819	0.00079	0.05743	0.00734	0.02899	0.00145	0.0355		103		14.1431	48
¹³⁷ Cs	661.6	0	0	0	0	0	0	0	0	0	0	0.01209	0.00060	0.85		0.0		0	0

NUCLIDE	ENERGY	AREA	±	c/s	±	BKG	±	BKG/s	±	NET c/s	± NET	Efficiency eeae	± Efficiency	FY	Corrections	Bq/kg	Total Dose Rate	± Bq/kg	nGy/h
²³⁴ Th	63	707	137	0.03359	0.00651	465.1	80	0.00465	0.0008	0.02894	0.00656	0.01335	0.00067	0.037		121		28.0168	56
²³⁵ U	143	222	88.8	0.01055	0.00422	172.7	51.81	0.00173	0.00052	0.00882	0.00425	0.02920	0.00146	0.109	0.72	4.11		2.7658	
²¹⁴ Pb	352	8942	123	0.42488	0.00584	1477	64	0.01477	0.00064	0.41011	0.00588	0.01868	0.00093	0.356		127		6.6081	59
²¹⁴ Bi	609	6582	102	0.31274	0.00485	1037	52.7	0.01037	0.00053	0.30237	0.00488	0.01280	0.00064	0.448		109		5.7049	50
²¹⁴ Bi	1764	1171	41	0.05564	0.00195	236	23.6	0.00236	0.00024	0.05328	0.00196	0.00615	0.00031	0.1531		117		7.2353	54
²²⁸ Ac	911	6660	84	0.31645	0.00399	411	39.3	0.00411	0.00039	0.31234	0.00401	0.00970	0.00048	0.29		229		11.8061	142
²⁰⁸ Tl	583	9390	115	0.44617	0.00546	564	39.7	0.00564	0.0004	0.44053	0.00548	0.01319	0.00066	0.307		224		11.5429	140
²³⁴ Pa	1001	126	30	0.00599	0.00143	87.9	14.943	0.00088	0.00015	0.00511	0.00143	0.00909	0.00045	0.01021		113		32.3086	53
⁴⁰ K	1461	409	33	0.01943	0.00157	1313	42	0.01313	0.00042	0.0063	0.00162	0.00701	0.00035	0.1067		17		4.5566	1
²²⁶ Ra + ²³⁵ U	186	2535	162	0.12045	0.00770	819	79.3	0.00819	0.00079	0.11226	0.00774	0.02899	0.00145	0.0355		225		19.1353	
²²⁶ Ra (after Gilmore correction)	186	2535	162	0.12045	0.00770	819	79.3	0.00819	0.00079	0.11226	0.00774	0.02899	0.00145	0.0355	0.571	128.31		19.1353	
²²⁶ Ra ONLY ²³⁵ U from ²³⁴ Th	186	2535	162	0.12045	0.00770	819	79.3	0.00819	0.00079	0.06682	0.00774	0.02899	0.00145	0.0355		134	Average ²²⁶ Ra	16.8716	62
²²⁶ Ra ONLY ²³⁵ U from ²³⁴ Pa	186	2535	162	0.12045	0.00770	819	79.3	0.00819	0.00079	0.0696	0.00774	0.02899	0.00145	0.0355		139	144	16.9836	65
²²⁶ Ra ONLY ²³⁵ U from 143 keV	186	2535	162	0.12045	0.00770	819	79.3	0.00819	0.00079	0.079	0.00774	0.02899	0.00145	0.0355		158		17.3908	74
¹³⁷ Cs	661.6	0	0	0	0	0	0	0	0	0	0	0.01209	0.00060	0.85		0.0		0	0

Table 3.1.5.4: Bulk radionuclide content for the alumina (Al₂O₃; upper image) industrial product derived from bauxite ore and the red mud (lower image; see text below) after the Bayer process at the Aluminium S.A. industrial plant at Antikyra bay.

NUCLIDE	ENERGY	AREA	±	c/s	±	BKG	±	BKG/s	±	NET c/s	± NET	Efficiency eee	± Efficiency	FY	Corrections	Bq/kg	Total Dose Rate	± Bq/kg	nGy/h
								(100000s)				density 1.7g/cm ³	5%				0 nGy/h		
²³⁴ Th	63	377	67	0.0053	0.0009	465.1	80	0.00465	0.00080	0.00067	0.00124	0.01651	0.00083	0.037		3		5.8254	1
²³⁵ U	143	129	98	0.0018	0.0014	172.7	51.81	0.00173	0.00052	0.00009	0.00148	0.03652	0.00183	0.109	0.72	0.05		1.0658	
²¹⁴ Pb	352	1064	55	0.0150	0.0008	1477	64	0.01477	0.00064	0.00024	0.00101	0.02323	0.00116	0.356		0		0.3495	0
²¹⁴ Bi	609	733	43	0.0103	0.0006	1037	52.7	0.01037	0.00053	-0.00003	0.00080	0.01540	0.00077	0.448		0		0.3347	0
²¹⁴ Bi	1764	165	19	0.0023	0.0003	236	23.6	0.00236	0.00024	-0.00003	0.00036	0.00694	0.00035	0.1531		0		0.9663	0
²²⁸ Ac	911	317	33	0.0045	0.0005	411	39.3	0.00411	0.00039	0.00036	0.00061	0.01139	0.00057	0.29		0		0.5304	0
²⁰⁸ Tl	583	364	38	0.0051	0.0005	564	39.7	0.00564	0.00040	-0.00051	0.00067	0.01591	0.00080	0.307		0		0.3926	0
²³⁴ Pa	1001	65	16.9	0.0009	0.0002	87.9	14.943	0.00088	0.00015	0.00004	0.00028	0.01061	0.00053	0.01021		1		7.4642	0
⁴⁰ K	1461	890	73	0.0126	0.0010	1313	42	0.01313	0.00042	-0.00058	0.00111	0.00799	0.00040	0.1067		-2		3.7500	0
²²⁶ Ra + ²³⁵ U	186	698	71	0.0098	0.0010	819	79.3	0.00819	0.00079	0.00166	0.00128	0.03749	0.00187	0.0355		4		2.7643	
²²⁶ Ra (after Gilmore correction)	186	698	71	0.0098	0.0010	819	79.3	0.00819	0.00079	0.00166	0.00128	0.03749	0.00187	0.0355	0.571	2.04		2.7643	
²²⁶ Ra ONLY ²³⁵ U from ²³⁴ Th	186	698	71	0.0098	0.0010	819	79.3	0.00819	0.00079	0.00056	0.00128	0.03749	0.00187	0.0355		1	Average ²²⁶ Ra	2.7592	1
²²⁶ Ra ONLY ²³⁵ U from ²³⁴ Pa	186	698	71	0.0098	0.0010	819	79.3	0.00819	0.00079	0.00131	0.00128	0.03749	0.00187	0.0355		3	2	2.7621	1
²²⁶ Ra ONLY ²³⁵ U from 143 keV	186	698	71	0.0098	0.0010	819	79.3	0.00819	0.00079	0.00129	0.00128	0.03749	0.00187	0.0355		3		2.7621	1
¹³⁷ Cs	661.6	0	0	0	0	0		0	0	0	0	0.01447	0.00072	0.85		0.0		0	0

NUCLIDE	ENERGY	AREA	±	c/s	±	BKG	±	BKG/s	±	NET c/s	± NET	Efficiency eee	± Efficiency	FY	Corrections	Bq/kg	Total Dose Rate	± Bq/kg	nGy/h
								(100000s)				density 1.7g/cm ³	5%				295 nGy/h		
²³⁴ Th	63	4062	360	0.02589	0.00229	465.1	80	0.00465	0.00080	0.02124	0.00243	0.01965	0.00098	0.037		133		16.6539	62
²³⁵ U	143	1684	136	0.01073	0.00087	172.7	51.81	0.00173	0.00052	0.00901	0.00101	0.04533	0.00227	0.109	0.72	5.99		1.0219	
²¹⁴ Pb	352	53011	305	0.33792	0.00194	1477	64	0.01477	0.00064	0.32315	0.00205	0.02712	0.00136	0.356		153		7.7025	71
²¹⁴ Bi	609	39969	249	0.25478	0.00159	1037	52.7	0.01037	0.00053	0.24441	0.00167	0.01794	0.00090	0.448		139		7.0082	65
²¹⁴ Bi	1764	6991	98	0.04456	0.00062	236	23.6	0.00236	0.00024	0.04220	0.00067	0.00805	0.00040	0.1531		156		8.2053	73
²²⁸ Ac	911	47434	223	0.30237	0.00142	411	39.3	0.00411	0.00039	0.29826	0.00147	0.01324	0.00066	0.29		355		17.8202	221
²⁰⁸ Tl	583	69843	308	0.44521	0.00196	564	39.7	0.00564	0.00040	0.43957	0.00200	0.01854	0.00093	0.307		353		17.7065	220
²³⁴ Pa	1001	738	70	0.00470	0.00045	87.9	14.943	0.00088	0.00015	0.00383	0.00047	0.01233	0.00062	0.01021		139		18.4199	64
⁴⁰ K	1461	3596	90	0.02292	0.00057	1313	42	0.01313	0.00042	0.00979	0.00071	0.00927	0.00046	0.1067		45		3.9838	2
²²⁶ Ra + ²³⁵ U	186	15841	332	0.10098	0.00212	819	79.3	0.00819	0.00079	0.09279	0.00226	0.04387	0.00219	0.0355		272		15.1302	
²²⁶ Ra (after Gilmore correction)	186	15841	332	0.10098	0.00212	819	79.3	0.00819	0.00079	0.09279	0.00226	0.04387	0.00219	0.0355	0.571	155.34		15.1302	
²²⁶ Ra ONLY ²³⁵ U from ²³⁴ Th	186	15841	332	0.10098	0.00212	819	79.3	0.00819	0.00079	0.05851	0.00226	0.04387	0.00219	0.0355		172	Average ²²⁶ Ra	10.8390	80
²²⁶ Ra ONLY ²³⁵ U from ²³⁴ Pa	186	15841	332	0.10098	0.00212	819	79.3	0.00819	0.00079	0.05714	0.00226	0.04387	0.00219	0.0355		168	171	10.6807	78
²²⁶ Ra ONLY ²³⁵ U from 143 keV	186	15841	332	0.10098	0.00212	819	79.3	0.00819	0.00079	0.05968	0.00226	0.04387	0.00219	0.0355		175		10.9745	81
¹³⁷ Cs	661.6	0	0	0	0	0		0	0	0	0	0.01685	0.00084	0.85		0.0		0	0

Table 3.1.5.5: Natural radionuclides (Bq/kg) and total dose rate (nGy/h) of the studied Greek bauxites compared with relevant values from literature.

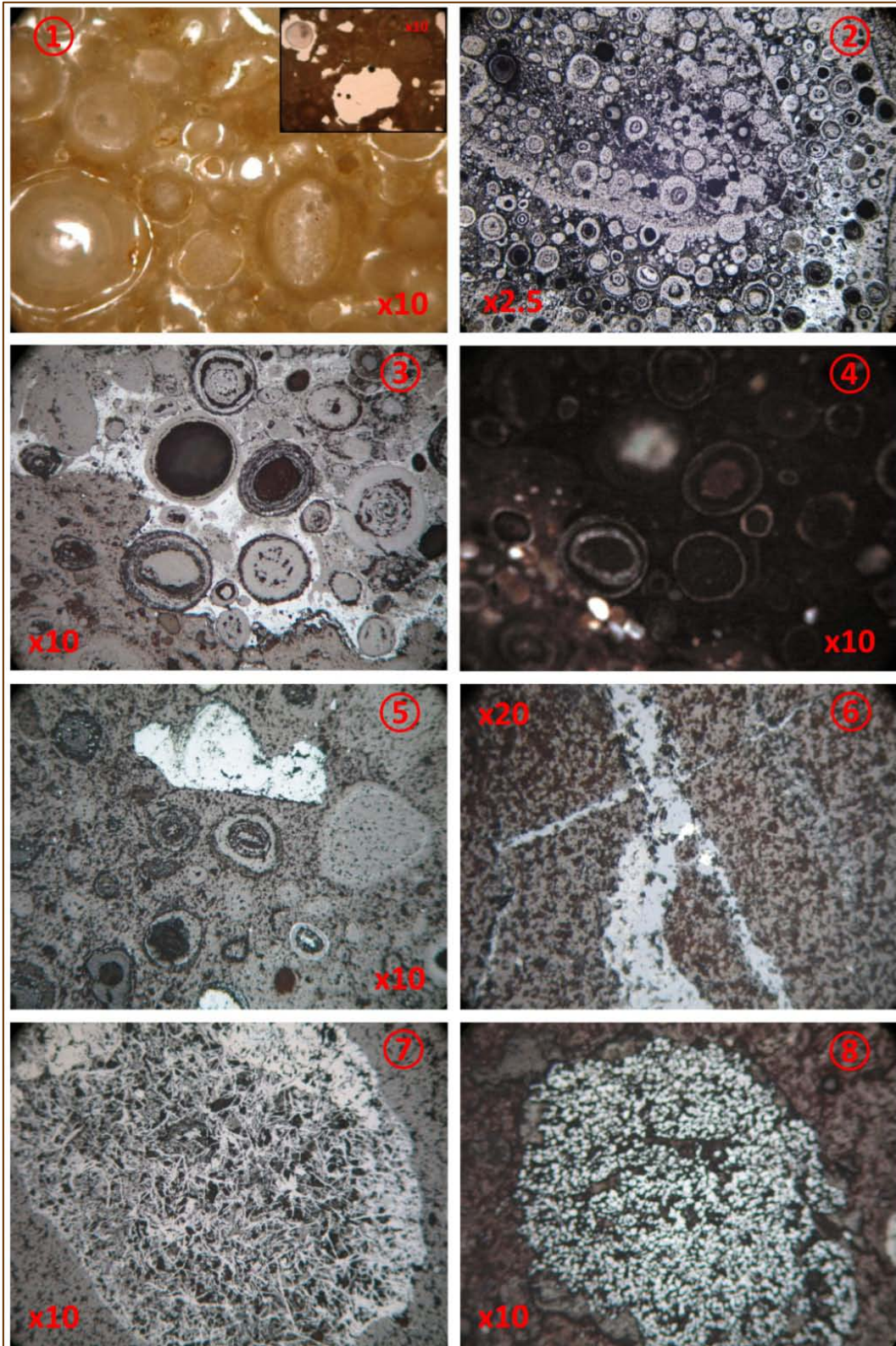
GREEK BAUXITES: Radioactivity (Bq/Kg) & Total Dose Rate (nGy/h)							
Greek bauxites (present study)		^{232}Th	^{238}U	^{226}Ra	^{40}K	^{137}Cs	Total Dose
Sample Code	Sample Description	(due to ^{228}Ac)	(due to ^{234}Th)				Rate
ALM0306_PL1_B1	<i>Fe-rich; Low grade; Diasporic; Red-brown</i>	192	69	138	15	0	174
ALM0306_PL1_B3	<i>Fe-rich; Low grade; Diasporic; Red-brown</i>	184	89	130	57	0	177
ELM0206_DV_B1	<i>Fe-rich; Low grade; Diasporic; Red-brown</i>	179	44	115	15	0	154
SAB0306_ASV	<i>Fe-rich; Low grade; Diasporic; Red-brown</i>	203	42	96	16	0	162
ALM0306_PL1_B2	<i>Fe-rich; Low grade; Boehmitic; Red-brown</i>	159	54	129	60	0	151
ELM0206_KV_B1	<i>Fe-rich; Low grade; Boehmitic; Red-brown</i>	155	27	64	109	0	130
ELM0206_2H1	<i>Fe-rich; Low grade; Boehmitic; Red-brown</i>	161	60	145	108	0	150
SAB0306_SKR	<i>Fe-rich; Low grade; Boehmitic; Red-brown</i>	166	38	83	49	0	137
ALM0306_PL1_BIW	<i>Fe-depleted; High grade; Diasporic; White-grey</i>	229	121	144	17	0	200
ALM0306_PL1_BS2	<i>Fe-depleted; High grade; Diasporic; White-grey</i>	191	118	160	12	0	186
Min – Max Values		155 – 229	27 – 121	64 – 160	17 – 117	0	130 – 200
Average Value		182	66	120	46	0	162
Greek bauxites (previous works)							
Greek bauxites (Papatheodorou et al., 2005)		205 – 226	143 – 248	74 – 150	28		

3.2. Mineralogy and geochemistry of bauxite in microscale

3.2.1. Optical microscopy investigation

The optical microscopic study has shown that the major mineral phases in the investigated bauxite samples from the Parnassos-Ghiona deposits are the two common AlOOH polymorphs diaspore / α -AlOOH (see image ① of **Figure 3.2.1.1**) and boehmite / γ -AlOOH (see image ⑧ of **Figure 3.2.1.1**), the typical Fe oxide (e.g., hematite; see images ②-⑦ of **Figure 3.2.1.1**) and oxyhydroxide (goethite; see image ⑦ of **Figure 3.2.1.1**), and the TiO₂ polymorph anatase (see inset of image ① of **Figure 3.2.1.1**), in accordance to bulk characterization. Iron sulphides, such as pyrite, have also been detected (see image ⑥ of **Figure 3.2.1.1**). Patches and veins of metallic minerals consisting of Fe oxides and few isolated sulfides (lighter areas; see image ⑥ of **Figure 3.2.1.1**) are included in diasporic matrix (darker areas containing also pisoliths). Most of the characteristic bauxitic pisoliths contain mainly diaspore together with finely dispersed hematite. Under the light of optical microscopic study, hematite can be present as smaller (see image ④ of **Figure 3.2.1.1**) or larger crystals (see image ⑤ of **Figure 3.2.1.1**) crystals close to pisoliths rims, and also as dispersed aggregates into (see image ③ of **Figure 3.2.1.1**) and nearby (see image ⑧ of **Figure 3.2.1.1**) the diasporic/boehmitic pisoliths.

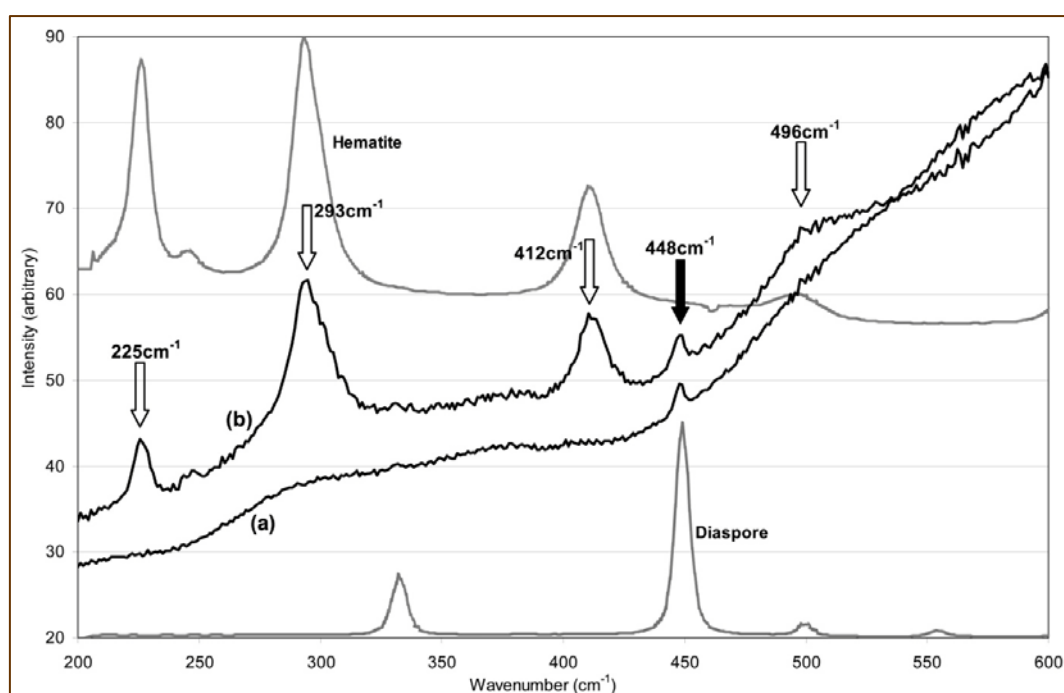
Figure 3.2.1.1: Representative microscopic images (x10 and x20) from Fe-depleted diasporic (ELM0206_SK_B1a: ①; inset image: ALM0306_PL1_BS2) and typical Fe-rich diasporic (ALM0306_PL1_B1: ② -④; ELM0206_DV_B1: ⑤-⑦) as well as Fe-rich boehmitic (ALM0306_PL1_B2⑧) bauxite samples using transmitted and reflected light.



3.2.2. AlOOH polymorph identification (Laser μ -Raman)

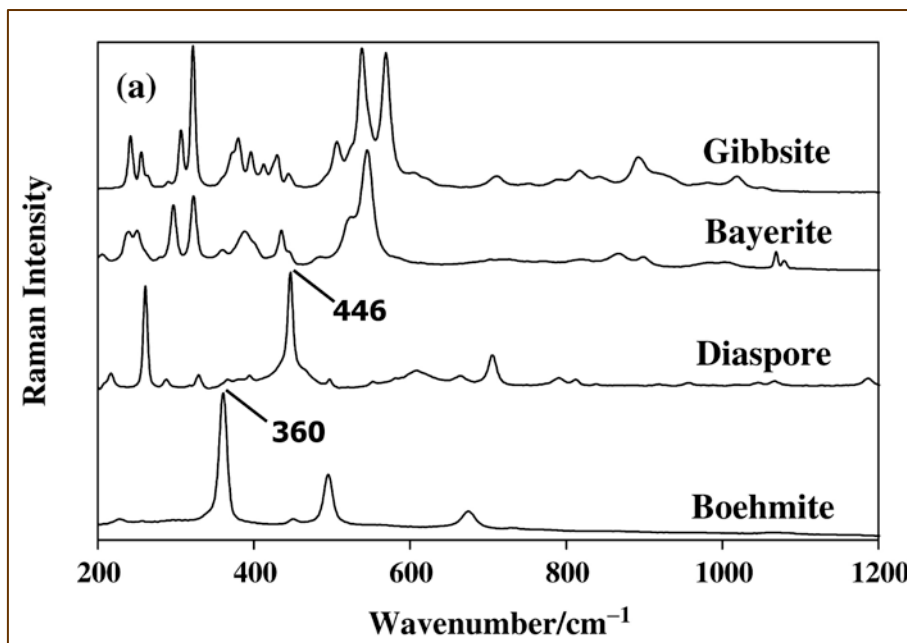
Conventional chemical methods are not recommended to characterize AlOOH polymorphs in bauxite samples. Thus powder XRD is fundamentally used in laboratory conditions. However it is rather difficult to use XRD for *in-situ* measurements in the field and in underground mining areas because portable XRD equipments are not greatly commercialized up to now. Therefore, it is important to suggest convenient spectroscopic methods, such as Laser μ -Raman, which can be easily used for phase determination in any case. The instrument is a bench system capable of confocal imaging with high spectral and spatial resolution. Representative Laser μ -Raman spectra of diasporic bauxite samples investigated during the present dissertation, both Fe-depleted (high grade) and Fe-rich (low grade), together with standard Raman spectra from the Mineral Spectroscopy Server of CalTech ([© Prof. G. Rossman, 2006](#)), are shown in **Figure 3.2.2.1**. It should be noted that the

Figure 3.2.2.1: Representative Laser μ -Raman spectra of diasporic bauxite samples in the low-wavenumber region (**a**: Fe-depleted and **b**: Fe-rich sample). The lower spectrum corresponds to the Mineral Spectroscopy Server diaspore and the upper one to a hematite standard.



spectra were obtained by focusing the laser beam on the diasporic matrix away from microscopically detectable metallic minerals including anatase grains. The diasporic bands are observed in the low-wavenumber region, namely between 200 cm^{-1} and 600 cm^{-1} . The most prominent are the 705 cm^{-1} , 446 cm^{-1} and 260 cm^{-1} , which are assigned to symmetric stretching modes (Ruan et al, 2001; Ruan et al., 2002). In the Fe-depleted diasporic bauxite samples the main $\alpha\text{-AlOOH}$ band appears at 448 cm^{-1} (black arrow in **Figure 3.2.2.2**), which is assigned to Al-O-Al stretching bend, and it is in good agreement with the results from the literature (Ruan et al., 2001; Ruan et al., 2002; see **Figure 3.2.2.2**). A number of strong peaks

Figure 3.2.2.2: Raman spectra of different AlOOH polymorphs (after Ruan et al., 2001). It is clearly marked the difference of the diasporic Raman band at 446 cm^{-1} from the one of the boehmite at 360 cm^{-1} , at the low-wavenumber region between 250 cm^{-1} and 600 cm^{-1} .

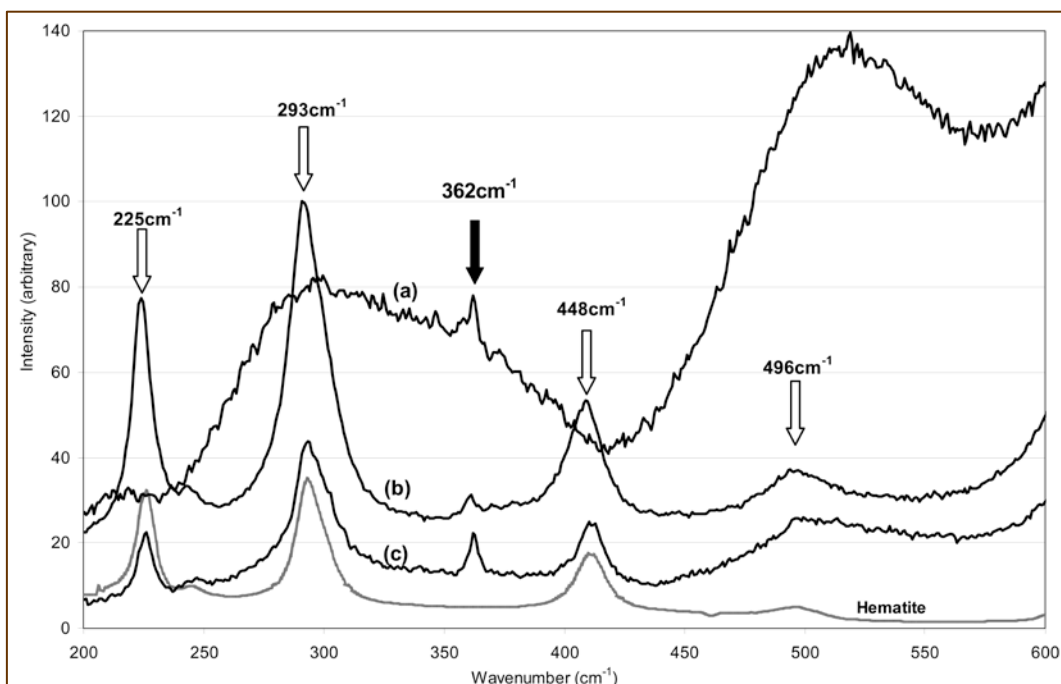


are also observed in the band range between 1000 and 2000 cm^{-1} which are attributed to fluorescence from the 633 nm He-Ne laser. Fluorescence peaks are wavelength-dependent and they should disappear when another laser is used, such as a Nd:YAG laser at 1064 nm . In synthetic diaspore a number of broad bands are observed with the 1064 nm laser in the $2800\text{-}3700\text{ cm}^{-1}$ region, attributed to the $\nu(\text{OH})$ stretching. These bands were not observed in

our spectra. The Fe-rich bauxite samples along with diaspore contain hematite (white arrows in **Figure 3.2.2.1**) with Raman bands at 612 cm^{-1} , 496 cm^{-1} , 412 cm^{-1} , 293 cm^{-1} and 225 cm^{-1} (Faria et al., 1997; Bersani et al., 1999; Chamritski & Burns, 2005; Zoppi et al., 2005; Zoppi et al., 2006).

Representative Laser μ -Raman spectra of boehmitic samples (Fe-rich bauxites) are shown in the low-energy region of **Figure 3.2.2.3**. According to the literature, the more intense boehmite peaks at the low-wavenumber region are at 674 cm^{-1} , 495 cm^{-1} and 360 cm^{-1} and they correspond to the hydroxyl translational modes. In our samples, we observe the 362 cm^{-1} band (Ruan et al., 2001; Ruan et al. 2002; see **Figure 3.2.2.3**). The spectrum (a) from **Figure 3.2.2.3** corresponds to the boehmitic matrix of the sample, at an area where metallic minerals, such as rounded hematite aggregates are not optically visible. This band (black arrow in **Figure 3.2.2.3**) is observed between the 412 cm^{-1} and 293 cm^{-1} hematite bands and it could be used as a rule of thumb to easily distinguish it from the diasporic peak, which is observed outside these hematite peaks (Faria et al., 1997; Bersani et al., 1999; Chamritski & Burns, 2005; Zoppi et al., 2005; Zoppi et al., 2006).

Figure 3.2.2.3: Representative Laser μ -Raman spectra of boehmitic bauxite samples in the low-wavenumber region (a, b, c: Fe-rich bauxites). The lower spectrum corresponds to the Mineral Spectroscopy Server hematite.



At this point one could suggest that the hematite Raman bands differ evidently to that of goethite, which may also be present in Fe-rich bauxites (either diasporic or boehmitic). In this case, the AlOOH polymorph bands (either at 448 cm^{-1} or at 362 cm^{-1}) are most probably expected to be distinguishable at the opposite sides of the main goethite band around 385 cm^{-1} (Faria et al., 1997; Bersani et al., 1999). Furthermore, it is also expected that diaspore and boehmite low-wavenumber Raman bands will be apparent if kaolinite is present, under the laser beam spot, inasmuch the main -very intense- kaolinite band appears at 140 cm^{-1} (Johnston et al., 1984; Frost et al., 1993).

In conclusion, the Laser μ -Raman spectroscopy could be applied for the fast determination of the AlOOH polymorphs and, as a consequence, the “type” of bauxite of the Parnassos-Ghiona active mining area (central Greece). In the case of the Fe-depleted (high-grade) diasporic bauxite, there is a clear diaspore Raman band at 448 cm^{-1} to be used as the characteristic band, while in the case of the typical red-brown diasporic bauxite the same band is accompanied by the unavoidable bands of hematite (Table 3.2.2.1). Besides, for the

Table 3.2.2.1: Summary of the Laser μ -Raman data.

	Raman bands (cm^{-1})	
	AlOOH polymorphs	Hematite ($\alpha\text{-Fe}_2\text{O}_3$)
Diasporic Type		
Fe-depleted bauxites	448	-
Fe-rich bauxites	448	412, 293, 225
Boehmitic Type		
Fe-rich bauxites	362	612, 412, 293, 225

Fe-rich boehmitic bauxite, the main Raman band of boehmite appears at 362 cm^{-1} , between two major hematite bands. It is, therefore, demonstrated that both diasporic and boehmitic bauxites can easily be characterized by recording Raman spectra in the $250\text{ cm}^{-1} - 600\text{ cm}^{-1}$ region. In this low-wavenumber region the bands of the AlOOH polymorphs do not interfere with bands from other bauxite minerals. A portable Raman system with a CCD acquisition

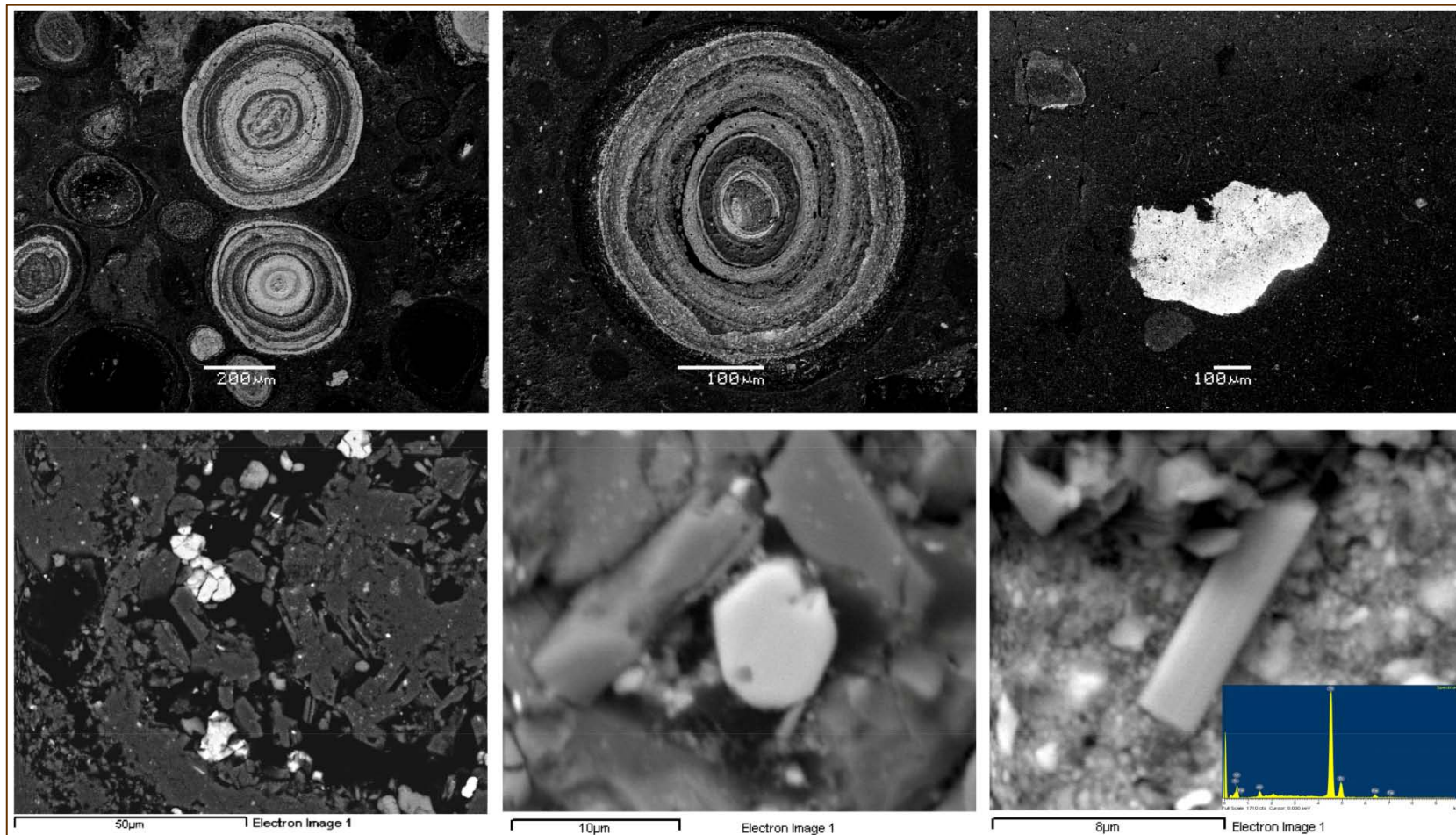
camera and with a laser operating at the wavelength of 1064nm could be used to rapidly acquire the narrow spectra range between 250cm^{-1} and 600cm^{-1} . The He-Ne laser with a wavelength of 633nm introduces significant fluorescence which might suppress the Raman peaks and make them invisible. However, it still can be used when the CCD is centred to cover the low wavenumber region but it may require longer integration times. The use of a powder XRD or of another time-consuming technique is not necessary in order to distinguish the type of bauxite (diasporic or boehmitic). This could be particularly useful in characterising similar in appearance samples, such as the massive red-brown samples (e.g., SAB0306_ASV and SAB0306_SKR) which could be of diasporic or boehmitic type. Future work could employ direct tests on site with a portable Raman system that has the above characteristics. Furthermore, one could proceed into calibrating a portable system to acquire quantitative or semi-quantitative information for precise quality assessment during production.

3.2.3. Chemical composition and element distribution and speciation in microscale (SEM-EDS/WDS, LA-ICP-MS, SR μ -XRF, μ -XAFS)

The SEM-EDS/WDS investigation proved the optical microscopy and spectroscopic observations, indicating that the major phases are Al-oxyhydroxides (diaspore/boehmite), Fe-oxides (mainly hematite), and Ti-oxides dispersed into the diasporic matrix (**Figure 3.2.3.1**). Remarkable minor quantities of Fe and Ti are always detectable in this diasporic matrix (see text below).

Furthermore, detailed SEM-EDS study on diaspore microcrystals revealed that they contain measurable quantities of Fe and Cr (**Table 3.2.3.1**) implying a novel low-T natural Fe-Cr-AlOOH. This is supported by Al, Cr, and Fe linescans and Fe/Al variations, showing rather homogeneous Cr and Fe distribution in microscale and also positive correlation of Fe and Al (**Figure 3.2.3.2**). Occasionally, the Fe contents are different in between the analyzed regions within a diaspore nodule. As shown in the **Figure 3.2.3.2**, the difference of Fe contents of 40 - 50 % at maximum is observed between their analyzed points. These observations suggest that though we propose the possibility of the presence of Fe in the structure of diaspore,

Figure 3.2.3.1: SEM-EDS data for major mineral phases into the studied bauxites. *Upper-left /-right images:* pisoliths containing AlOOH microcrystals with Fe, and Ti detectable quantities; *upper-right image:* hematite crystal; *lower images:* various usually fragmented anatase grains into diasporic matrix with Fe, and Ti detectable quantities (the EDS spectrum indicating only Ti is included in anatase).



some Fe portion would exist in the form of Fe *mineral nanoparticles* and/or Fe *nanominerals*. To meet this need, further rational microscopic study in nanoscale (FEG TEM-EDS & EELS; see text below), was performed to examine the above preliminary findings.

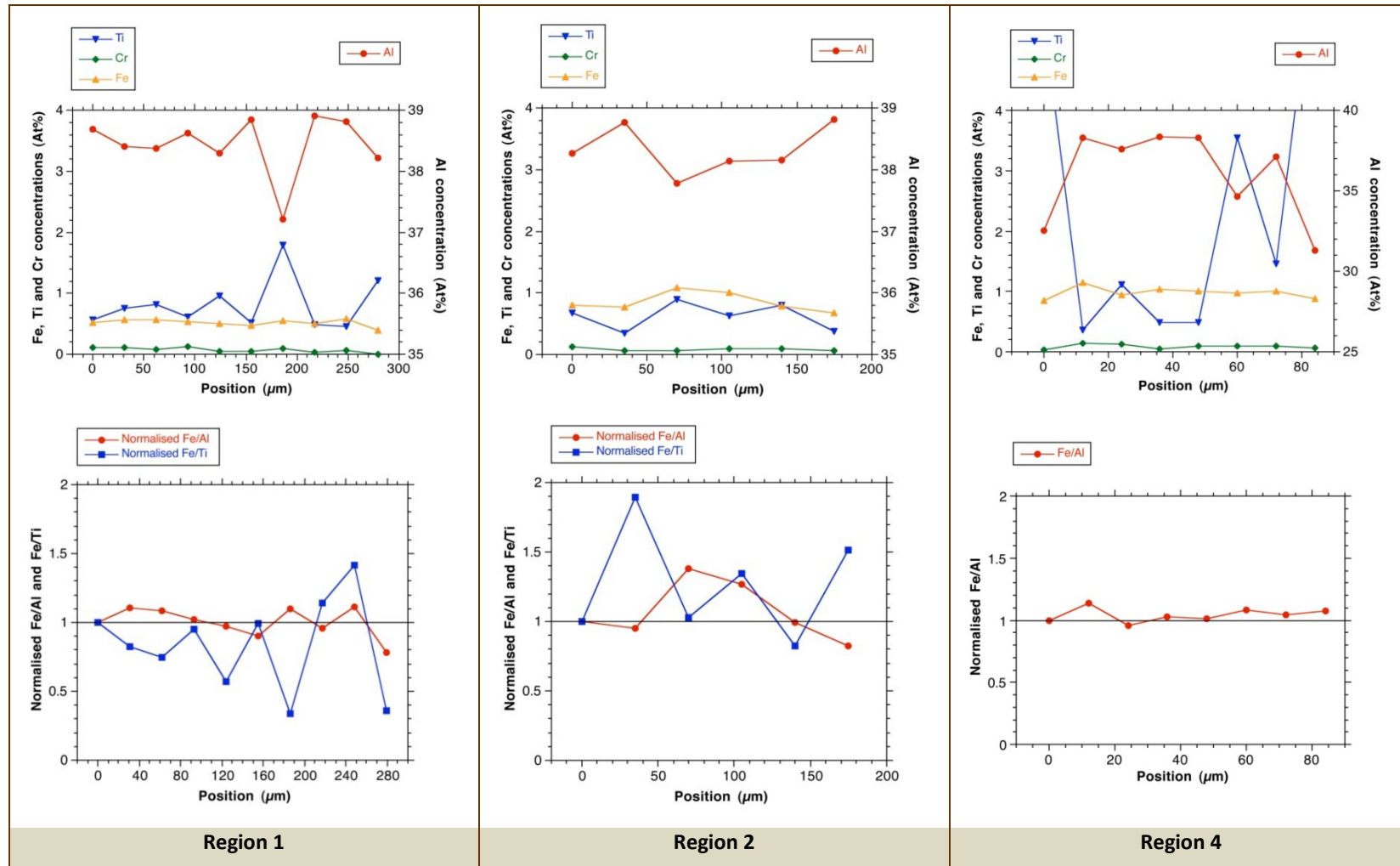
As it is mentioned above, Ti is inhomogeneously dispersed into the diaspore matrix, resulting always in a negative relationship to Al, and trivial Fe/Ti ratios (**Figure 3.2.3.2**). This can be attributed to occluded Ti minerals in microscale (TiO₂ polymorphs) or even Ti *mineral nanoparticles* or *nanominerals*, rather than to a distinct Fe-Cr-Ti-AlOOH phase. Thus, there is no particular relationship between the Fe and Ti contents, giving evidence for the absence of Fe-Ti oxides, and the presence of solely TiO₂ polymorphs which normally do not contain Fe.

Table 3.2.3.1: Chemical composition in microscale (SEM-EDS/WDS) of diaspore nodules in the Fe-depleted diasporic bauxite from Parnassos-Ghiona mining area (see **Figure 3.2.3.2**).

	Al (at%)	Fe (at%)	Ti (at%)	Cr (at%)	O (at%)
Region 1 (10)	38.44	0.52	0.82	0.06	60.16
Region 2 (6)	38.32	0.86	0.62	0.09	60.12
Region 3 (2)	37.12	1.32	1.21	0.12	60.24
Region 4 (8)	36.03	0.98	2.42	0.09	60.49
Region 5 (3)	37.87	1.09	0.76	0.13	60.15
Region 6 (5)	37.21	1.16	1.27	0.11	60.25
Region 7 (3)	38.34	1.02	0.46	0.09	60.09

The number in brackets shows analyzed data points and each concentration was obtained by averaging them.

Figure 3.2.3.2: SEM-WDS linescan analyses for Al, Fe, Ti, and Cr, in selected regions of diaspore nodules, including variation of normalized Fe/Al and Fe/Ti as a function of position.



In contrast to the latter, in some cases, Fe-Ti-oxides (predominantly determined as ilmenite), intergrown with Fe-oxides (hematite) can be rarely confirmed by SEM-EDS (**Figure 3.2.3.3**). A more careful investigation revealed the presence of detrital (clastic) zircons and chromites (**Figures 3.2.3.4 and 3.2.3.5**).

Figure 3.2.3.3: *Upper-left image:* SEM-EDS of Fe-Ti-oxide laths (lighter areas) intergrown with Fe-oxides (less light areas) into diaspore matrix with detectable amounts of Fe, Ti, and Si (darker areas); *Upper-right image:* Fe-Ti-oxide laths (darker areas) intergrown with Fe-oxides (lighter areas); *Lower-left image:* Fe-Ti-oxide laths (less light areas) intergrown with Fe-oxides (lighter areas) into diaspore matrix with detectable amounts of Fe, Ti, and Si (darker areas). *Lower-right image:* Zoom of the lower-left image. The measured amounts of Si in the diasporic matrix could be attributed to the presence of kaolin-group mineral phases.

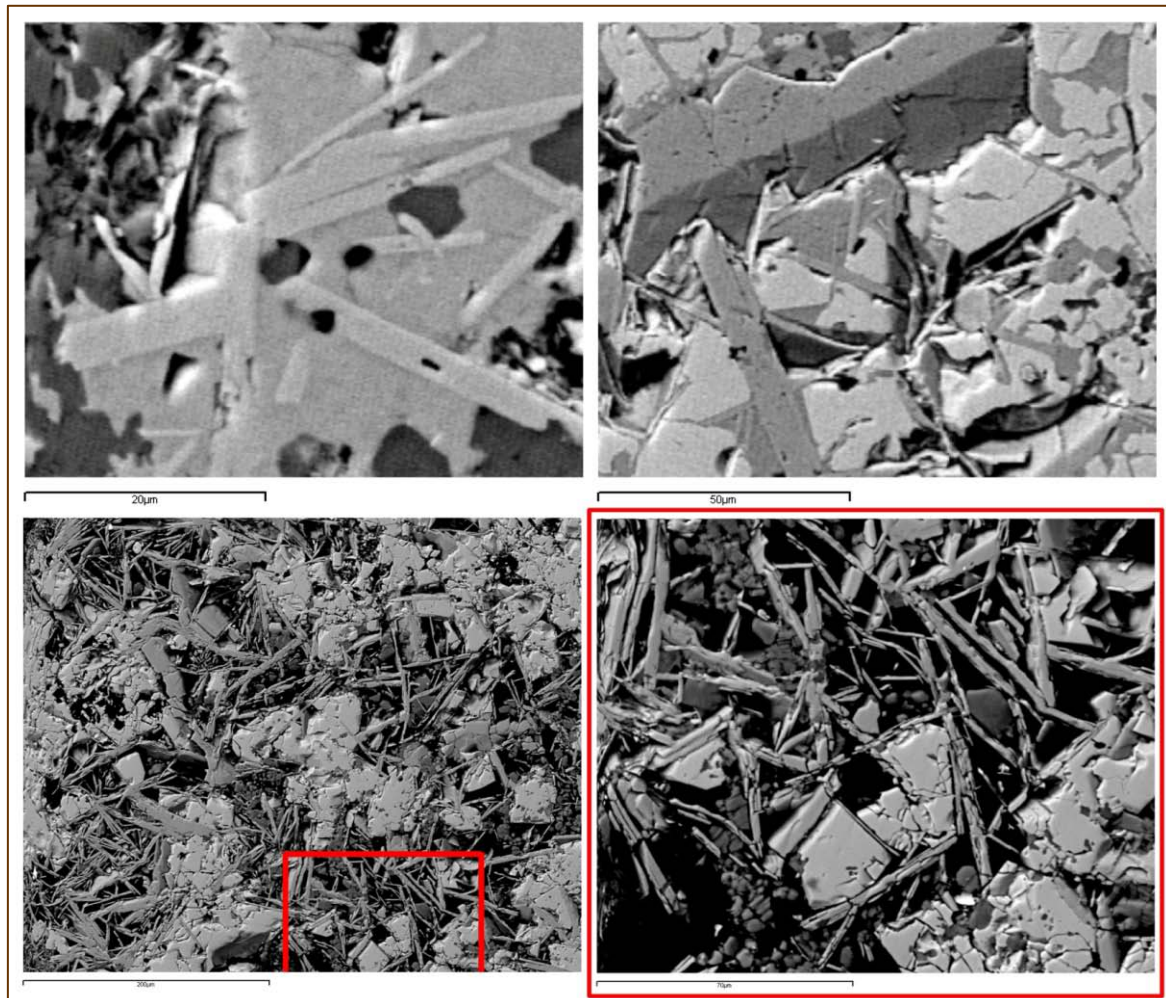


Figure 3.2.3.4: SEM-EDS data for minor (detrital) mineral phases in polished sections of bauxites (upper images: chromites; lower images: zircons). Abbreviations (Whitney & Evans, 2010): “dsp” for diaspor; “chr” for chromite; “zrn” for zircon.

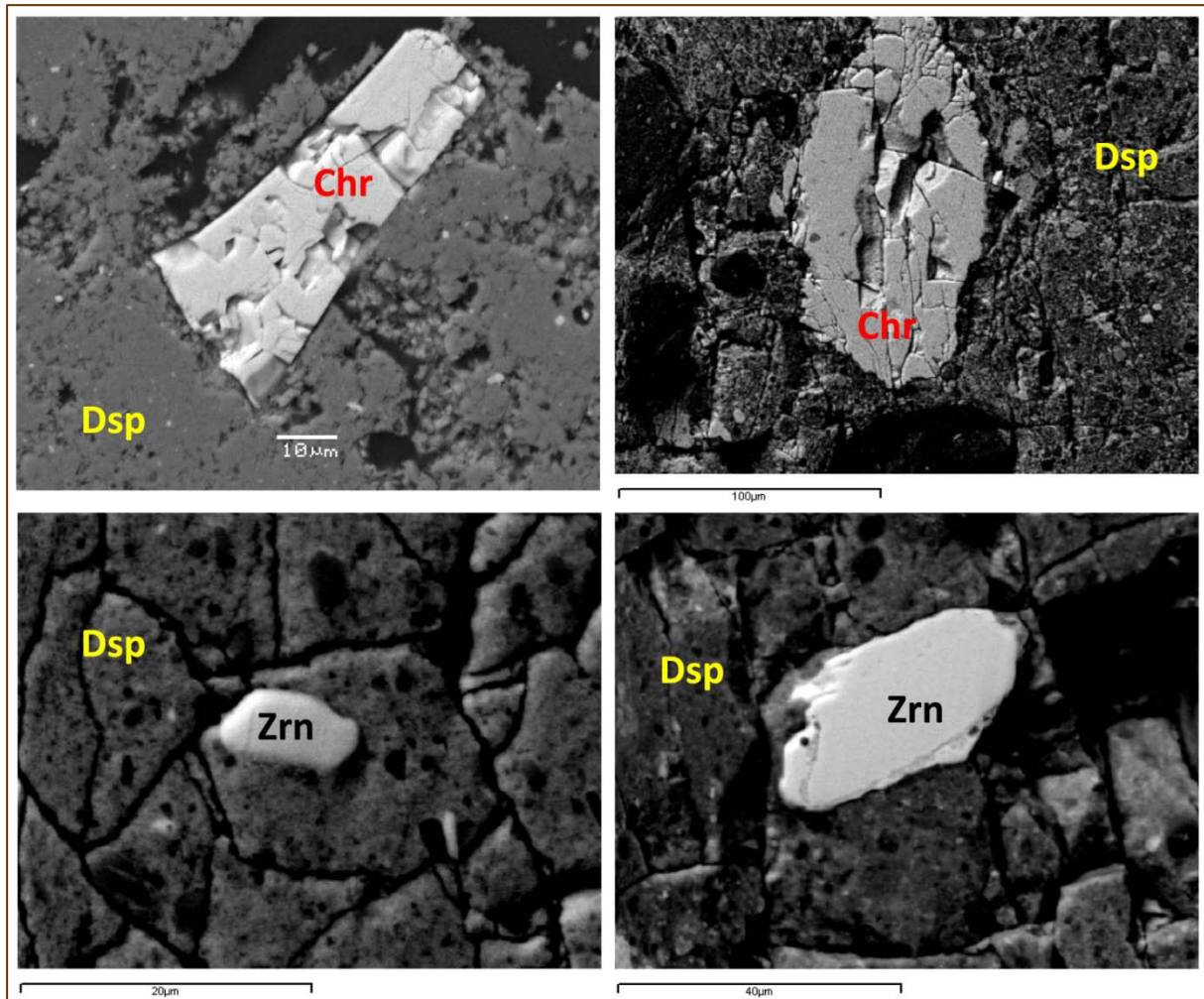
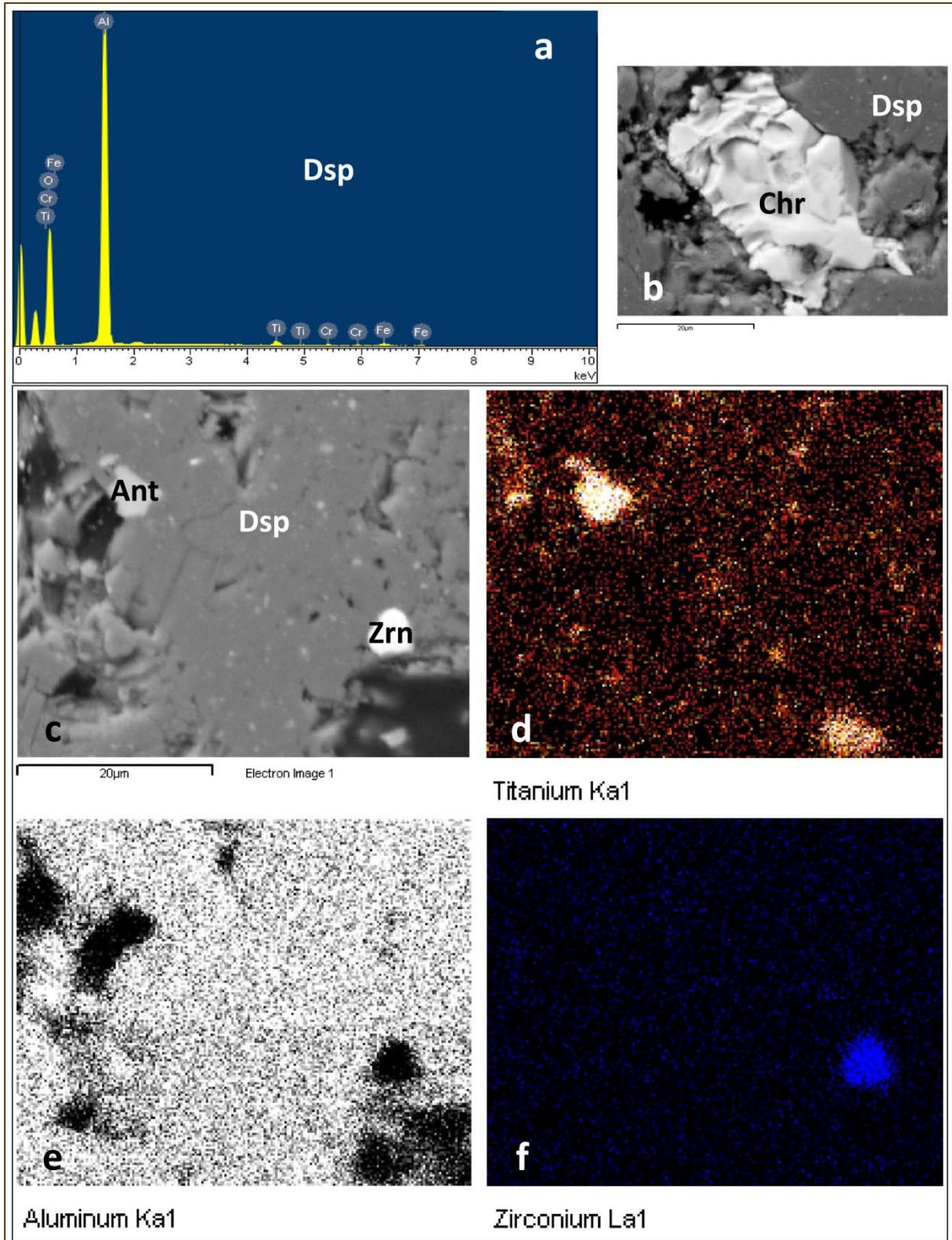


Figure 3.2.3.5: SEM-EDS/WDS data (**a**: X-ray spectrum, **b, c**: BSE images, and **d-f**: elemental maps) for a representative Fe-depleted diasporic karst-type bauxite from Parnassos-Ghiona mining area. Abbreviations (Whitney & Evans, 2010): “dsp” for diaspore; “ant” for anatase; “zrn” for zircon; “chr” for chromite.



The detrital chromite micro-grains appear fractured, with several cracks and fissures (highly cataclastic) and therefore, the precise elucidation of their chemical composition in microscale by SEM-EDS/WDS is rather difficult. In points where the polished surface of the crystals is appropriate for microanalyses, a set of data were collected for further evaluation. The overall suggestion is that part of the chromite grains are to some extent altered towards Fe-chromites, whereas there are also rather unaltered grains which fall in the fields of Al-chromite and Cr-spinel derived from alpine-type peridotites (**Figures 3.2.3.5 and 3.2.3.6**). In general, it is rather difficult to conclude regarding the exact parent ophiolites, though some grains lie close to the Othrys field. The observed alteration, if it is not exclusively related to primary higher P-T metamorphic processes (i.e., serpentinization) it can be due to transportation from parent peridotites, or due to in-situ lateritic weathering in tropical climate conditions, or perhaps due to further diagenetic (in fact low-grade metamorphism) and later epigenetic processes. A combination of all above geochemical processes could also be very likely. Similar altered detrital chromites, which however fall into the field of typical Fe-chromite, have been reported in the case of Greek laterites ([Michailidis et al., 1984](#); [Valeton et al., 1987](#); [Michailidis, 1990](#); [Eliopoulos & Economou-Eliopoulos, 2000](#)).

Figure 3.2.3.5:
Ternary plot of the cations Cr, Al, and Fe³⁺ contents of the chromites from the Parnassos-Ghiona bauxites ([Stevens, 1944](#)).

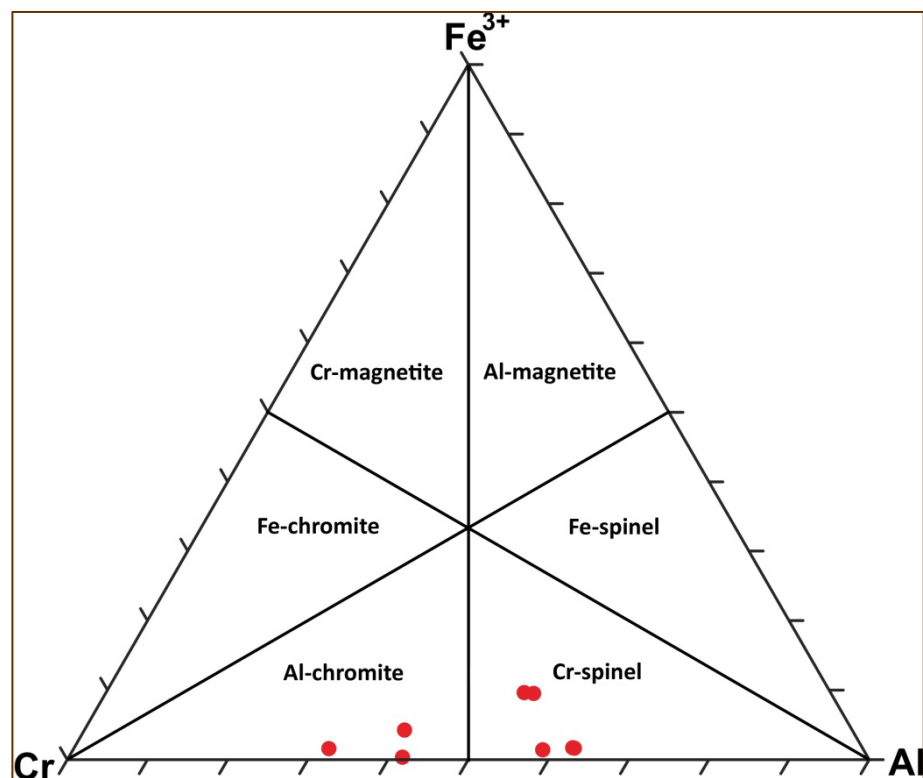
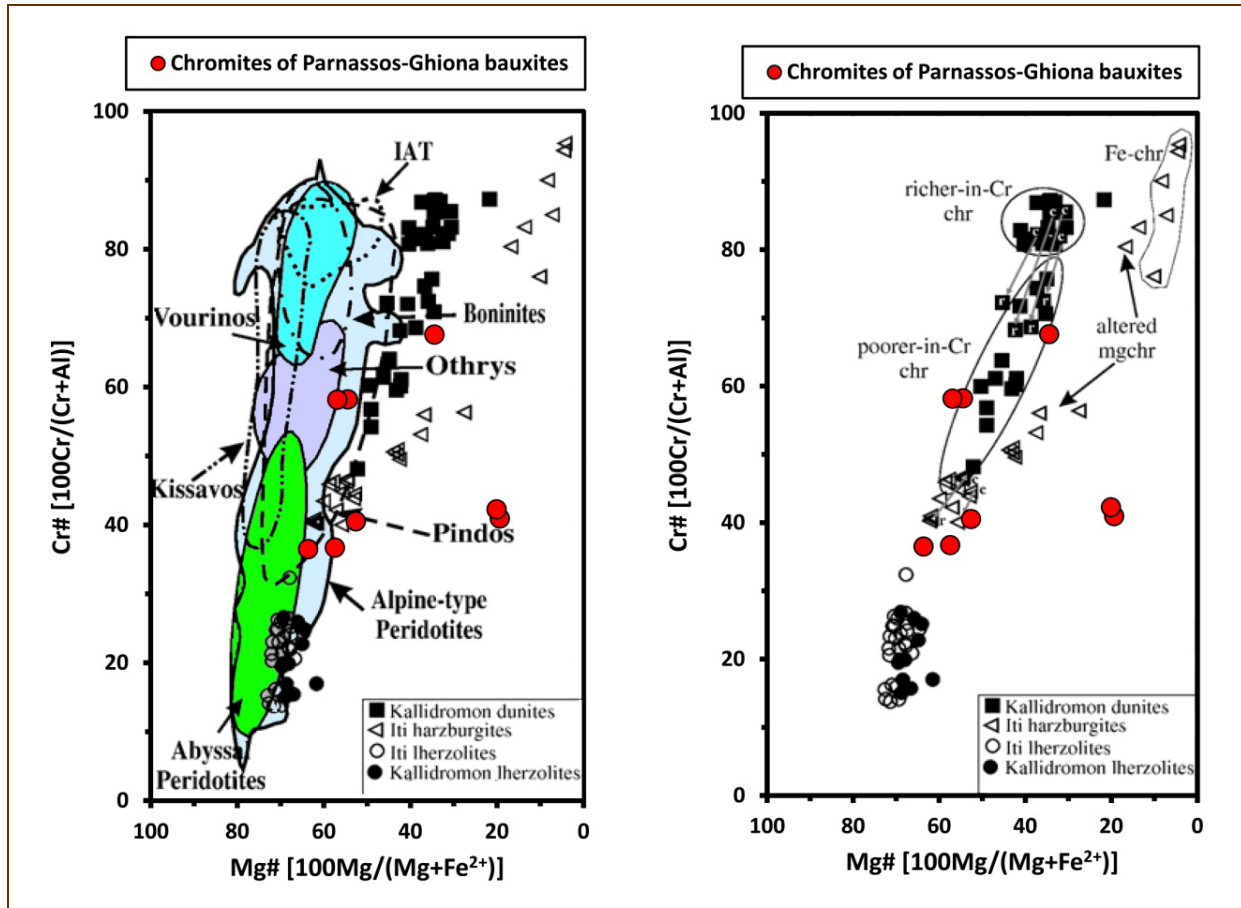
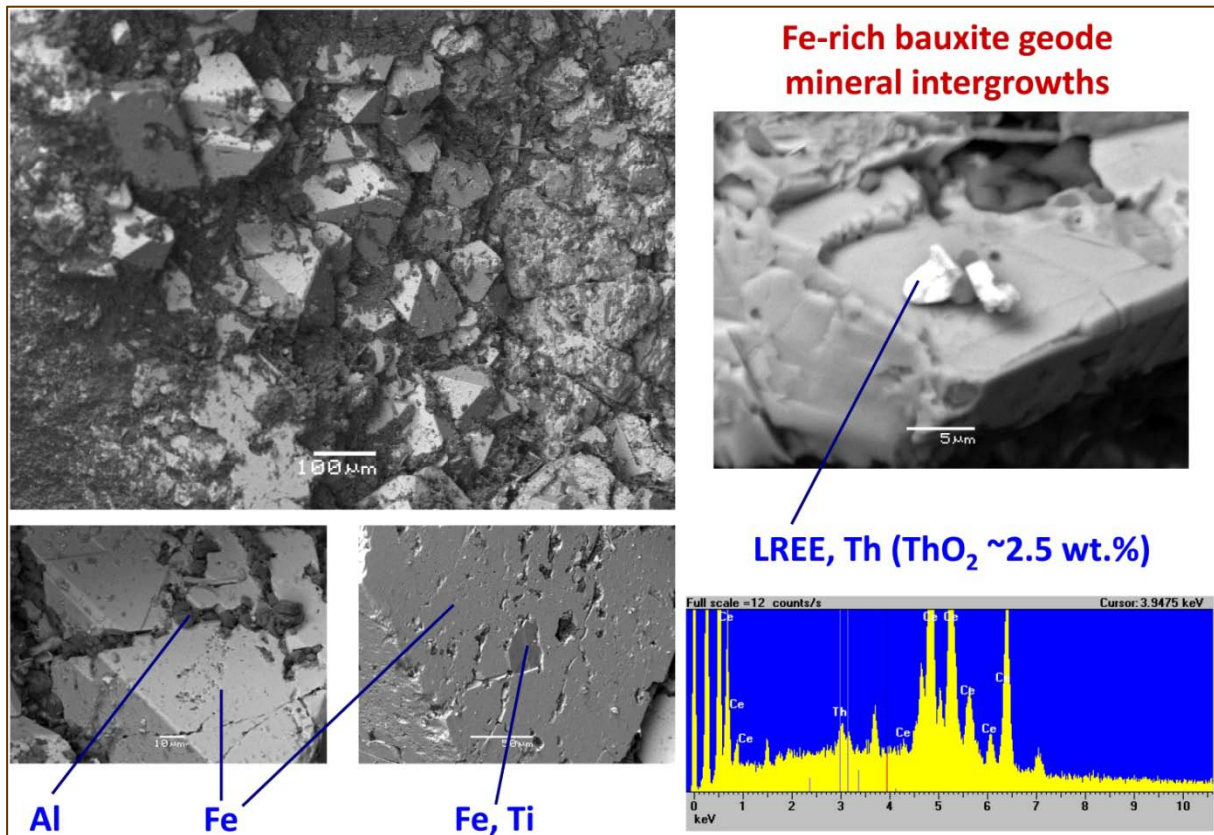


Figure 3.2.3.6: Chemical composition, in terms of Cr# [100 Cr/ (Cr+Al)] against Mg# [100 Mg/(Mg+Fe²⁺)], of detrital chromites occurring in Parnassos-Ghiona bauxites and comparison with spinels in ophiolitic rocks from Greece and the globe (after Karipi et al., 2007 and references therein).



The SEM-EDS investigation, aiming to detection of lanthanide (REE) and actinide (Th, U) minerals, prior to LA-ICP-MS studies (see text below), revealed the significant concentrations of Th into REE-fluorocarbonate minerals (mostly bastnäsite-/parisite-group; Grice et al., 2007; Maksimović & Pantó, 1996) with up to 2.5 wt.% ThO₂ (Figures 3.2.3.7 – 3.2.3.9). Previous microscopic studies about REE-phases in Greek bauxites have not reported the presence of Th (Ochsenkühn-Petropoulou & Ochsenkühn, 1995), while Th-containing Y-phosphates (Laskou & Andreou, 2003) have not been clearly approved in the frame of the present study. It is noteworthy that the obtained SEM-EDS results concerning the existence of Th in LREE-minerals in Greek bauxites are presented for the first time in the literature. It should also be emphasized that Th was not detected in AlOOH matrix or in any other Fe-, Ti-

Figure 3.2.3.7: SEM-EDS of Th-containing LREE minerals overgrown on Fe-oxide octahedral crystals into geode of Fe-rich bauxite.



and Fe-Ti-phase. Besides, there are few isolated Ce-Al-hydroxyphosphate grains corresponding to florencite (**Figure 3.2.3.10**). Finally, there are REE-phases coexisting with detrital Fe-Ni-sulfides and Co-Fe-Ni-sulfides and particularly pentlandite and Co-pentlandite (**Figure 3.2.3.11**). It should be noted that this is the first time in literature that such Ni-phases are demonstrated with regard to Parnassos-Ghiona bauxites.

Figure 3.2.3.8: SEM-EDS data for REE fluorocarbonate minerals $(\text{REE})^{3+}\text{Ca}^{2+}\text{F}(\text{CO}_3)_2$.

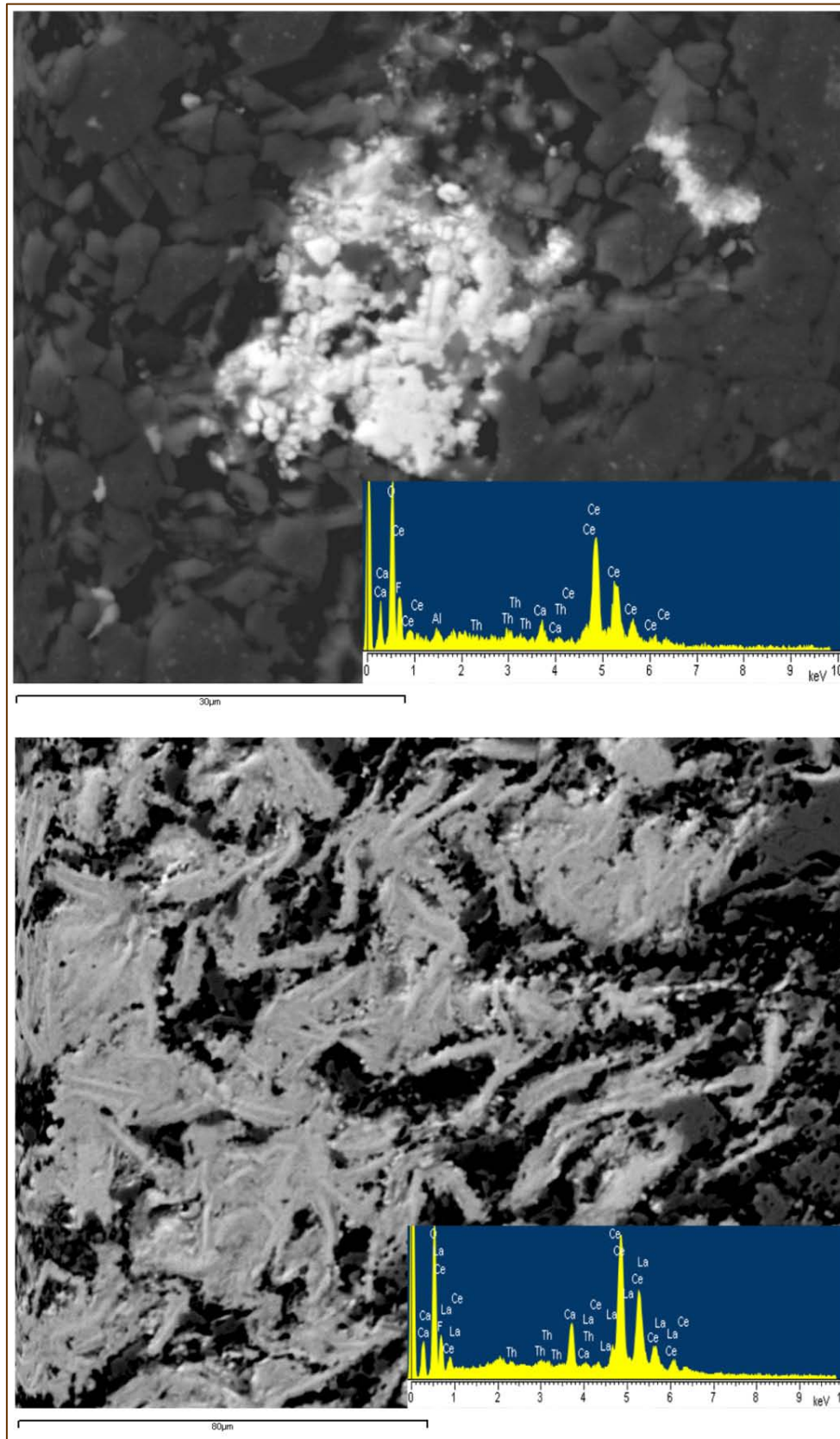


Figure 3.2.3.9: SEM-EDS elemental maps concerning REE minerals of Parnassos-Ghiona bauxites with Th up to 2.5 wt.%.

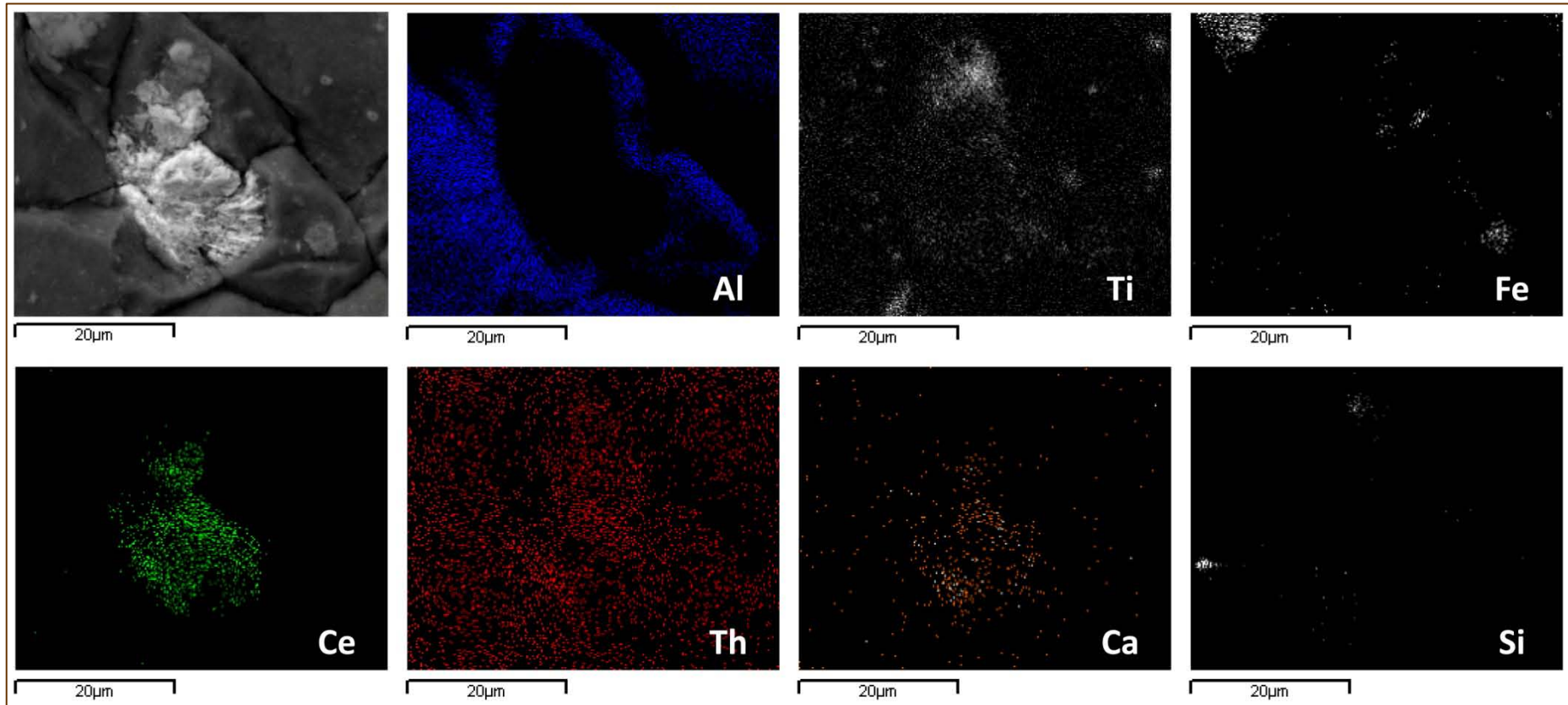


Figure 3.2.3.9: continued.

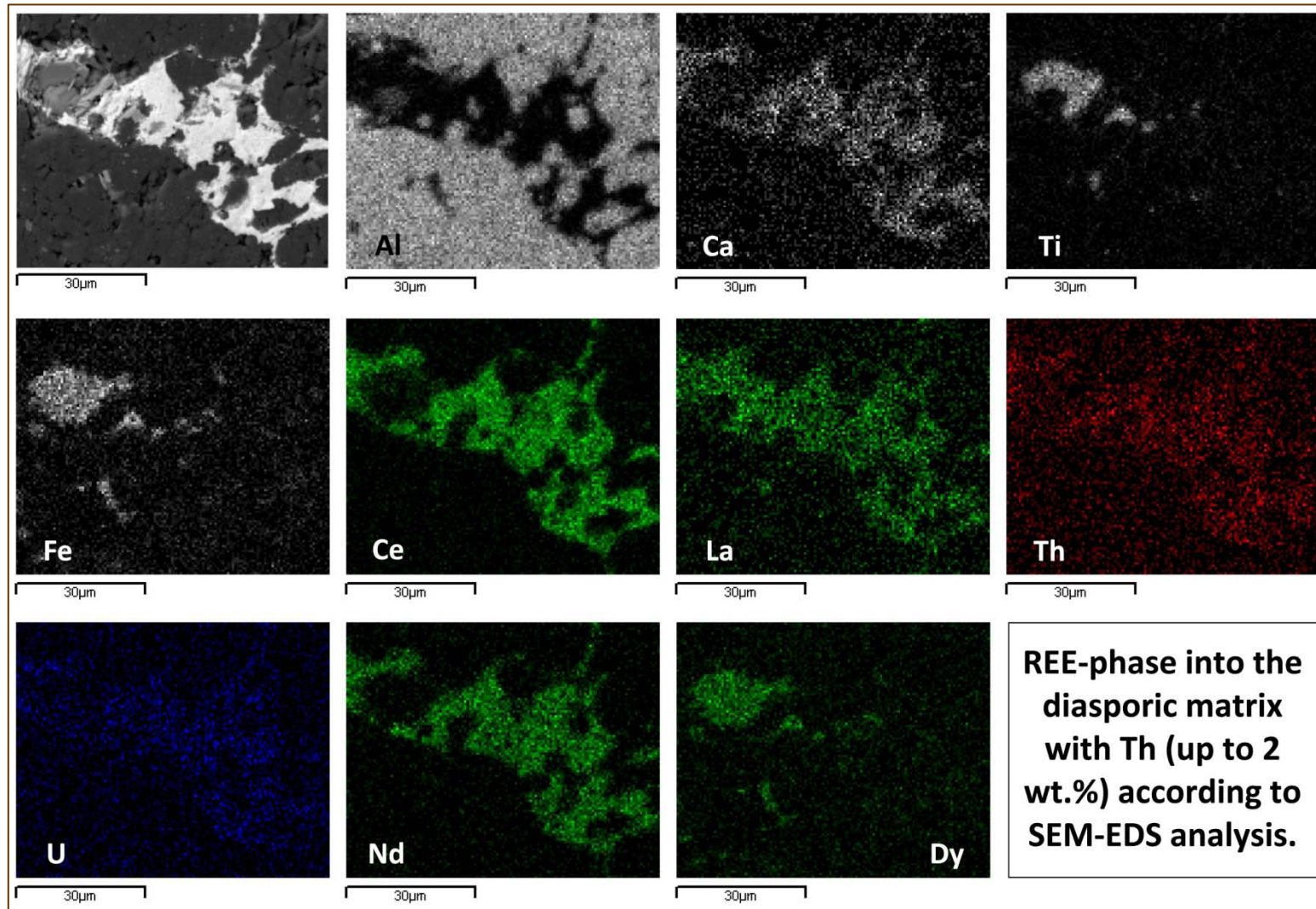


Figure 3.2.3.9: continued.

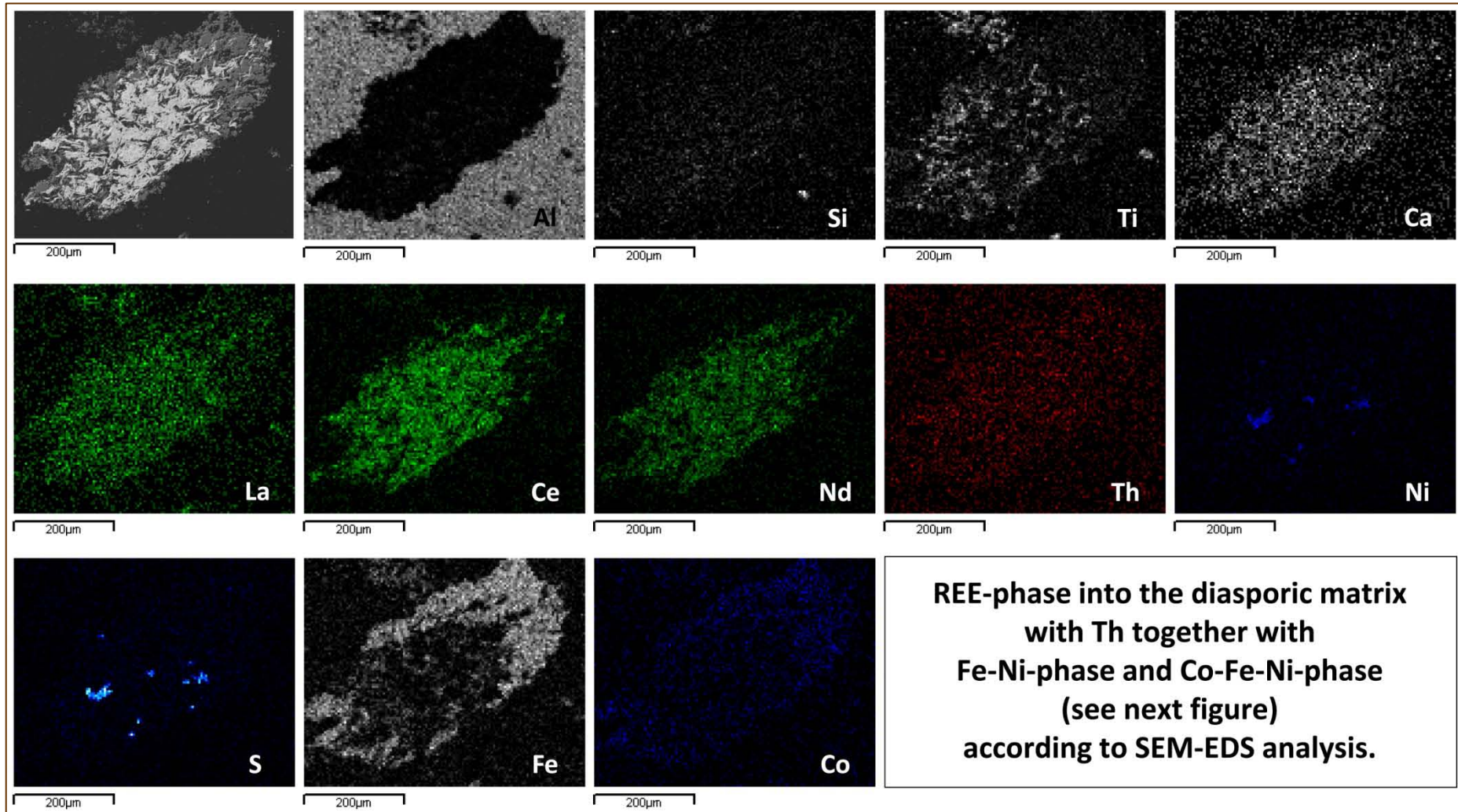


Figure 3.2.3.9: continued.

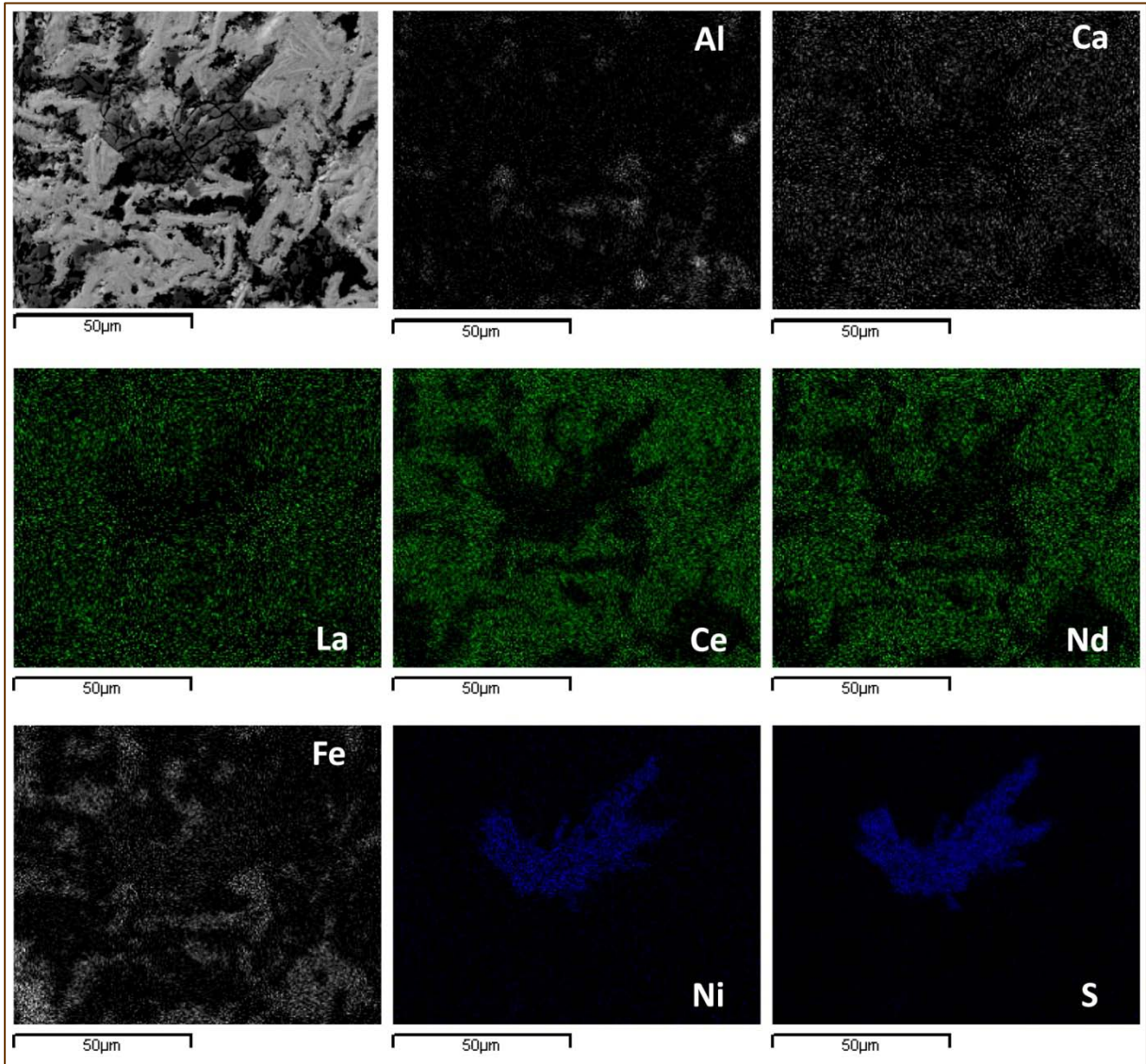


Figure 3.2.3.9: continued.

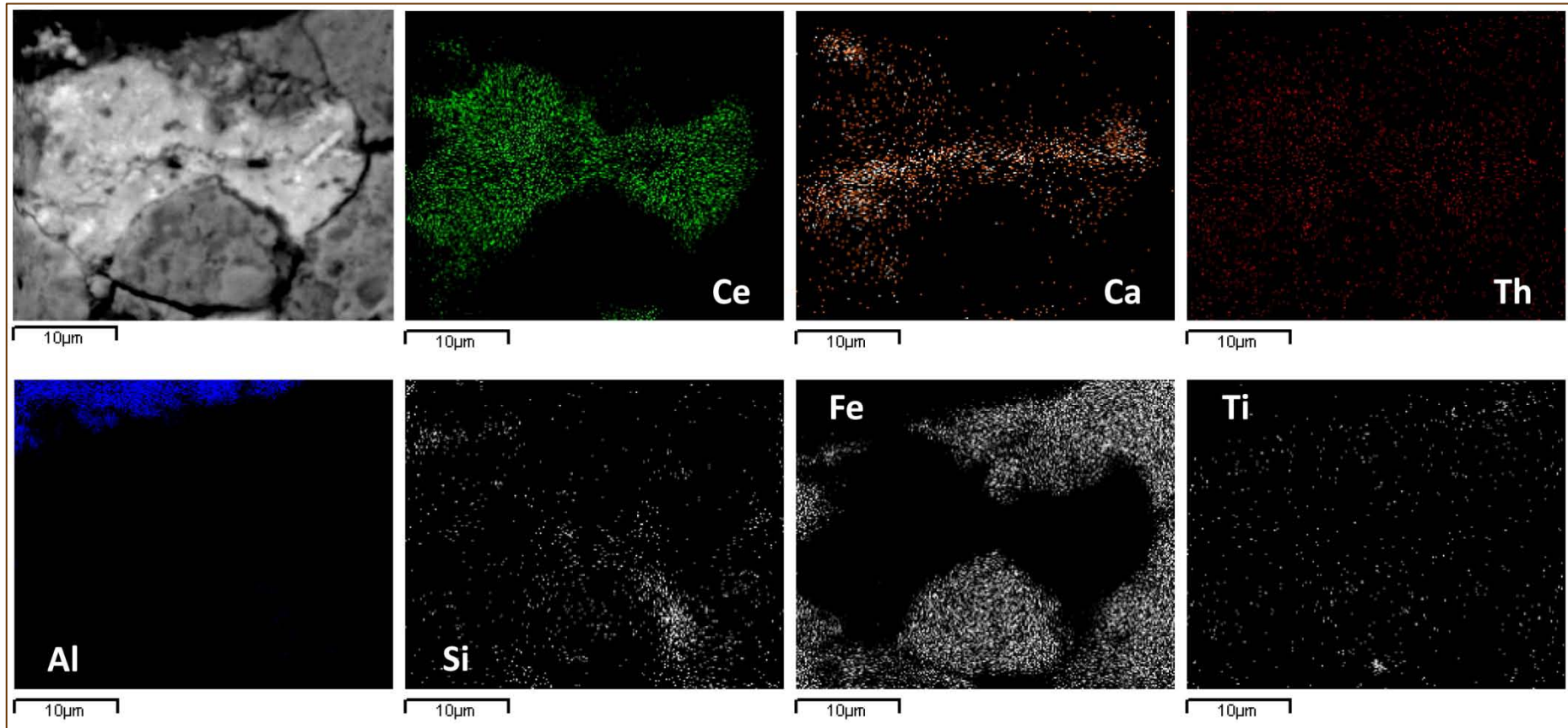


Figure 3.2.3.10: Florencite (Ce-Al-hydroxyphosphate) into the studied bauxites.

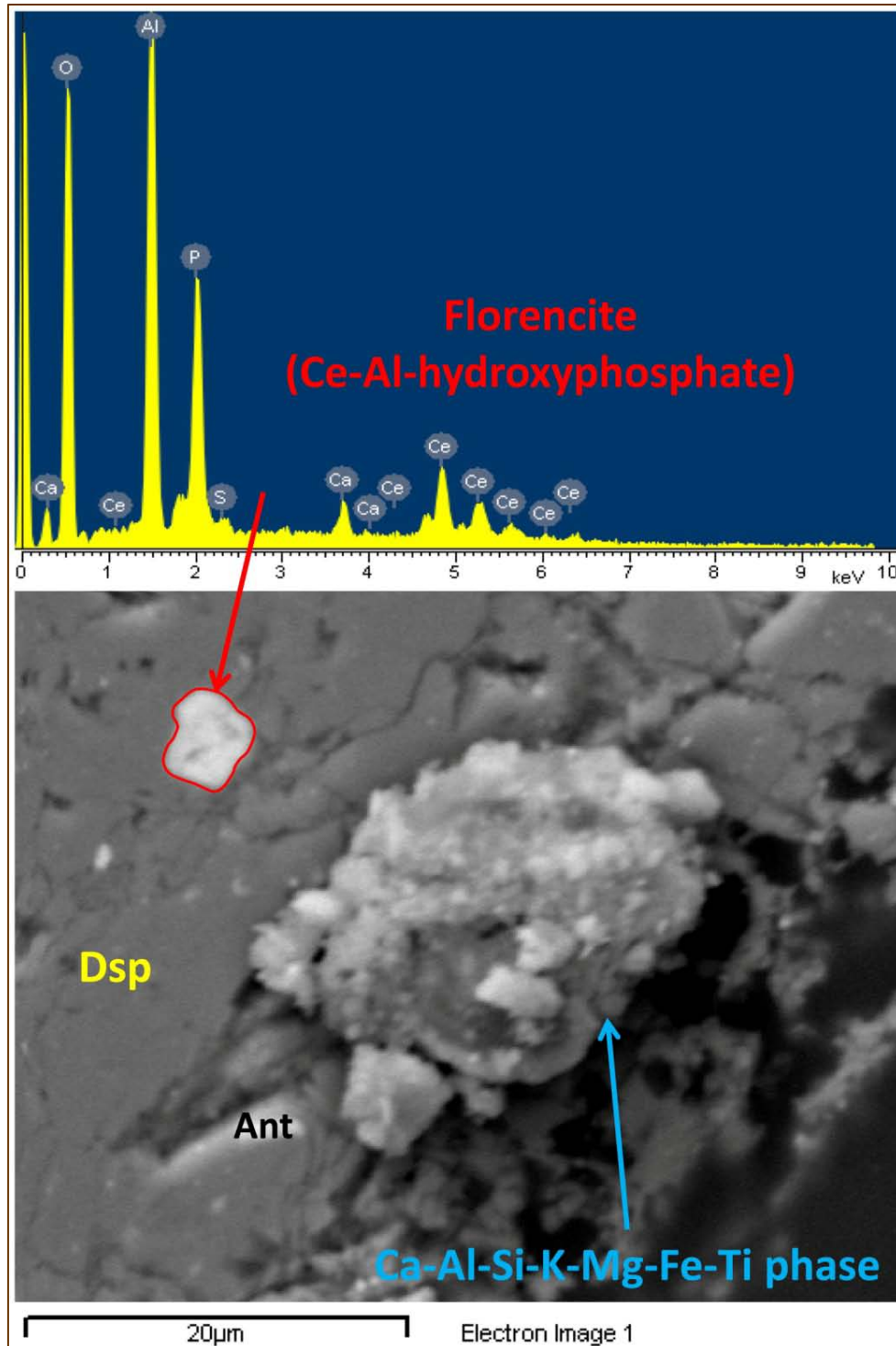
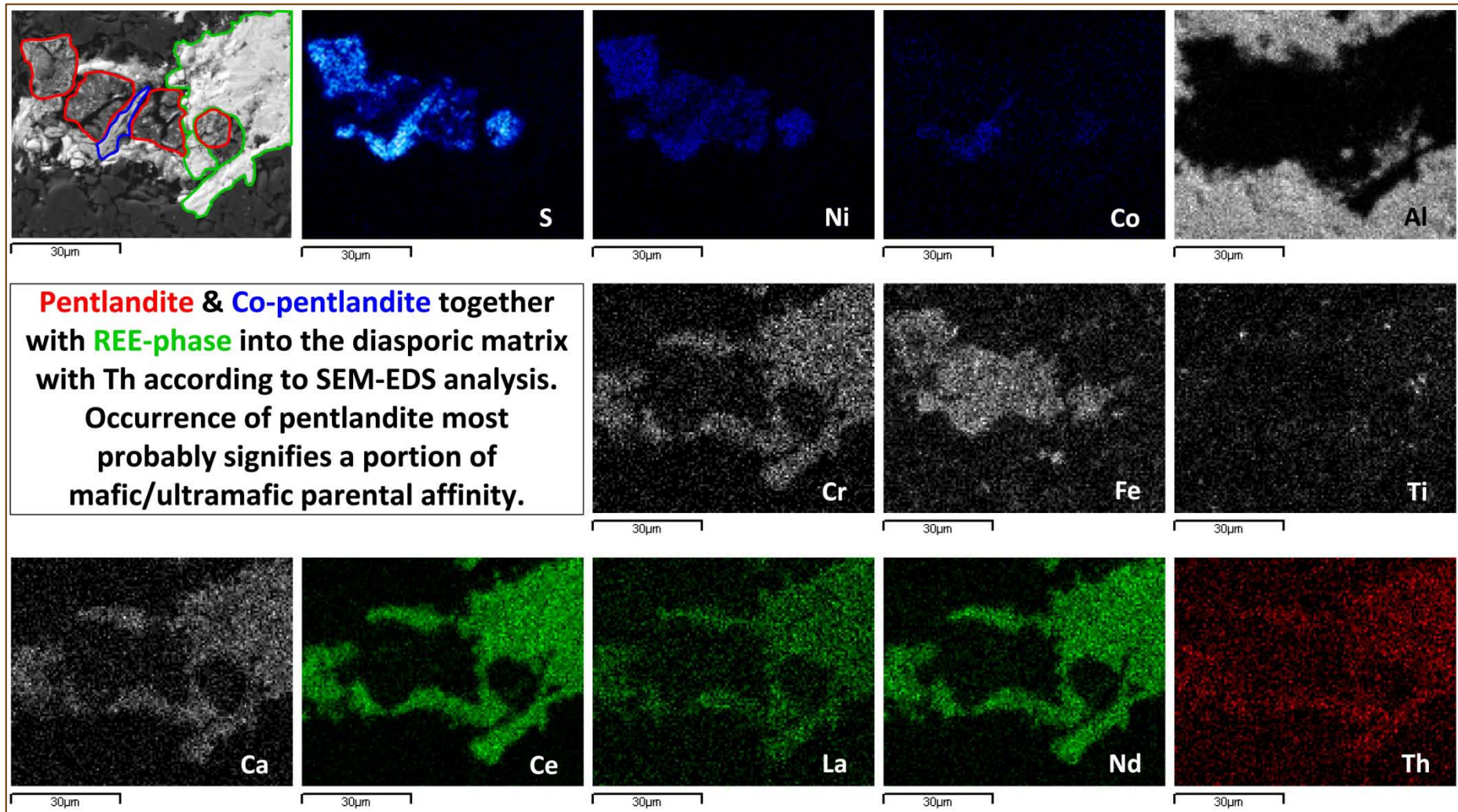


Figure 3.2.3.11: Pentlandite and Co-pentlandite together with REE-phases into Parnassos-Ghiona bauxites.



In the case of polished sections, the μ -XAFS spectra were obtained in micro-areas previously selected on the basis of optical microscopy, Laser μ -Raman and elemental maps from SR μ -XRF. The μ -XAFS spectra were recorded, in order to investigate the distribution and solid-state speciation of Cr and Th in Fe-depleted bauxite, as well as of As, V and Ga in Fe-rich samples.

Inasmuch the state of Fe into Fe-Cr-diaspore illustrated by the Mössbauer spectra, the samples were further subjected to Synchrotron-based techniques in microscale, in order to elucidate the nature of Cr previously detected by SEM-EDS/WDS. Prior to SR micro-XRF measurements proper micro-areas on polished sections were logged using an optical microscope in reflected light (**Figure 3.2.3.12** – upper left image). Particular micro-areas were also checked by means of Laser micro-Raman spectroscopy, in order to ensure pure diasporic regions for the acquisition of micro-XANES/-EXAFS spectra (see text below). The obtained micro-Raman spectra were compared to a standard Raman spectrum (red and black lines respectively in **Figure 3.2.3.12** – upper right image) from the Mineral Spectroscopy Server of CalTech ([© Prof. G. Rossman, 2006](#)). Laser micro-Raman investigation has been suggested, in the frame of this dissertation, as quick and accurate laboratory method for distinguishing diasporic from boehmite in the low-wavenumber region ($200\text{ cm}^{-1} - 600\text{ cm}^{-1}$) with distinct bands of the natural AlOOH polymorphs at 448 cm^{-1} for diasporic and 362 cm^{-1} for boehmite (see text above).

The SR micro-XRF maps for major elements (Al, Ti, Cr, and Fe) in the studied Parnassos-Ghiona bauxites are shown in the above **Figure 3.2.3.12**. It is clearly evident that the Al, Fe, and Cr are intercorrelated, whereas Ti exhibits a contrasting behavior especially at the center of pisoliths. The Cr *K*-edge micro-XANES spectra, obtained in diasporic regions and aiming in the elucidation of Cr oxidation state in diasporic, are presented in **Figure 3.2.3.13**. The processing of the spectra and the comparison with reference Cr^{3+} - and Cr^{6+} -materials results that Cr is present as trivalent, logically occupying octahedral sites in the structure of diasporic.

Figure 3.2.3.12: Optical microscopic -reflected light- image of diasporic pisoliths (upper left), previously checked for AlOOH polymorphs by Laser micro-Raman spectroscopy (upper right), studied into the ANKA SUL-X beamline vacuum chamber by means of SR micro-XRF spectroscopy for the achievement of Al, Ti, Cr, and Fe elemental maps (middle and lower images) and the acquisition of consequent micro-XANES/-EXAFS spectra (see text below).

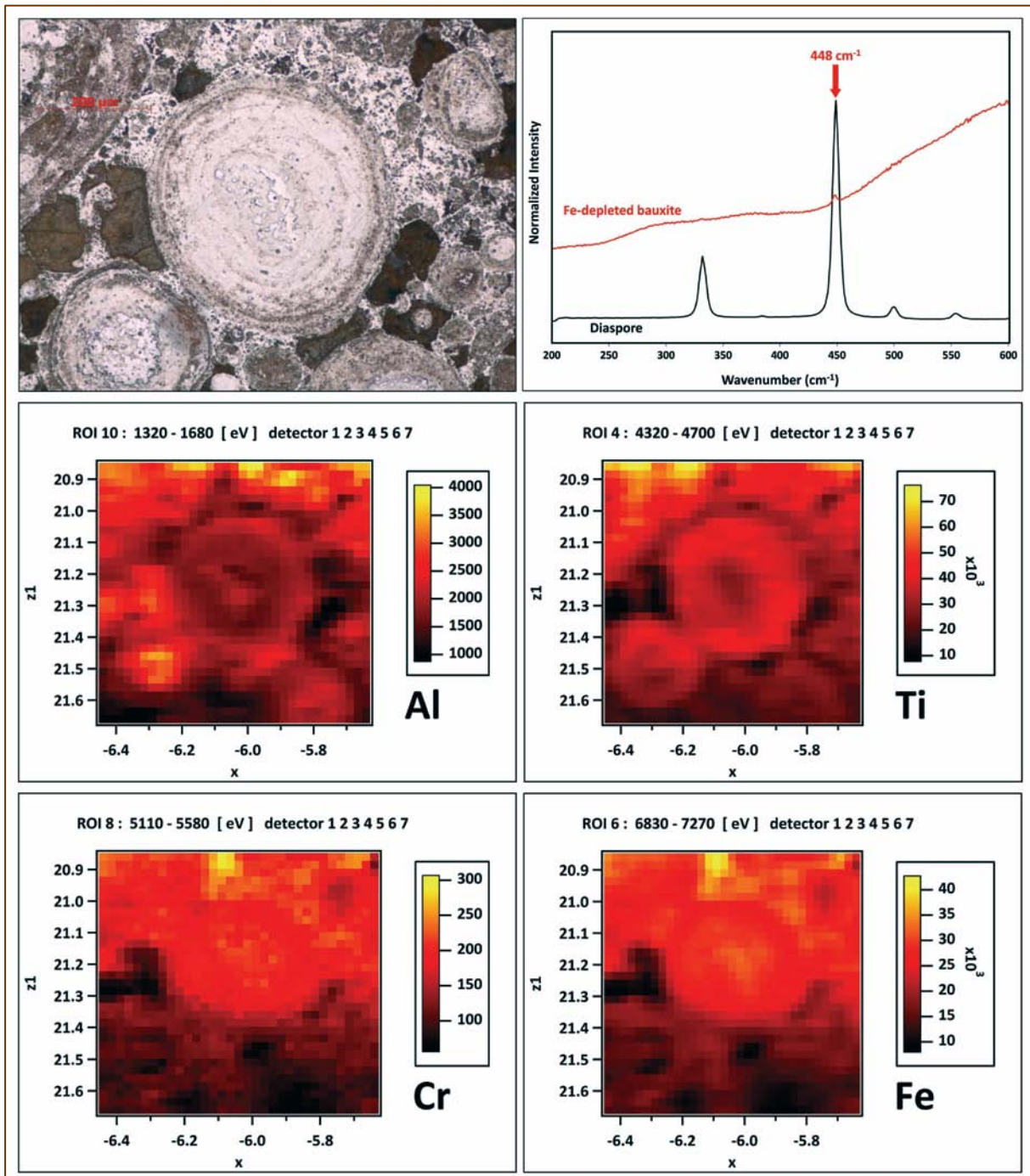


Figure 3.2.3.13: Normalized Cr *K*-edge micro-XANES spectra with regard to Al-Fe-Cr-rich (diasporic) micro-areas of pisoliths of Fe-depleted bauxite together with Cr reference materials. *Upper image:* The diasporic spectrum (blue-colored line) is depicted with all references of Cr³⁺ (FeCr₂O₄/chromite: green-colored line; Cr(NO₃)₃: red-colored line), Cr⁶⁺ (K₂Cr₂O₇: orange-colored line) and grimaldiite-type material (Cr-oxyhydroxide: violet-colored line); *Middle image:* The similarity of diasporic spectrum to Cr³⁺ reference materials is shown; *Lower image:* Enlarged view of the pre-edge region of the normalized Cr *K*-edge XANES spectrum of the studied sample focusing on the twin distinct pre-edge shoulders prior to the main absorption edge.

The Fourier transform (FT) of $\chi(k)$ of the Cr *K*-edge micro-EXAFS spectrum of diasporic

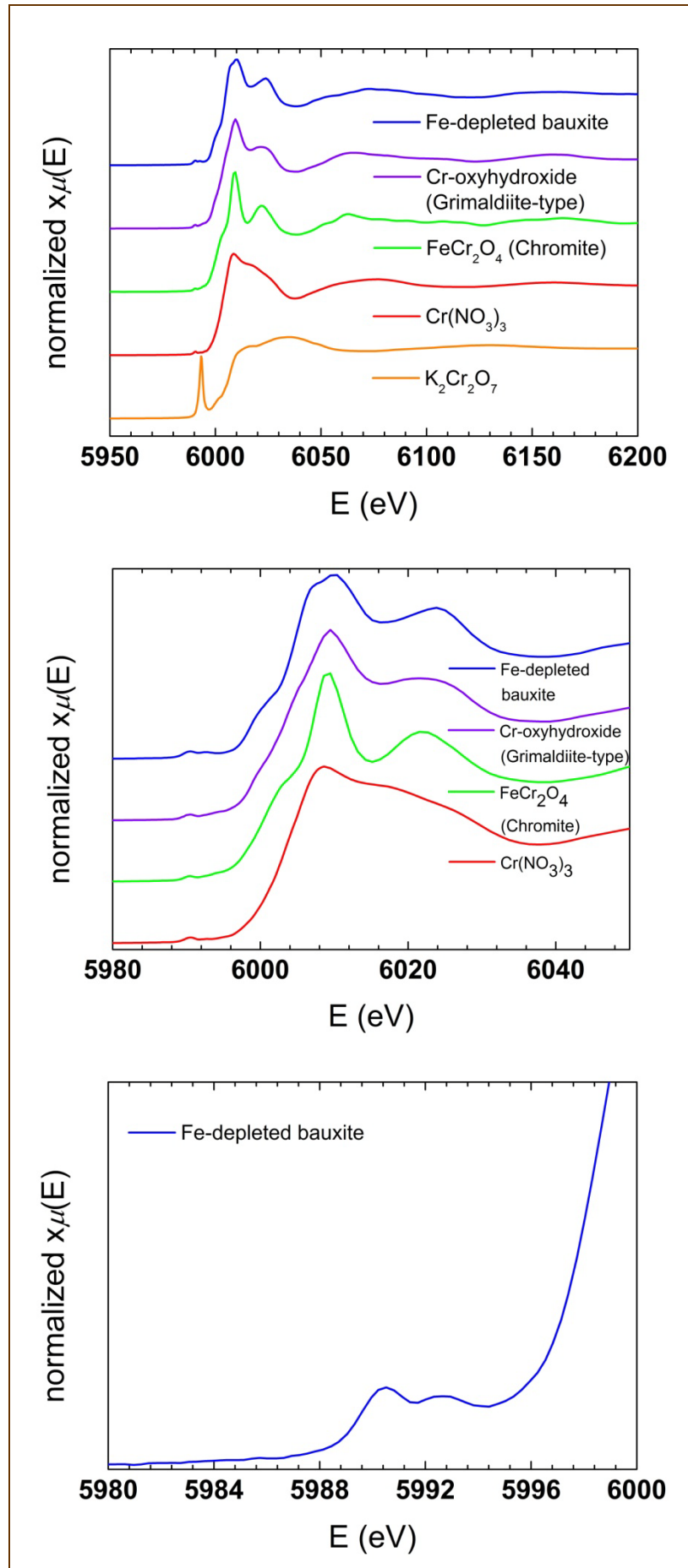


Figure 3.2.3.14: *Upper image:*

The Fourier transform (FT) of $\chi(k)$ of the Cr K-edge micro-EXAFS spectrum of diasporic pisoliths of Fe-depleted bauxite (blue-colored line);

Middle image:

The experimental FT plot in the magnitude part of $\chi(R)$ of the Cr K-edge EXAFS signal of the studied bauxite sample (blue-colored line);

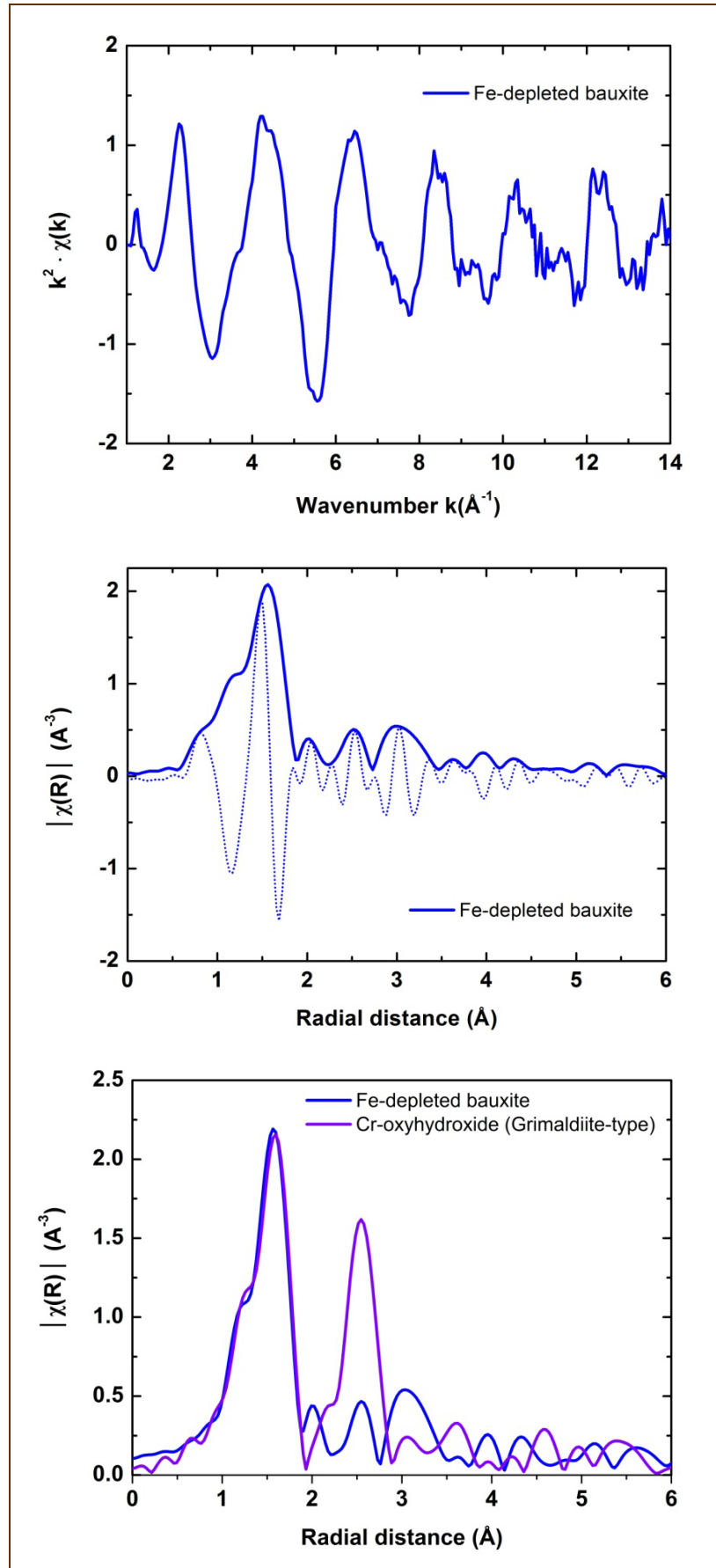
Lower image:

The experimental FT of $\chi(R)$ of the Cr K-edge EXAFS signal of the studied bauxite sample (blue-colored line) compared with the FT EXAFS signal of the Cr-oxyhydroxide (grimaldiite-type) reference material (violet-colored line).

All the Cr K-edge micro-EXAFS spectra have been processed using the ATHENA software package (Ravel & Newville, 2005).

pisoliths (Figure 3.2.3.14) indicates structural similarities of the studied sample and the Cr-oxyhydroxide (grimaldiite-

type) reference material. The interpretation of radial distribution functions – RDF spectra



(Figure 3.23.15) indicated that the first-shell fitting of Cr^{3+} in Cr^{3+} -(Fe^{3+})- AlOOH can adequately be performed using crystalline grimaldiite reference (Christensen et al., 1976; Christensen et al., 1977). The fitting gives for the interatomic distance, between the central atom of Cr and the first neighbor of O, a value of 1.965 Å which is reasonable for grimaldiite (Cr-O: 1.92 – 2.07 Å) and also for Al-O bond length in diaspore referred to vary from 1.851 to 1.982 Å (Busing & Levy, 1958; Hill, 1979). Thus, it is demonstrated that Cr exists as Cr^{3+} in the structure of diaspore, substituting Al^{3+} in octahedral sites ($^{[6]}\text{Cr}^{3+} \leftrightarrow ^{[6]}\text{Al}^{3+}$) as stands in the case of Fe^{3+} . This is observed for the first time in the literature for low-T (sedimentary) diaspore from karst type bauxite active mines of the Mediterranean bauxite belt (e.g., Valetton, 1972; Bárdossy, 1982; Valetton et al., 1987). It should be noted that previous EXAFS

Figure 3.2.3.15: The first shell, corresponding to Cr-O bond, EXAFS fit (Radial Distribution Function – RDF) plotted in $\chi(k)$ space (*upper image*), and also in the real part (*lower image*) of $\chi(R)$, using the ARTEMIS software package (Ravel & Newville, 2005).

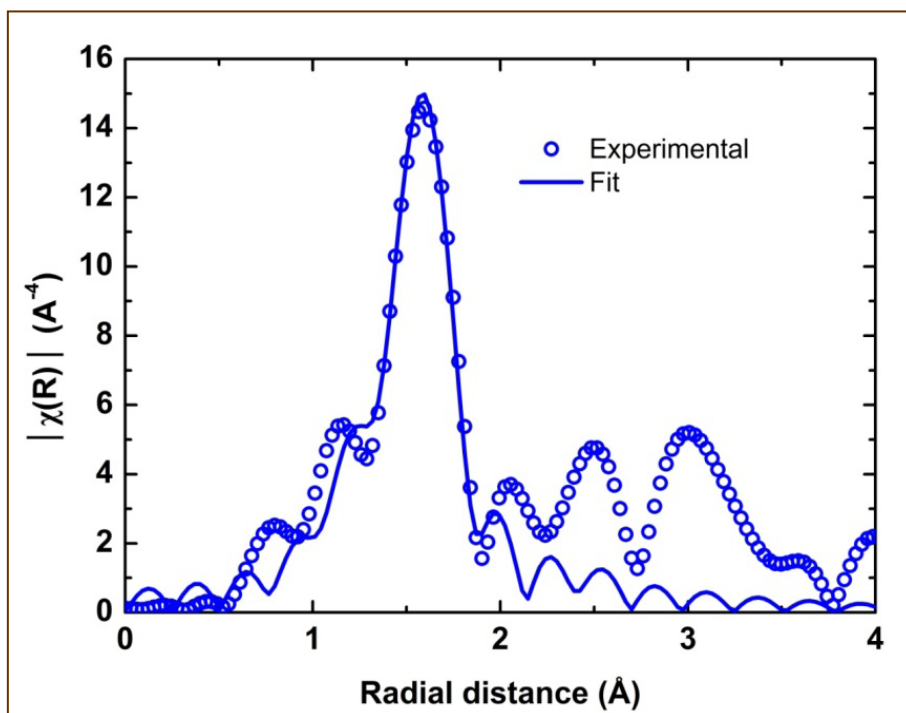
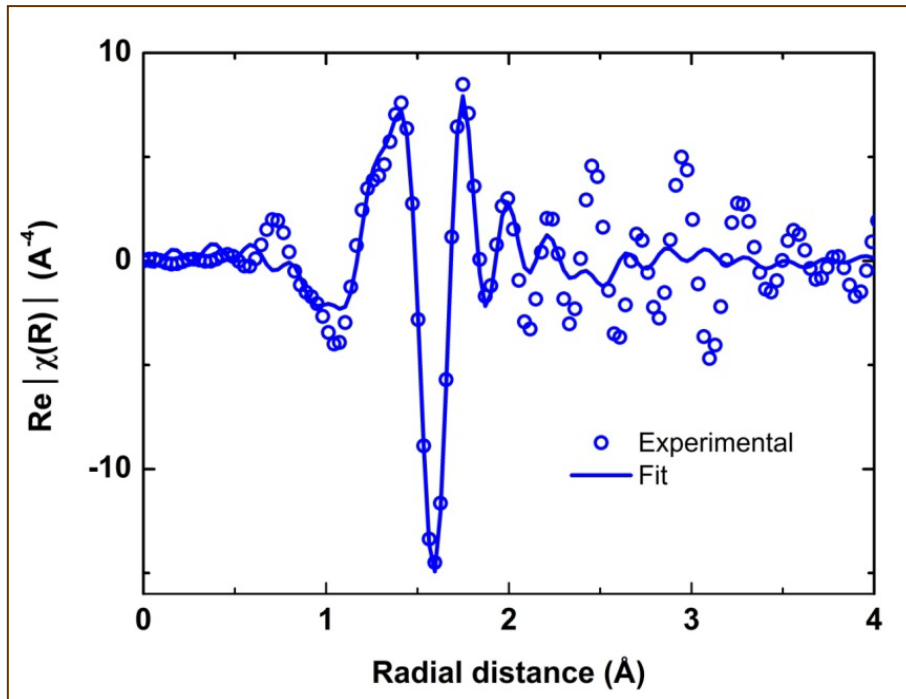


Figure 3.2.3.15: continued.

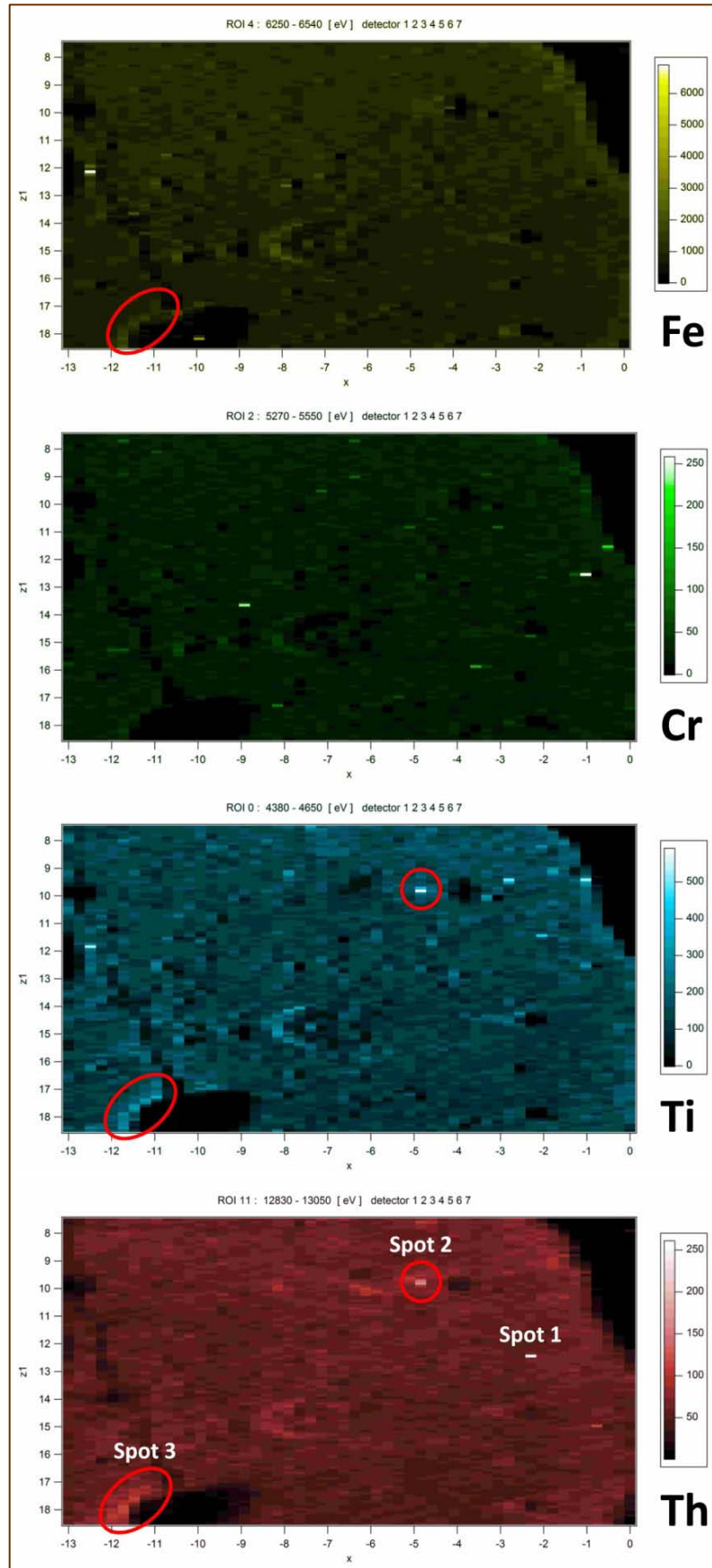


measurements for diasporite concerned only Fe^{3+} (Hazemann et al., 1992), and not Cr^{3+} , in green single crystal of “Anatolian” diasporite (zultanite), formed in higher T, and occurring in diasporite at the Muğla metabauxite deposit of Turkey (e.g., Hatipoğlu et al., 2010).

Nevertheless, the SR μ -XRF elemental maps supplying direct evidence that Th is associated with Ti- and Fe/Ti-containing phases into distinct pisoliths of Fe-depleted bauxite, presented in Figure 3.2.3.16. These phases, according to the present XRD and SEM-EDS data (see text above) and taking into account the data about Ti-phases in karst-type bauxites of the world (Valeton, 1972; Bárdossy, 1982), should be anatase and/or rutile and ilmenite. Our data are in line with previous bulk (Filippidis et al., 1997; Haridasan et al., 2008), SR μ -XRF (Garrett et al., 2001; Kappen et al., 2007), and LA-ICP-MS (Zack et al., 2002; Klemme et al., 2005) studies with regard to Th in synthetic and natural TiO_2 phases (rutile), as well as ilmenite occurring in geological materials other than bauxite (e.g., black sands).

Figure 3.2.3.16: SR μ -XRF elemental maps of Fe-depleted (diasporic) Parnassos-Ghiona bauxite, indicating the regions (spot 2 & spot 3) where μ -XAFS spectra were obtained (see text below).

The SR μ -XRF data about Th partitioning in Fe-depleted bauxite were complementary checked by applying LA-ICP-MS on seven selected anatase grains (up to 20 μm , see also anatase grains of **Figure 3.2.3.1**). The results shown in **Table 3.2.3.2** and **Figure 3.2.3.17** confirmed that Th concentration varies in the range of 13-117 ppm together with abundant Nb (947-11,865 ppm), Ta (55-982 ppm) and U (6-97 ppm). It is therefore demonstrated that Th is associated with Ti- and Fe/Ti-containing phases in microscale despite the

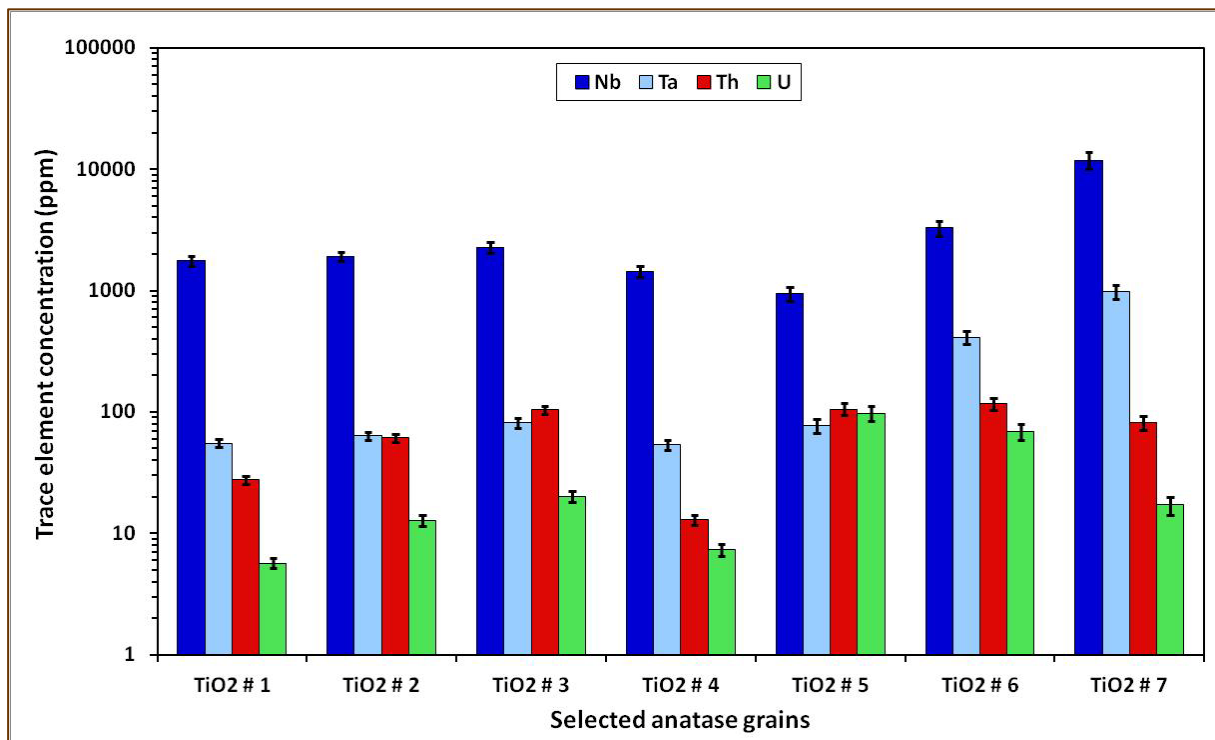


fact that bulk analyses (see text above) indicated no correlation of Th to Ti (effect of “scale-factor”; Bárdossy, 2007).

Table 3.2.3.2: LA-ICP-MS analyses of selected anatase (TiO₂) crystals from Fe-depleted bauxite from Parnassos-Ghiona (units in ppm).

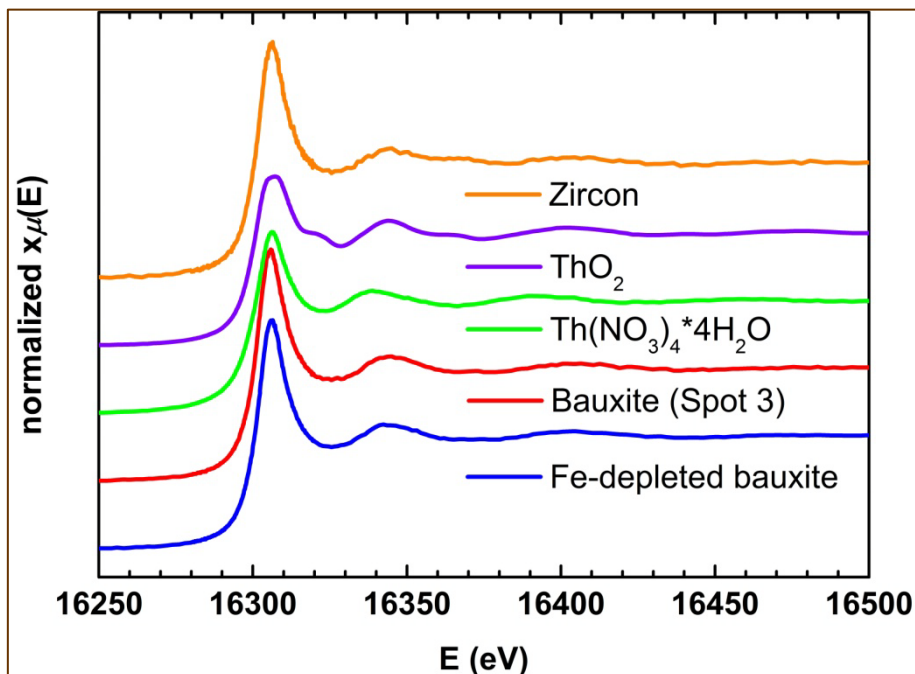
	Nb	Ta	Th	U
TiO₂ # 1	1759	55	28	6
<i>error (1 sigma)</i>	153	4	2	1
TiO₂ # 2	1913	64	61	13
<i>error (1 sigma)</i>	178	5	5	1
TiO₂ # 3	2278	82	104	20
<i>error (1 sigma)</i>	229	7	9	2
TiO₂ # 4	1443	54	13	7
<i>error (1 sigma)</i>	156	5	1	1
TiO₂ # 5	947	77	106	97
<i>error (1 sigma)</i>	129	9	12	13
TiO₂ # 6	3286	414	117	69
<i>error (1 sigma)</i>	481	53	14	10
TiO₂ # 7	11865	982	82	17
<i>error (1 sigma)</i>	1857	135	11	3

Figure 3.2.3.17: LA-ICP-MS results of selected anatase grains from Fe-depleted bauxite.



The recorded Th L_{III} -edge XAFS μ -XAFS spectra from Spot 3 (see SR μ -XRF maps in the above **Figure 3.2.3.16**) of Fe-depleted bauxite, together with bulk Th L_{III} -edge XAFS of bauxite and reference materials, are presented in **Figure 3.2.3.18**. The Th L_{III} -edge XAFS spectra of bauxite (bulk, and in microscale) show a shift towards higher energy in the first EXAFS oscillation as compared to $\text{Th}(\text{NO}_3)_4 \cdot 4\text{H}_2\text{O}$ possessing 12-coordinated Th ions (Charpin et al., 1987). This indicates, according to methodology of Harfouche et al. (2005), who studied the coordination of Zr^{4+} to zircon using Zr $L_{II/III}$ -edge XANES spectra, that Th most possibly undergoes to a coordination number lower than twelve ($\text{CN} < 12$). At the same time, there is a higher similarity to ThO_2 hosting 8-coordinated Th-ions (e.g., Figueiredo & Mirão, 2002). That means, Th in bauxite most likely reduces to a coordination number close to eight ($\text{CN} \approx 8$), i.e., higher than six ($\text{CN} > 6$), as well. The above data show that Th^{4+} ions do not replace 6-coordinated Ti^{4+} ions in distorted $[\text{TiO}_6]$ fundamental octahedral units (framework)

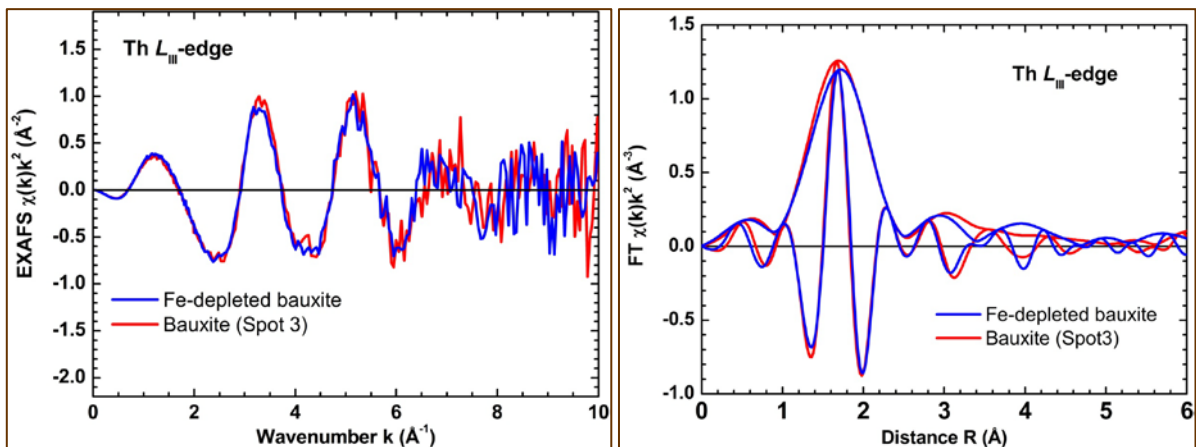
Figure 3.2.3.18: Th L_{III} -edge (μ)-XAFS spectra of Fe-depleted diasporic bauxite -micro (red line) and bulk (blue line)- compared to spectra of reference materials: $\text{Th}(\text{NO}_3)_4 \cdot 4\text{H}_2\text{O}$, ThO_2 and zircon (ZrSiO_4).



of anatase (Horn et al., 1972) and ilmenite lattice. It is known that Th is incorporated as impurity (from 0.5 to >5000 ppm; e.g., Poller et al., 2001) in natural zircon together with

several other trace elements (such as Hf, Y, P, U and REE; e.g., Poller et al., 2001; Grimes et al., 2007). According to Muñoz et al. (2003), $Zr \leftrightarrow Th$ substitution is possible because thorite ($ThSiO_4$) and zircon are isostructural ($I4_1/amd$). Additionally, Harfouche & Farges (2009) have mentioned a local expansion around actinides substituting for Zr, which is a function of the metamictisation degree. Thus, zircon hosts 8-coordinated Th ions in radiation-undamaged structure whereas their coordination drops to seven in the damaged structures. The similarity of Th L_{III} -edge XAFS spectra of bauxite to that of reference zircon (Figure 3.2.3.18), as well as to ThO_2 , indicates that Th ions (predominantly contained in anatase) are coordinated by about 7-8 oxygen atoms and therefore the coordination number is seven or eight (CN=7 or 8). This is supported by the evaluation of the EXAFS signals (Figure 3.2.3.19).

Figure 3.2.3.19: Experimental Th L_{III} -edge EXAFS signals (left image) and their Fourier transform (right image) using the EDA software package (Kuzmin, 1995).



The best-fits of the first peak contribution by one-component Gaussian model are shown in Figure 3.2.3.20. As one can see the agreement is acceptable, though a short k -space range strongly limits the resolution in R -space and also makes the values of coordination numbers - CN- to be strongly correlated with that of Debye-Waller factors σ^2 . In this case, the use of two models resulted in slightly different Radial Distribution Functions -RDFs- (Figure 3.2.3.21). The observed difference is due to the asymmetric shape of the RDF, which cannot be reproduced by the Gaussian model (Table 3.2.3.3).

The coordination number value, which is between seven and eight (CN=7.4 as revealed by regularization method), strongly supports the statement that Th^{4+} does not replace Ti^{4+} (CN=6) in anatase, and even ilmenite, framework.

Figure 3.2.3.20: First shell EXAFS fit using single-shell Gaussian model.

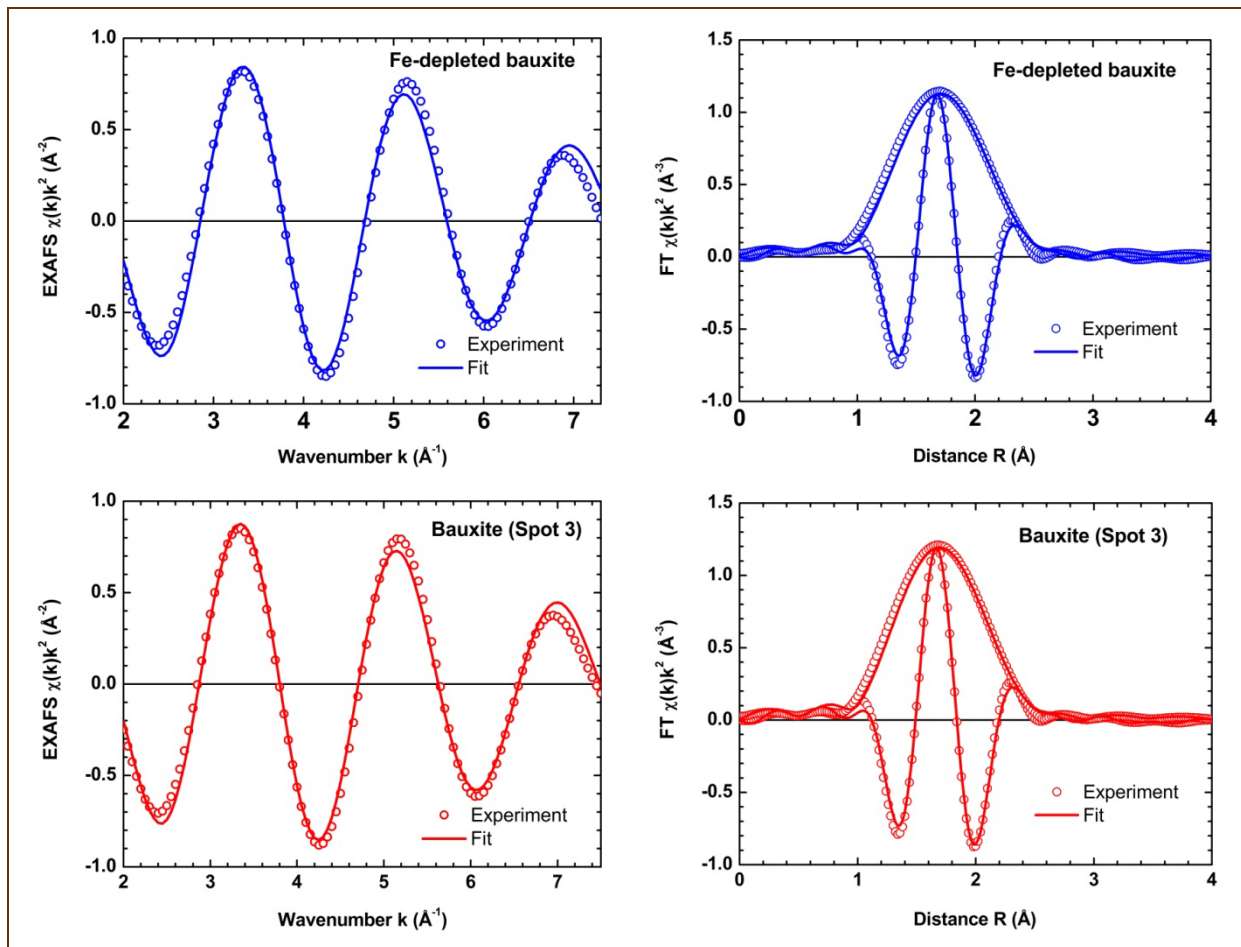
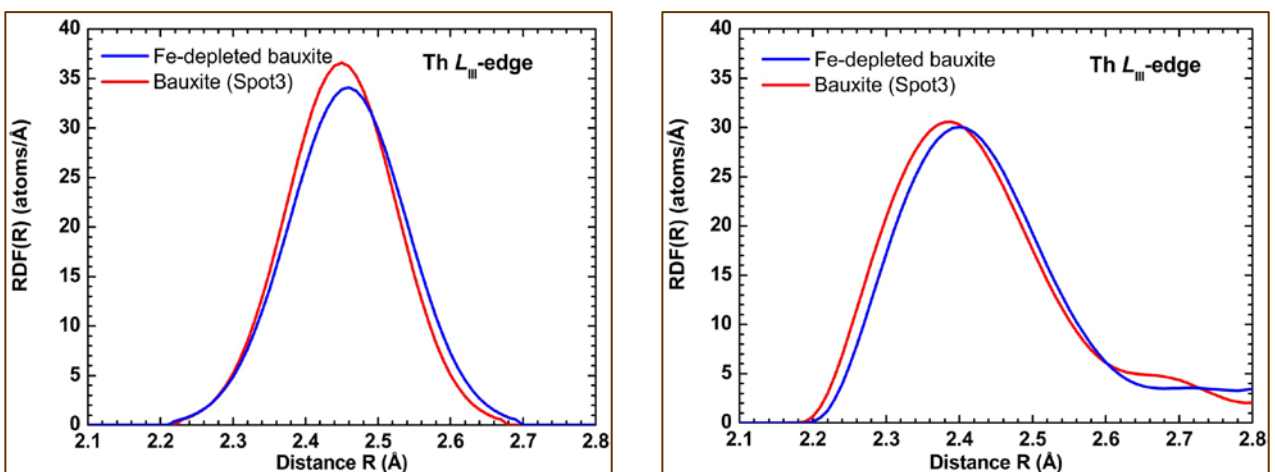


Figure 3.2.3.21: Radial Distribution Function -RDF- using conventional Gaussian model (left image) and regularization method (right image) of the studied bauxite (Kuzmin & Purans, 2000).



The formation of Th-polyhedra (perhaps distorted) by occupation of either extraframework sites or of defected/vacant (\square) sites is more probable (**Figure 3.2.3.22**). This is likely explained by the difficulty of Th^{4+} to replace directly Ti^{4+} in [6]-coordinated (octahedral) sites due to the large difference in the relevant ionic radii (0.940 Å and 0.605 Å respectively; Shannon, 1976). The above results give new aspects into mineral-chemistry of Th in karst-type bauxite and reveal the geochemical mechanisms allowing Ti- and Ti-Fe oxides, that deposited into cavities on karstic surfaces of carbonate platforms at low-temperature environments, together with insoluble chemical compounds (mostly Al-oxyhydroxides), to control the immobilization of dissolved Th ions.

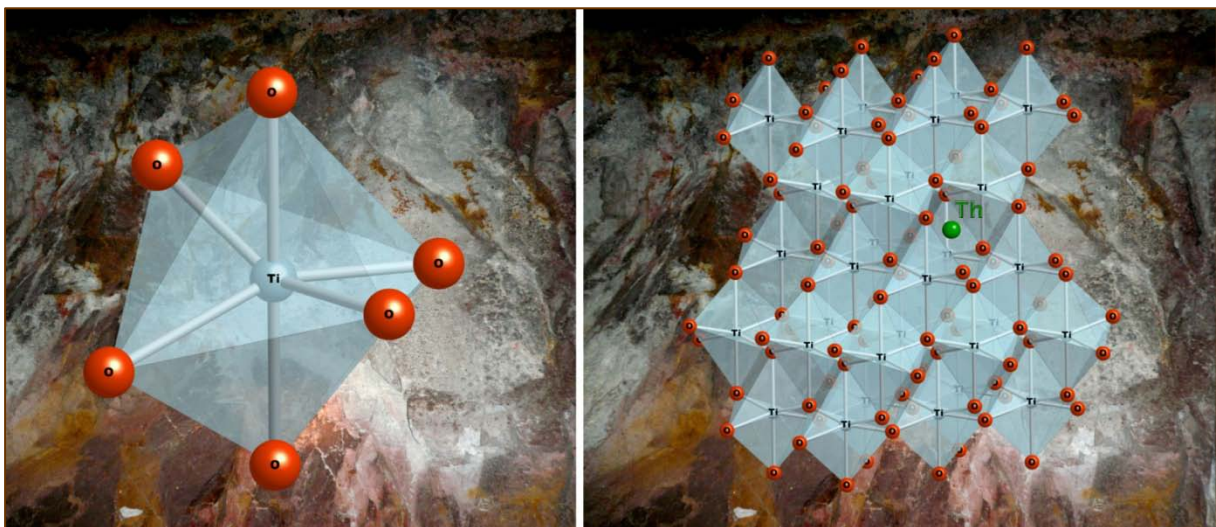
Table 3.2.3.3: Structural parameters obtained from the processing of the Th L_{III} -edge EXAFS signals using the EDA software package (Kuzmin, 1995).

Gaussian Model	Fe-depleted bauxite	Spot 3
CN ± 0.7	6.9	6.9
R (Å) ± 0.04	2.46	2.45
σ^2 (Å ²) ± 0.002	0.007	0.006

Regularization method	Fe-depleted bauxite	Spot 3
CN	7.4	7.4
R (Å)*	2.40	2.38

* This distance is the position of the RDF maximum.

Figure 3.2.3.22: $^{[6]}\text{Ti}^{4+}$ sites (left) and possible extraframework position of Th^{4+} into anatase structure (right).



The distribution of As in the studied bauxites cannot be sufficiently supported by means of SEM-EDS/WDS, in contrast to Greek laterites where this issue can be easily addressed using electron microprobe (Eliopoulos et al., 2012). Thus, the SR μ -XRF study revealed that As is associated to Fe-Cr-Ti into pisoliths, but not to S attributed to sulfides (Figure 3.2.3.23).

Figure 3.2.3.23: SR μ -XRF and μ -XAFS data, with regard to As *K*-edge XAFS study, of Fe-rich Parnassos-Ghiona bauxite.

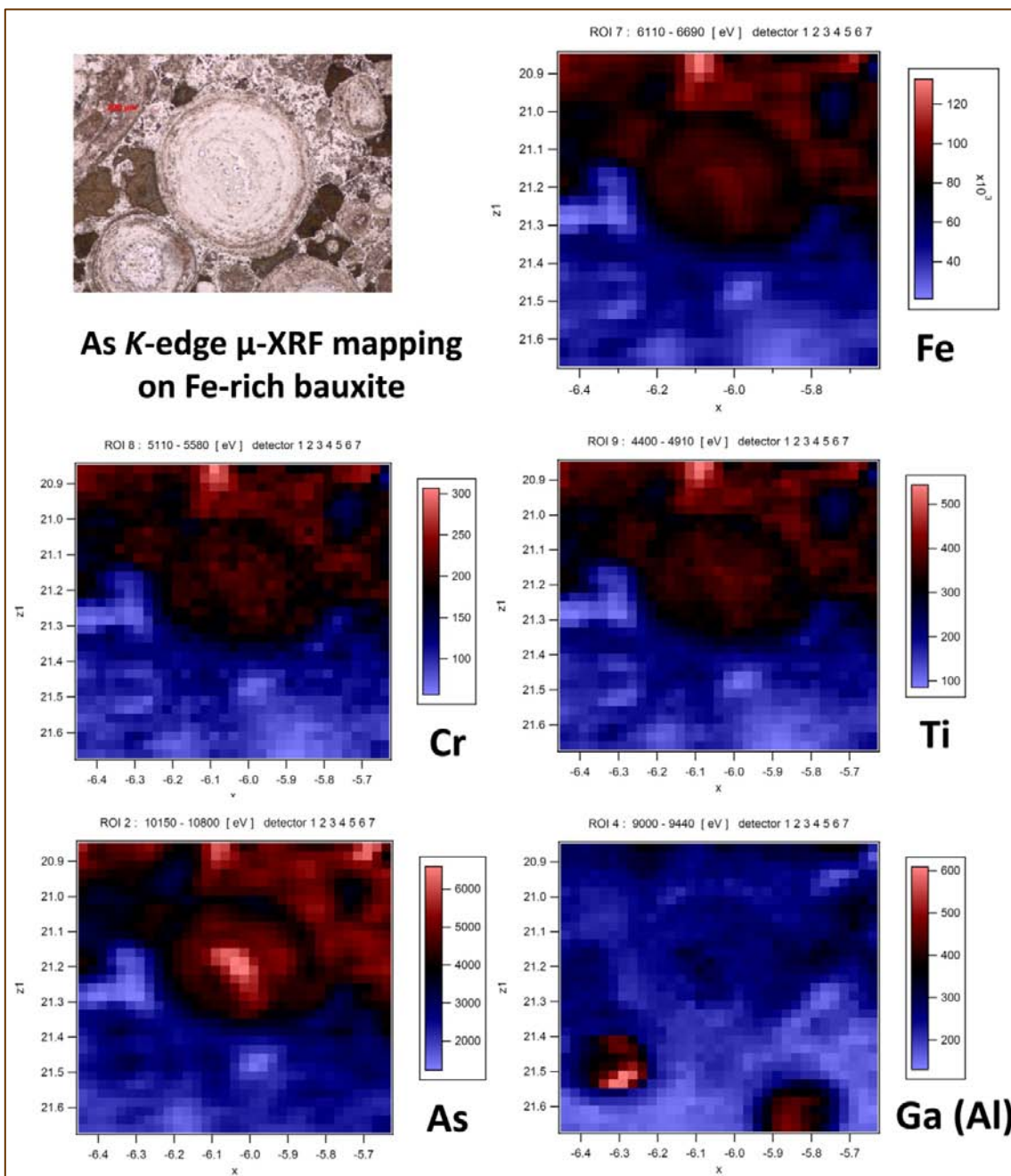
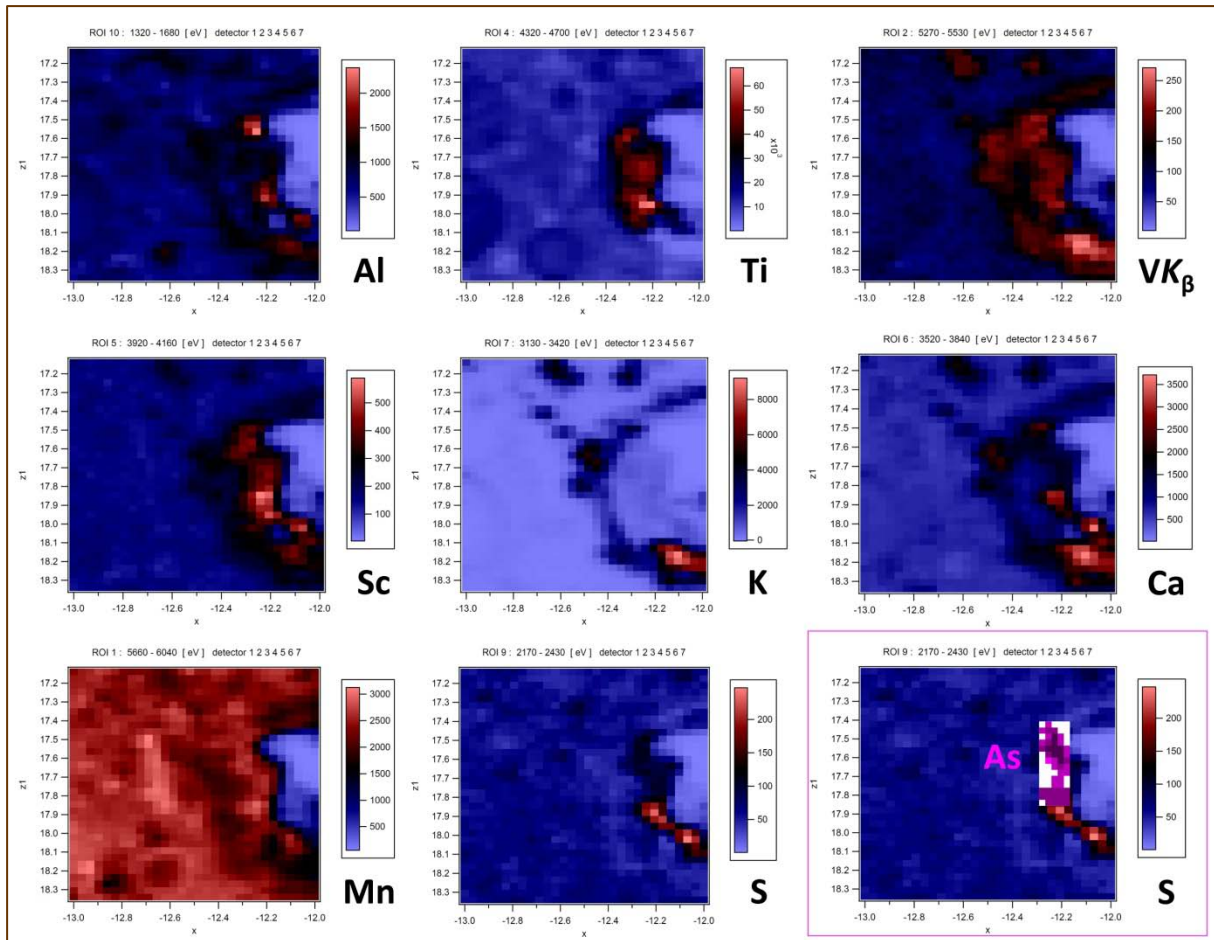


Figure 3.2.3.23: continued.



The solid-state speciation was also adequately investigated by means of μ -As *K*-edge XANES, indicated the presence of As^{5+} (Figure 3.2.3.24). Furthermore, though V is the most abundant trace element in the studied bauxites, it cannot be detectable by means of SEM-EDS/WDS microscopic investigation. However, the combined SR μ -XRF & μ -XAFS study in selected micro-areas between Fe-Cr-Ti and Al-(Ga) pisoliths of the studied Parnassos-Ghiona bauxite directly indicated that high-valence V (most likely V^{5+} though contribution of V^{4+} cannot be excluded) is related to Ca and K, but also possibly to Sc (Figures 3.2.3.25 and 3.2.3.26). Further processing of the XAFS data (i.e., EXAFS spectra) seems to be hardly reliable because REE L_3 - and L_2 -edges, as well as Cr *K*-edge, interfere with the V *K*-edge. Bulk

Figure 3.2.3.24:
Normalized As *K*-edge XANES spectrum of the studied bauxite compared with spectra of natural minerals (annabergite, and scorodite) and, also, with spectrum of a selected synthetic arsenite (arsenolite) used as reference materials.

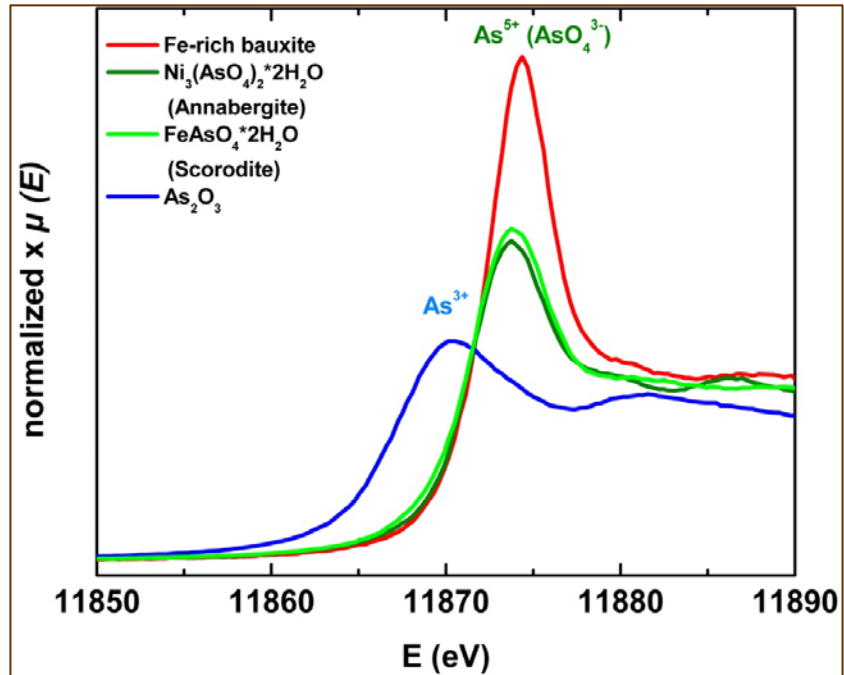
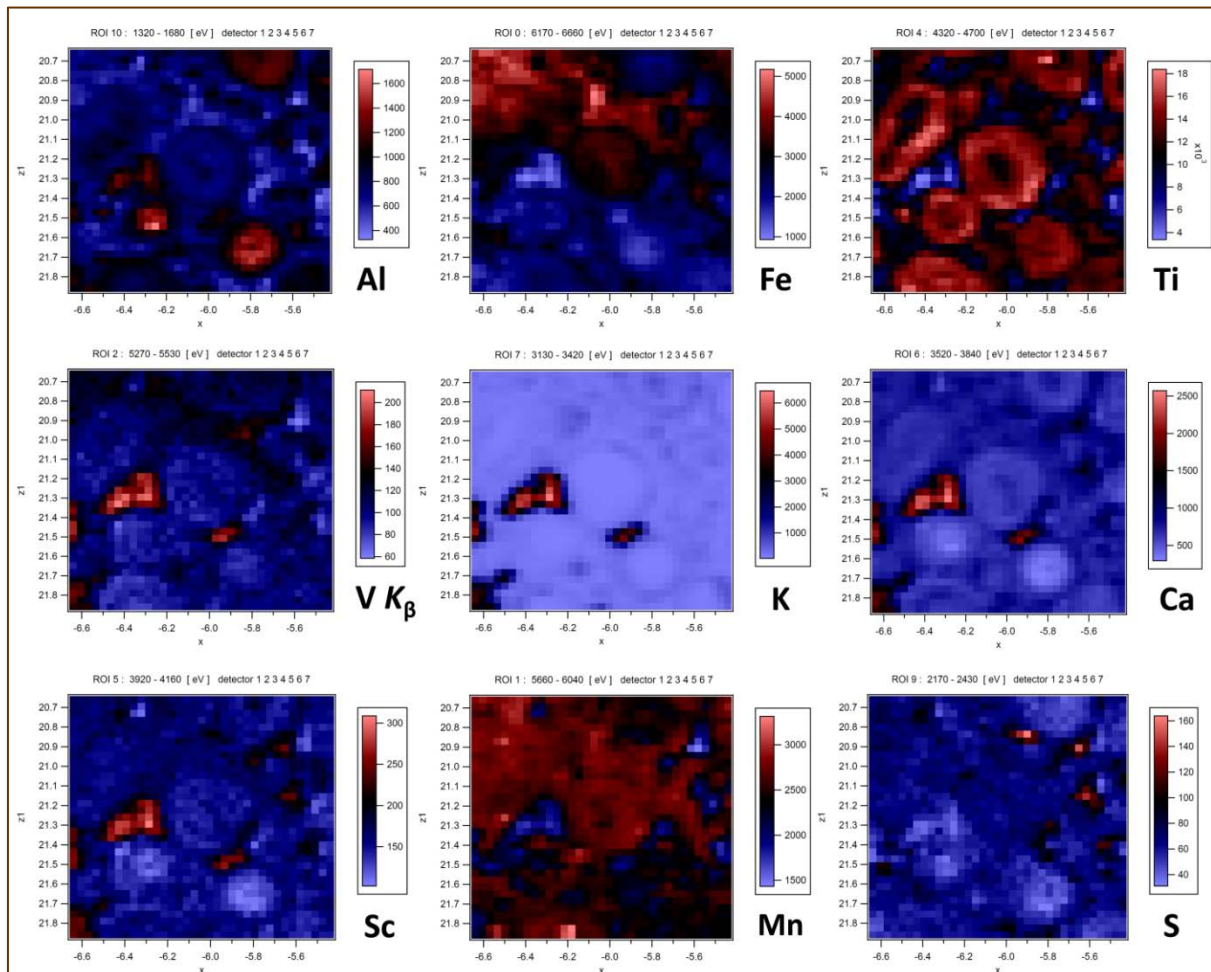
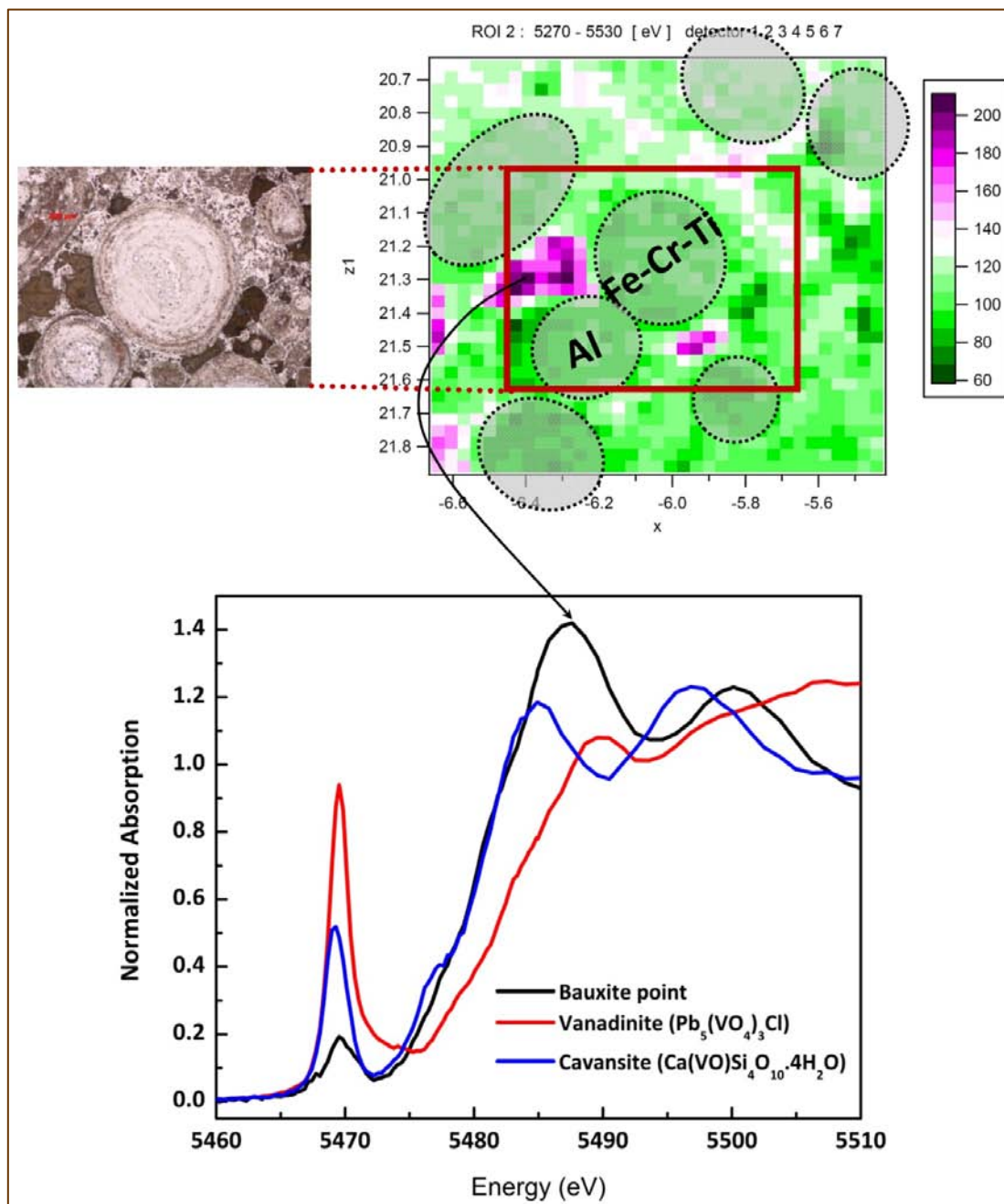


Figure 3.2.3.25: Representative SR μ -XRF data, with regard to V *K*-edge XAFS study, for Fe-rich Parnassos-Ghiona bauxite.



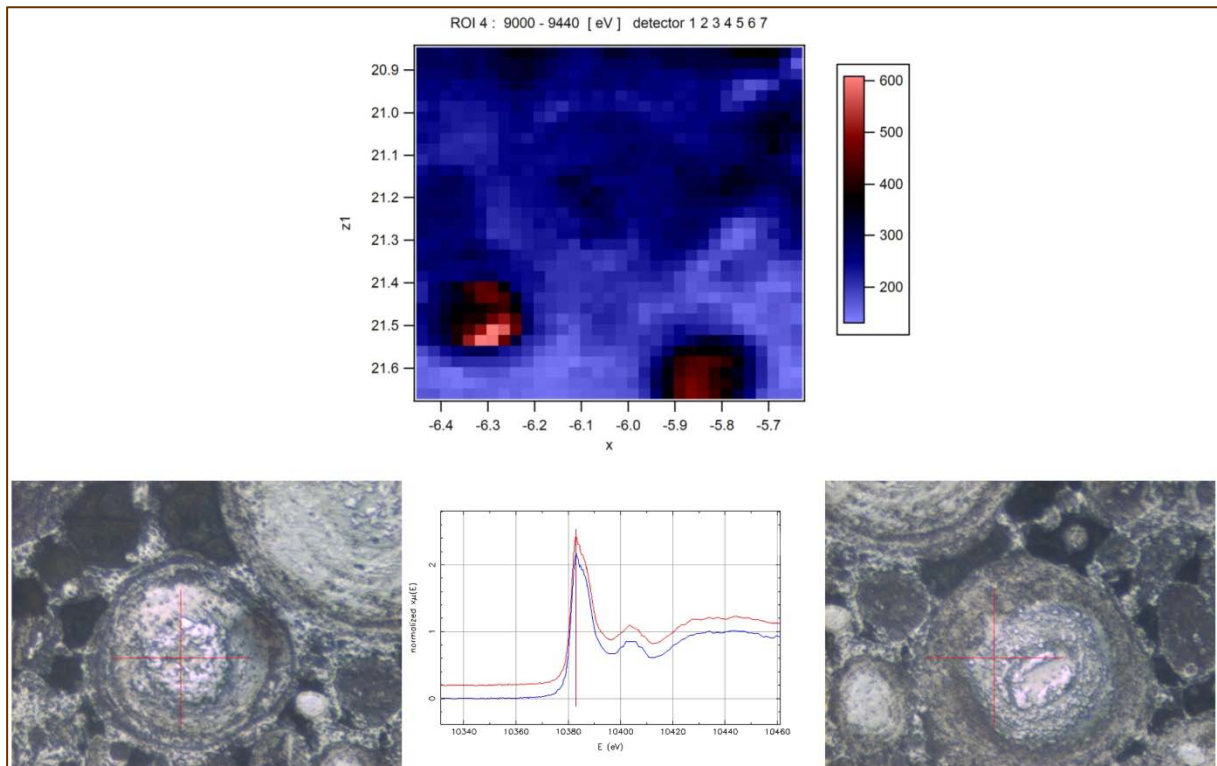
XAFS measurements of bauxite samples did not also give details for V due to the aforementioned effect. However, micro-XAFS spectra, measured at bauxite points, previously mapped by micro-XRF, were more reliable. In this case, the interference of Ti K_{β} -edge and Cr K_{α} -edge, led us to the usage of V K_{β} -edge for spectra acquisition.

Figure 3.2.3.26: Representative SR μ -XRF and μ -XANES data, with regard to V K_{β} -edge XAFS study, for Fe-rich Parnassos-Ghiona bauxite.



Finally, Synchrotron-based data with regard to Ga K-edge XANES study of Parnassos-Ghiona bauxites, related fundamentally to Al, are finally presented to **Figure 3.2.3.27**.

Figure 3.2.3.27: Representative SR μ -XRF and μ -XAFS data, with regard to Ga K-edge XAFS study, for Fe-rich Parnassos-Ghiona bauxite.



3.3. Mineralogy and geochemistry (phase identification, element distribution and solid-state speciation) of bauxite in nanoscale (FEG TEM-EDS & EELS)

Bright-field images of the studied bauxite obtained with FEG TEM-EDS, together with SAED patterns, EELS spectra, and elemental maps in nanoscale, are presented in **Figure 3.3.1** and **Figure 3.3.2**.

Figure 3.3.1: Ti mineral nanoparticles (TiO_2 polymorphs) occluded into diaspore of Fe-depleted karst-type bauxite, revealed by the FEG TEM-EDS & EELS data (BF images, SAED patterns, EDS elemental maps, and EELS spectra).

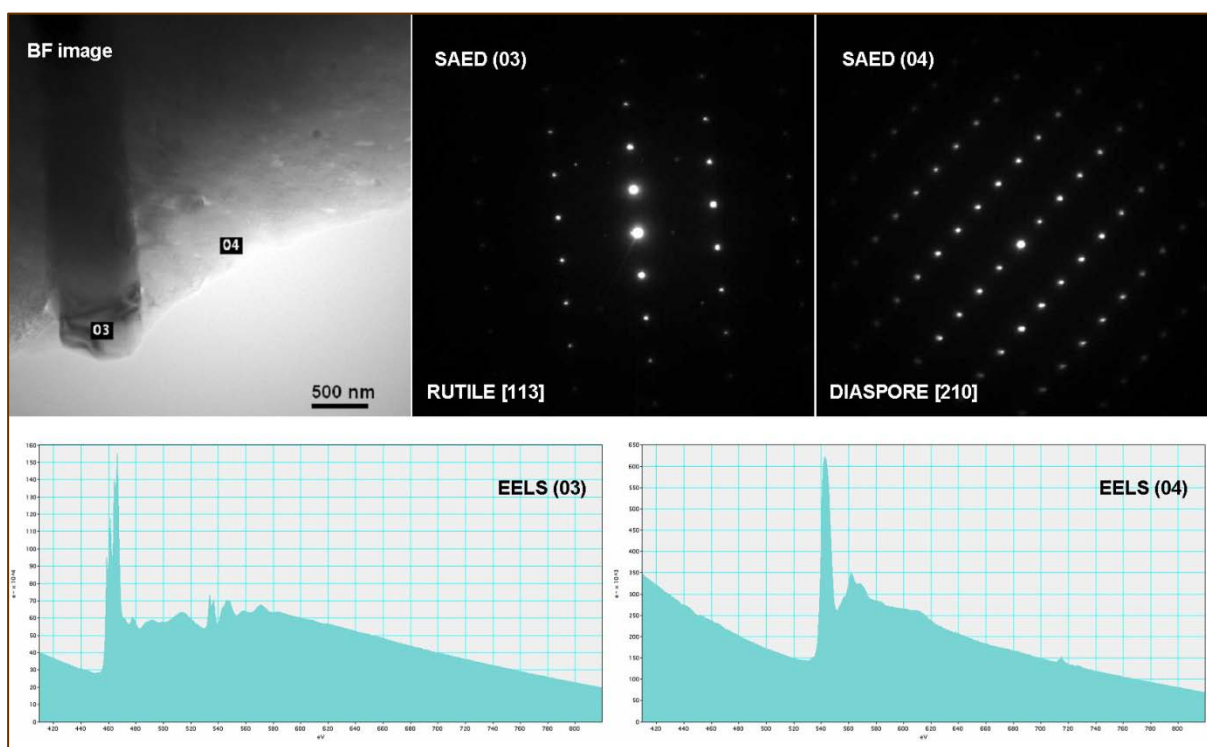
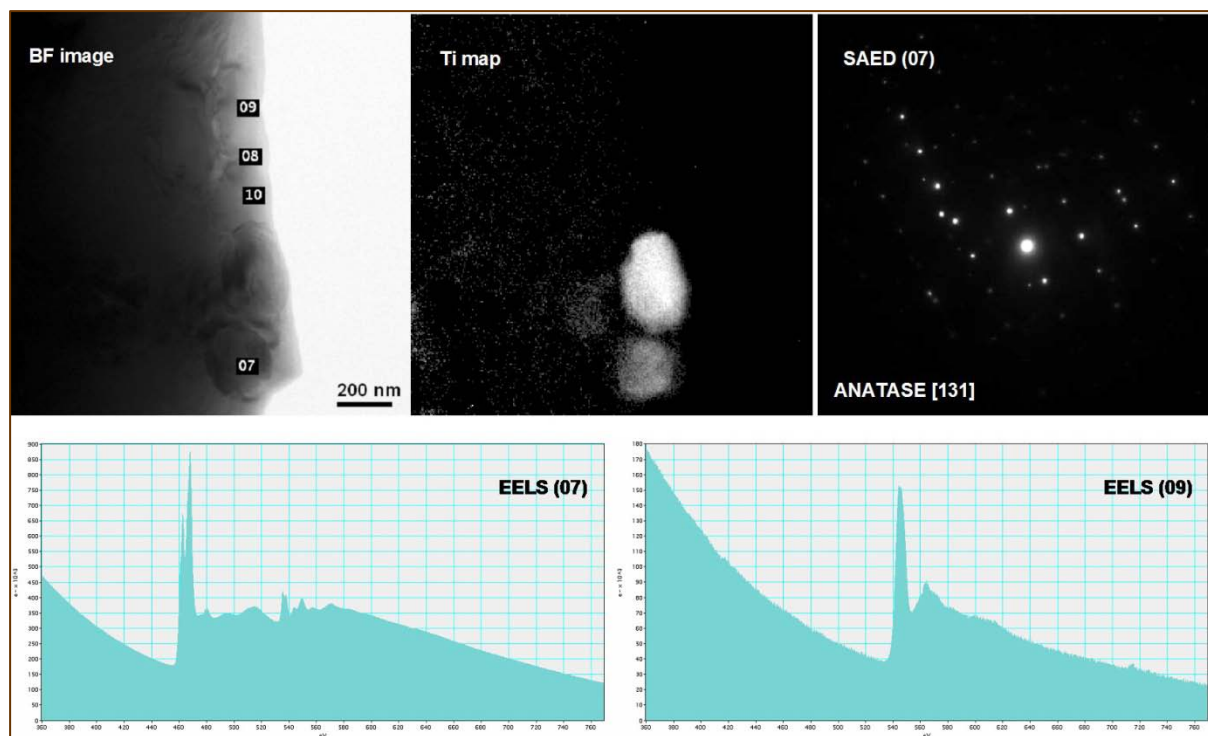
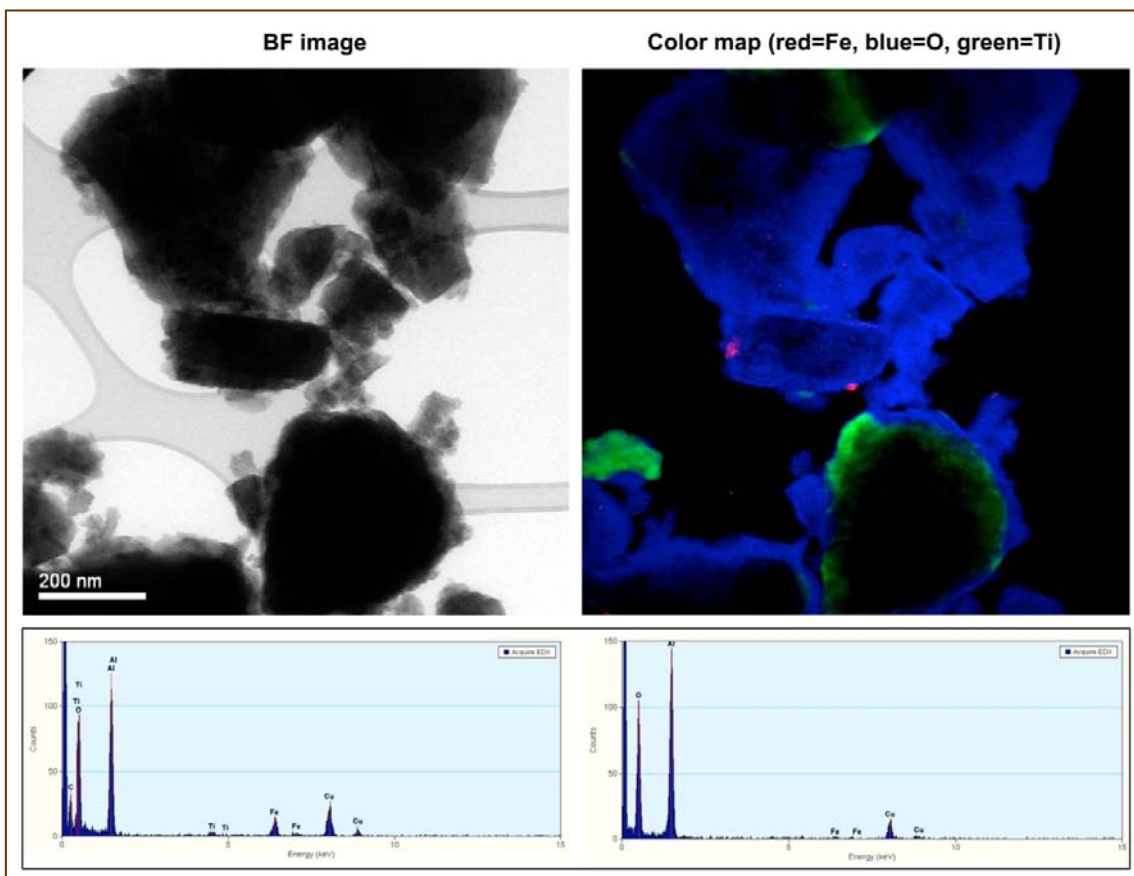
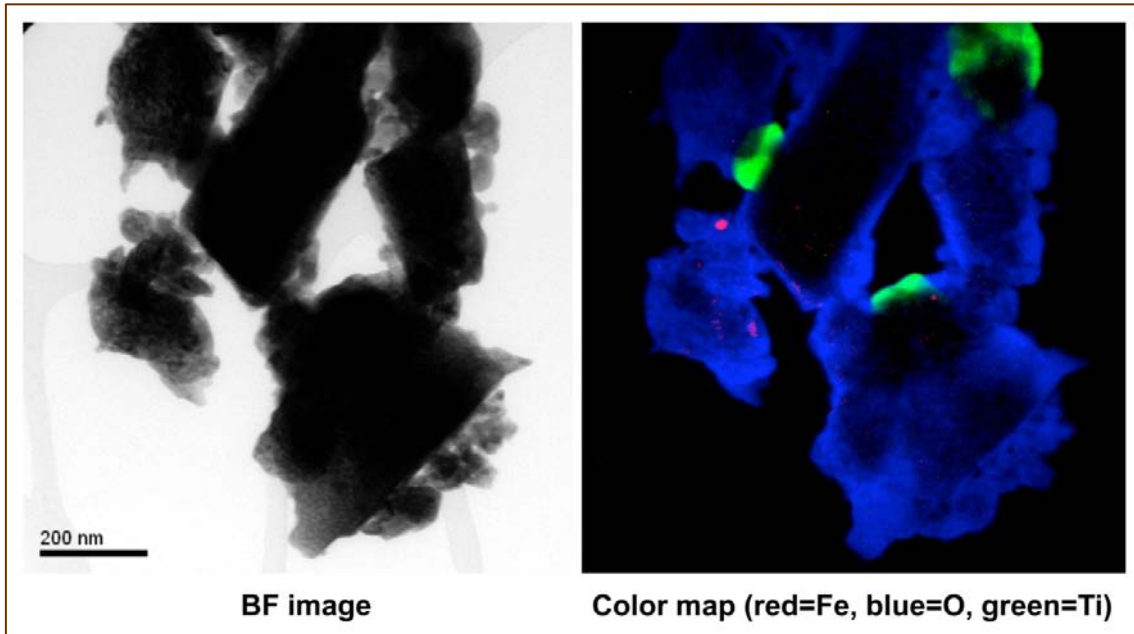


Figure 3.3.1: continued.



The geological material consists of a diaspore matrix containing α -AlOOH grains with 500-2000 nm in size. This is the first in the literature high-resolution TEM study of AlOOH polymorphs in karst-type bauxite, after the historical rough images taken by [Bárdossy & Mack \(1967\)](#) and some data reported by [Bárdossy & White \(1979\)](#). In particular, SAED pattern obtained from region 04 of [Figure 3.3.1](#) corresponds to diaspore [210], whereas the EELS spectra show signals of O (532 eV) and Fe (708 eV). The spectra from regions 08-10 were obtained from diaspore with a beam size of ~ 10 nm, which all show the presence of Fe, which was detected by SEM-EDS/WDS and recorded in the Mössbauer spectra (see text above). However, there are no detectable Fe nanoparticles in the above regions. The regions with brighter contrast appear to be pits or voids. It is noteworthy that Cr *mineral nanoparticles* and/or Cr *nanominerals* have not been identified in the TEM study. Thus, it is stated that Cr exists as Cr^{3+} ion (like Al^{3+}) in the diaspore structure. In contrast, Ti, except for

Figure 3.3.2: Fe nanominerals (25 - 45 nm), together with TiO₂ mineral nanoparticles, into diaspore of Fe-depleted karst-type bauxite, revealed by the FEG TEM-EDS data (BF images and EDS elemental maps).



the occurrence of anatase in microscale, it also appears in the form of both TiO₂ polymorphs in nanoscale. Relatively large, needle-like rutile is clearly observed in the diaspore matrix and SAED pattern, obtained from region 03 of **Figure 3.3.1**, corresponds to rutile [113]. This indicates that probably some of the Ti-oxide phases observed in the SEM-EDS/WDS study might be rutile, inasmuch the few rutile crystals observed in the TEM are elongated towards the microscale in the c-axis. Moreover, it is notable that EELS spectra, obtained from rutile, approved the presence of a Ti oxide but without a Fe signal. On the other hand, anatase crystals distribute widely into the diaspore matrix, and have a rounded shape with < ~500 nm in size. A SAED pattern obtained from region 07 of **Figure 3.3.1**, corresponds to anatase [131]. The EELS spectra obtained from the same region, shows signals of Ti (456, 462 eV) and O (532 eV), which also suggest the presence of anatase. Although EELS may allow distinguishing rutile and anatase (Brydson et al., 1989), it would be difficult to do it with the current spectra because of a little difference between two phases. However, the interesting point is that EELS of anatase also show that there are no Fe contents.

Therefore, the FEG TEM-EDS & EELS study confirms the absence of Fe-Ti oxides, and the presence of solely TiO₂ polymorphs which normally do not contain Fe. We could, therefore, demonstrate that Ti *mineral nanoparticles* (Waychunas, 2001; Udubasa et al., 2007; Hochella et al., 2008a; Hochella et al., 2008b; Wauchunas & Zhang, 2008; Plathe et al., 2010; Hochella et al., 2013) exist in karst-type bauxite, a significant Al-ore, from Greece. In a relevant recent study, Gan et al. (2013) have also reported TEM images of potential anatase grains (elemental maps in nanoscale and SAED patterns were not published) in the size 150 - 500 nm, but not rutile, in karst-type bauxites from northern Europe. The co-existence of two TiO₂ polymorphs in bauxite rises questions about the origin of rutile. Rutile is usually formed in high-T and -P, so it is common accessory mineral in metamorphic rocks (e.g., Goldsmith & Force, 1978) and is among the most stable detrital minerals in sedimentary systems (e.g. Zack et al., 2004). It may be also formed from conversion of metastable anatase at low-P and 600 °C (Jamieson & Olinger, 1969). However, according to Bárdossy (1982), rutile in karst-type bauxites, except for the form of clastic (detrital) grains in the size 10 to 200 µm, can also be low-T authigenic and rarely epigenetic in µm-sized veins along with anatase. Anatase is a typical low-T authigenic phase, which can be syngenetic (to diaspore) and early diagenetic (Bárdossy, 1982). It is obvious that, in contrast to anatase, the formation of rutile

in low-T Al-ore deposits has been remained questionable for a long time. However, it is now known that the process of anatase transformation to rutile may be take place in low-T at nanoscale, and thus there are particle size effects on transformation kinetics and phase stability in nanocrystalline TiO₂ (Gribb & Banfield, 1997; Smith et al., 2009; Zhou & Fichtorn, 2012). Taking into account all the above, we can also support the observations by Bárdossy (1982) and the “scale-effect” in bauxite minerals (Bárdossy, 2007) and suggest that rutile in can be authigenic at microscale and surely in nanoscale.

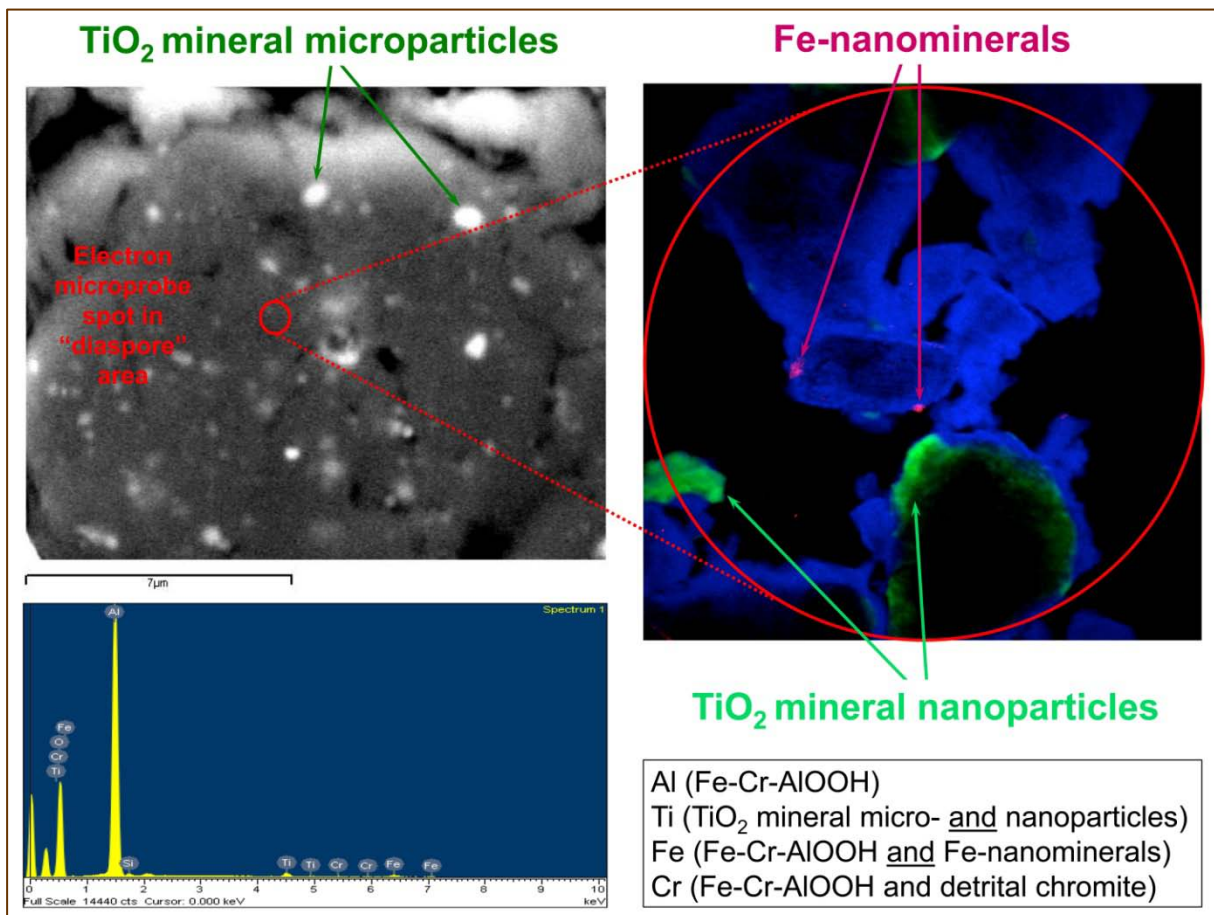
In order to characterize Fe nanoparticles in diaspore, more than 15 regions were thoroughly studied by electron nanoscopy and three of them were found to contain such materials. The precise phase identification was not feasible, because of aggregation with other phases, which make their lattice fringes totally invisible, or due to semi-amorphous/disordered or completely amorphous character. Thus, the study by FEG TEM-EDS & EELS revealed rounded Fe oxide nanoparticles between 25 and 45 nm in size (Figure 3.3.2). The EDS point analysis for a distinct Fe oxide particle with size 28 nm (Figure 3.3.2 – middle images) clearly proved significant Fe, while a region next to it does not comprise of Fe. That confirms that the detected Fe signal comes from the nanoparticle and not from the TEM specimen holder or the pole-piece. The results prove that Fe in the studied bauxite is present in the both forms, i.e., into the diaspore structure and also as nanoparticles occluded in the diaspore matrix. The exact nature of these Fe oxide nanoparticles is not absolutely clarified, but we can assume that they are not well-crystallized counterparts in nanoscale of typical Fe minerals such as magnetite and hematite, or even crystalline FeOOH polymorphs (goethite, lepidocrocite, akaganeite). The evaluation of the Mössbauer spectra gave proofs for the presence of maghemite, not localized by Laser micro-Raman and electron microscopic and nanoscopic techniques. Furthermore, magnetic susceptibility measurements gave evidence for probable existence of Al-maghemite. However, it is very reasonable to have semi-amorphous/disordered Fe nanoparticles, such as ferrihydrite-type phases (e.g., Gilbert et al., 2013) or completely amorphous phases, which can further undergo to crystalline Fe nanoparticles (e.g., Echigo et al., 2013). In another recent work Gan et al. (2013) reported TEM images of Fe phases in karst-type bauxites, and presumed to be typical crystalline *mineral nanoparticles*, and particularly hematite 80 nm in size. Nevertheless, the Fe nanoparticles of the present paper refer to untypical Fe minerals which

can be described as Fe *nanominerals* (Waychunas, 2001; Udubasa et al., 2007; Hochella et al., 2008a; Hochella et al., 2008b; Wauchunas & Zhang, 2008; Plathe et al., 2010; Hochella et al., 2013) and they can be crystalline, semi-amorphous/disordered or completely amorphous phases.

An overview of the nano-mineralogy and -geochemistry of Fe-depleted (high grade) diasporic karst-type bauxite from Parnassos-Ghiona mining area, revealed by a combination of spectroscopic, microscopic, and nanoscopic techniques, is graphically illustrated in **Figure 3.3.3**. According to this graphical depiction, the main conclusions concerning the nano-mineralogy and -geochemistry of the examined Greek industrial bauxite can be summarized as follows:

- The main crystalline mineralogical phase, comprising in fact the Al-matrix of the ore, is a novel type of Fe-Cr-diaspore, and particularly Fe³⁺-Cr³⁺-AlOOH (α -AlOOH) where ^[6]Fe³⁺ and ^[6]Cr³⁺ substitute for ^[6]Al³⁺ in the α -AlOOH structure.
- Except for Al, Fe and Cr, Ti is also a major metal in the ore, occurring in the form of TiO₂ polymorphs (anatase and rutile) detectable in microscale, as well as in nanoscale in the form of Ti *mineral nanoparticles*.
- In the case of Fe, except for Fe³⁺ ions in diaspore, there are also Fe oxide *nanominerals*, exhibiting most likely a maghemite-type composition or even a ferrihydrite-type character, implying semi-amorphous/disordered or completely amorphous nanoparticles.
- The Ti mineral nanoparticles and Fe nanominerals occluded into the Fe-Cr-diaspore, and described for first time in the literature with regard to karst-type bauxite deposits, illustrate the importance of nano-mineralogy, nano-geochemistry and, in general of nanogeoscience, in the exploration and exploitation of major Al mineral resources of the world.

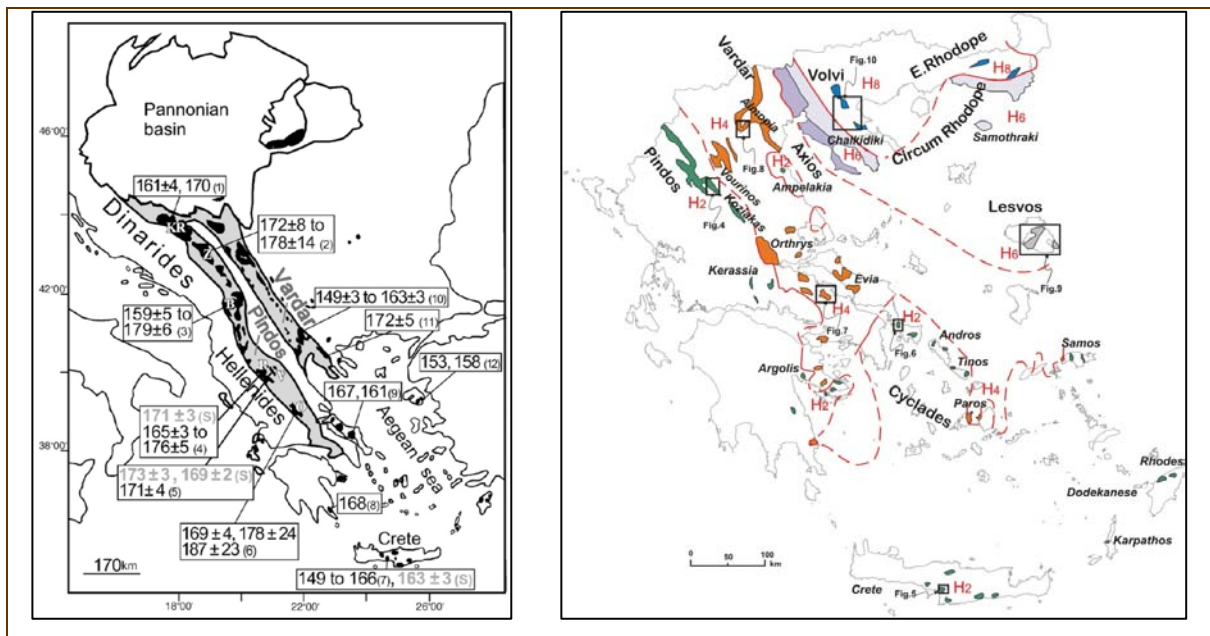
Figure 3.3.3: Overview of the nano-mineralogy and -geochemistry of Fe-depleted (high grade) diasporic karst-type bauxite from Parnassos-Ghiona mining area, Greece, based on a combination of spectroscopic (Laser micro-Raman, Mössbauer & magnetic susceptibility, SR micro-XRF, micro-XANES/-EXAFS), microscopic (SEM-EDS/WDS) and nanoscopic (FEG TEM-EDS & EELS) data.



3.4. Impact of mineralogy and geochemistry to the origin of the deposits

The host carbonates of karst bauxites are typical marine limestones and therefore, their dissolution to leave an insoluble residue is not considered a feasible bauxitization process (Bárdossy et al., 1977). This is also clear from the results of the present dissertation, indicating that Parnassos-Ghiona bauxites have practically nothing to do with the host carbonate rocks of Parnassos-Ghiona geotectonic zone. Thus, the studied bauxites from the current mines are evidently “allochthonous”, meaning that geological formations from other areas provided with Al-(and Fe-, Ti-, and Si)-rich materials filling the karst cavities. In fact, according to the results of the present dissertation, the avg. content of all studied bauxites for major elements (Al, Fe, Ti, Si, Mg, K, P, Cr, Mn, plus hydrous components expressed as LOI) is ~99.5 wt.% (min: ~97.6 wt.%; max: ~100 wt.%), and therefore the avg. of all trace elements is roughly below ~0.5 wt.%, i.e. < ~5000 ppm (generally, only V, Zr, Ni, Ce and Ga exceed 100 ppm; see text above). Evidently, major elements may reflect the origin of bauxite

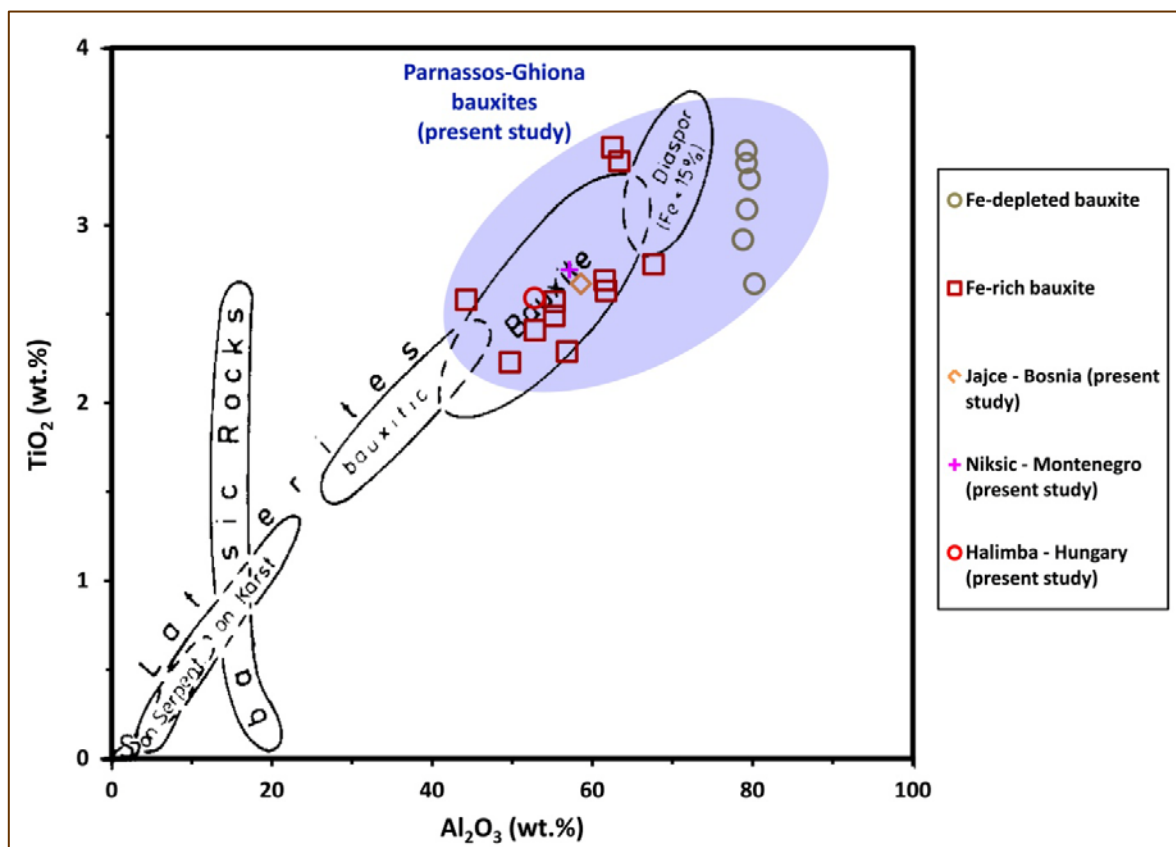
Figure 3.4.1: The main ophiolite outcrops, and their ages, of the Hellenides (Liati et al., 2004; Papanikolaou, 2009).



deposits, but, trace elements, though in low content, may provide with certain information by using various discrimination geochemical diagrams (e.g., [Rollinson, 1993](#)).

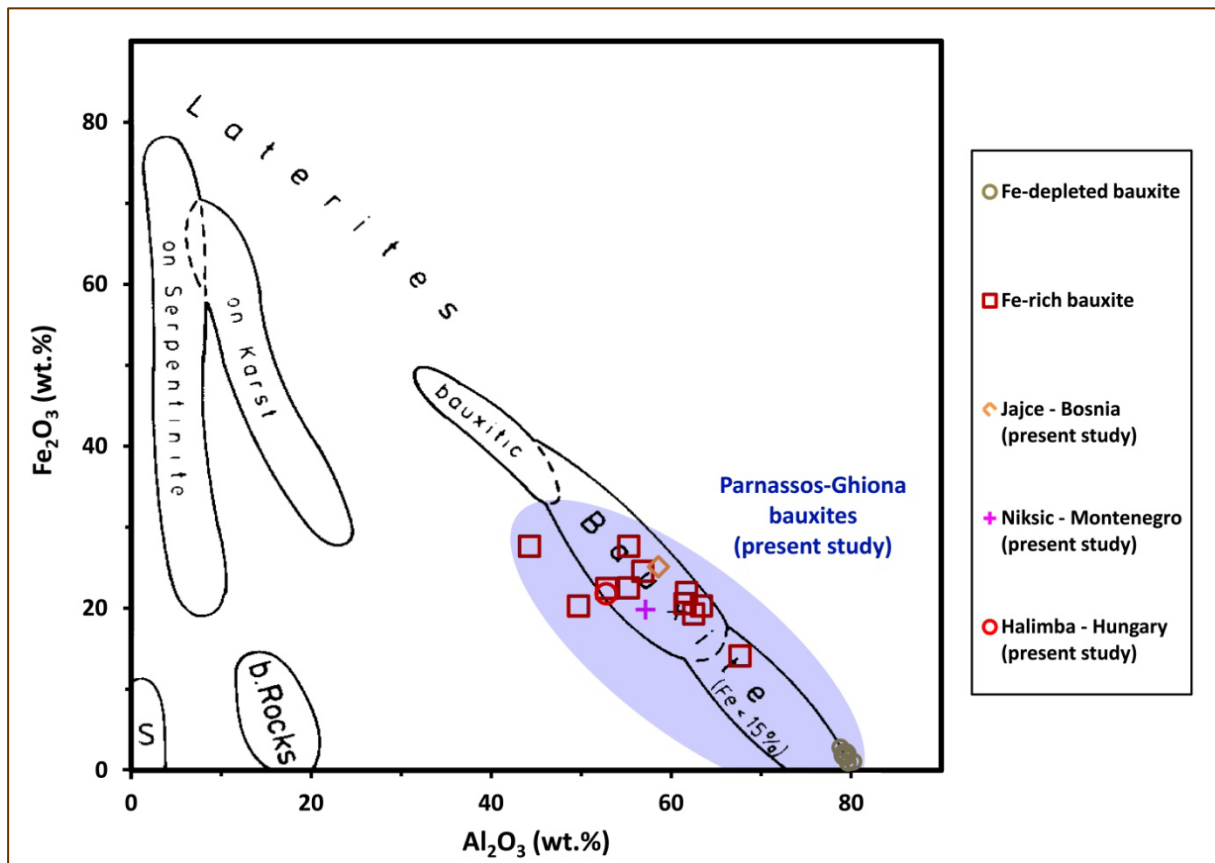
The vital contribution of the pre-Cretaceous (Middle-Upper Jurassic) ophiolites of the Hellenides ([Liati et al., 2004](#); [Papanikolaou, 2009](#); **Figure 3.4.1**) is more than obvious, due to the presence of detrital chromite grains, of possible zircon crystals from the basic members (gabbros) and the plagiogranites, and also of positive geochemical anomalies for relevant compatible elements (Ti, Cr, V, Ni, Sc). This is in accordance to all previous observations (e.g., [Valeton, 1987](#); [Petrascheck, 1989](#)). It is evident that the enrichment in other trace elements,

Figure 3.4.2: Binary correlation diagram of TiO_2 versus Al_2O_3 (after [Valeton et al., 1987](#) and references therein; in wt.%) for karst bauxites from Parnassos-Ghiona active mining area (present dissertation) as well as for karst bauxites from Balkan, and Hungarian active mines for comparison (present dissertation; [Bárdossy† – personal communication](#)).



namely some HFSE (Zr, Ce) and actinides (U, Th), can hardly be attributed to contribution of ophiolites and must be derived from pre-existing acidic geological formations. Thus, it should be mentioned that the co-existence of ophiolitic and acidic/felsic components is more than obvious, completely supporting the previous assumptions by [Valeton \(1985\)](#), [Valeton \(1987\)](#) and [Papastavrou & Perdikatsis \(1987\)](#).

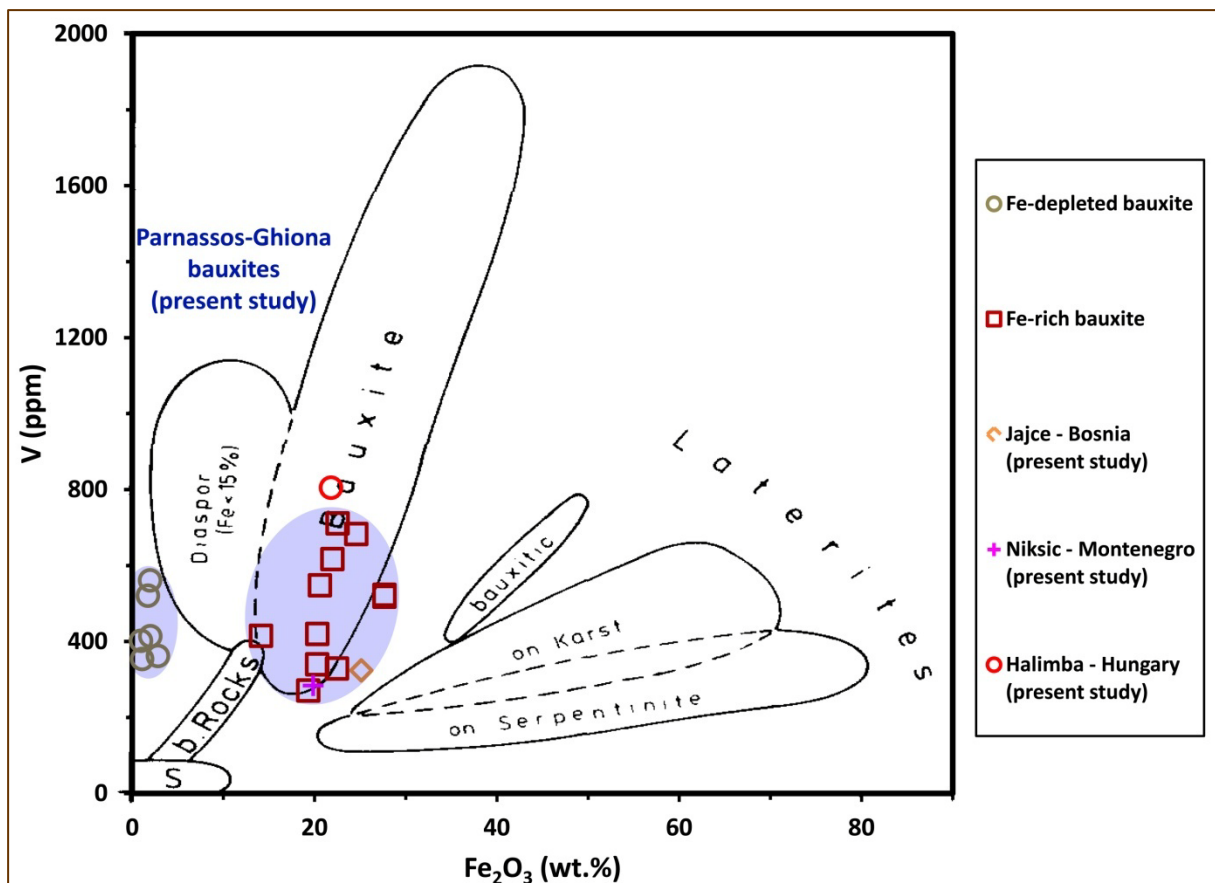
Figure 3.4.3: Binary correlation diagram of Fe_2O_3 versus Al_2O_3 (after [Valeton et al., 1987](#) and references therein; in wt.%) for karst bauxites from Parnassos-Ghiona active mining area (present dissertation) as well as for karst bauxites from Balkan, and Hungarian active mines for comparison (present dissertation; [Bárdossy† – personal communication](#)).



From the bulk geochemical point of view, various discrimination diagrams based on major elements and transition metals (Fe-Al: [Figure 3.4.3](#); V-Fe: [Figure 3.4.4](#)) and also rational (Ni-

Cr: **Figure 3.4.5**; LogCr-LogNi: **3.4.6**, La/Th-Hf; **Figure 3.4.7**) and contrasting trace elements (Zr-Cr-Ga: **Figure 3.4.8**; Th/Sc-Zr/Sc and Th/Sc-Cr/Th: **Figure 3.4.9**), clearly support the origin of bauxites from multiple (mixed) geological sources (**Figures 3.4.6 – 3.4.9**).

Figure 3.4.4: Binary correlation diagram of V – Fe₂O₃ (after Valeton et al., 1987 and references therein) for karst bauxites from Parnassos-Ghiona active mining area (present dissertation) as well as for karst bauxites from Balkan, and Hungarian active mines for comparison (present dissertation; Bárdossy† – personal communication).



The differences in the Ni/Cr ratio between the studied Parnassos-Ghiona industrial bauxites and bauxites from other Greek areas (Laskou, 1991; Laskou et al., 2011; Laskou & Economou-Eliopoulos, 2013) are clearly shown in the upper image of **Figure 3.4.5**. Additionally, analogous differences in the Ni/Cr ratio between the studied Parnassos-Ghiona

industrial bauxites, the studied Bosnian industrial bauxite (Jajce deposit; Bárdossy† – personal communication), the studied Montenegrin industrial bauxite (Niksic deposit; Bárdossy† – personal communication), the studied Hungarian bauxite (Halimba deposit; Bárdossy† – personal communication), other karst bauxites from the Parnassos-Ghiona area (Ochsenkühk & Parissakis, 1977; Laskou, 1991; Laskou & Economou-Eliopoulos, 2007; Eliopoulos & Economou-Eliopoulos, 2010; Laskou et al., 2011; Laskou & Economou-Eliopoulos, 2013), and the karst bauxites from other localities of the Mediterranean bauxite belt (Italian bauxites: Mongelli, 1997; MacLean et al., 1997; Mameli et al., 2007; Mondillo et al., 2011; Boni et al., 2013; Mongelli et al., 2014; Turkish bauxites: Özlü, 1978; Öztürk et al., 2002; Karadağ et al., 2009; Haniççi, 2013; Hungarian bauxites: Maksimović et al., 1991) are illustrated in the lower image of **Figure 3.4.5**.

Figure 3.4.5: Ni versus Cr binary diagrams (after Mongelli et al., 2014 – personal communication) illustrating the differences in the Ni/Cr ratio of the karst bauxites from the Mediterranean bauxite belt.

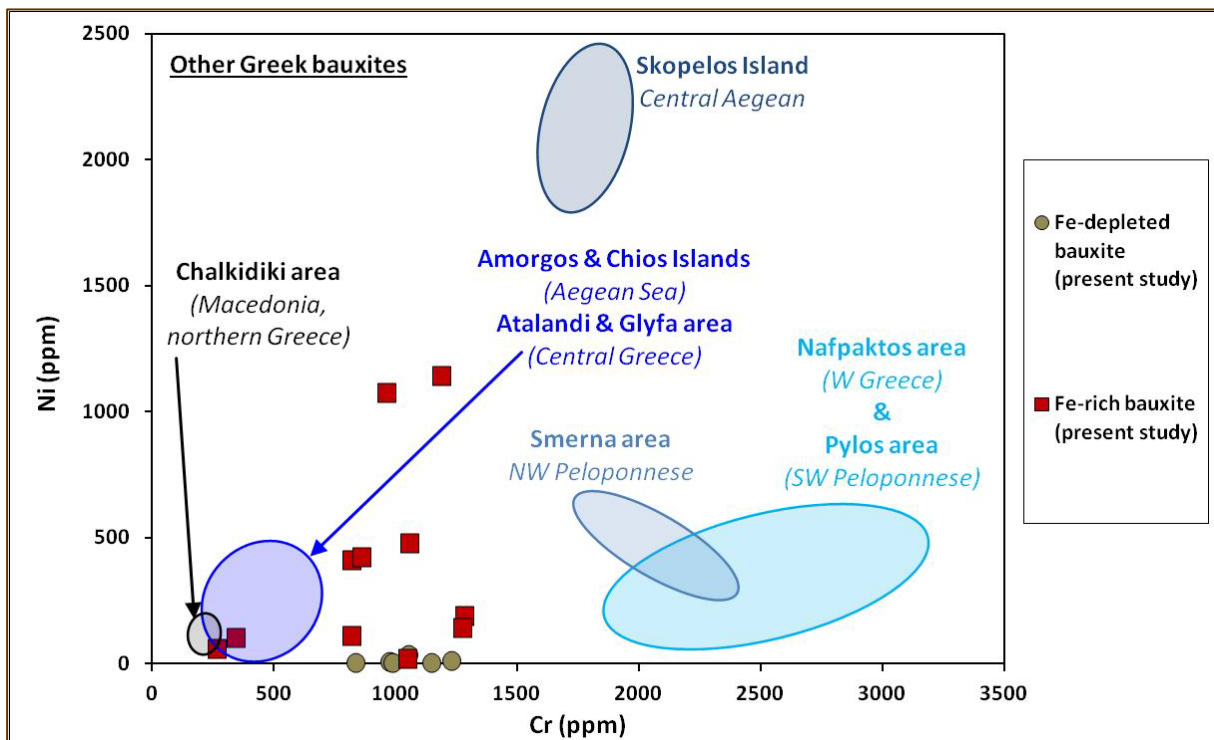


Figure 3.4.5: continued.

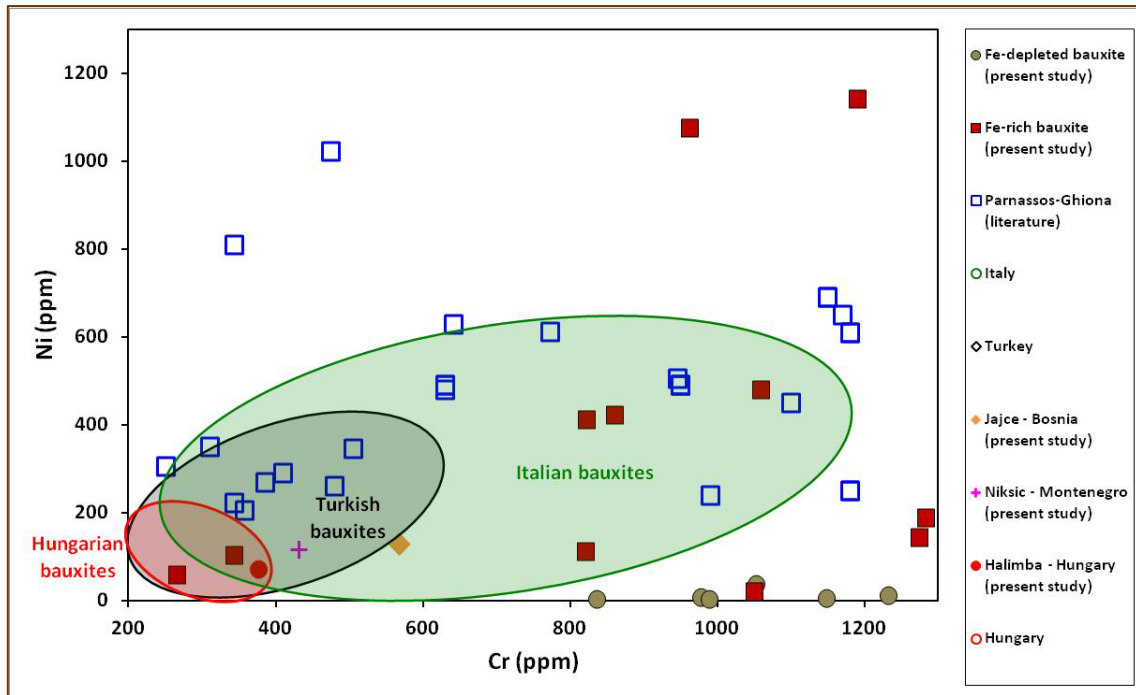


Figure 3.4.6: Binary diagram of Cr versus Ni (after Valeton, 1972 and references therein) for bauxites from Parnassos-Ghiona area (present dissertation), together with karst bauxites from Balkan (see legend), and Hungarian (see legend) active mines for comparison reason (present dissertation; Bárdossy† – personal communication).

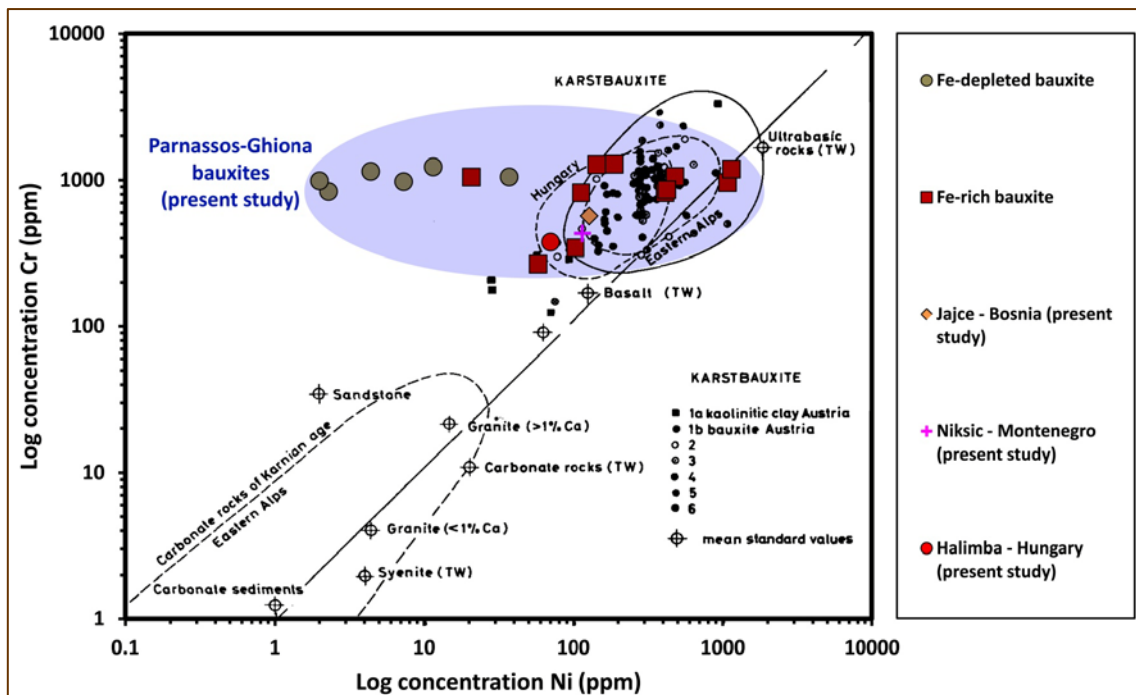


Figure 3.4.7: Binary correlation diagram of La/Th versus Hf (ppm) for karst bauxites from Parnassos-Ghiona active mining area. The value of UCC (Rudnick & Gao, 2003) is indicated for comparison reason.

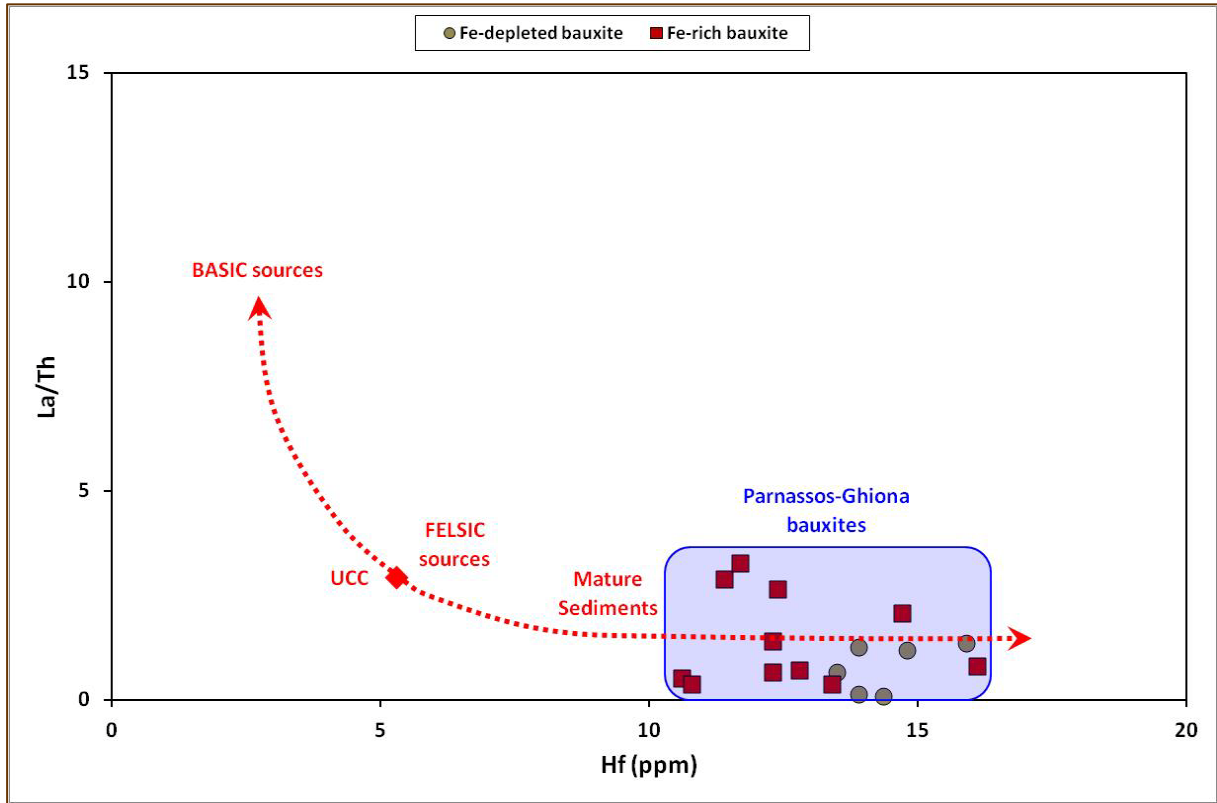


Figure 3.4.8: Triangular Zr-Cr-Ga

diagram showing the parental affinity of Parnassos-Ghiona karst bauxites (after Özlü, 1983).

The areas influenced by ultramafic, mafic, intermediary or argillaceous and acidic parent rocks are represented by I, II, III, and IV indexes, respectively (Özlü, 1983 and references therein).

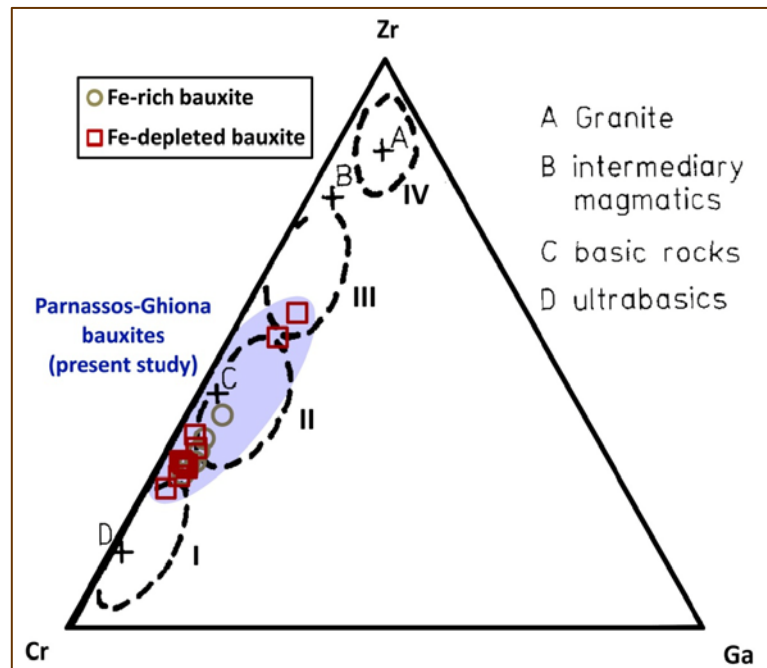


Figure 3.4.9: Binary correlation diagrams of $\text{Log}(\text{Th}/\text{Sc})$ vs $\text{Log}(\text{Zr}/\text{Sc})$ and $\text{Log}(\text{Th}/\text{Sc})$ vs $\text{Log}(\text{Cr}/\text{Th})$ indicating the provenance of karst bauxites from Parnassos-Ghiona active mining area (after Rollinson, 1993; Muftah et al., 2013 and references therein). The values of DMM (Depleted MORB Mantle; Salters & Stracke, 2004), avg. MORB (Sun & McDonough, 1989; Rollinson, 1993 and references therein), avg. diabase (Mason & Moore, 1982; Krauskopf & Bird, 1994), avg. crustal (Mason & Moore, 1982), UCC (Rudnick & Gao, 2003), avg. shale (Krauskopf & Bird, 1994), pelagic clays (Li, 1991 and references therein), and avg. granite (Mason & Moore, 1982; Krauskopf & Bird, 1994), are indicated for comparison.

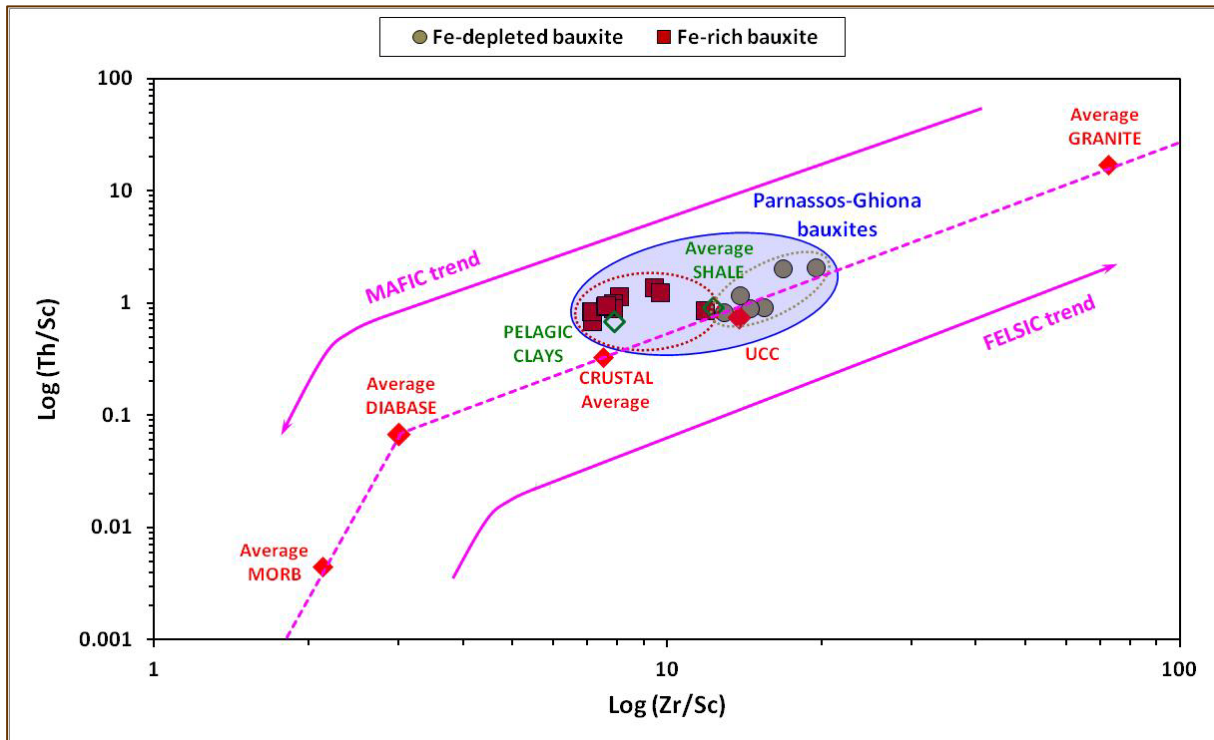
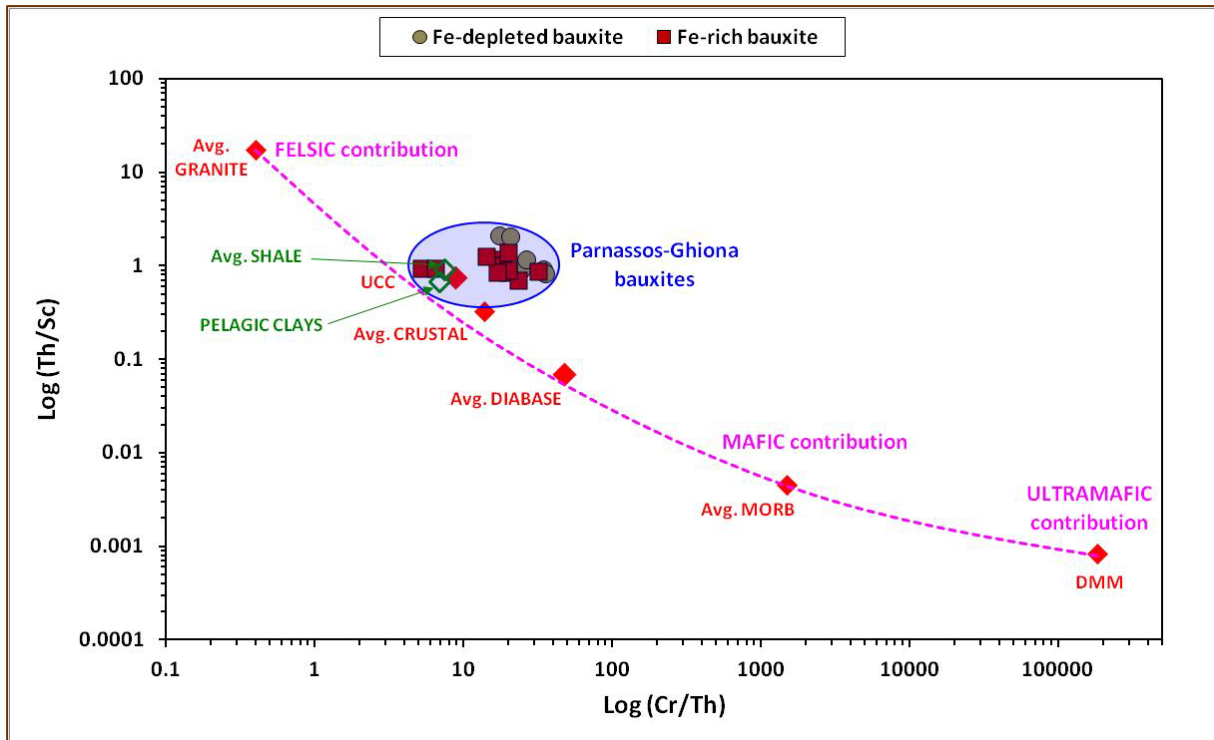
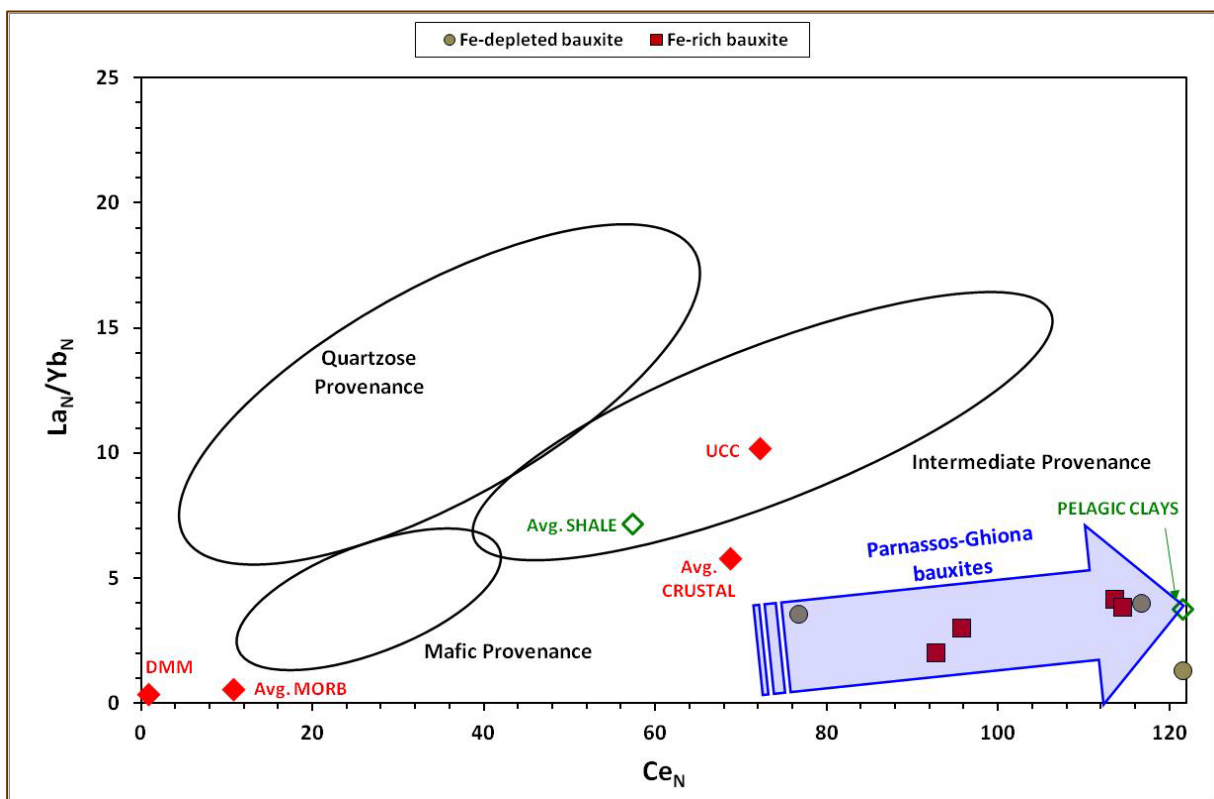


Figure 3.4.9: continued.



Furthermore, specific information about the origin of the studied Parnassos-Ghiona bauxites sampled from active mines, can be obtained using discrimination geochemical diagrams based on REE and REE anomalies, i.e., Eu/Eu^* and Ce/Ce^* (e.g., Rollinson, 1993; Alexander et al., 2000; Mameli et al., 2007; Leybourne & Johannesson, 2008 and references therein; Mondillo et al., 2011; Mongelli, et al., 2014; Mongelli, 2014 – personal communication; see Figures 3.4.10 – 3.4.17). The REE discrimination diagrams, in accordance to the previous trace element diagrams, clearly support the fact that bauxites concern mature (intensively re-processed) geological materials of multiple (mixed) sources (Figures 3.4.6 – 3.4.9). In particular, Eu_N values of the studied Parnassos-Ghiona bauxite samples (Figures 3.4.13 – 3.4.14), are demonstrated between the avg. volcanic, the avg. shale and the NASC symbols (after Leybourne & Johannesson, 2008 and references therein) and, particularly, into the “sediment-total”, the “sediment-partial” and the volcanic” field. In accordance to the previous statements about the provenance of the studied samples, this reflects the multiple sources of the studied Parnassos-Ghiona bauxites, too. For the first time in the literature, in these diagrams the studied Parnassos-Ghiona bauxites are illustrated to-

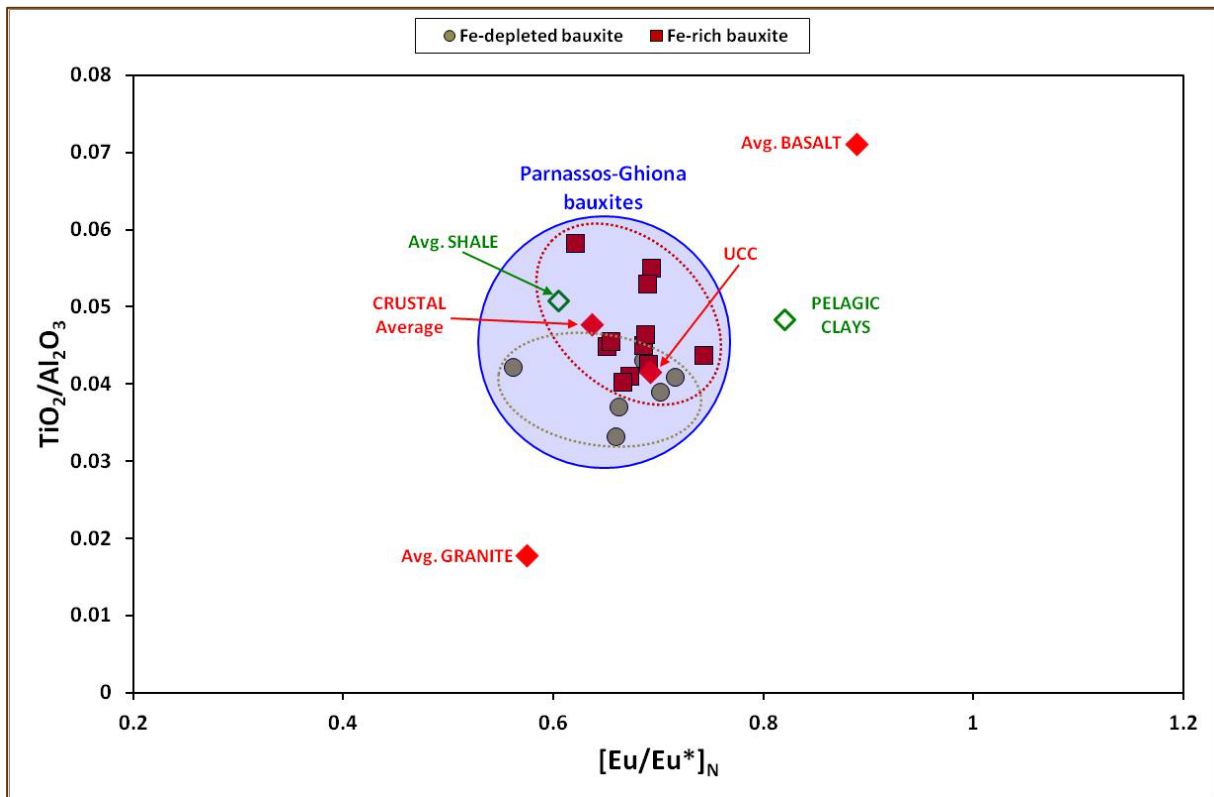
Figure 3.4.10: Binary plot of La_N/Yb_N versus Ce_N (normalized to chondrite; Haskin et al., 1968a; Haskin et al., 1968b; Haskin et al., 1971; Wakita et al., 1971; Boynton, 1985; Taylor & McClennan, 1985; Korotev, 1996a; Korotev, 1996b) showing the relation between the degree of REE fractionation (Rollinson, 1993) and the provenance (Alexander et al., 2000) for karst bauxites from Parnassos-Ghiona active mining area. The values of DMM (Depleted MORB Mantle; Salters & Stracke, 2004), avg. MORB (Sun & McDonough, 1989; Rollinson, 1993 and references therein), UCC (Rudnick & Gao, 2003), avg. crustal (Mason & Moore, 1982), avg. shale (Krauskopf & Bird, 1994), and pelagic clays (Li, 1991 and references therein), are indicated for comparison. Ce anomalies calculated as: $Ce/Ce^* = 3(Ce/Ce_{ch})/\{2(La/La_{ch})+(Nd/Nd_{ch})\}$ after German & Elderfield (1990). Some of the studied Parnassos-Ghiona bauxite samples cannot be illustrated into the depicted field that is limited by the La_N/Yb_N and Ce_N values. This is due to their enormous Ce_N values (see blue semi-transparent arrow).



gether with other bauxites from Parnassos-Ghiona area from the literature (Ochsenkühn-Petropoulou et al., 1994; Ochsenkühn et al., 1995; Laskou et al., 2011; Laskou & Economou-

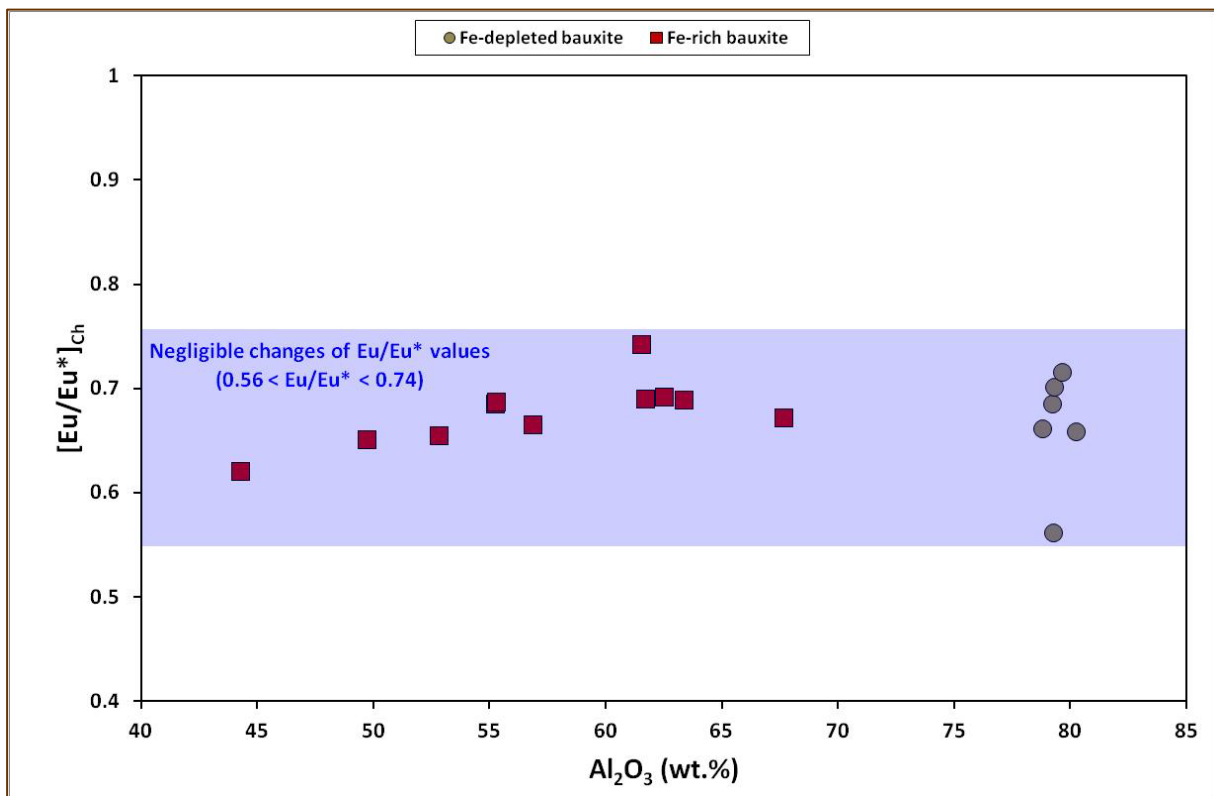
Eliopoulos, 2013), together with bauxites derived from other Greek localities (excluding those of Parnassos-Ghiona mining area: Laskou et al., 2011; Laskou & Economou-Eliopoulos, 2013, and including one isolated sample from Amorgos Island Laskou & Economou-Eliopoulos, 2013), for comparison reason. Furthermore, the studied Greek bauxites are addi-

Figure 3.4.11: Binary diagram of $\text{TiO}_2/\text{Al}_2\text{O}_3$ versus Eu anomalies (normalized to chondrite; Haskin et al., 1968a; Haskin et al., 1968b; Haskin et al., 1971; Wakita et al., 1971; Boynton, 1985; Taylor & McClennan, 1985; Korotev, 1996a; Korotev, 1996b) for the studied bauxites from Parnassos-Ghiona active mining area (after Mameli et al., 2007 and Mondillo et al., 2011). The values of avg. granite (Mason & Moore, 1982; Krauskopf & Bird, 1994), avg. basalt (Mason & Moore, 1982; Krauskopf & Bird, 1994), UCC (Rudnick & Gao, 2003), avg. crustal (Mason & Moore, 1982), avg. shale (Krauskopf & Bird, 1994), and pelagic clays (Li, 1991 and references therein), are indicated for comparison. Eu anomalies calculated as: $\text{Eu}/\text{Eu}^* = 2(\text{Eu}/\text{Eu}_{\text{Ch}})/\{(\text{Sm}/\text{Sm}_{\text{Ch}})+(\text{Gd}/\text{Gd}_{\text{Ch}})\}$ after Liu et al. (2013).



tionally depicted together with karst bauxites from the Mediterranean bauxite belt, such as Hungarian (Halimba deposit: present dissertation; Bárdossy, 2011 – personal communication), Bosnian (Jajce deposit: present dissertation; Bárdossy, 2011 – personal communication), Montenegrin (Niksic deposit: present study; Bárdossy, 2011 – personal communication) and Italian (Mondillo et al., 2011; Boni et al., 2013; Mongelli et al., 2014), as

Figure 3.4.12: Binary diagram of Eu anomaly (normalized to chondrite; Haskin et al., 1968a; Haskin et al., 1968b; Haskin et al., 1971; Wakita et al., 1971; Boynton, 1985; Taylor & McClelland, 1985; Korotev, 1996a; Korotev, 1996b) versus Al_2O_3 showing the negligible changes during intense weathering phenomena (Mameli et al., 2007; Mondillo et al., 2011) for karst bauxites from Parnassos-Ghiona active mining area. Eu anomalies calculated as: $\text{Eu}/\text{Eu}^* = 2(\text{Eu}/\text{Eu}_{\text{ch}})/\{(\text{Sm}/\text{Sm}_{\text{ch}})+(\text{Gd}/\text{Gd}_{\text{ch}})\}$ after Liu et al. (2013).



well as Turkish (Karadağ et al., 2009; Hanilçi et al., 2013). Karst-type bauxites from the Irano-Himalayan bauxite belt (i.e., Iran: Zarasvandi et al., 2008; Esmaeily et al., 2010) as well as from the East Asian bauxite belt (i.e., Chinese Salento-type karstic bauxites: Liu et al., 2010,

and Chinese Permian karst-type bauxites: [Li et al., 2013](#); [Liu et al., 2013](#)) are illustrated for comparison reasons. Despite the significant multiple source of the studied bauxites, it is noteworthy to mention the differences between them and other Greek bauxites (especially that of Amorgos Island, and those of Iran and China). Turkish, Italian, Balkan, and Hungarian karst bauxitic samples seem to have less or more the same provenance ([Figure 3.4.14](#) and [Figure 3.4.15](#)).

Figure 3.4.13: Bivariate plots of Eu versus Ce anomalies (normalized to NASC; [Gromet et al., 1984](#)) for the studied bauxites from Parnassos-Ghiona active mining area (after [Leybourne & Johannesson, 2008](#) and references therein). Eu anomalies calculated as: $\text{Eu}/\text{Eu}^* = 2(\text{Eu}/\text{Eu}_{\text{NASC}})/\{(\text{Sm}/\text{Sm}_{\text{NASC}})+(\text{Gd}/\text{Gd}_{\text{NASC}})\}$ from [Liu et al. \(2013\)](#). Ce anomalies calculated as: $\text{Ce}/\text{Ce}^* = 3(\text{Ce}/\text{Ce}_{\text{NASC}})/\{2 \text{La}/\text{La}_{\text{NASC}}+(\text{Nd}/\text{Nd}_{\text{NASC}})\}$ after [German & Elderfield \(1990\)](#).

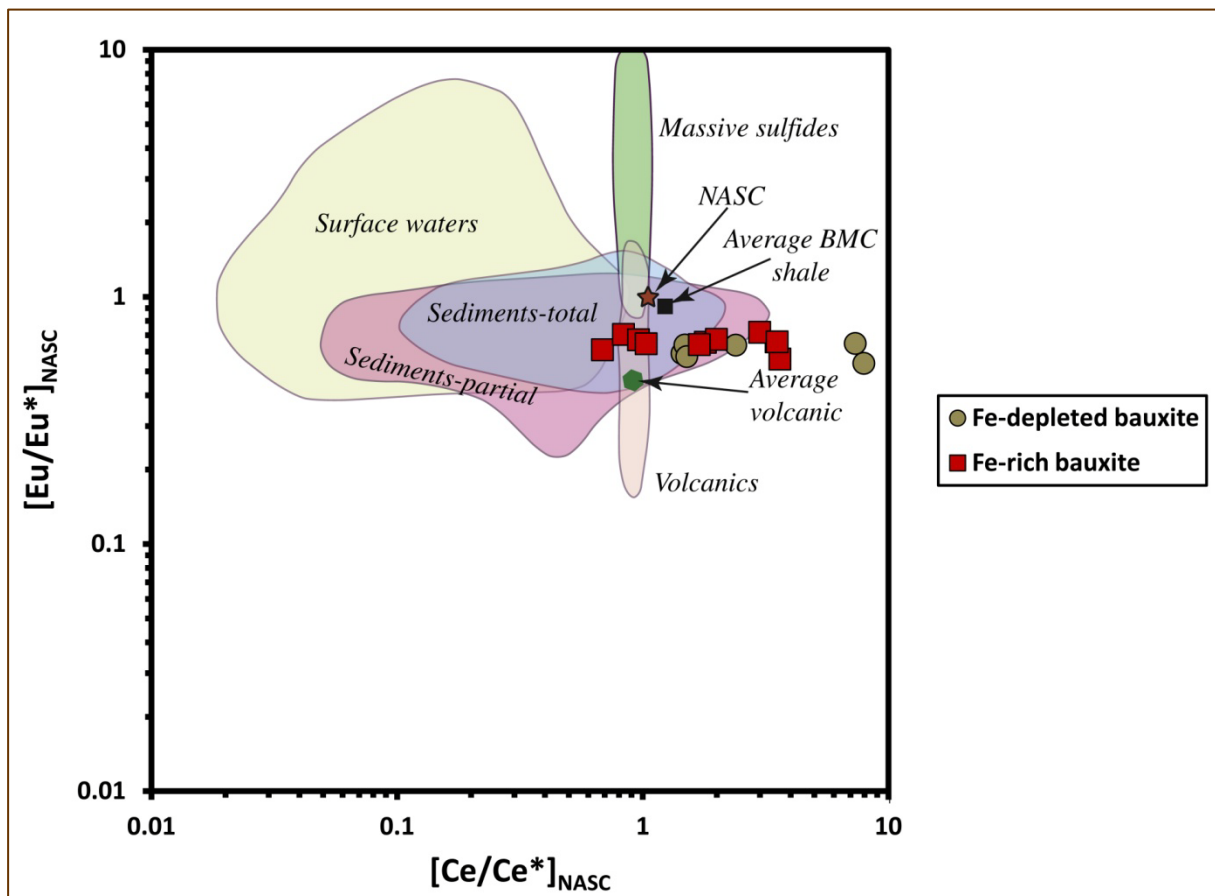
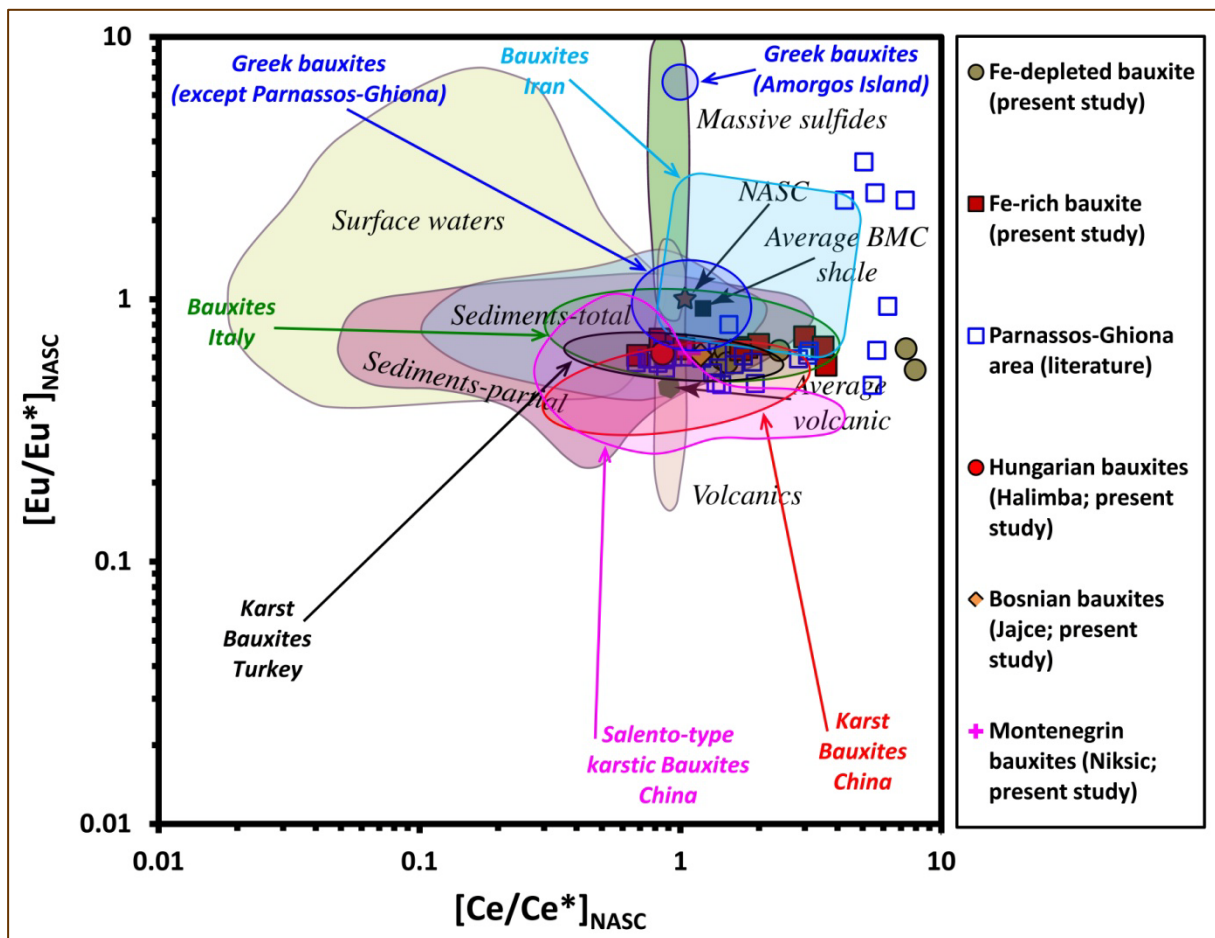


Figure 3.4.14: Bivariate plot (after Leybourne & Johannesson, 2008 and references therein) of Eu versus Ce anomalies (normalized to NASC; Gromet et al., 1984) for the studied Parnassos-Ghiona bauxites in comparison with other Greek bauxites from literature, together with karst bauxites from the Mediterranean bauxite belt, and with Chinese and Iranian karst-type bauxites. Eu anomalies calculated as: $Eu/Eu^* = 2(Eu/Eu_{NASC}) / \{(Sm/Sm_{NASC}) + (Gd/Gd_{NASC})\}$ after Liu et al. (2013). Ce anomalies calculated as: $Ce/Ce^* = 3(Ce/Ce_{NASC}) / \{2 La/La_{NASC} + (Nd/Nd_{NASC})\}$ after German & Elderfield (1990).



Nevertheless, it should be noted that La/Gd as a measure of LREEs/HREEs, plotted versus to Eu/Eu^* , is useful in the classification of REE deposits and the interpretation of their origin (Castor & Hedrick, 2006; see Figures 3.4.16 and 3.4.17). Carbonatites are considered to be mantle-derived rocks with little or no contribution from the crust, while monazite placer de-

posits plot in a region with high La/Gd and low Eu/Eu*, due to contribution from crustal rocks. Moreover, the Fe-REE deposits occupy a linear region giving the impression to link the carbonatite and peralkaline HREE deposit regions, proposing mixed crustal and mantle sources. In accordance, the studied Parnassos-Ghiona bauxites exhibit a similar mixed parental affinity (**Figure 3.4.16**). In general, the majority of karst-type bauxite from the Medi-

Figure 3.4.15: Binary diagram of Sm/Nd versus Eu anomalies (normalized to NASC; [Gromet et al., 1984](#)) indicating the position of the karst bauxites from Parnassos-Ghiona active mining area between the mixing curves of standard lithologies (after [Mongelli, et al., 2014](#); [Mongelli, 2014 – personal communication](#)). Eu anomalies calculated as: $Eu/Eu^* = 2(Eu/Eu_{NASC}) / \{(Sm/Sm_{NASC}) + (Gd/Gd_{NASC})\}$ after [Liu et al. \(2013\)](#). Ce anomalies calculated as: $Ce/Ce^* = 3(Ce/Ce_{NASC}) / \{2 La/La_{NASC} + (Nd/Nd_{NASC})\}$ after [German & Elderfield \(1990\)](#). The values of felsic volcanic ([Condie, 1993](#)), cratonic sediments ([Condie, 1993](#)), PAAS ([Taylor & McClennan 1985](#)), and andesite ([Taylor & McClennan 1985](#)) as well as the values of hanging wall limestone and bedrock limestone (present dissertation), are indicated for comparison in order to be consistent with that of [Mongelli et al. \(2014\)](#).

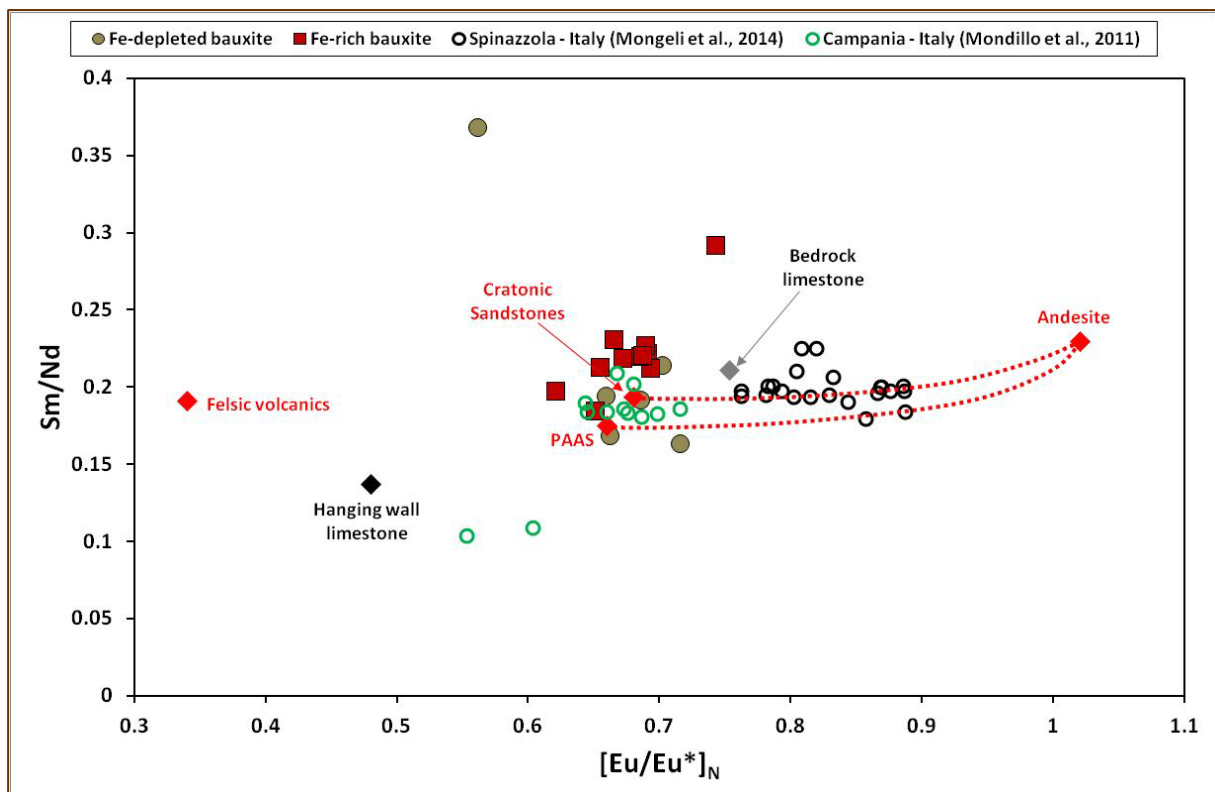
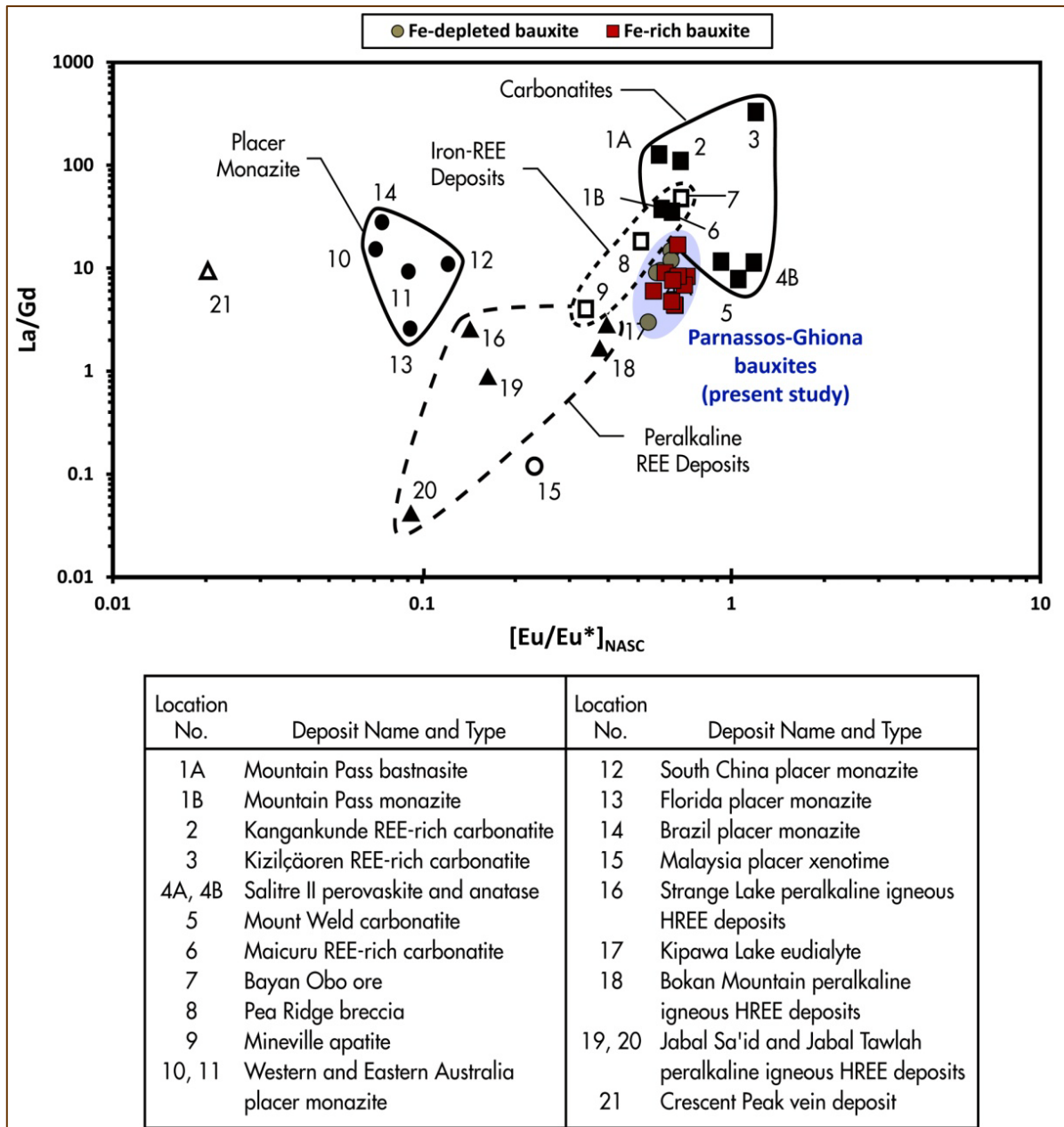
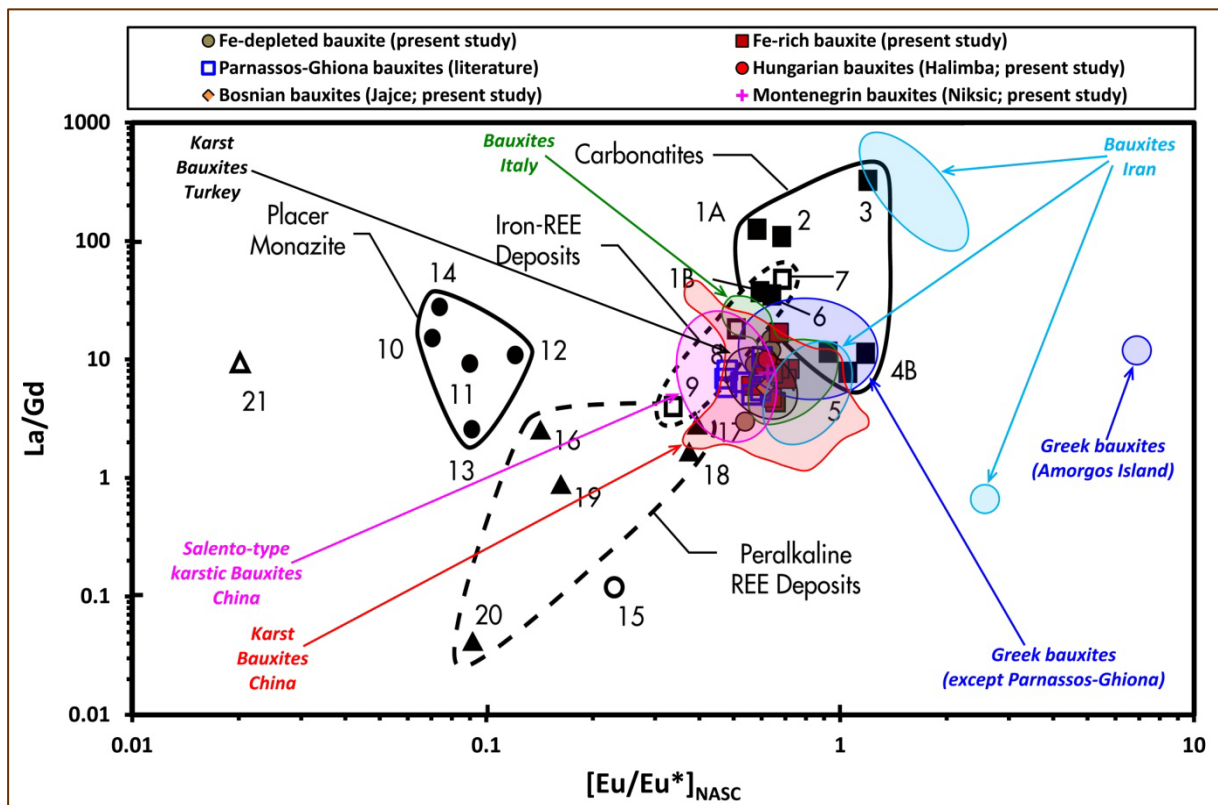


Figure 3.4.16: Bivariate plots of La/Gd versus Eu anomalies (normalized to NASC; Gromet et al., 1984) for the studied bauxites from Parnassos-Ghiona area as compared to samples from various REE deposits (after Castor & Hedrick, 2006, and references therein). Eu anomalies were calculated as: $\text{Eu}/\text{Eu}^* = 2(\text{Eu}/\text{Eu}_{\text{NASC}})/\{(\text{Sm}/\text{Sm}_{\text{NASC}}) + (\text{Gd}/\text{Gd}_{\text{NASC}})\}$ from Liu et al. (2013).



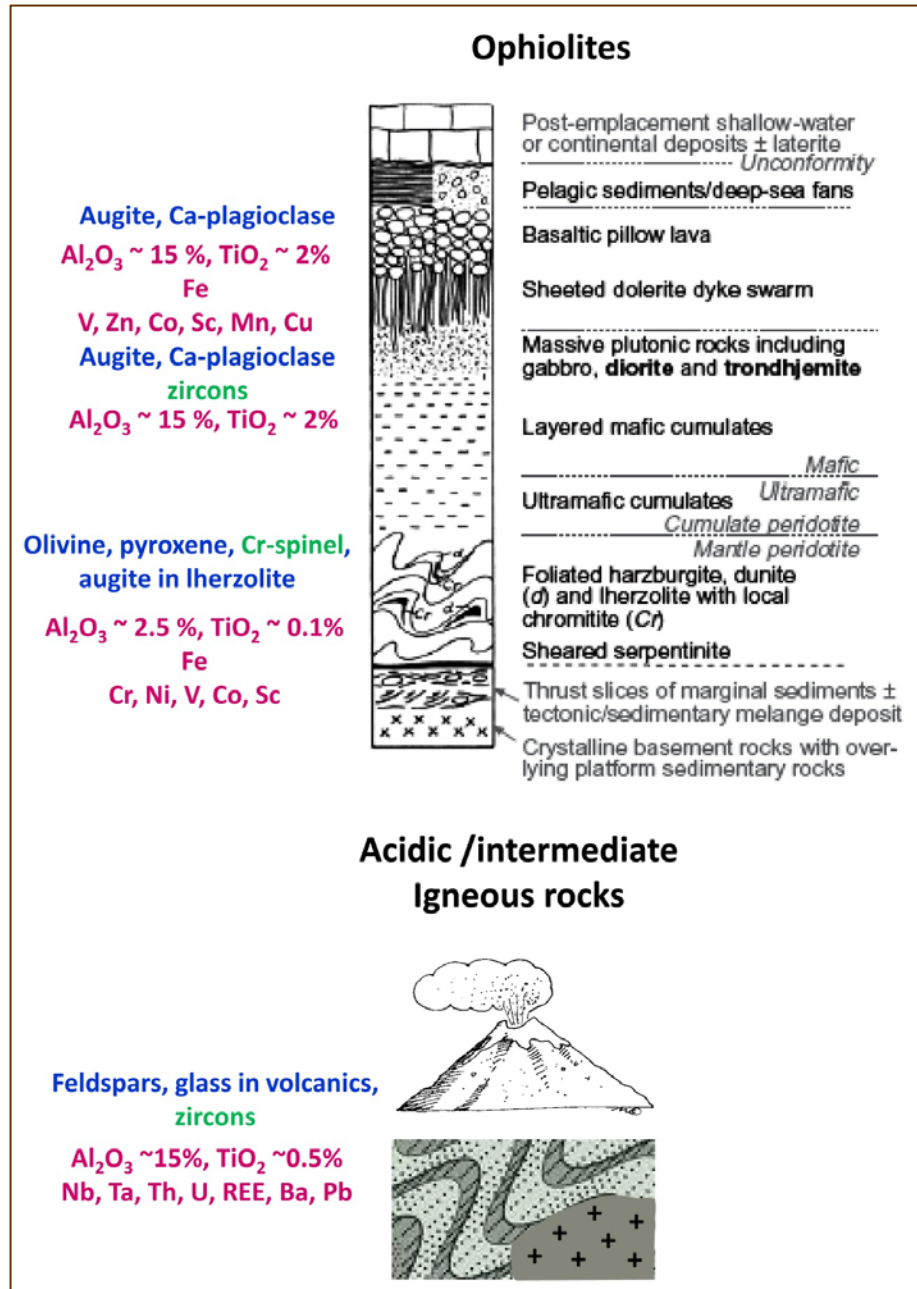
terranean, Irano-Himalayan, and East Asian belt, show a mixed origin. However, some karst-type bauxites from Irano-Himalayan belt show a rather different affinity, lying closer to carbonatites region (Figure 3.4.17).

Figure 3.4.17: Bivariate plots (after [Castor & Hedrick, 2006](#) and references therein) of La/Gd versus Ce anomalies (normalized to NASC; [Gromet et al., 1984](#)) for the studied Parnassos-Ghiona bauxites, for other Parnassos-Ghiona bauxites from the literature ([Ochsenkühn-Petropoulou et al., 1994](#); [Ochsenkühn et al., 1995](#); [Laskou et al., 2011](#); [Laskou & Economou-Eliopoulos, 2013](#)), for other Greek bauxites (except Parnassos-Ghiona ones; [Laskou et al., 2011](#); [Laskou & Economou-Eliopoulos, 2013](#)), for one significant bauxitic sample from Amorgos Island ([Laskou & Economou-Eliopoulos, 2013](#)), together with karst bauxites from the Mediterranean belt (Hungary – Halimba deposit: present dissertation; Bosnia – Jajce deposit: present dissertation; Montenegro – Niksic: present dissertation; Italy: [Mondillo et al., 2011](#); [Boni et al., 2013](#); [Mongelli et al., 2014](#); Turkey: [Karadağ et al., 2009](#); [Haniççi et al., 2013](#)). Karst-type bauxites from the Irano-Himalayan bauxite belt (Iran; [Zarasvandi et al., 2008](#); [Esmaeily et al., 2010](#)) and from the East Asian bauxite belt (i.e., Chinese Salento-type karstic bauxites: [Liu et al., 2010](#); Chinese Permian karst bauxites: [Li et al., 2013](#); [Liu et al., 2013](#)) together with as well as major REE deposits (see REE legend of the figure above) are also illustrated for comparison reasons. Eu anomalies calculated as: $Eu/Eu^* = 2(Eu/Eu_{NASC}) / \{(Sm/Sm_{NASC}) + (Gd/Gd_{NASC})\}$ from [Liu et al. \(2013\)](#).



Taking into account all the above, it is evident that acidic igneous rocks, predominantly volcanic, also contributed, besides ophiolites, to the formation of Parnassos-Ghiona bauxite deposits (**Figure 3.4.18**).

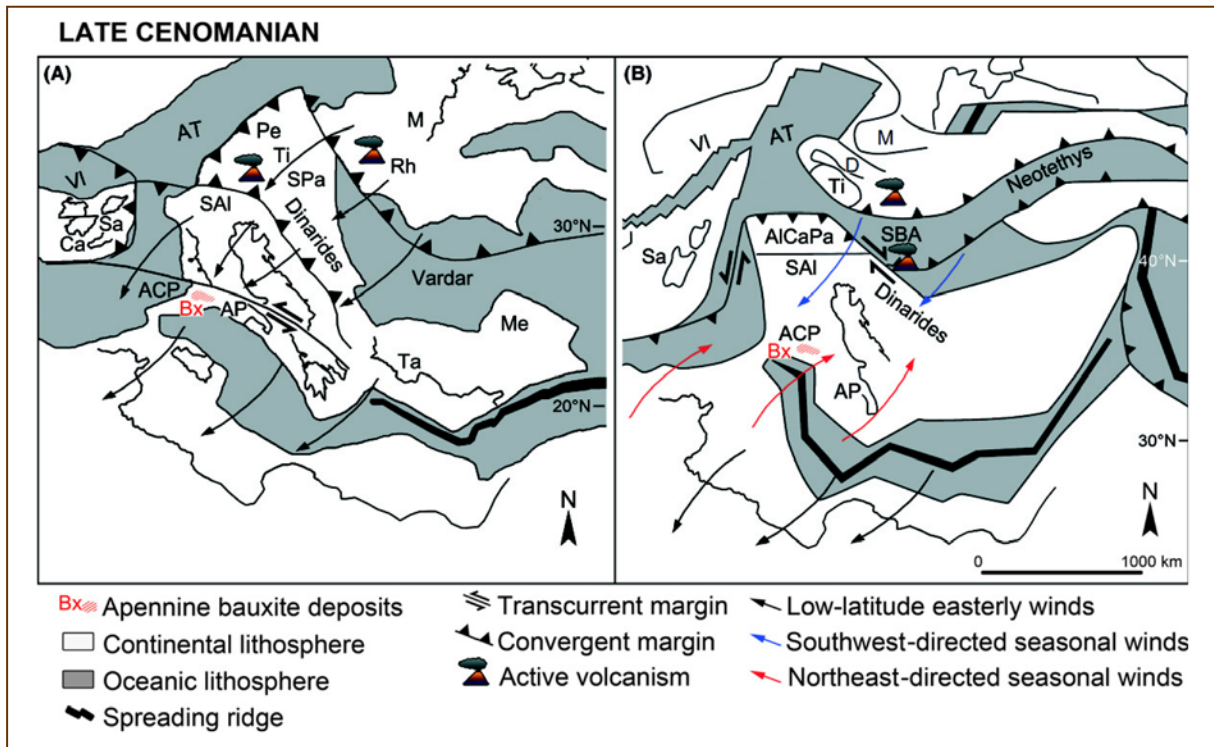
Figure 3.4.18:
Geological formations provided with chemical elements in karst bauxites of Parnassos-Ghiona area.



However, the exact source and age of the acidic rocks is still questionable. Regarding Italian karst-type bauxites, it has been proposed that may have formed from

windblown acidic-intermediate pyroclastic material (volcanic ash) which covered the carbonate platform(s) as a thin blanket and was subjected to lateritization and local remobilization (Bárdossy et al., 1977). Accordingly, Boni et al. (2012) reported, on the basis of zircon U-Pb isotopic data, contemporary Cretaceous volcanic sources, indicating remote origin (**Figure 3.4.19**) from the Dinaric and Carpatho-Balkan orogenic belts (Pamić et al., 2000).

Figure 3.4.19: Dinaric and Carpatho–Balkan Cretaceous volcanic sources of Italian karst bauxites (Boni et al., 2012)



In the case of Greek bauxites, and particularly of Parnassos-Ghiona bauxites, the aforementioned contemporary remote Cretaceous volcanic sources seem not to be particularly involved; inasmuch there must be neighboring pre-Cretaceous sources (Papanikolaou 2014 – personal communication; present dissertation). These sources concern most probably Triassic volcanic rocks showing a variable composition, from sub-alkaline basalts to rhyolite (Pe-Piper, 1982; Pe-Piper, 1998; Monjoie et al., 2008; Tsikouras et al., 2008, Barth & Gluhak, 2009; Koutsovitis et al., 2012; Figure 3.4.20), volcano-sedimentary complexes formed during the rifting stage of Permo-Triassic age (Papanikolaou, 2009; Papanikolaou, 2013), and perhaps also Paleozoic igneous rocks (~ 300 Ma) occurring in the pre-Alpine basement of areas such as the central Evia Island (Papanikolaou, 2009; Papanikolaou, 2013; Papanikolaou 2014 – personal communication).

Figure 3.4.20: Triassic volcanic rocks of Greece and eastern Mediterranean (upper image: Pe-Piper, 1998; lower image: Monjoie et al., 2008).

Therefore, it can be concluded that pre-Cretaceous (Middle-Upper Jurassic) ophiolitic rocks (in particular basaltic minerals provided with Al), as well as pre-Jurassic acidic igneous rocks (in particular volcanic glass provided also with Al), may have contributed to later (Jurassic-Cretaceous) bauxites of Parnassos-Ghiona. The suggested structures of Hellenides involved in the genesis of the Parnassos-Ghiona bauxites are shown in **Figure 3.4.21** (Papanikolaou, 2009; Papanikolaou, 2013; Papanikolaou, 2014 – personal communication; present dissertation), where the parent rocks, which had been tectonically emplaced prior to the genesis of the Parnassos-Ghiona bauxites, are illustrated. These geological multi-sources provided with bauxitic material that filled the paleo-karst carbonate cavities of the Parnassos-Ghiona geotectonic zone.

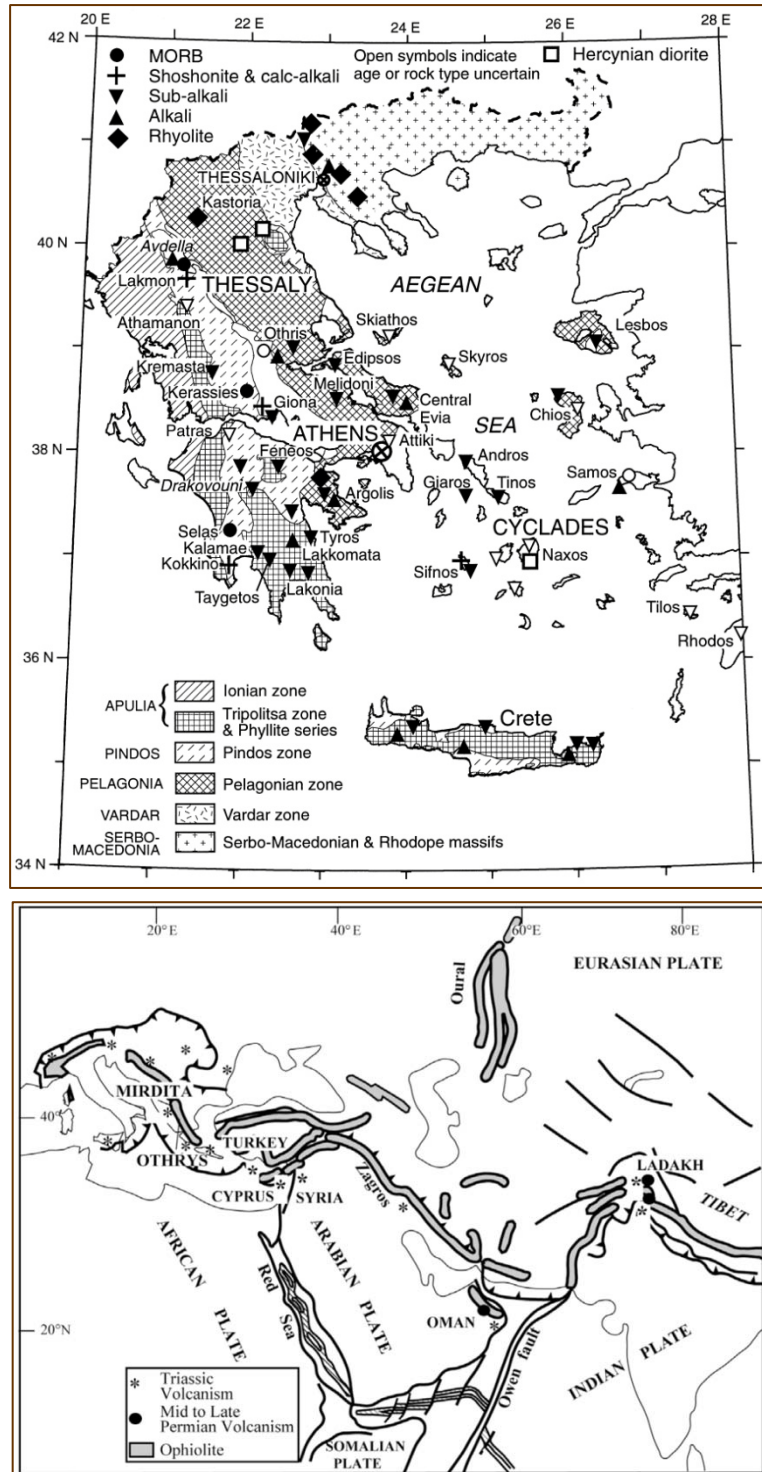


Figure 3.4.21: Schematic representation of the complex geological structures of Hellenides involved in the genesis of the Parnassos-Ghiona bauxites (Papanikolaou, 2014 – personal communication; present dissertation). Upper image: sources of Parnassos-Ghiona bauxites that supplied with material, which subsequently was transferred and trapped in the palaeo-karst cavities of carbonate platforms prior to the genesis of bauxites (modified after Papanikolaou, 2009); Lower image: Illustration of the volcano-sedimentary complex, the ophiolite complex the Mesozoic carbonate platforms formed the Parnassos-Ghiona carbonate sequence, and the flysch deposits of the two tectonostratigraphic models of the Hellenic terranes from which the karst carbonate cavities were being supplied by: continental/platforms (a) and oceanic (b) (Papanikolaou, 2013).

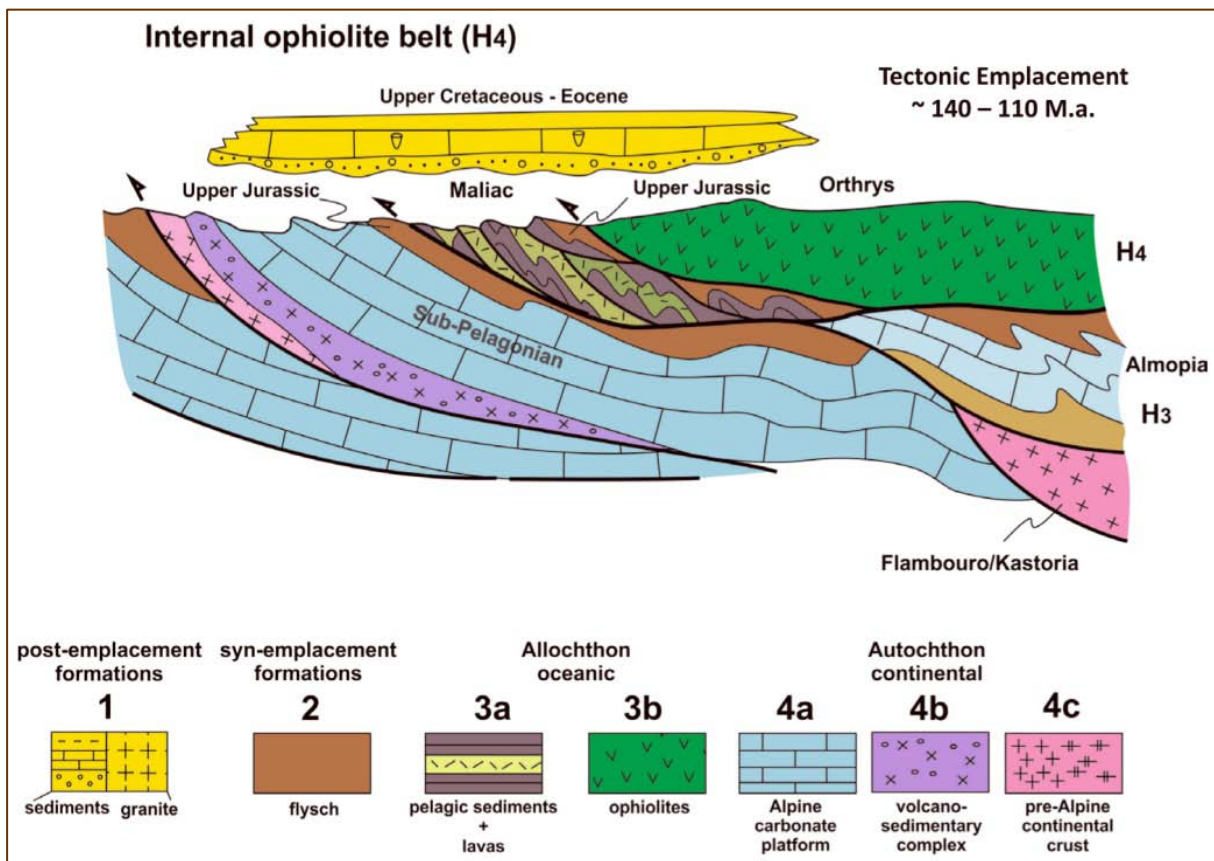
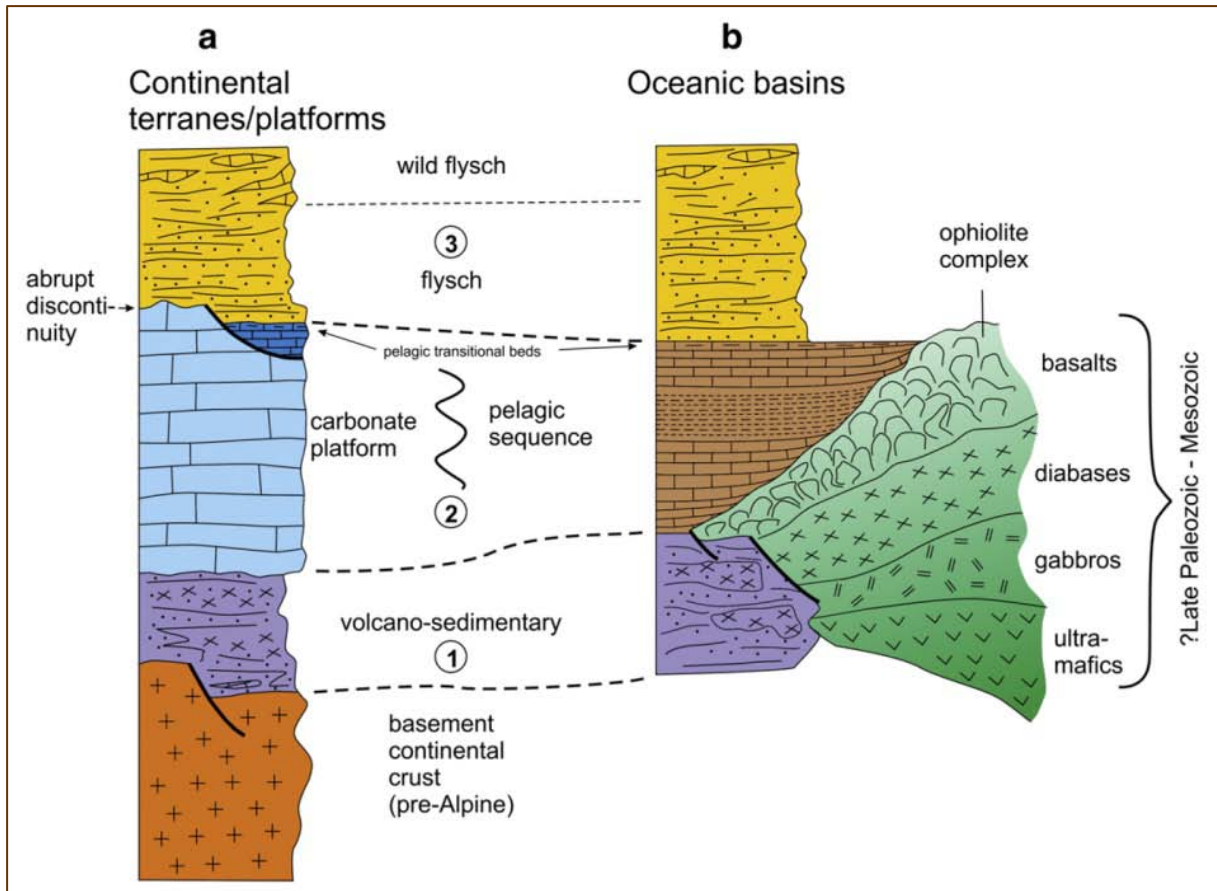


Figure 3.4.21: continued.



3.5. Comparison of bauxite with red mud

3.5.1. Red mud characterization in bulk, microscale and nanoscale

According to powder-XRD patterns (upper image of **Figure 3.5.1.1**) red mud contains hematite ($\alpha\text{-Fe}_2\text{O}_3$), calcite (CaCO_3), gibbsite & diaspore (AlOOH -polymorphs) and Na-Ca-Al-silicate-carbonate & Ca-Al-hydroxysilicate phases (cancrinite- & “hydrogarnet”-type phases). “Hydrogarnet” may correspond to katoite ($\text{Ca}_3\text{Al}_2(\text{SiO}_4)_{3-x}(\text{OH})_{4x}$, $x=1.5\text{-}3.0$ or $\{\text{Ca}_3\}[\text{Al}_2](\square_3)(\text{OH})_{12}$; [Grew et al., 2013](#)), on the basis of previous measurements ([Pontikes et](#)

Figure 3.5.1.1: PXRD pattern of the studied red mud from Greece (raw material: upper image; acetic acid-leached coarse fraction sample: lower image; fine fraction sample: inset of the lower image).

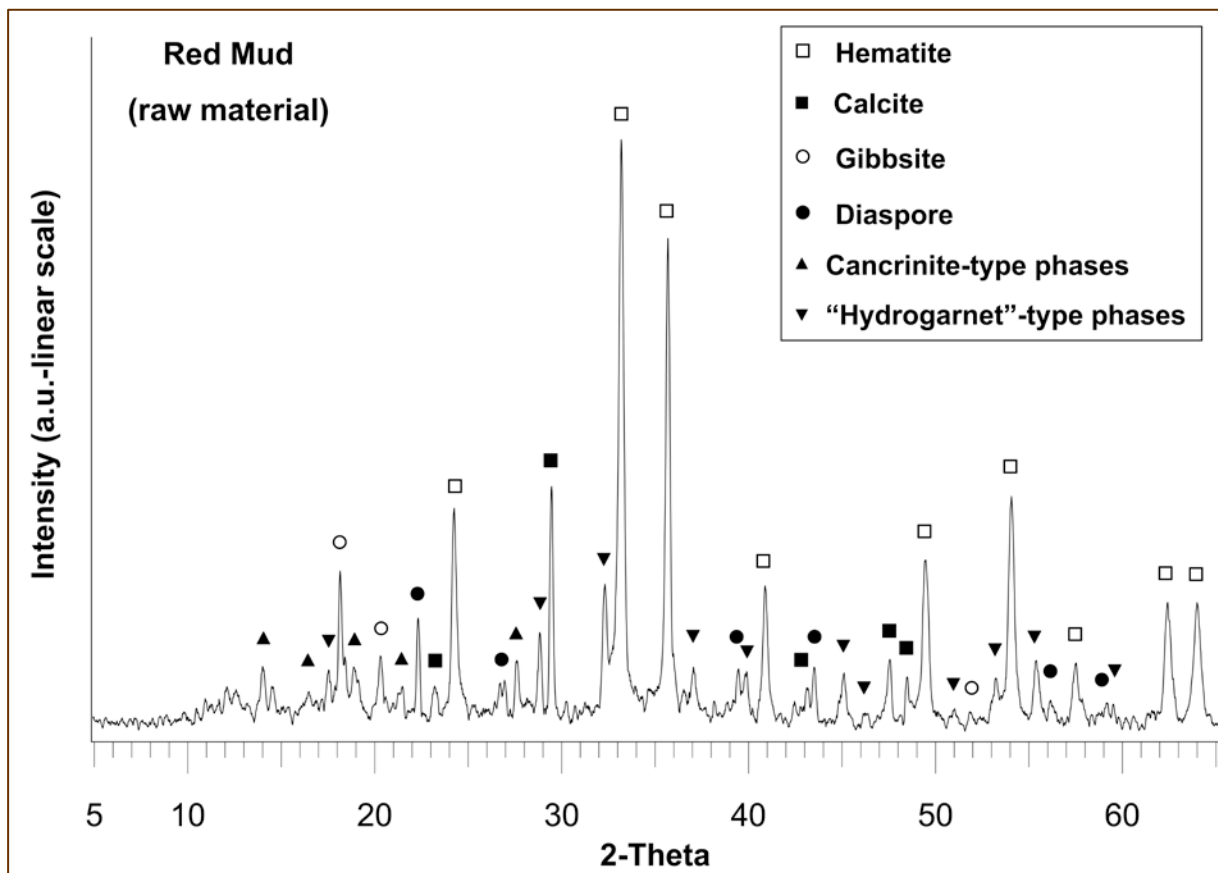
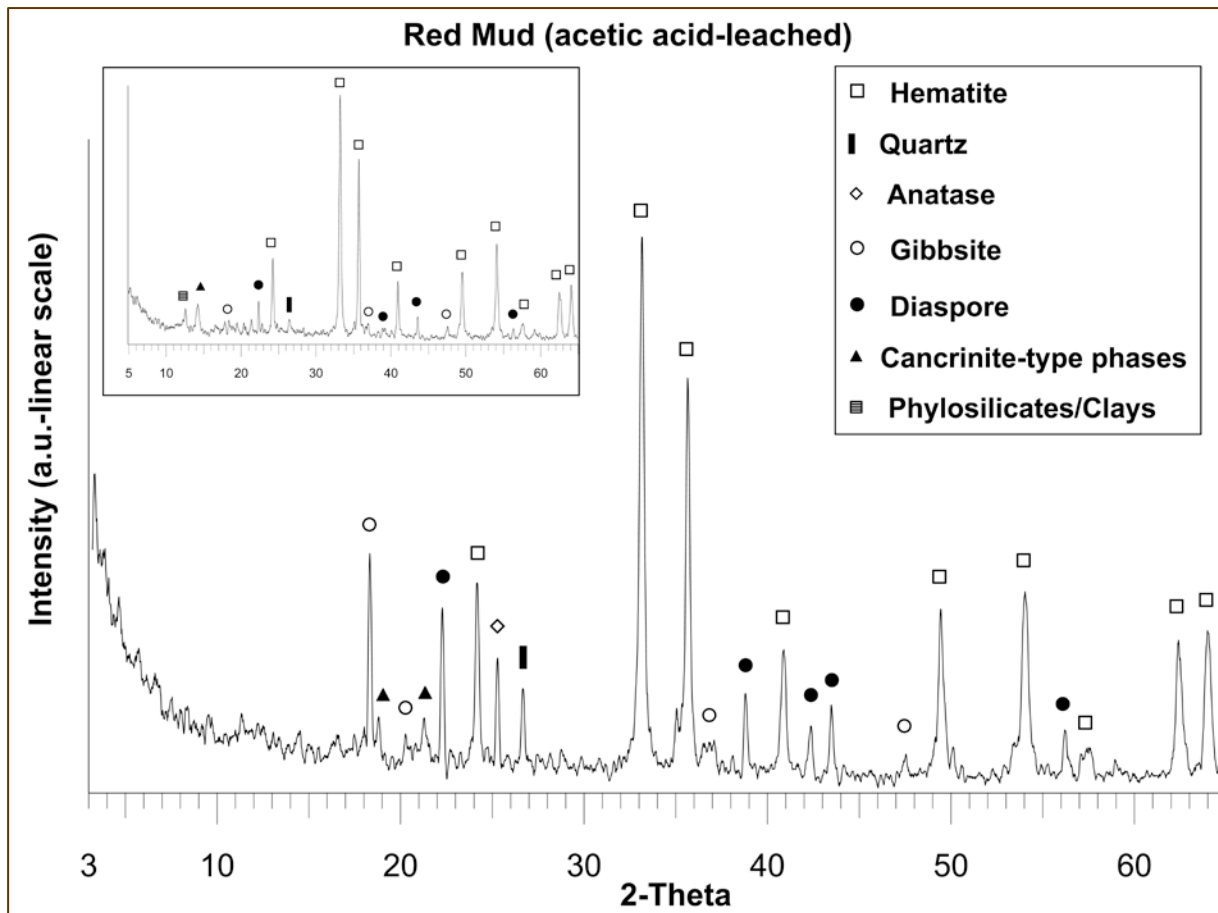


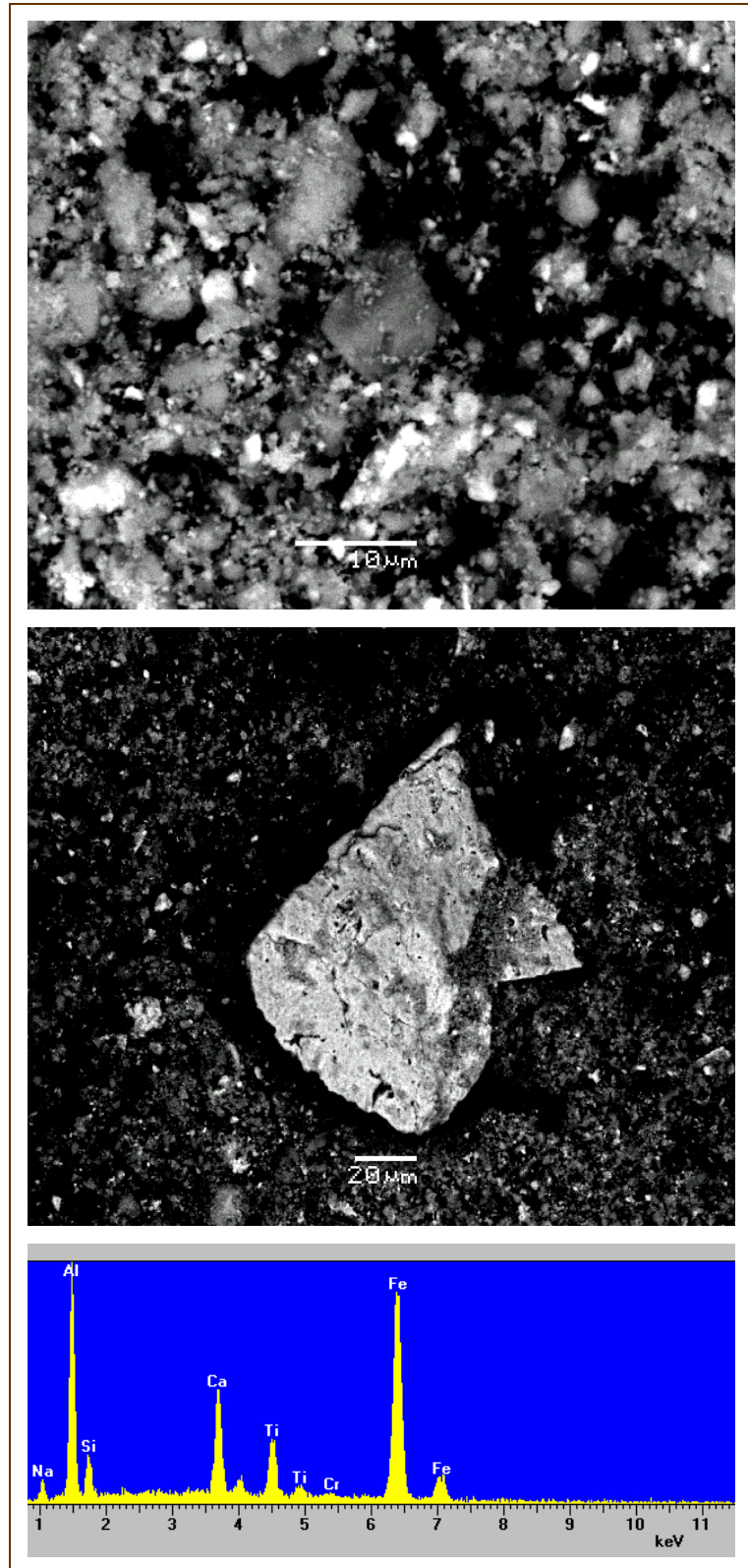
Figure 3.5.1.1: continued.



al., 2006). It should be noted that the same crystalline phases have also been detected in red mud from Ajka alumina plant accident (Burke et al., 2012). The same phases have been detected in the case of seawater-treated samples. On the other hand, carbonate minerals (at least calcite), and also Ca-Al-hydroxysilicate phases, are practically absent in red mud samples leached with acetic acid solutions. There is also a severe decrease in intensity of cancrinite [$\text{Na}_6\text{Ca}_2\text{Al}_6\text{Si}_6\text{O}_{24}(\text{CO}_3)_2$] peaks, in accordance to previous observations, for acid-treated red mud, by Liang et al. (2014). At the same time, distinct peaks of anatase, quartz and phyllosilicates/clay-like phases are revealed in the powder-XRD patterns of the acetic acid-leached red mud (inset of the lower image of Figure 3.5.1.1).

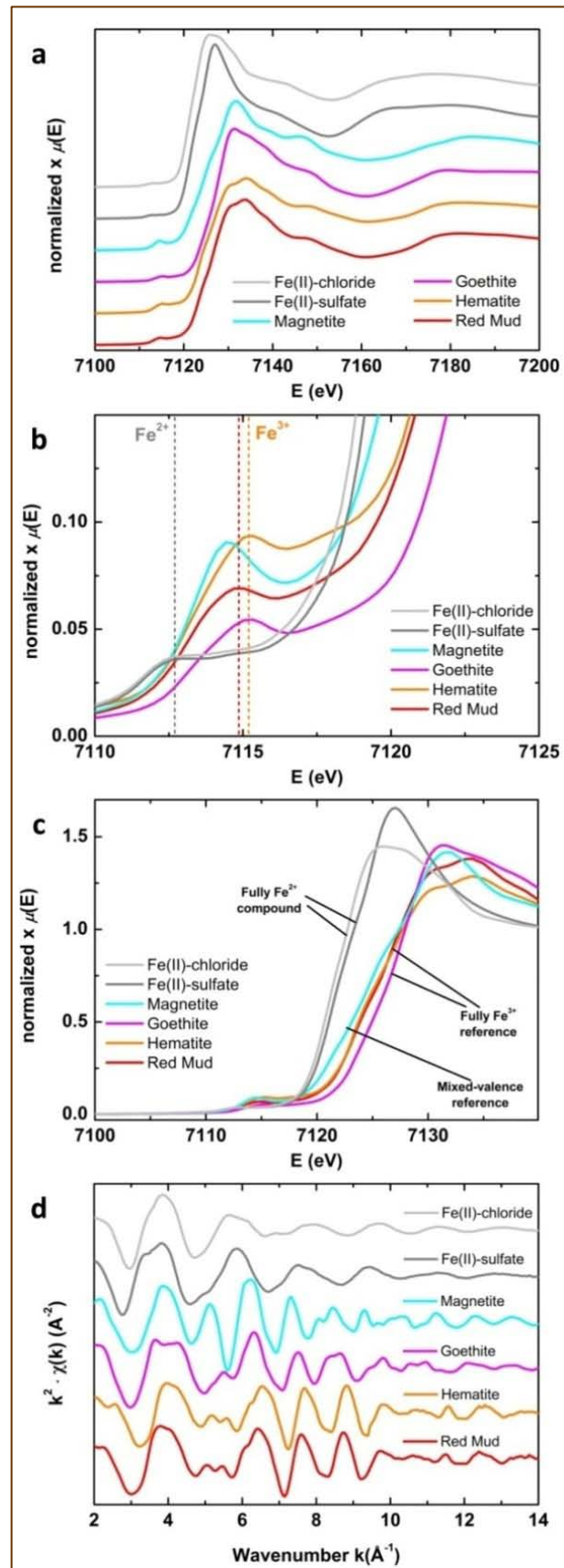
Thus, Fe-oxides, Ti-oxides, AlOOH-polymorphs and clay-like phases are resistant in seawater and acetic acid solutions (see also [Liang et al., 2014](#) and [Smičiklas et al., 2014](#)). Concerning the raw material, Fe, Al, Ca, Ti, Na and Si, and also O and H, are the elements corresponding to XRD-detected solids, while phases related to other elements of interest, such as actinides (namely Th), Cr, V, As, Pb, as well as REE, are not detectable. The same stands for seawater- and acid-treated red mud. However, Cr, together with above major elements, are additionally indicated by SEM-EDS data (**Figure 3.5.1.2**), into an “Al-Fe-Ca-Ti-Si-Na-Cr matrix” appearing in microscale. It is notable that all microareas of the material checked by SEM-EDS follow the same spectral pattern, and therefore there is an apparent homogeneity, in terms of composition, in microscale.

Figure 3.5.1.2: Morphology and chemical composition (major elements) of raw red mud, in microscale, obtained using conventional SEM-EDS.



Taking into account PXRD, it could be assumed that this matrix is an admixture of nanocrystalline phases and potential amorphous and/or poorly crystalline phases. The Fe oxidation state in the material was measured using Fe *K*-edge XANES spectroscopy (Figures 3.5.1.3 – 3.5.1.7), which showed that Fe exists in trivalent state corresponding evidently to the XRD-detected crystalline α -Fe₂O₃ (hematite). However, the further evaluation of the spectra, focusing in the $1s \rightarrow 3d$ pre-edge region (e.g., Waychunas et al., 1983; Bajt et al., 1994; Westre et al., 1997; Galois et al., 2001; Wilke et al., 2001; Berry et al., 2003; Regelin et al., 2014; Henderson et al., 2014 and references therein), revealed that except Fe³⁺, assigned to hematite and goethite component, there is also a minor ferrous Fe contribution. That could be due to small amounts of magnetite component

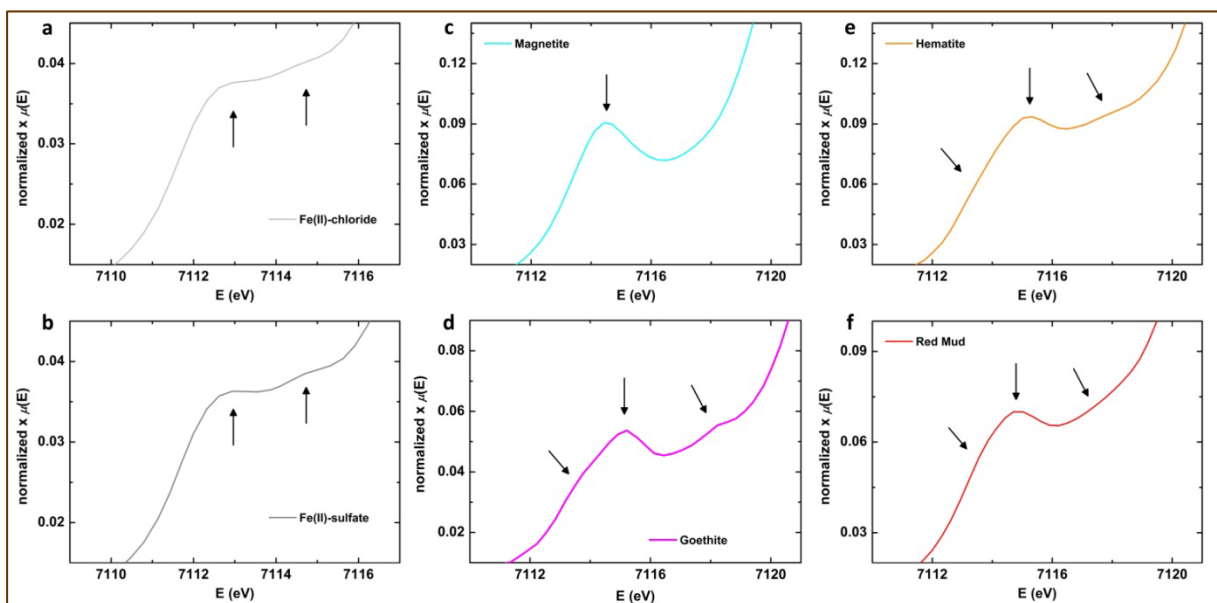
Figure 3.5.1.3: Normalized Fe *K*-edge XANES spectrum of red mud together with, Fe³⁺, Fe²⁺ and mixed-valence reference materials (a); zoom of the pre-edge region also illustrating Fe²⁺ and Fe³⁺ boundaries (b); the energy shift at the main rising part of the *K* absorption edge (c); the Fourier transform (FT) of $\chi(k)$ of the experimental Fe *K*-edge EXAFS signals (d).



($\text{Fe}^{3+}\text{Fe}^{2+}\text{O}_4$), not detectable by powder-XRD, as concluded from the Linear Combination Fitting procedure (LCF), dispersed into the “Al-Fe-Ca-Ti-Si-Na-Cr matrix” in nanoscale. However, in general, the solid-state structural environment of Fe atoms in red mud shows similarities with that in hematite and goethite. To stress structural relationships of Fe between the studied red mud and the measured Fe^{3+} reference materials (hematite and goethite, containing relevant hematite- and goethite-type $^{6}\text{Fe}^{3+}$ components), a comparison method, known as “fingerprinting” (Henderson et al., 2014, and references therein) and the Linear Combination Fitting (LCF) procedure (e.g., Regelink et al., 2014), has been successfully applied.

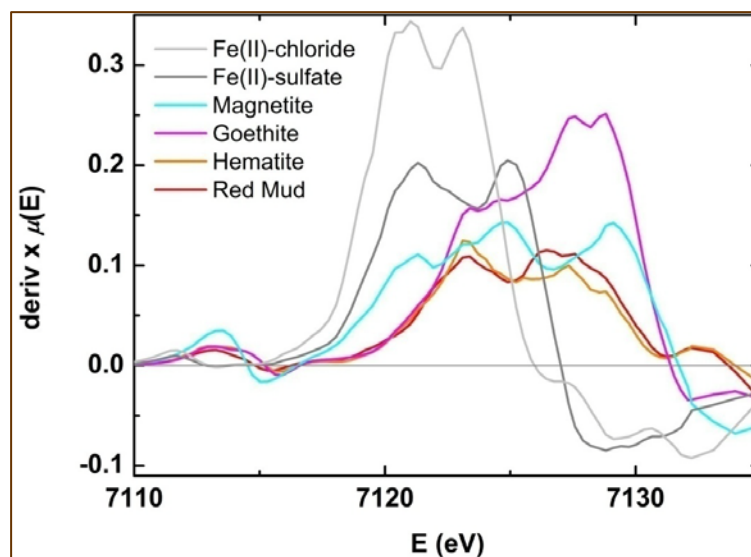
Primarily, the Fourier transform (FT) of $\chi(k)$ of the experimental Fe *K*-edge EXAFS signal of the studied red mud was compared with the EXAFS signals of hematite, goethite, and magnetite as well as with EXAFS signals of the divalent standards (image **d** of Figure 3.5.1.3).

Figure 3.5.1.4: Expanded views focusing in the $1s \rightarrow 3d$ pre-edge region of the experimental Fe *K*-edge XANES spectra of selected synthetic ferrous standards (Fe(II)-chloride: **a**; Fe(II)-sulfate: **b**), natural mixed-valence ($\text{Fe}^{3+}/\Sigma\text{Fe}\neq 1$) iron oxide (magnetite: **c**), synthetic and natural ferric crystalline references (goethite: **d**; hematite: **e**), and of the studied red mud sample (**f**). All pre-edge features are indicated by arrows.



Afterwards, further comparison among the FT of $\chi(k)$ of the Fe *K*-edge EXAFS signals of the red mud – hematite pair (image **a** of **Figure 3.5.1.6**) addressed significant spectral similarities among the first comparative pair, as their EXAFS signals match perfectly each other. Analogous spectral similarities between the red mud and the goethite were revealed, as resemblances at the red mud –

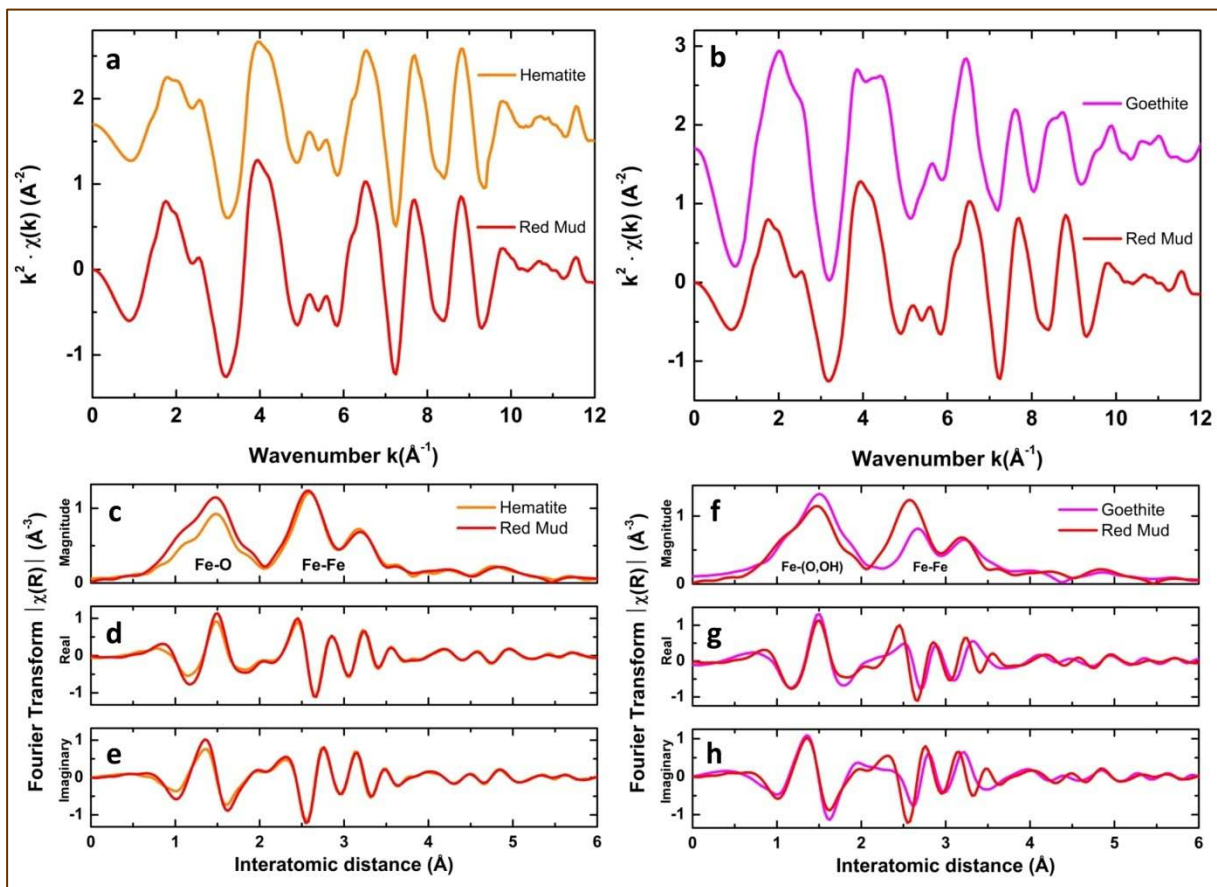
Figure 3.5.1.5: The first derivative spectra of the Fe *K*-edge XANES of the measured references and the studied red mud.



goethite pair were depicted (image **b** of **Figure 3.5.1.6**). In principal, a distinguished well-formed first peak was appeared, while a splitting phenomenon at higher interatomic distance, dividing the next to the first neighbor Fe-Fe atomic shell into two sub-shells, was also observed creating the second and the third peak, respectively (images **c** & **f** of **Figure 3.5.1.6**). This split is common for Fe oxides and oxyhydroxides (e.g., Manceau & Combes, 1988; Manceau & Drits, 1993; Singh et al., 2000; Cornell & Schwertmann, 2003, and references therein). It is noteworthy to mention that the ratio of the second to third peak intensity varies depending on the studied material (Manceau & Combes, 1988), and its intensity is equally enhanced both in the red mud and the hematite, and significantly lesser in goethite FT EXAFS signals. Since the experimental FT of $\chi(R)$ in the magnitude part of the Fe *K*-edge EXAFS signal of the red mud strongly resemble with that of hematite (image **c** of **Figure 3.5.1.6**), possible structural similarities between them can be extrapolated. This hypothesis can alternatively be supported by the similarities appearing at the experimental FT plot in the real (image **d** of **Figure 3.5.1.6**) and the imaginary part (image **e** of **Figure 3.5.1.6**) of $\chi(R)$ of their comparative Fe *K*-edge EXAFS signals. Intensity and shape differences between the peaks of the measured hematite and those of literature (Manceau & Combes, 1988; Manceau & Drits, 1993; Singh et al., 2000) can be attributed to different type of hematite reference (i.e., present sample is a natural pure -grey- hematite type contrary to the natural or synthetic red hematite type usually was used), to transition metals

incorporation into hematite structure (Singh et al., 2000) and to different experimental conditions. The above peak-to-peak comparison of the FT of $\chi(R)$ of the EXAFS signals directly illustrates that the first peak of the red mud matches perfectly with the first peak of hematite corresponding to an O_2 first neighbor (Fe-O shell) surrounding by Fe atoms (e.g., Manceau & Combes, 1988; Manceau & Drits, 1993; Singh et al., 2000; Cornell & Schwertmann, 2003). Besides, the above confirmatory evidence of the presence of a second

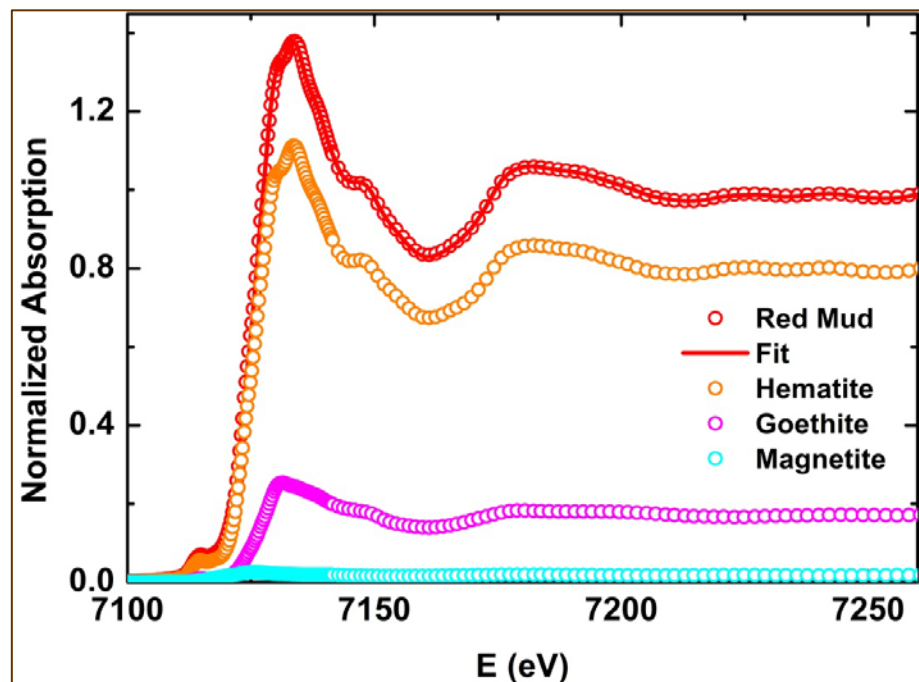
Figure 3.5.1.6: The Fourier transform (FT) of $\chi(k)$ of the experimental Fe *K*-edge EXAFS signal of the studied red mud comparing with EXAFS signals of pure-grey hematite (a), and goethite (b). Respectively, the experimental FT plots in the magnitude (c and f), the real (d and g), and the imaginary part (e and h) of $\chi(R)$ stressing spectral similarities between the Fe *K*-edge EXAFS signals of the red mud and the ferric references (hematite and goethite), using the ATHENA software package (Ravel & Newville, 2005). The second and the third peaks at the FT plot of $\chi(R)$ of the goethite (f) correspond to edge- and to corner-sharing (Manceau & Drits, 1993).



and a third peak establishes the existence of extended local environment around the Fe absorbing atom beyond its first coordination shell in the red mud and, predominantly, the resemblances of the second strongest and third peaks between the FT of $\chi(R)$ EXAFS signal of red mud and hematite can be attributed to the structural similarities among the Fe-Fe shells corresponding to the nearest and the next-to-nearest Fe neighboring atom, respectively (e.g., Manceau & Combes, 1988; Manceau & Drits, 1993; Singh et al., 2000; Cornell & Schwertmann, 2003). Nevertheless, since the experimental FT of $\chi(R)$ in the magnitude part (image **f** of **Figure 3.5.1.6**) of the Fe *K*-edge EXAFS signal of the red mud is not far away from that of goethite-type $^{[6]}\text{Fe}^{3+}$ component, possible structural similarities, also, between them cannot be excluded. This can be yielded by the experimental FT plot in the real (image **g** of **Figure 3.5.1.6**) and the imaginary part (image **h** of **Figure 3.5.1.6**) of $\chi(R)$ of the compared Fe *K*-edge EXAFS signals. Proportionally to the comparison of red mud to hematite component, the previous assessment also stands for the comparison of red mud to goethite component. Hence, the latter comparative finding denotes that the first peak of the red mud can be related not only to the first O^{2-} neighbor anion (as in the previous case of hematite-type $^{[6]}\text{Fe}^{3+}$ component) but, also, to a OH^- neighbor anion (as in the case of goethite-type $^{[6]}\text{Fe}^{3+}$ component), while the presence of Fe-Fe configuration in the red mud local structural environment is confirmed by the depiction of the second and third peaks corresponding to edge- and corner-sharing linkages, likewise also as in the case of goethite (e.g., Manceau & Combes, 1988; Manceau & Drits, 1993; Cornell & Schwertmann, 2003). Despite slight differences of the second peak between the red mud and the goethite reference (image **f** of **Figure 3.5.1.6**), the spectral similarities indicate that the majority of Fe atoms in red mud occupy hematite- and goethite-type octahedra ($^{[6]}\text{Fe}^{3+}$). The first ones correspond primarily to hematite (detected by both XRD and STEM-EDS/EELS) whereas the second ones have not been undoubtedly ascribed in a particular crystalline phase either in microscale or in nanoscale. Furthermore, on the basis of local structural differences between well-crystalline hematite and goethite (Manceau & Drits, 1993) and the established spectral similarities, the latter suggestion can drive to the assumption that part of the ferric basic structural units of the red mud can be linked to each other by face-linkages (due to structural similarities of red mud with hematite components), in addition to the other two type of linkages, while proportionally the rest of them might be linked only through corner- and edge-linkages existing only in goethite local structure (due to structural similarities between the red mud

and the goethite component). Since the second and the third peaks at the FT plot of $\chi(R)$ of the goethite correspond to different type of linkage of octahedra and, particularly, to edge- and to corner-sharing, respectively (Manceau & Drits, 1993), differences in the intensity between the second peak of the red mud and the second peak of the goethite FT EXAFS signal (image f of Figure 3.5.1.6) could be indirectly attributed to a possible less proportion of ferric octahedra linked by edge-linkages, though it is known that interatomic distances across edge- and face-sharing octahedra are too close to be separated by EXAFS (Manceau & Combes, 1988). Besides, and taking into account the structural characteristics of both hematite and goethite local environment (e.g., Cornell & Schwertmann, 2003, and references therein), it can be also assumed that apart from the Fe^{3+} ions in red mud surrounded by O^{2-} anions producing pairs of $\text{Fe}(\text{O})_6$ octahedra (as in the case of hematite-type structure; see Cornell & Schwertmann, 2003, and references therein), a substantial part of this cation can be surrounded by three O^{2-} and three OH^- anions forming $\text{FeO}_3(\text{OH})_3$ octahedra in the local environment of red mud (as in the case of goethite-type structure; see Cornell & Schwertmann, 2003, and references therein). Complementary to the depicted hematite-type structural characteristics of the red mud, the considerable amount of goethite-type structural signature approved by the “fingerprinting” method, can alternatively be explained by

potential epitaxial growth of goethite onto hematite resulting from the structural relationships between the (003) plane of hematite and the (100) goethite planes (Cornell & Schwertmann, 2003, and references



therein). The above polyhedral approach can be semi-quantitatively reflected and affirmed by the LCF procedure of the Fe *K*-edge XANES analysis using the Athena software package (Ravel & Newville, 2005). The LCF procedure (R-factor=0.0000475; chi-square=0.00206; Reduced chi-square=0.0000139; see: **Figure 3.5.1.7**) yielded Fe atoms corresponding 80.9 % to hematite component (attributed fundamentally to hematite XRD-detectable crystals -in fact nano-hematite proved by STEM-EDS/EELS), 17.3 % to goethite component (belonging to rather unknown phase either in microscale or nanoscale), and 1.8 % to magnetite component (in fact nano-magnetite, as indicated by STEM-EDS/EELS).

Regarding chemical composition of red mud, XRF and ICP-OES/MS measurements proved major Fe, Al, Ca, Si, Ti, Na, C, and significant volatiles (LOI) comprise 86.5 wt.% and 13.6 wt.% of the composition respectively. Concerning trace elements, when normalized to average Greek bauxites, UCC (Rudnick & Gao, 2003) and chondrites (McDonough & Sun, 1995), the material is depleted in Ga (following the chemical behavior of Al) and enriched -among others- in Cr (2403 ppm), V (1081 ppm), Ni (903 ppm), As (164 ppm), Pb (120 ppm), as well as in Cd, but also in Nb, Y, Ta, and REEs (**Table 3.5.1.1** and **Figure 3.5.1.8**).

Table 3.5.1.1: Major and trace element concentrations in the studied red mud according to XRF and ICP-OES/MS measurements. Commonly, the elements comprise the LREE and HREE groups are arbitrary defined (Mariano & Mariano, 2012; Gambogi, 2013; Zepf, 2013).

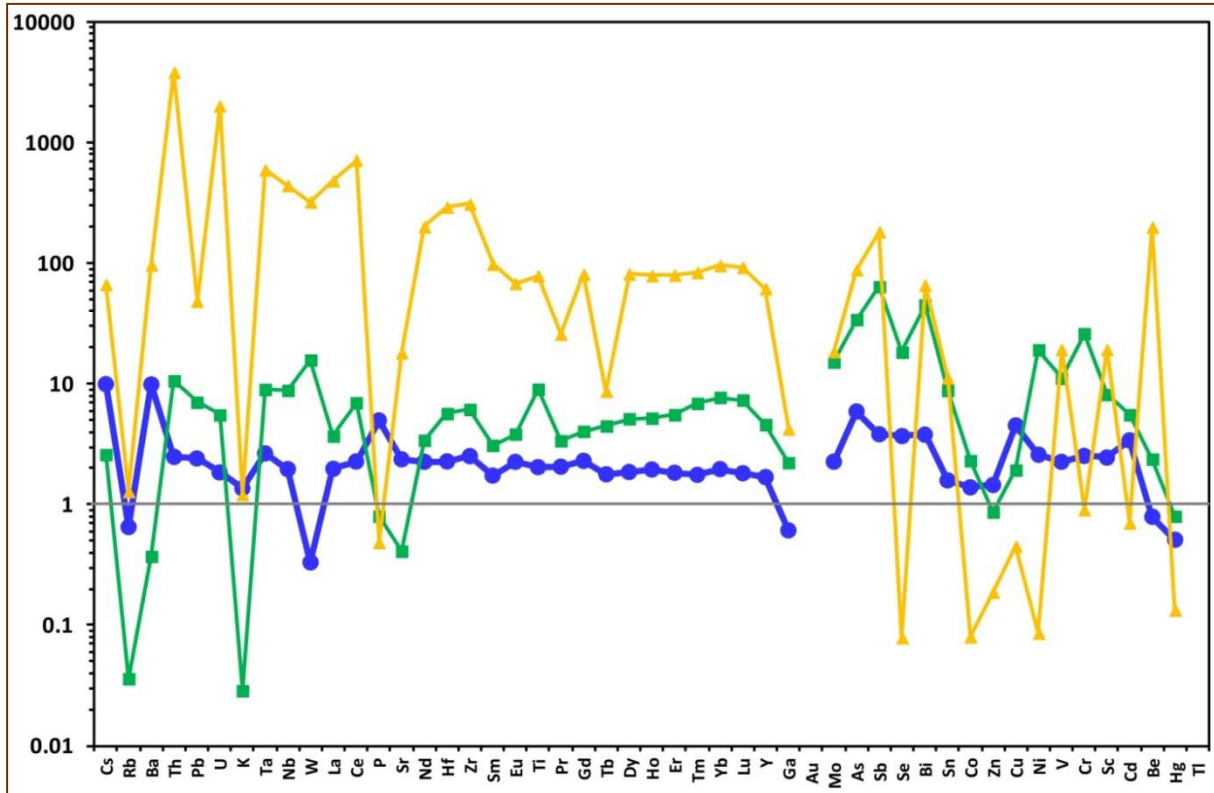
Fe₂O₃	(wt.%)	41.27	Cr	(μg g ⁻¹)	2403	Y	(μg g ⁻¹)	97	Gd	(μg g ⁻¹)	16	Br	(μg g ⁻¹)	4
Al₂O₃	(wt.%)	15.90	Zr	(μg g ⁻¹)	1188	Nd	(μg g ⁻¹)	92	Yb	(μg g ⁻¹)	15	Tb	(μg g ⁻¹)	3
CaO	(wt.%)	12.99	V	(μg g ⁻¹)	1081	Zn	(μg g ⁻¹)	58	U	(μg g ⁻¹)	15	Rb	(μg g ⁻¹)	3
SiO₂	(wt.%)	6.12	Ni	(μg g ⁻¹)	902	Cu	(μg g ⁻¹)	54	Sm	(μg g ⁻¹)	15	Lu	(μg g ⁻¹)	2
TiO₂	(wt.%)	5.78	Ce	(μg g ⁻¹)	439	Co	(μg g ⁻¹)	40	Te	(μg g ⁻¹)	13	Tm	(μg g ⁻¹)	2
Na₂O	(wt.%)	2.86	Ba	(μg g ⁻¹)	234	Ga	(μg g ⁻¹)	39	Er	(μg g ⁻¹)	13	Se	(μg g ⁻¹)	2
Total C	(wt.%)	1.53	As	(μg g ⁻¹)	164	Hf	(μg g ⁻¹)	30	Cs	(μg g ⁻¹)	13	Cd	(μg g ⁻¹)	0.5
LOI	(wt.%)	13.6	Sr	(μg g ⁻¹)	131	W	(μg g ⁻¹)	30	Ta	(μg g ⁻¹)	8	Ag	(μg g ⁻¹)	0.3
MgO	(wt.%)	0.21	Pb	(μg g ⁻¹)	120	Sb	(μg g ⁻¹)	26	Ge	(μg g ⁻¹)	8	Hg	(ng g ⁻¹)	40
P₂O₅	(wt.%)	0.12	La	(μg g ⁻¹)	115	Pr	(μg g ⁻¹)	24	Bi	(μg g ⁻¹)	7	Au	(ng g ⁻¹)	bdl
K₂O	(wt.%)	0.08	Sc	(μg g ⁻¹)	114	Dy	(μg g ⁻¹)	20	Be	(μg g ⁻¹)	5	ΣLREE*¹	(μg g ⁻¹)	704
Total S	(wt.%)	0.07	Th	(μg g ⁻¹)	111	Sn	(μg g ⁻¹)	19	Ho	(μg g ⁻¹)	4	ΣHREE*²	(μg g ⁻¹)	157
MnO	(wt.%)	0.03	Nb	(μg g ⁻¹)	106	Mo	(μg g ⁻¹)	17	Eu	(μg g ⁻¹)	4	ΣREE*³	(μg g ⁻¹)	976

*¹ ΣLREE group includes the lanthanide elements from La through Gd (Gambogi, 2013; Zepf, 2013).

*² ΣHREE group includes the lanthanide elements from Tb through Lu, including Y (Gambogi, 2013; Zepf, 2013).

*³ ΣREE group comprises of the 15 lanthanide elements including Sc, and Y (Gambogi, 2013; Zepf, 2013).

Figure 3.5.1.8: Spider diagrams of the red mud elemental content normalized: (a) to the avg. of the chemical composition of Greek bauxites from Parnassos-Ghiona area, solid circles; (b) to the reference values of Upper Continental Crust/UCC (Rudnick & Gao, 2003), solid squares; (c) to chondrite (McDonough and Sun, 1995), solid triangles.



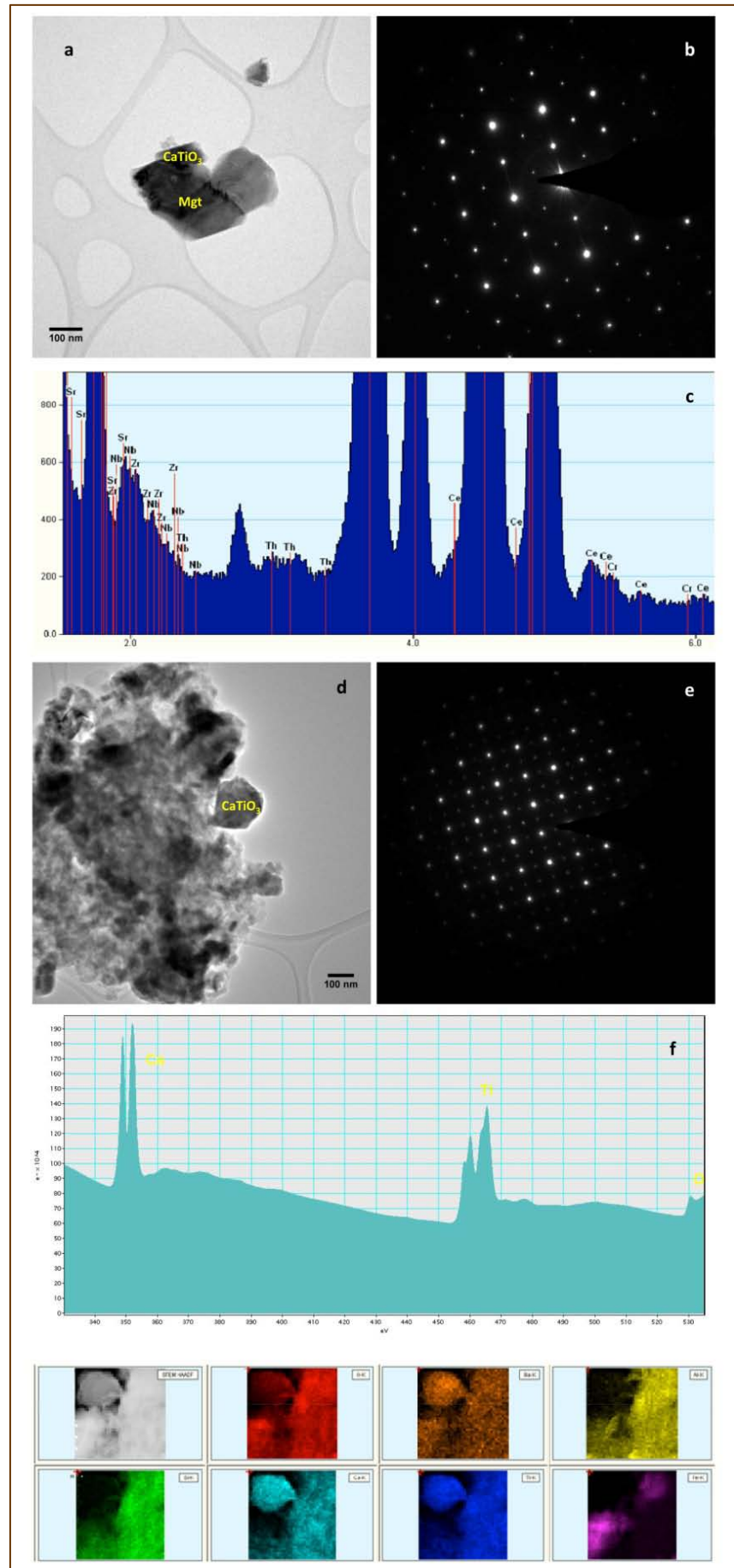
Moreover, remarkable amount of Th (111 ppm) has been determined. The latter, and also minor U (15 ppm), are responsible for radioactivity (352 and 134 Bq Kg⁻¹ for ²³²Th and ²³⁸U respectively) with total dose rate 285 nGy h⁻¹ (Table 3.5.1.2). It should be mentioned that the radioactivity of Greek red mud due to Th is relevant to that of similar materials from the globe, except the Australian red mud reaching 1900 Bq kg⁻¹ (Beretka & Mathew, 1985; O'Connor, 2005). The studied red mud shows higher Th radioactivity in comparison with the average of Greek bauxites from Parnassos-Ghiona mines (av. 188 Bq Kg⁻¹, av. total dose rate: 155 nGy h⁻¹, n=10). The same stands for radioactivity due to U whereas both materials exhibit similar values due to ⁴⁰K.

Table 3.5.1.2: Natural radionuclides (Bq/Kg) and total dose rate (nGy/h) of the studied red mud and typical Greek bauxites compared with relevant values from literature.

RED MUD: Radioactivity (Bq/Kg) & Total Dose Rate (nGy/h)						
<u>Red Mud Greece</u>	²³² Th (due to ²²⁸ Ac)	²³⁸ U (due to ²³⁴ Th)	²²⁶ Ra	⁴⁰ K	¹³⁷ Cs	Total Dose Rate
Red Mud - Greece (present study)	355	133	171	45	0	295
Red Mud - Greece (Papatheodorou et al., 2005)	15 – 412	52 – 400	13 – 185	72 – 160	1 – 5	
Red Mud - Greece (Pontikes et al., 2006)	472	149	379	21		
Red Mud - Greece (Samouhos et al., 2013)	346	182	232	45		
Red Mud - Worldwide (previous works)						
Red Mud - Turkey (Akinçi & Artir, 2008)	539	218	210	112		
Red Mud - Turkey (Turhan et al., 2011)	342 – 357		128 – 285	94 – 110		
Red Mud - Hungary (Somlai et al., 2008)	219 – 392		225 – 568	5 – 101		
Red Mud - Hungary (Jobbágy et al., 2009)	285 – 380		150 – 700	5 – 101		
Red Mud - Hungary (Jobbágy et al., 2009)	87 – 545		102 – 506	47 – 212		
Red Mud - Hungary (Ruyters et al., 2011)	640	550		250	5.5	
Red Mud - Spain (Rubinos & Barral, 2013)	598	350	203	62		
Red Mud - Germany (Von Philipsborn & Kühnast, 1992)	183	85	122			
Red Mud - Jamaica (Pinnock, 1991)	328 – 350		370 – 1047	265 – 335		
Red Mud - Australia (Beretka & Mathew, 1985)	1129		326	30		
Red Mud - Australia (Cooper et al., 1995)		400	310	350		
Red Mud - Australia (O' Connor, 2005)	1000 – 1900	150 – 600		70 – 230		
Red Mud - China (Wang, 1992)	705	477		153		
Red Mud - China (Wang & Liu, 2012)	360 – 475		125 – 620	67 – 247		

According to STEM-EDS/EELS study (**Figures 3.5.1.8 – 3.5.1.12**), one of the nanoscale Ti-phases, constituting the microscale “Al-Fe-Ca-Ti-Si-Na-Cr matrix”, is a perovskite-type phase with a major composition $\text{Ca}_{0.8}\text{Na}_{0.2}\text{TiO}_3$ (e.g., Connelly et al., 2005). Several other elements, namely Ce, Nb, Zr, Cr, and maybe Sr, are additionally hosted as impurities, implying a minor contribution of a loparite-type phase ($\text{Ce}(\text{Ti},\text{Nb})\text{O}_3$). It is noteworthy to emphasize that this phase also hosts detectable amounts of Th (estimated to ca. 100 ppm) and is commonly observed close to nanoscale -Th-free- Fe-oxides, namely nano-hematite/Ti-hematite and nano-magnetite/Ti-magnetite (**Figures 3.5.1.8 – 3.5.1.9**). The Ti content in both nano-Ti-hematite and -magnetite has been measured up to 5 wt.%. Small amounts of Ti, Si, Al, Cr and probably P, also occur. Concerning intergrown nano-perovskite, the viewing directions used for achievement of electron diffraction patterns, consistent with the perovskite structure, were [100] and [101] (sample tilted by 45°). According to the diffraction patterns, the observed nano-perovskite exhibits significant twinning. Subsequently, the presence of Ca, Ti,

Figure 3.5.1.8: STEM-EDS/EELS data of Ca-Na-(Ce-Nb-Zr-Cr)-nanoperovskite. Nanoperovskites are illustrated in the BF images (a, and d). The viewing directions for their electron diffraction patterns - SAED- are the [100] (b), and the [101] (e), respectively. A sharp peak at 2.77 KeV is due to the Si escape peak for Ti K α (c). Representative EELS spectrum (f) of the nano-perovskite showing the presence of Ca, Ti, and O, as well as the absence of N. STEM-EDS integrated intensity elemental maps of the nano-perovskite. Abbreviation (Whitney & Evans, 2010): “mgt” for magnetite.



and O. On the contrary, it confirmed the absence of N (N K edge: 401 eV), which was “artificially” detected in the EDS. The EELS measurement supports the phase to be CaTiO_3 (Calvert et al., 2006). Since there is no evidence for other phases, neither in microscale nor in

Figure 3.5.1.9: STEM-EDS data concerning nano-Fe-oxides. Representative BF images of nano-hematite/Ti-nano-hematite (a) and nano-magnetite/Ti-nano-magnetite intergrown with nano-perovskite (b). STEM-EDS integrated intensity elemental maps of the nano-magnetite with the nano-perovskite; Na signals on the nano-magnetite come from background noise. Abbreviations (Whitney & Evans, 2010): “hem” for hematite; “mgt” for magnetite.

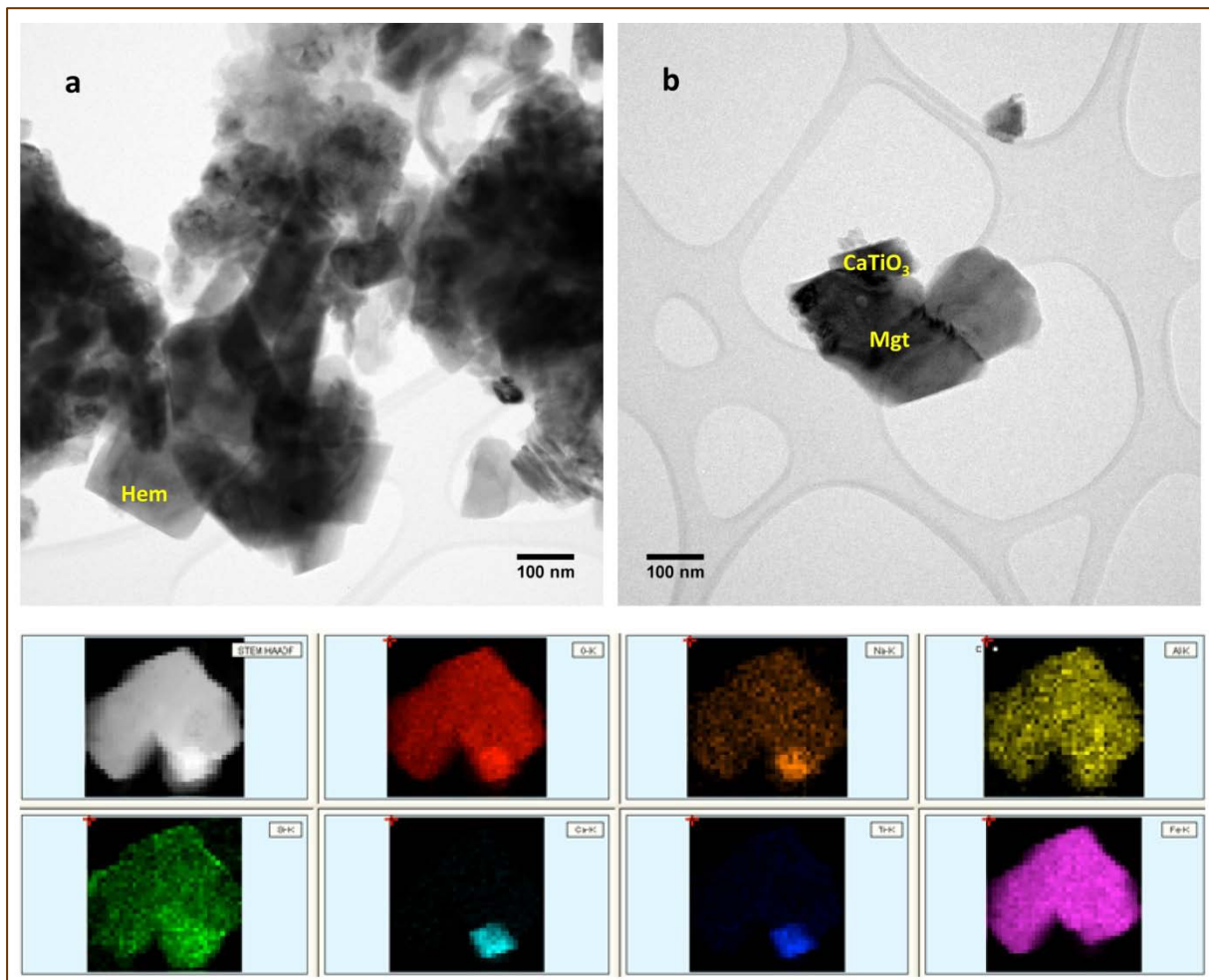
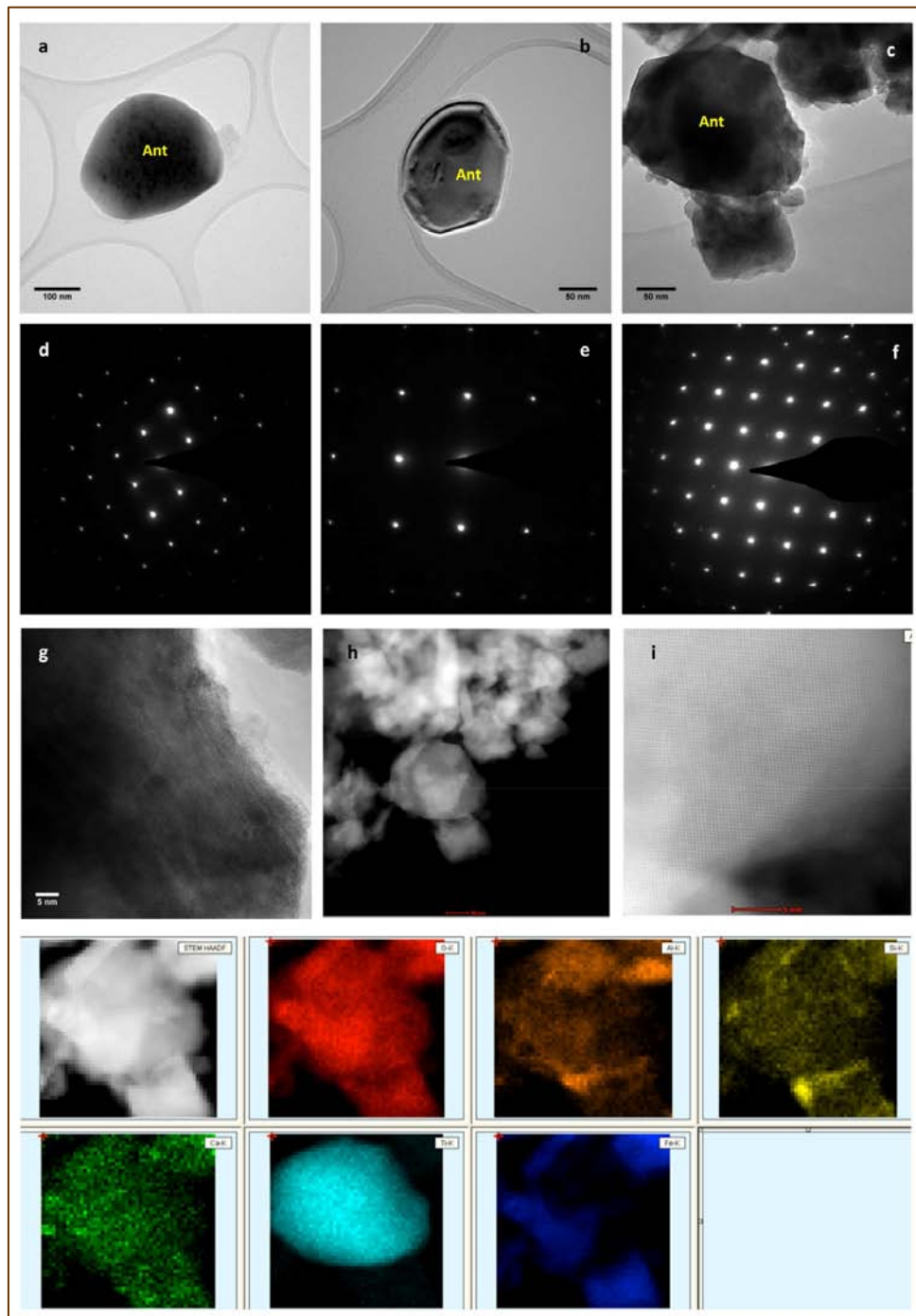


Figure 3.5.1.10: STEM-EDS/EELS data of nano-Ti-oxides (nano-anatase). Representative nano-anatase particles are illustrated in the BF images (**a**, **b**, and **c**). The viewing direction for their electron diffraction patterns -SAED- are the [111] (**d**), the [001] (**e**), and the [111] (**f**), respectively. Several planar defects, common in anatase, can be seen in the HRTEM image (**g**). STEM-HAADF (**h**) and HR-STEM-HAADF (**i**) images show no apparent sign of Th. STEM-EDS integrated intensity elemental maps of the nano-magnetite with the nano-anatase. Abbreviation (Whitney & Evans, 2010): “Ant” for anatase.



nanoscale, hosting Th, it can be considered that the aforementioned nano-perovskite is the carrier of the whole Th (and the related radioactivity) of the studied Greek red mud. Except the nano-Ca-Na-Ti-oxide and nano-Fe-Ti-oxides, distinct -Th free- nano-Ti-oxides have been revealed. In particular, three TiO₂ nanoparticles were studied and all were identified to be nano-anatase (**Figure 3.5.1.10**). They have rounded shapes with a smooth surface and some planar defects common for anatase. Besides, Th-free nano-AlOOH corresponding to nano-diaspore (**Figure 3.5.1.11**), and Th-free clay-like nanoparticles, as well as minor titanite, in association with nano-Fe-oxides and nano-Ca-Na-Ti-oxide have also been confirmed. These clay-like phases look to contain Si, Al, Ca, Ti and O as major elements and C, P and S as minor elements (**Figure 3.5.1.12**). Thus, the STEM-EDS & STEM-EELS study revealed that both the initial and acid-treated “Al-Fe-Ca-Ti-Si-Na-Cr matrix”, as appeared in microscale, is actually an aggregate of several Al-, Fe-, Ca-, Ti-, Si-, Na-, Cr- (and also S-, P-, Ce-, Nb-, Zr-, and maybe Sr-) nanoparticles, including the Th-hosting nano-perovskite.

Figure 3.5.1.11: HRTEM data including BF image (a) and SAED pattern (b) concerning the nano-AlOOH phase (nano-diaspore). The viewing direction for the electron diffraction pattern is [100]. Abbreviation ([Whitney & Evans, 2010](#)): “Dsp” for diaspore.

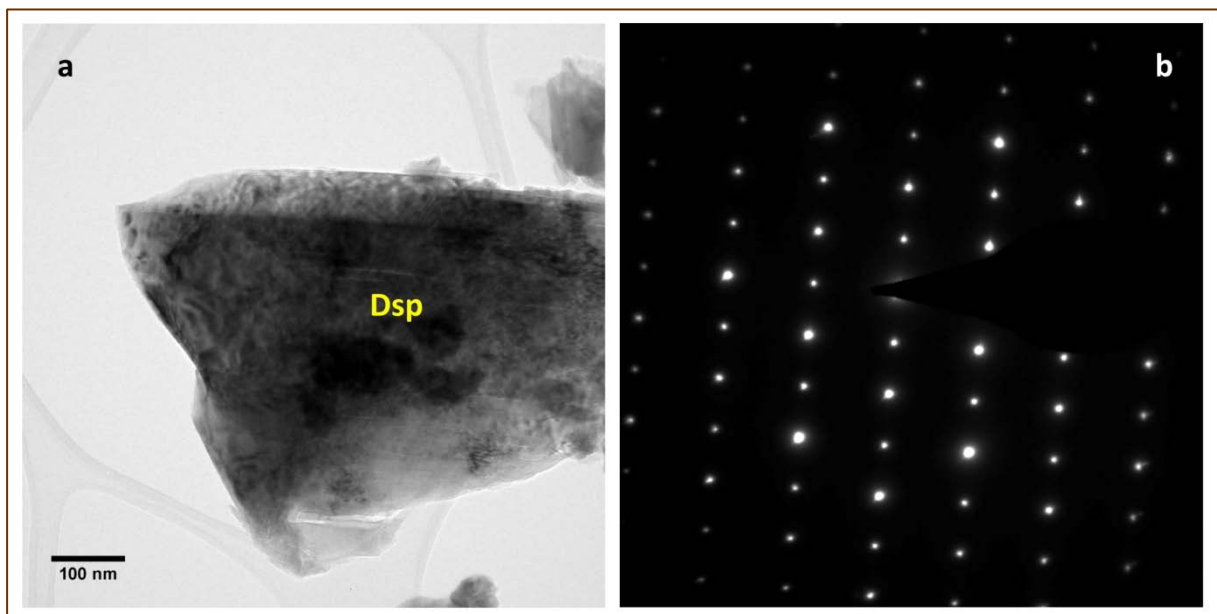
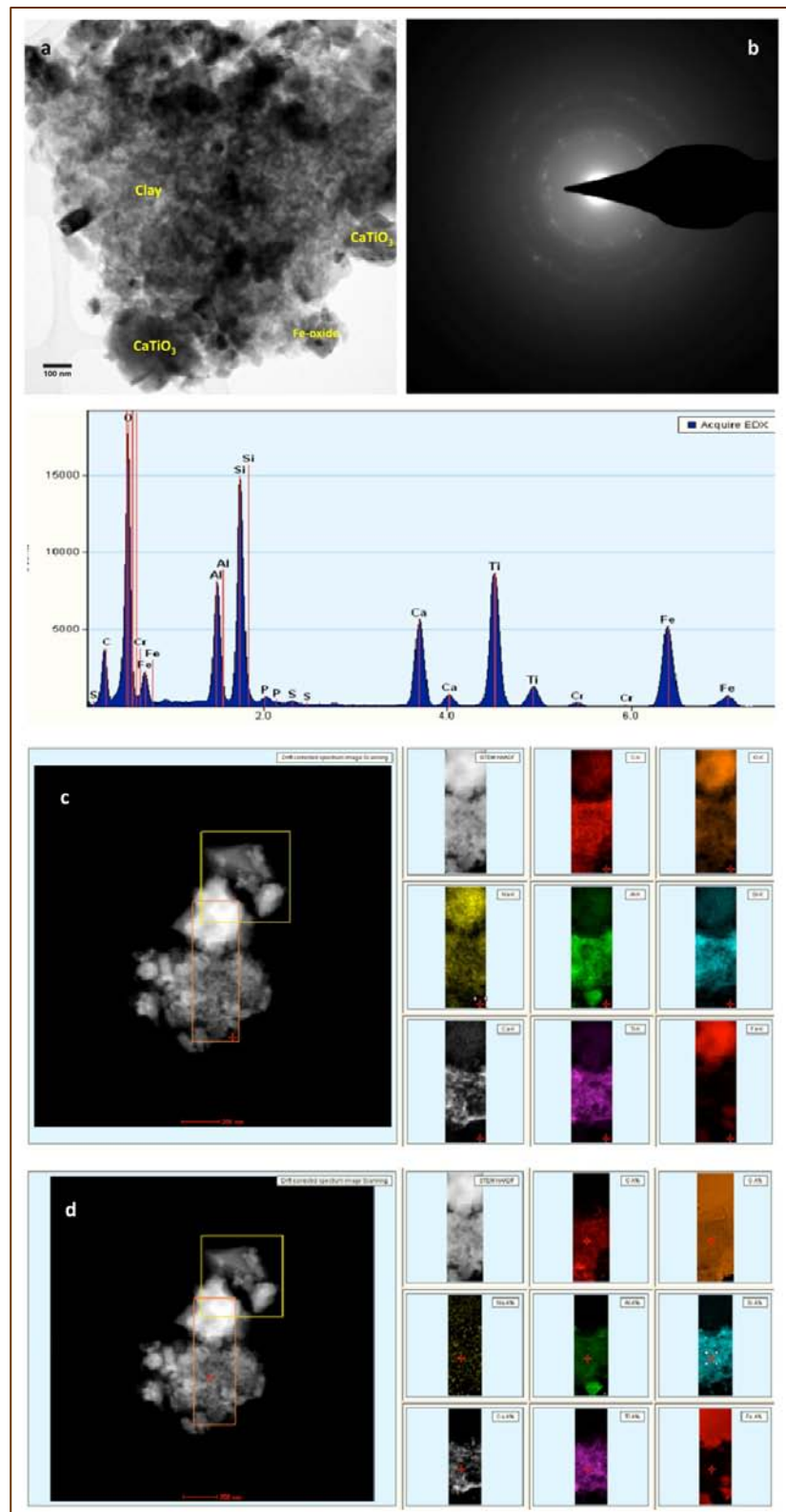
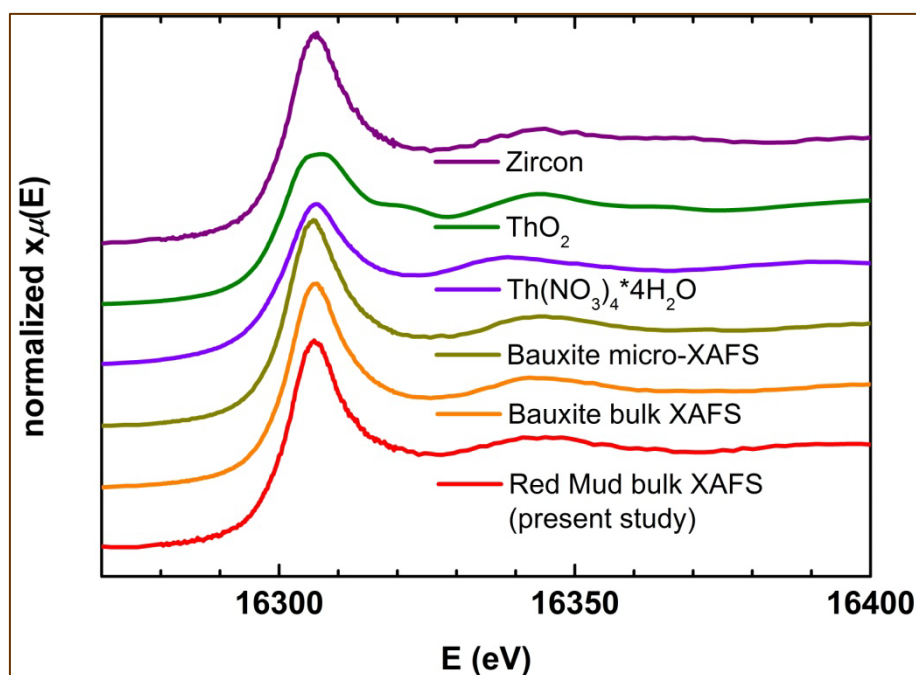


Figure 3.5.1.12: STEM-EDS data of clay-like nanoparticle together with nano-perovskites and nano-Fe-oxides. BF image (a), SAED pattern (b), and a STEM-EDX spectrum of clay-like nanoparticles are illustrated. STEM-EDS elemental maps from an observed similar area are depicted, using the integrated intensity (c) as well as the qualification method (d), indicate the existence of titanite as Si and Ca are present. Ca distribution does not match with Si or Al, meaning that it might exist not only in the form of the clay-like mineral but also in titanite. In these maps (c, and d), from the top, Fe-oxide, clay-like and nano-diaspore nanoparticles can be observed.



Details on the structural characteristics of Th, assigned to nano-perovskite, have been obtained by XAFS (Th L_{III} -edge XANES and EXAFS) spectra and processing using the ATHENA and EDA software packages (Ravel & Newville, 2005; Kuzmin, 1995). Th L_{III} -edge bulk XANES of red mud together with bulk & micro-XANES of Greek bauxite (see text above), in comparison with spectra of reference materials, indicated that the valence of Th is typical 4+ (see **Figure 3.5.1.13**). The experimental Th L_{III} -edge EXAFS spectrum of the studied red mud,

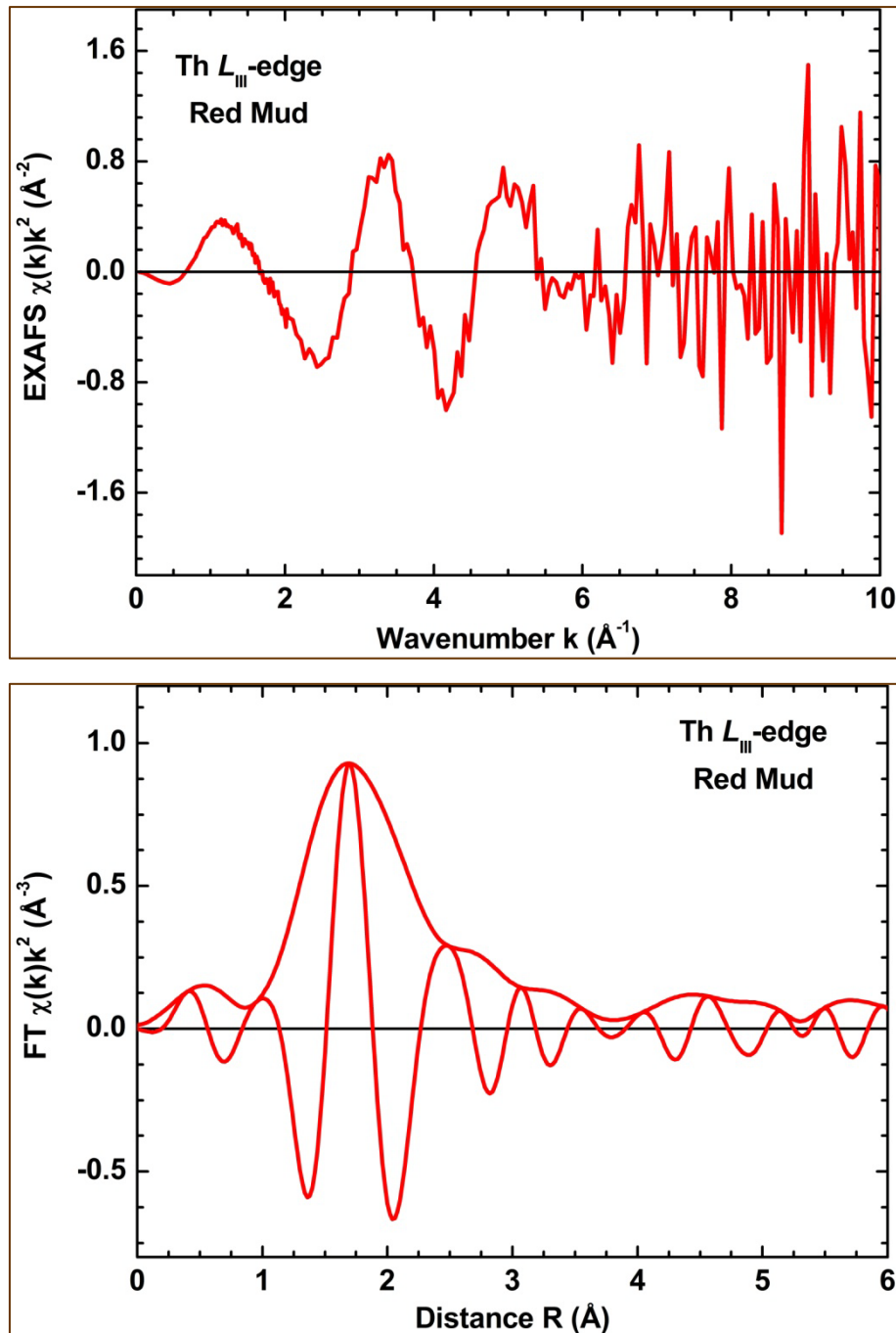
Figure 3.5.1.13: Th L_{III} -edge bulk XANES of red mud together with bulk & micro-XANES of Greek bauxite (see text above) compared with spectra of reference materials.



which was measured in the fluorescence mode, is rather noisy above $k=6 \text{ \AA}^{-1}$ (upper image of **Figure 3.5.1.14**). This fact limits the accuracy of the analysis, as well as it reduces its resolution in the R-space. The EXAFS spectrum does not also show any evidence for significant high frequency contributions. This fact is consistent with the shape of the EXAFS spectrum Fourier transform (lower image of **Figure 3.5.1.14**) which consists of a single broad peak located at 1.6 \AA . Thus, the contribution of outer coordination shells around thorium is

smearred out, and only analysis of the nearest environment can be performed. The first peak contribution into the total EXAFS spectrum was singled out by the Fourier filtering procedure

Figure 3.5.1.14: Experimental Th L_{III} -edge EXAFS spectrum (upper image) and its Fourier transform – FT (lower image) for the red mud sample.



and best fitted using two different approaches: the one-component Gaussian model (Aksenov et al., 2006) and the regularization method (Kuzmin & Purans, 2000). It is considerable that in the second method the radial distribution function (RDF) could have an arbitrary shape and, thus, may possibly account for anharmonicity and disorder effects. In the both models, the theoretical backscattering amplitude and phase shift functions for the Th-O atom pair were calculated by the ab initio real-space FEFF8 code (Ankudinov et al., 1998) using a complex Hedin-Lundqvist exchange-correlation potential accounting for inela-

Figure 3.5.1.15: Best-fit results for the first shell Th L_{III} -edge EXAFS in red mud using the one-shell Gaussian model (a), and the regularization method (b). Comparison of the radial distribution functions (RDF's), obtained from the first shell Th L_{III} -edge EXAFS (c) using the one-shell Gaussian model (dashed line) and the regularization method (solid line). The blue bars indicate the position of the Ca-O distances in CaTiO_3 perovskite (Buttner & Maslen, 1992).

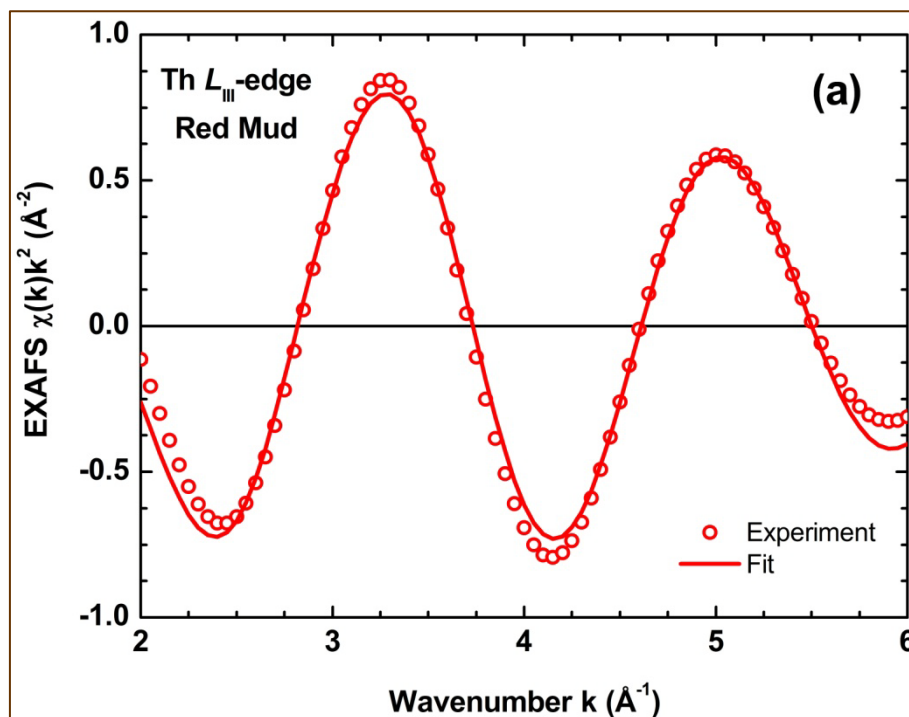
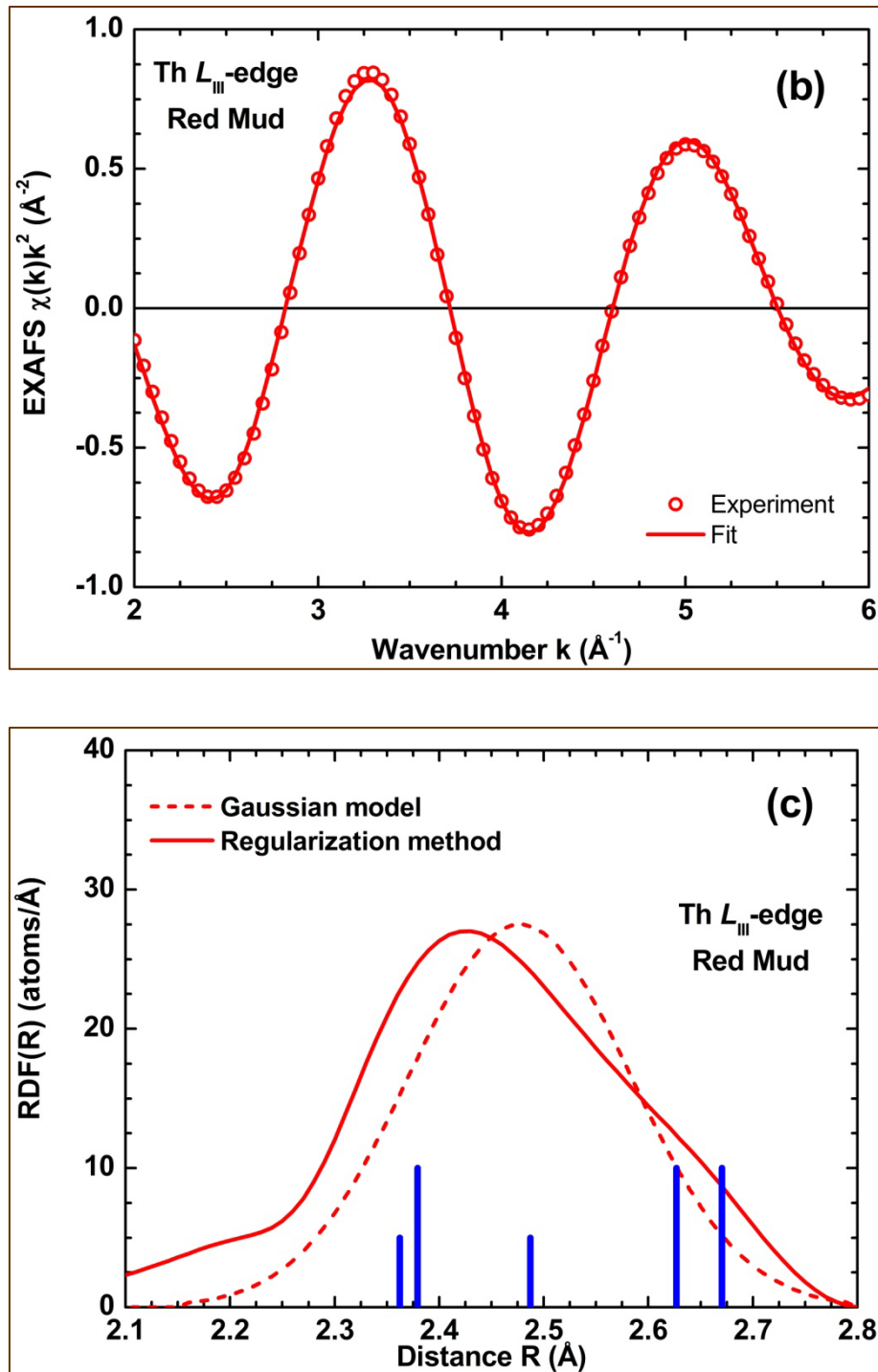


Figure 3.5.1.15: continued.



stic effects. The results of the best fits, obtained within the two models (i.e., Gaussian and regularization method) in the k-space range from 2 to 6 Å⁻¹, are shown in the upper and middle images of **Figure 3.5.1.15**, respectively, and the corresponding RDF's of them are given in the lower image of **Figure 3.5.1.15**. The regularization method results better agreement, suggesting a deviation of the RDF shape from the Gaussian form. The numerical values of structural parameters for both models are given in **Table 3.5.1.3**. For the sake of discussion it is noteworthy that due to the short k-range interval of the EXAFS spectrum there is a strong correlation between the value of the coordination number N and that of the Debye-Waller factor σ^2 . The local environment of Th ions in red mud is not very far from that in Fe-depleted bauxite (see text above), but is significantly more disordered as is evidenced by the larger value of the Debye-Waller factor in the Gaussian model and broad RDF's in **Figure 3.5.1.15**.

Table 3.5.1.3: Th structural parameters for the studied red mud, in comparison with Greek bauxite values (see text above), obtained from the processing of the EXAFS signals using the EDA software package (Kuzmin, 1995).

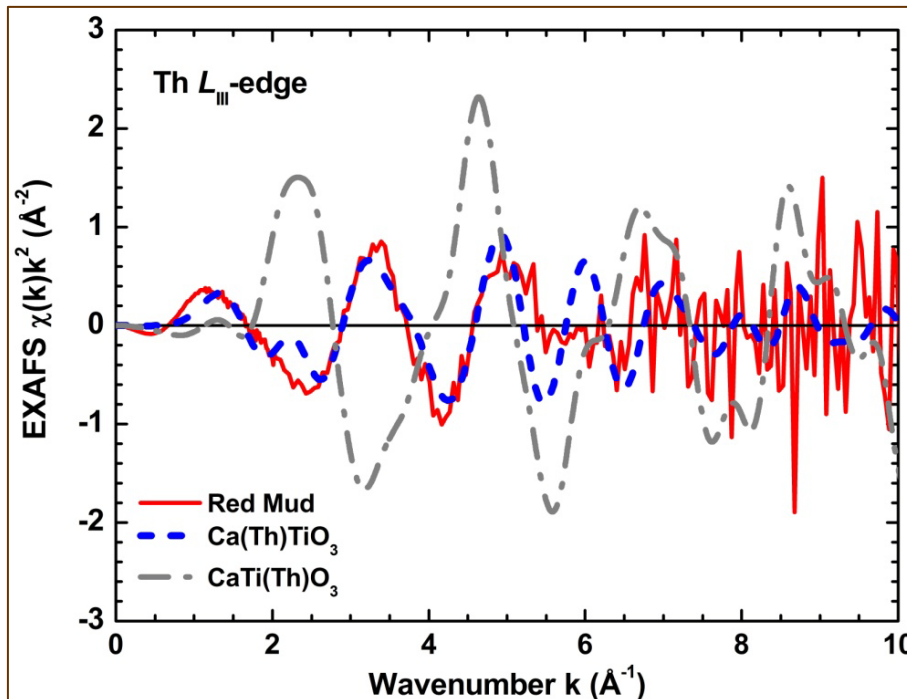
	Red Mud (present study) Th L _{III} -edge bulk-EXAFS	Bauxite (Gamaletsos et al., 2011)	
		Th L _{III} -edge bulk-EXAFS	Th L _{III} -edge Micro-EXAFS
<i>Gaussian model</i>			
CN ±0.7	7.3	6.9	6.9
R (Å) ±0.04	2.48	2.46	2.45
σ^2 (Å ²) ±0.002	0.011	0.007	0.006
<i>Regularization method</i>			
CN	8.0	7.4	7.4
R (Å)*	2.42	2.40	2.38

* This distance is the position of the RDF maximum.

As in the case of Fe-depleted bauxite (see text above), the Th ions in red mud are coordinated by about 7-8 oxygen atoms. This coordination number of thorium is smaller

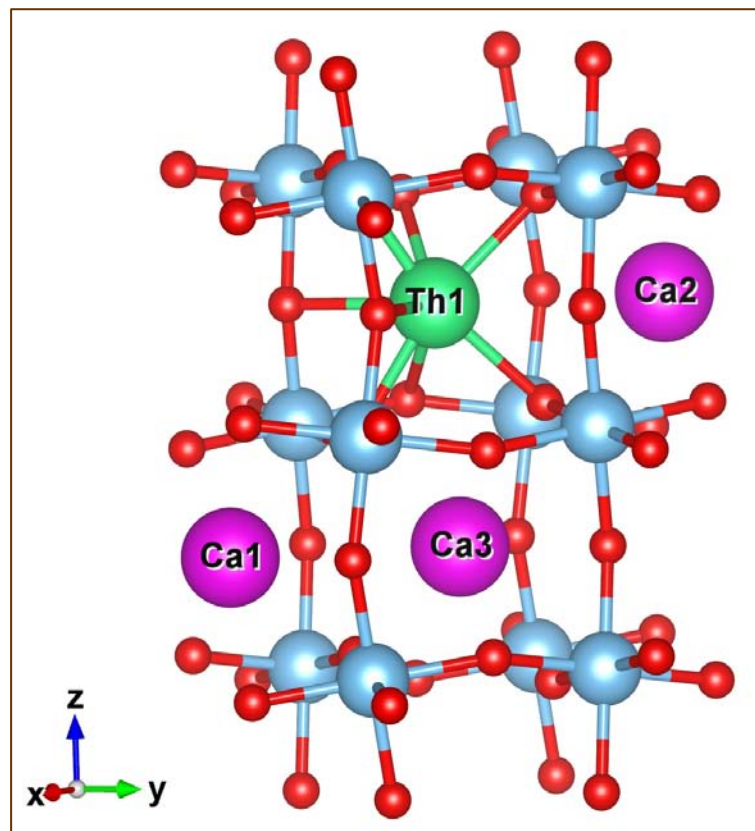
than that in Th-nitrate (N=12), being in agreement with the difference in the mean Th-O distances. However, it is notable that in the case of bauxite, being the parent material of red mud, Th is hosted in microscale anatase (TiO_2 polymorph), and there is no evidence for any perovskite phase. It is known that Th^{4+} in the structure of CaSiO_3 perovskite, synthesized at high temperature (and occasionally at high pressure), may fundamentally occupy “large” Ca dodecahedral sites ($^{[12]}\text{Ca}^{2+}$) or “small” Si octahedral sites ($^{[6]}\text{Si}^{4+}$) (Gréaux et al., 2012). On the other hand, in the structure of CaTiO_3 perovskite⁸, Ti appears as $^{[6]}\text{Ti}^{4+}$, whereas Ca may be $^{[8]}\text{Ca}^{2+}$, or even $^{[7]}\text{Ca}^{2+}$, compared to $^{[12]}\text{Ca}^{2+}$ in the ideal perovskite structure. As one can see in the lower image of **Figure 3.5.1.15**, the distribution of the Ca-O distances in CaTiO_3 perovskite agrees well with the shape of the Th-O RDF in red mud, obtained by the regularization method.

Figure 3.5.1.16: The experimental (solid line) and the calculated (blue dashed line – Th at the Ca site; grey dash-dotted line – Th at the Ti site) Th L_{III} -edge EXAFS spectra for the red mud and Th-substituted CaTiO_3 perovskite, respectively.



Therefore, we decided to simulate the Th L_{III} -edge EXAFS signal by the FEFF8 code for the case of Th absorbing atom substituting calcium or titanium in CaTiO_3 perovskite. The calculated Th L_{III} -edge EXAFS signals are compared with the experimental one for red mud in **Figure 3.5.1.16**. In the frame of this simulation, the atom positions were fixed as in orthorhombic CaTiO_3 perovskite-type structure (Buttner & Maslen, 1992), and all Debye-Waller factors were set to zero that explains smaller damping of the calculated EXAFS amplitude at larger k-values. As one can see, the model of Th at the Ca site (Ca(Th)TiO_3) gives the overall amplitude and the main frequency of the EXAFS signal close to the experimental one, whereas the model of Th at the Ti site (CaTi(Th)O_3) differs from the experiment significantly both in amplitude and frequency. Unfortunately, the weak contribution of the outer shells in the experimental Th L_{III} -edge EXAFS spectrum (upper image of **Figure 3.5.1.14**) in red mud does not allow us to make unambiguous conclusion on the Th location. However, taking into account the above in conjunction with the best-fit EXAFS results ($R=2.42\text{-}2.48$ Å and $\text{CN}=7\text{-}8$), we could presume that Th, hosted in the low-T & low-P novel Ca-Na-(Ce-Nb-Zr-Cr)-nanoperovskite of red mud, occupies Ca^{2+} sites rather than Ti^{4+} sites (lower image of **Figure 3.5.1.17**).

Figure 3.5.1.17: The structure of orthorhombic CaTiO_3 perovskite (Buttner & Maslen, 1992) with Th substituting Ca. Oxygen, titanium, and calcium atoms are illustrated by red-, blue-, and magenta-colored balls, respectively, whereas the thorium atom is indicated by green-colored ball.



3.5.2. Leaching experiments for red mud and bauxites

Leaching experiments for red mud, in conjunction with SF-ICP-MS, using Mediterranean seawater from Greece, indicated significant release of V, relatively to seawater composition (Li, 1991), depending on solid/liquid (S/L) ratio (Figure 3.5.2.1). Thus, V appears to be the most mobile element, perhaps due to its main association with rather soluble phases. This is in accordance to previous leaching NEN7341 tests concerning red mud calcined in inert and reducing atmosphere (Pontikes et al., 2006), as well as in good agreement with recent studies about V in red mud from the accident of Ajka alumina plant (Burke et al., 2012; Burke et al., 2013). According to the above studies, presenting V *K*-edge XANES spectra, the element in red mud from Ajka is pentavalent associated with a Ca-Al-hydroxysilicate phase corresponding to “hydrogarnet”-type phase. We can, therefore, assume that in Greek red mud, having the same phase composition with the Hungarian one, V is present most likely as VO_4^{3-} anions, which are mobile in seawater. On the other hand, V in Australian red mud has been reported as tetravalent and/or trivalent related to ilmenite and/or goethite (Gräfe et al., 2011). However, ilmenite has not been detected in the studied Greek red mud either by XRD or STEM-EDS/EELS (see text above), whereas the actual presence of goethite, either in microscale or nanoscale, cannot completely be confirmed. Traces of As and Cr have also been detected, relatively to seawater composition (Li, 1991), after prolonged exposure in lower S/L, while Pb is practically immobile. Based on previous Cr *K*-edge XANES and TEM, Cr is associated to hematite (Gräfe et al., 2011; Burke et al., 2012) showing less solubility. The most interesting point is that Th, related to radioactivity, seems to be remarkably immobile in seawater, at least after 12 months leaching tests (Figure 3.5.2.1). However, taking into account XRD and microscopic study in microscale (SEM-EDS), one can say that there is no clear evidence of the Th-hosting phase(s) into red mud. That was finally realized by combination of STEM-EDS/EELS and Th L_{III} -edge EXAFS spectroscopy, as mentioned above. Analogous leaching experiments with Mediterranean seawater from Greece carried out for comparison reasons, regarding the basic parent material (Parnassos-Ghiona industrial bauxite), showed negligible V, As, Cr, Pb, and Th release (typical Fe-rich bauxite: see Figure 3.5.2.2; Fe-depleted high grade bauxite: see Figure 3.5.2.3). The effect of solid/liquid ratio is also depicted, indicating that the lower S/L ratio causes a relative increase on the solubilization of heavy metals in Greek industrial bauxites, during the experiment.

Figure 3.5.2.1: Results from leaching experiments for red mud, with Mediterranean seawater and variable solid/liquid (S/L) ratios, concerning V, As, Cr, Pb and Th.

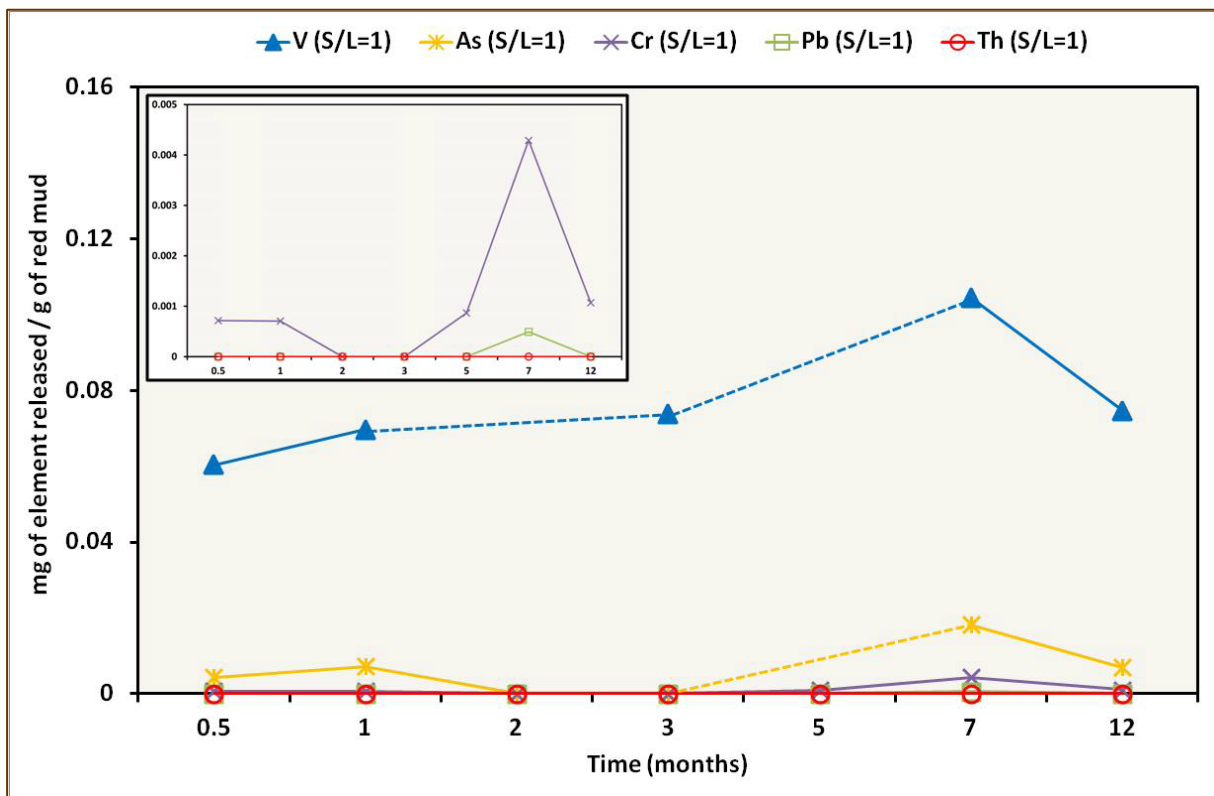
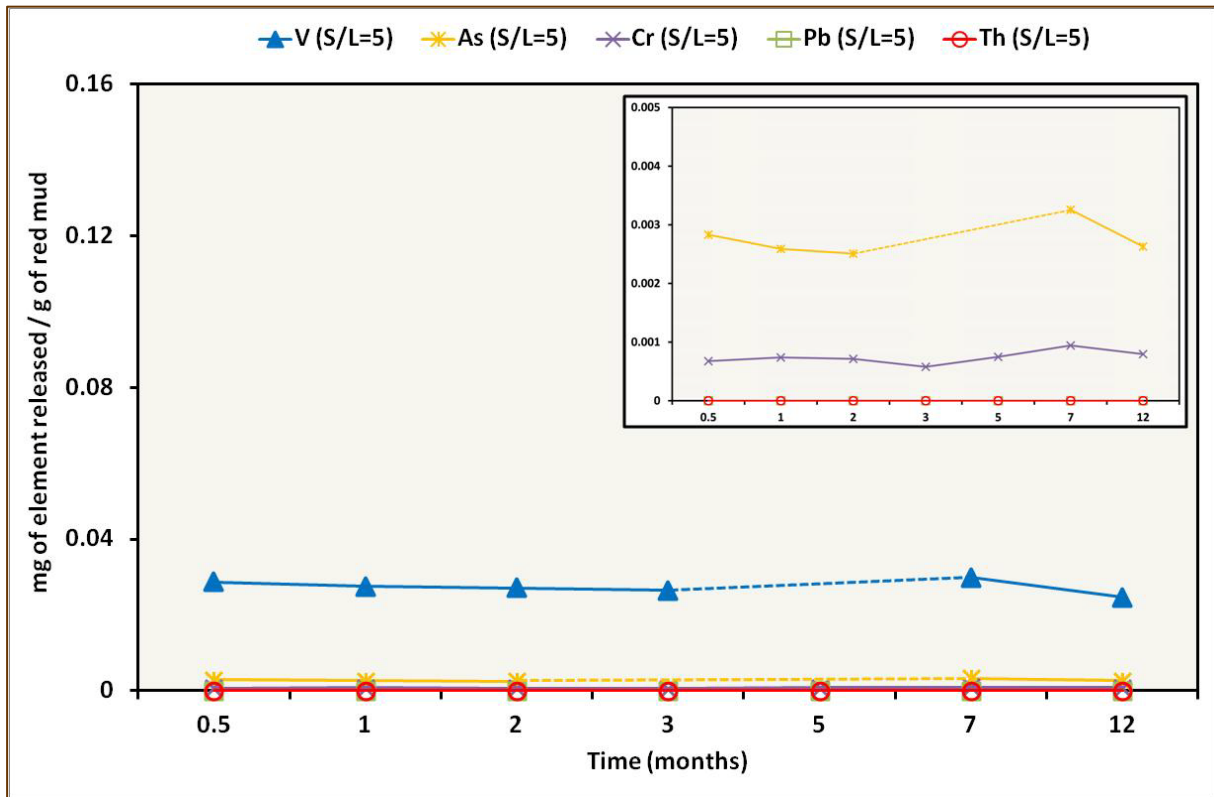


Figure 3.5.2.1: continued.

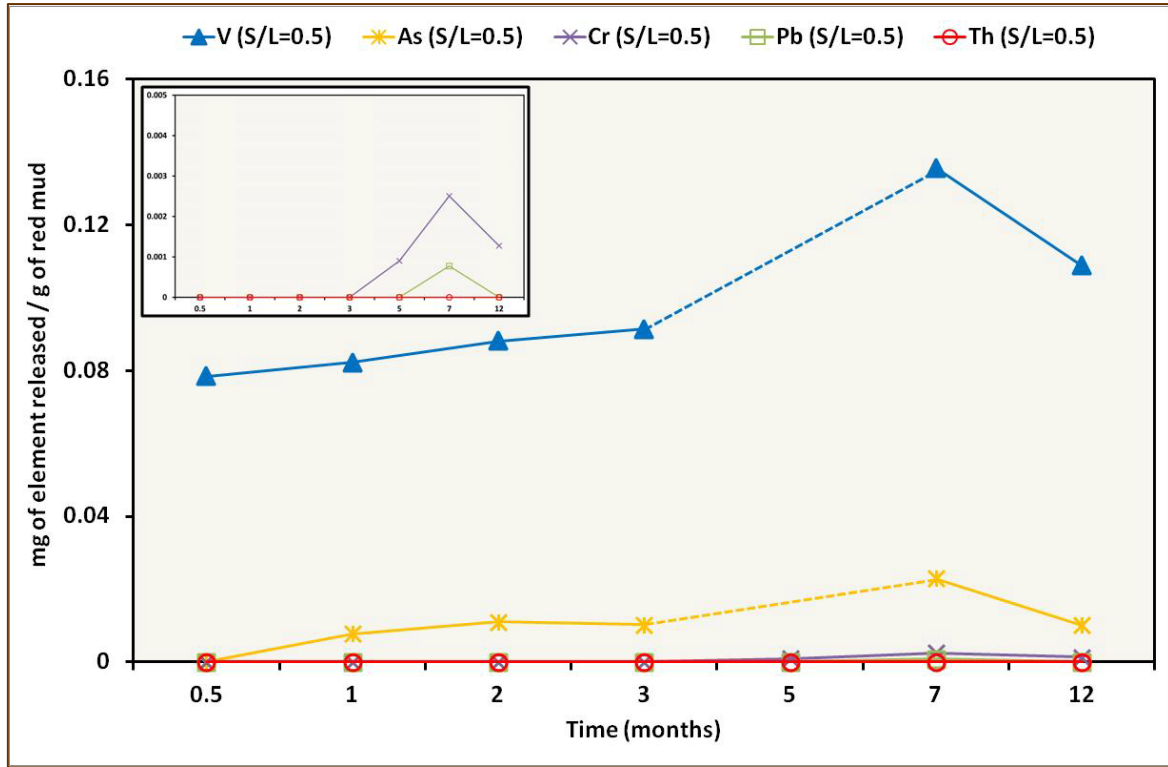


Figure 3.5.2.2: Results from leaching experiments showing the V, As, Cr, Pb, and Th negligible release from typical Fe-rich (low grade) bauxite leached by Greek seawater.

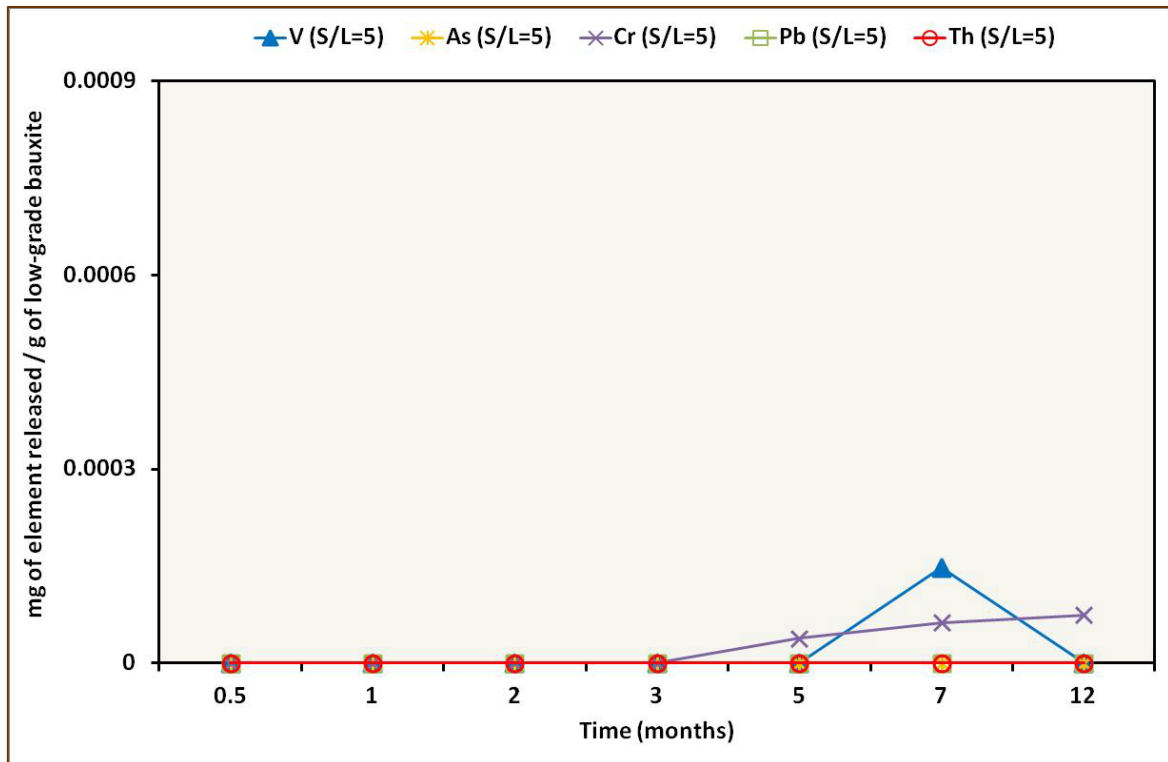


Figure 3.5.2.2: continued.

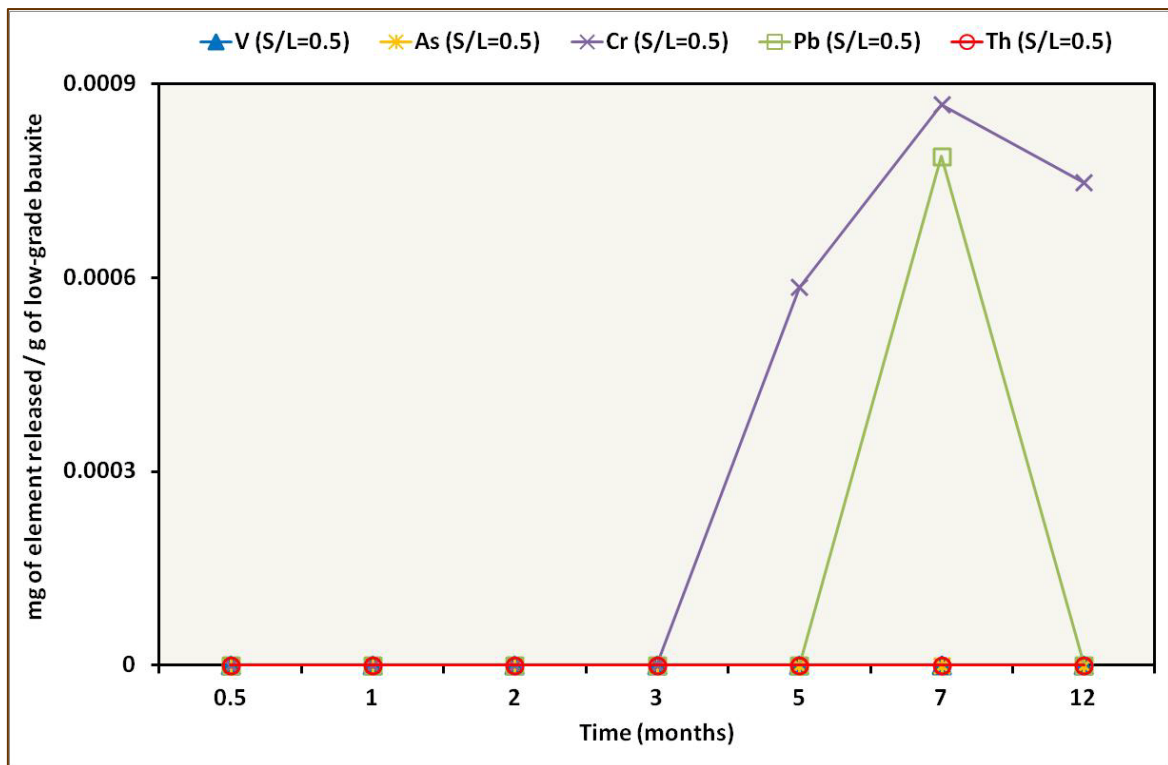
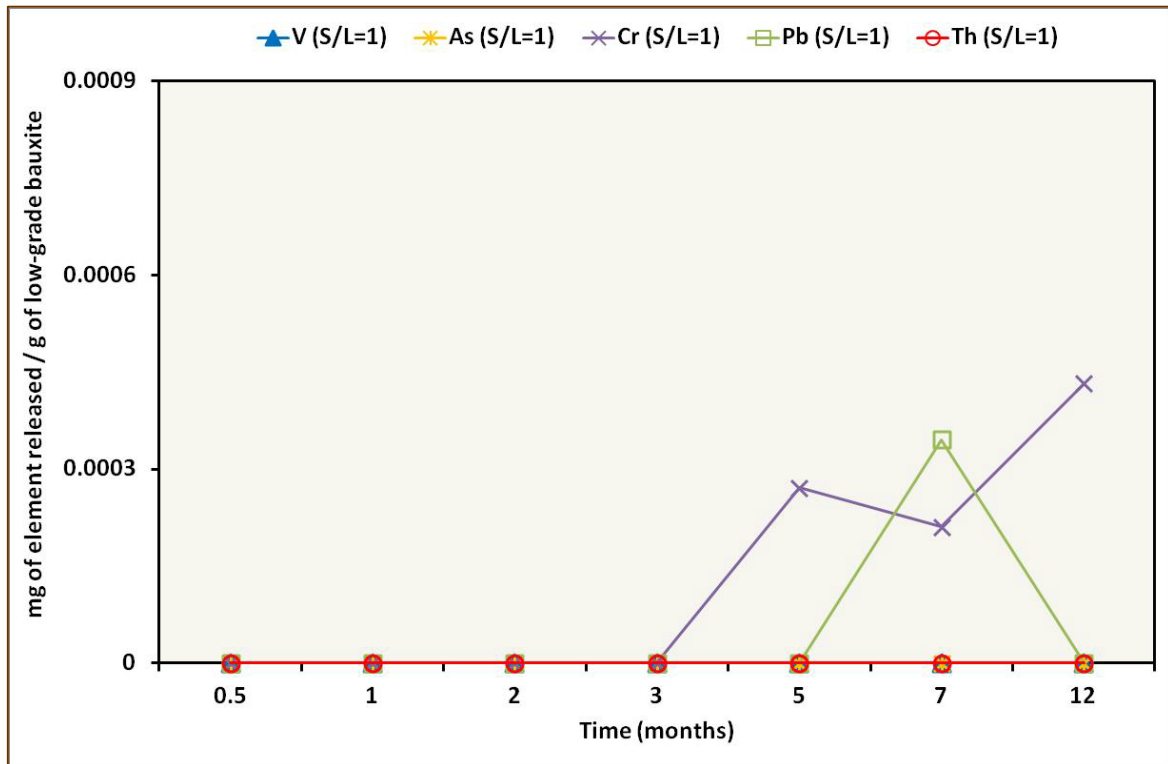


Figure 3.5.2.3: Results from leaching experiments showing the V, As, Cr, Pb, and Th negligible release from Fe-depleted (high grade) bauxite leached by Greek seawater.

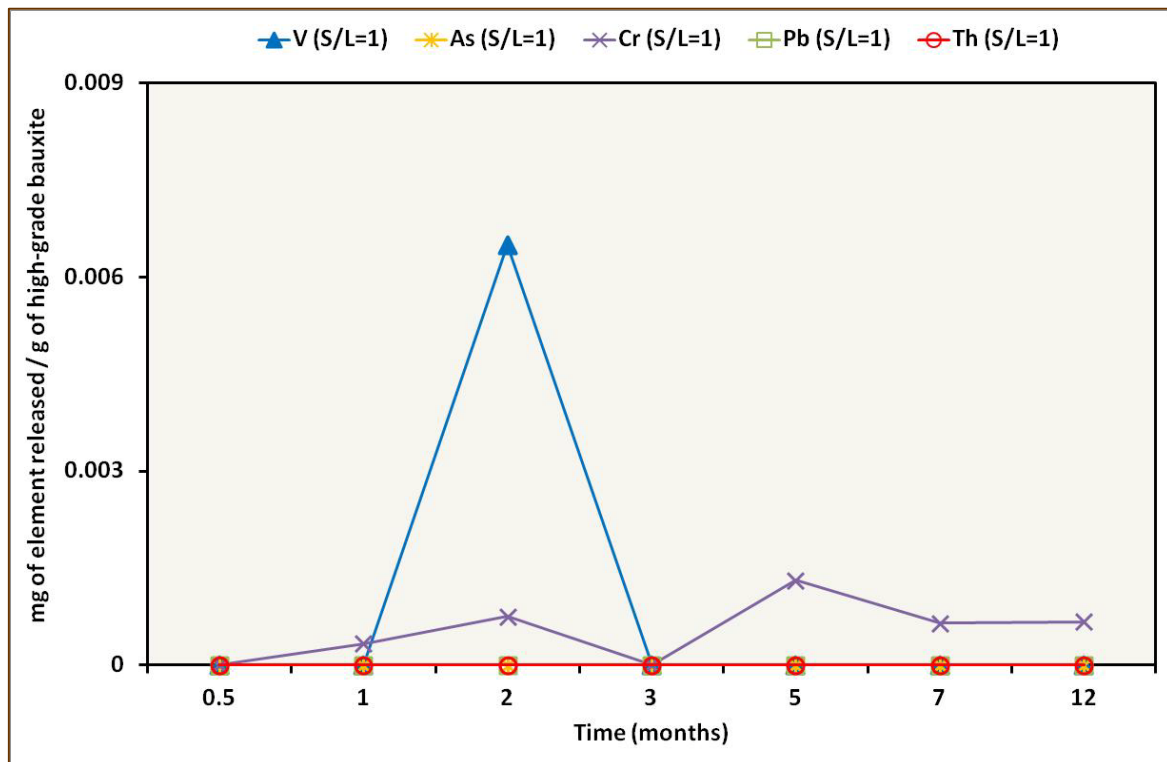
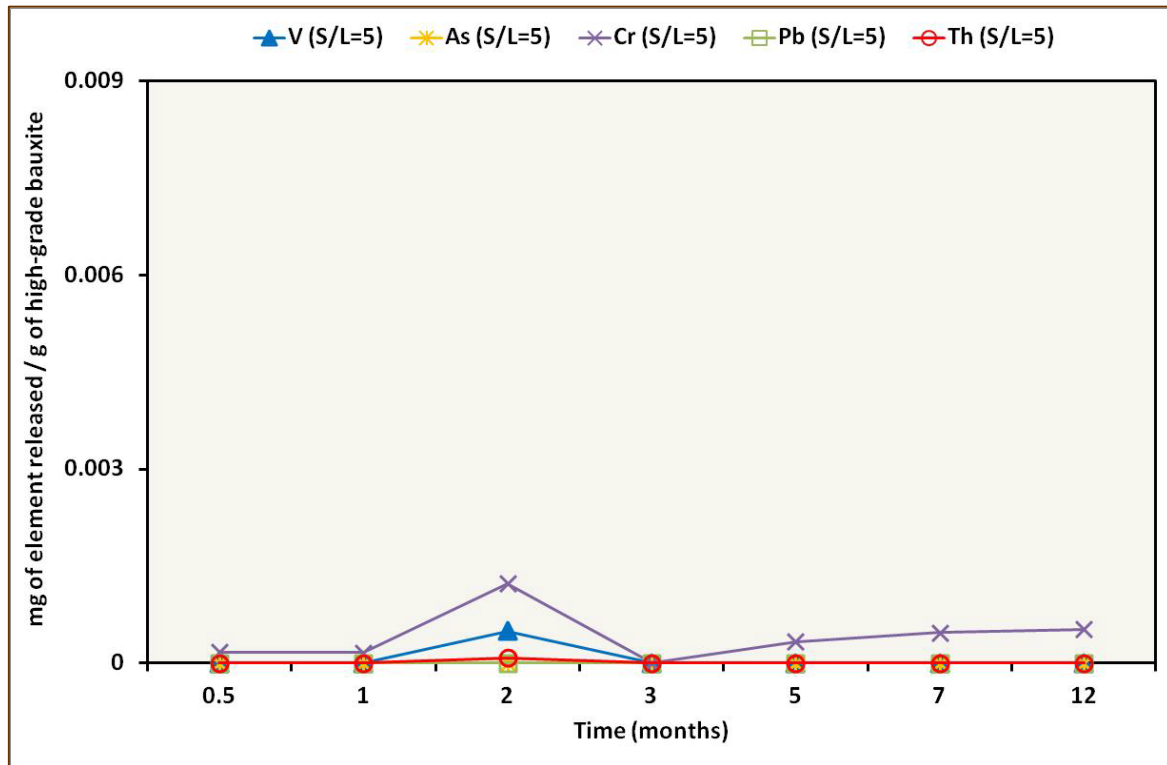
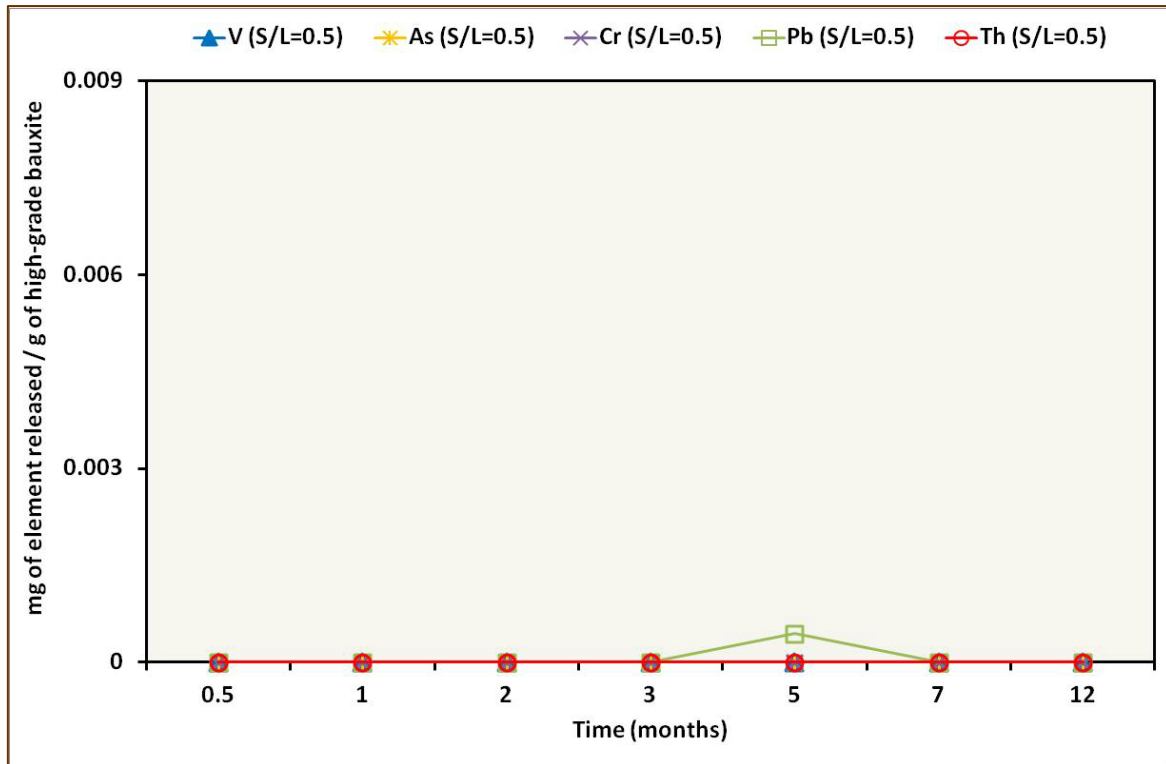


Figure 3.5.2.3: continued.



Additional acetic acid-leaching experiments with red mud, indicated significant release of V, as in the case of seawater, and much more release of Cr (**Figure 3.5.2.4**), a phenomenon also mentioned by [Rubinos et al. \(2013\)](#). Nevertheless, it is worthy to note that the release of REE is quite remarkable (for LREE release: see **Figure 3.5.2.5**; for HREE release: see **Figure 3.5.2.6**), giving facts for potential recovery technologies inasmuch future availability of REEs is of great concern due to monopolistic supply conditions, environmentally unsustainable mining practices, and rapid demand growth (e.g., [Catinat et al., 2010](#); [Alonso et al., 2012](#)). This is in line with previous relevant works for Greek red mud with regard to acid-recovery of lanthanides and Y ([Ochsenkühn-Petropulu et al., 1994](#); [Lympelopoulou, 1996](#); [Ochsenkühn-Petropulu et al., 1996](#); [Ochsenkühn-Petropoulou et al., 2002](#)). In either case, the negligible effect of solid/liquid (S/L) ratio is also presented indicating that the percentage of released elements -including the rare earth elements- from leached red mud is not severely affected

Figure 3.5.2.4: Results from leaching experiments showing the release of Σ LREE, and Σ HREE, together with Cr, V, Th, As, Pb, Nb, and Ta from Greek red mud leached by concentrated acetic acid.

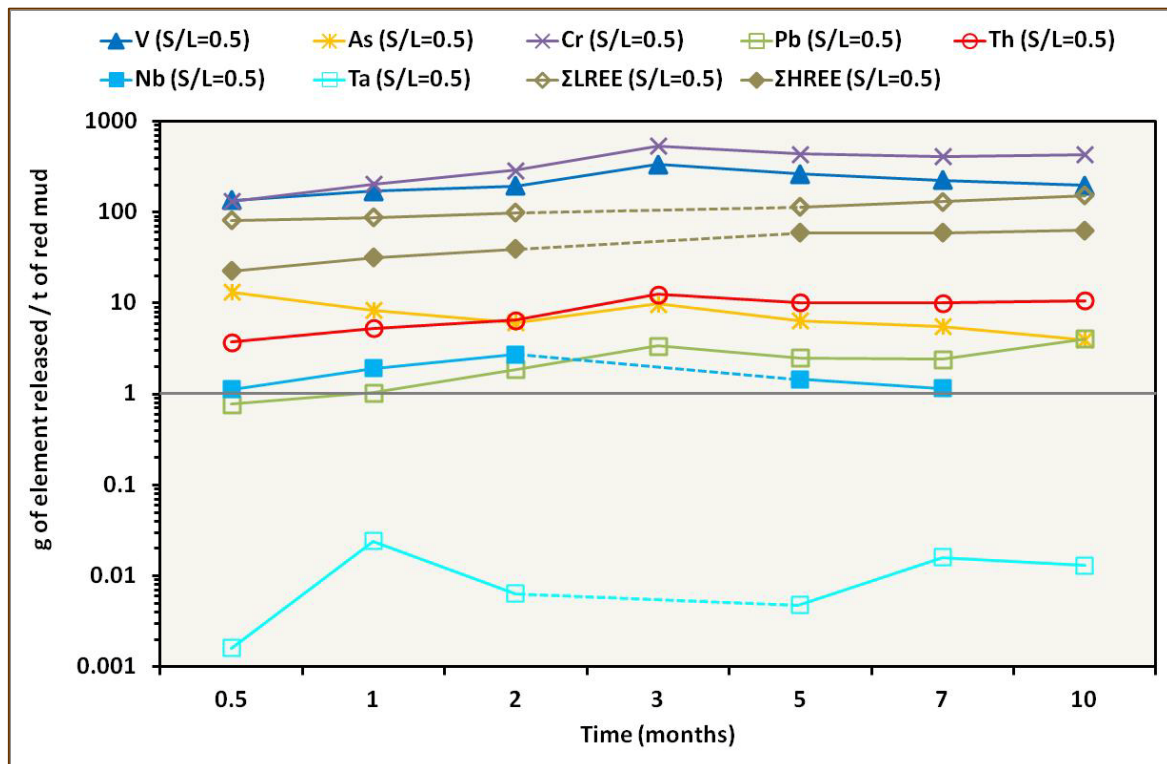
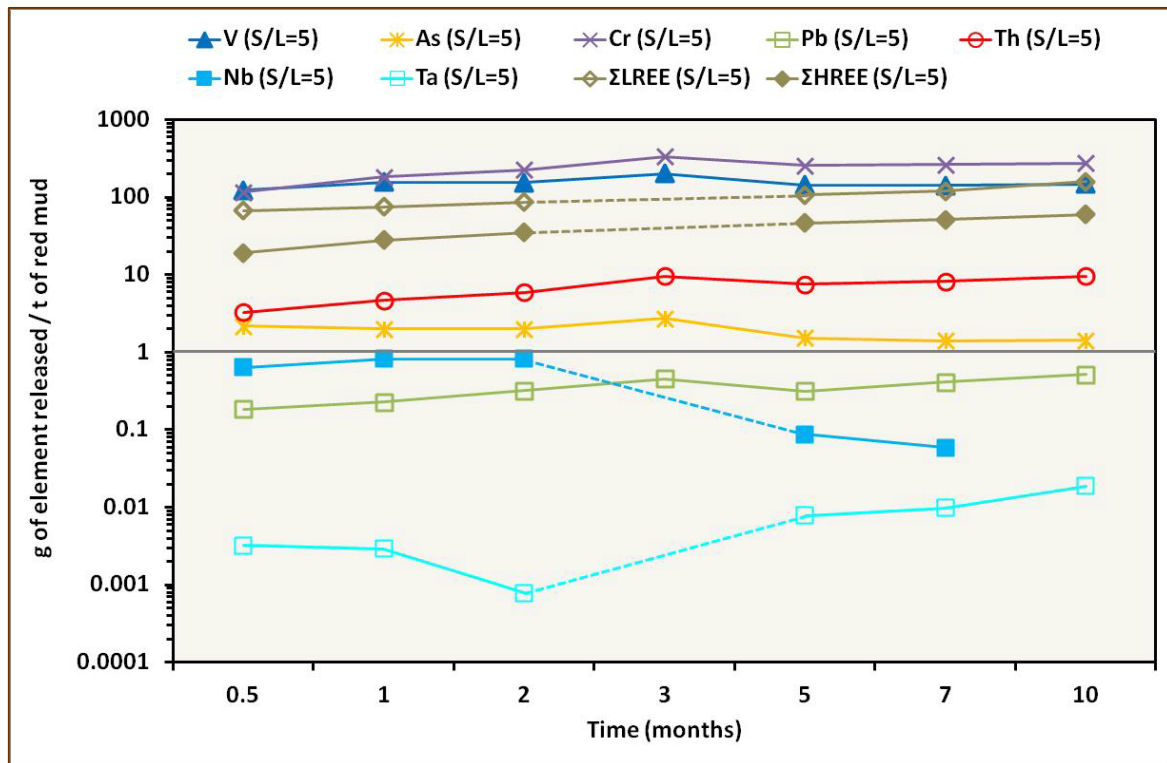


Figure 3.5.2.5: Results from leaching experiments showing the LREEs (La, Ce, Pr, Nd, Sm, Eu, and Gd) release (g) per 1 ton of Greek red mud leached by concentrated acetic acid.

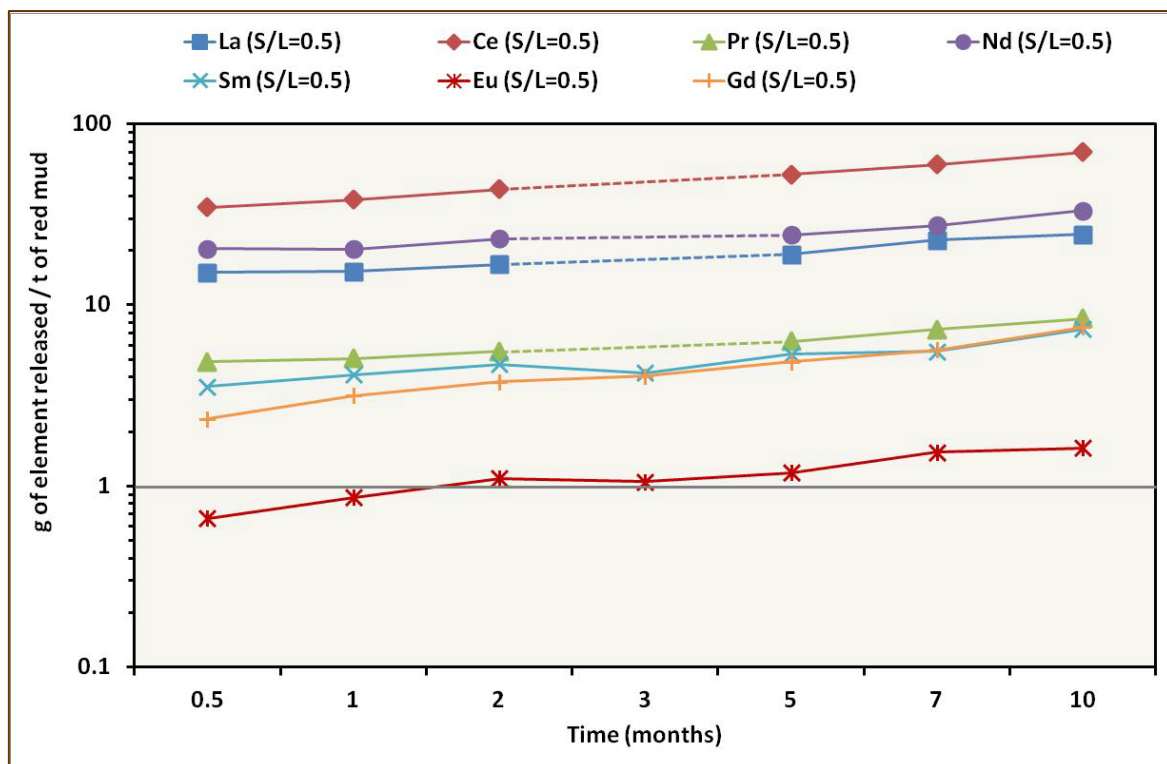
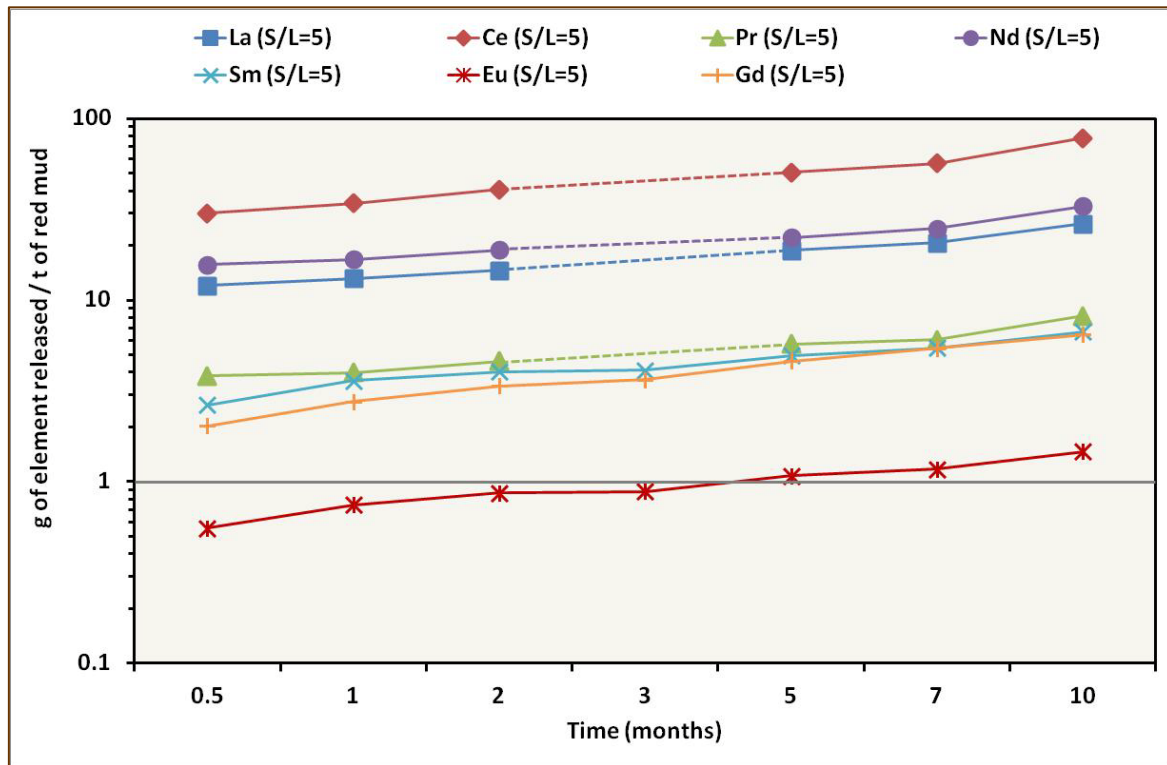
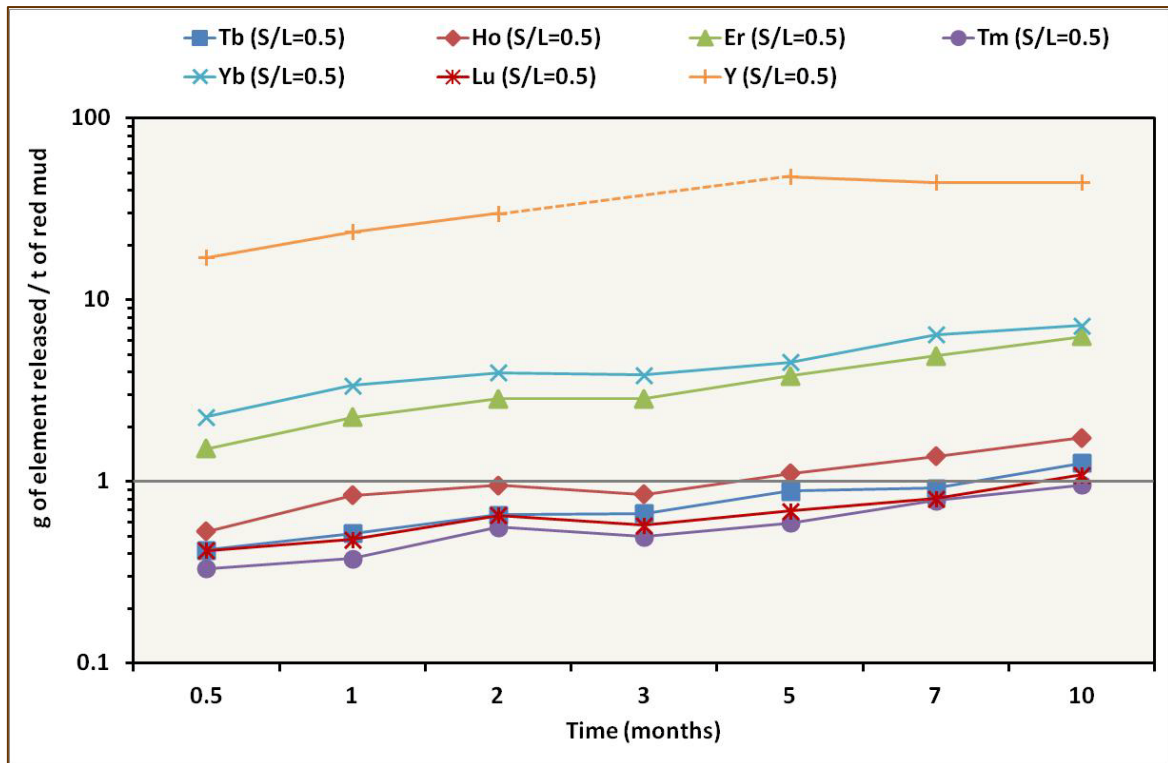
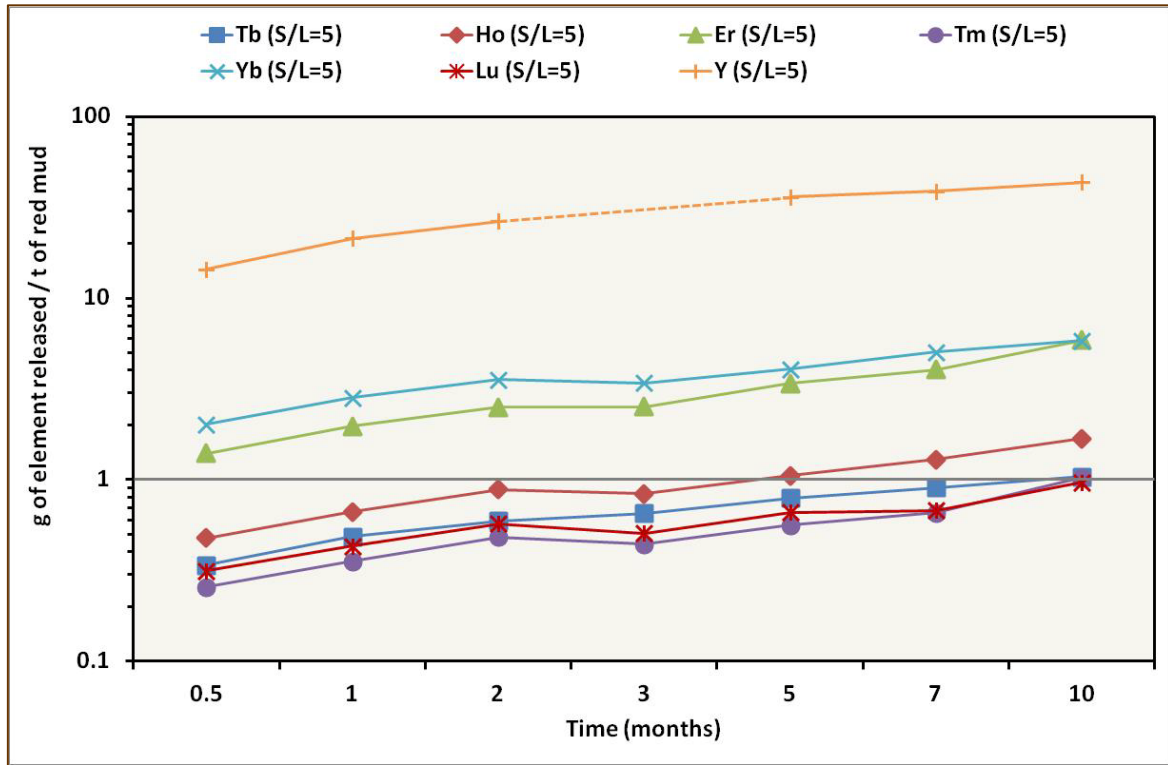


Figure 3.5.2.6: Results from leaching experiments showing the HREEs (Tr, Ho, Er, Tm, Yb, Lu, and Y) release (g) per 1 ton of Greek red mud leached with concentrated acetic acid.



by the S/L ratio, during the experiment. Similar leaching experiments with the Fe-rich (low grade) and Fe-depleted (high grade) Parnassos-Ghiona bauxites, presented for first time in the literature, also indicated significant recovery of REE (**Figures 3.5.2.7 – 3.5.2.10**). In the case of bauxites, the mobility of REE in acid is due to presence of LREE-minerals (mostly bastnäsite/parisite-group; see text above). Despite the fact that the mobility of Th in acid-treated red mud is enhanced, as it is compared to its negligible mobilization in seawater environment, considerable amount of this actinide element seems to remain in this residue.

Figure 3.5.2.7: Results from leaching experiments, relative to S/L ratio effect, showing the LREEs (La, Ce, Pr, Nd, Sm, Eu, and Gd) release from Greek Fe-rich (low grade) bauxite leached by concentrated acetic acid.

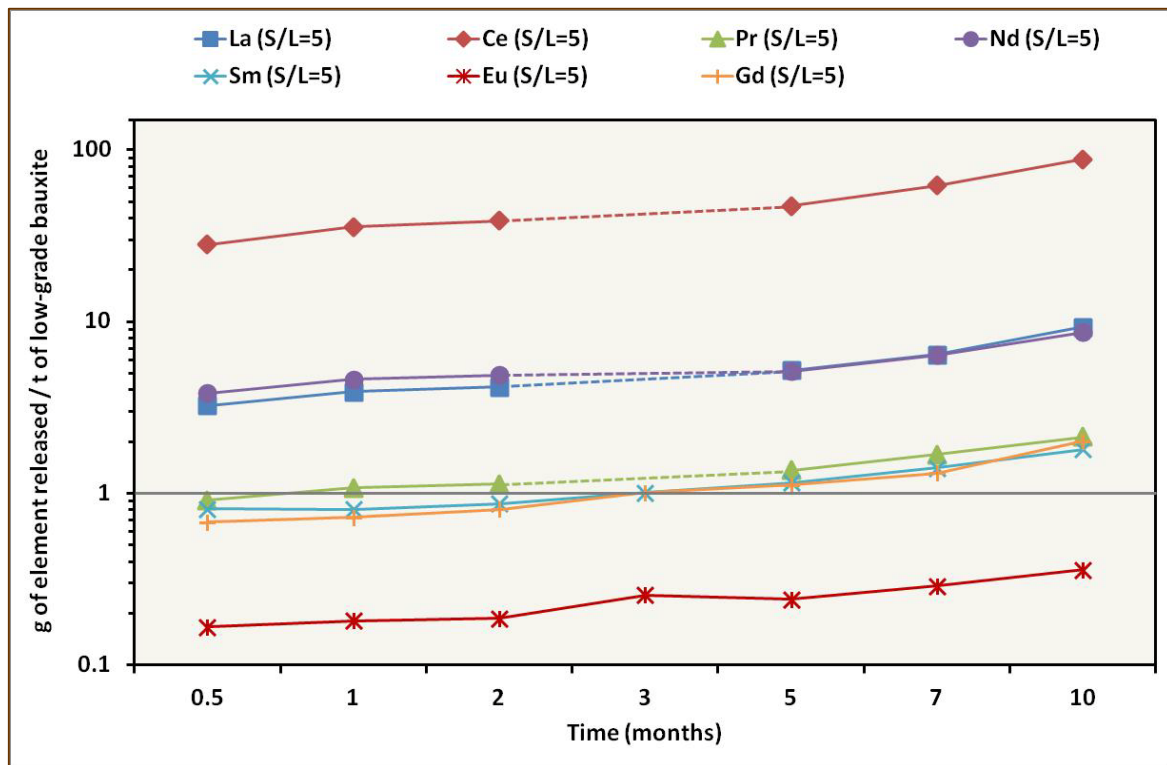


Figure 3.5.2.7: continued.

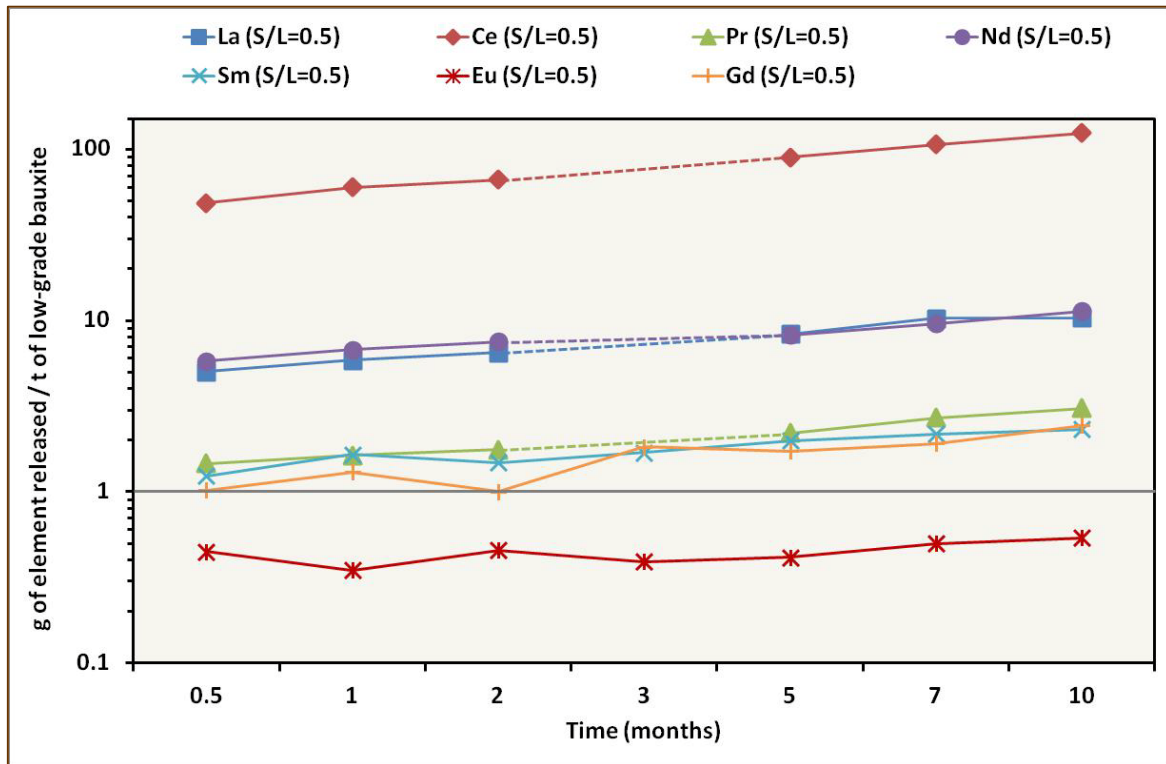


Figure 3.5.2.8: Results from leaching experiments, relative to S/L ratio effect, showing the HREEs (Tr, Ho, Er, Tm, Yb, Lu, and Y) release from Greek Fe-rich (low grade) bauxite leached by concentrated acetic acid.

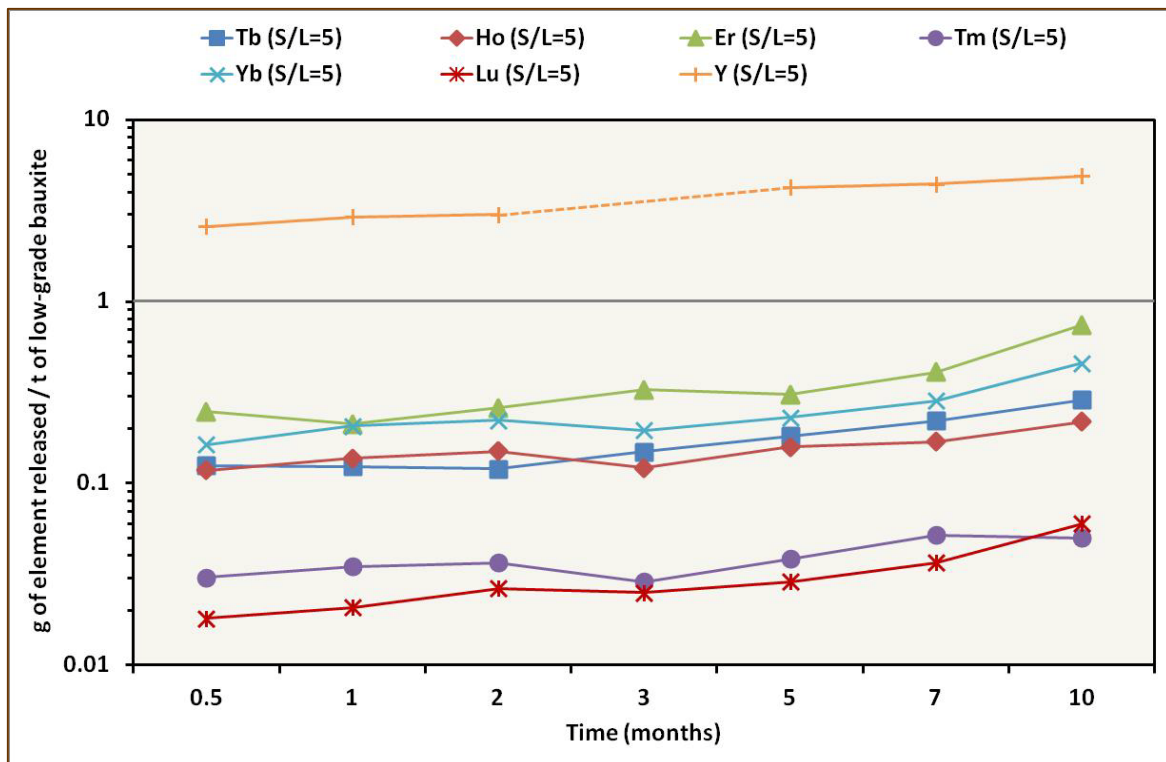


Figure 3.5.2.8: continued.

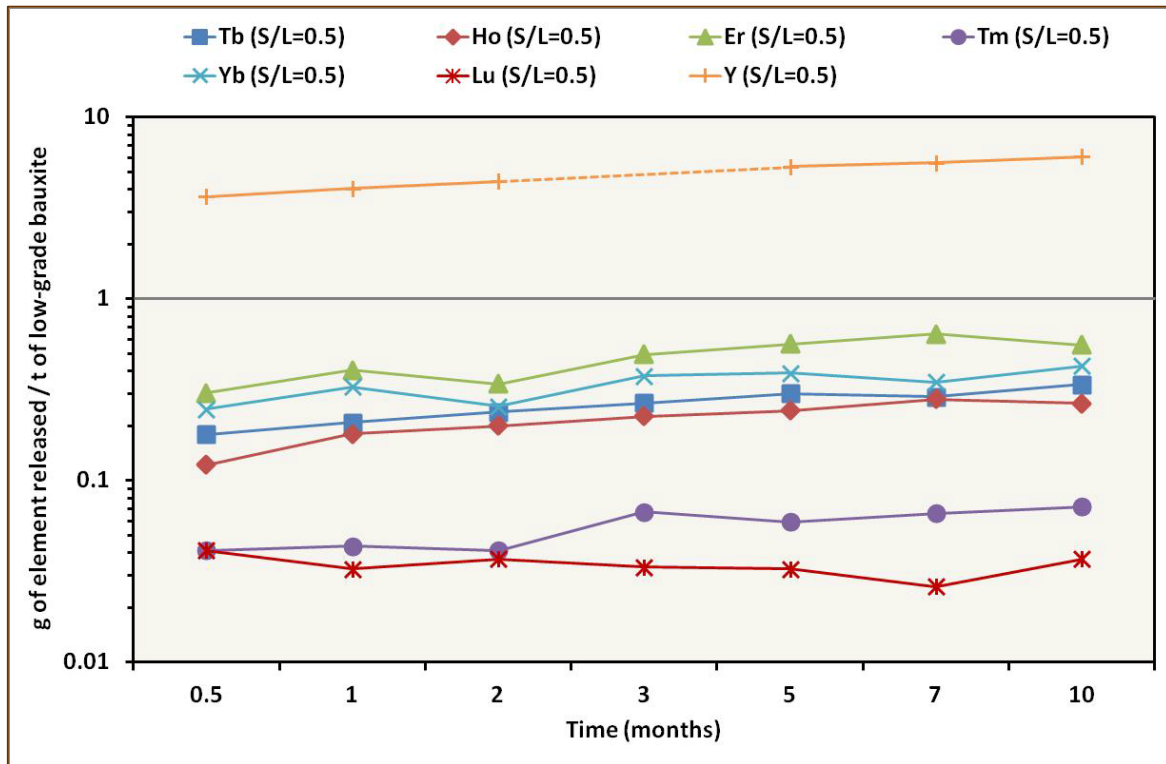


Figure 3.5.2.9: Results from leaching experiments, relative to S/L ratio effect, showing the LREEs (La, Ce, Pr, Nd, Sm, Eu, and Gd) release from Greek Fe-depleted (high grade) bauxite leached by concentrated acetic acid.

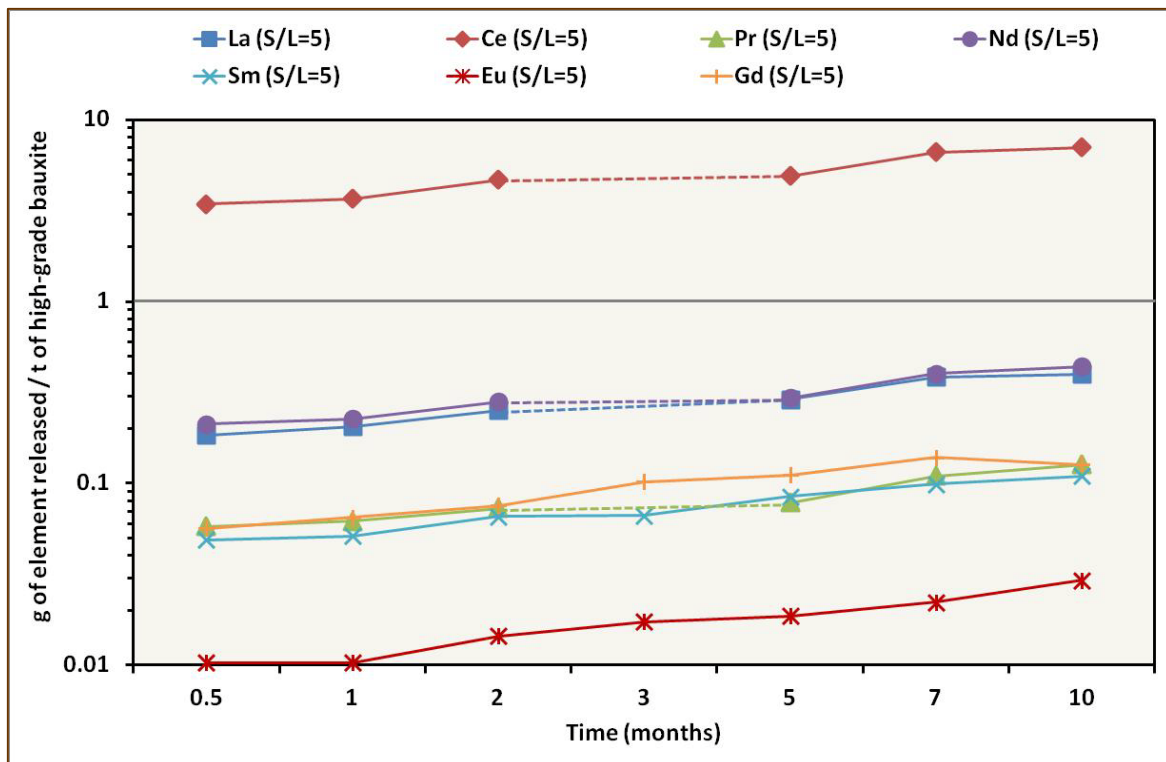


Figure 3.5.2.9: continued.

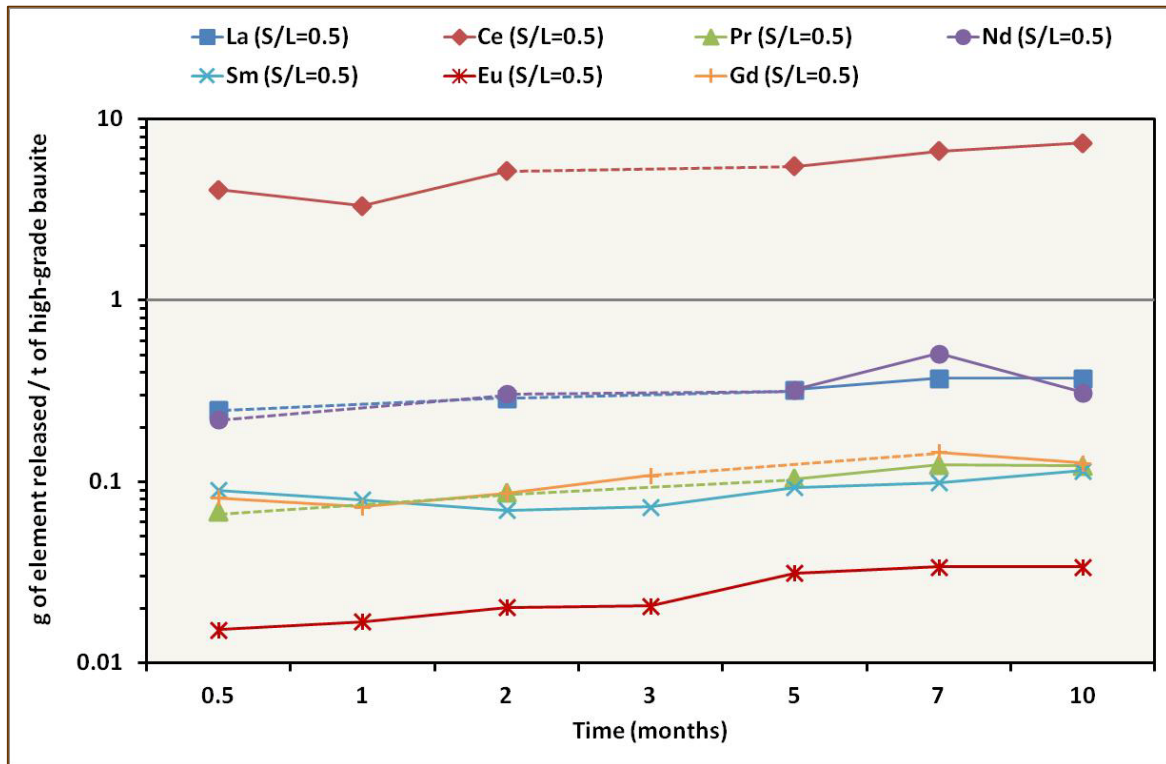


Figure 3.5.2.10: Results from leaching experiments, relative to S/L ratio effect, showing the HREEs (Tr, Ho, Er, Tm, Yb, Lu, and Y) release from Greek Fe-depleted (high grade) bauxite leached by concentrated acetic acid.

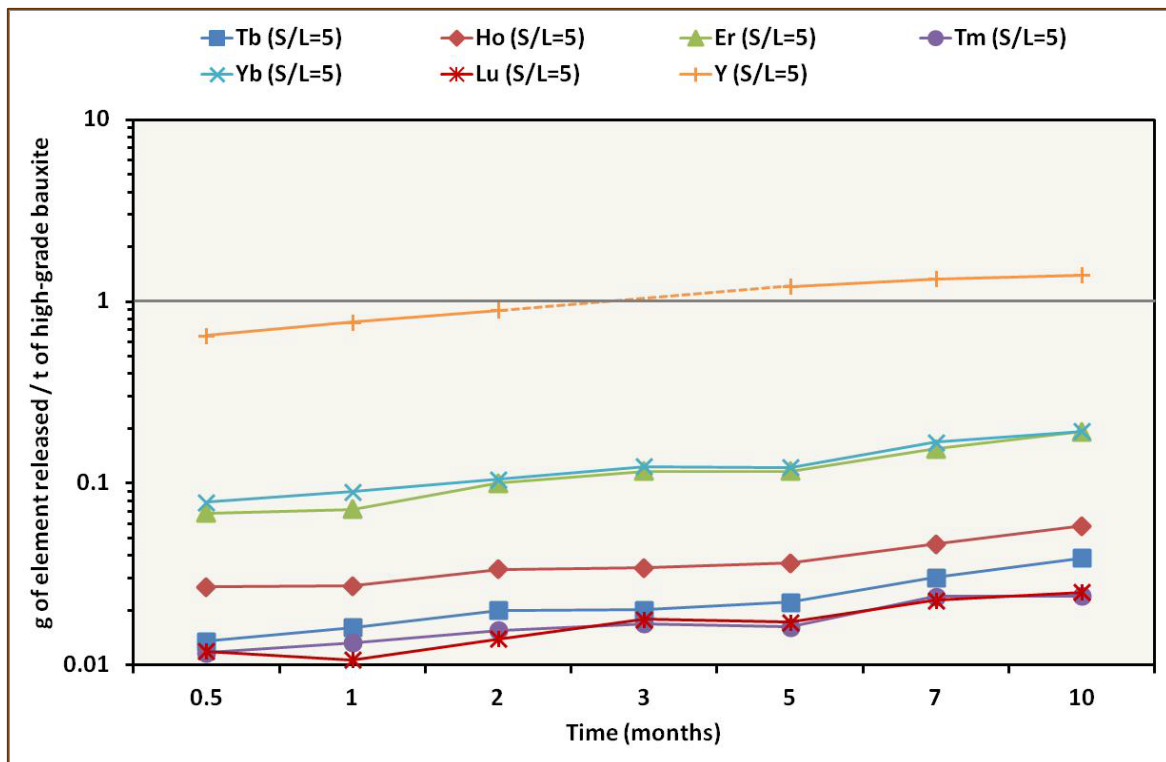
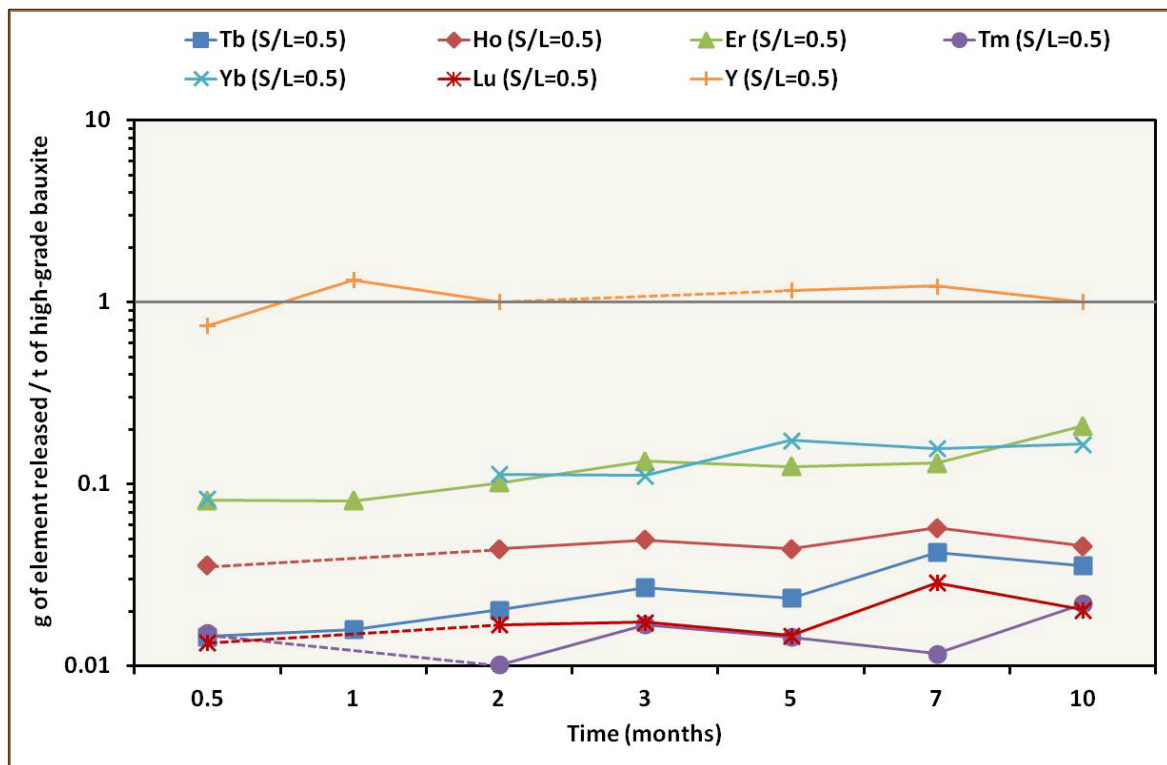


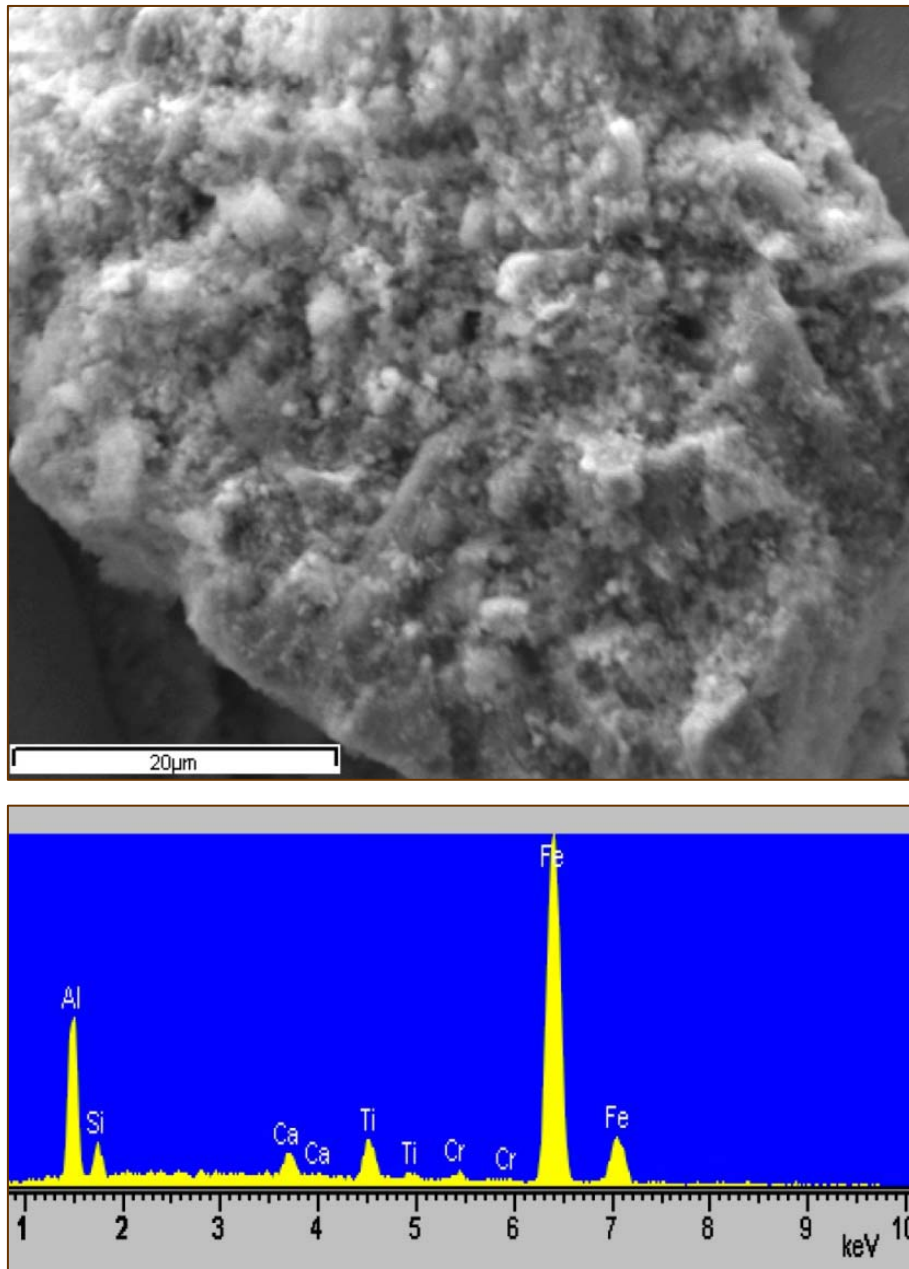
Figure 3.5.2.10: continued.



This robustly proves the aforementioned acid-insoluble and, of course, seawater-insoluble, solid nanophase (not apparent in the SEM-EDS study) hosting immobile Th, into the “Al-Fe-Ca-Ti-Si-Na-Cr matrix”. The difference, in microscale, between the initial and acid-treated “Al-Fe-Ca-Ti-Si-Na-Cr matrix”, affects mainly the lowering of Ca-K α X-ray emission peak in the EDS spectra (see SEM-EDS of raw red mud in **Figure 3.5.1.2** and **Figure 3.5.2.11**) attributed to the loss of Ca-carbonate minerals and Ca-Al-hydroxysilicate phases.

As mentioned above, the STEM-EDS/EELS study, in combination with Th L_{III} -edge XANES and EXAFS, revealed that both the initial and acid-treated “Al-Fe-Ca-Ti-Si-Na-Cr matrix”, as appeared in microscale, is actually an aggregate of several Al-, Fe-, Ca-, Ti-, Si-, Na-, Cr- (and also S-, P-, Ce-, Nb-, Zr-, and maybe Sr-) nanoparticles, including the Th-hosting nanoperovskite. It is, herein, stated that the above nanophase is the reason of low Th release in acid medium, and subsequently that explains the Th immobility in Greek red mud as exposed in Mediterranean seawater.

Figure 3.5.2.11: Morphology and chemical composition (major elements) of the studied red mud in microscale by SEM-EDS, after acid-leaching.



4. BIBLIOGRAPHY

- [1] Abhilash, Sinha, S., Sinha M. K. and Pandey B. D. (2014) Extraction of lanthanum and cerium from Indian red mud. *Int. J. Min. Process.* **127**, 70-73.
- [2] Adams J. A. S. and Richardson K. A. (1960) Thorium, uranium and zirconium concentrations in bauxite. *Econ. Geol.* **55**, 1653-1675.
- [3] Agatzini-Leonardou S., Oustadakis P., Tsakiridis P. E. and Markopoulos, Ch. (2008) Titanium leaching from red mud by diluted sulfuric acid at atmospheric pressure. *J. Hazard. Mater.* **157**, 579-586.
- [4] Akinci A. and Artir R. (2008) Characterization of trace elements and radionuclides and their risk assessment in red mud. *Mater. Charact.* **59**, 417-421.
- [5] Aksenov V. L., Kovalchuk M. V., Kuzmin A. Yu., Purans, Yu. and Tyutyunnikov S. I. (2006) Development of methods of EXAFS spectroscopy on Synchrotron radiation beam: Review. *Crystallogr. Rep.* **51**, 908-935.
- [6] Alexander J. L., Bailev E. H. and Pickering K. T. (2000) Using rare earth elements as provenance indicators in mudrocks from a range of tectonic settings. In: Goldschmidt 2000 Conference, September 3rd – 8th, Oxford, UK, *J. Conf. Abstr.* **5** (2), 134.
- [7] Alonso E., Sherman A. M., Wallington T. J., Everson M. P., Field F. R., Roth R. and Kirchain R. E. (2012) Evaluating Rare Earth Element Availability: A Case with revolutionary demand from clean technologies. *Environ. Sci. Technol.* **46**, 3406-3414.
- [8] Anders E. and Ebihara M. (1982) Solar-system abundances of the elements. *Geochim. Cosmochim. Acta* **46**, 2363-2380.
- [9] Anders E. and Grevesse N. (1989) Abundances of the elements: Meteoritic and solar. *Geochim. Cosmochim. Acta* **53**, 197-214.
- [10] ANKA Instrumentation Book (2012) ANKA Synchrotron Radiation Facility, Karlsruhe Institute of Technology, a member of the Helmholtz Association. IPS, Institute for

Photon Science and Synchrotron Radiation; Hermann-von-Helmholtz-Platz 1, 76344 Eggenstein-Leopoldshafen, Germany, pp. 92. (<http://www.anka.kit.edu/943.php>)

- [11] Ankudinov A. L., Ravel B., Rehr J. J. and Conradson S. D. (1998) Real-space multiple-scattering calculation and interpretation of x-ray-absorption near-edge structure. *Phys. Rev. B* **58** (12), 7565-7576.
- [12] Aplin A. C. (1984) Rare earth element geochemistry of Central Pacific ferromanganese encrustations. *Earth Planet. Sci. Lett.* **71**, 13-22.
- [13] Aragon R., Buttrey D., Shepherd J. and Honig J. (1985) Influence of nonstoichiometry on the Verwey transition. *Phys. Rev. B* **31** (1), 430-436.
- [14] Arčon I., Kolar J., Koder A., Hanžel D. and Strlič M. (2007) XANES analysis of Fe valence in iron gall inks. *X-Ray Spectrom.* **36**, 199-205.
- [15] Aronis G. A. (1955) Geographical distribution, geological placing and aspects on the genesis of the Greek bauxites. *Bull. Geol. Soc. Greece* **2**, 55-79. (In Greek – English abstract)
- [16] Arp T. (1985) Geologische Kartierung des Gebietes um Tithronion im Kallidromengebirge, Mittelgriechenland und petrographische Bearbeitung des Karstbauxites (b1). Unpublished PhD Thesis, University of Hamburg, Hamburg, Germany, 213 pp. (In German)
- [17] Arrio M. -A., Rossano S., Brouder Sh., Galois L. and Calas G. (2000) Calculation of multipole transitions at the Fe K pre-edge through $p-d$ hybridization in the Ligand Field Multiplet model. *Europhys. Lett.* **51**, 454-460.
- [18] Augustithis S. S., Mack E. and Vgenopoulos A. (1978) Textural and geochemical comparisons of the oolitic and pisolitic structures of the Parnassus bauxites and the Ni-Cr-Fe laterites of Larymna/Lokris and Euboea, Greece. In: Proceedings of 4th International Congress for the Study of Bauxites, Alumina and Aluminum, October 9-12, National Technical University of Athens, Athens, Greece, pp. 15-34.

- [19] Augustithis S. S., Mposkos E. and Vgenopoulos A. (1980) Diffusion rings (sphaeroids) in bauxite. *Chem. Geol.* **30**, 351-362.
- [20] Bajt S., Sutton S. R. and Delaney J. S. (1994) X-ray microprobe analysis of iron redox states in silicates and oxides using X-ray absorption near edge structure (XANES). *Geochim. Cosmochim. Acta* **58**, 5209-5214.
- [21] Ballaran T. B., Bromiley G., Demouchy S., Dubrovinskaia N. Dubrovinsky L., Frost D., Heidelbach F., Jacobsen S., Keyssner S., Klasinski K., Langenhorst F., Liebske C., Marton F., McCammon C., Rubie D., Seifert F., Steinle-Neumann G., Terasaki H. and Terry M. (2004) From crust to core and back. Geomaterials Research at Bayerisches Geoinstitut, Universität Bayreuth, Bayreuth, Germany, pp. 78. (http://www.bgi.uni-bayreuth.de/organization/bgibrochure/FromCrustToCore/FromCrustToCore_HR040421_web.pdf)
- [22] Barker S. L. L., Hickey K. A., Cline J. S., Dipple G. M., Kilburn M. R., Vaughan J. R. and Longo A. A. (2009) Uncloaking invisible gold: use of nanosims to evaluate gold, trace elements, and sulfur isotopes in pyrite from Carlin-type gold deposits. *Econ. Geol.* **104**, 897-904.
- [23] Barth M. G. and Gluhak T. M. (2009) Geochemistry and tectonic setting of mafic rocks from the Othris Ophiolite, Greece. *Contrib. Mineral. Petrol.* **157**, 23-40.
- [24] Bárdossy G. (1982) Karst bauxites: bauxite deposits on carbonate rocks. In: *Developments in Economic Geology* **14**, edited by Bárdossy G., Elsevier, Amsterdam, The Netherlands, 441 pp.
- [25] Bárdossy G. (2007) The Halimba bauxite deposit. In: *Occasional Papers of the Geological Institute of Hungary*, edited by Maros G., Geological Institute of Hungary **208**, pp. 119.
- [26] Bárdossy G. and Aleva G. J. J. (1990) Lateritic bauxites. Development in economic geology, **27**, Elsevier, Amsterdam, pp. 624.
- [27] Bárdossy G. and Brindley G. W. (1978) Rancieite associated with a karstic bauxite deposit. *Am. Mineral.* **63**, 762-767.

- [28] Bárdossy G., Csanády A. and Csordás A. (1978) Scanning electron microscope study of bauxites of different ages and origins. *Clay. Clay Miner.* **26**, 245-262.
- [29] Bárdossy G., Jonás K., Imre A. and Solymár, K. (1977) Interrelation of bauxite texture, micromorphology, mineral individualism and heteromorphism. *Econ. Geol.* **72**, 573-581.
- [30] Bárdossy G. and Mack E. (1967) Zur Kenntnis der Bauxite des Parnass-Kiona-Gebirges. *Miner. Deposita* **2**, 334-348. (In German)
- [31] Bárdossy G. and Pantó Gy. (1971) Investigation of Bauxites with Help of Electron-Probe. *Mineral. Petrol. (former: Tschermaks Min. Petr. Mitt.)* **15**, 165-184.
- [32] Bárdossy G. and White J. L. (1979) Carbonate inhibits the crystallization of aluminum hydroxide in bauxite. *Science* **203**, 355-356.
- [33] Beretka J. and Mathew P. J. (1985) Natural radioactivity of Australian building materials, industrial wastes and by-products. *Health Phys.* **48** (1), 87-95.
- [34] Berner R. A. (1999) Atmospheric oxygen over Phanerozoic time. *Proc. Natl. Acad. Sci. USA* **96**, 10955-10957.
- [35] Berry A. J., O'Neill H. St. C., Jayasuriya K. D., Campbell S. J. and Foran G. J. (2003) XANES calibration for the oxidation state of iron in a silicate glass. *Am. Mineral.* **88**, 967-977.
- [36] Berry A. J., Yaxley G. M., Woodland A. B. and Foran G. J. (2010) A XANES calibration for determining the oxidation state of iron in mantle garnet. *Chem. Geol.* **278**, 31-37.
- [37] Bersani D., Lottici P.P. and Montenero A. (1999) Micro-Raman Investigation of Iron Oxides Films and Powders Produced by Sol-Gel Syntheses. *J. Raman Spectrosc.* **30**, 355-360.
- [38] Bian Z., Miao X., Lei S., Chen S., Wang W. and Struthers S. (2012) The challenges of reusing mining and mineral-processing wastes. *Science*, **337**, 702-703.

- [39] Biermann M. (1983) Zur Mineralogie, Geochemie und Genese des Karstbauxites (B3 – Horizont) an der Grenze Unter-Oberkreide in Mittelgriechenland. Unpublished PhD Thesis, University of Hamburg, Hamburg, Germany, 134 pp. (In German)
- [40] Boni M., Reddy S. M., Mondillo N., Balassone G. and Taylor R. (2012) A distant magmatic source for Cretaceous karst bauxites of Southern Apennines (Italy), revealed through SHRIMP zircon age dating. *Terra Nova* **24** (4), 326-332.
- [41] Boni M., Rollinson G., Mondillo N., Balassone G. and Santoro L. (2013) Quantitative mineralogical characterization of karst bauxite deposits in the southern Apennines, Italy. *Econ. Geol.* **108**, 813-833.
- [42] Boulangé B. and Colin F. (1994) Rare earth element mobility during conversion of nepheline syenite into lateritic bauxite at Passa Quatro, Minas Gerais, Brazil. *Appl. Geochem.* **9**, 701-711.
- [43] Bowen N. L. (1922) The reaction principle in petrogenesis. *J. Geology* **3**, 177-198.
- [44] Boynton W. V. (1985) Cosmochemistry of the rare earth elements: Meteorite studies, In: Rare earth element geochemistry, edited by Henderson P., Developments in Geochemistry 2, Elsevier, Amsterdam, pp. 115-152.
- [45] Brady P. V. (1996) The physics and chemistry of mineral surfaces. Edited by Brady P. V. (Ed), CRC Press – Taylor & Francis Group, Boca Raton, FL, 384 pp., ISBN-13: 978-0849383519.
- [46] Brenker F. E. and Jordan G. (2010) Nanoscopic approaches in Earth and planetary sciences. In: *EMU Notes in Mineralogy*, edited by Brenker F. E. and Jordan G., European Mineralogical Union and the Mineralogical Society of Great Britain & Ireland **8**, 382 pp., ISBN: 978-0-903056-25-0.
- [47] Brydson R., Sauer H., Engel W., Thomass J. M., Zeitler E., Kosugi N. and Kuroda H. (1989) Electron energy loss and X-ray absorption spectroscopy of rutile and anatase: a test of structural sensitivity. *J. Phys. Condens. Matter.* **1**, 797-812.

- [48] Burke I. T., Mayes W. M., Peacock C. L., Brown A. P., Jarvis A. P. and Gruiz K. (2012) Speciation of arsenic, chromium, and vanadium in red mud samples from the Ajka spill site, Hungary. *Environ. Sci. Technol.* **46**, 3085-3092.
- [49] Burke I. T., Peacock C. L., Lockwood C. L., Stewart D. I., Mortimer R. J. G., Ward M. B., Renforth P., Gruiz K. and Mayes W. M. (2013) Behavior of aluminum, arsenic, and vanadium during the neutralization of red mud leachate by HCl, gypsum, or seawater. *Environ. Sci. Technol.* **47**, 6527-6535.
- [50] Busing W. R. and Levy H. A. (1958) A single crystal neutron diffraction study of diaspore, $\text{AlO}(\text{OH})$. *Acta Cryst.* **11**, 798-803.
- [51] Buttner R. H. and Maslen E. N. (1992) Structural parameters and electron difference density in BaTiO_3 . *Acta Cryst. B* **48**, 764-796.
- [52] Calagari A. A. and Abenini A. (2007) Geochemical investigations on Permo-Triassic bauxite horizon at Kanisheeteh, east of Bukan, West-Azarbaidjan, Iran. *J. Geochem. Explor.* **94**, 1-18.
- [53] Calas G. and Petiau J. (1983) Coordination of iron in oxide glasses through high-resolution K-edge spectra: information from the pre-edge. *Solid State Comm.* **48**, 625-629.
- [54] Calvert C. C., Rainforth W. M., Sinclair D. C. and West A. R. (2006) EELS characterization of bulk $\text{CaCu}_3\text{Ti}_4\text{O}_{12}$ ceramics. *Micron.* **37**, 412-419.
- [55] Casey W. H., Rustad J. R., Banerjee D. and Furrer G. (2005) Large molecules as models for small particles in aqueous geochemistry research. *J. Nanopart. Res.* **7**, 377-387.
- [56] Cashion J. D., Cook P. S. and Brown L. J. (1986) Minerals, sediments and coals. *Hyperfine Inter.* **27**, 23-34.
- [57] Castor S. B. and Hedrick J. B. (2006) Rare Earth Elements, pp. 769-792. (<http://www.segemar.gov.ar/bibliotecaintemin/LIBROSDIGITALES/Industrialminerals&rocks7ed/pdf/papers/058.pdf>)

- [58] Catinat M., Anciaux P., Backman C. M., Bosmans W., Buchholz P., Ferri A., Gernuks M., Gunn A., Hagelüken C., Hebestreit C., Hocquard C., Horninger S., Jones M., Kavina P., Kertesz B., Koskinen K. R., Lawlor N., Mager D., Marklund U., Moll S., Morliere A., Reimann M., Reller A., Weber L., Wyart-Remy M., Franco Amendes A., Gandenberger C., Le Guern Y., Marscheider-Weidemann F. and Tercero Espinoza L. (2010) Critical raw materials for the EU. In: Report of the Ad-hoc Working Group on defining critical raw materials, European Commission, 85 pp.
- [59] Chakhmouradian A. R. and Zaitsev A. N. (2012) Rare earth mineralization in igneous rocks: sources and processes. *Elements* **8**, 347-353.
- [60] Chamritski I. and Burns G. (2005) Infrared and Raman-Active Phonons of Magnetite, Maghemite and Hematite: A Computer Simulation and Spectroscopic Study. *J. Phys. Chem.* **109**, 4965-4968.
- [61] Charpin P. P., Chevrier G., Lance M., Nierlich M., Vigner N. D., Livet J. and Musikas C. (1987) Structure du nitrate de thorium(IV) Tétrahydraté. *Acta Cryst.* **C43**, 1239-1941. (In French)
- [62] Christensen A. N., Hansen P. and Lehmann M. S. (1976) Isotope effects in the bonds of beta-CrOOH and beta-CrOOD. *J. Solid State Chem.* **19**, 299-304.
- [63] Christensen A. N., Hansen P. and Lehmann M. S. (1977) Isotope effects in the bonds of α -CrOOH and α -CrOOD. *J. Solid State Chem.* **21**, 325-329.
- [64] Ciobanu C. L., Cook N. J., Utsunomiya S., Kogagwa M., Green L., Gilbert S. and Wade B. (2012) Gold-telluride nanoparticles revealed in arsenic-free pyrite. *Am. Mineral.* **97**, 1515-1518.
- [65] Ciobanu C. L., Cook N. J., Utsunomiya S., Pring A. and Green L. (2011) Focused ion beam-transmission electron microscopy applications in ore mineralogy: Bridging micro- and nanoscale observations. *Ore Geol. Rev.* **42**, 6-31.

- [66] Collins R. N., Clark M. W. and Payne T. E. (2014) Solid phases responsible for Mn^{II}, Cr^{III}, Co^{II}, Ni, Cu^{II} and Zn immobilization by a modified bauxite refinery residue (red mud) at pH 7.5. *Chem. Engineer. J.* **236**, 419-429.
- [67] Combes P. -J. (1979) Observations sédimentologiques, paléogéographiques, minéralogiques et géochimiques sur les bauxites du deuxième horizon dans la zone du Parnasse (Grèce) – *Sedimentological, paleogeographical, mineralogical and geochemical observations on the bauxites of the second horizon in the Parnassus zone.* *Bull. Soc. Geol. France* **XXI (4)**, 485-494. (In French)
- [68] Combes P. -J. (1984) Regards sur la géologie des bauxites; aspects récents sur la genèse de quelques gisements à substratum carbonate – *A look at the geology of bauxite; recent data on the genesis of some deposits in carbonate rock.* Bulletin des Centres de Recherches Exploration-production Elf-Aquitaine, **8 (1)**, pp. 251-274.
- [69] Combes P. -J. and Andreou G. (1983) Utilisation de la paléogéographie pour la prospection de bauxite dans une région de nappe: Un exemple au nord de Distomon (zone du Parnasse, Grèce) – *Paleogeography as an important support for the bauxite prospection in regions with nappe tectonics: An example to the north of Distomon (Parnassus zone, Greece.* Proceedings of the 5th Int. Congress ICSOBA, Zagreb, Yugoslavia, 26-28 September 1983, par l'Académie Yougoslave des Sciences et des Arts **13 (18)**, Zagreb, Yugoslavia, pp. 223-231. (In French)
- [70] Combes P. -J., Fourcade E., Masse J. P. and Philip J. (1981) Observations stratigraphiques et paléontologiques sur la Crétacé de la zone du Parnasse – *Stratigraphical and paleontological observations on the Cretaceous of the Parnassos zone (Greece).* In: Travaux du Comité International pour l'étude des bauxites, de l'alumine et de l'aluminium, Proceedings of the ICSOBA – AIM Conference, Cagliari, Italy, 27-28 September 1979, par l'Académie Yougoslave des Sciences et des Arts **11 (16)**, Zagreb, Yugoslavia, pp. 347-365. (In French)
- [71] Condie K. C. (1993) Chemical composition and evolution of the upper continental crust: contrasting results from surface samples and shales. *Chem. Geol.* **104**, 1-37.

- [72] Cooper M. B., Clarke P. C., Robertson W., McPharlin I. R. and Jeffrey, R. C. (1995) An investigation of radionuclide uptake into food crops grown in soils treated with bauxite mining residues. *J. Radioanal. Nucl. Chem.* **194** (2), 379-387.
- [73] Connelly N. G., Damhus T., Hartshorn R. M. and Hutton A. T. (2005) Nomenclature of inorganic chemistry IUPAC Recommendations 2005. In: The Royal Society of Chemistry: 2005. <http://old.iupac.org/publications/books/author/connelly.html>.
- [74] Cornell R. M. and Schwertmann U. (2003) *The Iron Oxides: Structure, Properties, Reactions, Occurrences and Uses*. 2nd edition, Wiley-VCH Verlag GmbH & Co. KGaA, 664 pp., ISBN: 3-527-30274-3.
- [75] Cosmidis J., Benzerara K., Gheerbrant E., Estève I., Bouya B. and Amaghazaz (2013) Nanometer-scale characterization of exceptionally preserved bacterial fossils in Paleocene phosphorites from Ouled Abdoun (Morocco). *Geobiology* **11**, 139-153.
- [76] Cromer D. T. and Herrington K. (1955) The structures of anatase and rutile. *J. Am. Chem. Soc.* **77**, 4708-4709.
- [77] Deditius A. P., Utsunomiya S., Reich M., Kesler S. E., Ewing R. E., Hough R. and Walshe J. (2010) Trace metal nanoparticles in pyrite. *Geochim. Cosmochim. Acta* **74**, Suppl. A216 (abstr.).
- [78] Deditius A. P., Utsunomiya S., Reich M., Kesler S. E., Ewing R. E., Hough R. and Walshe J. (2011) Trace metal nanoparticles in pyrite. *Ore Geol. Rev.* **42**, 32-46.
- [79] Demichelis R., Noel Y., Civalleri B., Roetti C., Ferrero M. and Dovesi R. (2007) The vibrational spectrum of α -AlOOH diaspore: An ab initio study with the CRYSTAL Code. *J. Phys. Chem.* **111**, 9337-9346.
- [80] De Carlo E.H. and McMurtry G. M. (1992) Rare earth element geochemistry of ferromanganese crusts from the Hawaiian archipelago, Central Pacific. *Chem. Geol.* **95**, 235-250.

- [81] De Wolff P. M. and Visser J. W. (1964) Absolute Intensities – Outline of a Recommended Practice: Technique for obtaining absolute intensities with internal standard. Report 641.109, Technisch Physische Dienst, Delft, Netherlands. Reprinted (1988), *Powder Diffraction*, **3**, 202-204.
- [82] Di Benedetto F., D'Acapito F., Fornaciai G., Innocenti M., Montegrossi G., Pardi L. A., Tesi S. and Romanelli M. (2010) A Fe K-edge XAS study of amethyst. *Phys. Chem. Min.* **37**, 283-289.
- [83] Douvallet L., Martin F., Soubières F., Salvi S., Melfi A. J. and Fortuné J.P. (1999) The mobility of zirconium and identification of secondary Zr-bearing phases in bauxite from Poços de Caldas, Minas Gerais, Brazil: A mass-balance and X-ray absorption spectroscopic study. *Can. Mineral.* **37**, 635-651.
- [84] Drake M. J. and Richter K. (2002) Determining the composition of the Earth. *Nature* **416**, 39-44.
- [85] Dyar M. D., Agresti D. G., Schaefer M. W., Grant C. A. and Sklute E. C. (2006) Mössbauer spectroscopy of earth and planetary materials. *Annu. Rev. Earth Planet. Sci.* **34**, 83-125.
- [86] Dyar M. D., Delaney J. S., Sutton S. R. and Schaefer M. W. (1998) Fe³⁺ distribution in oxidized olivine: A synchrotron micro-XANES study. *Am. Mineral.* **83**, 1361-1365.
- [87] Echigo T., Monsegue N., Aruguete D. M., Murayama M. and Hochella M. F. Jr. (2013) Nanopores in hematite (α -Fe₂O₃) nanocrystals observed by electron tomography. *Am. Mineral.* **98**, 154-162.
- [88] Economopoulos I.E. and Vgenopoulos A.G. (1998) An approach concerning bauxites, bauxitization and mining in Greece. *Min. Wealth* **109**, 21-34.
- [89] Economopoulou-Kyriakopoulou N. (1991) A comparative geochemical and mineralogical study of bauxitic horizons in central Greece. Unpublished PhD Thesis, National Technical University of Athens, Athens, Greece, 119 pp. (In Greek)

- [90] Elderfield H. and Graves M. J. (1981) Negative cerium anomalies in the rare earth element patterns of oceanic ferromanganese nodules. *Earth Planet. Sci. Lett.* **55**, 163-170.
- [91] Eliopoulos D.G. and Economou-Eliopoulos M. (2010) Arsenic distribution in laterite deposits of the Balkan Peninsula. In: Proceedings of XIX Congress of the Carpathian Balkan Geological Association, Greece, 23-26 September 2010, School of Geology, Aristotle University of Thessaloniki, *Scientific Annals* **100**, pp. 325-332.
- [92] Eliopoulos D.G. and Economou-Eliopoulos M. (2000) Geochemical and mineralogical characteristics of Fe–Ni- and bauxitic-laterite deposits of Greece. *Ore Geol. Rev.* **16**, 41-58.
- [93] Eliopoulos D.G., Economou-Eliopoulos M., Apostolikas A. and Golightly J. P. (2012) Geochemical features of nickel-laterite deposits from the Balkan Peninsula and Gordes, Turkey: The genetic and environmental significance of arsenic. *Ore Geol. Rev.* **48**, 413-427.
- [94] England K. E. R., Charnock J. M., Patrick R. A. D. and Vaughan D. J. (1999) Surface oxidation studies of chalcopyrite and pyrite by glancing-angle X-ray absorption spectroscopy (REFLEXAFS). *Mineral. Mag.* **63**, 559-566.
- [95] Engvik A. K., Golla-Schindler U., Berndt J., Austrheim H. and Putnis A. (2009) Intragranular replacement of chlorapatite by hydroxy-fluor-apatite during metasomatism. *Lithos* **112**, 236-246.
- [96] Enserink M. (2010) After red mud flood, scientists try to halt wave of fear and rumors. *Science* **330**, 432-433.
- [97] Esmaily D., Rahimpour-Bonab H., Esna-Ashari A. and Kananian A. (2010) Petrography and geochemistry of the Jajarm karst bauxite ore deposit, NE Iran: Implications for source rock material and ore genesis. *Turk. J. Earth Sci.* **19**, 267-284.
- [98] Evensen N. M., Hamilton P. J. and O'Nions R. K. (1978) Rare-earth abundances in chondritic meteorites. *Geochim. Cosmochim. Acta* **42**, 1199-1212.

- [99] Faria D.L.A., Venâncio Silva S. and Oliveira M.T. (1997) Raman Microspectroscopy of Some Iron Oxides and Oxyhydroxides. *J. Raman Spectrosc.* **28**, 873-878.
- [100] Fegley B. Jr. and Schaefer L. (2010) Cosmochemistry. In: *Principles and Perspectives in Cosmochemistry*, edited by Goswami A. and Reddy B. E., Astrophysics and Space Science Proceedings – Lecture notes of the Kodai School on “Synthesis of Elements in Stars”, Kodaikanal Observatory, India, April 29 – May 13, 2008, Springer-Verlag, Berlin-Heidelberg, Germany, pp. 347-377, ISBN: 978-3-642-10351-3.
- [101] Figueiredo M. O. and Mirão J. (2002) Electronic state of oxygen in oxide minerals: an XAS study on the influence of cationic environment. *Eur. J. Mineral.* **14**, 1061-1067.
- [102] Figueiredo M. O., Silva T. P. and Veiga J. P. (2010) The blue of iron in mineral pigments: a Fe K-edge XANES study of vivianite. *Appl. Phys. A* **99**, 357-361.
- [103] Filimonova L. G. and Trubkin N. V. (2008) Micro- and nanoparticles of zincite and native zinc from disseminated mineralization of metasomatic rocks in the Dukat ore field. *Geol. Ore Depos.* **50**, 153-163.
- [104] Filippidis A., Misaelides P., Clouvas A., Godelitsas A., Barbayiannis N. and Anousis I. (1997) Mineral, chemical and radiological investigation of a black sand at Touzla Cape, near Thessaloniki, Greece. *Environ. Geochem. Hlth.* **19**, 83-88.
- [105] Francombe M. H. (1957) Lattice changes in spinel-type iron chromites. *J. Phys. Chem. Solids* **3** (1-2), 37-43.
- [106] Frost R.L., Fredericks P.M. and Bartlett J.R. (1993) Fourier transform Raman spectroscopy of kandite clays. *Spectrochim. Acta* **49A** (5/6), 667-674.
- [107] Fysh S. A. and Clark P. E. (1983) A Mössbauer study of the iron mineralogy of acid-leached bauxite. *Hydrometallurgy* **10**, 285-303.
- [108] Fysh S. A., Cashion J. D. and Clark P. E. (1983) A Mössbauer study of the iron mineralogy of acid-leached bauxite. *Clay. Clay Min.* **31** (4), 285-292.

- [109] Galoisy L., Calas G. and Arrio M. A. (2001) High-resolution XANES spectra of iron in minerals and glasses: structural information from the pre-edge region. *Chem. Geol.* **174**, 307-319.
- [110] Gambogi J. (2013) Rare Earths; USGS Minerals Yearbook – 2011; U.S. Department of the Interior, U.S. Geological Survey: Washington, DC, 2013; pp 60.1-60.12.
- [111] Gan B. K., Taylor Z., Xu B., Van Riessen A., Hart R. D., Wang X. and Smith P. (2013) Quantitative phase analysis of bauxites and their dissolution products. *Int. J. Miner. Process.* **123**, 64-72.
- [112] Garrett R. F., Blagojevic N., Cai Z., Lai B., Legnini D. G., Rodrigues W. and Stampfl A. P. J. (2001) Synchrotron X-ray microprobe analysis of radioactive trace elements in mineral sands. *Nucl. Instrum. Meth. A* **467-468**, 897-900.
- [113] Gelencsér A., Kováts N., Turóczy B., Rostási Á., Hoffer A., Imre K., Nyirő-Kósa I., Csákberényi-Malasics D., Tóth A., Czitrovsky A., Nagy A., Nagy S., Ács A., Kovács A., Ferincz Á., Hartyáni Z. and Pósfai M. (2011) The Red Mud Accident in Ajka (Hungary): Characterization and potential health effects of fugitive dust. *Environ. Sci. Technol.* **45**, 1608-1615.
- [114] Gendler T. S., Shcherbakov V. P., Dekkers M. J., Gapeev A. K., Gribov S. K., and McClelland (2005) The lepidocrocite-maghemite-haematite reaction chain-I. Acquisition of chemical remanent magnetization by maghemite, its magnetic properties and thermal stability. *Geophys. J. Int.* **160** (3), 815-832.
- [115] Georgalas G. (1946) Geological studies in Greece. *Nature* **157**, 289-290.
- [116] German C. R. and Elderfield H. (1990) Application of the Ce anomaly as a paleoredox indicator: The ground rules. *Paleoceanography* **5**, 823-833.
- [117] Gilbert B., Erbs J. J., Lee Penn R., Petkov V., Spagnoli D. and Waychunas G. A. (2013) A disordered nanoparticle model for 6-line ferrihydrite. *Am. Mineral.* **98**, 1465-1476.

- [118] Godelitsas A. and Astilleros J. M. (2010) Dissolution, sorption/(re)precipitation, formation of solid solutions and crystal growth phenomena on mineral surfaces: implications for the removal of toxic metals from the environment. In: EMU Notes in Mineralogy, Ion partitioning in ambient-temperature aqueous systems, edited by: Prieto M. and Stoll H., vol. **10** (8), pp. 289-324. ISBN: 978-0-903-05626-7.
- [119] Goldsmith R. and Force E. R. (1978) Distribution of rutile in metamorphic rocks and implications for placer deposits. *Miner. Deposita* **13**, 329-343.
- [120] Göttlicher J., Steininger R. and Simon R. (2006) Combination of micro X-ray techniques: the synchrotron radiation laboratory for environmental studies at ANKA. In: 12th European Conference on X-Ray Spectrometry (EXRS 2006), Paris, France, 19-23 June 2006, (abstr.).
- [121] Gräfe M., Landers M., Tappero R., Austin P., Gan B., Grabsch A. and Klauber C. (2011) Combined application of QEM-SEM and hard X-ray microscopy to determine mineralogical associations and chemical speciation of trace metals. *J. Environ. Quality* **40**, 767-783.
- [122] Gréaux S., Farges F., Gautron L., Trcera N., Flank A. -M. and Lagarde P. (2012) X-ray absorption near edge structure (XANES) study of the speciation of uranium and thorium in Al-rich CaSiO₃ perovskite. *Am. Mineral.* **97**, 100-109.
- [123] Grew E. S., Locock A. J., Mills S. J., Galuskina I. O., Galuskin E. V., and Hålenius U. (2013) Nomenclature of the garnet supergroup. *Am. Mineral.* **98**, 785-811.
- [124] Gribb A. A. and Banfield J. F. (1997) Particle size effects on transformation kinetics and phase stability in nanocrystalline TiO₂. *Am. Mineral.* **82**, 717-728.
- [125] Grice J. D., Maisonneuve V. and Leblanc M. (2007) Natural and synthetic fluoride carbonates. *Chem. Rev.* **107**, 114-132.
- [126] Grimes C. B., John B. E., Kelemen P. B., Mazdab F. K., Wooden J. L., Cheadle M. J., Hanghøj K. and Schwartz J. J. (2007) Trace element chemistry of zircons from oceanic crust: A method for distinguishing detrital zircon provenance. *Geology* **35** (7), 643-646.

- [127] Gromet L. P., Dymek R. F., Haskin L. A. and Korotev R. L. (1984) The “North American shale composite”: Its compilation, major and trace element characteristics. *Geochim. Cosmochim. Acta* **48**, 2469-2482.
- [128] Gu H. and Wang N. (2013) Leaching of uranium and thorium from red mud using sequential extraction methods. *Fresen. Environ. Bull.* **22** (9A), 2763-2769.
- [129] Hanchar J. M. and van Wenstrenen W. (2007) Rare earth element behavior in zircon-melt systems. *Elements* **3**, 37-42.
- [130] Haniilçi N. (2013) Geological and geochemical evolution of the Bolkardaği bauxite deposits, Karaman, Turkey: Transformation from shale to bauxite. *J. Geochem. Explor.* **133**, 118-137.
- [131] Harfouche M. and Farges F. (2009) XAFS study of actinides in natural minerals analogues of ceramics for nuclear waste. In: Proceedings of the 25th European Crystallographic Meeting, ECM-25, Istanbul, Turkey, *Acta Cryst.* **A65**, s118.
- [132] Harfouche M., Farges, F., Crocombette J. P. and Flank A. M. (2005) XAFS and molecular dynamics study of natural minerals, analogues of ceramics for nuclear waste storage. *Phys. Scripta* **T115**, 928-930.
- [133] Haridasan P. P., Pillai P. M. B., Tripathi R. M. and Puranik V. D. (2008) Thorium in ilmenite and its radiological implications in the production of titanium dioxide. *Radiat. Prot. Dosim.* **129** (4), 381-385.
- [134] Haskin L. A., Haskin M. A., Frey F. A. and Wildman T. R. (1968a) Relative and absolute terrestrial abundances of the rare earths. In: Origin and distribution of the elements, edited by Ahrens L. H., Pergamon, Oxford, vol. **1**, pp. 889-911.
- [135] Haskin L. A., Wildeman T. R. and Haskin M. A. (1968b) An accurate procedure for the determination of the rare earths by neutron activation. *J. Radioanal. Chem.* **1**, 337-348.
- [136] Haskin L. A., Helmke P. A., Paster T. P. and Allen R. O. (1971) Rare earths in meteoritic, terrestrial, and lunar matter. In: Activation analysis in geochemistry and

cosmochemistry, edited by Brunfelt A. and Steinnes E., Proc. NATO Conf. on Activation Analysis in Geochemistry, Universitetsforlaget, Oslo, pp. 201-218.

- [137] Haskin M. A. and Haskin L. A. (1996) Rare earths in European shales: a redetermination. *Science* **154**, 507-509.
- [138] Hatch J. R. and Leventhal J. S. (1992) Relationship between inferred redox potential of the depositional environment and geochemistry of the Upper Pennsylvanian (Missourian) Stark Shale Member of the Dennis Limestone, Wabaunsee County, Kansas, U.S.A.. *Chem. Geol.* **99**, 65-82.
- [139] Hatipoğlu M., Helvacı C., Chamberlain S. C. and Babalık H. (2010) Mineralogical characteristics of unusual "Anatolian" diasporite (zultanite) crystals from the İlbirdağı diasporite deposit, Turkey. *J. Afr. Earth Sci.* **57**, 525-541.
- [140] Hazemann J. L., Manceau A., Saintavit Ph. and Malgrange C. (1992) Structure of the $\alpha\text{Fe}_x\text{Al}_{1-x}\text{OOH}$ solid solution. *Phys. Chem. Miner.* **19**, 25-38.
- [141] Hazemann J. L., Bézar J. F. and Manceau A. (1991) Rietveld studies of the aluminium-iron substitution in synthetic goethite. *Mater. Sci. Forum* **79**, 821-826.
- [142] Hazen R. M., Parineau D., Bleeker W., Downs R. T., Ferry J. M., McCoy T. J., Sverjensky D. A. and Yang H. (2008) Mineral evolution. *Am. Mineral.* **93**, 1693-1720.
- [143] Hazen R. M., Sverjensky D. A., Azzolini D., Bish D. L., Elmore S. C., Hinnov L. and Milliken R. E. (2013) Clay mineral evolution. *Am. Mineral.* **98**, 2007-2029.
- [144] Heijboer W. M., Glatzel P., Sawant K. R., Lobo R. F., Bergmann U., Barrea R. A., Koningsberger D. C., Weckhuysen B. M. and De Groot F. M. F. (2004) K β -detected XANES of framework-substituted FeZSM-5 Zeolites. *J. Phys. Chem. B* **108**, 10002-10011.
- [145] Hein J. R., Koschinsky A., Bau M., Manheim F. T., Kang J. K. and Roberts L. (2000) Cobalt rich ferromanganese crusts in the Pacific. In: Handbook of marine mineral deposits, edited by Cronan D. S., C R C Press NY, *Mar. Sci. Ser.* 239-280.

- [146] Helmy H. M., Ballhaus C., Fonseca R. O. C., Wirth R., Nagel T. and Treboux M. (2013) Noble metal nanoclusters and nanoparticles precede mineral formation in magmatic sulphide melts. *Nat. Commun.* **4**:2405, p. 1-7.
- [147] Henderson G. S., De Groot F. M. F. and Moulton B. J. A. (2014) X-ray absorption near-edge structure (XANES) spectroscopy. In *Reviews in Mineralogy and Geochemistry*; Henderson, G. S., Neuville, D. R., Downs, R. T., Eds.; Mineralogical Society of America: Washington, DC, **78**, pp. 75-138.
- [148] Hill R. J. (1979) Crystal structure refinement and electron density distribution in diaspore. *Phys. Chem. Miner.* **5**, 179-200.
- [149] Hill V. G., Weir C., Collins R. L., Hoch D., Radcliffe D., Wynter C. (1978) Application of Mössbauer spectroscopy to iron-57 bauxite. *Hyperfine Interact.* **4**, 444-447.
- [150] Hochella M. F. Jr. (2002a) There's plenty of room at the bottom: nanoscience in geochemistry. *Geochim. Cosmochim. Acta* **66**, 735-743.
- [151] Hochella M. F. Jr. (2002b) Nanoscience and technology: the next revolution in the Earth sciences: *Earth Planet. Sci. Lett.* **203**, 593-605.
- [152] Hochella M. F. Jr. (2002c) Sustaining Earth: thoughts on the present and future roles of mineralogy in environmental science. *Mineral. Mag.* **66**, 627-652.
- [153] Hochella M. F. Jr. (2006) The Case of nanogeoscience. *Ann. N. Y. Acad. Sci.* **1093**, 108-122.
- [154] Hochella M. F. Jr. (2008) Nanogeoscience: from origin to cutting-edge applications. *Elements* **4**, 373-379.
- [155] Hochella M. F. Jr. (2012) Nanominerals, mineral nanoparticles, and Earth processes: details on how nanoparticles work in the environment. *Bull. Am. Phys. Soc.* **57**, BAPS.2012.MAR.P36.1 (abstr.).

- [156] Hochella M. F. Jr., Aruguete D., Kim B. and Madden A. S. (2011) Naturally occurring inorganic nanoparticles: general assessment and a global budget for one of Earth's last unexplored major geochemical components. *Mineral. Mag.* **75**, #1031 (abstr.).
- [157] Hochella M. F. Jr., Aruguete D., Kim B. and Madden A. S. (2012) Naturally occurring inorganic nanoparticles: general assessment and a global budget for one of Earth's last unexplored geochemical components. In: *Nature's nanostructures*, edited by Barnard A. S. and Guo H., Pan Stanford Publishing, Australia, pp. 1-42.
- [158] Hochella M. F. Jr., Caraballo M. A. and Michel F. M. (2013) Should the definition of the term "mineral" be changed?: The case being made by environmental mineralogy and nanogeochemistry. In: GSA's 125th Anniversary Annual Meeting & Exposition, Denver, Colorado, USA, 27-30 October, *Book of Abstracts* **45 (7)**, 82 (abstr.).
- [159] Hochella M. F. Jr., Lower S. K., Maurice P. A., Penn R. L., Sahai N., Sparks D. L. and Twining B. S. (2008a) Nanominerals, mineral nanoparticles, and Earth systems. *Geochim. Cosmochim. Acta* **72**, Suppl. A382 (abstr.).
- [160] Hochella M. F. Jr., Lower S. K., Maurice P. A., Penn R. L., Sahai N., Sparks D. L. and Twining B. S. (2008b) Nanominerals, mineral nanoparticles, and Earth systems. *Science* **319**, 1631-1635.
- [161] Horn M., Schwerdtfeger C. F. and Meagher E. P. (1972) Refinement of the structure of anatase at several temperatures. *Z. Kristallogr.* **136**, 273-281.
- [162] Hough R. M. and Noble R. R. P. (2010) Colloidal gold nanoparticles in ore systems. *Geochim. Cosmochim. Acta* **74**, Suppl. A420 (abstr.).
- [163] Hough R. M., Noble R. R. P., Hitchen G. J., Hart R., Reddy S. M., Saunders M., Clode P., Vaughan D., Lowe J., Gray D. J., Anand R. R., Butt C. R. M. and Verrall M. (2008) Naturally occurring gold nanoparticles and nanoplates. *Geology* **36**, 571-574.
- [164] Hough R. M., Noble R. R. P. and Reich M. (2011) Natural gold nanoparticles. *Ore Geol. Rev.* **42**, 55-61.

- [165] Hough R., Reich M. and Noble R. (2012) Noble metal nanoparticles in ore systems. In: *Nature's Nanostructures*, edited by Barnard A. S. and Guo H., Pan Stanford Publishing, Australia, pp. 141-168.
- [166] Howard C. J., Sabine T. M. and Dickson F. (1991) Structural and thermal parameters for rutile and anatase. *Acta. Cryst.* **B47**, 462-468.
- [167] Hudson J. D. (1977) Stable isotopes and limestone lithification. *J. Geol. Soc. London* **133**, 637-660.
- [168] Hummer D. R. and Heaney P. J. (2007) Thermal expansion of anatase and rutile between 300 and 575 K using synchrotron powder X-ray diffraction. *Powder Diffraction*. **22**, 352-357.
- [169] Hurai V., Göttlicher J., Majzlan J., Huraiová M. (2008) Contrasting ferric iron contents in conjugate Fe oxide and silicate melts from Southern Slovakia determined using micro-XANES spectroscopy. *Can. Mineral.* **46**, 1173-1181.
- [170] Iatrou M., Papatheodorou G., Geraga M. and Ferentinos G. (2010) The study of heavy metal concentrations in the red mud deposits at the Gulf of Corinth, using multivariate techniques. Proceedings of 12th International Conference of Geological Society of Greece, Athens, Greece, 19-22 May 2010, Bull. Geol. Soc. Greece **XLIII** (2), 1018-1028.
- [171] Jackson S. E. (2001) The application of Nd: YAG lasers in LA-ICP-MS. Principles and Applications of Laser Ablation-Mass Spectrometry in the Earth. Mineralogical Association of Canada Short Course Series **29**, 29-46.
- [172] Jamieson J. C. and Olinger B. (1969) Pressure-Temperature studies anatase, brookite, rutile, and TiO₂(II): A discussion. *Am. Mineral.* **54**, 1477-1481.
- [173] Jobbágy V., Somlai J., Kovács J., Szeiler G. and Kovács T. (2009) Dependence of radon emanation of red mud bauxite processing wastes on heat treatment. *J. Hazard. Mater.* **172**, 1258-1263.

- [174] Johnston C.T., Sposito G., Bocian D.F. and Birge R.R. (1984) Vibrational spectroscopic study of the interlamellar kaolinite-dimethyl sulfoxide complex. *J. Phys. Chem.* **88**, 5959-5964.
- [175] Jones B. and Manning D. A. C. (1994) Comparison of geochemical indices used for the interpretation of palaeoredox conditions in ancient mudstones. *Chem. Geol.* **111**, 111-129.
- [176] Kakol Z., Sabol J., STICKLER J. and Honig J. (1992), Effect of low-level titanium(IV) doping on the resistivity of magnetite near the Verwey transition. *Phys. Rev. B* **46** (4), 1975-1978.
- [177] Kalaitidis S., Siavalas G., Skarpelis N., Araujo C. V. and Christanis K. (2010) Late Cretaceous coal overlying karstic bauxite deposits in the Parnassus-Ghiona unit, Central Greece: Coal characteristics and depositional environment. *Int. J. Coal Geol.* **81**, 211-226.
- [178] Kappen P., Dubrawski J. V. and Pigram P. J. (2007) XANES and micro-XRF investigations of ilmenite and derived products. In: HASYLAB Annual Report 2007, 919-920.
- [179] Karadağ M. M., Küpeli Ş., Arf. and Ayhan (2009) Rare earth element (REE) geochemistry and genetic implications of the Mortaş bauxite deposit (Seydişehir/Konya – southern Turkey). *Chemie Erde* **69**, 143-159.
- [180] Karagiannidi Th., Papaefthymiou H. and Papatheodorou G. (2009) Radioactive impact of a bauxite beneficiation plant in the Itea Gulf (Gulf of Corinth, Greece). *J. Radioanal. Nucl. Ch.* **279** (3), 923-934.
- [181] Karakitsios V., Tsikos H., Van Breugel Y., Bakopoulos I. and Koletti L. (2004) Cretaceous oceanic anoxic events in Western continental Greece. *Bull. Geol. Soc. Greece* **36**, 846-855.
- [182] Karipi S., Tsikouras B., Hatzipanagiotou K. and Grammatikopoulos T. A. (2006) Petrogenetic significance of spinel-group minerals from the ultramafic rocks of the Iti and Kallidromon ophiolites (Central Greece). *Lithos* **99**, 136-149.

- [183] Kim M. G., Cho H. S. and Yo C. H. (1998) Fe K-edge X-ray absorption (XANES/EXAFS) spectroscopic study of the nonstoichiometric $\text{SrFe}_{1-x}\text{Sn}_x\text{O}_{3-y}$ system. *J. Phys. Chem. Solids* **59**, 1369-1381.
- [184] Kirwan L. J., Deeney F. A., Croke G. M. and Hodnett K. (2009) Characterisation of various Jamaican bauxite ores by quantitative Rietveld X-ray powder diffraction and ^{57}Fe Mössbauer spectroscopy. *Int. J. Miner. Process.* **91**, 14-18.
- [185] Kiskyras D. (1960) Die mineralogische Zusammensetzung der griechischen Bauxite in Abhängigkeit von der Tektonik. *J. Mineral. Geochem. (former: Neues Jahrb. Mineral. Abhandl.)* **94**, 662-680. (In German)
- [186] Klemme S., Prowatke, S., Hametner K. and Günther D. (2005) Partitioning of trace elements between rutile and silicate melts: Implications for subduction zones. *Geochem. Cosmochem. Acta* **69** (9), 2361-2371.
- [187] Kloprogge J. T., Ruan H. D. and Frost R. L. (2002) Thermal decomposition of bauxite minerals: infrared emission spectroscopy of gibbsite, boehmite and diaspor. *J. Mater. Sci.* **37**, 1121-1129.
- [188] Klug A. and Farkas L. (1981) Structural investigations of polycrystalline diaspor samples by X-ray powder diffraction. *Phys. Chem. Miner.* **7**, 138-140.
- [189] Knauth L. P. and Kennedy M. J. (2009) The Late Precambrian greening of the Earth. *Nature* **460**, 728-732.
- [190] Kolesova V. A. and Ryskin Ya. I. (1962) Infrared absorption spectra of diaspor ($\alpha\text{-AlOOH}$), boehmite ($\gamma\text{-AlOOH}$) and GaOOH . *J. Struct. Chem.* **3** (6), 656-659.
- [191] Koneev R. I., Khalmatov R. A. and Mun Yu. S. (2010) Nanomineralogy and nanogeochemistry of ores from gold deposits of Uzbekistan. *Geol. Ore Depos.* **52**, 755-766.
- [192] Korotev R. L. (1996a) A self-consistent compilation of elemental concentration data for 93 geochemical reference samples. *Geostandard. Newslett.* **20**, 217-245.

- [193] Korotev R. L. (1996b) On the relationship between the Apollo 16 ancient regolith breccias and feldspathic fragmental breccias, and the composition of the prebasin crust in the Central Highlands of the Moon. *Meteor. Planet. Sci.* **31**, 403-412.
- [194] Korotev R. L. (2010) "Rare Earth Plots" and the concentrations of rare earth elements (REE) in chondritic meteorites. Available online at: <http://meteorites.wustl.edu/goodstuff/ree-chon.htm>, accessed on: February, 2010.
- [195] Koutsovitis P., Magganas A. and Ntaflou T. (2012) Rift and intra-oceanic subduction signatures in the Western Tethys during the Triassic: The case of ultramafic lavas as part of an unusual ultramafic-mafic-felsic suite in Othris, Greece. *Lithos* **144-145**, 177-193.
- [196] Krauskopf K. B. and Bird D. K. (1994) Introduction to geochemistry. McGraw-Hill International Editions, New York, USA, 667 pp. ISBN: 0-07-035820-6.
- [197] Kritsotakis K., Schulz-Dobrick B. and Panagos A.G. (1986) REE-Minerale in Griechischen Bauxiten. *Fortschritte der Mineralogie, Beiheft* **64** (1), 87. (In German)
- [198] Kuzmann E., Nagy S. and Vértés A. (2003) Critical review of analytical applications of Mössbauer spectroscopy illustrated by mineralogical and geological examples (IUPAC Technical Report). *Pure Appl. Chem.* **75**, 801-858.
- [199] Kuzmin A. (1995) EDA: EXAFS data analysis software package. *Physica B* **208&209**, 175-176.
- [200] Kuzmin A. and Purans J. (2000) Dehydration of the molybdenum trioxide hydrates $\text{MoO}_3 \cdot n\text{H}_2\text{O}$: in situ x-ray absorption spectroscopy study at the Mo K edge. *J. Phys.: Condens. Matter.* **12**, 1959-1970.
- [201] Larson A. C. and Von Dreele R. B. (2004) *General Structure Analysis System (GSAS)*. Los Alamos National Laboratory Report LAUR 86-748.

- [202] Lasaga A. C., Soler J. M., Ganor J., Burch T. E., Nagy K. L. (1994) Chemical weathering rate laws and global geochemical cycles. *Geochim. Cosmochim. Acta* **58** (10) 2361-2386.
- [203] Laskou M. (1981) Study of bauxite outcrops from the region of Eastern Greece. A contribution to the mineralogy, geochemistry, petrology and to origin of the bauxites. Unpublished PhD Thesis, University of Athens, Athens, Greece, 213 pp. (In Greek)
- [204] Laskou M. (1991) Concentrations of rare earths in Greek bauxites. *Acta Geol. Hung.* **34**, 395-404.
- [205] Laskou M. (2001) Chromite in karst bauxites, bauxitic laterites and bauxitic clays of Greece. In: Mineral deposits at the beginning of the 21st century, edited by Piestrzyński A. et al., Proceedings of the 6th Biennial SGA-SEG Meeting 2001, Krakow, Poland, 26-29 August 2001, Swets & Zeitlingen Publishers, Lisse, The Netherlands, pp. 1091-1094, ISBN: 90-2651-846-3.
- [206] Laskou M. (2005) Pyrite-rich bauxites from the Parnassos-Ghiona zone, Greece. In: Mineral Deposits Research: Meeting the Global Challenge, edited by Mao J. and Bierlein F. P., Proceedings of the 8th Biennial SGA Meeting 2005, Beijing, China, 18-21 August 2005, Springer-Verlag, Berlin-Heidelberg, Germany, pp. 1007-1010.
- [207] Laskou M. and Andreou G. (2003) Rare earth element distribution and REE-minerals from the Parnassos-Ghiona bauxite deposits, Greece. In: Mineral exploration and sustainable development, edited by Eliopoulos D. et al., Proceedings of the 7th Biennial SGA-SEG Meeting 2003, Athens, Greece, 24-28 August 2003, Millpress, Rotterdam, The Netherlands, pp. 89-92, ISBN: 90-77017-77-1.
- [208] Laskou M. and Economou M. (1991) Platinum group elements and gold concentrations in Greek bauxites. *Geol. Balcan.* **21**, 65-77.
- [209] Laskou M. and Economou-Eliopoulos M. (2005) Micro-organisms as fossils and present day development in Ni-laterites and bauxites of the Balkan Peninsula. In: Mineral Deposits Research: Meeting the Global Challenge, edited by Mao J. and Bierlein F. P.,

Proceedings of the 8th Biennial SGA Meeting 2005, Beijing, China, 18-21 August 2005, Springer-Verlag, Berlin-Heidelberg, Germany, pp. 1003-1006.

- [210] Laskou M. and Economou-Eliopoulos M. (2007) The role of microorganisms on the mineralogical and geochemical characteristics of the Parnassos-Ghiona bauxite deposits, Greece. *J. Geochem. Explor.* **93**, 67-77.
- [211] Laskou M. and Economou-Eliopoulos M. (2013) Bio-mineralization and potential biogeochemical processes in bauxite deposits: genetic and ore quality significance. *Miner. Petrol.* **107**, 471-486.
- [212] Laskou M., Economou-Eliopoulos M. and Mitsis I. (2010) Biomineralization of halotrichite on bauxite ores. *Geochim. Cosmochim. Acta* **74**, Suppl. A564 (abstr.).
- [213] Laskou M., Economou-Eliopoulos M. and Mitsis I. (2011) Bauxite ore as an energy source for bacteria driving iron-leaching and bio- mineralization. *Hell. J. Geosci.* **45**, 163-173.
- [214] Laskou M., Margomenou-Leonidopoulou G. and Balek, V. (2006) Thermal characterization of bauxite samples. *J. Therm. Anal. Calorim.* **84** (1), 141-145.
- [215] Laul J. C. (1979) Neutron activation analysis of geologic materials. In: *Atomic Energy Review* **17**, 603-695.
- [216] Lee Bray E. (2012) Bauxite and alumina [advanced released]. In: *2011 Minerals Yearbook*, edited by Lee Bray E., U.S. Department of the Interior, U.S. Geological Survey, pp. 10.1-10.13.
- [217] Leybourne M. I. and Johannesson K. H. (2008) Rare earth elements (REE) and yttrium in stream waters, stream sediments, and Fe-Mn oxyhydroxides: Fractionation, speciation, and control over REE + Y patterns in the surface environment. *Geochim. Cosmochim. Acta* **71**, 5962-5983.
- [218] Li Y. -H. (1991) Distribution patterns of the elements in the ocean: a synthesis. *Geochim. Cosmochim. Acta* **55**, 3223-3240.

- [219] Li Z., Din J., Liao C., Yin F. ǔ T., Cheng L. and Li J. (2013) Discovery of the REE minerals in the Wulong–Nanchuan bauxite deposits, Chongqing, China: Insights on conditions of formation and processes. *J. Geochem. Explor.* **133**, 88-102.
- [220] Liang W., Couperthwaite S. J., Kaur J., Yan C., Johnstone D. W. and Millar G. J. (2014) Effect of strong acids on red mud structural and fluoride adsorption properties. *J. Colloid Interf. Sci.* **423**, 158-165.
- [221] Liati A., Gebauer D. and Fanning C. M. (2004) The age of ophiolitic rocks of the Hellenides (Vourinos, Pindos, Crete): first U-Pb ion microprobe (SHRIMP) zircon ages. *Chem. Geol.* **207**, 171-188.
- [222] Ling M. -X., Liu Y. -L., Williams I. S., Teng F. -Z., Yang X. -Y., Ding X., Wei G. -J., Xie L. -H., Deng W. -F. & Sun W. -D. (2013) Formation of the world's largest REE deposit through protracted fluxing of carbonatite by subduction-derived fluids. *Sci. Rep.* **3**: 1776, 1-8.
- [223] Linnert C., Robinson S. A., Lees J. A., Bown P. R., Pérez-Rodríguez I., Petrizzo M. R., Falzoni F., Littler K., Arz J. A. and Russell E. E. (2014) Evidence of global cooling in the Late Cretaceous. *Nat. Comm.* **5**:4194, 1-7.
- [224] Liu G., Bangs C. E. and Müller D. B. (2011) Unearthing potentials for decarbonizing the U.S. aluminum cycle. *Environ. Sci. Technol.*, **45**, 9515-9522.
- [225] Liu G. and Müller D. B. (2013a) Centennial Evolution of Aluminum In-Use Stocks on Our Aluminized Planet. *Environ. Sci. Technol.*, **47**, 4882-4888.
- [226] Liu G. and Müller D. B. (2013b) Mapping the global journey of anthropogenic aluminum: A trade-linked multilevel material flow analysis. *Environ. Sci. Technol.*, **47**, 11873-11881.
- [227] Liu X., Wang Q., Deng J., Zhang Q., Sun S. and Meng J. (2010) Mineralogical and geochemical investigations of the Dajia Salento-type bauxite deposits, western Guangxi, China. *J. Geochem. Explor.* **105**, 137-152.

- [228] Liu X., Wang Q., Feng Y., Li Z. and Cai S. (2013) Genesis of the Guangou karstic bauxite deposit in western Henan, China. *Ore Geol. Rev.* **55**, 162-185.
- [229] Liu Y. -G., Miah M. R. U. and Schmitt R. A. (1988) Cerium: A chemical tracer for paleo-oceanic redox conditions. *Geochim. Cosmochim. Acta* **52**, 1361-1371.
- [230] Lodders K. (2010) Solar system abundances of the elements. In: *Principles and Perspectives in Cosmochemistry*, edited by Goswami A. and Reddy B. E., Astrophysics and Space Science Proceedings – Lecture notes of the Kodai School on “Synthesis of Elements in Stars”, Kodaikanal Observatory, India, April 29 – May 13, 2008, Springer-Verlag, Berlin-Heidelberg, Germany, pp. 379-417, ISBN: 978-3-642-10351-3.
- [231] Lüttge A., Bolton E. W. and Lasaga A. C. (1999) An interferometric study of the dissolution kinetics of anorthite: The role of reactive surface area. *Am. J. Sci.* **299**, 652-678.
- [232] Lympelopoulou Th. (1996) Determination and extraction of rare earth elements from bauxites and red mud. Unpublished PhD Thesis, National Technical University of Athens, Athens, Greece, 183 pp. (In Greek)
- [233] Ma C. and Rossman G. R. (2013) Nanomineralogy of gemstones: From genesis to discovery. *Mineral. Mag.* **77(5)**, 1661 (abstr.).
- [234] Mack E. and Petrascheck W.E. (1978) Palaeogeographie, Verteilung und Qualität der Bauxite im Parnass-Kjona Gebirge. 4th Intern. Congr. ICSOBA, **2**, 526-539.
- [235] MacLean W. H., Bonavia F. F. and Sanna G. (1997) Argillite debris converted to bauxite during karst weathering: evidence from immobile element geochemistry at the Olmedo Deposit, Sardinia. *Mineral. Depos.* **32**, 607-616.
- [236] Maksimović Z. and Bish D. L. (1978) Brindleyite, a nickel-rich aluminous serpentine mineral analogous to berthierine. *Am. Mineral.* **63**, 484-489.

- [237] Maksimović Z., Mindszenty A. and Pantó G. (1991) Contribution to the geochemistry of Hungarian karst bauxites and the allochthony/autochthony problem. *Acta Geol. Hungarica* **34** (4), 317-334.
- [238] Maksimović Z. and Pantó G. (1991) Contribution to the geochemistry in the karst-bauxite deposits of Yugoslavia and Greece. *Geoderma* **51**, 93-109.
- [239] Maksimović Z. and Pantó G. (1996) Authigenic rare earth minerals in karst-bauxites and karstic nickel deposits. In: Rare Earth Minerals: Chemistry, origin and ore deposits, edited by Jones A. P., Wall F. and Williams C. T., Chapman & Hill, London, UK, pp. 257-279.
- [240] Maksimović Z. and Papastamatiou J. (1973) Distribution d'oligoéléments dans les gisements de bauxite de la Grèce centrale. Symp. ICSOBA, Nice, 33-46.
- [241] Mameli P., Mongelli G., Oggiano G. and Dinelli E. (2007) Geological, geochemical and mineralogical features of some bauxite deposits from Nurra (Western Sardinia, Italy): insights on conditions of formation and parental affinity. *Int. J. Earth Sci. (Geol. Rundsch)* **96**, 887-902.
- [242] Manceau A. and Combes J. M. (1988) Structure of Mn and Fe oxides and oxyhydroxides: a topological approach by EXAFS. *Phys. Chem. Miner.* **15**, 283-295.
- [243] Manceau A. and Drits V. A. (1993) Local structure of ferrihydrite and ferrihydrite by EXAFS spectroscopy. *Clay Min.* **28**, 165-184.
- [244] Manceau A. and Gates W. P. (1997) Surface structural model for ferrihydrite. *Clays Clay Min.* **45**, 448-460.
- [245] Manceau A., Gorshkov A. I. and Drits V. A. (1992) Structural chemistry of Mn, Fe, Co, and Ni in manganese hydrous oxides: Part I. Information from XANES spectroscopy. *Amer. Mineral.* **77**, 1133-1143.
- [246] Mariano A. N. and Mariano A. Jr. (2012) Rare earth mining and exploration in North America. *Elements* **8**, 369-376.

- [247] Mason B. and Moore C. B. (1982) Principles of geochemistry. John Willey & Sons, New York, USA, 344 pp. ISBN: 0-471-57522-4.
- [248] Masuda A., Nakamura N. and Tanaka T. (1973) Fine structure of mutually normalized rare-earth patterns of chondrites. *Geochim. Cosmochim. Acta* **37**, 239-248.
- [249] Mayanovic R. A., Anderson A. J., Meredith P. R. and Bassett W. A. (2010) In situ XAS study on Zn²⁺ and Ni²⁺ adsorption on Fe₃O₄ nanoparticles in supercritical aqueous fluids. *Geochim. Cosmochim. Acta* **74**, Suppl. A681 (abstr.).
- [250] Mayes W. M., Jarvis A. P., Burke I. T., Walton M., Feigl V., Klebercz O. and Gruiz K. (2011) Dispersal and attenuation of trace contaminants downstream of the Ajka bauxite residue (red mud) depository failure, Hungary. *Environ. Sci. Technol.* **45**, 5147-5155.
- [251] Mazumdar A., Banerjee D. M., Schidlowski M. and Balaram V. (1999) Rare-earth elements and Stable Isotope Geochemistry of early Cambrian chert-phosphorite assemblages from the Lower Tal Formation of the Krol Belt (Lesser Himalaya, India). *Chem. Geol.* **156**, 275-297.
- [252] McDonough W.F. and Sun, S. -S. (1995) Composition of the Earth. *Chem. Geol.* **120**, 223-253.
- [253] McClennan S. M. (1989) Rare earth elements in sedimentary rocks: influence of provenance and sedimentary processes. In: Geochemistry and mineralogy of rare earth elements, edited by Lipin B. R. and McKay G. A., *Reviews in Mineralogy*, **21**, pp.169-200.
- [254] Merino E., Nahon D. and Wang Y. (1993) Kinetics and mass transfer of pseudomorphic replacement: Application to replacement of parent minerals and kaolinite by Al, Fe, and Mn oxides during weathering. *Am. J. Sci.* **293**, 135-155.
- [255] Mettos A., Rondoyanni T. and Ioakim C. (2009) Reconsideration of the structural relationship between the Parnassus-Ghiona and Vardoussia geotectonic zones in central Greece. *Int. J. Earth Sci. (Geol Rundsch)* **98**, 1927-1934.

- [256] Michailidis K. (1990) Zoned chromites with high Mn-contents in the Fe-Ni-Cr-laterite ore deposits from the Edessa area in Northern Greece. *Mineral. Deposita* **25**, 190-197.
- [257] Michailidis K., Kassoli-Fournaraki A. and Sklavounos S. (1984) Chromites and magnetite in the laterite ore occurrences of Karydia, Edessa region (Northern Greece). *Sci. Annals Eac. Sci. Univ. Thessaloniki* **24**, 111-132
- [258] Mierdel K., Keppler H., Smyth J. R. and Langenhorst F. (2007) Water solubility in aluminous orthopyroxene and the origin of Earth's asthenosphere. *Science* **315**, 364-368.
- [259] Miranda C. R. and Matsuoka T. (2008) Nanogeoscience: there's plenty of room at the ground. *Geochim. Cosmochim. Acta* **72**, Suppl. A634 (abstr.).
- [260] Mondillo N., Balassone G., Boni M. and Rollinson G. (2011) Karst bauxites in the Campania Apennines (southern Italy): a new approach. *Period. Mineral.* **80** (3), 407-432.
- [261] Mongelli G. (1997) Ce-anomalies in the textural components of Upper Cretaceous karst bauxites from the Apulian carbonate platform (southern Italy). *Chem. Geol.* **140**, 69-76.
- [262] Mongelli G., Boni M., Buccione R. and Sinisi R. (2014) Geochemistry of the Apulian karst bauxites (southern Italy): Chemical fractionation and parental affinities. *Ore Geol. Rev.* **63**, 9-21.
- [263] Monjoie P., Lapierre H., Tashko A., Mascle G. H., Dechamp A., Muceku B. and Brunet P. (2008) Nature and origin of the Triassic volcanism in Albania and Othrys: a key to understanding the Neotethys opening?. *Bull. Soc. Géol. Fr.* **179** (4), 411-425.
- [264] Moore D. M. and Reynolds R. C. Jr. (1997) X-Ray diffraction and the identification and analysis of clay minerals. Oxford University press, New York, USA, 373 pp. ISBN: 0-19-508713-5.
- [265] Morin F. J. (1950) Magnetic Susceptibility of α -Fe₂O₃ and α -Fe₂O₃ with added titanium. *Phys. Rev.* **78** (6), 819-820.

- [266] Muftah A. M., Pavlakis P., Godelitsas A., Gamaletsos P. and Boaz N. (2013) Paleogeography of the Eosahabi River in Libya: New insights into the mineralogy, geochemistry and paleontology of Member U1 of the Sahabi Formation, northeastern Libya. *J. Afr. Earth Sci.* **78**, 86-96.
- [267] Muñoz M., Argoul P. and Farges F. (2003) Continuous Cauchy wavelet transform analyses of EXAFS spectra: A qualitative approach. *Am. Mineral.* **88**, 694-700.
- [268] Murad E. (2005) Characterization of a standard bauxite and its deferration products by Mössbauer spectroscopy. *Miner. Eng.* **18**, 984-986.
- [269] Murakami T., Kogure T., Kadohara H. and Ohnuki T. (1998) Formation of secondary minerals and its effect on anorthite dissolution. *Am. Mineral.* **83**, 1209-1219.
- [270] Murphy K. and Dymond J. (1984) Rare earth elements fluxes and geochemical budget in the eastern equatorial Pacific. *Nature* **307**, 444-447.
- [271] Musić S., Dragčević Z., Lahodhy-Sarc O., Nagy-Czakó I. and Vértés A. (1980) Mössbauer effect study of some Yugoslav bauxites. *J. Phys. Colloques* **41** (C1), 305-306.
- [272] Muxworthy A. R. (1999) Low-temperature susceptibility and hysteresis of magnetite. *Earth Planet. Sci. Lett.* **169** (1-2), 51-58.
- [273] Nadin E. (2007) The secret lives of minerals. *Engineer. Sci.* **70**, 10-20. ISSN 0013-7812.
- [274] Nakamura N. (1974) Determination of REE, Ba, Fe, Mg, Na, and K in carbonaceous and ordinary chondrites. *Geochim. Cosmochim. Acta* **38**, 757-775.
- [275] Nia R. (1968a) Geologische und petrographische Untersuchungen zum Problem der Boehmit-Diaspor-Genese in griechischen Oberkreide-Bauxiten der Parnass-Kiona-Zone. Unpublished PhD Thesis, University of Hamburg, Hamburg, Germany, 133 pp. (In German)

- [276] Nia R. (1968b) Zur Bedeutung der methodischen Probennahme für genetische Untersuchungen von Bauxit-Lagerstätten am Beispiel der Oberkreide-Bauxite der Parnass-Kiona-Zone Griechenlands. *Miner. Deposita* **3**, 368-374. (In German)
- [277] Nia R. (1971) Genesis of boehmite and diasporite in Greek Upper Cretaceous bauxites of the Parnasse-Gjona zone. Proceedings of the 2nd Int. Symp. ICSOBA, Budapest, 69-98.
- [278] Nicolas, J. and Bildgen, P. (1979) Relations between the location of the karst bauxites in the northern hemisphere, the global tectonics and the climatic variations during geological time. *Palaeogeogr. Palaeoclimatol. Palaeoecol.* **28**, 205-239.
- [279] Nishi M., Irifune T., Tsuchiya J., Tange Y., Nishihara Y., Fujino K. and Hiro Y. (2014) Stability of hydrous silicate at high pressures and water transport to the deep lower mantle. *Nat. Geosci.* **7**, 224-227.
- [280] Norton S. A. (1973) Laterite and bauxite formation. *Econ. Geol.* **68**, 353-361.
- [281] Oakes M., Weber R. J., Lai B., Russell A. and Ingall E. D. (2012) Characterization of iron speciation in single particles using XANES spectroscopy and micro X-ray fluorescence measurements: insight into factors controlling iron solubility. *Atmos. Chem. Phys.* **12**, 745-756.
- [282] Ochsenkühn K.M., Fafouteli P. and Ochsenkühn-Petropoulou M. (2002) Determination and distribution of gold in Greek bauxites of the Parnassos-Ghiona area by gamma-spectroscopy after ion exchange separation. *J. Radioanal. Nucl. Chem.* **253**, 257-262.
- [283] Ochsenkühn K.M., and Ochsenkühn-Petropoulou M. (1982) Studie der Verteilung und Korrelation von Spurenelementen in den Parnassos Bauxiten. Griechisches Ministerium Für Forschung und Technologie, Athens, Greece. (in German)
- [284] Ochsenkühn K.M., Ochsenkühn-Petropoulou M. and Parissakis G. (1995) Activation analysis of bauxitic materials by epithermal irradiation. *J. Radioanal. Nucl. Chem.* **190**, 71-79.

- [285] Ochsenkühn K. M. and Parissakis G. (1977) Quantitative Untersuchungen von Bauxiten Zentralgriechenlands mittels Atomabsorptions-spectroscopie und Flemmenatomemission. *Microchim. Acta* **1**, 447-457. (In German)
- [286] Ochsenkühn-Petropoulou M. Th., Hatzilyberis K. S., Mendrinos L. N. and Salmas C. E. (2002) Pilot-plant investigation of the leaching process for the recovery of scandium from red mud. *Ind. Eng. Chem. Res.* **41**, 5794-5801.
- [287] Ochsenkühn-Petropoulou M. and Ochsenkühn K. M. (1995) Rare earth minerals found in Greek Bauxites by SEM and EPMA. *Eur. Microsc. Anal.* **49**, 13-14.
- [288] Ochsenkühn-Petropoulou M., Ochsenkühn K.M. and Luck J. (1991) Comparison of inductively coupled plasma mass spectrometry with inductively coupled plasma atomic emission spectrometry and instrumental neutron activation analysis for the determination of rare earth elements in Greek bauxites. *Spectrochim. Acta* **46**, 51-65.
- [289] Ochsenkühn-Petropulu M., Lyberopulu Th., Ochsenkühn K. M. and Parissakis G. (1996) Recovery of lanthanides and yttrium from red mud by selective leaching. *An. Chim. Acta* **319** (1-2), 249-254.
- [290] Ochsenkühn-Petropulu M., Lyberopulu Th. and Parissakis G. (1994) Direct determination of lanthanides, yttrium and scandium in bauxites and red mud from alumina production. *An. Chim. Acta* **296** (3), 305-313.
- [291] Ochsenkühn-Petropulu M., Lyberopulu Th. and Parissakis G. (1995) Selective separation and determination of scandium from yttrium and lanthanides in red mud by a combined ion exchange/solvent extraction method. *An. Chim. Acta* **315** (1-2), 231-237.
- [292] O'Connor B. H. (2005) In Alcoa Submission to Radiation Health and Safety Advisory Council NORM Discussion Papers, 2004: cited in Cooper, M. B. report prepared for the Radiation Health and Safety Advisory Council; 2005.

- [293] Oelkers E. H. and Schott (1995) Experimental study of anorthite dissolution and the relative mechanism of feldspar hydrolysis. *Geochim. Cosmochim. Acta.* **59** (24), 5039-5053.
- [294] Ohta A., Ishii S., Sakakibara M., Mizuno A. and Kawabe I. (1999) Systematic correlation of the Ce anomaly with the Co/(Ni+Cu) ratio and Y fractionation from Ho in distinct types of Pacific deep-sea nodules. *Geochem. J.* **33**, 399-417.
- [295] O'Reilly S. E. and Hochella M. F. Jr. (2003) Lead sorption efficiencies of natural and synthetic Mn and Fe-oxides. *Geochim. Cosmochim. Acta* **67** (23), 4471-4487.
- [296] Ostergren J. D., Bargar J. R., Brown G. E. Jr. and Parks G. A. (1999) Combined EXAFS and FTIR investigation of sulfate and carbonate effects on Pb(II) sorption to goethite (α -FeOOH). *J. Synchrotron Rad.* **6**, 645-647
- [297] Özdemir Ö. (1987) Inversion of titanomaghemites. *Phys. Earth Planet. Interiors.* **46** (1-3), 184-196.
- [298] Özdemir Ö. and Banerjee S. K. (1984) High-temperature stability of maghemite (γ -Fe₂O₃), *Geophys. Res. Lett.* **11** (3), 161-164.
- [299] Özlü N. (1983) Trace-element content of "karst bauxites" and their parent rocks in the Mediterranean belt. *Miner. Deposita.* **18**, 469-476.
- [300] Öztürk H., Hein J. R. and Hanilçi N. (2002) Genesis of the Doğankuzu and Mortaş bauxite deposits, Taurides, Turkey: Separation of Al, Fe, and Mn and implications for passive margin metallogeny. *Econ. Geol.* **97**, 1063-1077.
- [301] Pačevski A., Moritz R., Kouzmanov K., Marquardt K., Živković P. and Cvetković L. (2012) Texture and composition of Pb-bearing pyrite from the Čoka Marin polymetallic deposit, Serbia, controlled by nanoscale inclusions. *Can. Mineral.* **50**, 1-20.
- [302] Palenik C. S., Utsunomiya S., Reich M., Kesler S. E., Wang L. and Ewing R. C. (2004) "Invisible" gold revealed: direct imaging of gold nanoparticles in a Carlin-type deposit. *Am. Mineral.* **89**, 1359-1366.

- [303] Palme. H. (1988) Chemical abundances in meteorites. Reviews in Modern Astronomy, edited by Klare G., Springer-Verlag Berlin-Heidelberg, Germany, pp. 28-51.
- [304] Pamić J., Belak M., Bullen T. D., Lanphere M. A. and McKee E. H. (2000) Geochemistry and geodynamics of a Late Cretaceous bimodal volcanic association from the southern part of the Pannonian Basin in Slavonija (Northern Croatia). *Mineral. Petrol.* **68**, 271-296.
- [305] Papanikolaou D. (2009) Timing of tectonic emplacement of the ophiolites and terrane paleogeography in the Hellenides. *Lithos* **108**, 262-280.
- [306] Papanikolaou D. (2013) Tectonostratigraphic models of the Alpine terranes and subduction history of the Hellenides. *Tectonophysics* **595-596**, 1-24.
- [307] Papassiopi N., Vaxevanidou K. and Paspaliaris I. (2010) Effectiveness of iron reducing bacteria for the removal of iron from bauxite ores. *Miner. Eng.* **23**, 25-31.
- [308] Papastamatiou J. (1960) La géologie de la région montagneuse du Parnass-Kiona-Oeta. *Bull. Géol. Soc. Fr.* **7**, 398-409.
- [309] Papastamatiou J. (1964) Les gisements de bauxite en Grèce. Proceeding of the 1st Symp. ICSOBA, Zagreb, Yougoslavia, 285-293.
- [310] Papastamatiou J. and Maksimovic Z. (1970) Contribution to the study of genesis of Greek bauxites: chemical and mineralogical composition of Mandra II bauxite deposits. *Ann. Inst. Geol. Pub. Hung.* **3**, 391-402.
- [311] Papastavrou S. (1974) Einige Bemerkungen zur Relation zwischen Verkarstungsbahnen und Längserstreckung der Bauxitlager bei Sideroport-Bela. *Ann. Fac. Phys. – Math., Univ.*, 1-99.
- [312] Papastavrou S. (1986) Greek bauxites (description – classification – distribution – problems). Mineral Deposits Research, IGME, Internal Report. Athens, pp. 30 (In Greek)

- [313] Papastavrou S. and Perdikatsis V. (1987) U-Th and REE concentrations in bauxites and new aspects about the origin of bauxites in the Iti-mountains (C.Greece). In: Mineral Deposits of the Tethyan Eurasian Metallogenic Belt between the Alps and the Pamirs, edited by Janković S., UNESCO/IGCP Project No 169: Geotectonic Evolution and Metallogeny of Mediterranean and SW Asia, Department of Mineral Exploration, Faculty of Mining and Geology, Belgrade University, pp. 111-118.
- [314] Papatheodorou G., Papaefthymiou H., Maratou A. and Ferentinos G. (2005) Natural radionuclides in bauxitic tailings (red-mud) in the Gulf of Corinth, Greece. *Radioprotection* **40**, 549-555.
- [315] Paspaliaris J. (1985) A contribution to the optimization of diasporic bauxite leaching process. Unpublished PhD Thesis, National Technical University of Athens, Athens, Greece, 185 pp. (In Greek)
- [316] Paulik F. and Paulik J. (1978) Simultaneous techniques in thermal analysis. A review. *Analyst* **103** (1226), 417-437.
- [317] Perdikatsis V. (1992) Quantitative mineralogical analysis of bauxites by X-ray diffraction with the Rietveld method. *Acta Geol. Hung.* **35**, 447-457.
- [318] Petrascheck W. E. (1989) The genesis of allochthonous karst-type bauxite deposits of southern Europe. *Miner. Deposita* **24**, 77-81.
- [319] Pe-Piper G. (1982) Geochemistry, tectonic setting and metamorphism of mid-Triassic volcanic rocks of Greece. *Tectonophysics* **85**, 253-272.
- [320] Pe-Piper G. (1998) The nature of Triassic extension-related magmatism in Greece: evidence from Nd and Pb isotope geochemistry. *Geol. Mag.* **135** (3), 331-348.
- [321] Piegras D. J. and Jacobsen S. B. (1992) The behavior of rare earth elements in seawater: Precise determination of variations in the North Pacific water column. *Geochim. Cosmochim. Acta* **56**, 1851-1862.

- [322] Pinnock W. R. (1991) Measurements of radioactivity in Jamaican building materials and gamma dose equivalents in a prototype red mud house. *Health Phys.* **61** (5), 647-651.
- [323] Piper D. Z. (1974) Rare earth elements in ferromanganese nodules and other marine phases. *Geochim. Cosmochim. Acta* **38**, 1007-1022.
- [324] Plathe K. L., Von der Kammer F., Hassellöv M., Moore J., Murayama M., Hofmann T. and Hochella M. F. Jr. (2010) Using FIFFF and a TEM to determine trace metal-nanoparticle associations in riverbed sediment. *Environ. Chem.* **7**, 82-93.
- [325] Plathe K. L., Von der Kammer F., Hassellöv M., Moore J., Murayama M., Hofmann T. and Hochella M. F. Jr. (2013) The role of nanominerals and mineral nanoparticles in the transport of toxic trace metals: Field-flow fractionation and analytical TEM analyses after nanoparticle isolation and density separation. *Geochim. Cosmochim. Acta* **102**, 213-225.
- [326] Poller U., Huth J., Hoppe P. and Williams I. S. (2001) REE, U, Th, and Hf distribution in zircon from Western Carpathian Variscan granitoids: A combined cathodoluminescence and ion microprobe study. *Am.J.Sci.* **301**, 858-876.
- [327] Pontikes Y. (2007) Utilization of red mud in the heavy clay industry. Ph.D. Thesis, University of Patras, Patras, Greece, 515 pp. (In Greek)
- [328] Pontikes Y., Vangelatos I., Boufounos D., Fafoutis D. and Angelopoulos G. N. (2006) Environmental aspects on the use of Bayer's process bauxite residue in the production of ceramics. Proceedings of the International Ceramics Congress and 4th Forum on New Materials. Sicily, Italy, 4-9 June 2006, *Advances in Science and Technology* **45**, 2176-2181.
- [329] Proost K., Janssens K., Wagner B., Bulska E. and Schreiner M. (2004) Determination of localized Fe²⁺/Fe³⁺ ratios in inks of historic documents by means of μ -XANES. *Nucl. Instrum. Meth. B* **213**, 723-728.
- [330] Qu Y. and Lian B. (2013) Bioleaching of rare earth and radioactive elements from red mud using *Penicillium tricolor* RM-10. *Biores. Technol.* **136**, 16-23.

- [331] Quartieri S., Triscari M., Sabatino G., Boscherini F. and Sani A. (2002) Fe and Mn K-edge XANES study of ancient Roman glasses. *Eur. J. Mineral.* **14**, 749-756
- [332] Rajani R. P., Banakar V. K., Parthiban G., Mudholkar A. V. and Chodankar A. R. (2005) Compositional variation and genesis of ferromanganese crusts of the Afanasiy-Nikitin Seamount, Equatorial Indian Ocean. *J. Earth Syst. Sci.* **114** (1), 51-61.
- [333] Raj D., Harchand K. S. and Maini V. (1993) Characterization of iron minerals in bauxite. *Nucl. Instrum. Meth. B* **76**, 242-243.
- [334] Raj D., Harchand K. S., Aggarwal S. and Taneja S. P. (2004) High temperature transformation of iron minerals in bauxite. *Hyperfine Inter.* **153**, 153-158.
- [335] Rariei B., Mollai H. and Ghorbani M. (2008) The genesis of Late Triassic allochthonous karst-type bauxite deposits of the Kisejin area, Ab-e-Garm district, Iran. *N. Jb. Geol. Paläont. Abh.* **250** (2), 217-231.
- [336] Ravel B. and Newville M. (2005) ATHENA, ARTEMIS, HEPHAESTUS: data analysis for X-ray absorption spectroscopy using IFEFFIT. *J. Synchrotron Radiat.* **12**, 537-541.
- [337] Readman P. and O'Reilly W. (1970) The synthesis and inversion of non-stoichiometric titanomagnetites. *Phys. Earth Planet. Interiors* **4** (2), 121-128
- [338] Regelink I. C., Voegelin A., Weng L., Koopmans G. F. and Comans R. N. J. (2014) Characterization of colloidal Fe from soils using field-flow fractionation and Fe K-edge X-ray absorption spectroscopy. *Environ. Sci. Technol.* **48**, 4307-4316.
- [339] Reich M., Deditius A., Chryssoulis S., Li J.-W., Ma C.-Q., Parada M. A., Barra F. and Mittermayr F. (2013) Pyrite as a record of hydrothermal fluid evolution in a porphyry copper system: a SIMS/EMPA trace element study. *Geochim. Cosmochim. Acta* **104**, 42-62.
- [340] Reich M., Hough R. M., Deditius A., Utsunomiya S., Ciobanu C. L. and Cook N. J. (2011) Nanogeoscience in ore systems research: principles, methods, and applications. Introduction and preface to the special issue. *Ore Geol. Rev.* **42**, 1-5.

- [341] Reich M., Utsunomiya S., Kesler S. E., Wang L., Ewing R. C. and Becker U. (2006) Thermal behavior in metal nanoparticles in geologic materials. *Geology* **34**, 1033-1036.
- [342] Retallack G. J. (2010) Lateritization and bauxitization events. *Econ. Geol.* **106**, 655-667.
- [343] Retzmann K. (1986) Zur mineralogie, geochemie und genese des karstbauxites (B2-horizont) an der Grenze Jura/Kreide in Mittelgriechenland. Unpublished PhD Thesis, University of Hamburg, Hamburg, Germany, 146 pp. (In German)
- [344] Rivas-Sánchez M. L., Alva-Valdivia L. M., Arenas-Alatorre J., Urrutia-Fucugauchi J., Perrin M., Goguitchaichvili A., Ruiz-Sandoval M. and Ramos Molina M. A. (2009) Natural magnetite nanoparticles from an iron-ore deposit: size dependence on magnetic properties. *Earth Planets Space* **61**, 151-160.
- [345] Robb L. (2005) Introduction to ore-forming processes. Wiley-Blackwell (former Blackwell Publishing company), Malden, USA, 384 pp., ISBN: 978-0-632-06378-9.
- [346] Rodríguez-Carvajal J. (1993) Recent advances in magnetic structure determination neutron powder diffraction. *Physica B* **192**, 55-69.
- [347] Rollinson, H., 1993. Using geochemical data; evaluation, presentation, interpretation. Pearson Education Limited, 352 pp. ISBN: 9-780582-067011.
- [348] Royer D. L. (2006) CO₂-forced climate thresholds during the Phanerozoic. *Geochim. Cosmochim. Acta* **70**, 5665-5675.
- [349] Ruan H. D., Frost R. L. and Kloprogge J. T. (2001) Comparison of Raman spectra in characterizing gibbsite, bayerite, diaspore and boehmite. *J. Raman Spectrosc.* **32**, 745-750.
- [350] Ruan H. D., Frost R. L., Kloprogge J. T. and Duong L. (2002) Far-infrared spectroscopy of alumina phases. *Spectrochim. Acta Part A* **58**, 265-272.
- [351] Rubinos D. A. and Barral M. T. (2013) Fractionation and mobility of metals in bauxite red mud. *Environ. Sci. Pollut. Res.* **20**, 7787-7802.

- [352] Rudnick R. and Gao S. (2003) Composition of the continental crust. In *Treatise on Geochemistry*; Holland, H. D., Turekian, K. K., Eds.; Elsevier – Pergamon: Oxford, **3**, pp. 1-64.
- [353] Ruyters S., Mertens J., Vassilieva E., Dehandschutter B., Poffijn A. and Smolders E. (2011) The red mud accident in Ajka (Hungary): plant toxicity and trace metal bioavailability in red mud contaminated soil. *Environ. Sci. Technol.* **45**, 1616-1622.
- [354] Salters N. J. M. and Stracke A. (2004) Composition of the depleted mantle. *Geochem. Geophys. Geosyst.* **5** (5), 1-27.
- [355] Samouhos M., Taxiarchou M., Tsakiridis P. E. and Potiriadis K. (2013) Greek “red mud” residue: A study of microwave reductive roasting followed by magnetic separation for a metallic iron recovery process. *J. Hazard. Mater.* **254-255**, 193-205.
- [356] Sato C., Kazama S., Sakamoto A. and Hirayanagi K. (2013) Behavior of radioactive elements (uranium and thorium) in Bayer process. In: *Essential Readings in Light Metals: Alumina and Bauxite, Volume 1*, Donaldson, D. Raahauge, B. E., Eds; John Wiley & Sons, Inc.: Hoboken, NJ, USA, 1986, doi: 10.1002/9781118647868.ch25
Published Online: Apr 8, 2013, 191-197.
- [357] Sánchez del Río M., Sodo A., Eeckhout S. G., Neisius T., Martinetto P., Dooryhée E. and Reyes-Valerio C. (2005) Fe K-edge XANES of Maya blue pigment. *Nucl. Instrum. Meth. B* **238**, 50-54.
- [358] Schiermeier Q. and Balling Y. (2010) Analysis lags on Hungarian sludge leak. *Nature News*, (<http://www.nature.com/news/2010/101011/full/news.2010.531.html>)
- [359] Scotese C. R. (2001) Atlas of Earth history. Vol. **1**, Paleogeography, PALEOMAP Project, Arlington, Texas, pp. 52. (*Plate tectonic maps and continental drift animations by Scotese C. R., PALEOMAP Project www.scotese.com*)
- [360] Sen I. S. and Peucker-Ehrenbrink B. (2012) Anthropogenic disturbance of element cycles at the Earth’s surface. *Environ. Sci. Technol.* **46**, 8601-8609.

- [361] Shannon R. D. (1976) Revised effective ionic radii and systematic studies of interatomic distances in halides and chalcogenides. *Acta Cryst.* **A32**, 751-767.
- [362] Shulman R. G., Yafet Y., Eisenberger P. and Blumberg W. E. (1976) Observation and interpretation of x-ray absorption edges in iron compounds and proteins. *Proc. Natl. Acad. Sci.* **73**, 1384-1388.
- [363] Sigrist J. A., Gaultois M. W. and Grosvenor A. P. (2011) Investigation of the Fe K-edge XANES spectra from $\text{Fe}_{1-x}\text{Ga}_x\text{SbO}_4$: Local versus nonlocal excitations. *J. Phys. Chem.* **115**, 1908-1912.
- [364] Singh B., Sherman D. M., Gilkes R. J., Wells M. and Mosselmanns J. F. M. (2000) Structural chemistry of Fe, Mn, and Ni in synthetic hematites as determined by extended X-ray absorption fine structure spectroscopy. *Clays Clay Min.* **48**, 521-527.
- [365] Skarpelis N., Perlikos P., Gale N. and Gale-Stos S. (1989) Rare earth elements and gold in lateritic derived sedimentary nickeliferous iron ores: The Marmeiko deposit, Beotia, continental Greece. *Bull. Geol. Soc. Greece* **26**, 121-128. (In Greek)
- [366] Skelton P. W., Spicer R. A., Kelley S. P. and Gilmour I. (2006) *The Cretaceous world*, edited by Skelton P. W., Cambridge University Press, Cambridge, UK, 360 pp., ISBN: 0-521-53843-2.
- [367] Smičiklas I., Smiljanić S., Perić-Grujić A., Šljivić-Ivanović M., Mitrić M. and Antonović D. (2014) Effect of acid treatment on red mud properties with implications on Ni(II) sorption and stability. *Chem. Engineer. J.* **242**, 27-35.
- [368] Smykatz-Kloss W., Heide K. and Klinko W. (2003) Applications of thermal methods in the geosciences. In: *Handbook of thermal analysis and calorimetry – applications to inorganic and miscellaneous materials*, edited by Brown M. E. and Gallagher P. K., Elsevier, vol. **2**, pp. 451-593.
- [369] Smith S. J., Stevens R., Liu S., Li G., Navrotsky A., Boerio-Goates J. and Woodfield B. F. (2009) Heat capacities and thermodynamic functions of TiO_2 anatase and rutile: Analysis of phase stability. *Am. Mineral.* **94**, 236-243.

- [370] Soler J. M. and Lasaga A. C. (1996) A mass transfer model of bauxite formation. *Geochim. Cosmochim. Acta* **60** (24), 4913-4931.
- [371] Solymár K., Má dai F. and Papanastasiou D. (2005) Effect of bauxite microstructure on beneficiation and processing. In: *Alumina and bauxite*, edited by Kvande H., *Proceedings of the TMS Annual Meeting 2005*, 13-17 February 2005, San Francisco, California, Light Metals TMS, pp. 47-52.
- [372] Somlai J., Jobbágy V., Kovács J., Tarján J. and Kovács T. (2008) Radiological aspects of the usability of red mud as building material additive. *J. Hazard. Mater.* **150**, 541-545.
- [373] Spathi A. (1972) Distribution of trace elements in the bauxite bearing limestones of the Parnassos-Ghiona area. *Bull. Geol. Soc. Greece* **9** (2), 177-205. (In Greek)
- [374] Stanley S. M. (2008) Effects of global seawater chemistry on biomineralization: Past, present, and future. *Chem. Rev.* **108**, 4483-4498.
- [375] Steuber T., Raeder M. and Walter J. (1994) Parnassus – Pelagonian transitional facies recorded in the Cretaceous Paleokastron section (W. Beothia, central Greece). *Bull. Geol. Soc. Greece* **30** (2), 177-185.
- [376] Steuber T., Rauch M., Masse J. -P., Graaf J. and Malkoč M. (2005) Low-latitude seasonality of Cretaceous temperatures in warm and cold episodes. *Nature* **437**, 1341-1344.
- [377] Stevens R.E. (1944) Composition of some chromites of the Western hemisphere. *Am. Mineral.* **29**, 1-34.
- [378] Sun S. -S. and McDonough W. F. (1989) Chemical and isotopic systematics of oceanic basalts: implications for mantle composition and processes. In: *Magmatism in the Ocean Basins*, edited by Saunders A. D. and Norry M. J., Geological Society of London, Spec. Publ., vol. **42**, pp. 313-345.
- [379] Tauxe L. (1998) Paleomagnetic principles and practice. In: *Modern Approaches in Geophysics*, vol. 17, Kluwer Academic Publishers, New York, **XI**, pp. 301.

- [380] Taylor S. R. and McLennan S. M. (1985) The continental crust: Its composition and evolution, Blackwell, Oxford, 312 pp.
- [381] Thiagarajan N. and Aeolus Lee C. -T. (2004) Trace-element evidence for the origin of desert varnish by direct aqueous atmospheric deposition. *Earth Planet. Sci. Lett.* **224**, 131-141.
- [382] Tsakanika L. V., Ochsenkühn-Petropoulou M. Th. and Mendrinou L. N. (2004) Investigation of the separation of scandium and rare earth elements from red mud by use of reversed-phase HPLC. *Anal. Bioanal. Chem.* **379**, 796-802.
- [383] Tsakiridis P. E., Agatzini-Leonardou S. and Oustadakis P. (2004) Red mud addition in the raw meal for the production of Portland cement clinker. *J. Hazard. Mater.* **B116**, 103-110.
- [384] Tsikos H., Karakitsios V., Van Breugel Y., Walsworth-Bell B., Bombardiere L., Petrizzo M. R., Damsté J. S. S., Schouten S., Erba E., Silva I. P., Farrimond P., Tyson R. V. and Jenkyns H. C. (2004) Organic-carbon deposition in the Cretaceous of the Ionian Basin, NW Greece: the Paquier Event (OAE 1b) revisited. *Geol. Mag.* **141**, 401-416.
- [385] Tsikouras B., Pe-Piper G., Piper D. J. W. and Hatzipanagiotou K. (2008) Triassic rift-related komatiite, picrite and basalt, Pelagonian continental margin, Greece. *Lithos* **104**, 199-215.
- [386] Tsirambides A. and Filippidis A. (2012a) Greece seeks mineral lifeboat. *Industr. Miner.* January 2012, 38-45.
- [387] Tsirambides A. and Filippidis A. (2012b) Metallic mineral resources of Greece. *Cent. Eur. J. Geosci.* **4**, 641-650.
- [388] Turhan Ş., Arıkan İ. H., Demirel H. and Güngör N. (2011) Radiometric analysis of raw materials and end products in the Turkish ceramics industry. *Radiat. Phys. Chem.* **80**, 620-625.

- [389] Udubasa G., Constantinescu S., Popescu-Pogrion N., Hirtopanu P. and Udubasa S. S. (2007) Nano-minerals identification by different physical techniques. *Rom. Rep. Phys.* **59**, 819-824.
- [390] Valeton I. (1985) Alpine orogeny and genesis of nickel laterites and bauxites during Jurassic and Cretaceous in Greece. In: International Congress of the International Committee for Study of Bauxite, Alumina & Aluminum (ISCOBA), Travaux International Symposium on Bauxite Prospecting and Mining, Tapolca, Hungary, October 2-5, 1985, v. **19**, pp. 33-51.
- [391] Valeton I. (1972) *Bauxites*. Elsevier, Amsterdam, The Netherlands, 226 pp.
- [392] Valeton I. (1991) Processes of allochthony and autochthony in bauxites on carbonate platforms of the Mediterranean area. *Min. Wealth* **71**, 13-28.
- [393] Valeton I. (1994) Element concentration and formation of ore deposits by weathering. *Catena* **21**, 99-129.
- [394] Valeton I., Biermann M., Reche R. and Rosenberg F. (1987) Genesis of nickel laterites and bauxites in Greece during the Jurassic and the Cretaceous and their relation to ultrabasic rocks. *Ore Geol. Rev.* **2**, 359-404.
- [395] Vangelatos I., Angelopoulos G. N. and Boufounos D. (2009) Utilization of ferroalumina as raw material in the production of Ordinary Portland cement. *J. Hazard. Mater.* **168**, 473-478.
- [396] Varnavas S. and Achilleopoulos P. P. (1995) Factors controlling the vertical and spatial transport of metal-rich particulate matter in seawater at the outfall of bauxitic red mud toxic waste. *Sci. Total Environ.* **175**, 199-205.
- [397] Varnavas S., Ferentinos G. and Collins M. (1986) Dispersion of bauxitic red mud in the Gulf of Corinth, Greece. *Mar. Geol.* **70**, 211-222.

- [398] Vaughan D. J. and Pattrick R. A. D. (1995) Mineral surfaces. In: Mineralogical Society Series, edited by Vaughan D. J. and Pattrick R. A. D. (Eds), Chapman and Hall, London, pp. 370.
- [399] Vavadakis D., Agioutantis Z., Xenidis A. and Boufounos D. (2006) Simulation of bauxite residues disposal in abandoned mine open pits. Proceedings of the 2nd International Conference on: "Advances in Mineral Resources Management and Environmental Geotechnology", Hania, Crete, Greece, Sept 25-27, 2006; Agioutantis, Z., Komnitsas, K., Eds.; Heliotos Conferences: Santorini, 2006.
- [400] Veizer J., Ala D., Azmy K., Bruckschen P., Buhl D., Bruhn F., Carden G. A. F., Diener A., Ebner S., Godderis Y., Jasper T., Korte C., Pawellek F., Podlaha O. G. and Strauss H. (1999) $^{87}\text{Sr}/^{86}\text{Sr}$, $\delta^{13}\text{C}$ and $\delta^{18}\text{O}$ evolution of Phanerozoic seawater. *Chem. Geol.* **161**, 59-88.
- [401] Velde B. and Meunier A. (2008) The origin of clay minerals in soils and weathered rocks. Springer-Verlag, Berlin-Heidelberg, Germany, 406 pp., ISBN: 978-3-540-75633-0.
- [402] Verwey E. J. W. (1939) Electronic conduction of magnetite (Fe_3O_4) and its transition point at low temperatures. *Nature* **144**, 327-328.
- [403] Vgenopoulos A. and Daskalakis K. (1991) Remarks on the genesis and ore-dressing of the alluvial bauxite occurrences of Parnassos-Gkiona-Elikon. *Acta Geol. Hung.* **34** (4), 405-407.
- [404] Von Philipsborn H. and Kühnast E. (1992) Gamma spectrometric characterization of industrially used African and Australian bauxites and their red mud tailings. *Radiat. Prot. Dosim.* **45**, 741-743.
- [405] Wakita H., Rey P. and Schmitt R. A. (1971) Elemental abundances of major, minor, and trace elements in Apollo 11 lunar rocks, soil and core samples. Proceedings of the Apollo 11 Lunar Science Conference, pp. 1685-1717.
- [406] Wang K. (1992) Levels of radioactivity in the red mud and red mud cement and its dose rate for local residents. *Huanjing Kexue.* **13** (5), 90-93.

- [407] Wang P. and Liu D. -Y. (2012) Physical and chemical properties of sintering red mud and Bayer red mud and the implications for beneficial utilization. *Materials* **5**, 1800-1810.
- [408] Wang Q., Deng J., Liu X., Zhang Q., Sun S., Jiang C. and Zhou F. (2010) Discovery of the REE minerals and its geological significance in the Quyang bauxite deposit, West Guangxi, China. *J. Asian Earth Sci.* **39**, 701-712.
- [409] Wang Q., Liu X., Yan C., Cai S., Li Z., Wang Y., Zhao J. and Li G. (2012) Mineralogical and geochemical studies of boron-rich bauxite ore deposits in the Songqi region, SW Henan, China. *Ore Geol. Rev.* **48**, 258-270.
- [410] Wang Y., Bryan C. and Xu H. (2003) Nanogeochemistry: geochemical reactions and mass transfers in nanopores. *Geology* **31**, 387-390.
- [411] Waychunas G. A. (2001) Structure, aggregation and characterization of nanoparticles. In: *Nanoparticles and the environment*, edited by Banfield J. F. and Navrotsky A., *Reviews in Mineralogy and Geochemistry*, Mineralogical Society of America **44**, pp. 105-166.
- [412] Waychunas G. A., Apte M. J. and Brown G. E. Jr. (1983) X-ray K-edge absorption spectra of Fe minerals and model compounds: near edge structure. *Phys. Chem. Miner.* **10**, 1-9.
- [413] Waychunas G. A. and Zhang H. (2008) Structure, chemistry, and properties of mineral nanoparticles. *Elements* **4**, 381-387.
- [414] Weldt M., Reich M., Chryssoulis S., Deditius A., Palacios C., Zúniga A. and Alvear M. (2010) 'Invisible' Ag and Au in supergene Cu-sulfides: EMPA, SIMS and TEM constraints. *Geochim. Cosmochim. Acta* **74**, Suppl. A1124 (abstr.).
- [415] Wen X., De Carlo E. H. and Li Y. H. (1997) Interelement relationship in ferromanganese crusts from the Central Pacific Ocean. Their implications for crust genesis. *Mar. Geol.* **136**, 277-297.

- [416] Westre T. E., Kennepohl P., DeWitt J. G., Hedman B., Hodgson K. O. and Solomon E. I. (1997) A multiplet analysis of Fe *K*-edge 1s → 3d pre-edge features of iron complexes. *J. Am. Chem. Soc.* **119**, 6297-6314.
- [417] Whitney D. L. and Evans B. W. (2010) Abbreviations for names of rock-forming minerals. *Am. Mineral.* **95**, 185-187.
- [418] Wickersheim K. A. and Korpi G. K. (1965) Interpretation of the infrared spectrum of boehmite. *J. Chem. Phys.* **42** (2), 579-583.
- [419] Wilke M., Farges F., Petit P. -E., Brown G. E. Jr. and Martin F. (2001) Oxidation state and coordination of Fe in minerals: An Fe *K*-XANES spectroscopic study. *Am. Mineral.* **86**, 714-730.
- [420] Wilke M., Hahn O., Woodland A. B. and Rickers K. (2009) The oxidation state of iron determined by Fe *K*-edge XANES – application to iron gall ink historical manuscript. *J. Anat. At. Spectrom.* **24**, 1364-1372.
- [421] Wirth R., Reid D. and Schreiber A. (2013) Nanometer-sized platinum-group minerals (PGM) in base metal sulfides: New evidence for an orthomagmatic origin of the Merensky Reef PGE ore deposit, Bushveld complex, south Africa. *Can. Mineral.* **51**, 143-155.
- [422] Xu H. and Barnard A. S. (2008) Nano-minerals: size-dependent crystal structure, shape and chemical reactivity changes. *Geochim. Cosmochim. Acta* **72**, Suppl. A1045 (abstr.).
- [423] Zack T., A. Kronz A., Foley S. F. and Rivers T. (2002) Trace element abundances in rutiles from eclogites and associated garnet mica schists. *Chem. Geol.* **184**, 97-122.
- [424] Zack T., Von Eynatten, H. and Kronz A. (2004) Rutile geochemistry and its potential use in quantitative provenance studies. *Sediment. Geol.* **171**, 37-58.
- [425] Zarasvandi A., Carranza E. J. M. and Ellahi S. S. (2012) Geological, geochemical, and mineralogical characteristics of the Mandan and Deh-now bauxite deposits, Zagros Fold Belt, Iran. *Ore Geol. Rev.* **48**, 125-138.

[426] Zarasvandi A., Charchi A., Carranza E. J. M. and Alizadeh B. (2008) Karst bauxite deposits in the Zagros Mountain Belt, Iran. *Ore Geol. Rev.* **34**, 521-532.

[427] Zepf V. (2013) Rare earth elements: What and where they are. In Rare Earth Elements: A new approach to the nexus of supply, demand, and use: Exemplified along the use of Neodymium in permanent magnets; Zepf, V., Ed.; Springer Theses; Springer-Verlag, Berlin-Heidelberg, Germany, pp. 11-39.

[428] Zhou Y. and Fichtorn K. A. (2012) Microscopic view of nucleation in the anatase-to-rutile transformation. *J. Phys. Chem. C* **116**, 8314-8321.

[429] Zoppi A., Lofrumento C., Castellucci E.M., Dejoie C. and Sciau Ph. (2006) Micro-Raman study of aluminium-bearing hematite from slip of Gaul sigillata wares. *J. Raman Spectrosc.* **37**, 1131-1138.

[430] Zoppi A., Lofrumento C., Castellucci E.M. and Migliorini M.G. (2005) The Raman spectrum of hematite: Possible indicator for a compositional or firing distinction among terra sigillata wares. *Annal. Chim.* **95**, 239-246.

[431] Zou H., McKeegan K. D., Xu X. and Zindler A. (2004) Fe-Al-rich tridymite-hercynite xenoliths with positive cerium anomalies: preserved lateritic paleosols and implications for Miocene climate. *Chem. Geol.* **207**, 101-116.

[432] Živković Ž. D. and Blečić D. (1988) Comparative thermal analysis of commercial and low grade bauxites. *J. Therm Anal.* **33**, 413-419.

[433] Živković Ž. D., Štrac N. D. and Šesták J. (1988) Thermal decomposition of low-grade high-silicon boehmite bauxite. *Thermochim. Acta* **233**, 97-105.

5. Platon N. Gamaletsos Curriculum Vitae

Name: Platon Gamaletsos
Father Name: Nikolaos Gamaletsos (Rear Admiral / Inspector General of Hellenic Navy)
Mother Name: Argyroula Gamaletsou (Commander / Hellenic Navy)
Birth: 04 Oct 1973
Citizen/Nationality: Greek/Hellenic
Languages: Greek (mother tongue), English (professional working proficiency)

EDUCATION

- ◆ **PhD** in mineralogy & geochemistry of Al ore deposits and metallurgical residues, University of Athens, Greece (2014)
- ◆ **Courses** on Synchrotron-based X-ray spectroscopies and training as assistant beamline scientist at the ANKA Synchrotron, KIT, Germany (2010-2014).
- ◆ **Courses** on clay mineralogy, thermal analyses, FTIR spectroscopy, Mössbauer spectroscopy and gamma-ray spectrometry at Universities of Thessaloniki and Ioannina, Greece (2006-2010).
- ◆ **BSc** in Geology & Geoenvironment, University of Athens, Greece (2005).

COLLABORATION WITH INDUSTRY

- ALUMINIUM S.A., Greece (<http://www.alhellas.gr>)
- S&B Industrial Minerals S.A., Greece (<http://www.sandb.com>)
- ELMIN S.A., Greece (<http://www.elmin.gr>)
- Ajkai Timfoldgyar Alumina Plant owned by MAL Magyar Aluminium Co. Ltd., Hungary (<http://english.mal.hu/engine.aspx>)
- BENTOMINE KIMOLIAN ENTERPRISES S.A. (<http://bentomine.gr/>)
- APOTEFROTIRAS S.A., Greece (<http://www.apotefrotiras.gr/>)

FELLOWSHIPS, GRANTS, HONORS & AWARDS

- **Grant of Fellowship by KIT/ANKA** as Assistant Beamline Scientist at SUL-X Beamline of ANKA Synchrotron (2012).
- **ANKA Synchrotron Highlights 2010/2011** (The nature of thorium in Greek aluminium ores and their residues).

- **Grant by Deutsche Mineralogische Gesellschaft – DMG** for participation in the Course “*XAFS spectroscopy: Introduction, measurement, data evaluation*”, ANKA Synchrotron (2010).

RESEARCH INTERESTS

My research interests are related to material characterization techniques and the study of mineral resources, metallurgical residues, mining & industrial wastes in different scales, with emphasis to micro- and nano-scale, using a variety of laboratory and large-scale facilities (Synchrotron) techniques.

PARTICIPATION IN RESEARCH PROJECTS (related to PhD)

- **Speciation of iron in Aluminium ores (bauxites) and their residues (red mud) from active mining areas (Greece)** - funded by KIT (2012).
- **Speciation of iron in Cr-spinels from Chromium mines in Northern Greece** - funded by KIT (2012).
- **The nature of Ag and Au in mining products of Chalkidiki (Greece)** - funded by KIT (2012).
- **Distribution and speciation of contaminants in bauxite and red mud from Ajka alumina plant, Hungary** - funded by KIT (2012).
- **Thorium chemistry in Greek bauxites and bauxite-tailings (red mud) using X-ray absorption spectroscopy** - funded by EU (2009)
- **Partitioning and speciation of Cr in high-quality diasporic bauxite from Greece** - funded by EU (2009).

Member of Scientific Societies

- The Geochemical Society (USA) (<http://www.geochemsoc.org/>)
- European Association of Geochemistry (EAG) (<http://www.eag.eu.com/>)
- Hellenic Nuclear Physics Society (<http://nuclpart.phys.uoa.gr/HNPS/>)
- Geological Society of Greece (<http://www.geosociety.gr/>)
- Geotechnical Chamber of Greece (<http://www.geotee.gr/>)
- Red Mud Project (<http://redmud.org>)
- NuSTRAP group (<http://magneticmoments.info/nustrap/index.php>)
- The Scientific Society of the Mineral Wealth Technologists of Greece

6. Platon N. Gamaletsos Publications

Reviewed Articles

- S.P. Kiliyas, P. Nomikou, D. Papanikolaou, P.N. Polymenakou, A. Godelitsas, A. Argyraki, S. Carey, **P. Gamaletsos**, T.J. Mertzimekis, E. Stathopoulou, J. Goettlicher, R. Steininger, K. Bejelou, I. Livanos, C. Christakis, C.B. Croff and M. Scoullas: New insights into hydrothermal vent processes in the unique shallow-submarine arc-volcano Kolumbo, Santorini, *Sci. Rep.* **3:2421 (2013) 1-13**.
- A.M. Muftan, P. Pavlakis, A. Godelitsas, **P. Gamaletsos** and N. Boaz: Paleogeography of the Eosahabi River in Libya: New Insights into the Mineralogy, Geochemistry and Paleontology of Member U1 of the Sahabi Formation, Northeastern Libya, *J. Afr. Earth Sci.* **78 (2013) 86-96**.
- **P. Gamaletsos**, A. Godelitsas, T.J. Mertzimekis, J. Göttlicher, R. Steininger, S. Xanthos, J. Berndt, S. Klemme and G. Bárdossy: Thorium partitioning in Greek industrial bauxite investigated by synchrotron radiation and laser-ablation techniques, *Nucl. Instrum. Meth. B.* **269 (2011) 3067-3073**.
- I. Kougemitrou, A. Godelitsas, C. Tsabaris, V. Stathopoulos, A. Papandreou, **P. Gamaletsos**, G. Economou and D. Papadopoulos: Characterisation and management of ash produced in the hospital waste incinerator of Athens, Greece, *J. Hazard. Mater.* **187 (2011) 421-432**.
- A. Godelitsas, **P. Gamaletsos** and M. Roussos-Kotsis: Mordenite-bearing tuffs from Prassa quarry, Kimolos Island, Greece, *Eur. J. Mineral.* **22/6 (2010) 797-811**.
- E. Dotsika, D. Psomiadis, D. Poutoukis and **P. Gamaletsos**: Isotopic analysis for degradation diagnosis of calcite matrix in mortar and plaster, *Anal. Bioanal. Chem.* **395 (2009) 2227-2234**.

Chapters in Books

- **P. Gamaletsos**, A. Godelitsas, E. Dotsika, E. Tzamos, Jörg Göttlicher and A. Filippidis: Geological sources of As in the environment of Greece: a review, In: the volume "Threats to the Quality of Groundwater Resources: Prevention and Control" (A.

Scozzari and E. Dotsika, Eds), Springer's review series **"The Handbook of Environmental Chemistry"**. (in press).

Selected Conference Abstracts & Chapters in Proceedings

- A. Godelitsas, I.Tr. Tzifas, **P. Gamaletsos**, G. Economou, P. Megalovasilis and P. Nomikou: Rare earth elements and strategic metals mineralogy and geochemistry of coastal black sands in islands from Hellenic Volcanic Arc: The case of Nisyros, In: Proceedings of the **"ERES 2014 – The 1st conference on European Rare Earth Resources"**, Milos Island, Greece, September 4-6, 2014 – **Book of Proceedings, 348-362.**
- A. Godelitsas, I.Tr. Tzifas, **P. Gamaletsos**, T.J. Mertzimekis, J. Goettlicher and R. Steininger: Uranium distribution and speciation in phosphatized limestones of NW Greece, In: Proceedings of the **"Uranium Mining and Hydrogeology 2014 International Conference and UMREG 2014 | UMH VII"**, Freiberg, Saxony, Germany, September 21-25, 2014. (accepted)
- A. Godelitsas, G. Stamatakis, **P. Gamaletsos** and M. Stamatakis: Occurrence, properties and uses of mordenite-bearing tuffs from Milos-Kimolos-Polyegos volcanic field (Greece): A review, In: Proceedings of the **"9th International Conference on the Occurrence, Properties, and Utilization of Natural Zeolites – Zeolite 2014"**, Belgrade, Serbia, June 8-13, 2014. (Conference Extended Abstract – in press)
- **P. Gamaletsos**, A. Godelitsas, A. Kuzmin, M. Lagos, S. Xanthos, T.J. Mertzimekis, J. Goettlicher, R. Steininger, C. Zarkadas, A. Komelkov, Y. Pontikes and G.N. Angelopoulos: New insights into environmental characterization of bauxite residues (red mud) from Greece, In: Proceedings of the **"23rd Annual V.M. Goldschmidt Conference"**, Florence, Italy, August 25-30, 2013, **Mineralogical Magazine, 77 (5), 1136.**
- A. Filippidis, A. Godelitsas, N. Kantiranis, **P. Gamaletsos**, E. Tzamos and S. Filippidis: Neutralization of sludge and purification of wastewater from Sindos industrial area of Thessaloniki (Greece) using natural zeolite, In: Conference of the **"13th International Congress of the Geological Society of Greece: Exploration & Exploitation of Mineral Resources"**, Chania, Crete, Greece, September 5-8, 2013 – **Bulletin of Geological Society of Greece** (Chapter in Proceedings – in press)
- J. Goettlicher, R. Steininger, **P. Gamaletsos**, A. Godelitsas, M. Kersten, J. Majzlan, F. Meirer, T.J. Mertzimekis, B. Pemmer, G. Pepponi, P. Roschger, G. Schmidt, C. Strelj, P.

Wobrauschek and N. Zoeger: Environmental Research at the SUL-X Beamline of the Synchrotron Radiation Source ANKA, In: ***Mineralogical Society's Annual Conference 2011 "Frontiers in Environmental Geoscience"***, Wales, UK, June 21-24, 2011.

- A. Godelitsas, **P. Gamaletsos**, T.J. Mertzimekis, J. Göttlicher and R. Steininger: The nature of thorium in Greek aluminium ores and their residues, **Karlsruhe Institute of Technology, ANKA Synchrotron Radiation Facility - Annual Report 2010 / ANKA Highlights 2010/2011, 10-12.**
- **P. Gamaletsos**, A. Godelitsas, T.J. Mertzimekis, J. Göttlicher, R. Steininger, S. Xanthos, S. Klemme and G. Bárdossy: Spectroscopic investigation of thorium in Greek bauxite, In: *Proceedings of the "ECAART10 – 10th European Conference on Accelerators in Applied Research and Technology"*, Athens, Greece, September 13-17, **2010**. (Conference Abstract)
- **P. Gamaletsos**, A. Godelitsas, A.P. Douvalis, J. Göttlicher, T. Zorba, K. Chrissafis, K.M. Paraskevopoulos and T. Bakas: Spectroscopic (Mössbauer, XANES and FTIR) and thermal investigation of Greek bauxites from the Parnassos-Ghiona active mining area, In: *Proceedings of the "XXV Panhellenic Conference on Solid State Physics and Materials Science"*, Thessaloniki, Greece, September 20-23, **2009**, 355. (Conference Extended Abstract)
- I. Mitsis, A. Godelitsas, J. Göttlicher, R. Steininger, **P. Gamaletsos**, M. Perraki and M. Stamatakis: Chromium bearing clays from Crommyonia volcanic area, Greece, In: *Proceedings of the "14th International Clay Conference, Italy"*, Castellaneta Marina, Italy, June 14-20, **2009**, 491. (Conference Abstract)
- **P. Gamaletsos**, A. Godelitsas, A.P. Douvalis, T. Kasama, R.E. Dunin-Borkowski, J. Göttlicher, N. Church, G. Economou and T. Bakas: Partitioning and speciation of Fe, Ti and Cr in high-quality diasporic bauxite from Greece, In: *Proceedings of the "19th Annual V.M. Goldschmidt Conference"*, Davos, Switzerland, June 21-26, 2009 – ***Geochimica et Cosmochimica Acta 73 (2009) Suppl.1, S. A409.***
- **P. Gamaletsos**, A. Godelitsas, E. Chatzitheodoridis and D. Kostopoulos: Laser μ -Raman investigation of Greek bauxites from the Parnassos-Ghiona active mining area, ***Bulletin of Geological Society of Greece XXXX (2007) 736-747.***